Fabrication of the Nanomolecular Devices of ZnO for Solar Hydrogen Production

A
THESIS
Submitted for the Award of
Doctor of Philosophy
Degree
In Chemistry
(Faculty of Science)
to the
University of Kota, Kota
By
RAJESH KUMAR MEENA

Under the Supervision of
Dr. Neelu Chouhan

Department of Pure & Applied Chemistry
University of Kota, Kota
(Rajasthan)
2018

University of Kota, Kota

M. B. S. Road, Near Kabir Circle,
Swami Vivekanand Nagar, Kota (Rajasthan)-324005

Dr. Neelu Chouhan
Associate Professor
Department of Pure and Applied Chemistry,
University of Kota, Kota- (Raj.)-324005
Tel: 91-0744-2411742;
Fax No. - 91-0744-2411742
Email: niloochauhan@hotmail.com & neeluchouhan@uok.ac.in

Certificate

It is to certify that, The thesis entitled *"Fabrication of the Nanomolecular Devices of ZnO for Solar Hydrogen Production"* submitted by *Rajesh Kumar Meena* (Enrolment No RS/ 1766/13) is an original piece of research work carried out by the candidate under my supervision.

He has completed the following requirement as per Ph.D regulation of the University.

a) Course work as per the University rules.

b) Residential requirement of the university (200 days).

c) Regularly submitted annual progress reports.

d) Presented his work in the departmental committee.

e) Published/accepted minimum of one research paper in a referred research journal.

I recommend the submission of thesis.

Date: **Dr. Neelu Chouhan,**

ABSTRACT

Energy played a crucial role in the development of human race's life style. Currently, the energy is generated through consumption of fossil fuel, which are depleting day by day. Furthermore, these fuels contain carbonaceous materials, which upon oxidation causes pollution that disturb the ecological equilibrium of the mother earth that resulted in various natural disasters. Therefore, it is a high time to work on to find the better substitution of the conventional energy sources. And hydrogen can be a best solution to this problem as it can play a role of fuel as well as energy carrier. But currently, the hydrogen is produced by using steam reforming of hydrocarbon that themselves produces the huge pollution. Therefore, it is necessary to degrade pollution by forming hydrogen using clean/green methods. Artificial photosynthesis can be better choice to produce green hydrogen by splitting of water by using sunlight and photocatalyst in water. Hence in this research work, we had synthesised and characterised (using advance analytical techniques such as, UV-Visible spectrophotometer, FTIR spectrophotometer, XRD, FESEM, HRTEM, EDS, PL, Cyclic voltmeter, etc.) total four composite systems using different types of silver nanoparticles, ZnO nanorods and 1.5%loading of Pt i.e. Pt/Ag(Ajwain seeds)@ZnO, Pt/Ag(Fenugreek)@ZnO, Pt/Ag(Tea leaves) @ZnO and Pt/Ag(shikakai pods) @ZnO. Beside above four systems, we had also synthesized one more system i.e. 1.5%Pt/CdS@ZnO. All of these five systems were used to generate hydrogen gas by splitting of water. And the systems Ag@ZnO was also successfully used to degrade pollutant PAP(p-aminophenol) into PNP(p-nitrophenol). Therefore, we established that the Ag@ZnO systems are quite benign materials for significant high water splitting for hydrogen production in comparison to chemically synthesized CdS@ZnO as well as they show good catalytic properties for pollutant degradation.

Key Words: Hydrogen generation, Pollutant degradation, Water splitting, UV-Visible spectrophotometer, FTIR spectrophotometer, XRD, FESEM, HRTEM, EDS, PL.

Candidate's Declaration

I hereby certify that the work, which is being presented in the thesis, entitled **"*Fabrication of the Nanomolecular Devices of ZnO for Solar Hydrogen Production*"** in partial fulfillment of the requirement for the award of the Degree of Doctor of Philosophy, carried under the supervision of **Dr. Neelu Chouhan,** Department of Pure & Applied Chemistry, University of Kota, Kota, Rajasthan and submitted to the **Research Section**, University of Kota, Kota. The work was approved by Senior Research Committee of the University. I have presented my ideas in my own words and adequately cited and referred from the original sources. The work presented in this thesis as not been submitted elsewhere for the award of any other degree of diploma from any Institutions. I also declare that I have adhered to all principles of academic honesty and integrity and have not misrepresented or fabricated or falsified any idea/data/fact/source in my submission.

Date:

Place : Kota   **Rajesh Kumar Meena**

ACKNOWLEDGEMENTS

execution of this research work in the best possible way. She educated me on different aspects of the subject and told about the importance of work discipline as well as she encouraged me to reach much above than my natural abilities.

*I am also grateful to **Prof. Ashu Rani**, Dean PG of the University along with all **faculty member of** the Department including **Dr. Bhawani Singh, Dr. Sushil Sharma, Dr. Shweta Vyas** and **Mr. Ankit Sharma,** for their valuable support and inspirations during this research. I express my heart-felt gratitude to **all faculty members of the University,** who have been very kind enough to extend their help at various phases of this research.*

*My special words of thanks should also go to **Prof. Suresh Chand Ameta,** Professor and Director, Department of Chemistry, Pacific University, Udaipur for his guidance and support throughout the research work.*
*It is an honour for me to convey my special regards to **Prof. Pahup Singh, Prof. I.K.Sharma, Mr.Hanuman Singh Shakawat, Dr.Rakshit Ameta, Dr.Pragati Fageria, Dr.Amit Kotiya, Dr.Amanpal, Mr.Mohtashim Reza, Dr.Akhtar Khan, Dr.Dinesh Chand Sharma, Dr.Usha Pillai, Dr.Vijay Devra, Dr.Bharti Sharma, Dr.Shweta Saxena, Dr. Pallavi Sharma, Dr.Shweta Nagar, Dr. Neeru Choudhary, Dr.Ruchi Sahu, Dr.Deepak Sharma and Dr.Ashish Sharma** for their genuine interest, continuous encouragement and optimistic support. I would also expree my heartfelt thanks to my seniors **Dr.Renu Hada, Dr.Sakshi Kabra, Dr.Khushboo Shirivastava, Dr.Stuti Katara, Dr.Niharika shringi, and Dr.Priynka rajoriya** for their guidance and moral support.*

*In my daily work I have been blessed with a friendly and cheerful group of my labmates researchers, these are **Kavita Nagar**, **Niranjan Kumar Mandawat, Neeta Gurbani, Khaksaha Ansari, Tripti Bermen, Naval Kishore Sahu, Pragya Khandal, Sangeeta Yadav, Hariom Gour, Deepak Karsoliya, Kiran, Nidhi Gautam, Jaswant, Deepa, Kuldeep, Hanny, Megha Gang, Kanchan, Dr. Aruna, Dr. Ankita Jain, Dr. Shikha Jain, Dr. Priya Vijayvergiya, Dr.Dhanraj, Dr.Shivraj, Niharika Nagar, Gajala Tazwar,** who always helped me out in my difficult time.*

*I wish to convey my humble feelings of respect to my parents **Sh. Shriniwas Meena** and **Smt. Kamala Devi** for their affection, care, inspiration, and constant encouragement, for pursuing higher studies. They are always with me and their teachings have always been a source of inspiration to me in the journey of my life which has no destination. In fact, I am*

List of Abbreviation

AU	Arbitrary Unit
BE	Binding Energy
BET	Brunauer-Emmett-Teller
CPS	Cycles per Second
CTAB	Cetyltrimethylammonium Bromide
CTR	Charge transfer resistance
CV	Cyclic voltammetry
DLE	Deep Level Emissions
DR	Diffusion Resistance
DRS	Diffuse Reflectance Measurement
DSC	Differential Scanning Calorimetry
DTA	Differential Thermal Analysis
EM	Electron Microscopy
EDS	Energy Dispersive Spectroscopy
EIS	Electrochemical impedance spectroscopy
EDX	Energy Dispersive X-ray
eV	Electron Volt
FTIR	Fourier Transform Infrared Spectroscopy
FWHM	Full Width Half Maxima
H	Hour
HRSEM	High Resolution Scanning Electron Microscopy
HRTEM	High Resolution Transmission Electron Microscopy
M	Molar
Min	Minute
mL	Milliliter
mM	Millimolar
Mn	million
μM	Micromolar
NIR	Near-infrared Radiation
nm	Nanometer
NP	Nanoparticle

List of Abbreviation

NR	Nanorod
PED	Potential Energy Distribution
PL	Photoluminescence
PXRD	Powder X-ray Diffraction
QSE	Quantum size Effect
Sec	Second
SAED	Selected Area Electron Diffraction
SEM	Scanning Electron Microscopy
SPB	Surface Plasmon Band
SPR	Surface Plasmon Resonance
STEM	Scanning Transmission Electron Microscopy
TEM	Transmission Electron Microscopy
UV	Ultra Violet
WBG	Wide Band Gap
XAS	X-ray absorption spectroscopy
XPS	X-ray Photoelectron Spectroscopy
XRD	X-ray Diffraction

Table of contents

Chapter 1

I ntroduction

ABSTRACT

This chapter give a general introduction of the current status of the fuel and the impact of its application on environment. There are a good number of renewable fuels that can replace the conventional fuels i.e. tidal, solar, geothermal, water, wind and radiation energy, etc. Out of these renewable energies, hydrogen is a good substitute of conventional fuels. Steam reforming of hydrocarbons is the most popular way used to produce hydrogen at industrial level along with other methods such as electrolysis and thermolysis of water. Production of the hydrogen by splitting of water using sunlight and photocatalyst is a one of the greener way to generate hydrogen. Here, a comprehensive literature survey was made to identify the low cost, environmentally benign, stable in (light and water) and abundant material (photocatalyst) to be used for water splitting. The literature survey of the conductive oxides, sulphides and nitrides oxysulphides, and oxynitrides was carried out to provide the background of the materials used for water splitting. Pure, doped or composite-ZnO based materials, was reviewed under this chapter is used for setting the parameters of the fabrication of nanomolecular devices to produce hydrogen through photocatalytic water splitting. This will guides us in identification of the key parameters for the synthesis of nanomolecular devices. This is highly needed to understand the significance of ZnO nanomolecular devices. The theoretical background of the fabrication of the nanomolecular devices and water splitting phenomenon was also discussed in brief.

Key Words: Nanomolecular devices, water splitting, renewable energies, hydrogen production, oxides, sulphides, nitrides, oxysulphides, and oxynitrides etc.

1.1 Introduction of research work

Day by day growing demands of energy going hand in hand with its potential bad impact on environment. The world's increasing population and the continuous industrial expansion are two major driving factors behind the increasing energy conflicts. Moreover, limited availability of the conventional fuels, along with inflaming fuel prices, attracted the concern of layman towards the energy supply, energy security and climate changes. [1] This burning issue comply the world community to think about the better substitute of the conventional fossil fuel in the form of the alternative fuels. Major alternative/substantial fuel resources are hydrogen, wind, geothermal, solar, tidal, nuclear, hydrothermal, water flow, hydroelectric, photovoltaic, and many more. If we are not ready to adopt this transformation than the life on the planet became miserable in term of quality of life and health. [2] A number of recent studies show the direct use of hydrogen as a fuel, is a much cleaner and far less expensive fuel alternative. [3] Almost no pollution is produced by hydrogen engines because burning of the hydrogen gives water as its main product. Hydrogen is the lightest and most abundant (98% of the Universe mass) element of the Universe. Although hydrogen does not found naturally but it compound with the elements such as: metals, oxygen, carbon etc. [4]

In addition, hydrogen can carry energy and possess high energy efficiency (75%), and also useful as "chemical feedstock" in different industries. Furthermore, it can be envisioned that hydrogen could be a future energy source for homes, businesses, industries and for transportation. [3] Hydrogen can also contribute as an energy carrier or as an energy vector. [2]

1.2 Hydrogen as an energy carrier and fuel

Nowadays, hydrogen is being produced in large quantities for industrial and commercial purposes. Most of hydrogen production requires fossil fuels as feed stocks. It uses steam to reform natural gas by utilizing electricity for electrolysis, which can be produced from natural gas, coal, petroleum feed stocks or nuclear energy [2-3]. Large scale production of hydrogen from renewable resource, is a great challenge. The hydrogen produced from the alternative renewable feed stocks, is considered as a secondary energy carrier. Table 1 summarizes the several approaches used to produce hydrogen with their advantages and disadvantages. Few

prominent methods of hydrogen production are as follows: 1) solar (photocatalytic), 2) biomass gasification / hydrogen produced using biological organisms (bacteria or algae) and 3) photovoltaic or hydrogen produced using photo electrochemical cells. [4]

Table 1 Common Renewable/ Alternative Energy Technologies

Sl. No.	Technology	Advantages	Limitations
1.	**Solar-hydrogen**	Use of renewable energy. Environmental friendly. High energy power. Abundant and cheap materials Use of water or organic sources	Clear sky is required Low conversion efficiency Low hydrogen production efficiencies. Current lack of efficient infrastructure to store, transport and distribute hydrogen. Hydrogen production costs.
2.	**Photovoltaic**	Sunlight used Excess energy may be provided	Required clear sky Expensive technology
3.	**Wind Power**	Operated day/night	High cost Exposition to high wind
4.	**Hydroelectric**	Provides water/power Day/night operation	Requires a lots of water
5.	**Tidal power**	Constant operation for day/night	Limited to coasts
	Geothermal power	Constant operation for day/night	Limited access to site of geothermal activity
	Biomass	Constant operation for day/night	Green house gases are emitted

Table 1 reported that hydrogen can be generated from different sustainable sources at the minimum or low harm to our environment. That can reduce the gap between power consumer (industrial or public sector) and power supplier. That will lower the oil dependency as well as excessive green house gas CO_2 emissions. [2] Table 2 further describes the major characteristics of the hydrogen as a future fuel and energy carrier.

Table 2 Properties of hydrogen fuel in comparaison to other popular fuels i.e. CH$_4$, gasoline & diesel.

Properties / Fuel	H$_2$	CH$_4$(CNG)	Gasoline	Diesel
Molecular weight	2 (No-carbon)	16 (75% carbon)	100-105 (C$_4$-C$_{12,}$ 88%)	200-300 (C$_9$-C$_{25}$, 87%)
Density (g/l)	0.0899(g) 70.990 (l)	1.8160 (g) 422.36 (l)	-	-
Auto ignition Temperature (^{o}C)	385	540-630	260-460	180-320
Air/ fuel ratio	34.3	17.2	14.6	14.5
Ignition energy(mJ)	0.002	0.28	0.24	-
Diffusion coefficient cm^3/sec)	0.61	1.90	21.34	-
Energy Density KJ/Kg	142.00	45.30	48.6	33.8
Combustion temperature (^{o}C)	2318 (O$_2$)	1914 (O$_2$)	2307	2327
Combustion range in air (%)	4-75	5.3-15	1.4-7.6	0.6-5.5
Explosive range in air (%)	13-79	19	-	-
Octane rating	130	87-93	91-99	-
Fuel efficiency in combustion internal engine (%)	60	-	22	45

Heterogeneous photocatalysis can be used as an ideal technology to produce hydrogen and to remove a wide range of organic pollutants, [5] simultaneously. Heterogeneous photocatalysis has also been used for water/air purification, [6-8] due to its low cost, environmental-friendly and potentially efficient properties. [9]

1.3 Current energy status

Energy is a lever to trigger the speed of the development in all segments of life (economical, social and political) for the safer, affordable, cleaner and more habitable environmental conditions, for better standard of living. Secured, uninterrupted, affordable and adequate amount of the energy supply, are also required to sustain the global economic growth and stability. Worldwide our current energy storage contains 1047.7 billion barrels of oil, 5501.5 trillion SCF(standard cubic foot) of natural gas and 984 billion tons of coal as conventional energy sources that might be sufficient to satisfy our energy needs for 40.2, 53.8 and 205 years, respectively. Moreover, these energy sources are not proportionately distributed throughout the world. For example, USA contains about 25% of world coal reserves while Middle East countries accounts for about 60% of oil reserves. This resulted in energy insecurity among the countries, which did not have inadequate energy assets/ supply that consequent the most probable grounds for the political disturbances. According to the

estimated record nearly one-quarter of world's population (1. 6 billion) yet to have electricity today. However, the continuous increase in energy requirement has been putting a lot of pressure on the conventional energy sources. But the limited availability of the fossil fuels and corresponding environmental threats, compel us to explore more alternative resources for uninterrupted supply of the energy. All conventional sources of energy are carbon rich and so their combustion leads to CO_2 emission (main green house gas) that adds on extra burden on it's naturally occurrence amount. CO_2 is a green house gas absorbs the infrared part of the sun's radiation and re-radiates it to earth's surface that leads to trap the heat and keep the earth 30 degrees warmer than it would be otherwise - without greenhouse gases, earth would be too cold to live. But the additional CO_2 leads to the extra raise in temperature. [10] As a consequences earth's average temperature increases, which will result in unpredictable changes in weather patterns in the form of floods, droughts and submerging of low-lying areas due to melting of ice at poles. The concentration level of CO_2 in atmosphere is around 390 ppm (in Jan 2011) and scientists suggest that this value might be drop to 350 ppm otherwise it might be directed to irreversible catastrophic effects. The amount of carbon dioxide emission was 27 Giga tons in 2005 and expected to boost up to 42 Giga tons in 2030 and 62 Giga tons in 2050. Country wise contribution in CO_2 emission is shown in Figure 1.1. (A) (US Environmental Protection Agency, 2013) Most of these emissions are coming from power sectors, industries and transportation sectors.
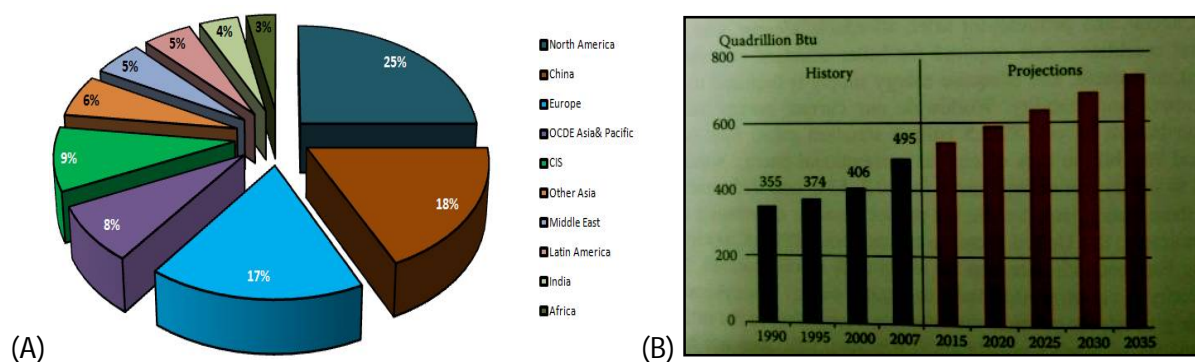
Figure 1.1 (A) Country wise per capita CO_2 emission in percentage. **(B)** World energy consumption history (1990-2011) and futuristic energy projections (2011-2035).

Our energy consumption history (1990-2011) Figure 1.1(A) and futuristic energy projections (2011-2035), are shown in Figure 1.1(B) which will be increases by the rate of 1.4 percent per year till 2035. This energy consumption profile reflected with the world average capacity of energy utilization rates have continued to rise with time, from about 65 percent in 1990 to about 80 percent today, with some more increases will anticipated in the future. That imposed

the severe challenges in front of us as the threat of disruptive climate challenges and huge capital investments in energy segment. Both become the problematic issues for developed and developing countries. According to a report, there is irrational ratio of the population and energy consumption rate found among the developed (20% and 60%) and developing countries (80% and 40%). [11] To meet these demands without further damaging the environment is a greatest challenge of the time. There are two main approaches to achieve the longing energy scenario: the first scenario involved the replacement of the long-term development process with the advanced energy-productive technologies and/or implementation of the hybrid processes instead of the conventional fuels to reduce the fuel consumption by reducing the climate change effect via the new advanced technologies used for gas conversion So, more fixations of the gases to value-added products will achieved. The second scenario includes the development of the alternative energy resources. The renewable resources, i.e. biomass, hydropower, wind, solar, geothermal and biofuels, are economically, socially and environmentally, sustainable. But no single approach is able to achieve this hercules goal. Therefore, a number of energy scenarios are given by different agencies i.e. energy information administration (EIA), World Energy Council (WEC) international energy agency (IEA), and many more, using different proportion of both approaches. Most comprehensive and authentic analysis on world energy scenario, based on world's facts and perceptions, was given by the International Energy Agency (IEA), which has constituted by a committee of 5000 experts from 39 countries on Energy Research and Technology to develop a strategy for the world energy scenario for 2050. In their report, they concluded the world energy consumption will be double by 2050 and carbon emission rate will increase by 2.5 factors. Their recommended focused on alternative resources of energy. To shape the world energy future, IEA projected a strategically energy scenario planning for 2050, which is represented by the Figure 1.2. [12] This includes step by step process to achieve the desired scenario. Process initiated by identifying the scope of the scenario then defining the main driving forces behind it. For developing the scenario model a system dynamics of the future energy market will be analyzed by identification of the interrelationship among the driving forces. Continuation of the status quo is not sustainable due to the raising the demand of the energy, particularly from fossil fuel and unacceptable level of the CO_2 emission. Therefore, by employing the existing technologies or the technologies under the development, a path towards the clean, clever and competitive energy, would be established by utilizing the sustainable energy solutions. Afterwards the possible future energy scenario (few models suggested by IEA, are the baseline for the accelerated technologies and blue map) models

would be developed. Where, they assume the future energy demand and level of the CO_2 emissions in the light of above defined driving forces. And accordingly they would set the periodical goals to meet the most probabilistic energy assess and reduced CO_2 emission level for 2050 by utilizing the decision support software. Finally, the strategies will develop to accomplish the final goal. No single strategy is enough to reach the desired level of energy production, consumption and CO_2 reduction. Therefore, a fusion of the below mentioned strategies, might be used for achieving the desired goal:

(a)   Research development, demonstration and deployment on new technology.

(b)   Investment strategies

(c) CO_2 emission reduction

(d)   International collaborations

(e)   Governmental involvement

Beside this, by employing the technology already exist or under development, world could bring onto a much more sustainable energy path.
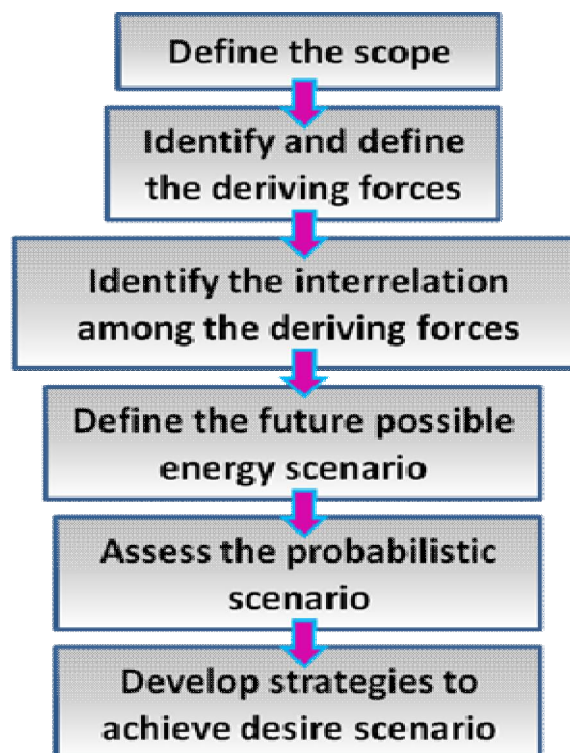
Figure 1.2 Stepwise energy scenario planning. [12]

1.4 Hydrogen energy and related concerns

Hydrogen is a pollution free promising substituent to the conventional source of energy with the properties like easy storage and high-energy efficiency. It is a most promising fuel, contains few drawbacks like handling of hydrogen in the form of compressed gas or liquid needs energy that adds extra costs [13] along with the limited number of infrastructure as fuelling station. The hydrogen production is currently depends on fossil fuel and several researches has been conducted to produce hydrogen from renewable resources through different methods.

1.5 Hydrogen evolution from renewable

The steam methane reforming is largely used to produce the hydrogen gas from the natural gas at high temperatures (up to 900°C) and pressures (1.5-3MPa). [14, 15] Furthermore, the coal gasification is also used to generate hydrogen at high temperatures and pressures (5MPa). [14] Biological methods like pyrolysis and gasification by using biomass materials are also used to produce hydrogen along with the by-products like CO, CO_2 and methane. Hydropower, wind power, and sunlight, etc, are also used as a renewable energy sources for the hydrogen production. out of which solar energy has been considered as a more promising source because of its good availability everywhere in abundance. The combination of solar energy and water resources in presence of the photocatalyst, can also provides a suitable method for hydrogen generation, known as solar water splitting, [16-18] which can be done mostly in three ways (1) thermo-chemical water splitting (highly expensive).[19] (2) photo-biological water splitting (bio-photolysis and organic bio-photolysis); and (3) photo-catalytic water splitting, which includes advantages of (a) low cost [20] (b) high solar-to-H_2 efficiency; (c) ability to separate H_2 and O_2 gas streams; and (d) flexible reactor size for small scale usage. [21] The Department of Energy (DOE), US had been ascertained a final goal of 26% efficiency of the solar to hydrogen energy conversion ratio, which needs a aggressive research to improve the current energy status. [22]

1.6 Selection criteria of photocatalytic material

The development of photocatalytic materials that can utilize maximum solar energy inputs to convert into either electric or chemical energy is one of the holy grails of future advancement in material research and technology that can direct the way in obtaining clean energy. At the molecular level, several physicochemical functions need to be integrated into one stable chemical system that can set the criteria, which must be satisfied simultaneously:

1. Band gap of the semiconducting material should lies between 1.6 eV (1.23 eV+ over potential) to 2.5 eV (larger than 2.43eV). Then, the material can harvest the visible part of the sunlight (which 52% of the total sunlight) and enhance the efficiency of the water splitting.

2. Band edge positions means that band edges of (VB and CB) must straddle between the redox potentials of the water i.e. (0.00 eV and 1.23 eV), respectively. Semiconductor materials must satisfy the minimum band gap requirement (~1.23 eV). But the materials of low band gap are visible light active but susceptible to photocorrosion and stable materials with a wider band gap absorb light only in the ultraviolet (UV) region (i.e. 5% of the whole sunlight spectrum). It has been found that the valence band (VB) holes are the powerful oxidant (+1.0 to +3.5V vs. NHE depending on the semiconductor and pH), while the conduction band (CB) electrons are good reductants (+0.5 to -1.5 V vs. NHE). Therefore, holes oxidise, water in to oxygen and electron reduce water into hydrogen.

3. Charge transfer is necessary at the photocatalytic surface and it must be fast enough to prevent photocorrosion and shifting of the band edges, which result in the loss of photon energy that can provide the efficient oxidation and reduction sites on the surface of the material.

4. Stability of the material in aqueous acidic/basic medium is essential (at least for 20 years). The hydrophilic and hydrophobic surface of the photocatalysts under light radiation is one of the important issues to maximize the photocatalytic effiency.

5. Aid of a cocatalyst for hydrogen generation is necessary, but some of the cocatalyst are highly active and induce a reverse reaction. That promotes the generation of water from molecular oxygen and hydrogen, which must be reduced. For example, $Pt@TiO_2^-$ anatase produce both reactions at surface, but addition of an iodine layer on the Pt surface prevents this backward reaction. [23]

6. Abundant availability can reduce the cost of the material and assure sustainability.

7. A complementary metal-oxide semiconductor (CMOS) compability and bio-compatibility of the photocatalytic material should be considered as a one parameter for their selection.
8. Nontoxic and easy to handle materials with good compatibility with sensitizers are important.

1.7 Hydrogen production by water splitting

The two half reactions of water splitting have been studied widely to examine the structural property relationships of the photocatalysts. Reactions use sacrificial reagents to improve the hydrogen and oxygen yield by promoting hydrogen and oxygen evolution reaction. The ratio of hydrogen and oxygen evolution during the water splitting is 2:1. Number of research and review articles have been published to explore the mechanism of photocatalytic water splitting. [24-26] Photon absortion is the initiation reaction, which generates numerous electron-hole pairs. Afterwards the charge carrier moves onto the photocatalyst surface to create the surface active sites. Finally, the photo-generated electrons used to reduce the water to prepare hydrogen and the holes to oxidize water molecules to give oxygen gas. The overall photocatalytic water splitting first reported by Fujishima and Honda by a titanium dioxide (TiO_2) electrode. [27] Numerous research studies of water splitting have been conducted on semiconductor materials, especially via heterogeneous catalysis. Semiconductors have non-overlapping valence bands and conduction bands. When sufficient light energy is applied, electrons will be jumped into the conduction band, by leaving holes in the valence band and enrich the population of the electrons in the conduction band. These electron-hole pairs play key roles in performing the redox reactions of water splitting. Electrons are responsible for reducing water/protons in to hydrogen molecules, and hydroxyl ions/ radicals that to be oxidized by the holes. To initiate the redox reactions, the upper most level of the valence band should be more positive than water oxidation level ($E_{O2/H2O}$, 1.23 V with respect to the Normal Hydrogen Electrode; NHE), while the lower most level of the conduction band that should be more negative than the hydrogen evolution potential ($E_{H2/H2O}$, 0 V *Vs*. NHE).

Oxidation Reaction

$$H_2O + 2h^+ \rightarrow 2H^+ + \frac{1}{2}O_2 \quad E^o \text{ Oxidation} = -1.23V \qquad\qquad .... (1)$$

Reduction Reaction

$$2H^+ + 2e^- \rightarrow H_2 \quad E^o \text{ Reduction} = 0.00V \qquad\qquad .... (2)$$

Overall Reaction

$$H_2O \rightarrow H_2 + \frac{1}{2}2O_2 \quad E = -1.23V \qquad\qquad .... (3)$$
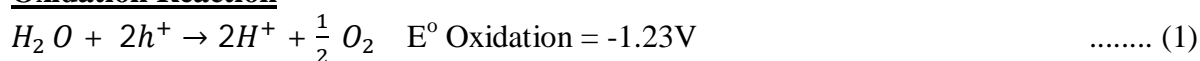
1.8 Electrochemistry of Water Splitting

1.8.1 Thermodynamic and Electrochemical aspects of water splitting

Solar water splitting is an energetically uphill chemical reaction that requires 1.23 V for the complete decomposition of pure water into hydrogen and oxygen. Usually, due to very low ionization (K_w= 1.0×10^{-14}) power, water splitting becomes thermodynamically (Gibbs free energy ΔG_o= 237kJ/mol, 2.46 eV per molecule) unfavourable at standard temperature and pressure. Where, ΔG calculated at 25^oC using the thermodynamic parameters (ΔH, ΔT, and ΔS) that required

$$\Delta G = \Delta H - T\Delta S = 285.83 \text{ kJ} - 48.7 \text{ kJ} = 237.13 \text{kJ} \qquad \text{......... (4)}$$

In the case of water electrolysis, Gibbs free energy represents the minimum work function i.e. necessary for the reaction to proceed and the reaction enthalpy is the amount of energy (both work and heat) that has to be provided so the reaction can proceed at the same temperature of the reactant. It also requires energy to overcome the changes in entropy of the reaction. Here, ΔG the electrical energy demand of the water splitting decreases with the temperature. Thus the useful electrical work requirement reduces on increasing the reaction temperature T. Heat demand ($T\Delta S$) gradually increases with temperature. Therefore, the total energy demand ΔH does not increase significantly with temperature.

Therefore, the process cannot proceed below 286 kJ/mol if no external heat energy is added. At this condition an electrolyzer operating at 1.48 V, would be 100% efficient. The positive value for ΔG (a measure of the thermodynamic driving force that makes a reaction occur) indicates that a reaction cannot proceed spontaneously without any large external inputs. The standard cell potential E^o of any reaction, related to the Gibbs free energy (ΔG^o= - nFE^o), is represented by the following equation:

$$E^o = - (\Delta G^o/nF) \qquad \text{............ (5)}$$

Where, n is the number of electrons transferred in the reaction and F is a proportionality constant in the Faraday units (96, 485 C/mol). Using above equation, the standard potential of the water electrolysis can be calculated as -1.229 V at 25° C. This cell potential belongs to the difference in potentials of the two half cell reactions occurring at the cathode (reduction;

hydrogen evolution reaction [HER] and anode (oxidation; oxygen evolution reaction [OER]). The Nernst equations for the half cell reactions of water splitting are mentioned below at pH 0 and 7.

Therefore, the minimum band gap for a suitable water splitting photocatalyst should be 1.23 eV. Accordingly, TiO_2, ZrO_2, $KTaO_3$, $SrTiO_3$, and $BiVO_4$ are good candidates for photocatalytic water splitting. [28-30] Except some typical exceptions i.e. SiC, InP, and CdS, etc, the most of the photocatalyst used for water splitting are oxide semiconductor that can be operated under ultraviolet (UV) light, which accounts for only ca. 4% of the total solar energy. [31-33] To have a visible light response (45% of the sunlight), the band gap of the semi conductors should be less than 3.00 eV, for this either new compound may be searched or doping of the elements such as N, B, S, C, P, etc should be done to the oxide semiconductors. Traditional water-splitting photocatalysts are based on transition metal oxides which form stable compounds due to the high electronegativity of oxygen atoms. [34] According to the d orbital structure of the transition metal oxides are classified into two catagories: (i) d^0 - and (ii) d^{10}- materials. Early the transition metals like Ti, V, Nb, and W have empty d-orbitals, thus having a low valence band energy. As a result, these materials have large band gaps, which make them less efficient for photocatalytic process. Strategies like doping are used to increase the light absorption efficiency of the main semiconductor. Zhao et al. successfully designed defect-enriched mesoporous black TiO_2 species via the high-temperature hydrogenation process that exhibited the excellent photocatalytic hydrogen evolution activity. [35] On the other hand, the late transition metals such as Mn, Fe, Co, and Ni, have fully occupied d-orbitals and their oxides had the small band gaps and the strong d-d electron transitions capability that play significant role in deciding band positions of these oxides. Fe_2O_3 is a typical example of this group due to its abundant avability and inexpensive nature, and it has been accounted as an attractive candidate for photocatalytic activities. [36-37] Having little polaron conductivity is the disadvantage of late transition metal oxides. [38] Wei et al have been reported that combining cations with s^2 material and d^0 typed materials with oxide, can also lowered the band gap. The coupling between s-band of s^2 cation and p-band of oxygen can increase the valence band level while the coupling between d-band of d^0 cations and p-band of oxygen can also lower the conduction band level. [39] A ternary oxides; $BiVO_4$ is a typical example of this type. Its photocatalytic properties have been

intensively studied over the years. [40-43] Further doping of $BiVO_4$ with the cations such as Ag^+, V^{5+}, and W^{6+} can also increases its electronic conductivity and causes better catalytic performance. [44-46] The ternary oxides including $CuWO_4$, $ZnFe_2O_4$, $CaFe_2O_4$, $CuBi_2O_4$, and $CuNb_3O_8$, etc are the good examples of the band gap tuning. [47-51] Besides metal doping techniques; nitrogen substitution to semiconductor can also decrease the band gap due to its higher-lying 2p orbital levels. [52-53] Like nitrogen, sulfur and selenium also possess higher-lying p-bands than those of oxygen; they can also be induced smaller band gap in materials than their parent oxides. [54-56] Moreover, modification of the catalysts with silicon, group III-V semiconductors, and carbon-based materials have been reported and proved to be efficient methods for developing photoactive materials. [57-59] Few of the prominent photocatlytic systems for water splitting with their hydrogen generation efficiency, are presented in Table 3. Where, the amount of active photocatalyst material, the type of the light source, turnover frequency and catalytic stability are different. After the electron-hole pairs are generated, these charge carriers need to move to the surface of the catalysts and catalyze water splitting at the interfaces between the electrode and electrolyte. The major challenge in this step is the recombination of electrons and holes. [35, 37] Before the photogenerated electron-hole pairs catalyze the redox reaction, they recombine in a short period of time. In general, the development of the fewer defects and addition of the cocatalsyt of small sized noble metals are believed to be able to inhibit the recombination of the electrons and holes. Nano sized materials can provide the short diffusion distances for the migration of the electrons and holes to the surface active sites that suppressed the probability of the carriers recombination. Lastly, these migrated electrons and holes will interact with surface active sites to perform the series of redox reactions to manufacture the hydrogen and oxygen, respectively. Sometimes, the bottom of the conduction bands of transition metal oxides are not sufficiently negative to start the hydrogen evolution reaction, so co-catalysts such as precious noble metals or their oxides to provide the assistance for water reduction [35]. However, the top level of valence bands of metal oxides is usually positive enough to oxidize water to oxygen without the aid of co-catalysts. Prominent ways to increase the efficiency of the photoctalyst are: band gap engineering, sensitization (dye / quantum dot), nanostructring, inorganic doing (metals/nonmetals), loading of noble metal (co-calayst), etc, as mentioned in Figure. 1.3. Moreover, water splitting into hydrogen and oxygen is an energy

demanding reaction, which is thermodynamically unfavourable and the backward reaction is more likely to occur. Therefore, the separation and removal of produced oxygen and hydrogen play a major role in this reaction.
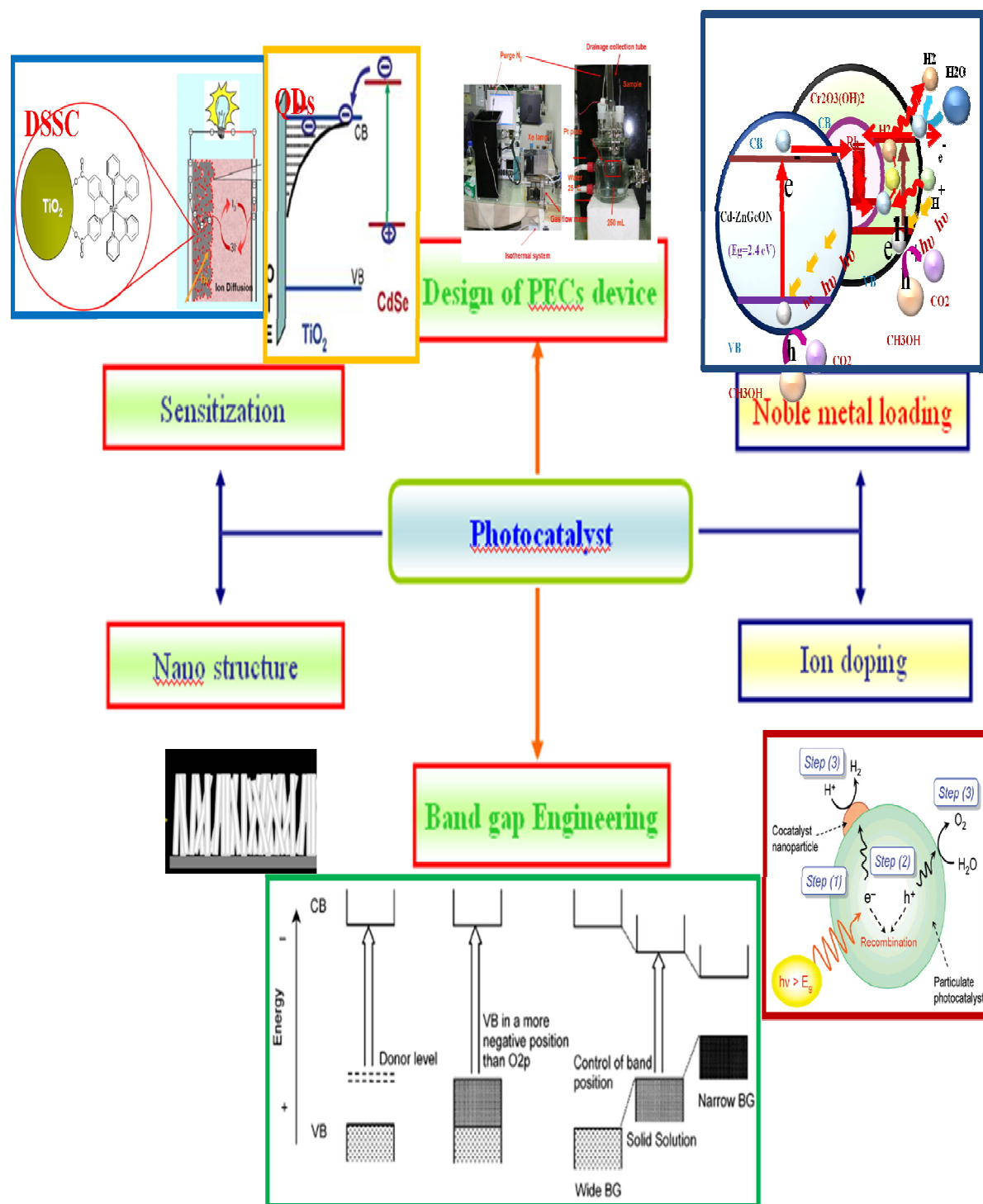
Figure 1.3 Modes of the modification of photocatalysts for water splitting.

Table 3 Recent visible light active photocatalysts for water splitting with their hydrogen generation efficiency.

Photocatalysts	Band Gap (eV)	Illumination	Hydrogen production	Ref.
Pt, Cr, Ta Dopped TiO_2	N/A	Visible light (>420)	11.7 μmol. $h^{-1}.g^{-1}$	[60]
Cu-Ga-In-S/TiO_2	N/A	300 W Xe arc lamp (385-740nm)	50.6 μmol. $h^{-1}.g^{-1}$	[61]
1 wt%Pt/C-HS-TiO_2	2.94	Visible light	5713.6 μmol. $h^{-1}.g^{-1}$	[62]
Platinized Sub-10nm rutile TiO_2 (1 wt%Pt)	2.7–2.9	Xe lamp (PLS-SXE,300 – 2500 nm) with (UV-REF: 320-400 nm, ca. 83 Mw.cm^{-2}; UV-Cut 400-780 nm, ca.80 Mw.cm^{-2})	932 μmol. $h^{-1}.g^{-1}$ Visible light 1954 μmol. $h^{-1}.g^{-1}$ Stimulated solar light	[63]
Rh-and La- codoped Sr TiO_3	N/A	300W Xe lamp fitted with a cutoff filter (λ>420nm)	84 μmol. $h^{-1}.g^{-1}$	[64]
$Cu_{1.94}$S-Zn_x Cd_{1-x}S (0≤X≤1)	2.57-2.9	visible-light irradiation (λ> 420 nm)	7735 μmol. $h^{-1}.g^{-1}$	[65]
MoS_2/Co_2O_3/ poly(heptazine imide)	N/A	Visible light irradiation	0.67 μmol. $h^{-1}.g^{-1}$	[66]
Bi_4NbO_8Cl	2.4	Visible light	6.25 μmol. $h^{-1}.g^{-1}$	[67]
CdS nanorods/ ZnS nanoparticale	N/A	Visible light irradiation(>420)	239,000 μmol. $h^{-1}.g^{-1}$	[68]
Ni/CdS/g-C_3N_4	N/A	300 W Xe lamp(≥420 nm	1258.7 μmol. $h^{-1}.g^{-1}$	[69]
CdS/WS/graphene	N/A	Visible light irradiation (>420nm)	1842 μmol. $h^{-1}.g^{-1}$	[70]
V-dopped TiO_2/RGO	N/A	Visible light irradiation	160 μmol. $h^{-1}.g^{-1}$	[71]
Pt/g-C_3N_4 Conjugated polumers	2.56	Visible light irradiation (>420nm)	1.2 μmol. $h^{-1}.g^{-1}$	[72]
Au-TiO_2 Nanohybrids	N/A	Vis- NIR irradiation (>420nm)	647,000 μmol. $h^{-1}.g^{-1}$	[73]
SrTiO_2:La,Rh/Au/BiVO_4:Mo	N/A	300W Xe lamp fitted with a cutoff filter(λ>420nm)	90 μmol. $h^{-1}.g^{-1}$	[74]
CoO_X -B/TiO_2-TaON	N/A	150 W Xe Lampe arc (>420 nm)	40 μmol. $h^{-1}.g^{-1}$	[75]
MoS_2/CuS_2	N/A	300W Xe lamp fitted with a cutoff filter(λ>420nm)	202 μmol. $h^{-1}.g^{-1}$	[76]
Copper-Organic Framework; H_2PtC_{16}	2.1	UV-Visible irradiation	30 μmol. $h^{-1}.g^{-1}$	[77]

1.9   Types of Photocatalytic Reactions

1.9.1 Photochemical Reactions

There are three components involved in Heterogeneous photochemical water splitting a catalyst, visible light absorber, and sacrificial electron donor. In photochemical reactions, there is a semiconductor-electrolyte junction at which the water splitting reaction takes place (Figure. 1.4). The essential potential for water splitting is produced at the semiconductor-liquid interface. Depending on the band edge position of the semiconductor, they can be active in hydrogen production, oxygen production, or overall water splitting [78].

(a)   **(b)**
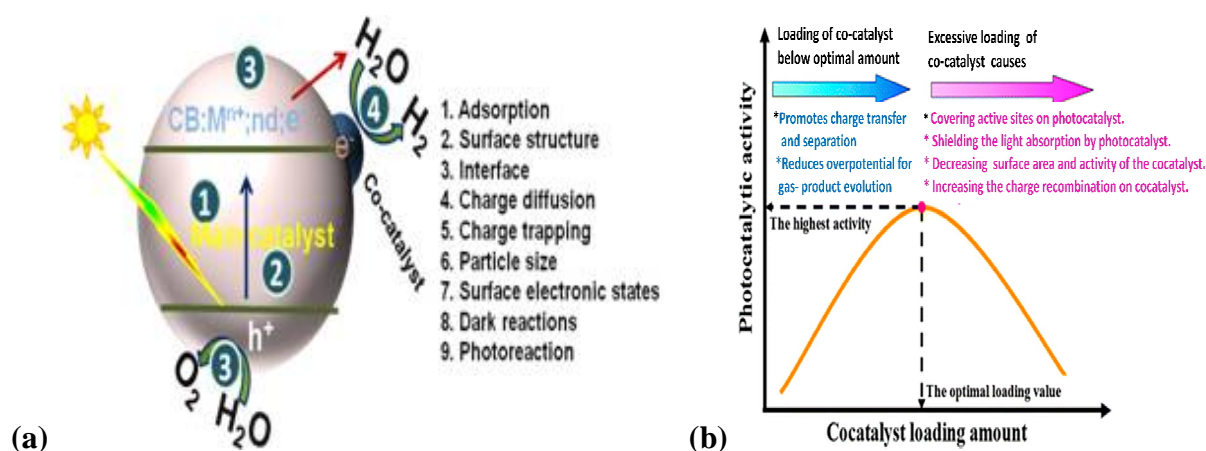
Figure 1.4 (a) Schematic representation of photocatalytical water splitting and **(b)** effect of loading of cocatalyst on main photocatalyst. [79]

1.9.2 Photo-Electrochemical Reactions

In photoelectrochemical (PEC) water splitting, a photocatalyst, which is a semiconductor, is irradiated by UV-visible light with energy higher or corresponding to the band gap of the semiconductor (Figure. 1.5). The light energy will be absorbed by the photocatalyst and results in charge separation at the valence band and conduction band. The holes are formed at the valence band, and the photo-excited electrons are located in the conduction band. The hole triggers the oxidation of water at the surface of conduction band while the photo-excited electrons at conduction band decrease the absorbed H^+ to H_2. Mainly in photoelectrochemical water splitting, semiconductors are use as a photocathode or photo-anode depending on the reaction, which is preferred. In photo-electrochemical water splitting, a semiconductor electrode should be in contact with an electrolyte, which includes a redox couple. In PEC water splitting, the overall reaction takes place at two different electrodes. In this process, the

potential, which is required for water splitting is being provided by illuminating the cathode or anode. [80]
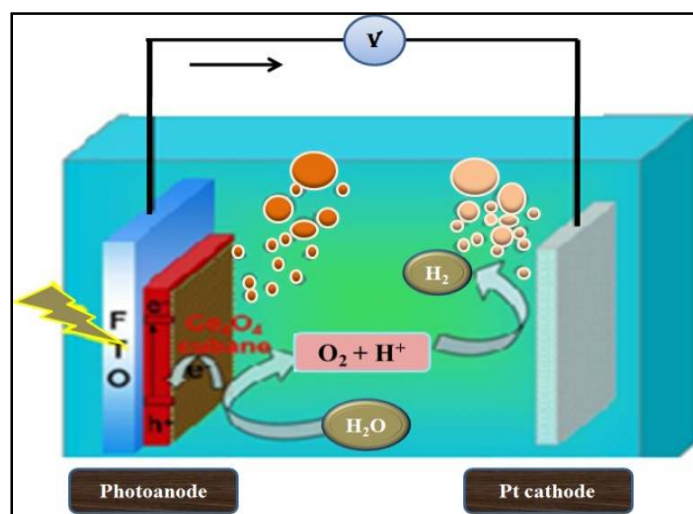
Figure 1.5 Schematic representation of photoelectrochemical water splitting. [80]

In particular, PEM water electrolysis, a proton exchange membrane (PEM), is applied which is well-suited for the combination with renewable energy sources. PEM electrolyzers have very good efficiency values at high current densities and they operate very dynamically at high pressures within a broad operating range. Fraunhofer ISE has been working for more than 25 years on component and system development as well as the integration of PEM electrolyzers in the energy system.

1.9.3 Thermochemical Reactions

In this process, the conversion of solar power to H_2 and synfuels with the utilization of the renewable is H_2O and CO_2 is seems to be a sound option. Artificial photosynthesis and photovoltaic-powered electrolysis of water are promising approaches, although their implementation is somewhat restricted because of the low solar to fuel conversion efficiency (η-solar-to-fuel) of <5% and <15%, respectively. [81-82] The other options would be a solar thermochemical process that provides a high theoretical efficiency and enables large-scale production of H_2 by using the thermal heating. [83] Research in thermochemical splitting of H_2O a begin in the early 1980s (84-85) and several thermochemical cycles have been examined. Thermochemical methods come under two main categories, the low-temperature multistep processes and the high-temperature two-step processes. The two-step process involving the thermal decomposition of metal oxides followed by reoxidation by reacting

with H_2O to yield H_2 is an attractive and viable process that can be rendered to become an isothermal process. Thermochemical splitting of H_2O at low temperatures ($<1,000°C$) is accomplished by a minimum of three steps as dictated by thermodynamic energy constraints. [86] Below mentioned examples the highlights of recent investigations of H_2O splitting by the low-temperature multistep process as well as the high temperature two-step process.

1.9.3.1 Low-temperature multistep cycles

Low-temperature cycles are advantageous due to low radioactive losses and availability of more heat resources, including nuclear waste heat sources. There has been a good deal of research in the past decades in this area and the performances of a few cycles such as the S-I and S-Br cycles as well as Fe-Cl, Hg-Br, and Cu-Cl cycles are noteworthy. [87]

1.9.3.2 Two-step thermochemical processes

The two-step metal oxide process carried out with the aid of solar concentrators and eliminates the necessity of separating of H_2 and O_2. The metal oxide (MO_{oxd}) reduced to the metal or to a lower valent metal oxide (MO_{red}) with the release of $O_2(g)$ during the endothermic step (T_{red}), and in the next step it gets reoxidized (T_{oxd}) on reaction with H_2O, releasing a stoichiometric amount of $H_2(g)$.

Thermochemical water splitting uses high temperatures by using energy from concentrated solar power or from the waste heat of nuclear power reactions and chemical reactions to produce hydrogen and oxygen from water. This is a long-term technological pathway, with potentially low or no greenhouse gas emissions. Thermochemical water splitting processes use high-temperature heat ($500°-2,000°C$) to drive a series of chemical reactions that produce hydrogen. The chemicals used in the process are reused within each cycle, creating a closed loop that consumes only water and produces hydrogen and oxygen. The necessary high temperatures can be generated in the following ways, Two examples of thermochemical water splitting cycles, the "direct" two-step cerium oxide thermal cycle and the "hybrid" copper chloride cycle, are illustrated in Figure 1.6 Typically direct cycles are less complex with fewer steps, but they require higher operating temperatures compared with the more complicated hybrid cycles.
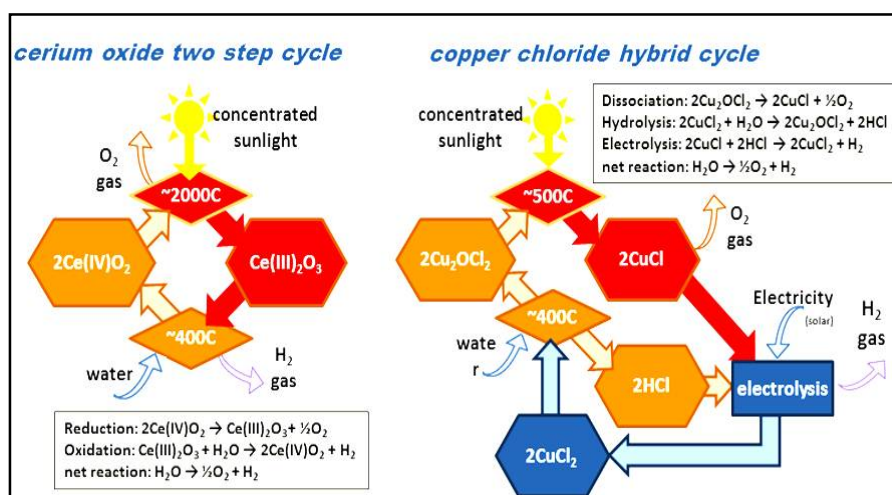
Figure 1.6 This illustrates the two examples of the thermochemical water-splitting cycles: (left) a two-step "direct" thermochemical cycle based on oxidation and reduction of cerium oxide particles; and (right) a multi-step "hybrid" thermochemical cycle based on copper chloride thermochemistry, which includes an electrolysis step that needs some electricity input.

1.9.4 Electrolysis

Hydrogen produced by water electrolysis is a key component for the energy economy. The electrochemical splitting of water by electrolysis (Figure 1.7) is a clean and efficient process to generate hydrogen if the electricity used for splitting the water comes from renewable energy sources. The resulting "green" hydrogen is a universal fuel that can be easily stored and used in many applications with the energy economy, transport sector or the chemical industry. Highly fluctuating and steadily increasing supply of electricity from renewable energy sources, can ensure a reliable energy supply that even provides a long-term or seasonal storage for future energy systems.
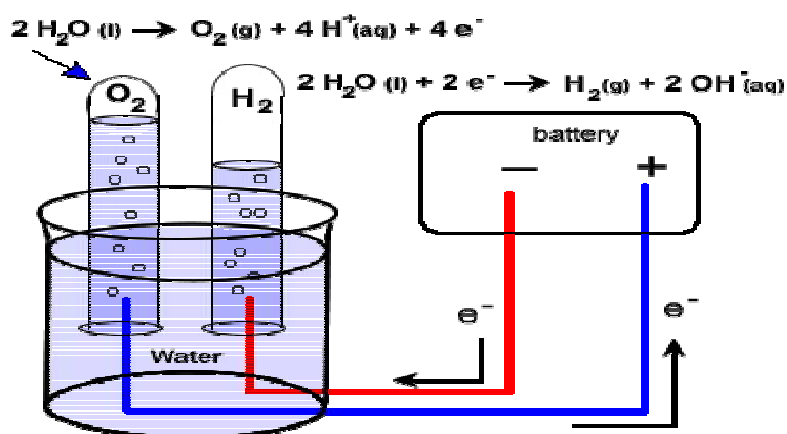
Figure 1.7 Schematic representation of electrolysis-water splitting.

1.9.4 Radiolysis

The current interest in non-traditional methods for the generation of hydrogen has prompted to revisit of radiolytic splitting of water, where the interaction of various types of ionizing radiation (α, β, and γ) with water to produce molecular hydrogen. This revaluation was further prompted by the current availability of large amounts of radiation sources present in the fuel discharged of nuclear reactors. This spent fuel is usually stored in water pools, awaiting permanent disposal or reprocessing. The yield of hydrogen resulting from the irradiation of water with β and γ radiation is low (G-values = <1 molecule per 100 electronvolts of absorbed energy) but this is largely due to the rapid re-association of the species arising during the initial radiolysis. The amount of hydrogen produced by radiolytic decomposition of water (Figure 1.8) is a complicated function of the water temperature, boiling strength, system pressure, absorbed fraction of radiation, and impurities in the water. If impurities are present or if physical conditions are created that prevent the establishment of a chemical equilibrium, the net production of hydrogen can be greatly enhanced. Another approach uses radioactive waste as an energy source for regeneration of spent fuel by converting sodium borate into sodium borohydride. By applying the proper combination of controls, stable borohydride compounds used as hydrogen fuel storage medium.
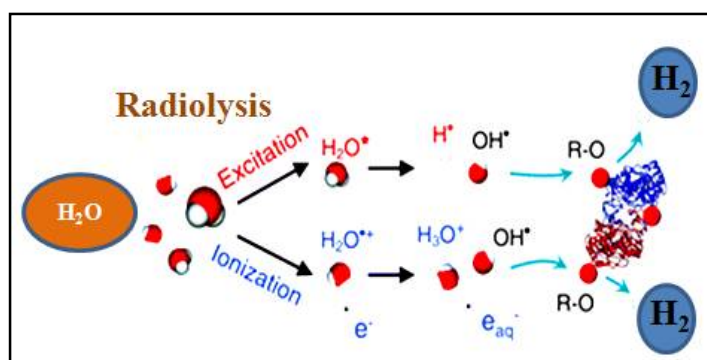
Figure 1.8 Hydrogen produced by radiolytic decomposition of water

1.9.5 Biolysis

In photolytic biological systems, microorganisms such as green microalgae or cyanobacteria, uses sunlight to split water (Figure 1.9) into oxygen and hydrogen ions. As generated hydrogen ions can be combined through direct or indirect routes to release hydrogen gas. Challenges of biolysis includes low yield of hydrogen production and the recombination of hydrogen with oxygen further produces water and safety issue created when oxygen mixed with hydrogen beyond certain concentrations. Researchers are developing some methods to meet out these challenges that allowed the microbes to produce hydrogen for longer periods

of time with increased yield. Some photosynthetic microbes also use sunlight to drive the breakdown of organic matter to release hydrogen, [88] under the process is known as photo-fermentative hydrogen production. But the low solar-to-hydrogen efficiency is a main constraint in making of commercial uses of hydrogen production. Hydrogen produced through the action of living organisms is called biohydrogen. This is a type of biofuel, like bio-ethanol, bio-diesel or bio-gas or bio-oil. There are three classes of biofuels:-

1. First generation – made from food crops

2. Second generation – made from non-food crops or wastes

3. Third generation (advanced) - made from microbes
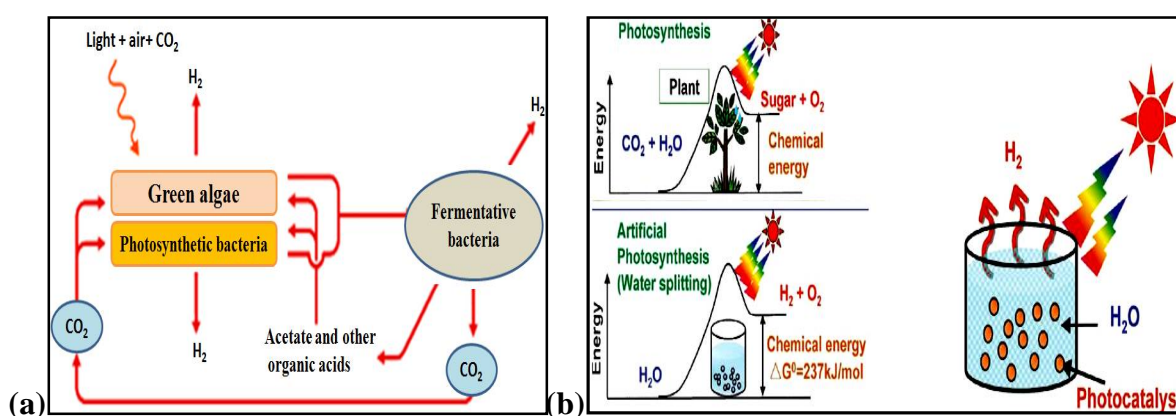
Figure 1.9 (a) Photobiological hydrogen production using water **(b)** photosynthesis and artificial water splitting

Advanced biofuels had several advantages over 1st and 2nd generation biofuels. Unlike, the advanced biofuels, first generation biofuels contributes a lot in increasing food prices. In comparison to second generation biofuels, advanced biofuels could capture sunlight energy 10 times more efficient by meaning of smaller areas or land are needed to produce large amount of fuel. Biohydrogen is an example of an advanced bio-fuel (or third generation biofuel). In advanced biofuel technologies, microbes are grown in special bioreactors by feeding them with the sunlight, waste organic materials, CO_2 from the air or from conventional gas plants. As they help in improving the growth of the microbes to produce the biofuels. Among the advanced biofuels, biohydrogen is particularly attractive because of the excellent properties of hydrogen as a fuel and ease to collect it from the bioreactor. Where, the purification of the biofuels such as bio oils from the microbial cell, is complex and expensive.

1.10 Photocatalyst Materials

1.10.1 Design and Description

As earlier mentioned, a suitable photocatalyst for complete water splitting should have a ideal band gap of 1.23 eV with no photocorrosion. In terms of water splitting, high crystallinity and small particle size are desired to minimize the recombination of photo-carriers i.e. electrons and holes. Metal oxides, sulfides, nitrides, and phosphates with d^0 and d^{10} metal cations have been used as water splitting catalysts. Group I, and Group II metals along with some lanthanides form perovskite materials can also be employed to catalyze photoelectron chemical (PEC) water splitting. The band diagram of the different semiconductors with respect to their redox potentials with respect to the water splitting requirement are summarized in the Figure 1.10. Advancement in photocatalysts by doping with some metal cations such as Ag^{2+}, Ni^{2+}, Cr^{3+}, and V^{5+}, are made to improve the solar energy conversion efficiency that can help to increase the visible light response. To prohibit the backward reaction of water splitting and to increase the hydrogen production yield, the suitable co-catalysts i.e. RuO_2, NiO, Au and Pt, can be added. In this section, we will focus on heterogeneous photocatalysts including metal oxides, metal sulfides, and metal nitrides.
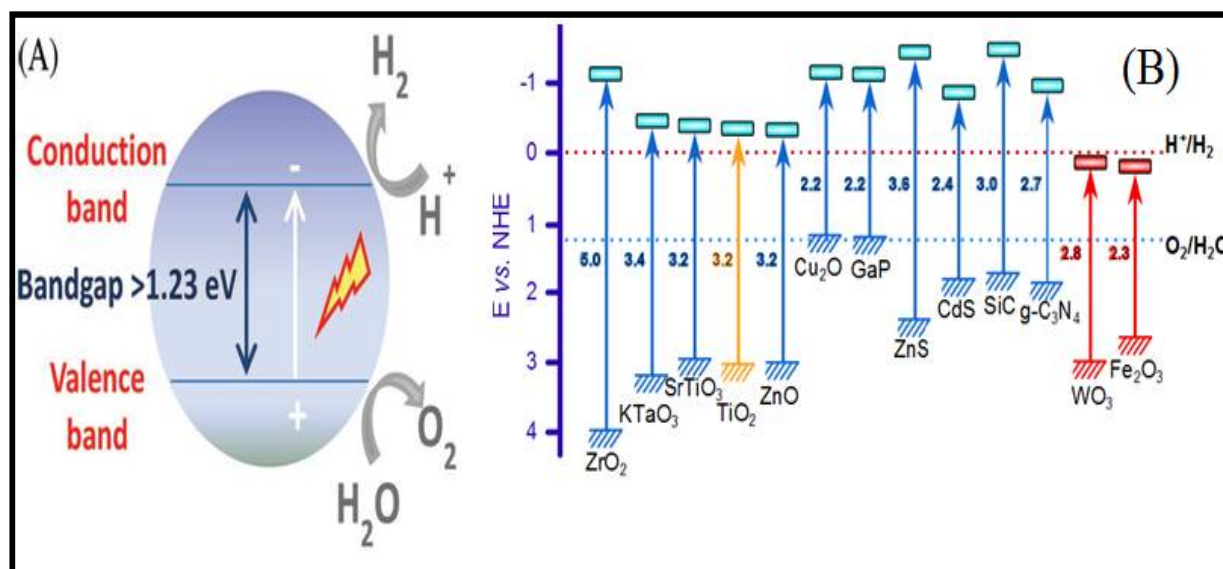
Figure 1.10 (A) Schematic of water splitting using semiconductor photocatalyst. **(B)** Band structure illustration of various semiconductors with respect to the redox potentials of water splitting. [89]

1.11 Oxide Photocatalysts: Challenges and Perspectives

Although, the oxide photocatalysts are a very common and famous class of photocatalyst, used for water splitting for a long time, due to their wide band gap (BG) they have some limitations, on which we need to focus our efforts. First, the study of oxide photocatalyst requires more devoted and goal-oriented efforts in the direction of overall efficient water splitting, as this field is quite complicated and the reported studies are quite scattered. A more systematic practical approach aligned with a theoretical scheme is needed to move toward this direction and to rationalize the major experimental observations. Second, new oxide photocatalyst materials with better performance at lower cost are required. In the long run, the cost of the material will be a driving factor even if the photocatalysis achieves high efficiency and stability under sunlight irradiation. Therefore, low cost material with stability and efficiency are in demand. Oxide materials, which have an apt BG with good light harvesting capacities, are still at the top of the "WANTED" list in the field of the functional materials. Third, new modified reactor designs are urgently needed in place of conventionally designs (typically slurry reactors and immobilized film reactors). [90]

1.11.1 Prominent oxide photocatalysts

1.11.1.1 Metal Oxides

A large number of representative metal oxides (such as ZnO, TiO_2, Fe_2O_3, WO_3, Cu_2O, Al_2O_3, Ga_2O_3, Ta_2O_5, CoO and ZrO_2, etc) have been widely studied for water splitting due to their high stability in aqueous solution and their low cost. However, most metal oxides suffers from the large band gaps that limits their ability to absorb visible light. Under the typical class of metal oxide, the valence band have O2p and metal s character and conduction band has metallic *nd* or *np* characters. Therefore, they might have relatively large band gap suchn as: ZrO_2(5.0 eV) SnO_2(3.68 eV), Nb_2O_5(3.5 to 4.8 eV), Cu_2O (2.2eV), In_2O_3 (3.75 eV), TiO_2 (3.2 eV) [91] ZnO (3.2 eV) [92], Ga_2O_3 (4.5 eV) [93], Al_2O_3 (8.8 eV) [94] etc.
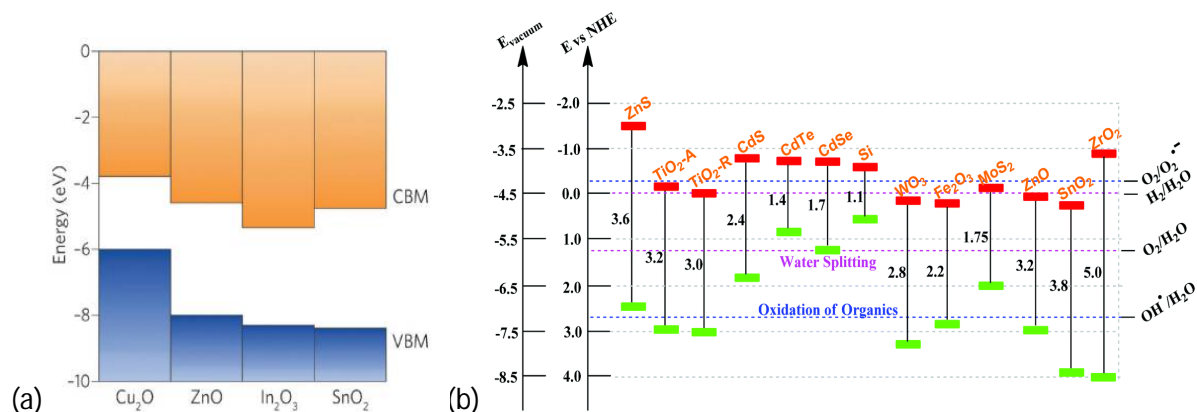
Figure 1.11 Typical valence and conduction band offsets of **(a)** Cu_2O, ZnO, In_2O_3 and SnO_2 [95] and **(b)** The band diagram of different popular semiconductors.

Table 4 Properties of the metal oxides with their band gap, donor concentration, valance bond voltage, conduction band voltage and E_B.

Photoanode	E_{BG}^{a}	Donor Concn.,^{b} cm^{-3}	E_{VB}^{c}	E_{CB} $\bullet$ V_{FB}^{d}	E_{B}^{e}
TiO_2	3.0	3×10^{20}	1.95	−1.05	1.0
SnO_2	3.5	2×10^{18}	2.8	−0.7	0.6
$SrTiO_3$	3.2	3×10^{20}	2.8	−1.3	1.3
$KTaO_3$	3.4	3×10^{20}	1.8	−1.4	1.2
Fe_2O_3	2.2	2.5×10^{17}	2.5	−0.3	-
$Fe_2O_3 + 1\% TiO_2$	2.2	6.4×10^{19}	-	-	-
$Fe_2O_3 + 1\% SnO_2$	2.2	7.8×10^{18}	-	-	-

Typical photocatalyst are discussed as follows:

1.11.1.1.1 TiO$_2$

TiO_2 (with band gap 3.2 eV) is the first ever photocatlyst that used for water splitting. [96] Titanium dioxide is a low-cost and nontoxic optoelectronic material that used to produce environmental friendly solar-hydrogen to support the future hydrogen economy. It found in three forms i.e rutile, anatase and brookite along with the two high pressure forms a monoclinic bad deleyite like form and an orthorhombic α-PbO_2-like form, in nature. Their strengths and weakness vary with the method of preparation. For example, the maximum value obtained for the photo-voltage of a photoelectrochemical cell using a TiO_2 photoanode is ~0.9 V. Hence, for TiO_2 (rutile, bandgap ≈ 3.0 eV) the conduction band edge potential is insufficiently negative to generate hydrogen at a useful rate. Consequently, it requires a bias

in order to decompose water by use of an externally applied bias voltage. Despite intensive research onto TiO_2, from both experimental and theoretical aspects, the understanding of the fundamentals of TiO_2 chemistry is still limited. Most of the microscopic mechanisms of the properties mentioned above have not been clarified but it was cleared that the surface chemistry of the TiO_2 has been expected to play an eminent role in solar hydrogen generation processes. In addition, a strong photocatalytic activity and photo induced hydrophilic conversion phenomena have also been observed on TiO_2 surfaces. Satoshi and Hiroshi in 2016, reported a visible-light-sensitive two-step overall water-splitting process for Pt/Cr, Ta doped -rutile (O_2) and -anatase (H_2) TiO_2 system, as shown in (Figure. 1.12 a), Li etal illustrated a Z scheme between the wide bandgap TiO_2 and narrow bandgap Ag_2S i.e. Ag_2S-Ag-TiO_2 (Figure 1.12 b), for photocatalytic hydrogen production under full-spectrum light illumination. The 30-mg Ag_2S-(Ag)-TiO_2 hybrid structures exhibit H_2 production rates at 1.3×10^{-7} and 1.9×10^{-8} mol/h under $\lambda < 400$ nm and $\lambda > 400$ nm, respectively. Pu etal compared the pure TiO_2, with Au NP and Au NR decorated- TiO_2 nanowires where the decorated electrodes exhibited significantly enhanced photoactivity in both the UV and visible regions. For Au NR-decorated TiO_2 electrodes, the photoactivity enhancement was, observed in the visible region only with the largest photocurrent generation achieved at 710 nm. Significantly, TiO_2 nanowires loaded with a mixture of Au NPs and NRs showed enhanced photoactivity in the entire UV-Visible region (Figure 1.12c).
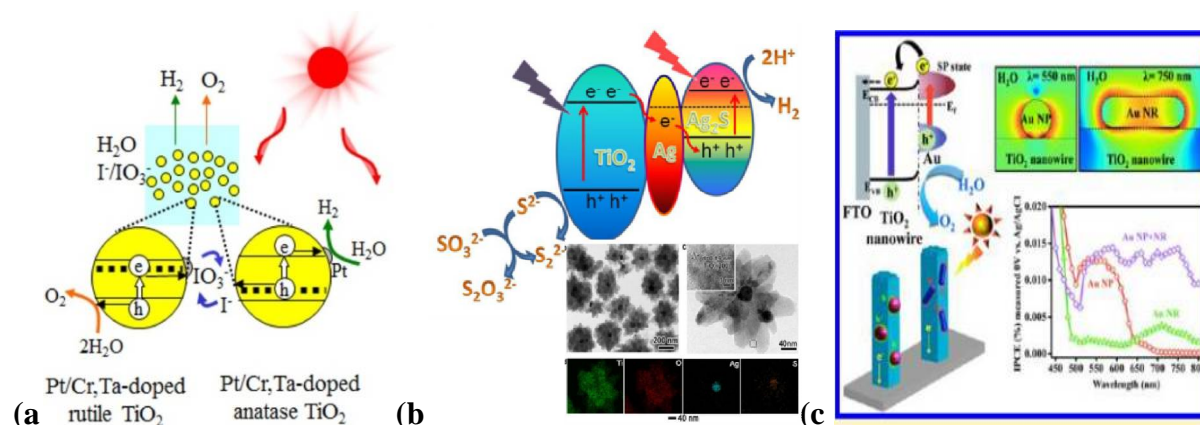
Figure 1.12 Visible-light-sensitive two-step overall water-splitting using TiO_2 based systems **(a)** Pt/Cr, Ta doped-rutile (O_2) and-anatase (H_2) TiO_2 system [97] **(b)** Ag_2S-Ag-TiO_2 [98] and **(c)** Au NP and Au NR decorated- TiO_2 nanowire [99].

1.11.1.1.2 Fe$_2$O$_3$

Mishra et al. [100] reported that Fe$_2$O$_3$ can be act as a photoanodic material for water oxidation. The band gap of Fe$_2$O$_3$ is 2.2 eV, which allows photon absorption under visible light irradiation. However, some mechanistic studies have been carried out to trace the water oxidation and reduction reactions. Haghighat et al. [101] have also been investigated the mechanism of water oxidation process on iron oxide surface by evaluating the electron-transfer rate on changing the pH and potential. Due to limitation of the severe bulk recombination, usage of α-Fe$_2$O$_3$ is not popular. Figure 1.13 suggested the ways for improvement of its photocatalytic property i.e. multilayered heterostructure, surface modification, doping with different materials and composite formation. Similar to the α-Fe$_2$O$_3$, WO$_3$ with the band gap 2.8 eV, is also act as photocatalyst for water oxidation because its valence band position which has a high onset potential suitable for water oxidation not for reduction. Moniz et al. [102] found that the main drawback of WO$_3$ is its instability toward anodic photocorrosion. These low Eg materials (e.g., Fe$_2$O$_3$ and WO$_3$) can be modified by doping it with metal cations or by forming heterojunctions with other semiconductors. [103]
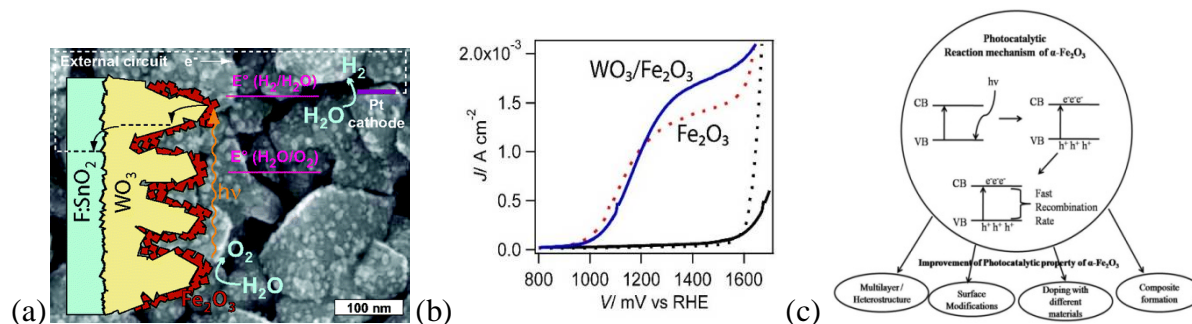
Figure 1.13 (a) Mechanistics of water oxidation on iron oxide and WO$_3$/Fe$_2$O$_3$ photocatalysts through evaluating the electron-transfer by changing the pH [102] **(b)** photo current density *Vs* applied voltage [103] and **(c)** modes of improvement in materialistic properties of Fe$_2$O$_3$, required for water splitting. [101]

1.11.1.1.1.3 WO$_3$

Mohamed et al. [104] Nanoporous and nanoflakes tungsten oxide (WO$_3$) films were produced on metallic W foil via one-step potentiostatic anodization method. The nanoflakes films conserved their topology under different annealing temperatures (up to 500°C) with particle sizes in the range of 46 nm. However, the nanoporous films showed a gradual deterioration in the porous structure upon annealing up to 500°C. The photoelectrochemical activity tests revealed that the nanoflakes annealed at 500°C exhibited a superior photocatalysis and achieved a photocurrent density of 1.17 mA cm^2 at 1.2 V$_{SCE}$ under AM 1.5 illumination.

1.11.1.1.4 CoO

Liao et al. [105] had testimony the CoO nanocrystals as HER photocatalyst for water splitting under visible light exposure. However, short lifetime and rapid deactivation of CoO nanoparticles that can limits their usage in water splitting. Morphology of nanomaterials can influence on the band-edge positions [106] and developing the CoO nanoparticles with different 1D morphology such as nanotubes or nanowires, can provide the more efficient photocatalystic material Zhan et al. [107] developed CoO nanowires on the carbon fiber papers with hydrogen generation rate of 81.3 mol g^{-1} h^{-1}, which indicated higher chemical stability in comparison with CoO nanoparticles.
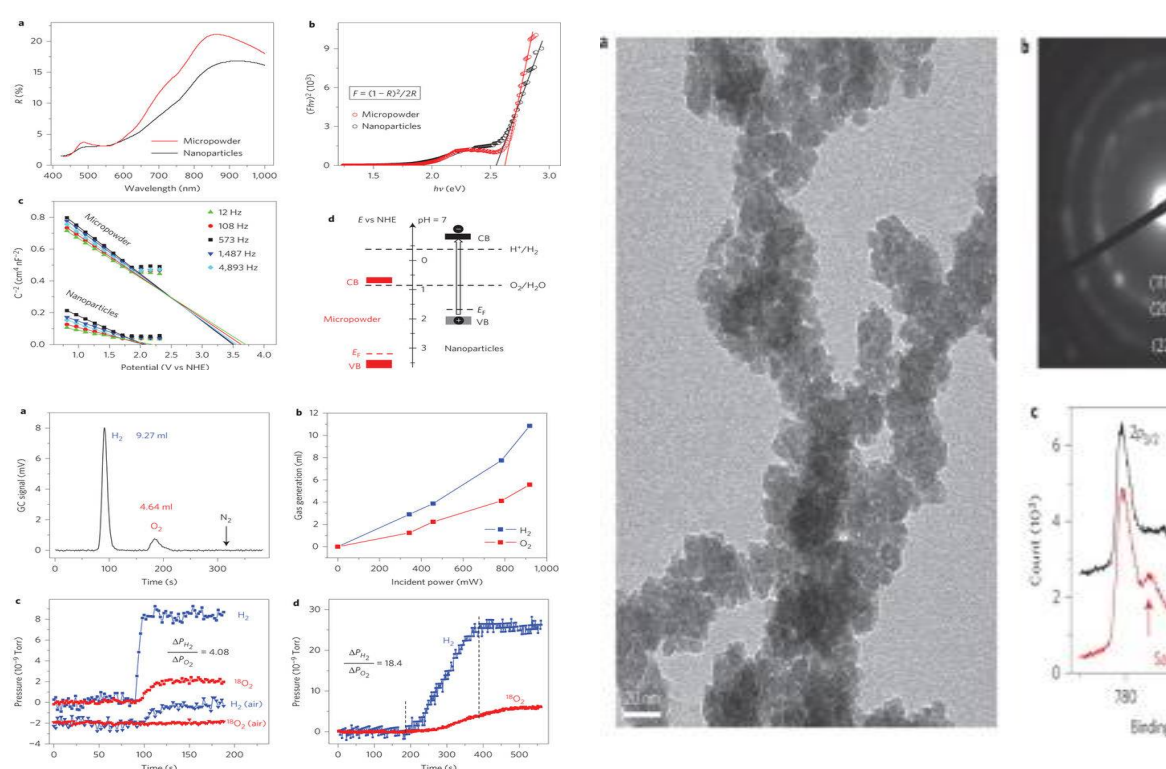
Figure 1.14 Water splitting into hydrogen and oxygen using CoO with its UV spectra, Mott schottky plot, SEM image and XPS spectra. [105]

1.11.1.1. 5 Tantalum oxide (Ta$_2$O$_5$)

Tantalum oxide (Ta$_2$O$_5$) has been an attractive semiconductor for photocatalytic water splitting [108-111] due to their wide band gap (about 4 eV), it is required to narrow the band gap that can be done by the doping of foreign ions. Lu et al. [108] described the Ta$_2$O$_5$ nanowires as an active photocatalysts, which generated hydrogen with the rate of 214 mmol

g^{-1} h^{-1} under Xe lamp irradiation without any cocatalyst. They concluded that the Ta_2O_5 nanowire with low dimensional structures provides a higher surface area with favorable carrier transport to harvest light for H_2 production. Tao et al.[109] explained the fabrication of the well dispersed mesoporous Ta_2O_5 submicrospheres at $R = 5\ °C/min$ that showed a considerably enhanced photocatalytic activity not only for hydrogen evolution but also for photodegradation of organic pollutants such as methylene blue and rhodamine B. The results here suggest that the meticulous control over the structural characteristics is an effective alternative to obtain highly efficient photocatalytic materials. Mao et al. [110] developed a H_2O_2-mediated hydrothermal method for the fabrication of the hydrophilic Ta_2O_5/graphene composite. The composite shows a superior H_2 productivity, up to 30 mmol g^{-1} h^{-1} for water splitting, corresponding to an apparent quantum efficiency of 33.8% at 254 nm. This superior performance is due to the hydrophilic nature of the composite with the ultrafine Ta_2O_5 nanoparticles (about 4.0 ± 1.5 nm), which are covalently bonded with the conductive graphene. The hydrophilic property of the composite is attributed to the use of H_2O_2 in the hydrothermal process. The ultrafine size of the Ta_2O_5 particles which are covalently bonded with the graphene sheets is attributed to the use of sonication in the synthesis process. Furthermore, the hydrophilic Ta_2O_5/Gr composite is durable, which is beneficial to long term photocatalysis. Zhu et al. [111] reported the gray Ta_2O_5 nanowires, which were modified by aluminum doping to improve electron density and photo electrochemical water splitting properties of the material. Where, the single-crystalline uniform Ta_2O_5 nanowires are prepared by a novel synthetic route. The formation of the nanowires, oriented in particular direction, result in the reduction of surface energy. These nanowires had been successfully applied to the photocatalytic H_2 evolution, pollutant degradation and dye-sensitized solar cells (DSSCs). The Ta_2O_5-based DSSCs revealed a significant photovoltaic response. As synthesised Ta_2O_5 nanowires possess high H_2 evolution efficiency with nearly 27-fold higher than the commercial powders, under the Xe lamp irradiation. A better performance for the photocatalytic degradation of the contaminant is also observed. Such improvements are ascribed to better charge transport ability for the single-crystalline wire and a higher potential energy of the conduction band.
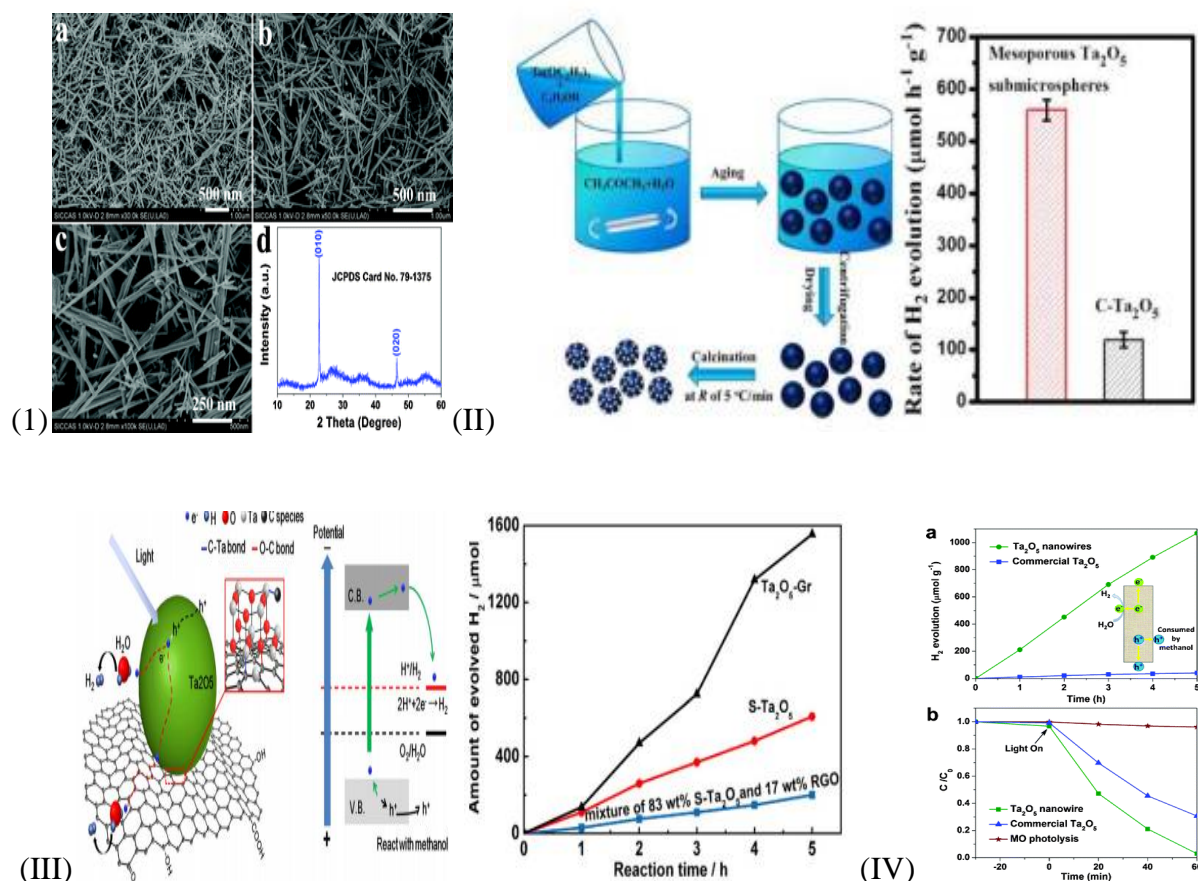
Figure 1.15 Modified Ta_2O_5 i.e. **(I)** wires structuring, [108] **(II)** mesoporus structure, [109] **(III)** addition of the reduced graphene oxide [110] and **(IV)** grey Ta_2O_5 for photocatalytic water splitting. [111]

1.11.1.1.6 Mixed metal oxide

Finally, it is valuable to extend the wavelength response region up to the near IR using appropriate supportive material to the main oxide photocatalyst assembly such as plasmonic photocatalysts, cocatalysts, or stand-alone photocatalysts. Most oxide materials are sensitive to the UV region (4% of sunlight) of the light and a handful of oxide photocatalysts can be worked under visible light (45% of sunlight). However, solar light contains a large proportion of energy in the near IR region, which is totally unexplored in this respect. Some studies have already demonstrated IR response (up to 1300 nm) using noble metal nanoparticles but the efficiency is low. [112] Transition metal oxides with d^n electronic configurations such as Fe_2O_3 (~2.0 eV) [113] and Co_3O_4 (~1.3 eV) [114] etc, showed increased light absorption but with decrease in charge carrier transfer efficiency due to small polaron dominated conductivity and high resistivity. [115, 116] Post-transition indirect band metal oxides (PbO

(2.1 eV) [115], SnO (2.4 eV) [116, 117] and Bi_2O_3 (2.5 eV) [118]) have occupied ns-orbital that leads to better photogeneration of charge carriers but their efficiency of carrier extraction process is less because their optical absorption band edges vary with the square root of the photon energy. Therefore, ternary metal oxide compounds or nanosturctures of the metal oxides have been employed to overcome these limitations using the photocatlyst like as: wormhole like mesoporous $Bi_{20}TiO_{32}$ [119] (with pore size 6.1nm and Eg = 2.5eV), NiO/NaTaO$_3$:La (with maximum apparent quantum yield 56% at 270 nm for water splitting) [120] $SnNb_2O_6$ [121] $A_{2-x}La_2Ti_{3-x}Nb_xO_{10}$ (A = K, Rb, Cs; x = 0, 0.5, 1.0), [122] NiO(0.15 wt %)/$Sr_2Ta_2O_7$ photocatalyst was 12% at 270 nm) [123] and $BiVO_4$ [124] $BiVO_4$ has been investigated with owning a low band gap (2.4-2.5 eV) and reasonable good aligned band edge positions suitable for the water redox potentials. [125-126]

$SrTiO_3$ (STO) has also been widely used for hydrogen production as a solid-state photocatalyst with a band gap of 3.2 eV, which has been explored for the overall water splitting under UV light irradiation. Since STO, is active towards water splitting only in the UV region with the solar to hydrogen conversion (STH). Doping can enhance the quantum efficiency of $SrTiO_3$ in the visible light region [127-128].
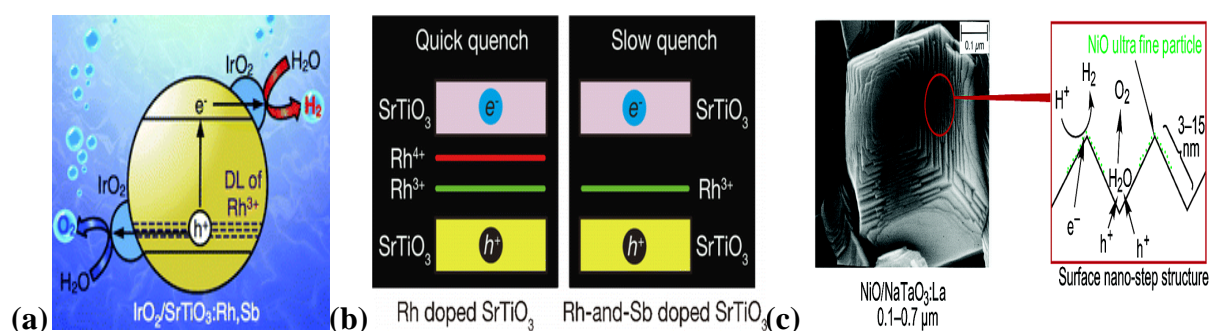
Figure 1.16 Mixed oxides **(a)** cocatalyst IrO_2 loaded Rh: Sb doped $SrTiO_3$ [128] **(b)** Rh:Sb doped $SrTiO_3$ [129] and **(c)** NiO/NaTaO$_3$:La, used for water splitting. [130]

Rh and Sb doped $SrTiO_3$ photocatalysts were prepared by hydrothermal synthesis. Figures 1.16 represents of effect of doping to STO. Rh doping to STO causes optical absorption centered at 580 and 420 nm, attributed to Rh^{4+} and Rh^{3+} species. Addition of Sb to Rh-doped $SrTiO_3$, result in the oxidation state of Rh shifts to be 3^+ and the absorption at 580 nm disappears. These doped and nondoped photocatalysts exhibit transient infrared absorption between 3000-1000 cm^{-1} due to excited electrons, when pumped by 355 or 532 nm light pulses. The absorbance decay was observed in a vacuum as a function of the microsecond

time delays to deduce the relative rate of electron-hole recombination. Doping of aliovalent metal cations to $SrTiO_3$ lowers the valence cation to introduce oxygen vacancies and decrease Ti^{3+} concentration, which is effective to enhance photocatalytic activity [129] have recently reported the photocatalytic behavior of the $SrTiO_3$ for the overall water splitting reaction their can significantly be improved to 30% at 360 nm by flux-mediated Al doping. In another study, Rh-doped $SrTiO_3$ is with a donor level in the band gap region of $SrTiO_3$: Rh that can averts the charge recombination and facilitates the hydrogen production (2223 mol h^{-1} g^{-1}) with respect to pure STO. Kato et al. in 2003, [130] investigated the highly efficient lanthanum-doped $NaTaO_3$ with high crystallinity and surface nanostructuring for overall water splitting into H_2 and O_2 under UV light irradiation.

1.11.1.1.7 Graphene Oxide

Graphene based nanocomposites or super carbons can also be proved as a good alternative material can be used for water splitting by using renewable energy that is solar energy. They can be fabricated using graphite as an initial material, as shown in Figure 1.17 a. They can also absorb over a wide range of wavelengths that is from IR through visible to UV region and can act as electron acceptors and transporters. Graphene is a large aromatic macromolecule with a flat monolayer of sp^2 bonded carbon atoms tightly packed into a 2D honeycomb lattice, which has no BG and has a unique band structure, in which the lowest unoccupied molecular orbital (HOMO) level (π) meet up at the dirac point, as shown in Figures 1.17 a and 1.17 b. This allows graphene to display quite high conductivity and electron mobility. Furthermore, the doping of the heteroatom or electrostatic field tuning makes graphene as n-or p-type semiconductor with a small BG that accompanied by detuning off the Fermi level from the Dirac point near to LUMO and HOMO [131]. Moreover, it has high thermal conductivity (~5000 Wm/K) [132], excellent mobility of the charge carriers (200,000 $cm^2V^{-1}S^{-1}$) [133] (Castro neto et al. 2009) a large specific surface area.
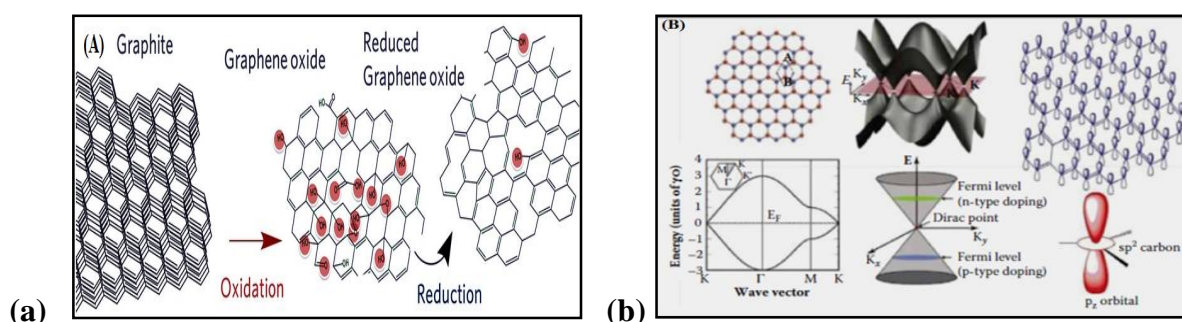
Figure 1.17 **(a)** the making of graphene based compounds from graphite. **(b)** Electronic structure of graphene. [131]

Specific surface area (2630 m^2/g) [134] easily functionalized in compared with carbon nanotubes, biodegradability [135], nontoxicity and good mechanical stability, [136] transparency, [137] large work function (4.42 eV) [138], which enables it to accept photogenerated electrons from CB of most of semiconductors and LUMO of dyes that results in suppression in charge recombination and enhance H$_2$ generation capacity. Accepted electrons can migrate across its 2D plane to a reactive site for hydrogen generation. Therefore, the roles of graphene as an electron acceptor and transporter need to be extensively investigated to enhance PEC/photocatalytic hydrogen generation. Moreover, the lateral size, layer thickness, homogeneity, and purity of the graphene are the qualities, which directed the material for high end uses in electronics and other devices. Furthermore, it might be suitable as a good electrode material for electronic devices due to its high thermal and chemical stability, low resistivity (10-30 per square), light weight, flexibility and transparency (>90% at 550 nm). [139] it has the potential to replace indium tin oxide (ITO) as an electrode material as it is thermally and chemically stable, highly conductive, flexible, and transparent. [140] Graphene based composite systems are classified into three categories: binary (one compound with graphene based composite), ternary (two compounds with graphene based composite) and dye sensitized (dye with graphene based composite). There typical examples are mentioned in Figures 1.18. TiO$_2$/graphene photocatalyst was first ever reported system for photocatalytic H$_2$ generation, as demonstrated in Figure 1.18 a and 1.18 b other binary systems are: graphenes with TiO$_2$ [141-142] ZnO, [137] ZnS 6H-SiC [143], BiOCl [144], 23.4% Zn$_x$ Cd$_{1-x}$ S, [145], CdSe [146] and CdTe [147].
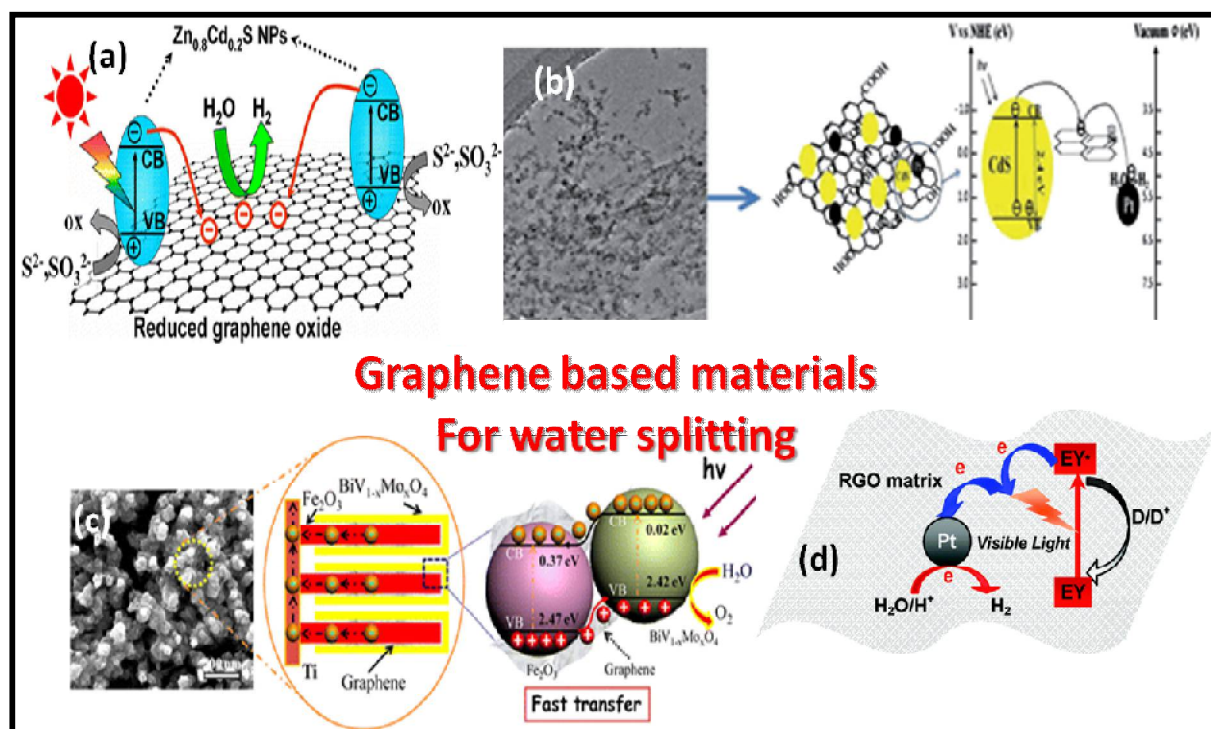
Figure 1.18 Schematic illustration of photocatalytic H_2 production by using graphene based materials with **(a)** $Zn_{0.8}Cd_{0.2}S$ NPs, [145] **(b)** CdS-Pt, [148] **(c)** $Fe_2O_3@BiV_{1-x}Mo_xO_4$ [149] and (d) dye (Eosin Y)-doped reduced graphene oxide under UV light irradiation [150].

In ternary graphene system, graphene acts as an electron mediator for water splitting in an ingenious Z-scheme that accelerates that transfer of electron from two different kind of semiconductor to the active sites of the graphene through the 2D plane. In a typical photoreduced graphene oxide (PRGO) is used as a mediator among Z-scheme semiconductors $BiVO_4$ and $Ru-SrTiO_3:Rh$. Under visible light illumination, photogenerated electrons of the CB of $BiVO_4$ transfer to $Ru-SrTiO_3:Rh$ via graphene as an electron conductor. The electrons in $Ru/SrTiO_3:Rh$ reduce water to H_2 on the Ru cocatalyst, while the holes in $BiVO_4$ oxidize water to O_2, accomplishing a complete water splitting. Similarly $Fe2O3@BiV1-x MOxO4$ works effectively for hydrogen generation by water splitting as shown in Figure 1.18c [149] In graphene based dye sensitized nano-coposite system, the dye (Eosin Y [EY], Rose Bengal [RB], Fluorescein and Rhodamine B, etc) molecules act as a photosensitizer and are first adsorbed on the surface of RGO sheet with dispersed Pt cocatalyst, which has excellent electron accepting and electron transporting properties; RGO can facilitate the electron transfer from excited dye (Eosin Y)-doped reduced graphene oxide molecule to the Pt cocatalyst, which promotes photocatalytic activity for hydrogen evolution (Figure 1.18 d). [150]

1.11.1.1.8 Oxynitride

Oxynitrides can be made by replacing few of the oxygen content by nitrogen at lattice sites, which intend to narrow the BG of the oxides, by pushing the VB towards the BG. Such a modification does not produce native point defects. This would otherwise be introduced in the case of N doping. Stoichiometric incorporation of the nitrogen also avoids the localized states induced by N doping and reduces the possible electron hole recombination. The solid solution of GaN and ZnO has been considered as a promising photocatalyst for the overall water splitting. [151] Although, the pristine GaN and ZnO are the poor visible light absorbers due to their wide band gaps but their solid solution $(Ga_{1-x}Zn_x)(N_{1-x}O_x)$ formed their will have new electronic states that considerably reduce the band gap. [152] Siritanaratkul et al in 2011 [153] studied the perovskite type crystal structured oxynitride compounds such as $CaNbO_2N$, $SrNbO_2$, $BaNbO_2N$, and $LaNbON_2$, etc. Maeda et al in 2011 [154] reported $SrNbO_2N$ (Eg = 1.8 eV) for photocatalytic hydrogen evolution under visible light from methanol solution. The photoelectrode of $SrNbO_2N$ on a transparent conducting surface shows water oxidation reaction without external bias. Higashi et al in 2009 [155] developed Tantalum based compounds such as $CaTaO_2N$ and $BaTaO_2N$ that to be utilized in Z-scheme photocatalysis. $CaTaO_2N$ and $BaTaO_2N$ loaded with Pt cocatalyst and coupled with Pt/WO_3, were used for Z-scheme water splitting. Maeda and Domen in 2014, [156] investigated a solid solution of $BaTaO_2N$ and $BaZrO_3$ for hydrogen and oxygen evolution, which showed improved performance compared with individual photocatalysts under visible light irradiation. Paven-Thivet et al in 2009 [157] developed a perovskite type compound $LaTiO_xN_y$ which shows high photocurrent density under visible light. Apart from the double perovskites that belongs to the general formula $AA'BB'O_6$. There are a several other compounds that show crystal structures close to the perovskite type structure. Theoretically, double perovskites offer a wider scope to design photocatalysts by selecting suitable cations and AA' and BB' sites in the lattice. Work on design and advancement of double perovskites is in progress.

1.11.1.1.9 Oxy Sulfides

Usually, oxides are active in UV light but its bandgap engineering can be done by in cooperating sulphur and metal ions. Hence, most of the oxysulfides are visible light active. For a typical example, Ishikawa et al [158] developed the oxysulfides with a similar

composition of sulfur and oxygen for photocatalysts. The mixed oxysulfide perovskite $Sm_2Ti_2S_2O_5$ (Eg = 2.0 eV) is known for water oxidation and reduction reaction for oxygen and hydrogen evolution, respectively, in the presence of sacrificial agent under low photon energy wavelength of 650 nm. The band structure of the phase reveals the presence of the sulfur that by narrowing the BG makes enable the compound for visible light absorption.

1.11.1.1.10 Metal Sulfides

Metal sulfide photocatalysts (MSP i.e. CdS and ZnS, etc), [159] with narrower band gap (in comparasion to metal oxide semiconductors) is considered as the most promising class of visible-light-driven photocatalyst for water splitting. [160] However, MSP are highly sensitive to photocorrossion due to rapid recombination of the photocarriers i.e. electrons and holes. Therefore, pristine MSP semiconductors usually show low hydrogen production rates [161-162] with less stability. To avoid this problem, MSPs can be coupled with other noble metals as a co-catalyst or form a heterojunction structure with other semiconductors. [163] In such case, the photogenerated electrons on the conduction band of semiconductor can be transferred to the conduction band of the MSP's that transferred to the electronic levels of the noble metals or to be delocalized through LSPR/ SPR. The whole assembly can be used for the photoreduction of water. Huang et al. [164] had synthesised the noble metal free hollow bimetallic sulfide materials ($M_xCo_{3-x}S_4$, M = Zn, Ni, and Cu) with a narrow band gap (Figure 1.19a). The bimetallic metal sulfides exhibit a hydrogen production rate comparable to Pt or Eosin Y dye sensitized TiO_2 coupled with C_3N_4 semiconductors. The H_2 evolution rates for CdS/Pt/Ga_2O_3 and CdS/Pt/In_2O_3 are found as high as 995.8 and 1032.2 $\mu mol\,h^{-1}$, respectively, under visible light (λ>420 nm) with high apparent quantum efficiencies of 43.6 and 45.3 % obtained at 460 nm, respectively, as shown in Figure 1.19b. These are much higher than those on Pt/CdS (108.09 $\mu mol\,h^{-1}$), Pt/Ga_2O_3 (0.12 $\mu mol\,h^{-1}$), and Pt/In_2O_3 (0.05 $\mu mol\,h^{-1}$). Nickel sulfide, in particular has proven to be enormously useful in raising the activity of semiconductors, when they use a co-catalyst along with TiO_2, CdS, and g-C_3N_4. [165] Unlike CdS, wide band gap ZnS (3.6 eV), responds weakly to visible light. [166, 167] Efforts have been made to improve the photoactivity of ZnS for hydrogen evolution.
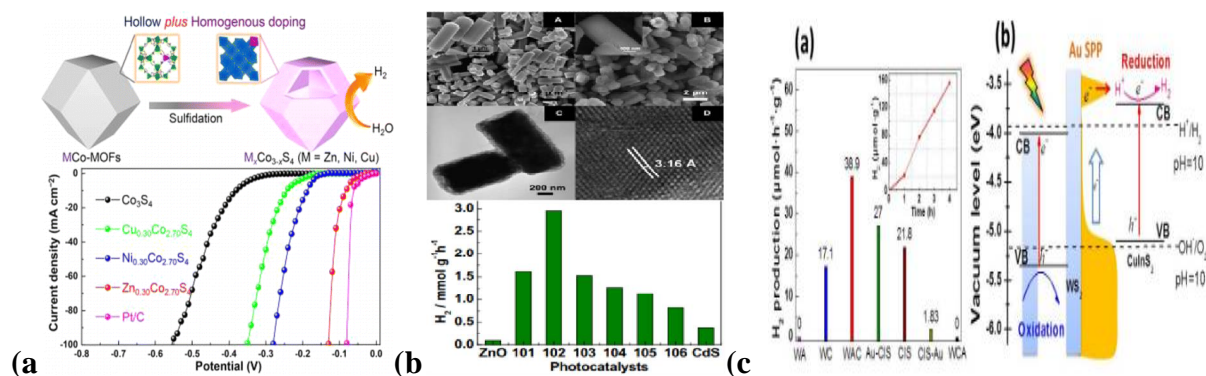
Figure 1.19 Metal sulphides used for water splitting i.e. **(a)** $M_xCo_{3-x}S_4$, M = Zn, Ni, and Cu) 164 **(b)** CdS/Pt/Ga_2O_3 and CdS/Pt/In_2O_3 core-shell nanorods **(c)** WS_2-Au-CIS [173]

Li et al. [168] have reported highly active solid solution system i.e. $Zn_{1-x}Cd_xS$ for visible-light irradiated hydrogen gas production from breaking of water. The band gaps of the solid solution photocatalysts can be narrowed by varying the Zn/Cd molar ratios with respect to the bare ZnS of large band gap that can favour the absorption of light photons. Although, the metal oxides with large band gaps are highly stable and can produced stable the composite material. [169] Some significant solid solutions of metal oxides (TaON, TiO_2 and ZnO) and CdS are studied by various groups. [170, 171] Nanocarbon with different morphology can combined with CdS to promote their catalytic behaviour towards water splitting by suppressing the charge recombination. Due to good compatibility of the carbon nanostructures and CdS and the high conductivity of carbon can improve the degree of the charge separation. Consequently, the catalytic behavior of the above nanocomposites will be improved. Different strategies for production of the carbon-based CdS nanocomposites that may include simple mixing of carbon-based nanomaterials with CdS or in-situ growing of the CdS at the graphene oxide surface by using oxygen moieties as the templates. [172] WS_2-Au-$CuInS_2$ has also been reported for photocatalytical H_2 production by insertion of gold nanoparticles between of WS_2 nanotubes and $CuInS_2$ (CIS) nanoparticles, as demonstrated in Figure 1.19c. [173] Addition of Au nanoparticles with WS_2 and $CuInS_2$ can lead to significant enhancement of light absorption, resulted in highest H_2 evolution efficiency for WS_2-Au-CIS due to the more rapid photogenerated carrier separation from the type II band structures and the localized surface plasmonic resonance (LSPR) associated with the Au nanoparticles.

1.11.1.1.11 Nitrides

To efficiently harvest solar light, nitrides and oxynitrides can be applied as photocatalysts for water splitting .The 2p orbitals corresponding to nitrogen in nitrides have higher energy than analogous orbitals of oxygen in metal oxides. Consequently, in nitrides lower energy is needed to excite electrons to the conduction band. Tantalum nitride (Ta_3N_5) also has been identified as an active photocatalyst for water splitting. In 2013, Zhen et al. reported a template-free synthesis of Ta_3N_5 nanorod, which was modified with $Co(OH)_x$ to be used as anode for photo electrochemical cell to split water. [174] Somewhere else, reported the Mg^{2+} and Zr^{4+} -modified Ta_3N_5 by partial substitution, which leads to the apparent decrease in onset potential for PEC water oxidation. [175] Such modification could be applied to other semiconductors in order to enhance photocatalytic activity. Oxynitrides and graphitic carbon nitrides ($g-C_3N_4$) combination with the narrow band gap of 2.7 eV have been utilized as photocatalysts to produce hydrogen due to their conduction band position shallower than hydrogen evolution potential and a valence band potential higher than the oxygen evolution potential. Hence, $g-C_3N_4$ could produce hydrogen from water under visible light (<540 nm) exposure in the presence of a sacrificial agent (oxidizing agent) without the assistance of any noble metal. However, pristine $g-C_3N_4$ shows a low affinity towards photocatalytic reactions. Wang et al. [176] have first time reported a graphitic semiconductor that was synthesized from cyanamide, which exhibited absorption in the visible light region and continued hydrogen production for 75 h. Band gap engineering for the $g-C_3N_4$ made to enhance the photocatalytic properties by in-cooperation of the non-metal (i.e., S, F, B, P) [177] and metal doping (i.e., Pt, Pd, Fe, Zn, Cu). [178] Furthermore, the degree of charge separation in $g-C_3N_4$ can be enhanced by application of the conductive graphene, carbon nanotubes, and reduced graphene oxide.

1.11.1.1. 12 Plasmonic material induced metal oxide photocatalysts

Ebbesen et al [179] introduced a new class of optoelectronic materials in the form of plasmonic photocatalytic materials that stimulated research in photocatalysis due to their good light harvesting qualities along with their BG breaking effect and sensitizer effect (Figure 1.20). To improve photocatalytic efficiency (due to the recombination of photo electrons and photoholes) and visible light response in photocatalytic water splitting process with nice stability, plasmonic photocatalytic materials are introduced. Because most commonly available and stable oxides have a wide BG, which allow them to absorb UV light,

and short BG materials did not sustain photoactivity for a long time. [180] SPR materials have two major parts: (1) nanoparticles of novel metals with localized surface plasmonic resonance (LSPR); and (2) Schottky junction at the junction of noble metal and semiconductor/polar material (support/carrier). In noble metal carried on semiconductor/polar material, LSPR adds on the assistance of the enhanced local heating effect, LSPR- powered e/h generation, enhanced UV-Vis absorption, reduced e/h diffusion length, enhanced local electric effect and molecular polarisation effect, quantum tunnelling effect, high catalytic effect, to the main photocatalytic unit. Hence, NPs of noble metals act as the thermal redox reaction-active centres on catalyst that can trap, scatter, and concentrate light and enhance the number of active sites, rate of electron-hole formation by providing a fast lane for charge transfer on the semiconductor surface. Few of the prominent members of this class are Au@ZnFe$_2$O$_4$, [181] Ag/TiO$_{2-x}$N$_x$, [182] Au /CuWO$_4$ [183], Au/ZnO [184], Au/TiO$_2$ [185], Au@ carbon quantum dots [186] etc, as shown in Figure 1.21a, 1.21b, 1.21c and 1.21d.
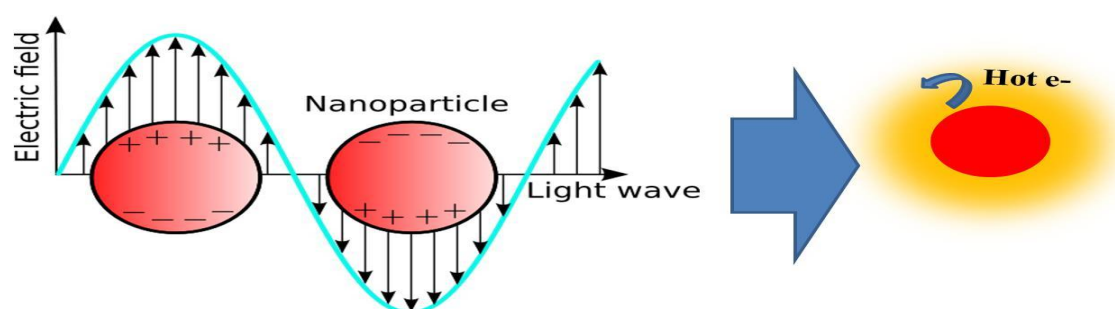
Figure 1.20 Schematic presentation of the localized surface plasmonic resonating electron of a noble metal. [181]
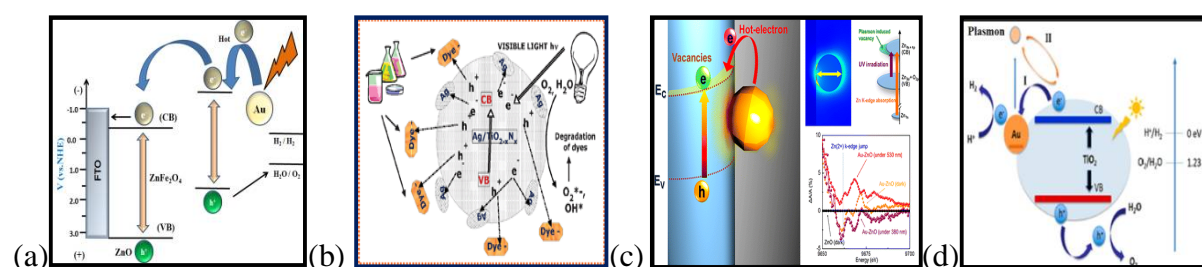
Figure 1.21 Representative examples of the surface activation by noble metal on catalytic surface by plasmonic photocatalysis in **(a)** Au@ZnFe$_2$O$_4$. A hot electron is transferred from CB of Au to the ZnFe$_2$O$_4$ and the same electron jumps into the CB of ZnO. [181] **(b)** Surface modification of Ag/TiO$_{2-x}$N$_x$.[182] **(c)** Au/ZnO, heterojunction between Au nanoparticles and ZnO semiconductors [184] and **(d)** Au/TiO$_2$, where pathway I shows the extraction of photo-generated electron from TiO$_2$ conduction band to Au NPs and pathway II shows the coupling of extraction of TiO$_2$ and surface plasmon of Au. [187]

Among various strategies to overcome fast charge recombination that result in low photocatalytic efficiency, [188, 189] plasmonic photocatalysis is the most promising approach to promote charge separation and visible light absorption [190,191]. Noble metal nanoparticles of Au [192-195], Ag [196] and Pd [197] have been applied to improve visible and near infrared (NIR) absorption and generate surface plasmon resonance (SPR) hot electrons.[191] The plasmonic properties of the metallic nanoparticles (normally Au Ag, Pd, Pt, Cu, etc) are very attracting due to their ability to promote catalytic reactions. Suitable photocatalyst combines an ability to dissociate water molecules with a band gap that absorbs light in the visible range and also enhance their stability in water and sunlight.

1.11.1.1.13 Z-Scheme Photocatalysts

Z-scheme photocatalysts has subsequently turned to achieving more efficient utilization of the visible light by widening the band of photo phonon-absorption and increasing the quantum efficiency of the photocatalyst. This can happen by combining the two wide band oxide photocatalysts (oxygen evolution reactant (OER) and hydrogen evolution reactant (HER)) in the redox pair of an electrolyte, one whose VB maxima exists below the oxidation potential of water is suitable for O_2 production and another with CBs that exist in the upper side of the reduction side of the water, is suitable for H_2 production, under the redox electrolyte system and light irradiation. This scheme is known as "Z-scheme or Tandem photocatalysis" that used for achieving the overall water splitting, which can show the similarity with the photosynthesis process occurs in the plants. To imitate the natural photosynthesis process of the green plants, where, the photosystems I and II harvest 700 and 680 nm photons, respectively, to oxidize water into O_2 and reduce water to generate glucose under sunlight, the artificial photosynthesis of the water was performed using photocatlyst in electrolyte medium. Similarly, the Z-scheme includes two step-photoexcitation using two different semiconductor powders electrodes (one having a VB position suitable for oxidation of water and other do reduction of water in a reversible donor/acceptor pair (so-called shuttle redox mediator) electrolyte as shown by Equations 6 to 9 and Figures 1.22a and 1.22b. The H_2 evolution process is the forward reaction (acceptor converted into donor) occurred due to the reduction of protons by CB electrons coupled with the backward reaction where, oxidation of water observed by the VB holes and oxidation of the donor to acceptor.

$2H^+ \rightarrow 2e^- + H_2$ (Photoreduction of H$^+$ to H$_2$) .... (6)

$D + nh^+ \rightarrow A$ (Photoreduction of D to A) .... (7)

$A + ne^- \rightarrow D$ (photoreduction of A to D) .... (8)

$2HO^- + 4h^+ \rightarrow O_2 + 4H^+$ (photooxidation of OH$^-$ to O$_2$) .... (9)
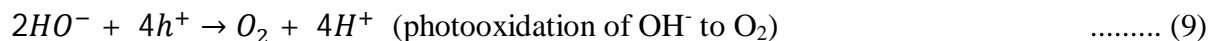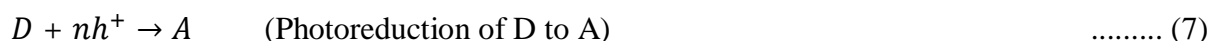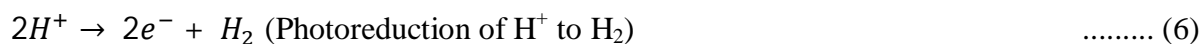
Few important Z scheme systems are discussed as follows:
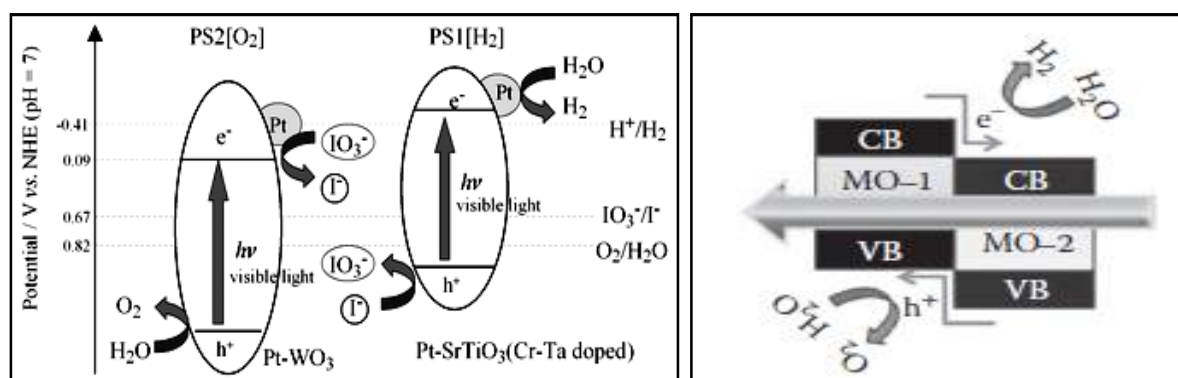
Figure 1.22 Z-scheme systems for photoelectrochemically water splitting by **(a)** two-photon process with a visible light response for Pt-WO$_3$ and Pt-SrTiO$_3$ (Cr-Ta doped) in mediator IO^{3-}/I$^-$. [199] **(b)** Combination of MO-1 and MO-2 for overall water splitting.

Kransnovskii and Brin [198] in 1962 reported the first case of Z-scheme water splitting by using the semiconductor such as TiO$_2$ and WO$_3$ in the presence of Fe^{+3}/Fe^{2+} as an electron acceptor. Simlarly, the system consisting Pt/SrTiO$_3$:Cr/Ta, Pt/WO$_3$ and IO^{3-}/I$^-$ redox couple shows that the QY is 0.1% at 420.7 nm. [199] Tabata et al. in 2010 [200] used the system Pt/ZrO$_2$/TaON and Ir/Rutile-TiO$_2$/Ta$_3$N$_5$ in the mediator IO^{3-}/I$^-$ for overall water splitting. In the process of the development of the better Z-scheme water splitting systems by studying various systems it was found that photocatalyst works efficiently in the presence of a shuttle redox mediator by creating active sites to promote surface chemical reactions and suppressing backward reactions involving redox mediators (Kudo and Miseki in 2009). [201] Where the redox cycle of the mediator challenges the reduction or oxidation process of water at the hydrogen and oxygen evolution sites. Sasaki et al in 2009 [202] includes Ru/SrTiO$_3$ and BiVO$_4$ as hydrogen and oxygen evolution catalyst (at pH = 3.5 maintained using H$_2$SO$_4$), respectively with 1.7% apparent efficiency and without an electron mediator. The results indicates that an inter-particle electron transfer occured between the two catalyst (Figure 1.23 a).
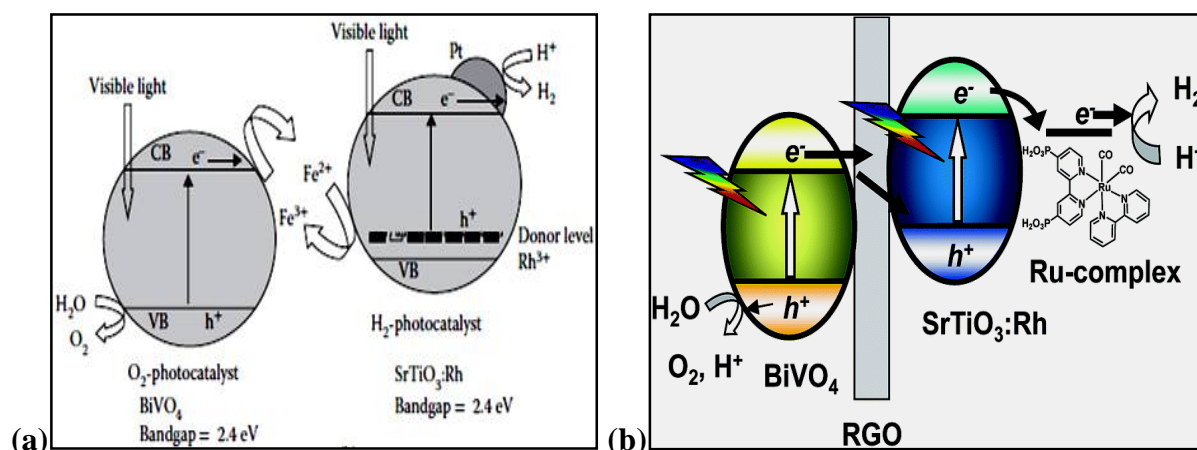
Figure 1.23 Schematic presentation of Z-scheme solid-state photocatalytic water splitting using **(a)** BViO$_4$ and SrTiO$_3$:Rh in mediator Fe^{2+} and Fe^{3+}. [199] and **(b)** cocatalyst Ru-complex ([Ru (2,2′-bipyridine) (4,4′-diphosphonate-2,2′- bipyridine)(CO)$_2$]$^{2+}$) associated with SrTiO$_3$:Rh (4%Rh) as a H$^+$ reduction photocatalyst coupled with BiVO$_4$ as a water oxidation photocatalyst in presence of the reduced graphene oxide as a solid-state electron mediator. [203]

A Z-scheme system powered photocatalytic water splitting reaction under visible light irradiation was also well demonstrated by utilizing a combination of a metal complex catalyst loaded reduced graphene oxide (RGO) with the semiconductor photocatalyst. Electrocatalyst Ru-complex [Ru(2,2-bipyridine) (4,4-diphosphonet-2,2-bipyridine)(CO)$_2$]$^{2+}$ loaded SrTiO$_3$:Rh (4 % Rh) and coupled with BiVO$_4$ to be worked as a H$^+$ reduction photocatalyst and water oxidation photocatalyst, respectively and RGO as a solid state electron transfer mediator, as shown by Figure 1.23 (b). Ma et al. in 2016 [204] also investigated a nanocomposite of C$_3$N$_4$/ RGO/bismuth tungsten oxide (Bi$_2$WO$_6$) as an effective electron transfer system foe cleavage of water. And, this system show much higher hydrogen production than the pristine samples, as shown in Figure 1.24 (a). Some other systems with parallel characters have also been investigated i.e. C$_3$N$_4$/BiVO$_4$ [205] and C$_3$N$_4$/AgPO$_4$.[206] Katsumata et al. in 2014 [207] studied a WO$_3$/C$_3$N$_4$ composite, and this composite with (Triethylene acetic acid) TEA as an electron donor was demonstrated for Z-scheme-type hydrogen production (AQY: 0.9% at 405 nm).
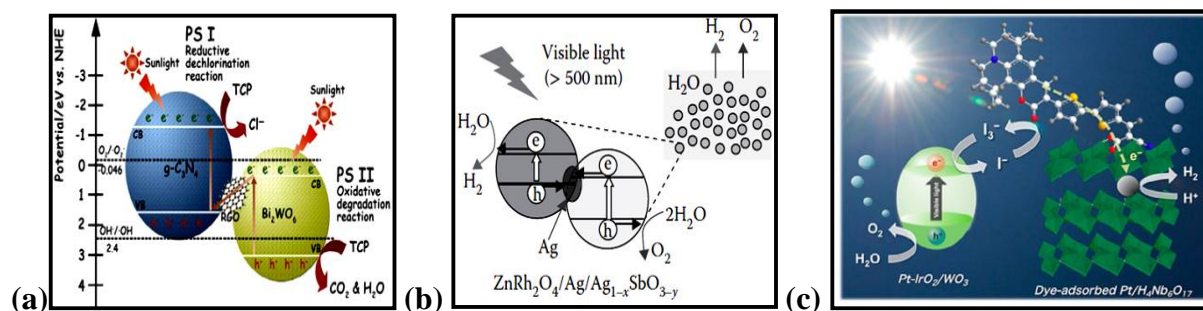
Figure 1.24 (a) RGO mediated C_3N_4-$BiWO_4$ hybrid Z-scheme-type photocatalyst [204] **(b)** Ag-embedded solid solution $ZnRh_2O_4/Ag/Ag_{1-x}SbO_{3-y}$ [208] and **(c)** Z-scheme-type organic-inorganic composite system for photocatalytic hydrogen production. Dye-sensitized nanosheets with WO_3 hybrid system. [211]

Kobayashi et al in 2014 [208] observed {$ZnRh_2O_4/Ag/Ag_{1-x}SbO_{3-y}$} system, where Ag acted as a solid state electron mediator for the electrons transfer from the CB of $Ag_{1-x}SbO_{3-y}$ to the VB of $ZnRh_2O_4$. The system simultaneously produced H_2 and O_2 from pure water at a molar ratio of ~2:1 under irradiation with visible light at 500 nm (Figure 1.24b) Gratzel [209] discussed the Z-scheme-type electron transfer for a complete water-splitting system, using a dye-sensitized photocatalyst. This system used a mesoporous WO_3 film as a OER catalyst for oxygen production, and a dye-sensitized mesoporous TiO_2 film as a catalyst for hydrogen generation.

Abe et al. in 2009 and 2013 [210, 211] studied the powder-type photocatalytic Z-scheme reaction with a coumarin-based dye-sensitized Z-scheme water-splitting system and iridium oxide (IrO_2)-Pt/ WO_3 and $Pt/H_4Nb_6O_{17}$ as photocatalysts in I^-/I^{3-} the mediator. It showed the complete water splitting under visible light irradiation with (Apparent quantum yield) AQY 0.05% at 480 nm (Figure 1.24c).

1.11.1.1.14 Doped metal oxide

When the BG energy of the metal oxide becomes smaller, the CB edge shifts towards positive side [212]. Thus, the CB edge of metal oxides having a small BG energy tends to locate quite close to the redox potential of H^+/H_2 redox couple (0 eV vs NHE). In some cases, it shifts to more positive potential than the redox potential of H^+/H_2 and loses their ability to reduce H^+ into H_2. A large amount work has been done to develop visible light responsive metal oxide photocatalysts such as the chemical doping of TiO_2 with transition metal ions or non metals

[213]. Various dopants including metal ions such as transition metals (Cu, Co, V, Mn, Fe, Zn, Ti, etc) [214], Cr [215], In [216], Ni [217], Mo [218], Ti [219, 220], Sn [221-223] and Fe [224, 225] and non-metal elements such as nitrogen [226], sulphur [227-228] silicon [229-230], boron [231], fluorine, phosphors, and carbon [232], as shown in Figure 1.25. Transitional metal ion doping and rare earth metal ion doping have been extensively investigated for enhancing TiO_2 photocatalytic activities [233-235]
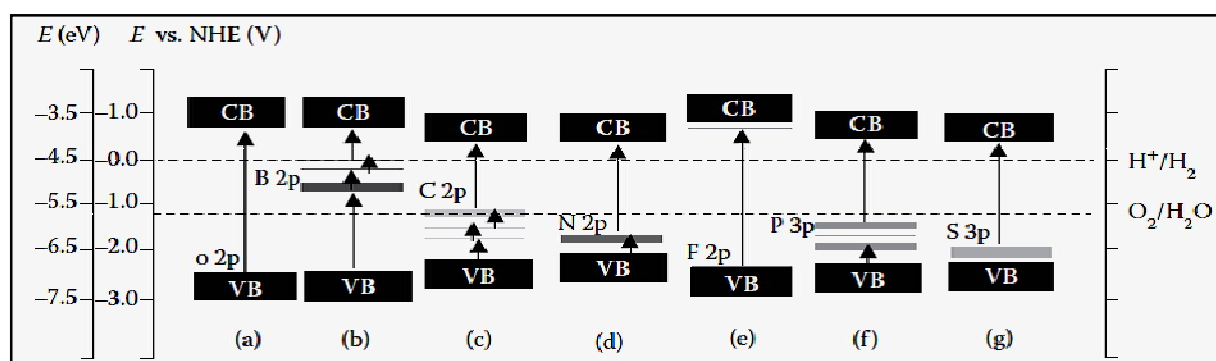
Figure 1.25 Effect of nonmetal element monodoping on band structure of $SrTiO_3$. **(a)** Undoped $SrTiO_3$, **(b)** one B atom doped $SrTiO_3$ at 4.167 atom%, **(c)** one C atom doped $SrTiO_3$ at 4.167 atom%, **(d)** one N atom doped $SrTiO_3$ at 4.167 atom%, **(e)** one F atom doped $SrTiO_3$ at 4.167 atom%, **(f)** one P atom doped $SrTiO_3$ at 4.167 atom%, and **(g)** one S atom doped $SrTiO_3$ at 4.167 atom%. The VB maximum and CB minimum values are given with respect to the NHE potential (V) and energy with respect to vacuum (eV). [236]

Since the discovery of the Fujishima and Honda for the UV light-driven photocatalytic water splitting with a promising photo-anode TiO_2 and Pt -cathode, the TiO_2 has became a widely studied material for many photocatalytic reactions are studied due to its high chemical stability and tenability of the electronic energy band gap.
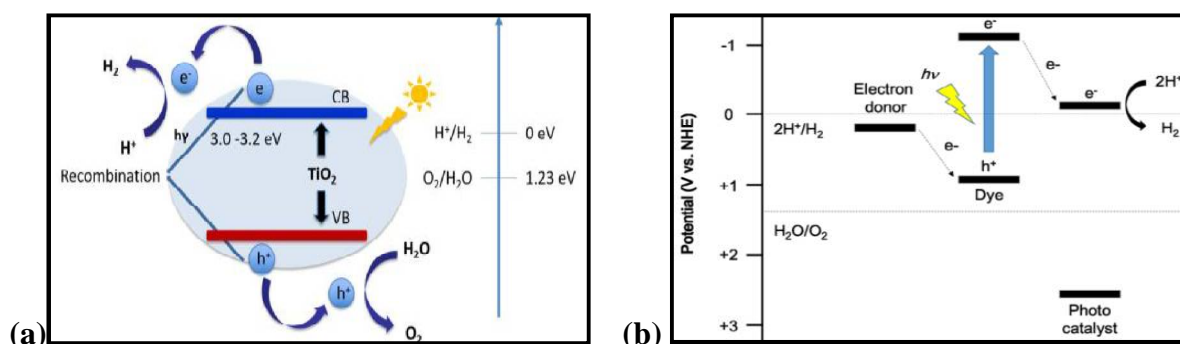
Figure 1.26 (a) A schemaic band gap illustration of TiO_2 [237] and **(b)** dye sensitized-photocatalysts for hydrogen production (water-splitting system using organic-inorganic composites).

The another method to extend the photocatalytic activity of TiO_2 to visible light region is by making solid state solution with metal oxide of small band gap or doping with non metals. The nice photocatalytic hydrogen evolution of $Pt-N-TiO_2$ over the pure TiO_2 and $N-TiO_2$, was investigated in an aqueous media in the presence of 20% ethanol as an electron donor under UV-light irradiation (Figure 1.26 a). Performance photocatalyst $Pt-N-TiO_2$ nanotubes was highly is the synergetic with the three time treated TiO_2 Degussa P-25, namely $Pt-N-TiO_2$ provides an increase in total production of hydrogen compared to the material TiO_2 Degussa P-25 and $N-TiO_2$. [237]

1.11.1.1.14 .1 Doping and defects in ZnO

In the recent years, much attention has been focused on wide band gap semiconductors materials because of their excellent potential for blue light emitting devices, short-wavelength laser diodes and detectors in UV-blue spectral region. Wide band gap semiconductor ZnO is gaining much importance for the possible application due to the capability of ultraviolet lasing at room temperature and possibilities to engineer the band gap. In order to attain the potential offered by ZnO, both high-quality n-and p-type ZnO are essential. But it is very difficult to obtain the bipolar carrier doping (both n and p types) in wide-band-gap semiconductors such as GaN and II-VI compound semiconductors including ZnS, ZnSe, and ZnTe. Unipolar doping has not been a surprising issue in wide-band-gap semiconductors: ZnO, GaN, ZnS, and ZnSe are easily doped to n-type, while p-type doping is difficult. All undoped ZnO to date has been found to be n-type, with donor concentrations typically around 1017 cm^{-3} for high-quality material. The situation is opposite for ZnTe where p-type doping is easily obtained, while n-type doping is difficult. The main characterization techniques used to find the shallow electrical defects in semiconductor materials are photoluminescence and temperature dependent Hall Effect measurements.

1.11.1.1.14 .1.1 N-type doping

ZnO has wurtzite structure, excess zinc is always found in ZnO. Due to this zinc excess, ZnO is a non-stoichiometric compound and n-type semiconductor. Undoped ZnO shows intrinsic n-type conductivity with high electron densities of about 10^{21} cm^{+3} value. Zinc interstitials Zn_i and the oxygen vacancy V are known as the dominant native donor in unintentionally ZnO film. But still it is debatable issue. Photoluminescence and temperature dependent Hall studies of electron irradiated ZnO have shown that zinc is the most likely candidate for purely

lattice-related dominant shallow donor, with an activation energy about 30-50 meV. It has been argued that the n-type conductivity of unintentionally doped ZnO film is only due to hydrogen (H), which is treated as a shallow donor with activation energy of 31 meV instead of Zn_i. This assumption is valid because hydrogen (H) is always present in all growth methods and can easily diffuse into ZnO in large amounts due to it large mobility. Hydrogen has been considered as a shallow donor candidate, much research has been done on hydrogen (H) in ZnO. During seeded chemical vapor transport (SCVT) growth of ZnO, it has been shown that hydrogen with activation energy 39 meV acts as main donor. This donor disappears through on annealing process [238, 239]. N-type doping of ZnO is relatively easy as compared to p-type doping. Group III elements Al, Ga and In as substitutional elements for Zn and group-VII elements Cl and I as substitutional elements for O can be used as n-type dopants. Doping with Al, Ga, and In has been attempted by many groups, resulting in high-quality, highly conductive n- type ZnO films. Al-doped ZnO films were grown by MOCVD. The films obtained through this method is high by conductive with minimum resistivity as compared to Ga- doped ZnO films by Chemical-vapor deposition [239-240].

1.11.1.1.14 .1.2 P-type doping

It is very difficult to obtain p-type doping in a wide band gap semiconductors. Acceptors in ZnO can also take place from both lattice defects and impurity atoms. The oxygen interstitial O_i and zinc vacancy V_{zn} are both known to be acceptors in ZnO. P-Type doping in ZnO may be possible by substituting either group-I elements (Li, Na, and K) for Zn sites acting as shallow acceptors and group-V elements (N, P, and As) are found to act as deep acceptors on O sites. It was shown that group-I elements could be better p-type dopants than group-V elements in terms of shallowness of acceptor levels. However, group-I elements tend to occupy the interstitial sites, due to their small atomic radii, rather than substitutional sites, and therefore, they can act as donors instead of acceptors. Moreover, significantly larger bond length for Na and K than ideal Zn-O bond length (1.93 Å) induces lattice strain, increasingly forming native defects such as vacancies which compensate the shallow dopants. Group V elements except N, both P and as, have a larger bonds lengths. That's why they are likely to form antisites to avoid the lattice strain. Unfortunately, for p-conduction these elements have a tendency towards antisite formation, i.e. they can substitute not only oxygen but also zinc atoms, in which case they act as donors. Nitrogen (N) appears to be good candidate for a shallow p-type dopant in ZnO with smallest ionization energy, although N is not soluble in ZnO, and doping can be achieved by ion implantation [239-241].

1.11.1.1.15 Dye-sensitized photocatalysts

Dye-sensitized photocatalytic water-splitting systems (dye-inorganic semiconductor) may be an alternative for hydrogen production under visible light irradiation. By using the visible-light absorption of dye molecules, photo-excited electrons can be efficiently transferred to inorganic semiconductors, and hydrogen can be produced by these electrons. Since the dye molecules are used to absorb the visible light, the inorganic semiconductors only need to be UV-responsive materials (>3.0 eV). As it is possible to separate charges from the dye to the inorganic semiconductor over a long distance, charge separation is easier than that in a inorganic- inorganic photocatalyst. In addition, since the photon energies absorbed can be changed by modification of the dye molecule, various inorganic semiconductors can be used in dye-sensitized photocatalytic water-splitting systems. Figure 1.26b shows two types of organic-inorganic composite photocatalysts. The mechanism of dye-sensitized photocatalysts is generally similar to that of dye-sensitized solar cells. The dye reaches the excited state by photoexcitation. The injected electrons travel to the surface of the inorganic semiconductor (or move to the co-catalyst) and react with protons to produce hydrogen (Figure. 1.26b). After that, electrons are injected from the excited state of oxidation potential of the dye to the CB of an inorganic semiconductor with a lifetime of several hundred femtoseconds [242-245].

1.12 Zinc Oxide

The native properties of wide-band-gap semiconductor (WBGS Eg=3.37eV) ZnO such as large exciton binding energy (~60 MeV) over TiO_2 (~6MeV) and GaN (~21 MeV), bio and complementary metal oxide semiconductor (MOS) compatibility, abundant availability, deep penetration power, efficient excitonic emission at room temperature [246] and short diffusion length for incident photon than TiO_2, made ZnO superior to others oxides of the same class. Furthermore, the 10 to 100 times greater carrier mobility of ZnO than the same of TiO_2. [247] It has the one of its kind optical and electrical properties, which can be used in number of applications. These characteristics empowered this compound as an extremely attractive material that to be used in versatile applications in optoelectronics, solar cell [248], SAW (surface acoustic wave) devices [249], gas sensors [250], UV photo detectors, laser diodes [251-252] and information storage device, heating mirrors, transparent electrodes [253] and so on.

(a)　　　　　　　　　　　(b)
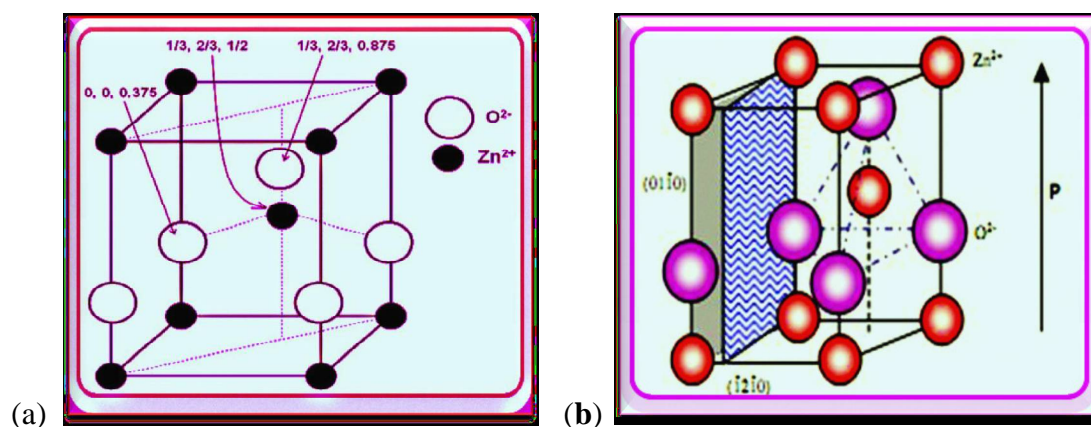
Figure 1.27 (a) Unit cell with ionic positions of 'Zn' & 'O' atoms and **(b)** Wurzite crystal structure with tetrahedral symmetry.

After the discovery of ZnO in 1930s, it come into limelight in mid 1950's but in 1970, researchers start losing interest in the material due to its limitation of p-type doping. Subsequently, advancement in the form of nanostructuring of the ZnO using different growth methods (such as magnetron sputtering, reactive evaporation, chemical vapor deposition, pulsed laser deposition [254], spray pyrolysis [255-257], aqueous chemical method [258], chemical bath deposition method [259], and electro deposition method [260]) in the mid of 1990s, reawakened the ZnO oriented research. Therefore, a new spring season of the ZnO research begins with the production of high quality p-type conducting ZnO nanomolecular devices for large number applications. Generally, zinc oxide crystallizes in two major forms, hexagonal wurtzite and cubic zinc blende with different parameters. The tetrahedral symmetry plays a vital role in deciding polarity along hexagonal axis, which gives rise to the piezoelectric property. The structure of ZnO, can be described as a number of alternating planes composed of tetrahedraly coordinated O_2^- and Zn^{2+} ions, stacked alternately along the c-axis and are shown in Figures 1.27a and 1.27b. The fundamental properties of ZnO are mentioned in Table 5. The most important band structure property of ZnO is that it possesses a direct band gap character. The lowest conduction band is s-type and the highest valence band is p- type with direct inter band transition occurred at the Brilliouin zone center, with k=0. The valence band is split by crystal field and spin orbit interaction into three states

named A, B, and C, which are associated with the free exciton binding energy as 63, 50, and 49 meV, respectively [261]. The undoped ZnO usually demonstrates n-type conductivity due to the presence of either Zn interstials or oxygen vacancies, [262] which is not suitable for device applications. High resistivity that results in the reoxidation of the zinc at ambient temperature, which may removes the source of conductivity. Therefore, a stable conductivity can be achived by introducing the elemental impurities into ZnO lattice. Table 6 represented the change in electrical properties with doping content of the different dopant element, carrier concentration and resistivity, etc.

Table 5 Physical properties of wurtzite ZnO material

Sr.No	Properties at 300K	Value	References
1	a	3.2496 (nm)	[263]
2	c	5.2042 (nm)	[263]
3	a/c	1.6018	[263]
4	u	0.3819565	[263]
5	Density	5.606(gm/cm^3)	[263]
6	Stable Phase	Wurtzite	[264]
7	Melting Phase	2248K	[264]
8	Bond Length	1.977μm	[264]
9	Thermal Conductivity	0.6, 1-1.2	[264]
10	Refractive Index	2.008- 2.009	[264]
11	Static Dielectric Constant	8.7	[264]
12	Intrinsic Carrier Conc.	<10^6 cm^3	[264]
13	Exciton Binding Energy	60 meV	[264]
14	Electron effective mass	0.24	[264]
15	Electron mobility at 300K	200cm^2/vs	[264]
16	Hole effective mass	0.59	[264]
17	Hall mobility at 300K	5-50cm^2/Vs	[264]
18	Cohesive Energy	1.89eV	[264]
19	Piezoelectric coefficient	0.27	[264]

Table 6 Effect of different dopants on electrical properties of ZnO nanomaterial

Doping Element	Doping Content (%)	Resistivity (10^{-4} cm)	Carrier Concentration (10^{20}cm^{-3})
Al	1.6-3.2	1.3	15
Ga	1.7-6.1	1.2	14.5
B	4.6	2	5.4
Y	2.2	7.9	5.8
In	1.2	8.1	3.9
Sc	2.5	3.1	6.7
Si	8	4.8	8.8
Ge	1.6	7.4	8.8
Ti	2.0	5.6	6.2
Zr	5.4	5.2	5.5
Hf	4.1	5.5	3.5
F	0.5	4	5

Doping of III groups impurities (substitutes for zinc atoms) like B [265], Al [266], Ga [267], In [268], Zr or VII group impurities (substitutes for oxygen atoms) like F, Cl, and I [269] to the ZnO lattice, play an important role in enhancing the quality of the ZnO. The doping leads to increase the carrier concentration and increase the concentration of the conducting electron that leads to reduce the resistivity. However, the excess of doping may generate the scattering centre by use of ionized impurity in ZnO lattice and leads to decrease the electron mobility. As a result the amount of doping must be controlled. In the last two decades, transparent conducting ZnO nanomaterial with resistivity's of the order of $10^{-4}\Omega$ cm, were prepared by impurity doping. The minimum resistivities and maximum carrier concentrations obtained for the ZnO nanomaterial prepared with the optimal doping contents for various doping elements were summarized in Table 6. [269] Actually, doping with group III elements have been attempted by many researchers. But it is very difficult to obtain p-type doping for wide band gap ZnO. It plays significant resistance for p-type doping. It appears that the most promising dopants for p-type materials are the group I elements like Li [270, 271], Na, K [272] and for Zinc sites they acting as shallow acceptors and group V elements like N [273, 274], P [275] and As sites which acted as deep acceptors for oxygen sites. Literature review [276, 277] shows that group I elements show better p-type dopants than group V elements. In case of group I elements, they occupy Zinc interstials, due to their small atomic radius, rather than substitution sites. They acted as donors instead of acceptors. ZnO is a piezoelectric material which as a key characteristic for the on water splitting or hydrogen production. ZnO also is a biocompatible, and it can be used in biomedical applications with or without further

modifications. Finally, ZnO is an environmentally benign and chemically stable material so it is favorable to practical applications.

1.12.1 Synthesis of ZnO

The variety of one- (1D), two- (2D), and three-dimensional (3D) nanometric structures of the zinc oxide can be produced by using different synthesis techniques that to be used for the applications in many fields of nanotechnology. One-dimensional structures are being made up by the large number of groups including nanorods, [278-280] needles, [281] -helixes, -springs and –rings, [282] ribbons, [283] –tubes, [284-286] –belts, [287] –wires, [288-290] etc. 2D Zinc oxide can be obtained in the shape such as nanotriangles, nanoplate/nanosheet and nanopellets [291, 292] Prominent examples of the 3D structures of the zinc oxide include flower, dandelion, snowflakes, coniferous urchin-like, etc. [293-296] Above structures are results of the synthesis method opted for the fabrication of the nanomaterial and reaction conditions. Following are the most frequently used chemical methods for the nano zincoxide synthesis.

1.12.1.1 Sol gel method

The sol-gel method of the ZnO synthesis is subject to interest of researchers because of its simplicity, low cost, reliability, repeatability and relatively mild conditions of synthesis. Therefore, this method often used to modify the zinc oxide surface with selected organic compounds, as shown in Figure 1.28 a.

1.12.1.2 Precipitation method

Controlled precipitation is a widely practiced method for obtaining zinc oxide as the product with the reproducible properties. The method involves fast and spontaneous reduction of a solution of zinc salt using a reducing agent (chemical/ green from part of the plant, fungi, bacteria, etc) to limit the growth of particles with specified dimensions, followed by the precipitation of a ZnO precursor from the solution. Afterwards this precursor undergoes the thermal treatment, followed by milling to remove impurities. The limitation of this process is difficulty in breaking down the agglomerates, because the calcined powders have a high level of agglomeration of particles. The process of precipitation can be controlled by parameters such as pH, temperature and time of precipitation. Typical process of the controlled precipitation of the zinc oxide was carried out by Wang et al. [297] where, the nanometric

zinc oxide was obtained by precipitation from aqueous solutions of NH_4HCO_3 and $ZnSO_4 \cdot 7H_2O$ by the way of the following reactions (10) and (11).

$$10NH_4HCO_3 + 5ZnSO_4 \cdot 7H_2O \rightarrow 5(NH_4)_2SO_4 + Zn_5(CO_3)_2(OH)_6 + 8CO_2 + 2H_2O ...(10)$$

$$Zn_5(CO_3)_2(OH)_6 \xrightarrow{\triangle} 5ZnO + 2CO_2 + 3H_2O \qquad ..... (11)$$

1.12.1.3 Solvothermal / Hydrothermal method

The hydrothermal method is better than other chemical methods as it does not required the organic solvents or additional processing of the product (grinding and calcination) or high temperature (need temperature 100-300 °C), which makes it a simple and environmentally friendly technique. The reduction of precursor takes place in an autoclave, under the gradual heating of the substances at the temperature of 100-300 °C for several days, followed by cooling. That leads to the formation of the nuclei and its growth with diverse shapes by growth along different dimensions. The properties of the resulting crystals depending on the composition of the starting mixture, the process temperature and pressure. The high degree of crystallinity of the product, and the high purity of the material obtained, as shown in Figure1.28 b.

1.12.1.4 Polyol method

This method is used for the production of well-controlled nanoparticles with higher crystallinity using polyethylene glycol as the polyol. In this process, Polyvinylpyrrolide (PVP) is also used as a stabilizer and shape-controlling reagent in the polyol synthesis methods. The precursor is thoroughly mixed with liquid polyol and heated to the boiling point of polyol. The used polyol acts as solvent, reducing agent, and stabilizer, thereby controlling the growth of particles and also preventing the aggregation of the particles. In this method, precursor compounds such as hydroxides, oxides, nitrates, sulfates, and acetates are either dissolved or suspended in a polyol, and the reaction mixture is then heated to reflux. As the temperature is increased, the reduction potential of the ethylene glycol increases, which leads to nucleation. During the reaction, the soluble metal precursor in polyol forms an intermediate compound and reduced to the metal nuclei, which will result in metal nanoparticles. The particle size can be controlled by adding foreign nuclei for heterogeneous nucleation and increasing temperature for thermal degradation of the polyol, as shown in Figure1.28 c.

1.12.1.5 Emulsion method

Microemulsions are thermodynamically stable, clear and isotropic mixtures of water, oil, and surfactant. Quite often cosurfactant is also added in to the mixtures. The aqueous phase may contain salt(s) and/or other ingredients, and the "oil" may actually be a complex mixture of different hydrocarbons and olefins. In contrast to ordinary emulsions, microemulsions form upon simple mixing of the components and do not require the high shear conditions generally used in the formation of ordinary emulsions. The three basic types of microemulsions are: direct (oil dispersed in water, o/w), reversed (water dispersed in oil, w/o) and bicontinuous. In ternary systems, such as microemulsions, where two immiscible phases (water and 'oil') are present with a surfactant, the surfactant molecules may form a monolayer at the interface between the oil and water, with the hydrophobic tails of the surfactant molecules dissolved in the oil phase and the hydrophilic head groups in the aqueous phase, as shown in Figure1.28 d.

1.12.1.6 Green Synthesis method

The nature is a huge active bio-laboratory that comprising of bio-organisms like plants, algae, fungi, yeast, etc. which are composed of the large number of phytochemicals. These naturally occurring biomolecules have been identified as an active species for the formation of the nanoparticles with in diverse shapes and sizes. The biogenic production is a better option due to its ease of fabrication via green route with non-toxic and non-poisonous ingredients, biocompatibility, mild reaction conditions, low cost, simplicity and eco-friendly nature of the reaction, are the benefits associated with the biogenic synthesis. Therefore, this can be used as an economic and valuable alternative for the large scale production of the metal nanoparticles. The use of the bio waste materials are not only reduces the cost of synthesis but also minimizes the need of using hazardous chemicals by practicing the greener, safe and environmentally benign protocols for nanopartical fabrication. It also focuses on the computational aspects of binding of biomolecules to nanoparticles and some other applications of the biosynthesized nanoparticles in biomedical, catalysis and biosensors fields. Large number of the biological materials/tools are adopted in this method , such as fungi [298-300], bacteria [301-303], Bengal gram bean [304], yeasts [305], capsicum annuum [306], quercetin [307], biomass of oat (Avena sativa) and wheat (Triticum aestivum) [308], honey [309], plants' extract, etc. A wide range of metal NPs such as Au [310-314], Ag [315-316], TiO_2 [317], In_2O_3 [318], ZnO [319], CuO [320], etc, have been synthesized using

herbal/ plant extracts. Several plants have been explored for the synthesis of metal NPs including medicinal plants. [319] Use of plant extract and microbial cells in the synthesis of metal NPs, was triggered by existence of the several organic group/compounds such as carbonyl groups, terpenoids, phenolics, flavonones, amines, amides, proteins, pigments alkaloids and other reducing agents of the plant extract, as shown in Figure 1.28e.
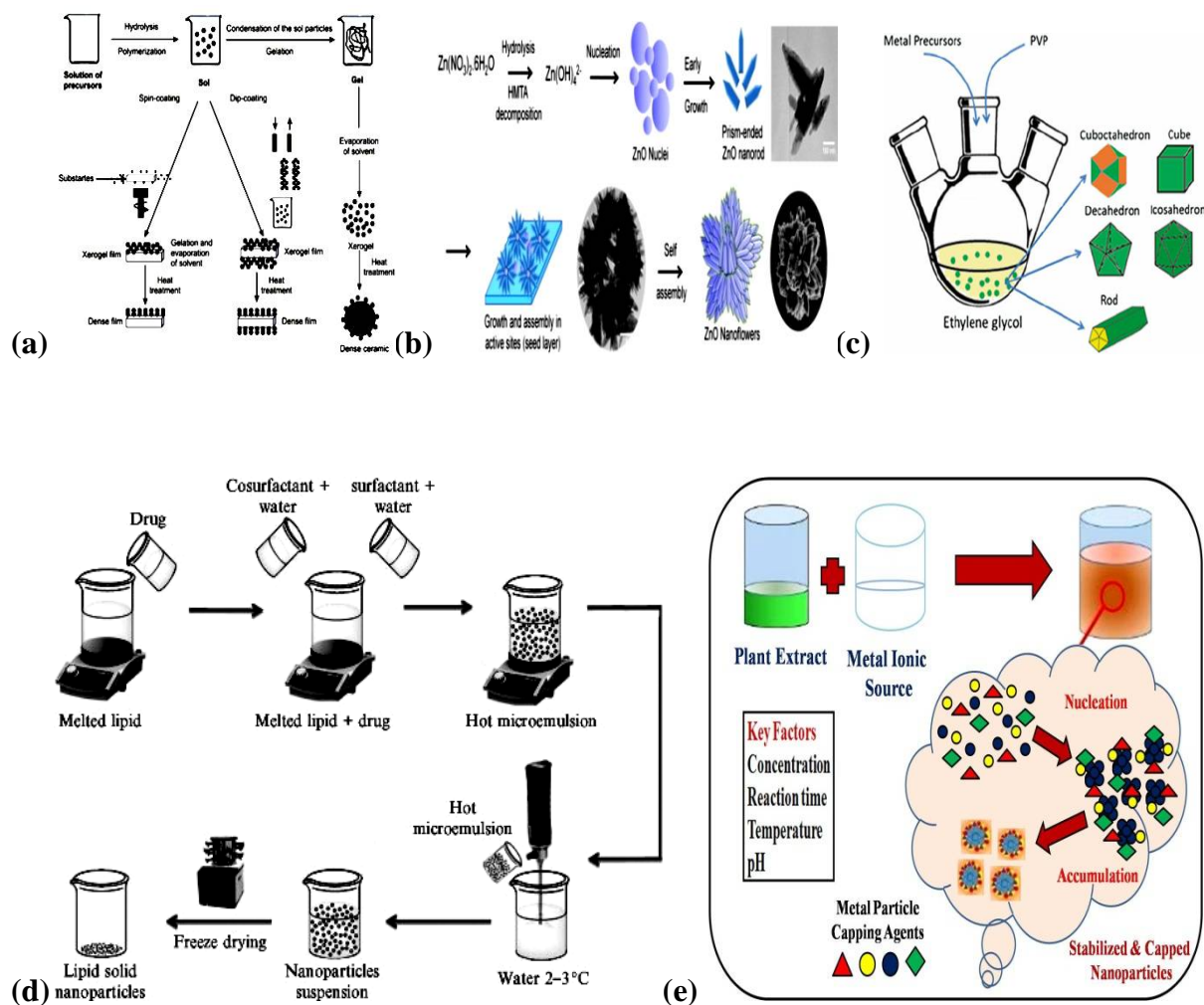
Figure 1.28 Schematic of the methods used for synthesis of ZnO **(a)** sol-gel method [321] **(b)** hydrothermal method [322] **(c)** polyol method [323] **(d)** emulsion method [324] and **(e)** green method with the formation of possible different morphologies.

1.12.2 Morphology of ZnO nanostructures

ZnO nanostructures have been attracting a great attention for their potential applications in various fields. A diversity of the ZnO nanostructures has been reported. Traditional morphologies, such as nanowires, [325-330] nanorods, [331-335] tetra pod nanorods, [336-

340] nanoribbons/belts, [341-343] etc. have been extensively reported for ZnONPs. Recently, novel morphologies like hierarchical nanostructures, [344] bridge/nail-like nanostructures, [345] tubular nanostructures, [346] nanosheets, [347] nanopropeller arrays, [348, 349] nanohelixes, [350] nanorings, [348-350] etc. have also been demonstrated. There are a variety of names describing the nanostructures, but their definitions are often arbitrary. The nanostructures usually have sizes ranging from several nanometers to a few hundred nanometers in at least one dimension. Taking nanowires as an example, they have diameters with several nanometers and lengths in micron scale. This is a reason why they are sometimes called as "one-dimensional (1-D)" nanostructures.
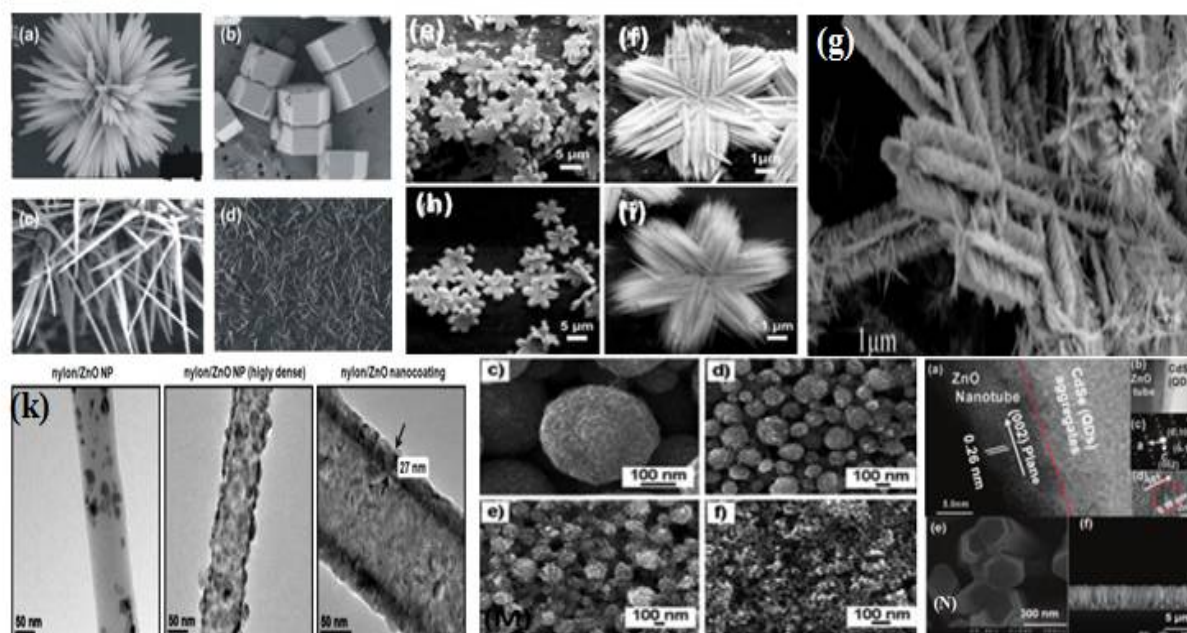
Figure 1.29 ZnO nanomolecules are fabricated in different shapes: **(a)** flower [351] **(b)** hexagonal [352] **(c)** wires [353] **(d)** tetropods [354] **(e-i)** flower [355] **(g)** brush [356] **(j)** flower [357] **(k)** particles and wire [358] **(l)** [359] **(m)** [360] and **(n)** [361]

Song etal. synthesized Zn(OH)F nanoflowers of six petals (Figures 1.29e, 1.29f, 1.29g, 1.29h, 1.29I and1.29j) [355-357] by microwave assisted ionic liquid route. Where, every petal is composed of lots of acicular nano-structure. Nanoporous ZnO is obtained by thermal decomposition of as-prepared Zn(OH)F in air, and the flower-like morphology is well retained. Ionic liquid 1-Butyl-3-methylimidazolium tetrafluoroborate is act as both the reactant and the template in the synthesis. As demonstrated in Figures l.29I, and reported by Patra etal, the growth of hexagonally shaped nanorods in a direction nearly perpendicular to

the substrate surface with a tip size of ∼50 nm and aspect ratio around 10. Formation of the Co (+2 and +3 oxidation states) doped hexagonal ZnO along the preferred *c*-axis. The doping of Co (+2 and +3 oxidation states) ions in ZnO nanorods was confirmed by presence of the absorption bands at 658, 617 and 566 nm in the UV-Vis spectra.

Figure 1.29m shows a schematic illustrating the hierarchical structure of the uniform submicrometer ZnO aggregates with almost perfect spherical shape and smooth surface can be seen in Figure 1.29m(c). Three other samples were prepared at slightly higher temperatures, and their SEM images (Figure 1.29m) reveal deteriorating aggregation and increasing surface roughness of the aggregates. All of the ZnO samples exhibit the hexagonal Wurtzite structure with lattice constants a=0.32 nm and c=0.52 nm. In Figure 1.29 n Chouhan etal. used the surfactant (CTAB)-controlled low cost fabrication of the ZnO NRs via reverse-micelles synthesis (Figure 1.29 n). Current work is focused on the performance of the nanomolecular photoelectrode of ZnO NRs by gradual surface modification for hydrogen production efficiency.

1.13 Application of nano zinc oxide in water splitting

Although, the oxide photocatlysts were used to split water for solar hydrogen production. But the most of powdered photocatalyst systems have wide band structures. Therefore they used to show low efficiency for water splitting. As a photoelectrode material ZnO has a limitation of a large band gap that prevents visible light absorption and show chemical in stability under both anodic and cathodic bias. Kyoung Shin Choi's group recently fabricated the cobalt oxide-phosphate cocatalyst that can be photo deposited on to the ZnO nanorod arrays [362] for improving the photocurrent onset potential by 0.23 V. Photodeposition was advantageous over electrodeposition, as it deposits the co-catalyst at locations with high photohole concentrations. Sun et al. also demonstrated the improved cathode photocurrents from the n-type ZnO nanowire arrays on p-Si wafers. The increased photocurrent was attributed to enhanced photocurrent carriers' separation at the n-ZnO/p-Si interface and reduction in light scattering from the nanorods surface. [363] Previously, Jin Zhang's group had demonstrated that non-sensitized nanoparticulate ZnO photoanodes supported photocurrents up to 175 mA cm^2 at 1.6 V (NHE) applied potential at pH = 7.4 and AM 1.5 illumination. [364]

A layered structure of $In_2O_3(ZnO)_m$ (m=3/9), crystallizes in a layered structure containing sheets of the octahedral InO_6 units alternating with the sheets of tetrahedral and trigonal-

pyramidal ZnO_4 units.[365] The band gaps for the material is 2.6 and 2.7 eV for m=3 and 9, respectively. Under visible light irradiation, both materials evolve small quantities of H_2/O_2 from aqueous solutions of methanol / $AgNO_3$ as electrolytes. [366]

Heterostructure $(ZnO)_1/(CdS)_{0.2}$ demonstrates the highest H_2 evolution rate of 1805 mmol h^{-1} g^{-1} among diffrent ZnO/CdS heterostructures, (Figure 1.30a) which has 14- and 40- times higher value than that of the pure CdS and ZnO photocatalysts, prepared by parallel synthesis routes. H_2 evolution from ZnO/CdS heterostructures gradually decreases with the increasing CdS molar ratios though their absorption edges are further extended. This is the possibly due to the decrease in oxidation reaction sites on the ZnO surface by post-deposited CdS. The optimal loading content of Pt was found to be 1 wt%, which gives the highest H_2 evolution (3870 mmol h^{-1} g^{-1}) rate and is twice that of the $(ZnO)_1/(CdS)_{0.2}$ alone. [367] It is known that Pt particles loaded on photocatalysts can trap excited electrons and act as H_2 evolution sites. (Figure 1.30 b)

Co-catalyst $Rh_{2-x}Cr_xO_3$ loaded $(Zn_{1+x}Ge)(N_2O_x)$ was studied by Lee etal., which is a solid solution between ZnO and $ZnGeN_2$ and prepared by the reaction between GeO_2 and ZnO under a NH_3 flow (20 mL min^{-1}) at 1123 K. Samples nitrided for 5-15 h under these conditions exhibit a single phase of wurtzitic $(Zn_{1+x}Ge)(N_2O_x)$, and are responsive to visible light with a band gap of ca. 2.7-2.8 eV. Modification of the optimized $(Zn_{1.44}Ge)(N_{2.08}O_{0.38})$ sample by loading with $Rh_{2-x}Cr_xO_3$ (3.0 wt % Rh, 0.2 wt % Cr) results in an effective photocatalyst for overall water decomposition with a quantum efficiency of ca. 0.20% at 420 nm. The material demonstrated the photocatalytic activity for overall water splitting under both ultraviolet (UV) and visible irradiation after surface modification with co-catalyst RuO_2. 5 wt% RuO_2 afforded the stoichiometric decomposition of the water in to the H_2 and O_2 with activities of 54.3μmol h^{-1} for H_2 and 27.5μmol h^{-1} for O_2 (Figure1.30 d). However, when the solid solution was loaded with a cocatalyst $Rh_{2-x}Cr_xO_3$ the mixed oxide consisting of 3.0 wt % Rh and 0.2 wt % Cr, the optimum activity of $(Zn_{1.44}Ge)(N_{2.08}O_{0.38})$ that increased to 414.5μmol h^{-1} for H_2 evolution and 202.3μmol h^{-1} for O_2 evolution. [368]

CdTe quantum dots sensitized nanowire of ZnO in a stable photocatalytic device dipped in a nonsacrifical electrolyte. The significant photocurrent and efficiency achieved here confirms that this structure can facilitate the stability and provide the true efficiency for the overall

water-splitting reaction in terms of the maximum photoconversion efficiency of 1.83 % which is more than 200 % higher than that of pristine ZnO nanowires. [369]
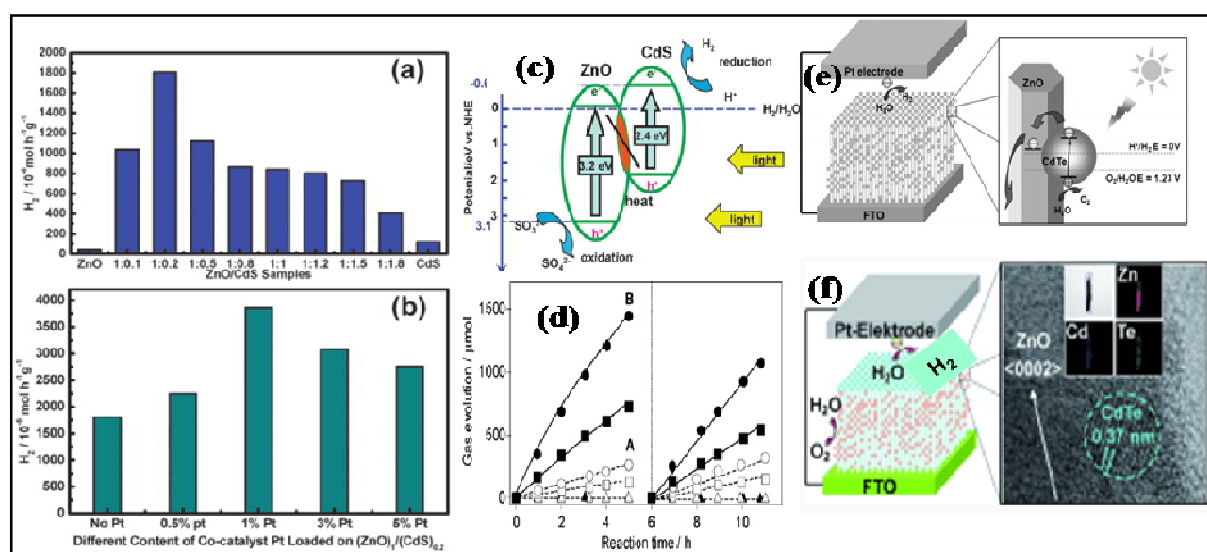
Figure 1.30 **(a)** & **(b)** H_2 evolution of the ZnO)$_1$/(CdS)$_{0.2}$ heterostructure with different content of loaded Pt. Measurement conditions: 0.2 g sample, 300 mL aqueous solution containing 0.1MNa$_2$S and 0.1MNa$_2$SO$_3$,and light source: 300 W Xe lamp [367] **(c)** Schematic of band structures in the Z-scheme mechanism in ZnO/CdS heterostructures. H_2 evolution of ZnO, (ZnO)$_x$/(CdS)$_y$ heterostructures and CdS, where x and y denote, the molar ratios of Zn and Cd precursors; **(d)** time courses of gas evolution for optimum (Zn$_{1+x}$Ge)(N$_2$O$_x$) loaded with (A) 5 wt % RuO$_2$ and (B) Rh$_{2-x}$Cr$_x$O$_3$ (3.0 wt % Rh, 0.2 wt % Cr) under UV-visible light (λ> 300 nm). Circles denote H_2 evolution, squares denote O_2 evolution, and triangles denote N_2 production and [368] **(e)** & **(f)** quantum dots of CdTe- doped ZnO for hydrogen generation using water splitting. [369]

Meda etal. have recently been reported an active RuO$_2$/GaN:ZnO system for overall water splitting. The material Ga$_{0.38}$N$_{0.33}$Zn$_{0.13}$O$_{0.16}$ (E$_g$=2.38 eV) is a solid solution of GaN (E$_g$=3.4 eV)) and (ZnO E$_g$=3.2 eV) that crystallised in a Wurtzite structure type. And its band gap depends upon the composition of the solid solution and it appeared to be due to a raised valence band edge that resulted from p-d electron repulsion of Zn (3d) and N (2p) electrons. The photocatalyst show the highest activity among the ZnO solid solutions that can use visible light up to about 450nm. After modification with RuO$_2$, Ga$_{0.38}$N$_{0.33}$Zn$_{0.13}$O$_{0.16}$ splits water stoichiometrically into H_2 and O_2 at very reasonably good rates under UV and visible light quantum yield (QE) 0.14% for 300-480 nm) light exposure. The good quantum yields of

these photocatalyst systems are exhibited for water splitting under visible light irradiation. [370-371] Cocatalyst RuO_2 can be replaced with other (Rh, Ir, and Pt) materials, [372] out of which a mixed Cr/Rh oxide is the most effective (QE=2.5%) coactalyst. [373-374]

As produced hydrogen can be used as an fuel for motor vehicles, lawn movers, cooking gas for burners, hydrogen-warmed house, fuel cell and hydrogenation reaction or generating H_2 atmosphere for chemical reactions and industrial uses for chemical synthesis, and so on. Few of the applications are illustrated by the Figures 1.31 a, 1.31 b, 1.31 c and 1.31 d. [375]
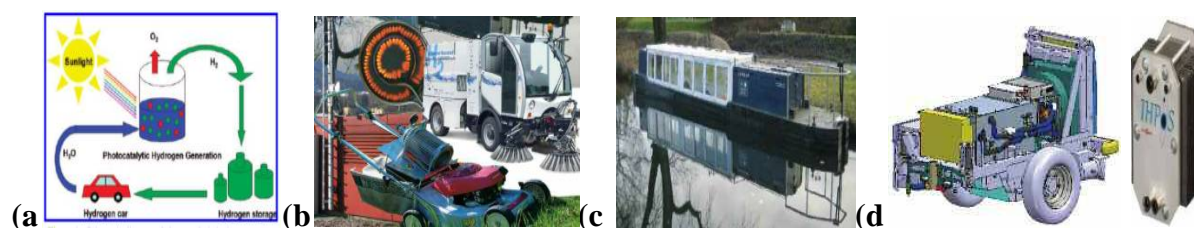
Figure 1.31 Application of hydrogen fuel as **(a)** fuel for car **(b)** fuel for hydrogen- burnner, road cleaner and loan mover **(c)** house warming (500 W commercial PEM - fuel cell by BFH-TI and CEKA AG typical applications) and **(d)** fuel cells. [375]

1.14 Scope of the Work

Day by day increasing price of conventional fuel, accompanied with the scarcity of the fuel compound the situation moving towards the energy crisis. To release the as created- energy pressure, green and abundant fuel is required and hydrogen might be the good fuel substitute. If the hydrogen (fuel with maximum efficiency~75%) generated by breaking of water using sunlight and photocatalyst, then it can assure to maintain the good health of our earth by reduce of CO_2 content. Moreover, the CO_2 content & low degradation of the chemical pollutant by using the same catalyst, adds on the metal nanoparticulated catalyst and their derivates have been attracted a great deal of attention and gained numerous achievements in the past years. This study has shown that at a definite point of their growth the particles become catalytic active and the grown up particles are showing the more catalytic properties than bulk metal. In order to fulfilling the growing demands of the versatile field, the reliable synthesis are required that can generate well-defined nanoparticles (with respect to shape and size) with a high degree of monodispersity. The synthesis of Ag and ZnO nanoparticles is carried out with specific attention to their future use in hydrogen generation from water

splitting and degradation of organic pollutants. This aim is being achieved through the green route of synthesis of Ag nanoparticles using green reductants (plant extraction i.e. TA, Tea, Fenugreek and Acacia) under the controlled synthesis conditions with respect to the time, temperature, pH as well as concentration, etc. The aqueous reduction method is currently selected for the synthesis of Ag nanoparticles because of its robust, cost effective, and efficient yield. This enables to achieve the properties such as the size, shape, solubility and surface functionality of the carefully tuned resulting nanoparticles. The diameter of the relatively monodisperse Ag nanoparticles is controlled under the range of approximately 12-40 nm by varying the nature concentration of reducing agent and time. Smaller nanoparticles obtained for higher concentration of plant extract content, because in this case more small nuclei can apparently become stabilized. This means that this method allows the formation of Ag nanoparticles of variable size that are stable under ambient conditions that is something typically and not achieved by simple chemical approaches. Such materials are being explored for many different applications, especially in catalysis. The current research work represents the development of innovative methodology of synthesis of the stable metal (Ag) and ZnO nano composites in application of the water splitting for hydrogen production reactions as well as organic pollutant (p-nitrophenol) degradation. Hydrogen production through water splitting is of great importance both from the chemical point of view and its commitment of the green fuel generation. The amounts of hydrogen production vary with the type of the reducing agent used in synthesis, the concentration nanoparticle, and the size/shape of nanocatalyst, etc. is investigated. Excelling catalytic activities of Ag and Ag-ZnO nanoparticle-based catalytic systems and nanocomposite (Pt/CdS/Co-ZnO) system over the bulk ZnO materials show a light on hydrogen production. Thus precise understanding of the mechanism of the green synthesis and their uses in the field of aforesaid applications is possible. The cost of synthesis and case of synthesis can make the use of the catalysts at industrial scale generation of hydrogen and degradation of pollutant.

1.15 REFERENCES

[1] B Johnston, MC Mayo, A. Khare **"**Hydrogen*: the energy source for the 21st century" Technovation* **(2005),** *25* (6): *569*-585.

[2] Michael Ball, Werner Weindorf, Ulrich Bünger, Chapter 10 in *"The Hydrogen Economy: Opportunities and. Challenges"*by Michael Ball and Martin Wietschel, *published by Cambridge. University Press, 24 September* (**2009),** ISBN 978-0521882163.

[3] G.P. Dunn, A.T. Bruce, H. Ikeda, L.J. Old, D. Schreiber, "Cancer immunoediting: From immuno-surveillance to tumor escape" *Nature Immunology* (**2002**), 3991-998.

[4] M. Momirlan, T. N. Veziroglu, "The properties of hydrogen as fuel tomorrow in sustainable energy system for a cleaner planet" *International Journal of Hydrogen Energy* (**2005),** 30: 795-802.

[5] A. Patsoura, D. I. Kondarides, X. E. Verykios, "Photocat- alytic degradation of organic pollutants with simultaneous production of hydrogen" *Catalysis Today* **(2007),** vol. 124, no. 3-494-102.

[6] A. Ortiz-Gomez, B. Serrano-Rosales, M. Salaices, H. de Lasa, "Photocatalytic Oxidation of Phenol: Reaction Network, Kinetic Modeling, and Parameter Estimation" *Industrial & Engineering Chemistry Research* **(2007),** 46 (23): 7394-7409.

[7] H. I brahim, H. de Lasa, "Photo-catalytic conversion of air borne pollutants: Effect of catalyst type and catalyst loading in a novel photo-CREC-air unit" *Applied Catalysis B: Environmental* (**2002**), 38 (3): 201-213.

[8] B. Serrano, H. de Lasa, "Photocatalytic Degradation of Water Organic Pollutants. Kinetic Modeling and Energy Efficiency" *Industrial & Engineering Chemistry Research* (**1997),** 36 (11): 4705-4711.

[9] Escobedo Salas, Salvador, Benito Serrano Rosales, Hugo de Lasa "Quantum Yield with Platinum Modified TiO$_2$ Photocatalyst for Hydrogen Production" *Applied Catalysis B: Environmental 140-141 (August)* (**2013),** 523-536.

[10] B. Van Ruijven, J. F. Lamarque, D. P. van Vuuren, "Emission scenarios for a global hydrogen economy and the consequences for global air pollution" *Glob. Environ.Chang.* **(2011),** 21: 983-94.

[11] H. Nezhad, "World Energy Scenarios to 2050: Issues and Options. Minnesota" *MN: State University of Minneapolis* **(2009).**

[12] H. Nezhad, "Software Tools for Managing Project Risk: Management Concepts. Vienna, VA" *Management Concepts* **(2007),** 1037-55.

[13] A. Midilli, M. Ay, I. Dincer, M.A. Rosen, "On hydrogen and hydrogen energy strategies I: Current status and needs" *Renew. Sustain. Energy Rev.* (**2005),** 9: 255-271.

[14] G.L. Chiarello, M.H. Aguirre, E. Selli, "Hydrogen production by photocatalytic steam reforming of methanol on noble metal-modified TiO$_2$" *J. Catal.* (**2010**), 273: 182-190.

[15] K. Hou, R. Hughes, "The kinetics of methane steam reforming over a Ni/-Al$_2$O catalyst" *Chem. Eng. J.* (**2001**), 82: 311-328.

[16] Q. Xie, Y. Wang, B. Pan, H. Wang, W. Su, X. Wang, "A novel photocatalyst LaOF: Facile fabrication and photocatalytic hydrogen production" *Catal. Commun.* (**2012**), 27: 21-25.

[17] J. Luo, J.H. Im, M.T. Mayer, M. Schreier, M.K. Nazeeruddin, N.G. Park, S.D. Tilley, H.J. Fan, M. Gratzel, "Water photolysis at 12.3% efficiency via perovskite photovoltaics and Earth-abundant catalysts" *Science* (**2014**), 345: 1593-1596.

[18] N.L. Wu, M.S. Lee, "Enhanced TiO$_2$ photocatalysis by Cu in hydrogen production from aqueous methanol solution" *Int. J. Hydrog. Energy* (**2004**), 29: 1601-1605.

[19] A. Steinfeld, "Solar hydrogen production via a two-step water-splitting thermochemical cycle based on Zn/ZnO redox reactions" *Int. J. Hydrog. Energy* (**2002**), 27: 611-619.

[20] N.S. Lewis, D.G. Nocera, "Powering the planet: Chemical challenges in solar energy utilization" *Proc. Natl. Acad. Sci. USA* (**2006**), 103: 15729-15735.

[21] A. Kudo, "Photocatalysis and solar hydrogen production" *Pure Appl. Chem.* (**2007**), 79: 1917-1927.

[22] Department of Energy. "Fuel Cell Technologies Office Multi-Year Research, Development, and Demonstration Plan" *Available online: http://energy.gov/eere/fuelcells/downloads/fuel-cell-technologies-office-multi-yearresearch.*

[23] Li W. X., "Photocatalysis of oxide semiconductors" *J. Aust. Ceram Soc.* (**2013**), 49: 41-6.

[24] A. Kudo, Y. Miseki, "Heterogeneous photocatalyst materials for water splitting" *Chem. Soc. Rev.* (**2009**), 38: 253-278.

[25] A.L. Linsebigler, J.T. Yates, Jr. G. Lu, "Photocatalysis on TiO$_2$ Surfaces: Principles, Mechanisms, and Selected Results" *Chem. Rev.* (**1995**), 95: 735-758.

[26] Z. Zou, J. Ye, K. Sayama, H. Arakawa, "Direct splitting of water under visible light irradiation with an oxide semiconductor photocatalyst" *Nature* (**2001**), 414: 625-627.

[27] A. Fujishima, K. Honda, "Electrochemical photolysis of water at a semiconductor electrode" *Nature* (**1972**), 238: 37-38.

[28] M. Halmann, M. Grätzel, "Energy Resources through Photochemistry and Catalysis" *Academic Press: New York, NY, USA* (**1983**).

[29] N. Serpone, E. Pelizzetti, "Photocatalysis: Fundamentals and Applications" *Wiley: New York, NY, USA* (**1989**).

[30] Y.V. Pleskov, Y.Y. Gurevich, "Semiconductor Photoelectrochemistry; Consultants Bureau" ***New York, NY, USA*** **(1986).**

[31] A. Kudo, Y. Miseki, "Heterogeneous photocatalyst materials for water splitting" ***Chem. Soc. Rev.*** **(2009),** 38: 253-278.

[32] A.L. Linsebigler, J.T. Yates, G. Lu, "Photocatalysis on TiO_2 Surfaces: Principles, Mechanisms, and Selected Results" ***Chem. Rev.*** **(1995),** 95: 735-758.

[33] Z. Zou, J. Ye, K. Sayama, H. Arakawa, "Direct splitting of water under visible light irradiation with an oxide semiconductor photocatalyst" ***Nature*** **(2001),** 414: 625-627.

[34] K. Sivula, R. van de Krol, "Semiconducting materials for photoelectrochemical energy conversion" ***Nat. Rev. Mater.*** **(2016),** 70: 15010:1-15010:7.

[35] W. Zhou, W. Li, J.Q. Wang, Y. Qu, Y. Yang, Y. Xie, K. Zhang, L. Wang, H. Fu, D. Zhao, "Ordered Mesoporous Black TiO_2 as Highly Efficient Hydrogen Evolution Photocatalyst" ***J. Am. Chem. Soc.*** **(2014),** 136: 9280-9283.

[36] A. Kay, I. Cesar, M. Gratzel, "New Benchmark for Water Photooxidation by Nanostructured Fe_2O_3 Films" ***J. Am. Chem. Soc.*** **(2006),** 128: 15714-15721.

[37] J.Y. Kim, G. Magesh, D.H. Youn, J.W. Jang, J. Kubota, K. Domen, J.S. Lee, "Single-crystalline, wormlike hematite photoanodes for efficient solar water splitting" ***Sci. Rep.***(**2013),** 3: 2681 1-2681:8.

[38] V.E. Henrich, P.A. Cox, "The Surface Science of Metal Oxides" ***Cambridge University Press: Cambridge, UK*** **(1996).**

[39] A. Walsh, Y. Yan, M.N. Huda, M.M. Al-Jassim, S.H. Wei, "Band Edge Electronic Structure of $BiVO_4$: Elucidating the Role of the Bi s and V d Orbitals" ***Chem. Mater.*** **(2009),** 21: 547-551.

[40] J.K. Cooper, S. Gul, F.M. Toma, L. Chen, P.A. Glans, J. Guo, J.W. Ager, J. Yano, I.D. Sharp, "Electronic Structure of Monoclinic $BiVO_4$" ***Chem. Mater.*** (**2014**), 26: 5365-5373.

[41] W. Lu, D. Yuan, J. Sculley, D. Zhao, R. Krishna, H.C. Zhou, "Sulfonate-grafted porous polymer networks for preferential CO_2 adsorption at low pressure" ***J. Am. Chem. Soc.*** **(2011),** 133: 18126-18129.

[42] A. Kudo, K. Ueda, H. Kato, I. Mikami, "Photocatalytic O_2 evolution under visible light irradiation on $BiVO_4$ in aqueous $AgNO_3$ solution" ***Catal. Lett.*** (**1998**), 53: 229-230.

[43] K. Sayama, A. Nomura, T. Arai, T. Sugita, R. Abe, M. Yanagida, T. Oi, Y. Iwasaki, Y. Abe, H. Sugihara, "Photoelectrochemical decomposition of water into H_2 and O_2 on porous $BiVO_4$ thin-film electrodes under visible light and significant effect of Ag ion treatment" ***J. Phys. Chem. B*** (**2006**), 110: 11352-11360.

[44] Y. Liang, T. Tsubota, L.P.A. Mooij, R. van de Krol, "Highly Improved Quantum Efficiencies for Thin Film $BiVO_4$ Photoanodes" ***J. Phys. Chem. C*** (**2011**)**,** 115: 17594-17598.

[45] H. Ye, J. Lee, J.S. Jang, A.J. Bard, "Rapid Screening of $BiVO_4$-Based Photocatalysts by Scanning Electrochemical Microscopy (SECM) and Studies of Their Photoelectrochemical Properties" ***J. Phys. Chem. C*** (**2010**), 114: 13322-13328.

[46] D.K. Zhong, S. Choi, D.R. Gamelin, "Near-Complete Suppression of Surface Recombination in Solar Photoelectrolysis by "Co-Pi" Catalyst-Modified $W:BiVO_4$" ***J. Am. Chem. Soc.***(**2011**)**,** 133: 18370-18377.

[47] J.E. Yourey, B.M. Bartlett, "Electrochemical deposition and photoelectrochemistry of $CuWO_4$, a promising photoanode for water oxidation" ***J. Mater. Chem.*** (**2011**)**,** 21: 7651-7660.

[48] K.J. McDonald, K.S. Choi, "Synthesis and Photoelectrochemical Properties of $Fe_2O_3/ZnFe_2O_4$ Composite Photoanodes for Use in Solar Water Oxidation" ***Chem. Mater.*** (**2011**), 23: 4863-4869.

[49] S. Ida, K. Yamada, T. Matsunaga, H. Hagiwara, Y. Matsumoto, T. Ishihara, "Preparation of p-Type $CaFe_2O_4$ Photocathodes for Producing Hydrogen from Water" ***J. Am. Chem. Soc.*** (**2010**)**,** 132: 17343-17345.

[50] R. Patil, S. Kelkar, R. Naphade, S. Ogale, "Low temperature grown $CuBi_2O_4$ with flower morphology and its composite with CuO nanosheets for photoelectrochemical water splitting" ***J. Mater. Chem. A*** (**2014**)**,** 2: 3661-3668.

[51] U.A. Joshi, P.A. Maggard, "$CuNb_3O_8$ A p-Type Semiconducting Metal Oxide Photoelectrode" ***J. Phys. Chem. Lett.*** (**2012**)**,** 3: 1577-1581.

[52] P. Zhang, J. Zhang, J. Gong, "Tantalum-based semiconductors for solar water splitting" ***Chem. Soc. Rev.*** (**2014**)**,** 43: 4395-4422.

[53] M. Higashi, K. Domen, R. Abe, "Highly Stable Water Splitting on Oxynitride TaON Photoanode System under Visible Light Irradiation" ***J. Am. Chem. Soc.*** (**2012**)**,** 134: 6968-6971.

[54] J. Zhao, T. Minegishi, L. Zhang, M. Zhong, M. Gunawan, M. Nakabayashi, G. Ma, T. Hisatomi, M. Katayama, S. Ikeda, "Enhancement of Solar Hydrogen Evolution from Water by Surface Modification with CdS and TiO_2 on Porous $CuInS_2$ Photocathodes Prepared by an Electrodeposition-Sulfurization Method" ***Angew. Chem. Int. Ed.*** (**2014**)**,** 53: 11808-11812.

[55] L. Zhang, T. Minegishi, M. Nakabayashi, Y. Suzuki, K. Seki, N. Shibata, J. Kubota, K. Domen, "Durable hydrogen evolution from water driven by sunlight using $(Ag, Cu)GaSe_2$ photocathodes modified with CdS and $CuGa_3Se_5$" ***Chem. Sci.*** (**2015**)**,** 6: 894-901.

[56] M. Moriya, T. Minegishi, H. Kumagai, M. Katayama, J. Kubota, K. Domen, "Stable Hydrogen Evolution from CdS-Modified $CuGaSe_2$ Photoelectrode under Visible-Light Irradiation" ***J. Am. Chem. Soc.* (2013),** 135: 3733-3735.

[57] B. Seger, A.B. Laursen, P.C.K. Vesborg, T. Pedersen, O. Hansen, S. Dahl, I. Chorkendorff, "Hydrogen Production Using a Molybdenum Sulfide Catalyst on a Titanium-Protected n+p-Silicon Photocathode" ***Angew. Chem. Int. Ed.* (2012),** 51: 9128-9131.

[58] C. Liu, J. Sun, J. Tang, P. Yang, "Zn-Doped p-Type Gallium Phosphide Nanowire Photocathodes from a Surfactant-Free Solution Synthesis" ***Nano Lett.* (2012),** 12: 5407-5411.

[59] J. Zhang, M. Zhang, R.Q. Sun, X. Wang, "A Facile Band Alignment of Polymeric Carbon Nitride Semiconductors to Construct Isotype Heterojunction" ***Angew. Chem.* (2012),** 124: 10292-10296.

[60] S. Tanigawa, H. Irie, "Visible-light-sensitive two-step overall water-splitting based on band structure control of titanium dioxide" ***Appl. Catal. B Environ.* (2016),** 180: 1-5.

[61] T.A. Kandiel, K. Takanabe, "Solvent-induced deposition of Cu-Ga-In-S nanocrystals onto a titanium dioxide surface for visible-light-driven photocatalytic hydrogen production" ***Appl. Catal. B Environ.* (2016),** 184: 264-269.

[62] Z. Zhu, J.Y. Chen, K.Y. Su, R.J. Wu, "Efficient hydrogen production by water-splitting over Pt-deposited C-HS-TiO_2 hollow spheres under visible light" ***J. Taiwan Inst. Chem. Eng.* (2016),** 60: 222-228.

[63] L. Li, J. Yan, T. Wang, Z.J. Zhao, J. Zhang, J. Gong, N. Guan, "Sub-10 nm rutile titanium dioxide nanoparticles for efficient visible-light-driven photocatalytic hydrogen production" ***Nat. Commun.* (2015),** 6: 5881.

[64] Q. Wang, T. Hisatomi, S.S.K. Ma, Y. Li, K. Domen, "Core/shell structured La- and Rh-Codoped $SrTiO_3$ as a hydrogen evolution photocatalyst in Z-scheme overall water splitting under visible light irradiation" ***Chem. Mater.* (2014),** 26: 4144-4150.

[65] Y. Chen, S. Zhao, X. Wang, Q. Peng, R. Lin, Y. Wang, R. Shen, X. Cao, L. Zhang, G. Zhou, "Synergetic Integration of Cu1.94S-ZnxCd1-xS Heteronanorods for Enhanced Visible-light-driven Photocatalytic Hydrogen Production" ***J. Am. Chem. Soc.* (2016),** 138: 4286-4289.

[66] D. Dontsova, C. Fettkenhauer, V. Papaefthimiou, J. Schmidt, M. Antonietti, "1,2,4-Triazole-Based Approach to Noble-Metal-Free Visible-Light Driven Water Splitting over Carbon Nitrides" ***Chem. Mater.* (2015),** 28: 772-778.

[67] H. Fujito, H. Kunioku, D. Kato, H. Suzuki, M. Higashi, H. Kageyama, R. Abe, "Layered Perovskite Oxychloride Bi_4NbO_8Cl: A Stable Visible Light Responsive Photocatalyst for Water Splitting" ***J. Am. Chem. Soc.* (2016),** 138: 2082-2085.

[68] D. Jiang, Z. Sun, H. Jia, D. Lu, P. Du, "A cocatalyst-free CdS nanorod/ZnS nanoparticle composite for high-performance visible-light-driven hydrogen production from water" ***J. Mater. Chem. A Mater. Energy Sustain.* (2016),** 4: 675-683.

[69] X. Yue, S. Yi, R. Wang, Z. Zhang, S. Qiu, "Cadmium Sulfide and Nickel Synergetic Co-catalysts Supported on Graphitic Carbon Nitride for Visible-Light-Driven Photocatalytic Hydrogen Evolution" ***Sci. Rep.* (2016),** 6: 22268:1-22268:9.

[70] Q. Xiang, F. Cheng, D. Lang, "Hierarchical Layered WS_2/Graphene-Modified CdS Nanorods for Efficient Photocatalytic Hydrogen Evolution" ***Chem Sus Chem* (2016),** 9: 996-1002.

[71] A.K. Agegnehu, C.J. Pan, M.C. Tsai, J. Rick, W.N. Su, J.F. Lee, B. J. Hwang, "Visible light responsive noble metal-free nanocomposite of V-doped TiO_2 nanorod with highly reduced graphene oxide for enhanced solar H_2 production" ***Int. J. Hydrog. Energy* (2016),** 41: 6752-6762.

[72] G. Zhang, Z.A. Lan, L. Lin, S. Lin, X. Wang, "Overall water splitting by Pt/g-C_3N_4 photocatalysts without using sacrificial agents" ***Chem. Sci.* (2016),** 7: 3062-3066.

[73] J. Zhang, X. Jin, P.I. Morales-Guzman, X. Yu, H. Liu, H. Zhang, L. Razzari, J.P. Claverie, "Engineering the Absorption and Field Enhancement Properties of Au-TiO_2 Nanohybrids via Whispering Gallery Mode Resonances for Photocatalytic Water Splitting" ***ACS Nano* (2016)**, 10: 4496-4503.

[74] Q. Wang, T. Hisatomi, Q. Jia, H. Tokudome, M. Zhong, C. Wang, Z. Pan, T. Takata, M. Nakabayashi, N. Shibata, "Scalable water splitting on particulate photocatalyst sheets with a solar-to-hydrogen energy conversion efficiency exceeding" 1. ***Nat. Mater.* (2016),** 15: 611-615.

[75] S.S. Gujral, A.N. Simonov, M. Higashi, X.Y. Fang, R. Abe, L. Spiccia, "Highly Dispersed Cobalt Oxide on TaON as Efficient Photoanodes for Long-Term Solar Water Splitting" ***ACS Catal.* (2016),** 6: 3404-3417.

[76] Y.J. Yuan, D.Q. Chen, Y.W. Huang, Z.T. Yu, J.S. Zhong, T.T. Chen, W.G. Tu, Z.J. Guan, D.P. Cao, "MoS_2 Nanosheet-Modified $CuInS_2$ Photocatalyst for Visible-Light-Driven Hydrogen Production fromWater". ***Chem Sus Chem* (2016),** 9: 1003-1009.

[77] Z.L. Wu, C.H. Wang, B. Zhao, J. Dong, F. Lu, W.H. Wang, W.C. Wang, G.J. Wu, J.Z. Cui, P. A Cheng, "Semi-Conductive Copper-Organic Framework with Two Types of Photocatalytic Activity" ***Angew. Chem.-Int. Ed.* (2016),** 55: 4938-4942

[78] N.S. Lewis, "Light work with water" ***Nature* (2001),** 414: 589-590.

[79] N Chouhan, RS Liu, J. Zhang, "Photochemical Water Splitting: Materials and Applications" ***CRC Press;* (2017),** Jan 27.

[80] S. Ikeda, T. Itani, K. Nango, M. Matsumura, "Overall water splitting on tungsten-based photocatalysts with defect pyrochlore structure" ***Catal. Lett.* (2004),** 98: 229-233.

[81] GP Smestad, A Steinfeld, "Photochemical and thermochemical production of solar fuels from H_2O and CO_2 using metal oxide catalysts" ***Ind Eng Chem Res*** **(2012),** 51: 11828-11840.

[82] CNR Rao, SR Lingampalli, S Dey, A Roy, "Solar photochemical and thermochemical splitting of water" ***Philos Trans A Math Phys Eng Sci*** **(2016),** 374: 20150088.

[83] CNR Rao, S Dey, "Generation of H_2 and CO by solar thermochemical splitting of H_2O and CO_2 by employing metal oxides" ***J Solid State Chem*** **(2016),** 242: 107-115.

[84] GE Eghi, "A decade of research on thermochemical hydrogen at the Joint Research Centre, Ispra" ***Int J Hydrogen Energy*** **(1986),** 11: 761-771.

[85] S Yalccin, "A review of nuclear hydrogen production" ***Int J Hydrogen Energy*** **(1989),** 14: 551-561.

[86] B Meredig, C Wolverton, "First-principles thermodynamic framework for the evaluation of thermochemical H_2O- or CO_2-splitting materials" ***Phys Rev B*** **(2009),** 80: 245119.

[87] T Kodama, N Gokon "Thermochemical cycles for high-temperature solar hydrogen production" ***Chem Rev*** **(2007),** 107: 4048-4077.

[88] https://www.energy.gov/eere/fuelcells/hydrogen-production-photobiological.

[89] W.J. Ong, L.L. Tan, Y.H. Ng, S.T. Yong, S.P. Chai, "Graphitic Carbon Nitride (g-C_3N_4) Based Photocatalysts for Artificial Photosynthesis and Environmental Remediation" ***Chem. Rev.*** **(2016),** 116: 7159-7329.

[90] W. Wunderlich, H. Ohta, K. Koumoto. "Enhanced effective mass in doped $SrTiO_3$ and related perovskites" ***Physica B*** **(2009),** 404: 2202-212.

[91] A. Walsh, Y. Yan, M.N. Huda, M.M. Al-Jassim, S. H. Wei, "Band Edge Electronic Structure of $BiVO_4$: Elucidating the Role of the Bi s and V d Orbitals" ***Chem. Mater.*** **(2009),** 21: 547-551.

[92] O. Madelung, "Semiconductors: Data Handbook; Springer Berlin Heidelberg: Berlin/Heidelberg" ***Germany*** **(2004)**.

[93] G. Schmitz, P. Gassmann, R. Franchy, "A combined scanning tunneling microscopy and electron energy loss spectroscopy study on the formation of thin, well-ordered Ga_2O_3 films on CoGa" (001). ***J. Appl. Phys.*** (**1998),** 83: 2533-2538.

[94] T.V. Perevalov, A.V. Shaposhnikov, V.A. Gritsenko, H. Wong, J.H. Han, C.W. Kim, "Electronic structure of Al_2O_3 Ab initio simulations and comparison with experiment" ***JETP Lett.*** **(2007),** 85: 165-168.

[95] B. Kramm, A. Laufer, D. Reppin, A. Kronenberger, P. Hering, A. Polity, B. K. Meyer, "The band alignment of Cu_2O/ZnO and Cu_2O/GaN heterostructures" ***Appl. Phys. Lett.*** **(2012),** 100: 094102.

[96] Akira Fujishima, Kenichi Honda, "Electrochemical Photolysis of Water at a Semiconductor Electrode" ***Nature***. **(1972),** 238 (5358): 37-8.

[97] Satoshi Tanigawa Hiroshi Irie, "Visible-light-sensitive two-step overall water-splitting based on band structure control of titanium dioxide" ***Applied Catalysis B: Environmental*** **(2016),** 1801-5.

[98] Yanrui Li, Leilei Li, Yunqi Gong, Song Bai, Huanxin Ju, Chengming Wang, Qian Xu, Junfa Zhu, Jun Jiang, Yujie Xiong, "Towards full-spectrum photocatalysis: achieving Z scheme between Ag_2S and TiO_2 by engineering energy band alignment with interfacial Ag" ***Nano Research.*****(2015),** 12274: 1-9.

[99] Ying-Chih Pu, Gongming Wang, Kao-Der Chang, Yichuan Ling, Yin-Kai Lin, Bob C. Fitzmorris, Chia-Ming Liu, Xihong Lu, Yexiang Tong, Jin Z. Zhang, Yung-Jung Hsu, and Yat Li. "Au Nanostructure-Decorated TiO_2 Nanowires Exhibiting Photoactivity Across Entire UV-visible Region for Photoelectrochemical Water Splitting" ***Nano Lett.*** **(2013),** 13: 3817-3823

[100] M. Mishra, D.M. Chun, "Fe_2O_3 as a photocatalytic material: A review" ***Appl. Catal. A Gen.*** **(2015),** 498: 126-141.

[101] S. Haghighat, J.M. Dawlaty, "Continuous representation of the proton and electron kinetic parameters in the pH-potential space for water oxidation on hematite" ***J. Phys. Chem. C*** **(2015),** 119: 6619-6625.

[102] S. Moniz, S.A. Shevlin, D. Martin, Z. Guo, J. Tang, "Visible-Light Driven Heterojunction Photocatalysts for Water Splitting, A Critical Review" ***Energy Environ. Sci.*** **(2015),** 8: 731-759.

[103] V.J. Babu, S. Vempati, T. Uyar, S. Ramakrishna, "Review of one-dimensional and two-dimensional nanostructured materials for hydrogen generation" ***Phys. Chem. Chem. Phys.*** **(2015**), 17: 2960-2986.

[104] M. Aya, Mohamed Seham A. Shaban Hussien A. El Sayed Nageh K. Allam "Morphology-photoactivity relationship: WO_3 nanostructured films for solar hydrogen production" ***International Journal of Hydrogen Energy*** **(2016),** Volume 41 Issue 2866-872.

[105] L. Liao, Q. Zhang, Z. Su, Z. Zhao, Y. Wang, Y. Li, X. Lu, D. Wei, G. Feng, Q. Yu, "Efficient solar water-splitting using a nanocrystalline CoO photocatalyst" ***Nat. Nanotechnol.*** (**2014),** 9: 69-73.

[106] J. Jasieniak, M. Califano, S.E. Watkins, "Size-Dependent Valence and Conduction Band-Edge Energies of Semiconductor Nanocrystals" ***ACS Nano*** **(2011),** 5: 5888-5902.

[107] X. Zhan, Z. Wang, F. Wang, Z. Cheng, K. Xu, Q. Wang, M. Safdar, J. He, "Efficient CoO nanowire array photocatalysts for H_2 generation" ***Appl. Phys. Lett.*** **(2014),** 105: 153903:1-153903:5.

[108] X. Lü, S. Ding, T. Lin, X. Mou, Z. Hong, F. Huang, "Ta_2O_5 nanowires: A novel synthetic method and their solar energy utilization" ***Dalton Trans.*** **(2012),** 41: 622-627.

[109] C. Tao, L. Xu, J. Guan, "Well-dispersed mesoporous Ta_2O_5 submicrospheres: Enhanced photocatalytic activity by tuning heating rate at calcinations" ***Chem. Eng. J.*** (**2013**)**,** 229: 371-377.

[110] L. Mao, S. Zhu, J. Ma, D. Shi, Y. Chen, Z. Chen, C. Yin, Y. Li, D. Zhang, "Superior H_2 production by hydrophilic ultrafine Ta_2O_5 engineered covalently on graphene" ***Nanotechnology*** (**2014**)**,** 25: 215401:1-215401:9.

[111] G. Zhu, T. Lin, H. Cui, W. Zhao, H. Zhang, F. Huang, "Gray Ta_2O_5 Nanowires with Greatly Enhanced Photocatalytic Performance" ***ACS Appl. Mater. Interfaces*** (**2016**)**,** 8: 122-127.

[112] J. M. Herrmann, "Heterogeneous photocatalysis: State of the art and present applications" ***Top. Catal.*** (**2005**)**,** 34: 49-65.

[113] U. Schwertmann, R. Cornell, "The Iron Oxides. Structure, Properties, Reactions Occurrences and Uses" ***VCH:Weinheim, Germany*** (**1996**).

[114] K.J. Kim, Y.R. Park, "Optical investigation of charge-transfer transitions in spinel Co_3O_4" ***Solid State Commun.*** (**2003**)**,** 127: 25-28.

[115] A. Walsh, G.W. Watson, "The origin of the stereochemically active Pb(II) lone pair: DFT calculations on PbO and PbS" ***J. Solid State Chem.***(**2005**)**,** 178: 1422-1428.

[116] A. Walsh, G.W. Watson, "Electronic structures of rocksalt, litharge, and herzenbergite SnO by density functional theory" ***Phys. Rev. B*** (**2004**)**,** 70: 235114:1-235114:7.

[117] J. Geurts, S. Rau, W. Richter, F.J. Schmitte, "SnO films and their oxidation to SnO_2: Raman scattering, IR reflectivity and X-ray diffraction studies" ***Thin Solid Films*** (**1984**)**,** 121: 217-225.

[118] V. Dolocan, "Some electrical properties of Bi_2O_3 thin films" ***Phys. Status Solidi*** (**1978**)**,** 45: K155-K157.

[119] L. Kong, H. Chen, W. Hua, S. Zhang, J. Chen, "Mesoporous bismuth titanate with visible-light photocatalytic activity" ***Chem. Commun.*** (**2008**)**,** 40: 4977-4979.

[120] H. Kato, K. Asakura, A. Kudo, "Highly efficient water splitting into H_2 and O_2 over lanthanum-doped $NaTaO_3$ photocatalysts with high crystallinity and surface nanostructure" ***J. Am. Chem. Soc.*** (**2003**)**,** 125: 3082-3089.

[121] Y. Hosogi, Y. Shimodaira, H. Kato, H. Kobayashi, A. Kudo, "Role of Sn^{2+} in the Band Structure of SnM_2O_6 and $Sn_2M_2O_7$ (M = Nb and Ta) and Their Photocatalytic Properties" ***Chem. Mater.*** (**2008**)**,** 20: 1299-1307.

[122] T. Takata, Y. Furumi, K. Shinohara, A. Tanaka, M. Hara, J. N. Kondo, K. Domen, "Photocatalytic Decomposition of Water on Spontaneously Hydrated Layered Perovskites" ***Chem. Mater.,*** (**1997**)**,** 9 (5): 1063-64.

[123] A. Kudo, H. Kato, S. Nakagawa, "Water Splitting into H_2 and O_2 on New $Sr_2M_2O_7$ (M = Nb and Ta) Photocatalysts with Layered Perovskite Structures: Factors Affecting the Photocatalytic Activity" ***J. Phys. Chem. B* (2000),** 104: 571.

[124] K. Sayama, A. Nomura, T. Arai, T. Sugita, R Abe, M. Yanagida, T. Oi, Y. Iwasaki, Y. Abe, H. Sugihara, "Photoelectrochemical decomposition of water into H_2 and O_2 on porous $BiVO_4$ thin-film electrodes under visible light and significant effect of Ag ion treatment" ***J. Phys. Chem. B*** (**2006**)**,** 110: 11352-11360.

[125] H. Kisch, "Visible Light Induced Photoelectrochemical Properties of n-$BiVO_4$ and n-$BiVO_4$/p-Co_3O_4" ***J. Phys. Chem. C*** (**2008**)**,** 112: 548-554.

[126] K. Sayama, A. Nomura, Z. Zou, R. Abe, Y. Abe, H. Arakawa, "Photoelectrochemical decomposition of water on nanocrystalline $BiVO_4$ film electrodes under visible light" ***Chem. Commun.*(2003),** 23: 2908-2909.

[127] R. Asai, H. Nemoto, Q. Jia, K. Saito, A. Iwase, A. Kudo, "A visible light responsive rhodium and antimony-codoped $SrTiO_3$ powdered photocatalyst loaded with an IrO_2 cocatalyst for solar water splitting" ***Chem. Commun.*** (**2014**)**,** 50: 2543-2546.

[128] K. Furuhashi, Q. Jia, A. Kudo, H. Onishi, "Time-Resolved Infrared Absorption Study of $SrTiO_3$ Photocatalysts Codoped with Rhodium and Antimony" ***J. Phys. Chem. C*** (**2013**)**,** 117: 19101-19106.

[129] H.W. Kang, S.N. Lim, D. Song, S. Bin Park, "Organic-inorganic composite of g-C_3N_4-$SrTiO_3$:Rh photocatalyst for improved H_2 evolution under visible light irradiation" ***Int. J. Hydrog. Energy*** (**2012**), 37: 11602-11610.

[130] <u>Hideki Kato</u>, <u>Kiyotaka Asakura</u>, <u>Akihiko Kudo</u>, "Highly Efficient Water Splitting into H_2 and O_2 over Lanthanum-Doped $NaTaO_3$ Photocatalysts with High Crystallinity and Surface Nanostructure" ***J. Am. Chem. Soc.*, (2003,)** 125 (10): 3082-3089.

[131] K. S. Novoselov, A. K. Geim, S. V. Morozov, "Electric field effect in atomically thin carbon films" ***Science* (2004),** 306: 666-669.

[132] S. Stankovich, D. A. Dikin, G. H. B. Dommett, "Graphene based composite materials" ***Nature* (2006),** 442: 282-286.

[133] A. H. Castro Neto, F. Guinea, N. M. R. Peres, K. S. Novoselov, A. K. Geim, "The electronic properties of graphene" ***Rev. Mod. Phys.*, (2009)** Vol. 81, No. 1, January-March.

[134] G. P. Kotchey, B. L. Allen, H. Vedala, "The enzymatic oxidation of graphene oxide" ***ACS Nano* (2011),** 5: 2098-108.

[135] A. Bianco, "Graphene: Safe or toxic? The two faces of the medal" ***Angew. Chem. Int. Engl.* (2013),** 52: 4986-97.

[136] R. R. Nair, P. Blake., A. N. Grigorenko, "Fine structure constant defines visual transparency of graphene" ***Science* (2008),** 320: 1308.

[137] T. F. Yeh, S. J. Chen, C. S. Yeh, H. Teng, "Tuning the electronic structure of graphite oxide through ammonia treatment for photocatalytic generation of H_2 and O_2 from water splitting" ***J. Phys. Chem. C*** **(2013),** 117: 6516-24.

[138] X. Huang, Z. Zeng, Z. Fan, J. Liu, H. Zhang, "Graphene-based electrodes" ***Adv. Mater.*** **(2012),** 24: 5979-6004.

[139] S. Bae, H. Kim, Y. Lee, "Roll-to-roll production of 30-inch graphene films for transparent electrodes" ***Nat. Nanotechnol.*** **(2010),** 5: 574-78.

[140] V. C. Tung, J. H. Huang, I. Tevis, "Surfactant-free water-processable photoconductive all-carbon composite" ***J. Am. Chem. Soc.*** **(2011),** 133: 4940-47.

[141] N. J. Bell, Y. H. Ng, A. Du, H. Coster, S. C. Smith, R. Amal, "Understanding the enhancement in photoelectrochemical properties of photocatalytically prepared TiO_2 reduced graphene oxide composite" ***J. Phys. Chem. C*** **(2011),** 115: 6004-6009.

[142] A. T. Garcia-Esparza, D. Cha, Y. Ou, J. Kubota, K. Domen, K. Takanabe, "Tungsten carbide nanoparticles as efficient cocatalysts for photocatalytic overall water splitting" ***Chem. Sus. Chem.*** **(2013),** 6 (1): 168-181.

[143] T. Jayasekera, K. W. Kim, M. B. Nardelli, "Electronic and structural properties of turbostratic epitaxial graphene on the 6H-SiC (000-1) surface" ***Mater. Sci. Forum*** **(2012),** 717-720 595-600.

[144] L Tian, J. Liu, C. Gong, L. Ye, L. Zan, "Fabrication of reduced graphene oxide-BiOCl hybrid material via a novel benzyl alcohol route and its enhanced photocatalytic activity" ***J. Nanopart. Res.*** **(2013),** 15: 1917.

[145] J. Zhang, J. Yu, M. Jaroniec, J. R. Gong, "Noble metal-free reduced graphene oxide-Zn x Cd$_{1-x}$ S nanocomposite with enhanced solar photocatalytic H_2-production performance" ***Nano Lett.*** **(2012b),** 12: 4584-89.

[146] X. Geng, L. Niu, Z. Xing, "Aqueous-processable noncovalent chemically converted graphene-quantum dot composites for flexible and transparent optoelectronic films" ***Adv. Mater.*** **(2010),** 22: 638-42.

[147] Z. Lu, C. X. Guo, H. B. Yang, "One-step aqueous synthesis of graphene -CdTe quantum dot-composed nanosheet and its enhanced photoresponses" ***J Colloid and Iter. Science*** **(2011),** 353 (2): 588-592.

[148] <u>Peng Gao, Jincheng Liu, Siewsiang Lee, Tong Zhang, Darren Delai Sun</u>, "<u>High quality graphene oxide-CdS-Pt nanocomposites for efficient photocatalytic hydrogen evolution</u>" ***J. Mater. Chem.,*** **(2012),** 22: 2292-2298 (Highest hydrogen evolution rate of 123 mL h^{-1} g^{-1})

[149] Y. Hou, F. Zuo, A. Dagg, P. Feng. "Visible light-driven α-Fe_2O_3 nanorod/graphene/ BiV_1 core/shell heterojunction array for efficient photoelectrochemical water splitting" ***Nano Lett.*** **(2012b),** 12 (12): 6464-73.

[150] N. J. Bell, *J. Phys. Chem., C* **(2011)** 115: 6004-09.

[151] K. Maeda, T. Takata, M. Hara, N. Saito, Y. Inoue, H. Kobayashi, K. Domen, "GaN:ZnO solid solution as a photocatalyst for visible-light-driven overall water splitting" *J. Am. Chem. Soc.*(**2005**), 127: 8286-8287.

[152] K. Maeda, K. Teramura, K. Domen, "Effect of post-calcination on photocatalytic activity of $(Ga_{1-x}Zn_x)(N_{1-x}O_x)$ solid solution for overall water splitting under visible light" *J. Catal.* **(2008),** 254: 198-204.

[153] B. Siritanaratkul, K. Maeda, T. Hisatomi, K. Domen. "Synthesis and photocatalytic activity of perovskite niobium oxynitrides with wide visible-light absorption bands" *Chem. Sus. Chem.* **(2011),** 4: 74-8.

[154] K. Maeda, M. Higashi, B. Siritanaratkul, R. Abe, K. Domen. "$SrNbO_2N$ as a water splitting photoanode with a wide visible-light absorption band" *J. Am. Chem. Soc.* **(2011),** 133: 12334-37.

[155] M. Higashi, R. Abe, T. Takata, K. Domen, "Photocatalytic overall water splitting under visible light using A TaO 2N (A) Ca, Sr, Ba) and WO_3 in a IO_3^-/I^- shuttle redox mediated system" *Chem. Mater.* **(2009),** 21: 1543-49.

[156] K. Maeda, K. Domen, "Preparation of $BaZrO_3$-$BaTaO_2N$ solid solutions and the photocatalytic activities for water reduction and oxidation under visible light" *J. Catal.* **(2014),** 310: 67-74.

[157] C. L. Paven-Thivet, A. Ishikawa, A. Ziani, "Photoelectrochemical properties of crystalline perovskite lanthanum titanium oxynitride films under visible light" *J. Phys.Chem. C* **(2009),** 113: 6156-62.

[158] A. Ishikawa, T. Takata, J. N. Kondo, M. Hara, H. Kobayashi, K. Domen, "Oxysulfide $Sm_2Ti_2S_2O_5$ as a stable photocatalyst for water oxidation and reduction under visible light irradiation ($\lambda \leq 650$ nm)" *J. Am. Chem. Soc.* **(2002),** 124: 13547-53.

[159] A.A. Ismail, D.W. Bahnemann, "Photochemical splitting of water for hydrogen production by photocatalysis: A review" *Sol. Energy Mater. Sol. Cells* **(2014**), 128: 85-101.

[160] H. Ahmad, S.K. Kamarudin, L.J. Minggu, M. Kassim, "Hydrogen from photo-catalytic water splitting process: A review. Renew" *Sustain. Energy Rev.* **(2015**), 43: 599-610.

[161] I. Majeed, M.A.A. Nadeem, M. Al-Oufi, M.A.A. Nadeem, G.I.N. Waterhouse, A. Badshah, J.B. Metson, H. Idriss, "On the role of metal particle size and surface coverage for photo-catalytic hydrogen production: A case study of the Au/CdS system" *Appl. Catal. B Environ.* (**2016**), 182: 266-276.

[162] M. Reza Gholipour, C.T. Dinh, F. Béland, T.O. Do, "Nanocomposite heterojunctions as sunlight-driven photocatalysts for hydrogen production from water splitting" *Nanoscale* **(2015**), 7: 8187-8208.

[163] J. Cao, J.Z. Sun, J. Hong, H.Y. Li, H.Z. Chen, M. Wang, "Carbon Nanotube/CdS Core-Shell Nanowires Prepared by a Simple Room-Temperature Chemical Reduction Method" ***Adv. Mater.*** (**2004**), 16: 84-87.

[164] Z.F. Huang, J. Song, K. Li, M. Tahir, Y.T. Wang, L. Pan, L. Wang, X. Zhang, J.J. Zou, "Hollow Cobalt-Based Bimetallic Sulfide Polyhedra for Efficient All-pH-Value Electrochemical and Photocatalytic Hydrogen Evolution" ***J. Am. Chem. Soc.*** (**2016**), 138: 1359-1365.

[165] J. Ran, J. Zhang, J. Yu, M. Jaroniec, S.Z. Qiao, "Earth-abundant cocatalysts for semiconductor-based photocatalytic water splitting" ***Chem. Soc. Rev.*** (**2014**), 43: 7787-7812.

[166] P. Reiss, M. Protière, L. Li, "Core/shell semiconductor nanocrystals" ***Small*** (**2009**), 5: 154-168.

[167] J. Zhang, J. Yu, M. Jaroniec, J.R. Gong, "Noble Metal-Free Reduced Graphene Oxide-ZnxCd$_{1-x}$S Nanocomposite with Enhanced Solar Photocatalytic H$_2$-Production Performance" ***Nano Lett.*** (**2012**), 12: 4584-4589.

[168] Li, Q.; Meng, H.; Zhou, P.; Zheng, Y.; Wang, J.; Yu, J.; Gong, J. "Zn$_{1-x}$Cd$_x$S solid solutions with controlled bandgap and enhanced visible-light photocatalytic H2-production activity" ***ACS Catal.*** (**2013**), 3: 882-889.

[169] Y.X. Pan, H.Q. Zhuang, J.D. Hong, Z. Fang, H. Liu, B. Liu, Y.Z. Huang, R. Xu, "Cadmium Sulfide Quantum Dots Supported on Gallium and Indium Oxide for Visible-Light-Driven Hydrogen Evolution fromWater" ***Chem Sus Chem*** (**2014**), 7: 2537-2544.

[170] X. Wang, G. Liu, G.Q. Lu, H.M. Cheng, "Stable photocatalytic hydrogen evolution from water over ZnO-CdS core-shell nanorods" ***Int. J. Hydrog. Energy*** (**2010**), 35: 8199-8205.

[171] J. Hou, Z. Wang, W. Kan, S. Jiao, H. Zhu, R.V. Kumar, "Efficient visible-light-driven photocatalytic hydrogen production using CdS@TaON core-shell composites coupled with graphene oxide nanosheets" ***J. Mater. Chem.*** (**2012**), 22: 7291-7299.

[172] S. Bai, X. Shen, "Graphene-inorganic nanocomposites" ***RSC Adv.*** (**2012**), 2: 64-98.

[173] Z. Cheng, Z. Wang, T.A. Shifa, F. Wang, X. Zhan, K. Xu, Q. Liu, J. He, "Au plasmonics in a WS$_2$-Au-CuInS$_2$ photocatalyst for significantly enhanced hydrogen generation" ***Appl. Phys. Lett.*** (**2015**), 107: 223902:1-223902:5.

[174] C. Zhen, L. Wang, G. Liu, G.Q.M. Lu, H.M. Cheng, "Template-free synthesis of Ta$_3$N$_5$ nanorod arrays for efficient photoelectrochemical water splitting" ***Chem. Commun.*** (**2013**), 49: 3019-3021.

[175] J. Seo, T. Takata, M. Nakabayashi, T. Hisatomi, N. Shibata, T. Minegishi, K. Domen, "Mg-Zr Cosubstituted Ta$_3$N$_5$ Photoanode for Lower-Onset-Potential Solar-Driven Photoelectrochemical Water Splitting" ***J. Am. Chem. Soc.*** (**2015**), 137: 12780-12783.

[176] X. Wang, K. Maeda, A. Thomas, K. Takanabe, G. Xin, J.M. Carlsson, K. Domen, M. Antonietti, "A metal-free polymeric photocatalyst for hydrogen production from water under visible light" ***Nat. Mater.*** **(2009**), 8: 76-80.

[177] G. Zhang, M. Zhang, X. Ye, X. Qiu, S. Lin, X. Wang, "Iodine modified carbon nitride semiconductors as visible light photocatalysts for hydrogen evolution" ***Adv. Mater.*** (**2014**), 26: 805-809.

[178] Z. Ding, X. Chen, M. Antonietti, X. Wang, "Synthesis of transition metal-modified carbon nitride polymers for selective hydrocarbon oxidation" ***Chem Sus Chem*** (**2011**), 4: 274-281.

[179] W. L. Barnes, A. Dereux, T. W. Ebbesen, "Surface plasmon subwavelength optics" ***Nature* (2003),** 424: 824-830.

[180] K. Hashimoto, H. Irie, A. Fujishima, "TiO_2 photocatalysis: A historical overview and future prospects" ***Jpn. J. Appl. Phys.* (2005),** 44: 8269.

[181] A. Sheikh, A. Yengantiwar, M. Deo, S. Kelkar, S. C. Ogale, "Near-field plasmonic functionalization of light harvesting oxide–oxide heterojunctions for efficient solar photoelectrochemical water splitting: The $AuNP/ZnFe_2O_4/ZnO$ system" ***Small* (2013),** 9 (12): 2091-96.

[182] J Virkutyte, RS. Varma, "Fabrication and visible light photocatalytic activity of a novel $Ag/TiO_{2-x}N_x$ nanocatalyst" ***New Journal of Chemistry* (2010),** 34 (6): 1094-1096.

[183] M Valenti, D Dolat, G Biskos, A Schmidt-Ott, WA. Smith, "Enhancement of the photoelectrochemical performance of $CuWO_4$ thin films for solar water splitting by plasmonic nanoparticle functionalization" ***The Journal of Physical Chemistry C.* (2015),** 119 (4): 2096-2104.

[184] HM Chen, CK Chen, CJ Chen, LC Cheng, PC Wu, BH Cheng, YZ Ho, ML Tseng, YY Hsu, TS Chan, JF. Lee, "Plasmon inducing effects for enhanced photoelectrochemical water splitting: X-ray absorption approach to electronic structures" ***ACS nano.* (2012),** 6 (8): 7362-7372.

[185] M Haro, R Abargues, I Herraiz-Cardona, J Martínez-Pastor, S. Giménez, "Plasmonic versus catalytic effect of gold nanoparticles on mesoporous TiO_2 electrodes for water splitting" ***Electrochimica Acta.* (2014),** 144: 64-70.

[186] Akansha Mehta, Pooja D., Anupma Thakur, Soumen Basu, "Enhanced photocatalytic water splitting by gold carbon dot core shell nanocatalyst under visible/sunlight" ***New J. Chem.,* (2017),** 41: 4573-4581.

[187] C.G. Silva, J.L. Faria, "Photocatalytic oxidation of benzene derivatives in aqueous suspensions: Synergic effect induced by the introduction of carbon nanotubes in a TiO_2 matrix" ***Appl. Catal. B Environ.*** (**2010**)**,** 101: 81-89.

[188] Z. Lou, B. Huang, Z. Wang, X. Ma, R. Zhang, X. Zhang, X. Qin, Y. Dai, M.H. Whangbo, "$Ag_6Si_2O_7$: A Silicate Photocatalyst for the Visible Region" ***Chem. Mater.*** (**2014**), 26: 3873-3875.

[189] H. Cheng, K. Fuku, Y. Kuwahara, K. Mori, H. Yamashita, "Harnessing single-active plasmonic nanostructures for enhanced photocatalysis under visible light" ***J. Mater. Chem. A*** (**2015),** 3: 5244-5258.

[190] Z. Bian, T. Tachikawa, P. Zhang, M. Fujitsuka, T. Majima, "Au/TiO_2 Superstructure-Based Plasmonic Photocatalysts Exhibiting Efficient Charge Separation and Unprecedented Activity" ***J. Am. Chem. Soc.*** (**2013),** 136: 458-465.

[191] C. Clavero, "Plasmon-induced hot-electron generation at nanoparticle/metal-oxide interfaces for photovoltaic and photocatalytic devices" ***Nat. Photonics*** (**2014),** 8: 95-103.

[192] S. Mubeen, J. Lee, D. Liu, G.D. Stucky, M. Moskovits, "Panchromatic Photoproduction of H_2 with Surface Plasmons" Nano Lett. (**2015),** 15: 2132-2136.

[193] Moskovits, M. "The case for plasmon-derived hot carrier devices" ***Nat. Nanotechnol.*** (**2015**), 10: 6-8.

[194] C. Liu, J. Tang, H.M. Chen, B. Liu, P. Yang, "A Fully Integrated Nanosystem of Semiconductor Nanowires for Direct SolarWater Splitting" ***Nano Lett.*** (**2013),** 13: 2989-2992.

[195] S. Mubeen, J. Lee, N. Singh, S. Krämer, G.D. Stucky, M. Moskovits, "An autonomous photosynthetic device in which all charge carriers derive from surface plasmons" ***Nat. Nanotechnol.*** (**2013),** 8: 247-251.

[196] G. Li, C. Cherqui, N.W. Bigelow, G. Duscher, P.J. Straney, J.E. Millstone, D.J. Masiello, J.P. Camden, "Spatially Mapping Energy Transfer from Single Plasmonic Particles to Semiconductor Substrates via STEM/EELS" ***Nano Lett.*** (**2015),** 15: 3465-3471.

[197] R. Long, Z. Rao, K. Mao, Y. Li, C. Zhang, Q. Liu, C. Wang, Z.Y. Li, X. Wu, Y. Xiong, "Efficient Coupling of Solar Energy to Catalytic Hydrogenation by Using Well-Designed Palladium Nanostructures" ***Angew. Chem.*** (**2015),** 127: 2455-2460.

[198] A. A. Krasnovskii, G. P. Brin, "Inorganic models of hills reaction" ***Dokl. Akad. Nauk. SSSR*** (**1962),** 147: 656-65.

[199] K. Sayama, K. Masuka, R. Abe, Y. Abe, H. Arakawa, "Stiochiometric water splitting into H_2 and O_2 using a mixture of two different photocatalysts and an IO^{3-}/I^- shuttle redox mediator under visible light irradiation" ***Chem. Commun.*** (**2001),** 2416-17.

[200] M. Tabata, K. Maeda, M. Higashi, "Modified Ta_3N_5 powder as a photocatalyst for O_2 evolution in a two-step water splitting system with an iodate/iodide shuttle redox mediator under visible light" ***Langmuir*** (**2010),** 26 (12): 9161-65.

[201] A. Kudo, Y. Miseki. "Heterogeneous photocatalyst materials for water splitting" ***Chem. Soc. Rev.*** (**2009),** 38: 253-78.

[202] Y. Sasaki, H. Nemoto, K. Saito, A. Kudo. "Solar water splitting using powdered photocatalysts driven by Z-schematic interparticle electron transfer without an electron mediator" ***J. Phys. Chem. C*** **(2009),** 113: 17536-42.

[203] H. Kato, M. Hori, R. Konta, Y. Shimodaira, A. Kudo. "Construction of Z-scheme type heterogeneous photocatalysis systems for water splitting into H_2 and O_2 under visible light irradiation" ***Chem. Lett.*** **(2004),** 33: 1348-49.

[204] D Ma, J Wu, M Gao, "Fabrication of Z-scheme g-C_3N_4/RGO/Bi_2WO_6 photocatalyst with enhanced visible-light photocatalytic activity" ***Chem Engineer J.*** **(2016),** 290: 136-146.

[205] N Tian, H Huang, Y He, "Mediator-free direct Z-scheme photocatalytic system: $BiVO_4$/g-C_3N_4 organic-norganic hybrid photocatalyst with highly efficient visible-light-induced photocatalytic activity" ***Dalton Trans.*** **(2015),** 44: 4297-4307.

[206] H Katsumata, T Sakai, T Suzuki, "Highly efficient photocatalytic activity of g-C_3N_4/Ag_3PO_4 hybrid photocatalysts through Z-scheme photocatalytic mechanism under visible light" ***Ind Eng Chem Res.*** **(2014),** 53: 8018-8025.

[207] H Katsumata, Y Tachi, T Suzuki, "Z-scheme photocatalytic hydrogen production over WO_3/g-C_3N_4 composite photocatalyst" ***RSC Adv.*** **(2014),** 4: 21405-21409.

[208] R. Kobayashi, S. Tanigawa, T. Takashima, B. Ohtani, H. Irie. "Silver-inserted heterojunction photocatalysts for Z-scheme overall pure-water splitting under visible-light irradiation" ***J. Phys. Chem. C*** **(2014),** 118 (39): 22450-456.

[209] M. Gratzel "Photoelectrochemical cells" ***Nature.*** **(2001),** 414: 338-344.

[210] R Abe, K Shinmei, K Hara, "Robust dyesensitized overall water splitting system with two-step photoexcitation of coumarin dyes and metal oxide semiconductors" ***Chem Commun.*** **(2009),** 3577-3579.

[211] R Abe, K Shinmei, N Koumura, "Visiblelight-induced water splitting based on two-step photoexcitation between dye-sensitized layered niobate and tungsten oxide photocatalysts in the presence of a triiodide/iodide shuttle redox mediator" ***J Am Chem Soc.*** **(2013),** 135: 16872-16884.

[212] D. E. Scaife, "Oxide semiconductors in photoelectrochemical conversion of solar energy" ***Sol. Energy*** **(1980),** 25: 41-54.

[213] M. R. Hoffmann, S. T. Martin, W. Y. Choi, D. W. Bahnemann. "Environmental applications of semiconductor photocatalysis" ***Chem. Rev.*** **(1995),** 95: 69-96.

[214] A. Hameed, M. A. Gondal, Z. H. Yamani. "Effect of transition metal doping on photocatalytic activity of WO_3 for water splitting under laser illumination: Role of 3D-orbitals" ***Catalysis Commun.*** **(2004),** 5(11): 715-19.

[215] S. Shen, C. X. Kronawitter, J. Jiang, P. Guo, L. Guo, S. S. Mao. "A ZnO/ZnO:Cr isostructural nanojunction electrode for photoelectrochemical water splitting" ***Nano Energy*** **(2013),** 2: 958-65.

[216] R. Sasikala, A. R. Shirole, V. Sudarsan, "Enhanced photocatalytic activity of indium and nitrogen co-doped TiO_2-Pd nanocomposites for hydrogen generation" ***Appl.Catal. A Gen.*** **(2010),** 377(1-2): 47-54.

[217] X. Hou, S. Jiang, Y. Li, J. Xiao, Y. Li. "Ni-doped InN/GaZnON composite, catalyst for overall water splitting under visible light irradiation" ***Int. J. Hydrogen Energy*** 40 (45): 15448-53.

[218] S. K. Pilli, T. E. Furtak, L. D. Brown, T. G. Deutsch, J. A. Turner, A. M. Herring. "Cobalt-phosphate (Co-Pi) catalyst modified Mo-doped $BiVO_4$ photoelectrodes for solar water oxidation" ***Energy Environ. Sci.*** **(2011),** 4: 5028-34.

[219] Y. S. Hu, A. K. Shwarsctein, G. D. Stucky, E. W. McFarland. "Improved photoelectrochemical performance of Ti-doped α-Fe_2O_3 thin films by surface modification with fluoride" ***Chem. Commun.*** **(2009),** (19): 2652-54.

[220] G. M. Wang, H. Y. Wang, Y. C. Ling, "Hydrogen-treated TiO_2 nanowire arrays for photoelectrochemical water splitting" ***Nano Lett.*** **(2011a),** 11: 3026-33.

[221] Y. C. Ling, G. M. Wang, D. A. Wheeler, J. Z. Zhang, Y. Li. "Sn-doped hematite nanostructures for photoelectrochemical water splitting" ***Nano Lett.*** **(2011),** 11: 2119-25.

[222] J. Frydrych, L. Machala, J. Tucek, "Facile fabrication of tin-doped hematite photoelectrodes: Effect of doping on magnetic properties and performance for light-induced water splitting" ***J. Mater. Chem.*** **(2012),** 22: 23232-39.

[223] J. Xu, C. Hu, Y. Xi, B. Wan, C. Zhang, Y. Zhang. "Synthesis and visible light photocatalytic activity of β-$AgVO_3$ nanowires" ***Solid State Sci.*** **(2012a),** 14: 535-39.

[224] A. P. Singh, S. Kumari, R. Shrivastav, S. Dass, V. R. Satsangi. "Iron doped nanostructured TiO_2 for photoelectrochemical generation of hydrogen. ***Int. J. Hydrogen Energy*** **(2008),** 33: 5363-68.

[225] Dholam, R. N. Patel, M. Adami, A. Miotello. "Hydrogen production by photocatalytic water-splitting using Cr- or Fe-doped TiO_2 composite thin films photocatalyst" ***Int.J. Hydrogen Energy*** **(2009),** 34: 5337-46.

[226] S. Hoang, S. W. Guo, N. T. Hahn, A. J. Bard, C. B. Mullins., "Visible light driven photoelectrochemical water oxidation on nitrogen-modified TiO_2 nanowires" ***Nano Lett.*** **(2012b),** 12: 26-32.

[227] E. M. Rockafellow, L. K. Stewart, W. S. Jenks. "Is sulfur-doped TiO_2 an effective visible light photocatalyst for remediation" ***Appl. Catal. B Environ.*** **(2009),** 91: 554-62.

[228] Q. J. Xiang, J. G. Yu, M. Jaroniec. "Nitrogen and sulfur co-doped TiO_2 nanosheets with exposed {001} facets: Synthesis, characterization and visible-light photocatalytic activity" ***Phys. Chem. Chem. Phys.*** **(2011b),** 13: 4853-61.

[229] A. Kay, I. Cesar, M. Gratzel. "New benchmark for water photooxidation by nanostructured α-Fe_2O_3 films" ***J. Am. Chem. Soc.*** **(2006),** 128: 15714-21.

[230] K. Sivula, F. Le Formal, M. Gratzel. "Solar water splitting: Progress using hematite (α Fe_2O_3) photoelectrodes" ***Chem. Sus. Chem.*** **(2011),** 4: 432-49.

[231] N. Lu, X. Quan, J. Y. Li, S. Chen, H. T. Yu, G. H. Chen. "Fabrication of boron-doped TiO_2 nanotube array electrode and investigation of its photoelectrochemical capability" ***J. Phys. Chem. C*** **(2007),** 111: 11836-42.

[232] Y. Park, W. Kim, H. Park, T. Tachikawa, T. Majima, W. Choi. "Carbon-doped TiO_2 photocatalyst synthesized without using an external carbon precursor and the visible light activity" ***Appl. Catal. B Environ.*** **(2009),** 91: 355-61.

[233] W. Y. Choi, A. Termin, M. R. Hoffmann. "The role of metal ion dopants in quantum-sized TiO_2: Correlation between photoreactivity and charge carrier recombination dynamics" ***J Phys Chem*** **(1994),** 84: 13669-79.

[234] M. I. Litter, "Heterogeneous photocatalysis transition metal ions in photocatalytic systems" ***Appl. Catal. B Environ.*** **(1999),** 23: 89-114.

[235] K. Wilke, H. D. Breuer. "The influence of transition metal doping on the physical and photocatalytic properties of titania" ***J. Photochem. Photobiol. A Chem.*** **(1999),** 121 (1): 49-53.
[236] C. Zhang, Y. Z. Jia, Y. Jing, Y. Yao, J. Ma, J. Sun. "Effect of non-metal elements (B, C, N, F, P, S) mono-doping as anions on electronic structure of $SrTiO_3$" ***Comput. Mater. Sci.*** **(2013a),** 79: 69-74.

[237] Septia Nurkhalisa, Hanifatun Maghfiroh, Eko Budi Wibowo, Emas Agus Prastyo Wibowo; "A Concept: Improved Hydrogen Production using Pt-N-TiO_2 under Visible Light via Photocatalysis Process" ***Chemistry Research Journal*** **(2017),** 2 (2): 90-95.

[238] S. Tuzemen, Emre Gur, **"**Principal issues in producing new ultraviolet light emitters based on transparent semiconductor zinc oxide" ***Optical Materials*** **(2007),** 30: 292-310.

[239] N. Izyumskaya, V. Avrutin, Ü. Özgür, Y. I. Alivov, H. Morkoç "Preparation and properties of ZnO and devices" ***Phys. stat. sol.*** **(2007),** 244: 51439-1450.

[240] Ü. Özgür, Ya. I. Alivov, C. Liu, A. Teke, M. A. Reshchikov, S. Dogan, V. Avrutin,S.J. Cho, H. Morkoçd, "A comprehensive review of ZnO materials and devices" ***Journal of applied physics*** **(2005),** 98: 041301-041404.

[241] D. C. Look, "Recent advances in ZnO materials and devices" ***Mat. Sci. Eng. B.*** **(2001),** 80: 383-387.

[242] H Furube, R Katoh, H Hara, "Ultrafast stepwise electron injection from photoexcited Ru-complex into nanocrystalline ZnO film via intermediates at the surface" ***J Phys Chem B.*(2003),** 107: 4162-4166.

[243] R Huber, S Spörlein, JE Moser, "The role of surface states in the ultrafast photoinduced electron transfer from sensitizing dye molecules to semiconductor colloids" ***J Phys Chem B.*(2000),** 104: 8995-9003.

[244] J Kallioinen, G Benkö, V Sundström. "Electron transfer from the singlet and triplet excited states of Ru(dcbpy)$_2$ (NCS)$_2$ into nanocrystalline TiO$_2$ thin films" ***J Phys Chem B.*(2002),** 106: 4396-4404.

[245] G Benkö, J Kallioinen, JEI Korppi-Tommola. Photoinduced ultrafast dye-to-semiconductor electron injection from nonthermalized and thermalized donor states. ***J Am Chem Soc.* (2002),** 124: 489-493

[246] Z. L. Wang, "Zinc oxide nanostructures: growth, properties and applications" ***J. Phys. Condense matter* (2004),** 303: R829

[247] E. Hendry, M. Koeberg, B. O Regan, M. Bonn, "Local field effects on electron transport in nanostructured TiO$_2$ revealed by terahertz spectroscopy" ***Nano Lett.,* (2006),** 6: 755

[248] H. H. Afifty, S. H. EL Hefnawi, A.Y. Eliwa, M. M. Abdel-Naby, N.M. Ahmed, ***Egypt. J. Solids* (2005),** Vol. (28) No. (2).

[249] G. Epurescu, N. D. Scarisoreanu, D.G. Matei, G. Dinescu, C. Ghica, L. C. Nistor, M. Dinescu, " Functional ZnO thin films obtained by radiofrequency beam assisted pulsed laser deposition" ***Romanian reports in Physics* (2008),**Vol. (60) No. (3): 807-814.

[250] A. Maldonado, S. T. Guerra, J. M. Cázares, M. de. La L. Olvera, "Physical and Sensing Properties of ZnO:F:Al Thin Films Deposited by Sol-Gel" ***Thin Solid Films* (2010),** 518: 1815-1820.

[251] S. Y. Lee, E. S.S him, H. S. Kang, S. S. Pang, J. S. Kang, "Fabrication of ZnO thin film diode using laser annealing" ***Thin Solid Films* (2005),** 473: 31.

[252] M. H. Huang, S. Mao, H. Feick, H. Yan, Y. Wu, H. Kind, E. Weber, R. Russo, P. Yang, "Room-Temperature Ul- traviolet Nanowire Nanolasers" ***Science* (2001),** 292: 1897.

[253] H. Liu, V. Avrutin, N. Izyumskaya, Ü.Özgür, H. Morkoç, "Transparent conducting oxides for electrode applications in light emitting and absorbing devices" ***Superlattices and Microstructures* (2010),** 48: 458-484.

[254] S. Singh, D. Nakamura, K. Sakai, T. Okada, M. S. Ramachandra Rao, "Investigation of lowtemperature excitonic and defect emission from Ni-doped ZnO nanoneedles and V-doped ZnO nanostructured film" ***New J. of Phys.* (2010),** 12: 023007.

[255] M. Caglar, S. Ilican, Y. Caglar, F. Yakuphanoglu, "The effects of Al doping on the optical constants of ZnO thin films prepared by spray pyrolysis method" *J. Mater Sci: Mater Electron* **(2008),** 19: 704-708.

[256] R. Ferro, J .A. Rodriguez, P. Bertrand, "Mixed $(ZnO)_X(CdO)_{1-X}$ policrystalline oxide films deposited by spray pyrolysis from metal nitrate solutions" *J. of materials science letters* **(2002),** 21: 1939-1941.

[257] P. M. Ratheesh Kumar, K. P. Vijayakumar, C. Sudha Kartha, "On the origin of blue-green luminescence in spray pyrolysed ZnO thin films" *J. Mater Sci* **(2007),** 42: 2598-2602.

[258] R. C. Pawar, J. S. Shaikh, N. L. Tarwal, M. M. Karanjkar , P. S. Patil, **"**Surfactant mediated growth of ZnO nanostructures and their dye sensitized solar cell properties" *J. Mater Sci: Mater Electron* **(2012),** 2: 349-355.

[259] A. D. A. Buba, J. S .A. Adelabu, "Optical and Electrical Properties of Chemically Deposited ZnO Thin Films" *The Pacific Journal of Science and Technology* **(2010),** 2: 429-434.

[260] D. Ramırez , D. Silva , H. Gomez , G. Riveros , R.E. Marotti , E.A. Dalchiele, "Electrodeposition of ZnO thin films with molecular oxygen and hydrogen peroxide as oxygen precursors" *Solar Energy Materials & Solar Cells* **(2007),** 91: 1458-1461.

[261] T.S. Kim, C. J. Youn, "Splitting of the valence band for polycristalline ZnO" *J. of the Korean Physical Society* **(2001),** Vol. 38 No.1: 42-46.

[262] S. J. Henley, M.N.R. Ashfold, D. Cherns, "The growth of transparent conducting ZnO films by pulsed laser ablation" *Surface and Coatings Technology* **(2004),** volumes 177-178, pages 271-276.

[263] Ü. Özgür, Ya. I. Alivov, C. Liu, A. Teke, M. A. Reshchikov, S. Doğan, V.Avrutin, S. J. Cho, H. Morkoç "A comprehensive review of ZnO materials and devices" *J. of Applied Physics* **(2005),** 98: 041301.

[264] C. Kilngshirn, "ZnO: From basics towards applications" *Phys. Stat. Sol. (b)* **(2007),** No. 9: 3027-3073.

[265] M. L. Addonizio, C. Diletto, "Doping influence on intrinsic stress and carrier mobility of LP-MOCVD-deposited ZnO: B thin films" *Solar Ener. Materi. & Solar Cells* **(2008),** 92: 1488-1494.

[266] A. Aiaddine, I. Rachidi, F. Bahsoun, Y. Mohanna, O. Bazzi, F. El Hai Hassan, *J. of Applied Sciences* **(2009),** 9 (8): 1588-1592.

[267] T. Minami, T. Miyata, Y. Honma, T. Ito, "Effect of spatial relationship between arc plasma and substrate on the properties of transparent conducting Ga-doped ZnO thin films prepared by vacuum arc plasma evaporation" *Thin Solid Films* **(2009),** 517: 6824-6828.

[268] S. Ilicana, Y. Caglar, M. Caglar, F. "Low-dimensional Systems and Nanostructures" *Yakuphanoglu Physica E35* **(2006),** 131-138.

[269] T. Minami, "New n-Type Transparent Conducting Oxides" *MRS Bulletin* **(2000),** 25: 38-44.

[270] E. M. El-Maghraby, "Temperature dependence of growth orientation and surface morphology of Li-doped ZnO thin films on SiO_2/Si substrates" *Cryst. Res. Technol.* **(2008),** 43, No. 9: 970-974.

[271] B. Xiao, Z. Ye, Y. Zhang, Y. Zeng, L. Zhu, B. Zhao, "Fabrication of p-type Li-doped ZnO films by pulsed laser deposition" *Applied Surface Science* **(2006),** 253: 895-897.

[272] W. Jun, Y. Yintang, "Deposition of K-doped *p* type ZnO thin films on (0001) Al_2O_3 substrates" *Materials Letters* **(2008),** 62: 1899-1901.

[273] X. D. Zhang, C. L. Liu, Z. Wang, Y. Y. Lu, L. J. Yin, "Photoluminescence and electrical properties of N-implanted ZnO films" *Nuclear Instruments and Methods in Physics Research B* **(2007),** 254: 83-86.

[274] Y. Zhang, J. Lu, L. Chen, Z. Ye, "Properties of N-doped ZnO thin films in annealing process" *Solid State Communications* **(2007),** 143: 562-565.

[275] D. S. Kim, llert, A. Lotnyka, R. Scholza, E. Pippel, S. Senza, H. Kalt, U. G. Oselea, M. Zachariasa, "Growth and optical properties of phosphorus-doped ZnO nanowires" *Solid State Communications* **(2007),** 143: 570-573.

[276] A.N. Banerjee, K. K. Chattopadhyay, "Recent Developments in the Emerging Field of Crystalline 'p-Type' Transparent Conducting Oxide Thin Films" *Progress in Crystal Growth and Characterization of Materials* **(2005),** 50: 52-105.

[277] Y. Yan, S. B. Zhang, "Control of doping by impurity chemical potentials: predictions for p-type Zno" *Physical Review Letters* **(2001),** Volume 86 Number 25 5723-5726.

[278] D. Banerjee, J.Y. Lao, D.Z. Wang, J.Y. Huang, Z.F. Ren, D. Steeves, B. Kimball, M. Sennett, "Large-quantity free-standing ZnO nanowires" *Appl. Phys. Lett.* **(2003),** 83: 2061-2063.

[279] Y.B. Hahn, "Zinc oxide nanostructures and their applications" *Korean J. Chem. Eng.* **(2011),** 28: 1797-1813.

[280] T. Frade, Melo, M.E. Jorge, A. Gomes, "One-dimensional ZnO nanostructured films: Effect of oxide nanoparticles" *Mater. Lett.* **(2012),** 82: 13-15.

[281] R. Wahab, S.G. Ansari, Y.S. Kim, H.K. Seo, H.S. Shin, "Room temperature synthesis of needle-shaped ZnO nanorods via sonochemical method" *Appl. Surf. Sci.* **(2007),** 253: 7622-7626.

[282] X. Kong, Y. Ding, R. Yang, Z.L. Wang, "Single-crystal nanorings formed by epitaxial self-coiling of polar-nanobelts" *Science* **(2004),** 303: 1348-1351.

[283] Z.W. Pan, Z.R. Dai, Z.L. Wang, "Nanobelts of semiconducting oxides" *Science* **(2001),** 291: 1947-1949.

[284] J.J. Wu, S.C. Liu, C.T. Wu, K.H. Chen, L.C. Chenm, "Heterostructures of ZnO-Zn coaxial nanocables and ZnO nanotubes" ***Appl. Phys. Lett.*** **(2002),** 81: 1312-1314.

[285] W.J Chen, W.L. Liu, S.H. Hsieh, T.K. Tsai, "Preparation of nanosized ZnO using α brass" ***Appl. Surf. Sci.*** **(2007),** 253: 6749-6753.

[286] J. Liu, X. Huang, J. Duan, H. Ai, P. Tu, "A low-temperature synthesis of multiwhisker-based zinc oxide micron crystals" ***Mater. Lett.*** **(2005),** 59: 3710-3714.

[287] Y. Huang, J. He, Y. Zhang, Y. Dai, Y. Gu, S. Wang, C. Zhou, "Morphology, structures and properties of ZnO nanobelts fabricated by Zn-powder evaporation without catalyst at lower temperature" ***J. Mater. Sci.*** **(2006),** 41: 3057-3062.

[288] B. Nikoobakht, X. Wang, A. Herzing, J. Shi, "Scable synthesis and device integration of self-registered one-dimensional zinc oxide nanostructures and related materials" ***Chem. Soc. Rev.*** **(2013),** 42: 342-365.

[289] L.C. Tien, S.J. Pearton, D.P. Norton, F. Ren, "Synthesis and microstructure of vertically aligned ZnO nanowires grown by high-pressure-assisted pulsed-laser deposition" ***J. Mater. Sci.*** **(2008),** 43: 6925-6932.

[290] J. Cui, Zinc oxide naniwires. and combs (Xu, T.; Ji, P.; He, M.; Li,) J. "Growth and structure of pure ZnO micro/nanocombs" ***J. Nanomater. Mater. Charact.*** **(2012),** 64: 43-52.

[291] W.S. Chiua, P.S. Khiew, M. Clokea, D. Isaa, T.K. Tana, R.S. Abd-Shukorb, M.A. Abd-Hamid, N.M. Huangc, H.N. Limd, "Photocatalytic study of two-dimensional ZnO nanopellets in the decomposition of methylene blue" ***Chem. Eng. J.*** **(2010),** 158: 345-352.

[292] M. Jose-Yacaman, C. Gutierrez-Wing, M. Miki, D.Q. Yang, K.N. Piyakis, E. Sacher, "Surface diffusion and coalescence of mobile metal nanoparticles" ***J. Phys. Chem. B*** **(2005),** 109: 9703-9711.

[293] V. Polshettiwar, B. Baruwati, R.S. Varma, "Self-asssembly of metal oxides into three-dimensional nanostructures: Synthesis and application in catalysis" ***ACS Nano*** **(2009),** 3: 728-736.

[294] Q. Xie, Z. Dai, J. Liang, L. Xu, W. Yu, Y. Qian, "Synthesis of ZnO three-dimensional architectures and their optical properties" ***Solid State Commun.*** **(2005),** 136: 304-307.

[295] J. Liu, X. Huang, Y. Li, K.M. Sulieman, F. Sun, X. He, "Selective growth and properties of zinc oxide nanostructures" ***Scr. Mater.*** **(2006),** 55: 795-798.

[296] M. Bitenc,; Z.C. Orel, "Synthesis and characterization of crystalline hexagonal bipods of zinc oxide" ***Mater. Res. Bull.*** **(2009),** 44: 381-387.

[297] Y. Wang, C. Zhang, S. Bi, G. Luo, "Preparation of ZnO nanoparticles using the direct precipitation method in a membrane dispersion micro-structured reactor" ***Powder Technol.*** **(2010),** 202: 130-136.

[298] N. Duran, P.D. Marcato, O.L. Alves, G.I.H. De Souza, E. Esposito, "Mechanistic aspects of biosynthesis of silver nanoparticles by several Fusarium oxysporum strains" *J. Nanobiotechnol.* **(2005)** 3: 1.

[299] D.S. Balaji, S. Basavaraja, R. Deshpande, D.B. Mahesh, B.K. Prabhakar, A. Venkataraman, "Extracellular biosynthesis of functionalized silver nanoparticles by strains of Cladosporium cladosporioides fungus" *Colloids Surf. B* **(2009),** 68: 88-92.

[300] A. Ahmad, P. Mukherjee, D. Mandal, S. Senapati, M.I. Khan, R. Kumar, M. Sastry, "Enzyme mediated extracellular synthesis of CdS nanoparticles by the fungus, Fusarium oxysporum" *J. Am. Chem. Soc.* **(2002),** 124: 12108.

[301] A. Ahmad, S. Senapati, M.I. Khan, R. Kumar, M. Sastry, "A novel extracellular synthesis of monodisperse gold nanoparticles using marine alga, Sragassium, wightii, greville" *Langmuir* **(2003),** 19: 3550.

[302] A. Ahmad, S. Senapati, M.I. Khan, R. Ramani, V. Srinivas, M. Sastry, "Intracellular synthesis of gold nanoparticles by a novel alkalo tolerant actinomycete, Rhodococcus species" *Nanotechnology* **(2003),** 14: 824.

[303] H. Lee, A.M. Purdon, V. Chu, R.M. Westervelt, "Controlled assembly of magnetic nanoparticles from magnetotactic bacteria using micro electromagnets arrays" *Nano Lett.* **(2004),** 4: 995-998.

[304] V. Armendariz, J.L. Gardea-Torresdey, M. Jose-Yacaman, J. Gonzalez, I. Herrera, J.G. Parsons, "Gold nanoparticles formation by oat and wheat biomasses" *Proceedings– Waste Research Technology Conference at the Kansas City, Mariott-Country Club Plaza* July 30-Aug 1, (**2002**).

[305] M. Kowshik, S. Ashtaputre, S. Kharrazi, W. Vogel, J. Urban, S.K. Kulkarni, K.M. Paknikar, "Extracellular synthesis of silver nanoparticles by a silver-tolerant yeast strain MKY3" *Nanotechnology* **(2003),** 14 (1): 95.

[306] K. Ghule, A.V. Ghule, J.Y. Liu, Y.C.J. Ling, "Microscale size triangular gold prisms synthesized using Bengal Gram beans (Cicer arietinum L.) extract and $HAuCl_4 \cdot 3H_2O$: A green biogenic approach" *Nanosci. Nanotechnol.* **(2006),** 6: 3746-3751.

[307] S. Li, Y. Shen, A. Xie, X.Yu, L. Qiu, L. Zhang, Q. Zhang, "Green synthesis of silver nanoparticles using. Capsicum annum **L**. extract" *Green Chem.* **(2007),** 9: 852-858.

[308] J.L. Gardea-Torresdey, J.G. Parsons, E. Gomez, J. Peralta-Videa, H.E. Troiani, P. Santiago, M. Yacaman, "Formation and growth of Au nanoparticles inside live alfalfa plants" *J. Nano Lett.* **(2002),** 2: 397-401.

[309] I.B. Obot, S.A. Umoren, A.S.J. Johnson, *Mater. Environ. Sci.* **(2013),** 4 (6): 1013-1019.

[310] E.M. Egorova, A.A. Revina, Physicochem. "Synthesis of metallic nanoparticles in reverse micelles in the presence of quercetin" *Eng. Asp.* **(2000),** 168: 87-96.

[311] Huang, Q. Li, D. Sun, Y. Lu, X. Yang, H. Wang, Y. Wang, W. Shao, N. He, J. Hong, C. Chen, "Biosynthesis of Silver and Gold Nanoparticles by Novel Sundried Cinnamomum camphora Leaf" *Nanotechnology* **(2007),** 8: 105104.

[312] B. Ankamwar, C. Damle, A. Ahmad, M. Sastry, "Biosynthesis of gold and silver nanoparticles using Emblica officinalis fruit extract, their phase transfer and transmetallation in an organic solution," *J. Nanosci. Nanotechnol.* **(2005),** 51665-1671.

[313] S.P. Chandran, M. Chaudhary, R. Pasricha, A. Ahmad, M. Sastry, "Synthesis of gold nanotriangles and silver nanoparticles using Aloe vera plant extract" *Biotechnol. Prog.* **(2006),** 22: 577-583.

[314] S.S. Shankar, A. Rai, A. Ahmad, M. Sastry, "Rapid synthesis of Au, Ag, and bimetallic Au core Ag shell nanoparticles using Neem (Azadirachta indica) leaf broth" *J. Colloid Interf. Sci.* **(2004),** 275: 496-502.

[315] R.P. Singh, S. Magesh, C. Rakkiyappan, " Formation of fenugreek (Trigonella foenum-graecum) extract mediated Ag nanoparticles: mechanism and applications" *Int. J. Bioeng. Sci. Technol.* **(2011),** 02 (03): 75-80.

[316] K. Govindaraju, S. Tamilselvan, V. Kiruthiga, G. Singaravelu, "Biogenic silver nanoparticles by Solanum torvum and their promising antimicrobial activity" *J. Biopestic.* **(2010),** (1): 3394-399.

[317] M. Sundarajan, S. Gowri, "Green synthesis of titanium dioxide nanoparticles by Nyctanthes arbour-tristis leaves extract" *Chalcogenide Lett.* **(2011),** 8 (8): 447-451.

[318] S. Maensiri, P. Laokul, J. Klinkaewnarong, S. Phokha, V. Promarak, S. Seraphin, J. Optoelectron. "Indium oxide (In_2O_3) nanoparticles using Aloe vera plant extract: synthesis and optical properties optoelectron" *Adv. Mater.* **(2008),** 10 (3): 161-165.

[319] H.M. Gong, L. Zhou, X.R.Su, S. Xiao, S.D. Liu, Q.Q.Wang, "Illuminating dark plasmons of silver nanoantenna rings to enhance exciton–plasmon interactions" *Adv.Funct. Mater.* **(2009),** 19: 298-303.

[320] N.P.S. Acharyulu, R.S. Dubey, V. Swaminadham, P. Kollu, S.V.N. Pammi, "Green synthesis of Cuo nanoparticles using Phyllanthus amarus leaf extract and their antibacterial activity against multidrug resistance bacteria" *Int. J. Eng. Res. Technol.* **(2014),** 3 (4): 639-641.

[321] L. Znaidi, "Sol-gel-deposited ZnO thin films: A review. Mater" *Sci. Eng.* **(2010),** 174: 18-30.

[322] Ruri Agung Wahyuono, Christa Schmidt, Andrea Dellith, Jan Dellith, Martin Schulz, Martin Seyring, Markus Rettenmayr, Jonathan Plentz, Benjamin Dietzek "ZnO nanoflowers-based photoanodes: Aqueous chemical synthesis, microstructure and optical properties" *Open Chem.,* (**2016**), 14: 158-169.

[323] Nabraj Bhattarai, Subarna Khanal, J. Jesus Velazquez-Salazar, Miguel Jose-Yacaman chapter 3 "Advanced Electron Microscopy in the Study of Multimetallic Nanoparticles" *Springer International Publishing Switzerland* **(2015),** 59-91.

[324] Maria Luisa Bondì, Roberto Di Gesù, "Emanuela Fabiola Craparo Chapter twelve Lipid Nanoparticles for Drug Targeting to the Brain" *Methods in Enzymology* **(2012),** 508: 229-251.

[325] Q. Wan, Q. H. Li, Y. J. Chen, T. H. Wang, X. L. He, J. P. Li, C. L. Lin, "Fabrication and ethanol sensing characteristics of ZnO nanowire gas sensors" *Appl. Phys. Lett.* **(2004)** 84: 3654-3656.

[326] S. Y. Li, P. Lin, C. Y. Lee, T. Y. Tseng, "Field emission and photofiuorescent characteristics of zinc oxide nanostructure synthesized by a metal catalyzed vapor-liquid-solid process" *J. Appl. Phys.* **(2004),** 95: 3711-3716.

[327] M. H. Huang, Y. Wu, H. Feick, N. Tran, E. Weber, P. Yang, "Catalytic growth of zinc oxide nanowires by vapor transport" *Adv. Mater.* **(2001),** 13: 113-116.
[328] B. D. Yao, Y. F. Chan, N. Wang, "Formation of ZnO nanostructures by a simple way of thermal evaporation" *Appl. Phys. Lett.* **(2002),** 81: 757-759.

[329] L. E. Greene, M. Law, J. Goldberger, F. Kim, J. C. Johnson, Y. Zhang, R. J. Saykally, P. Yang, "Low-Temperature Wafer-Scale Production of ZnO Nanowire Arrays" *Augew. Chem. Int. Ed.* **(2003),** 42: 3031-3034.

[330] C. Liu, J. A. Zapien, Y. Yao, X. Meng, C. S. Lee, S. Fan, Y. Lifshitz, S. T. Lee, "High-density, ordered ultraviolet light-emitting ZnO nanowire arrays" *Adv. Mater.* **(2003),** 15: 838-841.

[331] B. Liu, H. C. Zeng, "Hydrothermal synthesis of ZnO nanorods in the diameter regime of 50 nm" *J. Am. Chem. Soc.* **(2003),** 125: 4430-4431.

[332] M. Guo, P. Diao, S. Cai, "Hydrothermal Growth of Well-Aligned ZnO Nanorod Arrays: Dependence of Morphology and Alignment Ordering upon Preparing Conditions" *J. Solid State Chemistry* **(2005),** 178: 1864-1873.

[333] W. I. Park, Y. H. Jun, S. W. Jung, G. C. Yi, "Excitonic emissions observed in ZnO single crystal nanorods" *Appl. Phys. Lett.* **(2003),** 82: 964-966.

[334] A. B. Hartanto, X. Ning, Y. Nakata, T. Okada, "Growth mechanism of ZnO nanorods from nanoparticles formed in a laser ablation plume" *Appl. Phys. A* **(2003),** 78: 299-301.

[335] W. D. Yu, X. M. Li, X. D. Gao, "Using an elastomeric phase mask for sub-100nm photolithography in the optical near field" *Appl. Phys. Lett.* **(2004),** 84: 2658-2660.

[336] Y. Dai, Y. Zhang, Q. K. Li, and C. W. Nan, "Synthesis and optical properties of tetrapod-like zinc oxide nanorods" *Chem. Phys. Lett.* **(2002),** 358: 83-86.

[337] Y. Dai, Y. Zhang, Z. L. Wang, "The octa-twin tetraleg ZnO nanostructures" *Solid State Commun.* **(2003),** 126: 629-633.

[338] V. A. L. Roy, A. B. Djurišić, W. K. Chan, J. Gao, H. F. Lui, C. Surya, "Luminescent and structural properties of ZnO nanorods prepared under different conditions." ***Appl. Phys. Lett.*** **(2003),** 83: 141-143.

[339] J. M. Szarko, J. K. Song, C. W. Blackledge, I. Swart, S. R. Leone, S. Li, Y. Zhao, " Optical injection probing of single ZnO tetrapod lasers" ***Chem. Phys. Lett.*** **(2005),** 404: 171-176.

[340] H. Yan, R. He, J. Pham, P. Yang, "Morphogenesis of One-Dimensional ZnO Nano- and Microcrystals" ***Adv. Mater.*** **(2003),** 15: 402-405.

[341] Z. W. Pan, Z. R. Dai, Z. L. Wang, "Nanobelts of semiconducting oxides" ***Science*** **(2001),** 291: 1947-1949.

[342] H. Yan, J. Johnson, M. Law, R. He, K. Knutsen, J. R. McKinney, J. Pham, R. Saykally, P. Yang, "ZnO. Nanoribbon Microcavity Lasers" ***Adv. Mater.*** **(2003),** 15: 1907-1911.

[343] Y. B. Li, Y. Bando, T. Sato, K. Kurashima, "ZnO nanobelts grown on Si substrate" ***Appl. Phys. Lett.*** **(2002),** 81: 144-146.

[344] J. Y. Lao, J. G. Wen, Z. F. Ren, "Hierarchical ZnO Nanostructures" ***Nano Lett.*** **(2002),** 2: 1287-1291.

[345] J. Y. Lao, J. Y. Huang, D. Z. Wang, Z. F. Ren, "ZnO nanobridges and nanonails" ***Nano Lett.*** **(2003),** 3: 235-238.

[346] Y. J. Xing, Z. H. Xi, X. D. Zhang, J. H. Song, R. M. Wang, J. Xu, Z. Q. Xue, D. P. Yu, "Nanotubular structures of Zinc Oxide" ***Solid State Commun.*** **(2004),** 129: 671-675.

[347] J.H. Park, H.J. Choi, Y.J. Choi, S.H. Sohn, J.G. Park, "Ultrawide ZnO nanosheets" ***J. Mater. Chem.*** **(2004),** 1435-36.

[348] Z. L. Wang, X. Y. Kong, Y. Ding, P. Gao, W. L. Hughes, R. Yang, Y. Zhang, "Semiconducting and piezoelectric oxide nanostructures induced by polar surfaces" ***Adv. Funct. Mater.*** **(2004),** 14943-956.

[349] P. X. Gao, Z. L. Wang, "Quantifying oxygen diffusion in ZnO nanobelt" ***Appl. Phys. Lett.*** **(2004),** 84: 2883-2885.

[350] X. Y. Kong, Z. L. Wang, "Spontaneous polarization-induced nanohelixes, nanosprings, and nanorings of piezoelectric nanobelts" ***Nano Lett.*** **(2003),** 31625-1631.

[351] V. Polshettiwar, B. Baruwati, R.S. Varma, "Self-asssembly of metal oxides into three-dimensional nanostructures: Synthesis and application in catalysis" ***ACS Nano*** **(2009),** 3: 728-736.

[352] W.J. Chen, W.L. Liu, S.H. Hsieh, T.K. Tsai, "Preparation of nanosized ZnO using α brass" ***Appl. Surf. Sci.*** **(2007),** 253: 6749-6753.

[353] J. Cui, "Zinc oxide nanowires" **Mater Charact. (2012),** 64: 43-52.

[354] M. Bitenc, Z.C. Orel, "Synthesis and characterization of crystalline hexagonal bipods of zinc oxide" ***Mater. Res. Bull.* (2009),** 44: 381-38.

[355] JK Song, MB Zheng, ZJ Yang, HQ Chen, HY Wang, JS Liu, GB Ji, HQ Zhang, JM. Cao "Synthesis of Novel Flower-Like Zn(OH)F via a Microwave-Assisted Ionic Liquid Route and Transformation into Nanoporous ZnO by Heat Treatment" ***Nanoscale Res Lett* (2009),** 4 (12): 1512.

[356] Zhang Yuan, Xu Jiaqiang, Xiang Qun, Li Hui, Pan Qingyi, Xu Pengcheng, "Brush-Like Hierarchical ZnO Nanostructures: Synthesis, Photoluminescence and Gas Sensor Properties" ***J. Phys. Chem. C* (2009),** 113: 3430-3435.

[357] Salavati-Niasari Masoud, Mi Noshin, Davar Fatemeh**, "ZnO nanotriangles: Synthesis, characterization and optical properties" ***Journal of Alloys and Compounds* (2009),** 476: 908-912.

[358] F. Kayaci, C. Ozgit-Akgun, N. Biyikli, T. Uyar "Surface-Decorated ZnO Nanoparticles and ZnO Nanocoating on Electrospun Polymeric Nanofibers by Atomic Layer Deposition for Flexible Photocatalytic Nanofibrous Membranes" **RSC Advances (2013),** 3 (19): 6817-6820.

[359] M.K. Patra, K. Manzoor, M. Manoth, S.R. Vadera, N. Kumar "Studies on structural and magnetic properties of Co-doped pyramidal ZnO nanorods synthesized by solution growth technique" ***J. Phys. Chem. Solids* (2009),** 70: 659-664.

[360] D. Jezequel, J. Guenot, N. Jouini, F. Fievet, "Submicrometer zinc oxide particles: Elaboration in polyol medium and morphological characteristics" ***J. Mater. Res.,* (1995),** 10 77.

[361] N. Chouhan, L. Yeh, S. F. Hu, R. S. Liu, W. S. Chang, K. H. Chen. "CdSe(QDs)@ ZnO Nanotubes as an Effective Photoanode" ***Chem. Comm,* (2011),** 47: 3493-3495.

[362] E. M. P. Steinmiller, K. S. Choi, "Photochemical deposition of cobalt-based oxygen evolving catalyst on a semiconductor photoanode for solar oxygen production" ***Proc. Natl. Acad. Sci. U. S. A.,* (2009),** 106: 20633-20636.

[363] K. Sun, K. Madsen, P. Andersen, W. N. Bao, Z. L. Sun, D. L. Wang, "Metal on metal oxide nanowire Co-catalyzed Si photocathode for solar water splitting" ***Nanotechnology* (2012),** 23: 194013.

[364] A. Wolcott, W. A. Smith, T. R. Kuykendall, Y. P. Zhao, J. Z. Zhang, "Photoelectrochemical study of nanostructured ZnO thin films for hydrogen generation from water splitting" ***Adv. Funct. Mater.* (2009),** 19: 1849-1856.

[365] N. Kimizuka, M. Isobe, Nakamura, "Syntheses and singlecrystal data of homologous compounds, In_2O_3 $(ZnO)_m$ (**m** = 3, 4, and 5), $InGaO_3$ $(ZnO)_3$, and $Ga_2 O_3$ $(ZnO)_m$ (**m** = 7, 8, 9, and 16) in the In_2O_3 -$ZnGa_2 O_4$-ZnO system" ***M. J. Solid State Chem.*(1995),** 116 (1): 170-178.

[366] A. Kudo, Mikami, "New $In_2O_3 (ZnO)_m$ pholocatalysts with laminai structure for visible light-induced H_2 or O_2 evolution from aqueous solutions containing sacrificial reagents" *I. Chem. Lett.* **(1998),** 10: 1027-1028.

[367] Xuewen Wang, Gang Liu, Zhi-Gang Chen, Feng Li, Lianzhou Wang, Gao Qing Lu and Hui-Ming Cheng, "Enhanced photocatalytic hydrogen evolution by prolonging the lifetime of carriers in ZnO/CdS heterostructures" *Chem. Commun.,* **(2009),** 3452-3454.

[368] Yungi Lee, Kentaro Teramura, Michikazu Hara and Kazunari Domen. "Modification of $(Zn_{1+x}Ge)(N_2O_x)$ Solid Solution as a Visible Light Driven Photocatalyst for Overall Water Splitting" *Chem. Mater.* **(2007),** 19: 2120-2127.

[369] HM Chen, CK Chen, YC Chang, CW Tsai, RS Liu, SF Hu, WS Chang, KH Chen, "Quantum dot monolayer sensitized ZnO nanowire-array photoelectrodes: true efficiency for water splitting" *Angewandte Chemie.* **(2010),** Aug 9 122(34): 6102-5.

[370] K. Maeda, K. Teramura, T. Takata, M. Hara, N. Saito, K. Toda, Y. Inoue, H. Kobayashi, Domen, "GaN:ZnO Solid Solution as a Photocatalyst for Visible-Light-Driven Overall Water Splitting" *J. Am. Chem. Soc.* **(2005),** 127 (23): 8286-8287.

[371] K. Maeda, K. Teramura, T. Takata, M. Hara, N. Saito, K. Toda, Y. Inoue, H. Kobayashi, Domen, "GaN:ZnO solid solution as a photocatalyst for visible-light-driven overall water splitting" *K. J. Phys. Chem. B* **(2005),** 109 (43): 20504-20510.

[372] K. Maeda, K. Teramura, D. L. Lu, T. Takata, N. Saito, Y. Inoue, Domen, "Noble-metal/Cr_2O_3 core/shell nanoparticles as a cocatalyst for photocatalytic overall water splitting" *K. Angew. Chem., Int. Ed.* **(2006),** 45 (46): 7806-7809.

[373] K. Maeda, K. Teramura, D. L. Lu, T. Takata, N. Saito, Y. Inoue, Domen, "Characterization of Rh-Cr mixed-oxide nanoparticles dispersed on (Ga1-xZnx)(N1-xOx) as a cocatalyst for visible-light-driven overall water splitting" *K. J. Phys. Chem. B* **(2006),** 110 (28): 13753-13758.

[374] K. Maeda, K. Teramura, D. L. Lu, T. Takata, N. Saito, Y. Inoue, Domen, "Photocatalyst releasing hydrogen from water" *K. Nature* **(2006),** 440 (7082): 295-295.

[375] K. Yvon Lawn Mower, "Hydrogen-powered lawn mower: 14 years of operation" *Int. J. Hydrogen. Energy* **(2006),** 31.

Chapter 2

Instrumentation

ABSTRACT

The present chapter deals with the some of the important experimental techniques that used to conduct experiments for characterisation of the samples. In this chapter, we deals with the details (that includes the basic theories along with their principle and application part) of the various characterization techniques, which were used to characterized the as-synthesized nanocatalyst or molecular device.

Key Words: XRD, FESEM, HRTEM, EDS, FTIR, UV-Visible, PL, Cyclic Voltammetry and Water Splitting.

2.1 Instrumental techniques

This part discussed the basic theories and application of the advanced analytical analysis tools to characterise the samples that used in this study. The instrumental details of the analytical tools such as :x-ray diffraction (XRD), UV-VIS spectrophotometer, ATR (Attenuated total reflection) and Fourier Transmission Infrared (FTIR) spectroscopy, Field emission scanning electron microscopy (FE-SEM), transmission electron microscopy (TEM), Cyclic Voltammetry (CV), X-ray Absorption spectroscopy (XAS) and X-ray photoelectron spectroscopy (XPS) etc, were adopted to study the optical properties, crystallinity, functional groups, shape, size, sample purity and binding energy in the presence of nanocatalysts, chemical environment at bulk and surface.

2.1.1 Electron Microscopy (EM)

Electron microscopy is extremely versatile technique for providing morphological information over a wide range of resolution from 10 μm to 2Å. Particularly in the range where the specimen is so small (<1μm) that optical microscopes are not able to image it anymore. Electron microscopes operate in either transmission (TEM) or scanning (SEM) mode.

2.1.1.1 Transmission Electron Microscopy (TEM)

Transmission Electron Microscopy (TEM) is one of the most important tools used in nanotechnology for imaging nanomaterial with sub-nanometer resolution (High resolution TEM). In this technique, a thin specimen is imaged by an electron beam, which is irradiated through the sample at uniform current density. The typical acceleration voltage in an operational TEM is 80-200 KV. The electrons are emitted from a thermionic (tungsten or lanthanum hexaboride filament) or field emission (tungsten filament) electron guns. The set of the condenser lenses and illumination slit can control the area of specimen to be illuminated, as shown in Figure 2.1.

The function of the objective lens is the diffraction image formation by the sample. Electron diffraction images are used to identify the surface morphology of the material. To investigate the particle size distribution and crystalline nature of the metal nanoparticles. For this particular study the diffraction image mode is used to monitor the samples,. The electron intensity distribution of the specimen will be investigated with the help of the magnified three or four stage lens system and fluorescent screen. [1] The images of the samples are captured on a photographic plate or CCD camera. A full detailed description about the TEM can be found elsewhere [2] The analysing

capacity of TEM has been significantly enhanced by introduction of the several advanced techniques into the main instrument.
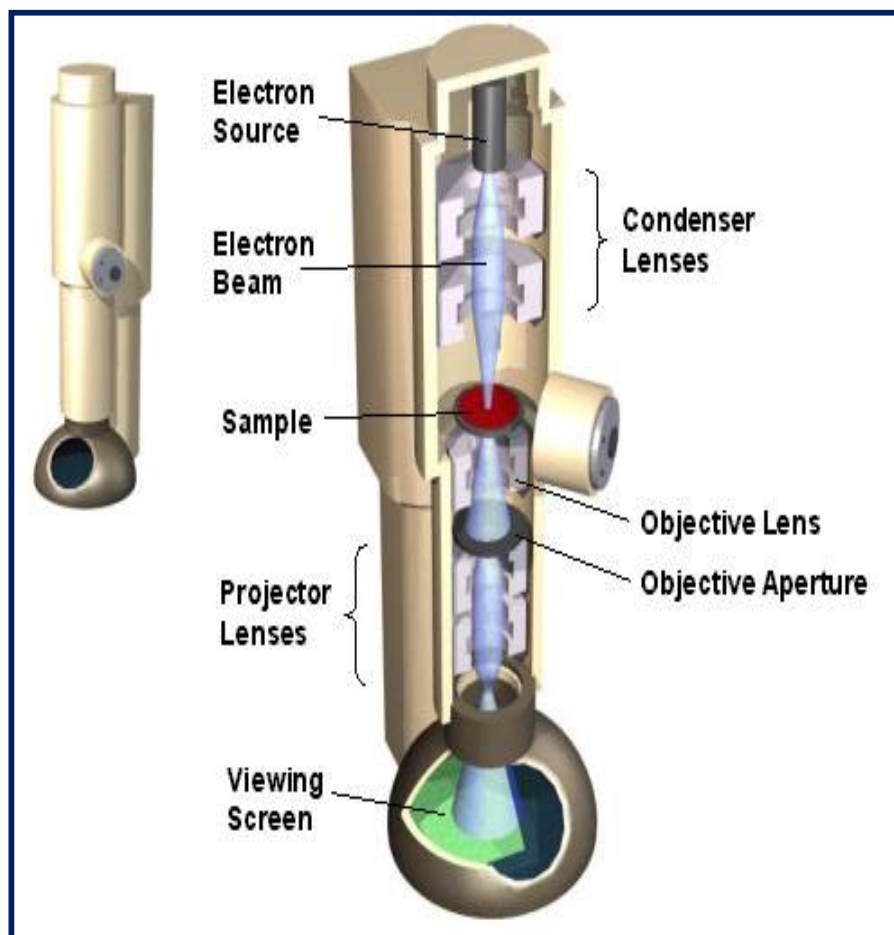
Figure 2.1 Setkch diagram of a Transmission Electron Microscope that to be used in the imaging and diffraction modes. [3]

TEM column alignment, applied voltage, angle/plane of incident light, magnification unit and several other factors are used to control / acquire good quality high resolution-TEM (HRTEM) images of the samples. TEM column alignment is needed to be carried out instrument alignment using electron gun and condenser lens alignment unit, plus astigmatic correction unit for condenser lenses and objective lens. Optimum focus is a crucial requirement of the HRTEM atomic image of a crystalline sample. TEM instrument of the Model- JEOL-2010F TEM, located

at Material Research Center (MRC) MNIT, Jaipur (Raj.), was used for the study. It has a operating voltage range from 20 to 200kV. TEM samples were prepared by taking small quantities of nanoparticles in alcohol was separated by centrifugation and gone through ultra sonication and the well dispersed suspensions were made. 3-4 Drops of the well dispersed solid samples in alcohol on a 300-mesh, were mounted on carbon-coated Cu grid (EM sciences) and after careful evaporation of the liquid in air, Cu grid with sample will be placed at sample holder for collecting the information regarding particle size, shape and determination of the size distribution of the as-synthesised nanoparticles. Electron diffraction patterns and EDX profile obtained from a field emission TEM were used to study the composition and morphology of the studied nanoparticles.

2.1.1.2 Scanning Electron Microscopy (SEM)

The Scanning electron microscope (SEM) is a representative electron microscope that is capable for producing high resolution images of a sample surface. This method was developed to overcome the limitations of optical microscopy to provide increased magnification and resolution. This is far superior to the optical systems. SEM is powerful tool for examining and interpreting microstructure of materials, and is widely used in the field of material science. The SEM technique is based on the interaction of an incident electron beam with the specimen. [4] SEM images have a characteristic three-dimensional appearance and are useful for judging the surface structure of the sample. By correlating the sample scan position with the resulting signal, a black and white image can be formed that is absolutely similar to what would be seen through an optical microscope. A schematic diagram of an SEM apparatus is given below in Figure 2.2.
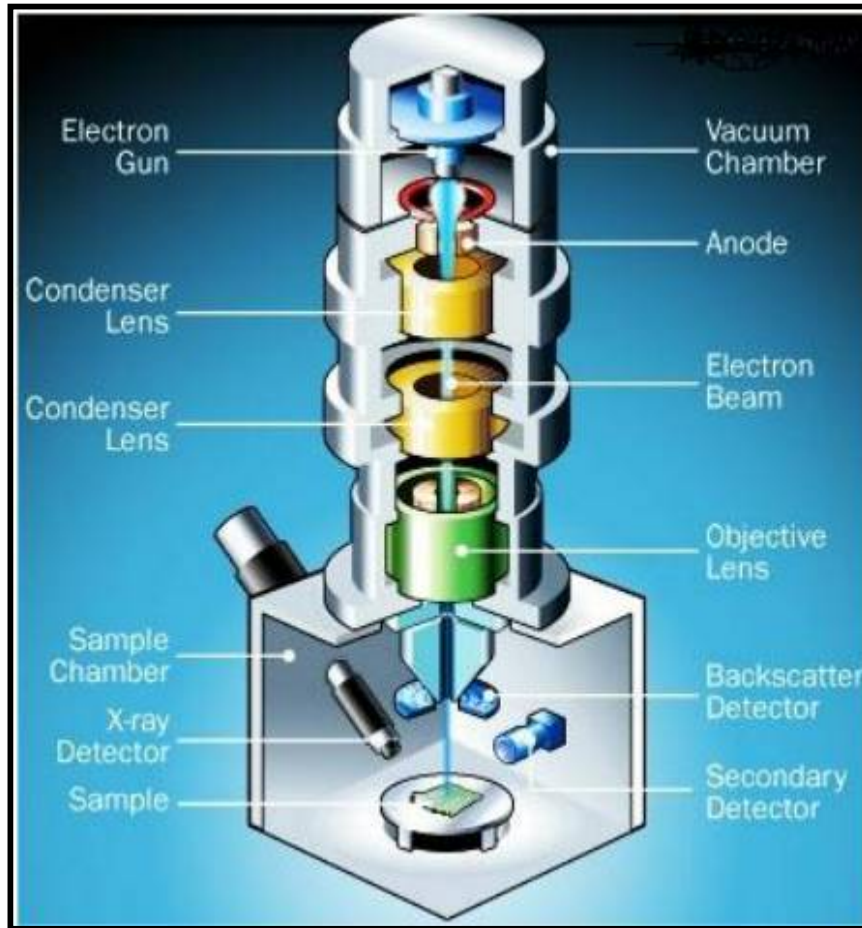
Figure 2.2 Schematic diagram of Scanning Electron Microscope [5]

SEM analysis technique is a very unique and versatile tool over the other complementary imaging modes. That can be use two different modes of analuses i.e.

(1) Specimen current imaging mode, in which the sample was illuminated by the electron beam to produce an image and controlled by the intensity of the electrical current.. It can often be used to show subsurface defects.

2) Backscatter imaging mode, which used high-energy electrons that emerged from the nearly 180 degrees from the irradiation beam direction. The backscatter electron yields is function of the average atomic number of each point on the sample, and thus can able to give us the information about the composition.

The detailed description of the technique and it practical application can be found elsewhere. [6] For this study FESEM analyses were done by using the instrument of make FEI Nova NanoLab situated at Material Research Center (MRC) MNIT, Jaipur (Raj.). This microscope is equipped with a field emission gun, operating at an accelerating voltage 0.2 to 30kV, with a claimed resolution images of 2 nm.

2.1.2 Fourier Transform Infrared (FTIR) Spectrophotometer

Fourier transform infrared (FTIR) Spectrophotoscopy is a energy dispersive technique that used for the many applications, where identification of bonding and group is required with higher sensitivity. [7] This technique is based on the vibrations of the atoms present with in a molecule where the IR spectrum obtained by passing IR radiation through a sample and used to detect the fraction of the incident radiation absorbed by the sample. The absorption spectrum corresponds to the frequency of a vibration and intensity of a sample molecule. [8] Moreover, chemical bonds and the motion of the molecules present in different environments, which will absorb the different intensities at varying frequencies. Thus, the frequencies of infrared radiation absorbed (peaks or signals) can be directly correlated to the bonds within the analysed compound. Because each inter-atomic bond might vibrate with different type of motions (stretching or bending). Therefore, an individual bond may absorb at more than one IR frequency. Usually, the stretching absorptions can produce the stronger peaks than bending. However, the Finger print region of absorptions can be useful in identification of the similar types of bonds.

One of the finest advantages of FTIR technology is that it can accept a wide range of sample such as gases, liquid, pastes, powders, films, fibers and surfaces can be examined through a sensible sampling technique. Attenuated total reflectance (ATR) spectrophotometer is also used for analysing the samples. Attenuated total Reflectance FTIR (ATR-FTIR) is a modified version of FTIR, where. The IR radiation falls onto the studing crystal. And attenuated IR radiations reflected from the surface of the materials, are used to identify the sample. This technique is especially useful for obtaining IR spectra of the difficult samples (such as thick or highly absorbing solid and liquid materials, including films, coatings, powders, threads, adhesive, polymers and aqueous samples) that cannot be examined by the normal transmission method.. ATR required a little amount of the sample with simple sample preparation method. The sampled

surface pressed into intimate optical contact with the lid of the crystal such as ZnSe, diamond or Ge.

In this work, FTIR spectrometer of Bruker -Tensor model, situated at Department of Pure & Applied Chemistry of University of Kota, Kota (Raj.) was used for the study. The sample for FTIR was prepared by mixing of the sample with dried KBr (1: 20) weight ratio and the spectrum was recorded in the range of 400-4000cm^{-1} with a resolution of 4cm^{-1}.
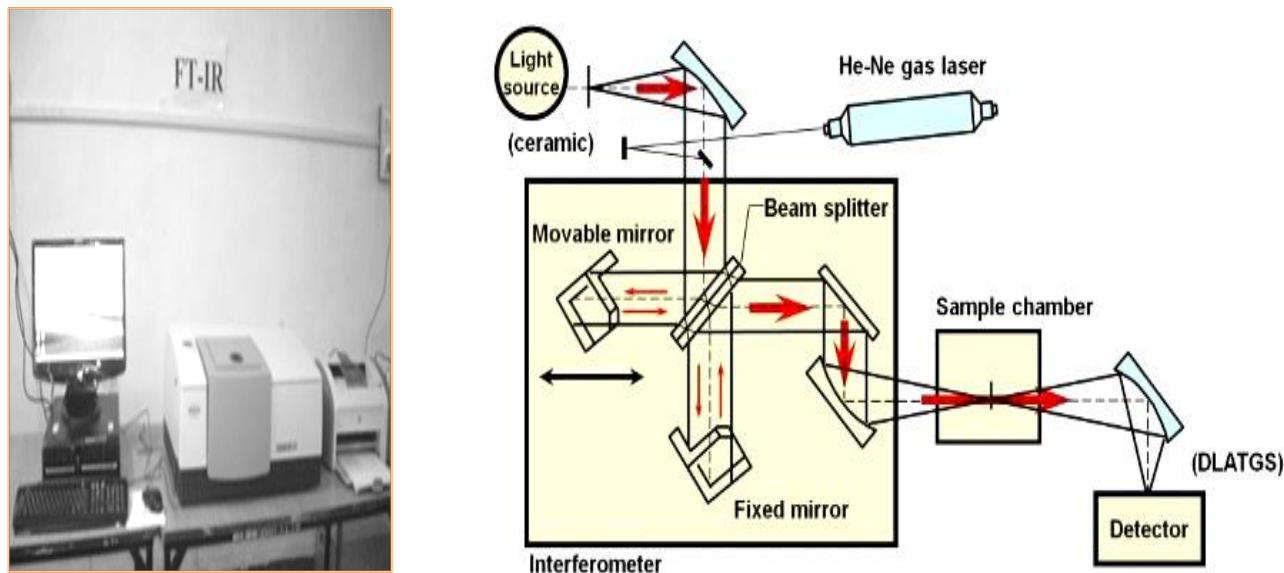
Figure 2.3 Schematic diagram of Fourier transform infrared (FTIR) spectrometer.

2.1.3 Ultraviolet -Visible Spectrophotometer

Ultraviolet-visible (UV-Vis) spectroscopy offers a relatively straight forward and effective way for quantitatively characterization of the wide range of the organic and inorganic compounds by determining the electronic transition and the band gap of a material. Furthermore, the instrument operates on the principle of absorption of photons that promotes the molecule to be in an excited state and it is an ideal technique for. UV-Vis analysis can be performed for the metal nanoparticles that dispersed in a solvent or embedded in to the insulator matrix. In such cases, absorption of incident radiation takes place on to the sample surface and due to surface plasmon resonance (SPR) of the metal nanoparticles the light waves trapped on the surface of the semiconductor because of their interaction with the free electrons of the noble metal/

nanoparticles with light. [9] Which is not found in the spectrum of their bulk counter parts. [10] The UV-Vis spectrum shows a characteristic absorption band at a specific wavelength depending upon the nature of nanoparticles, matrix, shape of the particles and their distribution. [11, 12, 13]
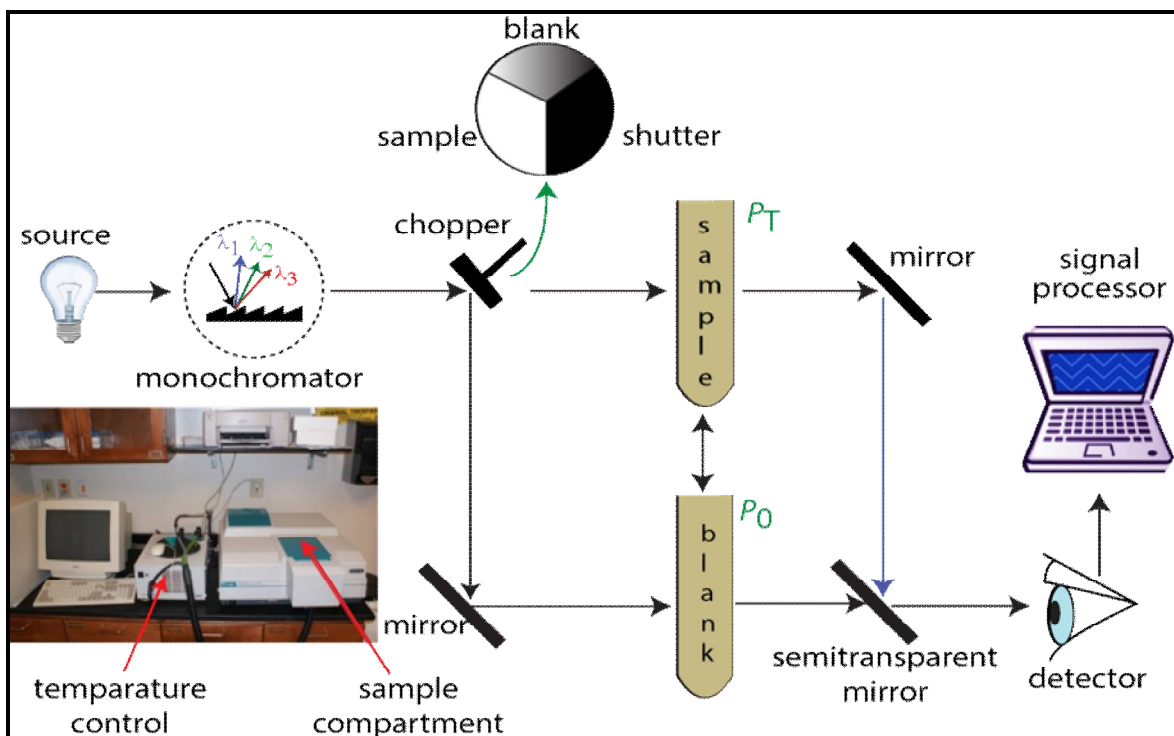
Figure 2.4 Schematic diagram of Ultraviolet-Visible Spectrophotometer

Furthermore, size-depending optical properties can be evaluated by the UV-visible spectrum, particularly at the atomic scales. Broadening or shifts of the peak along the absorption wavelength was found on varying different factors. [14, 15]

In this work UV-vis absorption spectra was recorded on a double beam spectrophotometer (LABINDIA Uv-Visible 3000+), situated at Department of Pure & Applied Chemistry, University of Kota, Kota (Raj.). The sample was dissolved in methanol, and placed in a quart's cuvette with path length was set to 1.0 cm for taking observation on the structure.

2.1.4 X-ray absorption spectroscopy (XAS)

X-ray absorption spectroscopy (XAS) is a technique is used when XRD fails to detect the atomic environment of the element f. When the x-rays fall upon the sample the oscillating electric field of

the electromagnetic radiation interacts with the electrons bounded with the atom. Afterwards either the radiation will be scattered or absorbed to excite the other electrons. A narrow monochromatic x-ray beam of intensity I_0 passing through a sample of thickness x, and afterwards the reduced intensity I detected at the receiving end as follows:

$$\ln (I_0 /I) = \mu\, x \qquad\qquad .... (1)$$

Where, μ is the linear absorption coefficient, which depends on the types of atoms and the density ρ of the material.
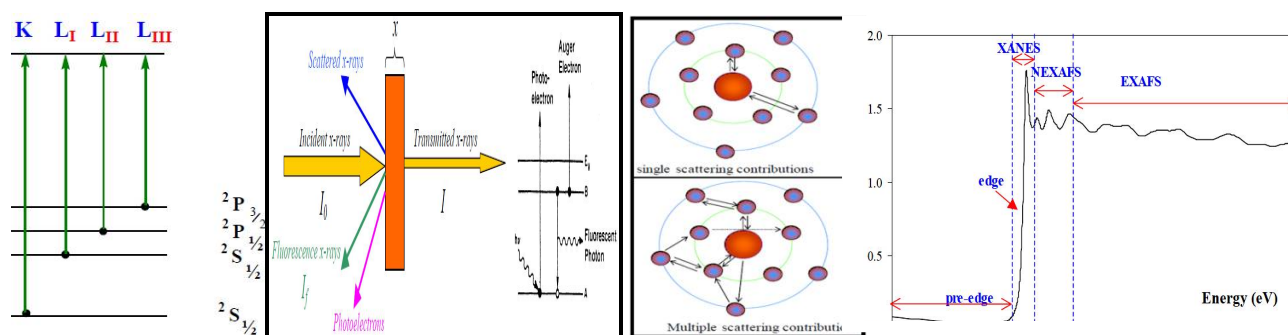
Figure 2.5 Schematic diagram of X-ray absorption spectroscopy (XAS)

At certain absorption energies, where the intensity increases drastically and gives rise to an absorption edge. Each of theedge corresponds to the energy of the incident photons that sufficient to cause excitation of a core electron of the absorbing atom to a continuum state, i.e. to produce a photoelectron. Thus, the energies of the absorbed radiation at these edges correspond to the binding energies of electrons in the K, L, M, etc- shells of the absorbing elements. Therefore, the absorption edges are indicated by the increasing energy, K, L_I, L_{II}, L_{III}, M_I,…. that corresponds to the excitation of an electron from the 1s ($^2S_{1/2}$), 2s ($^2S_{1/2}$), 2p ($^2P_{1/2}$), 2p ($^2P_{3/2}$), 3s ($^2S_{1/2}$), … to the other orbital (states), respectively. A XAS spectra is generally divided into four parts:

1) Pre-edge ($E < E_0$).

2) X-ray absorption near edge structure (XANES), where the energy of the incident x-ray beam is $E = E_0 \pm 10$ eV.

3) Near edge x-ray absorption fine structure (NEXAFS), in the region between 10 eV up to 50 eV above the edge.

4) Extended x-ray absorption fine structure (EXAFS), which starts approximately from 50 eV and continues up to 1000 eV above the edge.

The minor features in the pre-edge region occured due to the electron transitions from the core level to the higher unfilled or half-filled orbital (e.g. : $s \rightarrow p$, or $p \rightarrow d$). XANES region belongs to the transitions of core electrons to non-bound levels. Due to the high probability of such transition, a sudden raise in absorption intensity is observed. In NEXAFS, the ejected photoelectrons possess a low kinetic energy ($E-E_0$ is small) and experience strong multiple scattering among electrons of even higher coordinating shells. In EXAFS region, the photoelectrons with high kinetic energy ($E-E_0$ is large), are enriched with the single scattering of the electrons by the nearest neighbouring atoms.

2.1.5 X-Ray Diffraction

X-ray diffraction is a versatile, non-destructive method of analyses of the crystallinity, phase identification and quantitative determination of various crystalline forms, present in powder and solid samples. Diffraction occurs when the X ray waves interacted with a regular structure of crystal where the atomic distances are same as the wavelength of x-rays. For example, light can be diffracted by a grating having scribed lines spaced on the order of a few thousand angstroms (about the wavelength of light). It happens because of the X-rays have the wavelengths of order of a few angstroms, the same as typical inter-atomic distances in crystalline solids. That means X-rays can be diffracted from minerals which, by definition, are crystalline and have regularly repeating atomic structures. When certain geometric requirements are met, X-rays scattered from a crystalline solid can constructively interfere, producing a diffracted beam. In 1912, W. L. Bragg recognized a predictable relationship among several factors.

1. The distance between similar atomic planes in a mineral (the inter atomic spacing) which we call the d-spacing and measure in angstroms.

2. The angle of diffraction which we call the theta angle and measure in degrees. For practical reasons the diffractometer measures an angle twice that of the theta angle. Not surprisingly, we call the measured angle '2-theta'.

3. The wavelength of the incident X-radiation, symbolized by the Greek letter lambda and, in our case, equal to 1.54 angstroms.

$$n\lambda = 2d \sin\theta \qquad \qquad \text{........ (2)}$$

Where, λ- Wavelength of X-ray, d- Inter planer spacing,   θ- diffraction angle and n- 0,1,2,3….

(a) **(b)** **(c)**
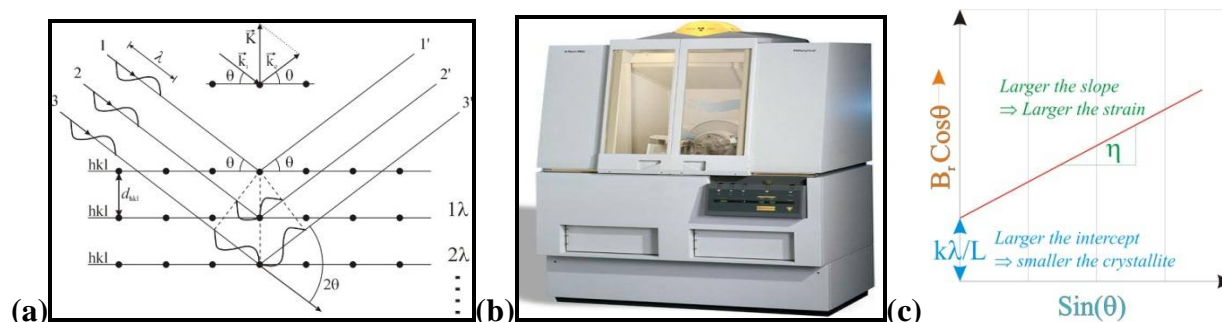
Figure 2.6: (a) Schematic diagram of Bragg's diffraction and (b) schematic diagram of PANalytical diffractometer (Model: DY-1656) (c) Wiliamson curve for particle size determination

Here, XRD was done by the X-ray diffraction of the as milled powder samples were performed using the diffractometer. X-Ray diffraction patterns were recorded from 20° to 90° with a PANalytical system diffractometer (Model: DY-1656) using Cu Kα (λ=1.542Ao) with an accelerating voltage of 40 KV. Data were collected with a counting rate of 1°/min. The Kα doublets were well resolved. From XRD, the crystallite size can be found out by using the Scherrer's formula,

$$P = 0.9\,\lambda / \beta \cos\theta \qquad \qquad \text{.......... (3)}$$

Where P-crystallite size, λ-wavelength (CuK$_\alpha$~1.54A0), β -full maxima half width, θ- diffraction angle, by applying Scherer's formula, the crystallite size of the nanostructure sample found out to be approximately similar to the value measured by particle size analyzer. Moreover, G.K.Williamson and his student, W.H.Hall [16] gives a formula (Equation no. 4) for particle size determination that based on the principle of the approximate formulae for size broadening, β, and strain broadening, β$_e$, vary quite differently with respect to Bragg angle, θ:

$$B_r \, Cos(\theta) = \frac{k\,\lambda}{L} + \eta \, Sin(\theta)$$

.... (4)

Williamson-Hall plot includes the all peak information beside the Scherrer formula, used the single maxima for particle size determination. Therefore, this method is more accurate than other methods.

2.1.6 Cyclic Voltammetry (CV)

Cyclic Voltammetry (CV) is an electrochemical technique which measures the current- voltage curve in an electrochemical cell under conditions where voltage is applied in excess of that can be predicted by the Nernst equation. The equipment required to perform cyclic voltammetry consists of a conventional three-electrode potentiostat connected to three electrodes (working, reference and auxiliary) immersed in a test solution. The potentiostat applies and maintains the potential between the working and reference electrode while at the same time measuring the current at the working electrode. Charge flows between the working electrode and the auxiliary electrode. CV is performed by cycling the potential of a working electrode, and measuring the resulting current. A cyclic voltammogram is obtained by applying a linear potential sweep (that is, a potential that increases or decreases linearly with time) to the working electrode. As the potential is swept back and forth past the formal potential, E° of an analyte a current flow through the electrode that either oxidizes or reduces the analyte. The magnitude of this current is proportional to the concentration of the analyte in solution, which allows cyclic voltammetry to be used in an analytical determination of concentration. A recording device (such as a computer or plotter) is used to record the resulting cyclic voltammogram as a graph of current versus potential. CV methods have found to be extensive applicable for the evaluation of thermodynamic and kinetic parameters such

as number of electrons change (n), heterogeneous rate constant (k_o), entropy (S), Gibb's free energy (G) and diffusion coefficient (D_o) etc, for a number of redox reactions and associated chemical reactions. These methods are especially useful in both oxidation and reduction process and to study the multiple electron transfer in an electrochemical reaction.
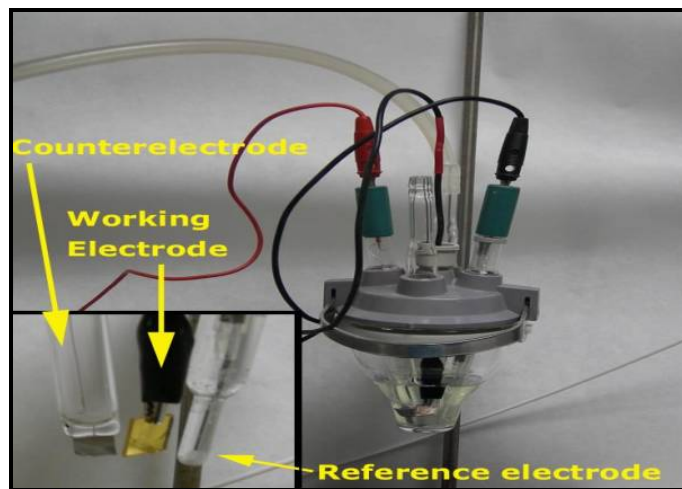
Figure 2.7 Schematic diagram of Electrochemical cell

We had use potentiostat of autolab metrohm model no. AUT50244, placed at the Pure & Applied Chemistry, University of Kota, Kota (Raj.), for cyclic voltametric study of the as synthesised system with respect to the time and concentration.

2.1.7 Spectrofluorimeter

Figure 2.8 depict the basic flow diagram of the spectrofluorimeter used for the measuring of the fluorescence that includes two wavelength selectors, one for selecting an excitation wavelength from the source and one for selecting the emission wavelength from the samples with the help of the absorption or interference filters. We had used the low-pressure Hg vapour lamp to provides the emission energy in the ultraviolet and visible region (254, 312, 365, 405, 436, 546, 577, 691, and 773 nm with the help of the monochromator and high-pressure Xe arc lamp as an excitation source, that gives us a continuous emission spectrum.
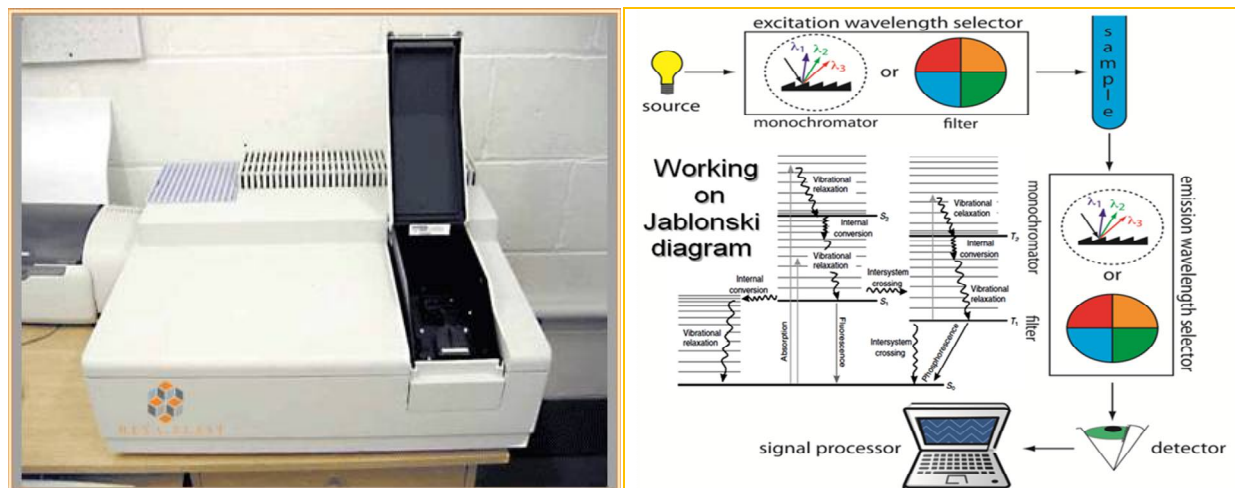
Figure 2.8 schematic diagrams for measuring fluorescence showing the placement of the wavelength selectors for excitation and emission. When a filter is used the instrument is called a fluorimeter, and when a monochromator is used the instrument is called a spectrofluorimeter. Jablonski diagram is shown in inset is the working principle of the spectrofluorimeter.

Photoluminescence spectroscopy is widely used to identify the optical and electronic properties of semiconductors and molecules. The photoluminescence is relaxation processes and divided into two categories: fluorescence and phosphorescence. When an analyte absorbsan ultraviolet or visible photon, one of its valence electrons jump from the ground state to an excited state by conservation of the electron's spin. Emission of a photon occur when electron moves from the singlet excited state to the singlet ground state or between any two energy levels with the same spin is known as fluorescence. It has an average lifetime of excited state of an electron is 10^{-5} - 10^{-8} s. Fluorescence, occurs in absence of the source of excitation. Emission from a triplet excited state to the singlet ground state or between any two energy levels that differ in their respective spin states–is called phosphorescence. Because the average lifetime for phosphorescence ranges from 10^{-4} -10^{4} s, phosphorescence may continue for some time after removing the excitation source. These techniques can be combined with microscopy, to trace the intensity or the lifetime of the photoluminescence across a sample i.e. either a solid or liquid sample.
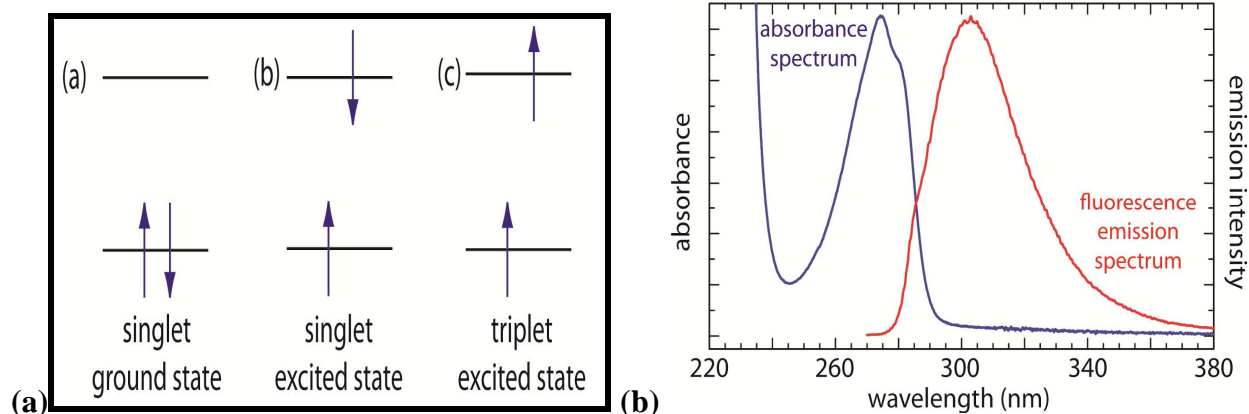
Figure 2.9 (A) Electron configurations for (a) a singlet ground state; (b) a singlet excited state; and (c) a triplet excited state. (B) Absorbance spectrum and fluorescence emission spectrum

In this work PL spectrum was recorded on spectrofluorimeter processor Shimadzu model (RF-5301 (PC) S CE (LVD) situated at Department of Pure & Applied Chemistry, University of Kota, Kota (Raj.).

2.1.8 Ultrasonic Processor

Ultrasonic processor of make cole-parmer and model EI-250UP of 250 watts (average) and 20+/-3 KHz frequency and with microprocessor based timer 0 to 20 minutes was used to prepare the sample for analysis. The instrument is located at Pure & Applied Chemistry, University of Kota, Kota (Raj.)

2.1.9 Centrifuge

Centrifuge (REMI model 8X15) is located at of Pure & Applied Chemistry, University of Kota, Kota (Raj.) with the swings of out four heads was used to separate nano particles from aqueous dispersion from colloidal solution and as separated silver nanoparticles are stabilized for the more than two months.

2.1.10 pH-Meter

Systronics digital pH meter of model MAC (MSW-552) was used for the pH determination for the synthesized nanoparticles and the reaction mixtures during the various steps of the synthesis process. The pH of the reduced solution of the nanoparticles was found to be basic in nature.

2.1.11 Water splitting Instrumentation

The catalyst (0.3 g) was suspended in 120 mL of 20% aqueous CH_3OH electrolyte in a double walled Pyrex glass reaction cell (volume ~220 mL, with water jacket) that was sealed with a rubber septum. To expel the air content from the solution, the sample was purged with Ar for 1 h prior to start the photochemical reaction. Ar gas flow continuously in inner jacket, to maintain 1 atm. pressure of the solution. Temperature of the outer jacket was set at $25^{\circ}C$. The suspension was irradiated with a 300 W Xe lamp (>420 nm, light intensity $1x10^{22}$ photons per hour Xe lamp-HX1, Model PE300UV). All the experiments are carried out under ambient conditions. Photocatalytic responses were hourly monitored in terms of the amount of the hydrogen generated at 1-4 h time intervals, using gas chromatograph (Shimazdu, Japan, thermal conductivity detector and molecular sieve with 5 A columns) throughout the course of the reaction.

Figure 2.10 Schematic diagram of Water Splitting Instrument

2.2 References

[1] L. Reimer*, **"**Transmission electron microscopy: physics of image formation and microanalysis" ***Springer-Verlag, Berlin: New York*** (**1989**).

[2] D. B. Williams, C. B. Carter, "Transmission electron microscopy: A textbook for material science" ***Plenum Press, New York*** (**1996**).

[3] http://commons.wikipedia.org/wiki/File:TEM-ray-Diag.basic.en.png, ***visited June*** (**2010**).

[4] P. J. Grundy, G. A. Jones, "Electron microscopy in the study of materials" *Edward Arnold, London* **(1976).**

[5] J. Goldstein, "Scanning electron microscopy and X-ray microanalysis: A text book for biologist, material scientist, geologist" *Plenum Press, New York* **(1992).**

[6] http://www.purdue.edu/REM/rs/sem.htm, *visited June* **(2010).**

[7] F. A. Settle, "Handbook of instrumental techniques for analytical chemistry" *Prentice Hall, Upper saddle River, N. J.,* **(1997).**

[8] B. Stuart, D. J. Ando, "Modern infrared spectroscopy" *Wiley, Chichester, New York* **(1996).**

[9] W. L. Brans, A. Dereux, T. W. Ebbesen, "Surface plasmon sub wavelength optics" *Nature* **(2003)** 424 824.

[10] J. J. Mock, D. R. Smith, S. Schultz, "Local refractive index dependence of plasmon resonance spectra from individual nanoparticles" *Nano Lett.* **(2003)** 3 485.

[11] F. Strelow, A. Fojtik, A. Henglein, "Chemisorption of phosphine on colloidal silver in aqueous solution" *J. Phys. Chem.* **(1994)** 98 3032.

[12] A. C. Templeton, J. J. Pietron, R. W. Murray, P. Mulvaney, "Solvent refractive index and core charge influences on the surface plasmon absorbance of alkanethiolate monolayer-protected gold clusters" *J. Phys. Chem. B* **(2000)** 104 564.

[13] (a) C. Bullen, P. Mulvaney, "The effects of chemisorption on the luminescence of CdSe quantum dots" *Langmuir* **(2006)** 22 3007. (b) A. Henglein, "Chemisorption effects on colloidal lead nanoparticles" *J. Phys. Chem. B* **(1999)** 103 9302.

[14] U. Kreibig, M. Vollmer, "Optical properties of metal clusters" *Springer, Berlin: New York,* **(1995).**

[15] A. D. Mcfarl, R. P. Van Duyne, "Single silver nanoparticles as real-time optical sensors with zeptomole sensitivity" *Nano Lett.* **(2003)** 3 1057.

[16] G.K. Williamson, W.H. Hall, "X-ray line broadening from filed Al and W" *Acta Metall.* (1953) 1, 22-31.

Chapter 3

Synthesis and Characterization: Co catalyst (Pt)/ Sensitizer (Ag or CdS) loaded- ZnO NRs

3.1 Synthesis of ZnO NRs by Hydrothermal Method and their Characterization

3.2 Synthesis and Characterization of biogenic Ag NPs prepared by using:

(I) Ajwain (Trachyspermum Ammi) seeds extract

(II) Fenugreek (Trigonella Foenum Graecum) seeds extract

(III) Tea (Camellia Sinensis) leaves extract

(IV) Shikakai (Acacia Concinna) pods extract

3.3 Synthesis and Characterization of Ag @ZnO NRs

3.4 Synthesis and Characterization of CdS @Co-ZnO NRs
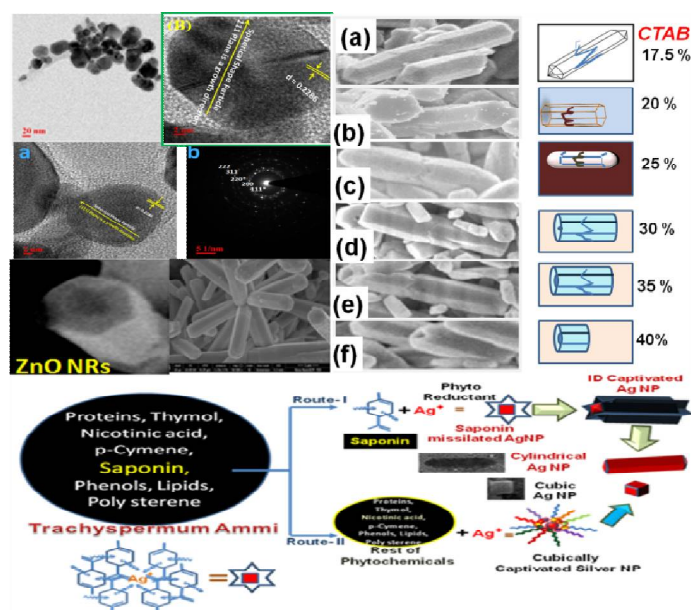
Chapter 3.1

Synthesis of ZnO NRs by Hydrothermal Method and their Characterization

ABSTRACT

Single crystal ZnO nanorods arrays were synthesized at low temperature in an aqueous solution containing zinc nitrate and hexamethylenetetramine by simple hydrothermal method. In this chapter ZnO, nanorods were synthesized using zinc acetate dihydrate as starting material for ZnO seed formation. Afterwards, the ZnO nanorods were hydrothermally synthesised using hexamethylenetetramine and zinc nitrate in a seeds (ZnO) grown at 90°C for 10h. The crystal structure, orientation and surface morphology were investigated by X-ray diffractometer and electron microscopy, respectively. Optical properties were studied using UV-visible spectroscopy. As prepared ZnO nanorods were employed as wide band gap semiconductor to split water for hydrogen generation when it decorated with Ag nanoparticles.

Key Words: ZnO nanorods, HMT, optical properties, hydrothermal method, hydrogen generation.

3.1.1 INTRODUCTION

Wide band gap II-VI semiconductor, zinc oxide (ZnO) has many applications such as transducers, gas sensors, and dye-sensitized solar cells, water splitting and other optoelectronic activities, etc. [1] Specially, ZnO have attracted considerable attention because they can be tailored in different morphologies to possess high electrical conductivity and high visible transmittance. ZnO is a self-excitation semiconductor, one of the most important promising materials which have been applied tomany fields such as transparent conductive contacts, solar cells, laser diodes, ultraviolet lasers, thin film transistors, optoelectronicand piezoelectric applications and surface acoustic wave devices. [2-5] ZnO films with well aligned sheets, rods, or wires may exhibit better performance due to high surface to volume ratio that can promote fast and effective path for electron transportation. Therefore, it is essential to control the morphology of zinc oxide. 1D- ZnO nanostructures such as nano tubes, nano wires, nanorods, nano belts, nano cables, and nano ribbons had stimulated considerable interest of researchers due to their applications in numeous fields. Several methods for the synthesis of nano structured ZnO have been explored, but some of them are highly power demanding (by means of temperature or pressure) or they used sophisticated fabrication techniques such as laser ablation, chemical vapour pressure deposition (CVD) method,etc, that can scaling up thecomplicacy of the method. One of the most promising andcost effective method to synthesize nanorods is the hydrothermal method, which comparatively needs low-temperature and lesscomplexity. Additionally, the above method has a high degree of versatility to modify several parameters, such as temperature, pH and concentration of reactants, which in turn could modify the morphology, size and shape of the nanozincoxide.

3.1.2 EXPERIMENTAL PROCEDURES

3.1.2.1 Preparation of ZnO seed powder

ZnO nanorods were grown via a two-step process. In the first step, a ZnO seeds was prepared by zinc acetate. In the second step, ZnO nano rods were grown by hydrothermal technique. In this process firstly 2 gm of zinc acetate powder exposed to the 350°C temperature in muffule furnace (350°C is the decomposition temperature of the zinc acetate) for 30 min to form ZnO seeds, by using below mentioned reactions:

$$Zn(CH_3COO)_2 . 2H_2O \xrightarrow{heat} Zn(CH_3COO)_2 + 2H_2O \tag{1}$$

$$4Zn(CH_3COO)_2 + 2H_2O \xrightarrow{heat} Zn_4O(CH_3COO)_6 + 2CH_3COOH \tag{2}$$

$$Zn_4O(CH_3COO)_6 + 3H_2O \xrightarrow{heat} 4ZnO + 6CH_3COOH \tag{3}$$

$$Zn_4O(CH_3COO)_6 \xrightarrow{heat} 4ZnO + 3CH_3COCH_3 + 3CO_2 \tag{4}$$
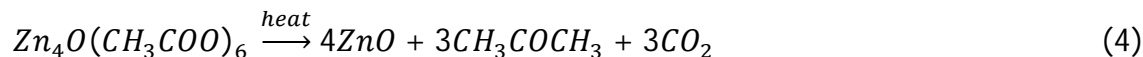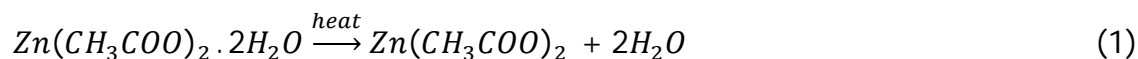
Figure 3.1 depicted the preparation procedure of ZnO seed powder.
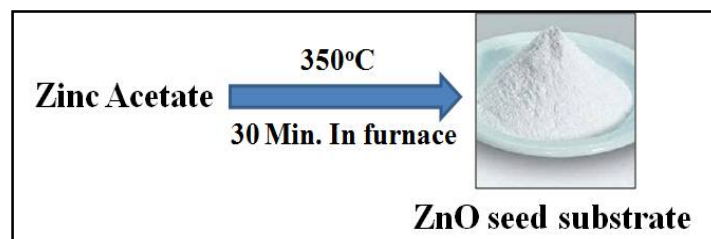
Figure 3.1 Preparation of ZnO seed powder

3.1.2.2 Preparation of ZnO nanorods

Hydrothermal method was carried out by suspending the ZnO seed powder. ZnO nanorods were grown using hydrothermal method by immersing a dilute seed solution in a glass beaker which contain 0.06 M zinc nitrate and 0.06 M hexamethylenetetramine (HMT) solution on 1:1 molar concentration, which is an optimized ratio to grow ZnO nano rods, as reported in our prior work. [6] The solution was heated in a hot air oven and maintained at 90°C for 24 hours.Zinc nitrate hexahydrate salt provides Zn^{2+} ions required for building up ZnO nanowires. Water molecules in the solution provide O^{2-} ions. The hexamethylenetetramine (HMT) actas a weak base during the ZnO nanowire growth by releasing NH_3 in to the solution, which would slowly hydrolyze in the water solution and gradually produce OH^-. [7] Which is very important for the synthesis process because if the HMT hydrolyzes fast to produces a lot of OH^- in a shortperiod of time, the Zn^{2+} ions in solution would precipitate out very quickly due to thehigh pH, which would have little contribution to the ZnO nanorods oriented growth, and eventually results in fast consumption of the nutrient and prohibits further growth of ZnO nanorods. The growth process of ZnO nanorods can be controlled through slow release of OH^- ion in a chemical reaction. That can be controlled by adjusting the reaction parameters, such as precursor concentration, growth temperatureand growth time, in order to push the reaction equilibrium forward or backward. Ingeneral, precursor concentration control the nanowire size and density. The growth time and temperature control the

ZnO nanorods morphology and aspect ratio. The synthesis of ZnO follows following reaction steps 5-12.

$$Zn(NO_3)_2 \leftrightarrow Zn^{2+} + NO_3^- \tag{5}$$

$$(CH_2)_4N_4 + 6H_2O \leftrightarrow 4NH_3 + 6HCHO \tag{6}$$

$$NH_3 + H_2O \leftrightarrow NH_3.H_2O \tag{7}$$

$$NH_3.H_2O \leftrightarrow NH_4^+ + OH^- \tag{8}$$

$$2H_2O \rightarrow OH^- + H_3O^+ K^{1/4} = 10^{-14} \tag{9}$$

$$Zn^{2+} + 4NH_3 \leftrightarrow [Zn(NH_3)_4]^{2+} \quad K = 10^{-9.58} \quad K = 10^{-9.58} \tag{10}$$

$$Zn^+ + 2OH^- \leftrightarrow Zn(OH)_2 \quad K = 3 \times 10^{-17} \tag{11}$$

$$Zn(OH)_2 \leftrightarrow ZnO + H_2O \tag{12}$$
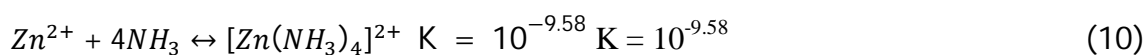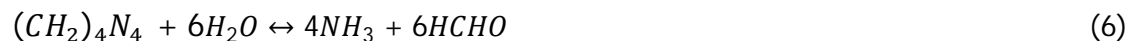
At the end of the growth period, as prepared solid is rinsed immediately with deionized water to remove the residuals from the surface and dried in air at room temperature. Afterwards the powder was further annealed in a muffle furnace at different temperatures, i.e. 300°C, 500°C and 700°C for 1 hour. The flow diagram shown in Figure 3.2 depicts the detailed preparation procedure of ZnO nanorods.
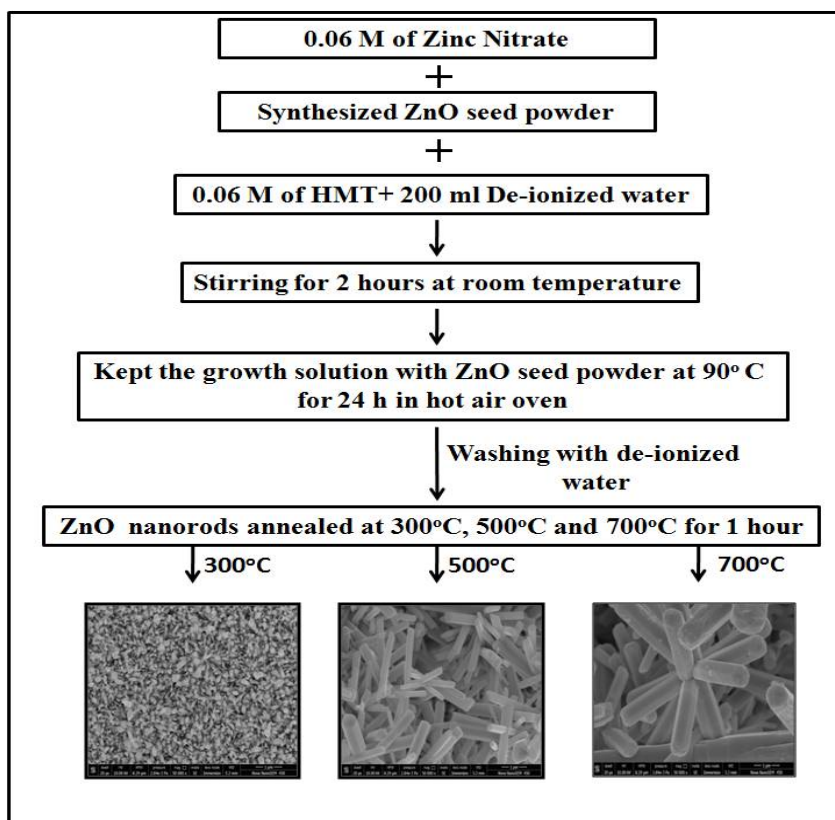
Figure 3.2 Flow chart for the preparation of ZnO nanorods

3.1.2.2.1 A proposed growth mechanism for ZnO nanorods

ZnO is a polar crystal charge species whose positive polar plane is rich in Zn and the negative polar plane is rich in O. [8] Several growth mechanisms have been proposed for aqueous chemical solution deposition. The most important growth path for a single crystal is the so called Ostwald ripening process. [9] This is a spontaneous process that occurs because larger crystals are more energetically favored than smaller crystals. In this case, kinetically favored tiny crystallites nucleate first in supersaturated medium are followed by the growth of larger particles, which is thermodynamically favoured due to the energy difference between large and smaller particles of high solubility based on the Gibbs-Thomson law. [10] The aqueous zinc nitrate and HMT can produce the following chemical reactions. (equation 13-17) The concentration of HMT plays a vital role in formation of the ZnO nanostructure. Since the concentration of the OH^- is strongly related to the reaction that produces nanostructures. Initially, due to decomposition of zinc nitrate hexahydrate and HMT at modrate temperature (90^oC), OH^- was introduced in Zn^{2+} aqueous solution and their concentration increased:

$$C_6H_{12}N_4 + 6H_2O \rightarrow 4NH_3 + 6\,HCHO \tag{13}$$

$$NH_3 + H_2O \rightarrow NH_4^+ + OH^- \tag{14}$$

$$Zn^{+2} + 2OH^- \rightarrow Zn(OH)_2 \rightarrow ZnO + H_2O \text{ (Rod fabrication)} \tag{15}$$

$$Zn^{+2} + 2\,OH^- \rightarrow Zn(OH)_2 + 2OH^- \rightarrow Zn(OH)_4^{2-} \tag{16}$$

$$nZn(OH)_4^{2-} \leftrightarrow n\,ZnO + n\,H_2O + 2n\,OH^- \tag{17}$$
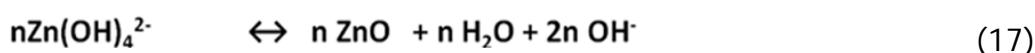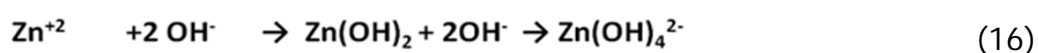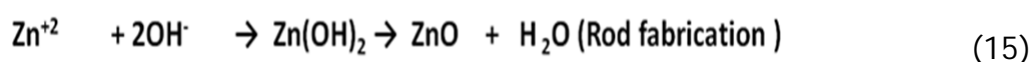
As precipitated colloidal $Zn(OH)_4$ clusters in solution were act partly as nuclei for the growth of ZnO nanorods. During the hydrothermal growth process, the $Zn(OH)_4$ dissolves with increasing temperature. When the concentrations of Zn^{2+} and OH^- reached at the critical value of the supersaturation, nucleation of the ZnO into the fine ZnO rods started in the aqueous complex solution. [11] That will reduce the interfacial free energy of the nanorods because the molecules situated at the surface are energetically less stable than the ones who is well ordered and packed in the interior. Since the (101) face has higher symmetry (C_{6v}) than the other faces growing along the c-axis (101) direction), it is the typical growth plane. The nucleation determines the surface-to-volume ratio of the ZnO nanorod. Then the dehydration reaction takes place by incorporation of growth units into crystal lattice of the nanorods. It is concluded that the growth mechanism is

determined by the thermodynamic factor and concentration of OH$^-$ as the kinetic factor in aqueous solution growth.

3.1.3 RESULTS AND DISCUSSION

3.1.3.1 Electron microscopic measurements

ZnO nanorods were synthesized by simple hydrothermal method at low growth temperature i.e. 90°C. The diffraction studies disclosed that the ZnO crystallized in the wurtzite phase with c-axis orientation. The wurtzite phase has been identified using x-ray diffraction method and confirmed by SAED pattern associated with HRTEM images. The surface morphology of the as- prepared ZnO nanorod has been studied by using SEM, TEM and HRTEM. Synthesized ZnO NRs can be used for further characterization after annealing at different temperatures i.e. 300°C, 500°C and 700°C. Morphological changes occured due to the annealing are represented by FESEM as shown in Figure 3.3a shows the FESEM image of the 300°C annealed-dense ZnO-NRs. The Figures 3.3b and 3.3c exhibits the increasing size of ZnO NRs annealed at 500°C and 700°C with increasing annealing temperature. The diameter and length of the ZnO NRs in the range 100-300 nm. The FESEM images of the ZnO NRs show the increase in annealing temperature (300°C, 500°C and 700°C) increases the size (300, 600 and 900 nm) as well as lengths of the nano rods. FESEM images of ZnO NRs also proved that higher temperatures of post-annealing give better crystal quality, but at very high-temperature and longer period of heating surface diffusion of Zn or ZnO can take place. [12] Figure 3.4a shows the high magnification TEM images of the ZnO NRs. Length and diameter of the ZnO NRs in the range of 50-300 nm. The TEM supported EDXS analysis of the samples depicted in Figure 3.4b that had proved the synthesis of the pure ZnO NRs with elements Zn and O.
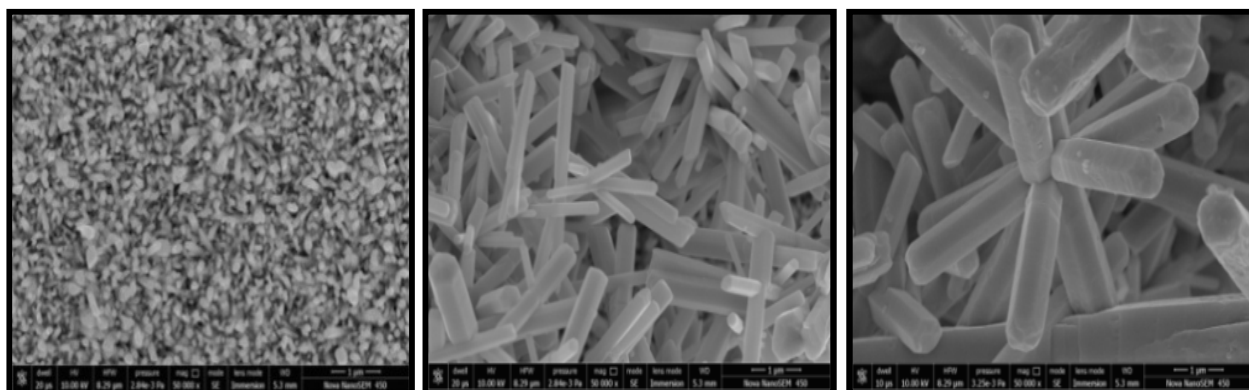
Figure 3.3 FESEM image of ZnO nanorods samples annealed at three different temperature (a) 300°C (b) 500°C and (c) 700°C. All have scale of 1μm length.

TEM images of the as-grown samples also confirm the high crystallinity of the ZnO NRs. The lengths and diameters of the NRs obtained from the TEM images are in close agreement with the FESEM images. Figure 3.4c shows the HRTEM lattice image taken for the single NRs with the lattice spacing is 0.36 Å which corresponds to the (101) plane. Figure 3.4d represents the SAEDpatternof the after annealed ZnO nanorods that confirm the formation of the one-dimensional single crystal with high crystallinity that grown with hexagonal shape.
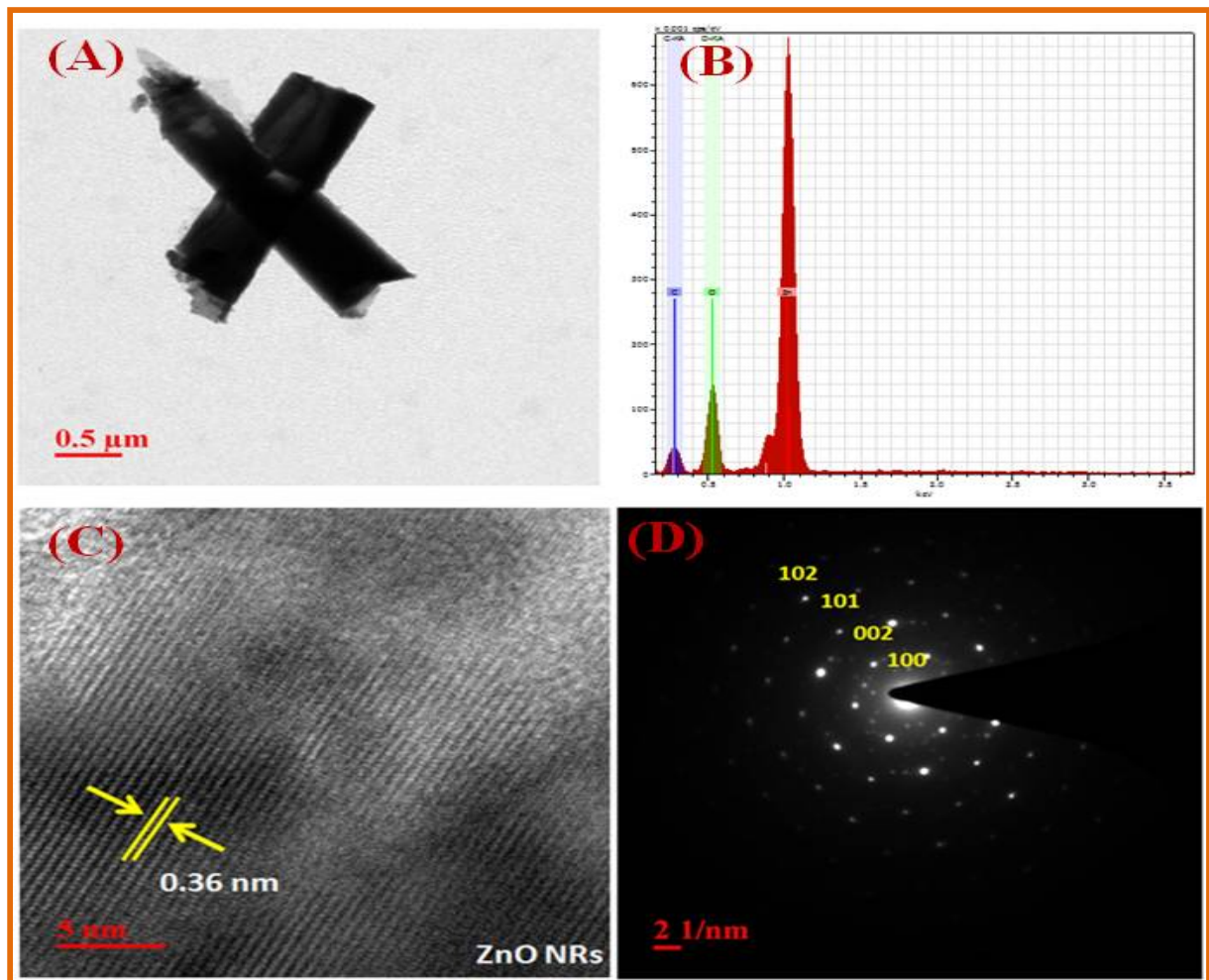
Figure 3.4 (a) TEM images of the hydrothermally prepared ZnO NRs **(b)** EDXS pattern image of the ZnO NRs.**(c)** HRTEM image of ZnO NRs **(d)** The SAED pattern of the corresponds to the ZnO NRs with high crystalline hexagonal wurtzite phase.
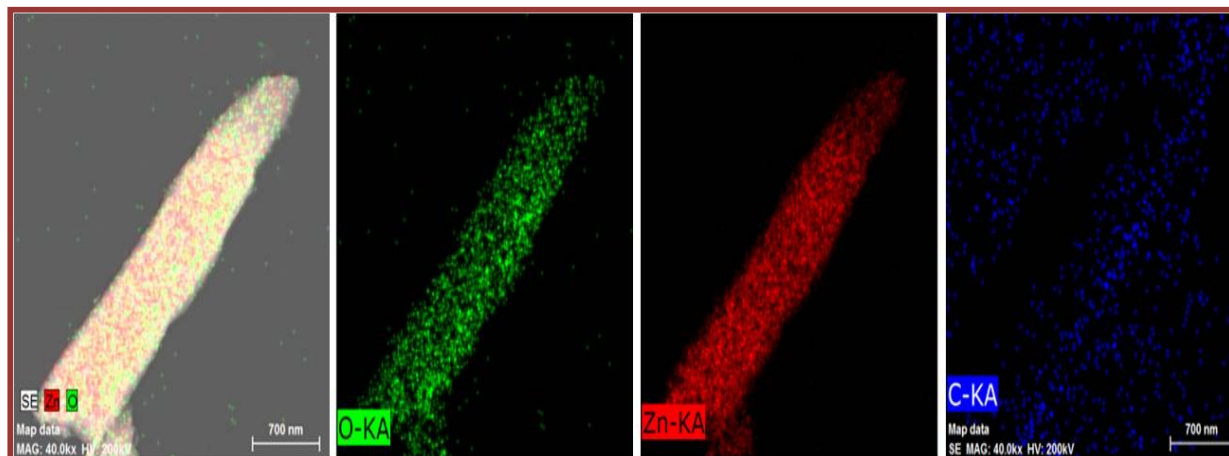
Figure 3.5 FESEM imageand its supported EDXS elemental mapping of the ZnO NRs and elemental mapping which depicts the distribution of constituents O(Kα_1), Zn(Lα_1), and C (Kα_1). Carbons from the tape used to spread the sample for analysis.

For the determination of the spatial distribution of Zn and O element in ZnO NRs, EDS mapping was employed to map the oxygen and zinc in the ZnO NRs without carbon content. Carbon showing in Figure 3.5, is comes from the carbon tape and which is correlates with the result obtained from FESEM, TEM and HRTEM and tell us that the oxygen is almost homogeneously spread element across the sample surface. This means the oxygen is included into Zn matrix of the NRs as well as into underlying 2D bottom layer between the rods.

3.1.3.2 X-ray diffraction studies

The crystal structure and growth orientation of the ZnO NRs were investigated by X-ray diffraction (XRD) patterns. X-ray diffraction spectra of the ZnO NR sannealed at different temperature are represented by the Figure 3.6. All the diffraction spectra indicates that the all samples are polycrystalline in nature with a hexagonal wurtzite structure, and the peaks with (100), (002), (102), (110), (103), (200), (112) and (201) reflections, in $2\theta = 20\text{-}70^{\circ}$ range that belong to the ZnO NRs. [13] As shown in Figure 3.6a, ZnO NRs have (101) reflection as the preferred orientation in case of all samples annealed at 300°C, 500°C and 700°C temperatures. This (101) preferred orientation result of the minimal surface energy in the hexagonal arrangement of the ZnO crystallites that corresponds to the densest packed plane. No bogus diffraction peaks corresponds to the high purity of the synthesized ZnO NRs. The intensity of the peaks increases with annealed temperature, indicating decreasing the size of ZnO NRs which in are in good harmony with the FESEM results and reported literature. [14-17]
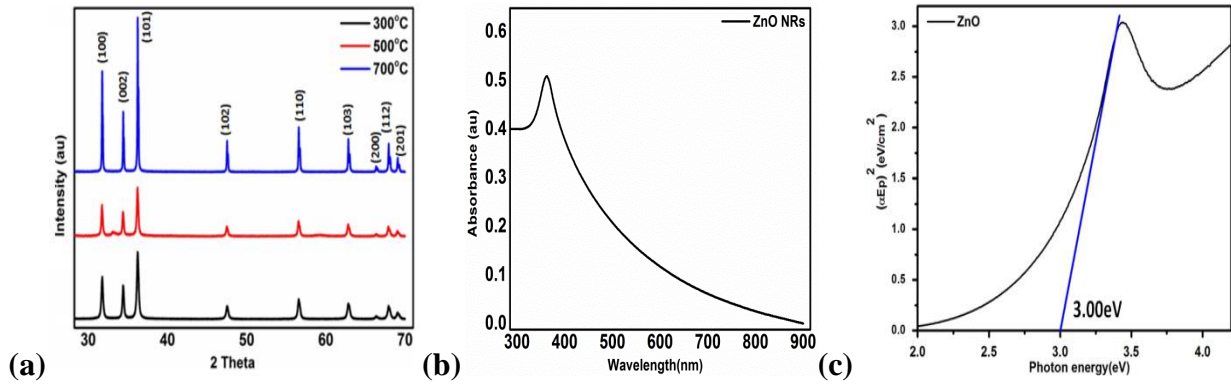
Figure 3.6 (a) XRD patterns of ZnO NRs anealed at different temperature i.e 300°C, 500°C and 700°C **(b)** UV-vis absorption spectra and **(c)** Kubelka Munk plot for the band gaps determination of ZnO nanorod.

3.1.3.3 UV-Visible studies

UV-Visible spectroscopic study of the as-synthesized ZnO nanorods was performed at room temperature using UV Visble spectroscopy. Deionised Millipore water (DIW) was used as the solvent throughout the experiment. The UV-visible spectrum shows a strong first excitonic absorption peak at 368 nm for ZnO nanorods as a result of near band gap excitonic emission. [18,19] When the optical transition energy moves from the top of the valence band to the bottom of the conduction bottom and the absorption maximum shifts to the shorter wavelength region. The stronger exciton effect is a character of quantum confinement in nanosemiconductors, in which the electrons, holes and excitons have limited space to move and their motion is possible for definite values of energies. In case of 1D nano structures, quantum confintment in two directions are achieved and electrons and excitoons can move in single direction (growth direction). Thus, their energy spectrum is quantized. The band gap of as synthesized ZnO nanorods is calculated using Kubelka Munk plot, i.e. plotted between photon energy and $(aEp)^{1/n}$ using equation (18) as shown in Figure 6(c).

$$a = (2.303*A)^{T} \text{ where Ep=h}\upsilon...... (18)$$

Where A is absorbance, T =2 (for direct band gap material), T=1/2 (for indirect band gap material). [20] The band gap calculated from Tauc plot is found to be 3.00 eV, which is lower than the bulk ZnO (3.2 eV).

3.1.3.4 PL studies

The photoluminescence studies had represented the presence of defects levels leading to luminescence phenomena. Figures 3.7a and 3.7b, represents PL emission spectrum of the samples recorded at an excitation wavelength 250 nm. This results shows one emission peaks in green region (at 501 nm) broad peak is generated by radial recombination of the photoexcited holes with respect to the oxygen vacancies. [21]
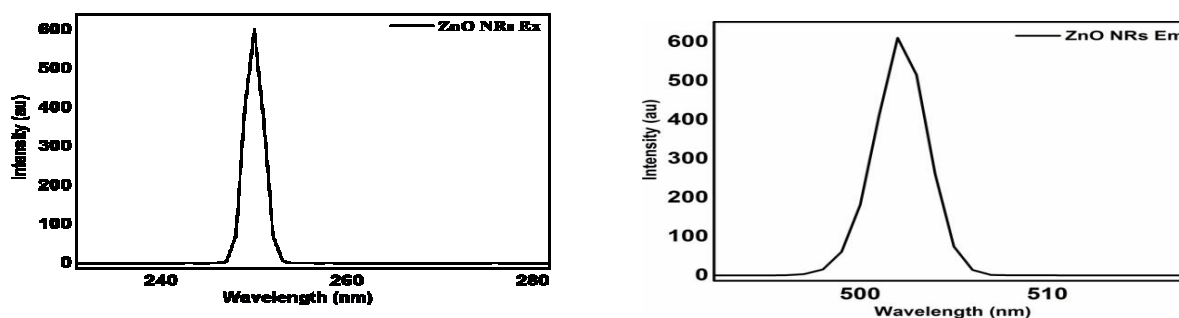
Figure 3.7 PL **(a)** excitation peak at 250 nm and **(b)** emission spectra at 501 nm at λ_{ex}= 250 nm of as-synthesized ZnO nanorods.

It is commonly known that the room-temperature PL spectra for ZnO usually show three major emission peaks at: 380 nm (UV peak), 500-520 nm (a green peak) and 600 nm (a red or orange). [22] The UV peak is recognized to band-edge emission, while the two broad visible bands are generally recognized todeep level defects in ZnO crystal, such as vacancies and interstitials of zinc and oxygen atoms. In this synthesis process green emission peaks are observed for our samples, which confirm the origins of the defect in ZnO nanorods samples. After annealing in hydrogen (in argon) at 700 °C for 30 min, the defect PL peak around at 501 nm observed due to the oxygen vacancies and zinc position at the interstitials. [23] The large surface area of the ZnO nanorods with small diameters generated along with the depletion layers near the nanorod's surface, plays an important role in the PL process. Close to the surface region, when electrons are excited to the conduction band, they are easily trapped by high-density surface states and are relaxed via a nonradiative process, so that the photon emissions can occur only in the central region of the ZnO nanorods (deep from the surface). When ZnO nanorods are annealed, more oxygen vacancies and zinc interstitials are created, which increases the emission centers of green peak around at 520 nm. At the same time, the free carrier density is also increased in ZnO and therefore it reduces the width of depletion region and increases the volume of bulk region, where radiative recombination occurs. [24] Consequently, the intensity of the green PL peak increases significantly. This implies that when ZnO nanorods are annealed at high temperature, new defects

of oxygen interstitials are created. The effect of increasing number of oxygen interstitial defects with increasing temperature of ZnO nanorods, shifted PL the emission peak toward the higher wavelength side.

3.1.4 CONCLUSION

The study accounts for the synthesis of highly crystalline, pure and hexagonal shaped ZnO nanorods by a simple hydrothermal technique. The samples annealed at three different temperatures 300°C, 500°C and 700°C. From the results of SEM, it was clearly observed that good quality ZnO nanorods are grown at the annealing temperature of 300°C, 500°C and 700°C. The UV-vis spectrum of the as synthesized ZnO nanorods indicates the blue shift in the spectra and exhibits a band gap of 3.1eV. PL spectrum of as synthesized ZnO nanorods indicates high emission peak in the green region with oxygen vacancy defects. Synthesized ZnO nanorods can withstand at very high temperature retaining the hexagonal symmetry. Therefore, can be used in various devices such as gas sensors, which is operated at very high temperature and specially for water splitting after decorated with cocatalyst.

3.1.5 REFERENCES

[1] D. Sharma, J.R., B.S. Kaith, M. Kaur, S. Sharma "Synthesis of ZnO nanoparticles and study of their antibacterial and antifungal properties" *Thin Solid Films* (**2010**), 519: 1224-1229.

[2] V.S. Khomchenkoa, T.G. Kryshtabb, A.K. Savina, "Fabrication and properties of ZnO:Cu and ZnO:Ag thin films" *Superlattices Microstruct .*(**2007**), (42): 94.

[3] D.P. Norton, Y.W. Heo, M.P. Ivill, K. Ip, S.J. Pearton, M.F. Chisholm, T. Steiner, "ZnO Growth, Doping & Processing" *Mater. Today* (**2004**), 7: 34-40.

[4] S.H. Jeong, J.W. Lee, S.B. Lee, J.H. Boo, "The insert of zinc oxide thin film in indium tin oxide anode for organic electroluminescence devices" *Surf. Coat. Technol.* (**2003**), 174: 187-192.

[5] J.F. Chang, H.H. Kuo, I.C. Leu, M.H. Hon, "The effects of thickness and operation temperature on ZnO: Al thin film CO gas sensor" *Sens. Actuators B* (**2002**), 84: 258-264.

[6] J. Deenathayalan, M. Saroja, M.Venkatachalam, P.Gowthaman, T.S.Senthil, "Effect of growth layer solution concentration on the structural and optical properties of hydrothermally grown zinc oxide nano rods" *Chalcogenide letters* (**2011**), 8: 549-554.

[7] Zhong Lin Wang, "Nanogenerators for Self-powered Devices and Systems" *Georgia Tech.,* U.S.A., (**2011**), June.

[8] H. Zhang, D. Yang, Y.J. Yi, X.Y. Ma, J. Xu, D.L. Que, J. "Low Temperature Synthesis of Flowerlike ZnO Nanostructures by Cetyltrimethylammonium Bromide-Assisted Hydrothermal Process" ***Phys. Chem. B* (2004),** 108: 3955-3958.

[9] O. Krichershy, J. Stavan, "Solvable dynamical model for a quantum measurement process. Hiromichi Nakazato and Saverio Pascazio" ***Phys. Rev. Lett.* (1993),** 70: 1473-1479.

[10] J.W. Mullin, Crystallization, third ed., ***Butterworth/Heinemann, Oxford* (1997),** 1436.

[11] **L**.G. Sillen, A.E. Martell, "Stability constants of metal-ion complexes" ***The Chemical Society, Burlington House, London* II**nd **Edition (1964),** 754.

[12] Akbar Zendehnam, Marzieh Shirazi, Samira Doulatshah, and Mahdieh Sadat "Effect of temperature and period of post-annealing on the optical properties of zno thin films" ***Armenian Journal of Physics*, (2010)** vol 3, 4, 305-311.

[13] Wei Huiying, Wu Youshi, Lun Ning, Hu Chunxia, "Hydrothermal synthesis and characterization of ZnO nanorods" ***Materials Science and Engineering A* (2005),** 393: 80-82.

[14] Y. Caglar, Silicon, M. Calagr, F.Yakuphanoglu, "Effects of in Al and Sn dopants on the structural and optical properties of ZnO thin films" ***Spec. Act. Part A* (2007),** 67: 1113-1119.

[15] A. Bougrine, A. El Hichou, M. Addou, J. Ebothe, A. Kachouane, M. Troyon," Microstructure and cathodoluminescence study of sprayed Al and Sn doped ZnS thin films" ***Mater Chem. Phys.* (2003),** 80: 438-445.

[16] E. Luna-Arredondo, A. Maldonado, R. Asomoza, D. Acosta, M. Melendez-Lira, M. Dela, L. Olvera, "Indium-doped ZnO thin films deposited by the sol-gel technique" ***Thin Solid Films* (2005),** 490: 132-136.

[17] X. Zi-qiang, D. Hong, L. Yan, C. Hang, "Al-doping effects on structure, electrical and optical properties of *c*-axis-orientated ZnO: Al thin films" ***Mater.Sci. Semiconductor. Process.* (2006),** 9132-135.

[18] Zhuo Wang, Xue-feng Qian, Jie Yin, Zi -Kang Zhu, "Large scale fabrication of Tower- like, Flower-like and Tube- like ZnO arrays by a simple chemical solution route" ***Langmuir* (2004),** 20: 3441-3448.

[19] Jian-Bai Xia, KW Cheah, "Quantum confinement effect in thin quantum wires "***Phys. Rev. B* (1997),** 55: 15688-15694.

[20] H Kumar, R Rani., "Structural and optical characterization of ZnO nanoparticles synthesized by microemulsion route" ***International Letters of Chemistry, Physics and Astronomy* (2013),** 14: 26-32.

[21] C Lin, Y Li "Synthesis of ZnO nanowires by thermal decomposition of zinc acetate dihydrate" ***Materials Chemistry and Physics* (2009),** 113: 334-337.

[22] S. A. Studenikin, N. Golego, M. Cocivera, "Fabrication of green and orange photoluminescent, undoped ZnO films using spray pyrolysis" *J. Appl. Phys.* **(1998),** 84: 2287-2294**.**

[23] K. Vanheusden, W. L. Waren, C. H. Seager, D. R. Tallant, J. A. Voigt, "Mechanisms behind green photoluminescence in ZnO phosphor powders" *J. Appl. Phys.* **(1996),** 79: 7983-7990.

[24] X. L. Wu, G. G. Siu, C. L. Fu, H. C. "Photoluminescence and cathodo luminescence (CL) spectra of stoichiometric" *Ong, Appl. Phys. Lett*., **(2001),** 78: 2285.

Chapter 3.2

Synthesis and Characterization of biogenic Ag NPs prepared by using:

(I)   Ajwain (Trachyspermum Ammi) seeds extract

(II)   Fenugreek (Trigonella Foenum Graecum) seeds extract

(III) Tea (Camellia Sinensis) leaves extract

(IV) Shikakai (Acacia Concinna) pods extract

3.2 Synthesis and Characterization of biogenic Ag NPs prepared by using:

(1)Ajwain (Trachyspermum Ammi) seeds extract

ABSTRACT

Plasmonic silver nanoparticles (AgNPs, size=3-50 nm) were synthesized by biogenic reduction of aqueous $AgNO_3$ using Trachyspermum ammi (TA, Ajwain) seeds extract. Effect of aging and increasing concentration ofTA, was observed on particle concentration/size and their corresponding catalytic activity. Surface plasmonic resonance band centered around 420 nm wavelength, recognized as first exitonic peak of UV–vis absorption spectra of Ag NPs, was used to estimate the particle size (10-30 nm) of Ag NPs. However, some cubic-structures along with the rod like patterns were grown along the 111plane. ATR and IR results suggested the presence of the reducing agent/phytochemicals (nicotinic acid, thymol, sugars, proteins, saponin, etc) incorporated NPs. Impedance study revealed that the rate of charge transfer in TA-Ag NPs aggregates is inversely proportional to the concentration of TA that confirms the stability of the AgNPs in water. These biogenic AgNPs are also characterized using by XRD, FESEM and HRTEM transmission electron microscopy (TEM) and their corresponding energy dispersive X-ray analysis (EDX), electrochemical impedance spectroscopy (EIS), cyclic voltammetry (CV) studies, etc. On the basis of the above observations and optoelectronic characteristics, the most probable mechanism of biogenesis of the stable Ag NPs, is suggested.

Key Words: SilverNanoparticles, plasmonics nano particles, Trachyspermum ammi (TA, Ajwain), Green Synthesis, FESEM, HRTEM, XRD, FTIR, Cyclic Voltammetry (CV) etc.

3.2 (I) 1 INTRODUCTION

Recently, metal nanoparticles (MNPs) have drawn enormous attention of researchers over their bulk equivalents due to their multipurpose applicability in diverse areas. [1-4] These are magnetic, electronic, catalytic, electrochemical, optoelectronics, antimicrobial, corrosion, inhibition and optical performances, and many more. Because of their unmatched fabulous qualities, they can affect human life in various avatars such as biosensors, nano-molecular optoelectronic devices, bio-mimetic materials, catalyst, biomedicine, industrial and environmental fields. There are two well-known approaches for fabrication of MNPs. First is bottom to top or small to big -approach, where the MNPs gain the final shape by addition of small building blocks and prepared by using supercritical liquid medium, templates, spinning, plasma or fire sparing, pyrolysis, sol-gel process, biological method, chemical vapour deposition, atomic condensation, etc. The second approach is top to bottom approach, which involves mechanical milling, electrochemical explosion, laser ablation, chemical etching, etc. Where, bigger particle cut down into small particles of different shapes. Morphology (dominated by the shape and size) of the MNPs is very important factor in deciding their optical, electronic, magnetic, and catalytic properties that can be engineered by controlling the dimensions of MNPs. The conventional methods popular for the synthesizing MNPs are namely: physical and chemical processs but their biogenic production is a better choice due to the use of non-toxic and non-poisonous ingredients, biocompatibility, mild reaction conditions, low cost, simplicity and eco-friendly nature of the reaction. The alleviate fabrication of MNPs via green route includes the above benefits of the biogenic synthesis that can make the MNPs production as an economic and valuable alternative for the large scale production. Biological tools or materials adopted in biogenic synthesis are fungi, [5-7] bacteria, [8-10] Bengal gram bean, [11] yeasts, [12] Capsicum annuum, [13] quercetin, [14] biomass of oat (Avena sativa) and wheat (Triticum aestivum), [15] honey,[16] part of plants' extract, etc. A wide range of metal NPs such as Au, [17-21] Ag, [22-23] TiO_2, [24] In_2O_3, [25] ZnO, [26] znd CuO, [27] etc, have been synthesized using herbal/ plant'parts extract in different shape and size. [26] Use of plant extract and microbial cells in the synthesis of metal NPs, was triggered by presence of the several organic group/compounds such as carbonyl groups, terpenoids, phenolics, flavonones, amines, amides, proteins, pigments alkaloids and other reducing agents present in the plant extract. In this research work, an aqueous seed extract of Trachyspermum ammi (TA; Ajwain) has been used to

grow the metal (silver) nanoparticles. This plant is the native of Egypt and cultivated in Iran, Iraq, Afghanistan, Pakistan and India. TA has a great medicinal and nutrition values because its seed extract consists of carbohydrates (-CHO, -OH), glucosides (6- O-β-glucopyranosyl oxythymol), oleoresin, saponin, phenols, volatiles (thymol, γ-terpinmene, para-cymene, α- and β-pinene, dipentene), proteins, fat, fibres, and minerals (P, Fe, Ca, etc). Furthermore, prominent principle oils such as, carvone (46%), dillapiole (9%) and limonene (38%) along with reducing agents (nicotinic acid), are also present in TA. Therefore, due to the presence of these biochemical ingredients, TA can be served as the reducing and capping agent without addition of any external stabilizing agent, during the synthesis process of NPs. Silver has long been famous for its good inhibitory effect towards many bacterial strains/microorganisms and catalytic activity. Therefore, commonly used in medical and industrial products that directly come in to the contact with the human body, such as shampoos, soaps, detergent, shoes, cosmetic products, and toothpaste, including the photocatalytic and pharmaceutical applications. Moreover, superiority of the nanosilver particles over other candidates of the same class is already established in terms of the small losses in optical frequency during the surface-plasmon propagation, high conductivity and stability at ambient conditions, less costlier price than other noble metals such as gold and platinum, high primitive character, and wide range of visible light absorption, etc. Which, prompt us to select silver as a plasmonic material for this study. MNPs of the noble metals (size <10nm) with localised spin plasmonic resonance (LSPR) are known as plasmonic material. Free electrons integrated with the photon energy produces a LSPR [28-32] on exposing nano-particles of noble metals to sunlight. Therefore, NPs of the noble metals will be act as the active centres on catalyst for the thermal redox reaction that can trap, scatter, and concentrate light [33-35], due to the fast charge transfert hat result in enhanced activities. Pure Ag NPs, as well as some chemically modified Ag NPs has also been in trend that to be used in various applications such as: cleaning water, catalyst, sensor, optoelectronic properties, eradication of organic pollutants, etc. Consequently, as-synthesized Ag NPs were rigorously investigated using advance techniques i.e. XRD (X-ray diffraction), UV-vis spectrophotometry, FTIR and ATR spectroscopy, scanning electron microscopy (SEM) and their corresponding energy dispersive X-ray analysis (EDX), transmission electron microscopy (TEM), high resolution transmission electron microscopy

(HRTEM), photoluminescence emission (PLE), cyclic voltammetry and electrochemical impedance spectroscopy (EIS), etc.

3.2(I) 2 EXPERIMENTAL DETAILS

3.2 (I) 2.1 TA seed Extract Preparation

Established procedure was adopted for preparing the aqueous extract of Trachyspermum ammi (TA; Ajwain) seeds [24] that include the washing of dry seeds of TA thoroughly with DIW to make them free form dust particles and surface contamination. Afterwads the seeds dried for 24 h in moisture free atmosphere and 2 g of dried seeds were soaked in 50 mL of pure DIW for 24 h. The extract was filtered using Whatmann filter paper No. 42. All other reagents employed in this study were of analytical grade and used as supplied without undertaking any further treatment. DIW water was used throughout the study.

3.2 (I) 2.2 AgNPs Synthesis

Silver nitrate (Merck, Germany) is used for generating silver metal ion in given solution. A fresh solution of aqueous 0.001 M $AgNO_3$ was prepared in deionised water (DIW, purified by Millipore assembly). Silver nanoparticles were synthesized using the procedure describe somewhere else. [25] 2.5 mL of the aqueous TA seeds' extract was added drop wise into the 25.0 mL of aqueous 0.001 M $AgNO_3$ that kept in a 50 mL boiling tube, at room temperature. Afterwards, the mixture was shifted in a desiccator at room temperature for aging (7 h, 24 h, 48 h, 7 days, 14 days, 21 days, etc) that leads to a biogenic chemical reduction of Ag^+ ions into Ag NPs. When transparent solution of $AgNO_3$ starting turning pink with time, is indication of the presence of Ag nanoparticles. Aging added fastness to the colour. Silver nanoparticles in aqueous phase are extremely stable without any precipitation and their stability for long period may be due to the antimicrobial properties of this plant. Highly dispersed colloidal Ag NPs were found soluble in water and stable at ambient condition for more than 6 months. After certain aging time, the suspension was centrifuged at 20,000 rpm for 20 min, which resulted in suspended solid settled at bottom of the centrifuge tube it was washed by hot DIW thrice prior to be used for further analysis (XRD, TEM, and FESEM with EDX, HRTEM, UV-vis, FTIR, PLE, and cyclic voltammetric study) and catalytic activity analysis.

3.2 (I) 2.3 Characterization and product analysis

3.2 (I) 2.3.1 Optical measurement

The Ag NPs were analyzed by X-ray diffraction (XRD) using a Bruker D2 Phase diffractometer that was operated in transmission mode with CuK_α radiation (λ = 1.5418 Å). The data were collected over the 2θ range from $20°$ to $90°$ at the interval of $0.02°$ with a counting time of 30 s per step. UV-visible absorption spectra were measured in the range of 200-800 nm by periodic sampling of 1 mL aliquot, in spectrophotometer (LAB India, UV 3000$^+$). The particle size of the Ag NPs was also monitored by considering the position of the first excitonic peak of the spectra. The FTIR spectra of the as-synthesized nanoparticles (in form of KBr pellet), were recorded in transmission mode at the frequency range between 4000 and 400 cm^{-1} with the resolution of 4 cm^{-1}, by using FTIR spectrophotometer (Tensor-27 Bruker, Germany with software OPUS version 5.1) for solid and ATR spectrophotometer (T-alpha, Bruker) for liquid samples. PL spectra were observed using a spectrofluorimeter (Shimazdu Model RF-5301; along with software PC-IV) equipped with a 150 W Xe lamp and a Hamamatsu R928 photo-multiplier tube at room temperature. The excitation and emission spectra were recorded at fixed slit width i.e. 5 nm. Morphology and elemental composition of the sample was checked using scanning electron microscopy (FESEM, JEOL JSM-6700F) and their corresponding energy dispersive X-ray spectrum (EDXS, OXFORD), respectively. EDXS measurement was carried out with the same instrument by focusing a particular area of the samples. TEM and HRTEM micrographs were recorded using an electron microscope (CM12, PHILIPS). The images were analyzed on the basis of the shape, size and crystallinity of Ag NPs at accelerating voltage of 200 kV. Samples were prepared by placing 3-4 drops of the well dispersed Ag NPs in ethyl alcohol solution on to a 300-mesh, carbon coated Cu grid (EM Sciences) and afterwards allowing the liquid to evaporate in air. For Ag NPs, the particle size distribution measure by randomly selected 30 particles.

3.2 (I) 2.3.2 Electrochemical measurements

Electrochemical experiments were performed in a conventional three-electrode glass cell of capacity 100 mL, using a potentiostat/ galvanostat (Auto Lab-PGSTAT 204 Metrohm, equipped with the software NOVA 3.1). Three types of electrode i.e. Pt-tipped carbon electrode, Pt-wire and a saturated Ag-AgCl electrode of were used as a working, counter and reference electrodes, correspondingly. In these experiments, all the potentials were reported against the Ag/AgCl reference electrode in naturally aerated and unstirred solutions at 303 K. Impedance

measurements were made at corrosion potentials over a frequency range of 100 kHz 10 mHz, with a signal amplitude perturbation of 5 mV.

3.2 (I) 3 RESULTS AND DISCUSSION

3.2 (I) 3.1 Crystallography of Ag NPs: XRD ànalysis

The powder XRD profile of the Ag NPs exhibited the major diffraction peaks indexed by the (111) plane at 37.554^o, (200) plane at 43.751^o, (220) plane at 64.021^o and (311) plane at $76.949^{°}$ that belongs to the cubic crystal system (a = 4.0686 Á) that matched well with the standard JCPDS card No. 04-0783 of the pure silver. These results attributed to the orientation of the crystal growth along the crystal 111 plane. Peak broadening noticed in XRD data of the silver nanoparticles was dedicated to the small particle size and associated spin plasmonic resonance phenomena. No bogus Bragg reflections were observed in the pattern due to crystallographic impurities in the sample, which reflected the presence of the 100% pure silver metal in the sample [36]. AgNPs was crystallized in the face centered cubic symmetry of the space group Fm-3m (Space group number: 225) and point group m3m. Debye Scherrer equation corresponding to the XRD profile (Figure 3.8) was used to calculate the particle size of the NPs, i.e. 12.74 nm, by utilizing following relationship Equation. (1). [37, 38]

$$B_{2\theta}\cos\theta \ = \ k\lambda/L \qquad \qquad ……….\ (1)$$

Where, θ = half of the diffraction angle of the strongest peak, λ=wavelength of the incident x-ray beam, L = average crystallite size ($\perp$ to surface of the specimen), Scherrer constant (k) = 0.62 to 2.08 (0.94 for FWHM of spherical crystals with cubic symmetry 0.89 for integral breadth of spherical crystals with cubic symmetry and $B_{2\theta}$= full width at half maximum).
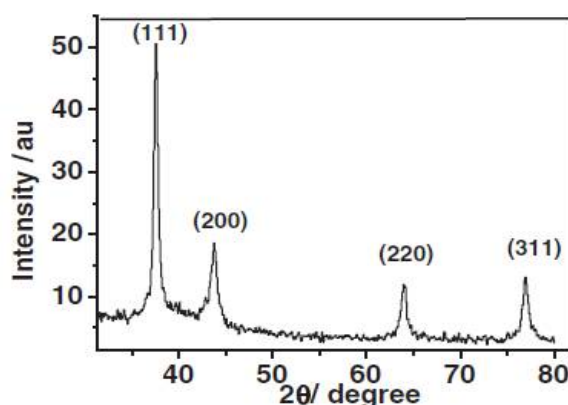
Figure 3.8 XRD pattern of biogenic TA supported Ag NPs with their refelection planes.

3.2 (I) 3.2Electron Microscopic study

FESEM and TEM images along with the corresponding EDX profile exhibited by Figures 3.9a, 3.9b and 3.9c, which reveals the information about their surface morphology, particle shape/size and elemental composition of the synthesized Ag NPs. Flocculated surface visualised by the FESEM and TEM images, indicates uniformly dispersed colloidal silver NPs in sample as visualised by Figure 3.9a. On minute observation of the TEM micrographs, it was found that the Ag NPs crystallized in two shapes i.e. features in the form of the dark cubes of size 5-20 nm (inset of Figure 3.9a). Where, Figure 3.9b shows the particle size distribution in the despersion.
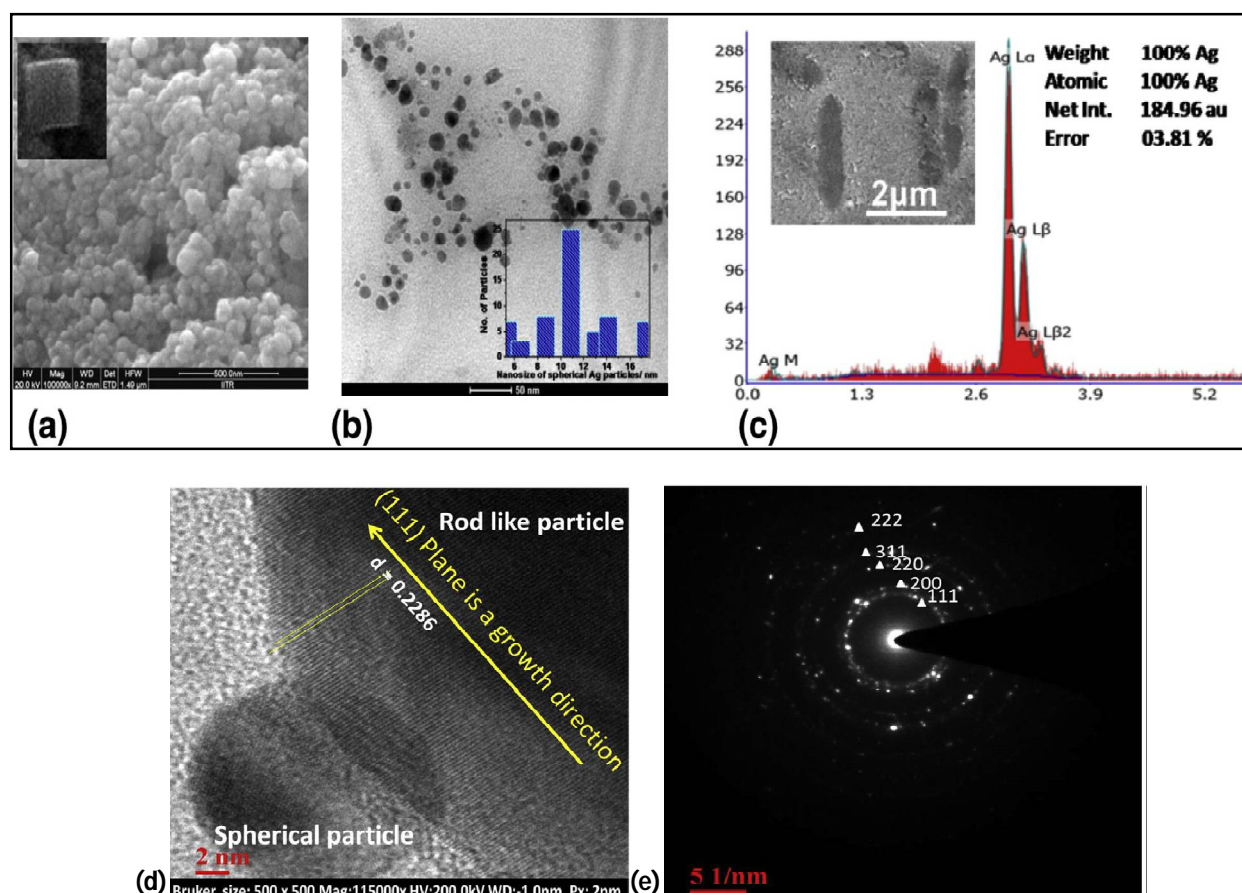
Figure 3.9 (a) FESEM images of silver nanoparticles, **(b)** TEM image and particle size distribution of Ag NPs and **(c)** corresponding EDX profile. Inset images (in a and c) are the magnified TEM images of the square and elongated Ag NPs. **(d)** HRTEM image of a 12.78 nm spherical and rod like structure that featuring d-spacing for the 111 plane and **(e)** cross-grating patterns (SAED pattern) consistent with the cubic structure for biogenic Ag NPs.

These features are result of the interaction between some of the interesting biochemicals present in aqueous TA extract and Ag^+ / Ag NPs. Figure 3.9c corresponds to the EDXS profile of the Ag NPs, collected at 3.2 KeV and used to exhibit the chemical composition of the silver NPs i.e. 100% pure Ag without any foreign contaminants and corresponds to the FESEM image. Few transparent features of gray elongated cylinderical particles of size 0.480×2 μm are demonstrated by inset of Figure 3.9c but the number of dark cubic structures are dominated over the rod shape structures. Figures 3.9d and 3.9e, represents the HRTEM images and corresponding SAED pattern of the as synthesized AgNPs. Figure 3.9d exhibits a high resolution TEM image featuring lattice fringes associated with a d-spacing of 0.2286 nm, consistent with the growth plane 111. The SAED pattern in Figure 3.9e exhibits polycrystalline diffraction rings consistent with 111, 200, 220, 311 and 222 cubic reflections.

One of the chief bio-constituent of TA is the surfactant; saponin (present as 38% limonene with cmc = 0.5-0.8 g/L), [39] which can induces micellization process and captivate silver ions through hydrophobic force, resulting into reduction in entropy. When the concentration of the surfactant is higher than it's CMC, the entropy penalty for Ag ions assembly formation is lesser than the entropy penalty for caging of Ag ions by surfactant into water. That causes the electrostatic interaction between surfactant and Ag ions that leads to elongated structures. Hydrophobic group of the surfactant sequestrated into the centre, which solubilised in bulk Ag ions by the virtue of head's group interaction with solvent and hydrophilic part extended away from the centre. Moreover, position strongly affects the micellisation process by reducing its surface and interfacial tension. [40] The carboxylic group belongs to saponin (responsible for stabilizing the silver nanoparticles) fasten to the hydrophobic a glycone part of the molecule, which dissociates slowly. It leads to grow molecular self assembling of surfactant around Ag NPs in a one dimensional way and induce the formation of the elongated filamentous nanoclusters. The extract also contains the carboxylic/phenolic group attached to the different moieties i.e. nicotinic acid, thymol, sugars, proteins, etc that also highly influence the surface activity, foam ability, and emulsifying ability of the surfactant. These carboxylic/phenolic groups dissociate into aqueous phase and form free carboxyl/phenoxide anions, which increases the solubility of molecule in water and promote the formation of cubical Ag NPs (Figure 3.10).
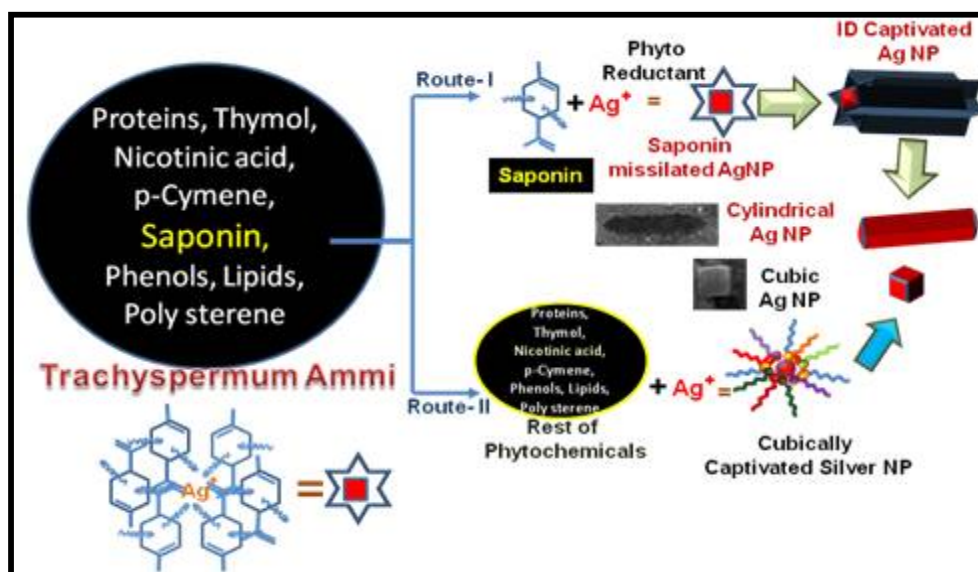
Figure 3.10 Schematic presentation of physical growth mechanism of Ag NPs from two routes that responsible for synthesis of spherical and cylindrical shaped silver nano particles.

3.2 (I) 3.3 Optical characterization

Presence of the Ag NPs, grown at different concentrations of TA and growth time, was successfully examined using UV-vis absorption spectrum (Figures 3.11a and 3.11b). UV spectra shown in Figure 3.11c, revealed the production of AgNPs in TA extract (Red line), where TA extract in absence of $AgNO_3$ didn't exhibit any peak in region 350-550 nm (Black line). Silver NPs exhibited an intense, small and broad absorption at 440 nm due to the surface plasmon resonance (it describes the collective excitation of the conduction electrons of metal in presence of light) excitation. [41] All absorption spectra possess two prominent peaks with maximas; first at 200 nm and second around 420-450 nm. Strong peak around 200 nm, usually caused by the general transition of electrons between the valence and conduction bands of Ag NPs. Second, broad but short peak found within the range of excitonic transitions between 415 nm and 460 nm, depending on TA extract concentration, structural, and aging conditions. [42-44] Figure 4a confirmed the formation of the Ag NPs at different concentrations (0.5, 1.0, 1.5, 2.0 and 2.5% (w/v)) of TA at fixed $AgNO_3$ concentration i.e. 0.001M $AgNO_3$ and 1 h aging. The increase in the intensity of the first excitonic peak at 446, 445, 446, 452, and 452 nm along with the broadness of the peak on raising the TA concentration, was observed. Furthermore, 2.0 and 2.5% TA concentrated samples has shown the same pattern and peak maxima (452 nm) (Figure 3.11a). Therefore, 2.0% TA samples were taken for optimisation through aging. The effect of aging on

Ag NPs grown in 2.0% of TA was explored by varying the growth time (24 h, 36 h and 48 h) on peak position viz. 448, 446 and 446 nm as shown in Figure 3.11b. [45]. The height of the first excitation peak for 24 h and 36 h aged samples are almost similar but rise in the peak height observed for the 48 h aged sample that confirmed the increase in concentration and a decrease in size of the Ag NPs (blue shift in peaks on aging), indicated a decrease in size of the Ag NPs. UV spectrum for 2.0% TA sample aged for 48 h and pure TA extract is demonstrated in Figure 3.11c. The presence of broad first excitonic peak between 333.7 and 650 nm (3.72-1.98 eV) at peak maxima at λ_{max}=446 nm (2.78 eV), confirms the formation of Ag NPs. Broadening to the optical absorption spectrum of Ag NPs, was originated by SPR phenomena. The surface plasmon resonance (SPR) is the coherent excitation of all the 'free' electrons within the conduction band. Because the SPR prohibits to give rise to the intensity of the absorption peak for very small Ag NP clusters. Hence, the short and broad peaks were observed. Such absorption spectra can be explained by Mie theory. [46] Mie theory describes the scattering of light (in various directions with varying efficiency) by small particles (an aggregation of material) that constitute a region with refractive index, different from the refractive index of its surroundings.
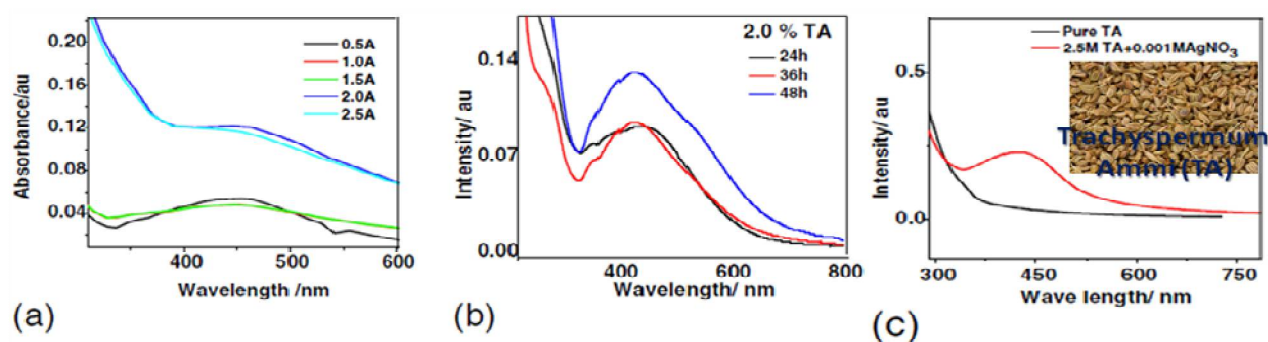
Figure 3.11 UV-Vis diffuse reflectance spectra of the **(a)** as-prepared Ag NPs at different concentrations of TA i.e. 0.5, 1.0, 1.5, 2.0 and 2.5%, **(b)** TA supported Ag NPs on aged at different time i.e. 24 h, 36 h, and 48 h and **(c)** comparative spectra of 2.5M Pure TA (Black solid line) and AgNPs synthesized by mixing of 2.5% TA and 0.001M AgNO₃ (Red solid line). Trachyspermum Ammi (TA) seeds are shown in Inset.

3.2 (I) 3.4 IR spectroscopic investigation

Figure 3.12a demonstrates the ATR (Attenuated total reflectance) spectrum of TA-stabilised Ag NPs that was used to study the effect of aging on bonding environment of the Ag NPs in presence of the phytochemicals that belongs to TA. Respective IR peaks of N-H or O-H and υ C=O groups,

were observed at different aging period i.e. 24 h (3315.74 & 1637.36 cm^{-1}), 36 h (3314.32 & 1635.59 cm^{-1}) and 48 h (3313.64 & 1635.69 cm^{-1}). Gradual shifting of peaks towards low wave number was observed for the TA and AgNO$_3$ mixture with aging that signifies the increase in bulkiness (heavier the molecule, lesser the frequency or wave number) of the molecular self assembly of TA due to the formation of the cluster of Ag NPs.
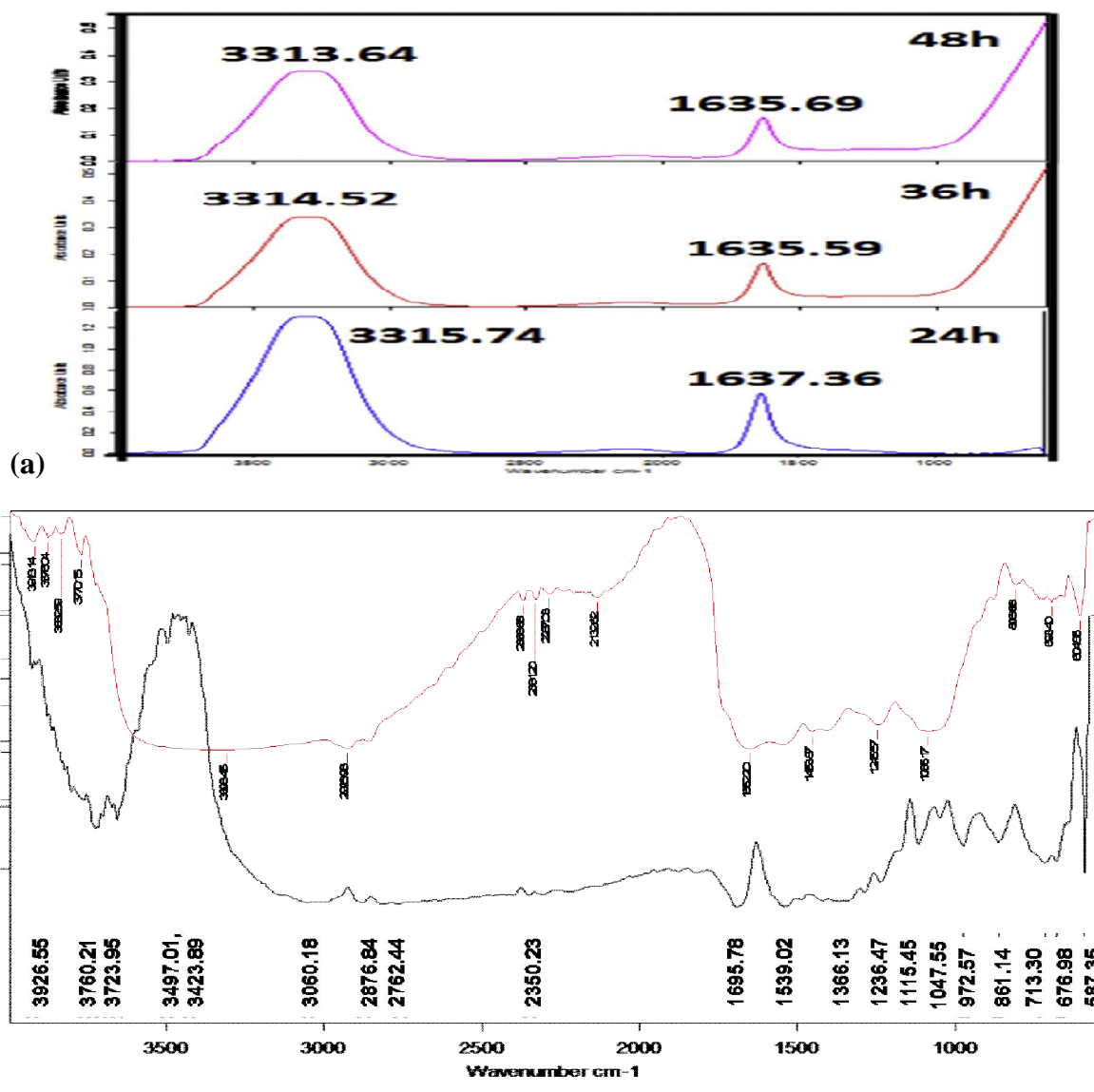
Figure 3.12 (a) ATR spectra of 2.5% TA supported Ag NPs with aging of 24 h, 36 h and 48 h and **(b)** FTIR spectrum of the 2.5% pure TA (Red solid line) extract and Ag NPs stabilised in 2.5% TA (Black solid line).

It was also justified from the FTIR study, which was carried out (Figure 3.12b) in the range of the wave number 4000-500 cm^{-1}. This technique is also used to recognize the most probable

interactions between the Ag ions and phytochemicals present in TA with time and the role of the chemical constituents of the TA in stabilization of Ag NPs. Pure 2.5% TA gave peaks at the wave number of 3918.14, 3876.04, 3832.59, 3770.15, 3308.45, 2926.98, 2368.65, 2331.20, 2237.03, 2132.62, 1652.2, 1453.87, 1245.57, 1085.17, 806, 693.40 and 604.85 cm^{-1}. Where, 2.5% TA stabilised AgNPs exhibits prominent peaks at the wave number 3926.55 (w), 3760.21 (w), 3723.95 (s), 3664.86 (s), 3497.01 (w), 3428.69 (w), 3060.18 (b), 2876.84 (w), 2762.44 (vw), 2350.23 (vw), 1695.78 (s), 1539.02 (w), 1366.14 (vw,b), 1236.47 (w), 1115.45 (s), 1047.55 (w), 972.57 (s), 861.14 (s), 713.30 (b,s), 676.98 (b,s) and 587.36 (vs) cm^{-1}. These peaks are representative of the respective functional groups belongs to the most probable biomolecular species, shown in Table 1. Similar to the ATR results, the shifting of the IR peaks towards the lower frequencies was observed due to the formation of the TA stabilised-Ag NPs. Characteristic intermolecular hydrogen bonding of the pure TA, is attributed to the broad band at 3308.45 cm^{-1}. Where, the sharp and well defined peaks at 3723.95 s and 3664.86 s in TA stabilised Ag NPs, are attributed to the intra-molecular hydrogen bond. [47] IR peak at 3428.69 cm^{-1} belongs to the OH stretching of alcohols and phenolic groups in TA stabilised Ag NPs. The frequencies between 3000-2800 cm^{-1} dedicated to the stretching modes of CH$_2$ group. The absorption band at 3060.18, 2876.84 and 1366.14 (vw,b) cm^{-1} might be linked with the asymmetric and symmetric stretching/wagging vibrations of CH$_2$ group, respectively. Distinguish peak at 3060.18 cm^{-1}, attributed to the poly substituted benzenes and aromatic CH$_2$ stretching vibrations. [48, 49] Sharp IR peaks at 1695.78 cm^{-1} suggested the presence of amide group [50], due to the carbonyl stretching of the proteins that strongly adsorbs the MNPs.

TA supported Ag NPs exhibits the strong bands at 972.57 and 861.14 cm^{-1} that identified as twisting and rocking modes of CH$_2$ bending. The secondary structures of the proteins were not affected during the reaction with Ag$^+$ ions or after binding with Ag nanoparticles. [51] Thus, the IR spectroscopic studies confirmed the presence of the amino acid that develop the strong binding, reducing and stabilizing ability with metal through carbonyl group. Thus, it is concluded that a layer of the bio-organics have formed on AgNPs to secure the nanoparticles. This layer acts as a capping agent to prevent agglomeration and provides the extra stability in aqueous medium. [52] The IR spectra also possess the peaks at 1321 and 1580 cm^{-1}, attributed to ν-C-N and δ-NH$_2$, respectively. [53] The position and relative intensity of these bands changes with respect to the pure amine (2083, 1514 cm^{-1}) groups. [54, 55] The variation in the -NH$_2$ and -NH infrared bands

suggests the links between the two or more nanoparticles. The typical bands at 1120 and 1480 cm^{-1} are representative of the ν-C-OC and δs-CH$_2$/ δa-CH$_3$ vibrations, respectively. [56]

Table 1 Representative bonding of functional groups and corresponding bio-molecules belonging to FTIR peaks positions (in wave number).

Wave number (cm^{-1})	Functional groups	Bio-molecules
587.35	CCC out of plane bending P-O bending	PO$_4$$^{3-}$
676.98	C-S str. O-Ag-O str.	Thiol, sulfide
713.30 b	N-H bonded, secondary amide	carvone
861.14	C-O str.	epoxide
972.57	C-H out of the plane bend	Trans RHC=CHR', fat oil
1047.55	Alkane, C-O str. P-O str.	Lipids, saponin
1115.45	C-O, C-N, C-C str.	Lipid, amino acid sugars
1236.47	C=S str.,	(RO)$_2$C=S, thioketone
1366.13	S=O str., ν-C–N,	(RO)$_2$SO$_2$, sulfuric ester, nicotinic acid
1539.02	C=N(plus C=C), δ-NH$_2$ str. Aromatic ring str.	Aromatic ring, pyrimidines, thymol
1695.78	Primary Amide , carboxylate C-O stretch, conjugated ketones H O-H bending HO-H	Proteins, thymol, nicotinic acid p-cymene
2350.23	NH$_2$$^{+}$, NH^{+} str.	Nicotinic acid
2762.44	C-H str. , –C(=O)H, aldehyde	Carbohydrates,
2876.84	-CH2- stretch (s), C-H str. methine	Aliphatic methylene group, limonene
3060.18	Alkane, aromatic C-H strech	Lipids, saponin poly sterene
3428.69	Asym.N-H str., carboxylate C-O sym. and asym. str. Bonded /non bonded OH group	Alcohols and phenols, thymol, nicotinic acid
3497.01	Intra- or inter-molecular Bonded OH	saponin
3664.86	free OH , primary NH amines asymmetric,	Amino acids
3723.95	free OH	saponin
3760.21	free OH	saponin
3926.55	C-H stretch of aromatic combination	All aromatic rings

The aromatic C-H out-of-plane deformations signals were observed in the range 720-1000 cm^{-1}. The out-of-plane and in-plane deformation of the phenyl ring are observed below 1000 cm^{-1} and these modes are not pure but contain a significant contribution from other modes and are substituent sensitive also, the spectral positions of the weaker γ-CH near 900 cm^{-1} correlates well

with the electron donating or electron attracting properties of the substituent. The CH in-plane deformations (δ-CH) were obtained at 972.57 s and 1047.55 cm^{-1} in the IR spectrum. Aromatic nitro compounds shows a C-N stretching vibration near 870 cm^{-1}and the ν- CN band is available at 861.14 cm^{-1} in the IR spectrum. The vibration modes of the various functional groups are variant with respect to the formation of the complex and to the adsorption at the nanoparticle's surface. It is suggested that the alkyl chains adopted the stretched conformation irrespective of the complex formation. Stretching also confirms the inter band and intra band transitions between electronic states of silver. IR study prove the presence of two kinds of chemicals in TA extract: one the reducing agent (nicotinic acid, polyphenols) that convert Ag$^+$ ions into Ag nanoparticles and second the capping agents/surfactant (carvone, thymols, sugars, proteins, lipids, saponin, etc), which can act as an scaffold for controlling size and shape of these nanoparticles, as it was mentioned in SEM/TEM/HRTEM study segment of this chapter.

3.2 (I) 3.5 Visible Photoluminescence

Figure 3.13 illustrated the excitation and emission spectra of biogenic silver nanoparticles that synthesized at 24 h aging time of AgNPs in 2.0% TA. Excitation spectra of the as-prepared AgNPs was obtained at λ=289 nm under the emission radiation of 565 nm and sharp PL emission spectrum of green light at λ$_{em}$=563 nm was found under the excitation of λ$_{ex}$= 285 nm. Excitation of electrons from the occupied d-bands into the states above the Fermi level and successive relaxation of electrons from an occupied sp-band to the holes takes place by the electron-phonon scattering process directed an energy loss, which is responsible for the visible light luminescence of the Ag nanoparticles. [57]
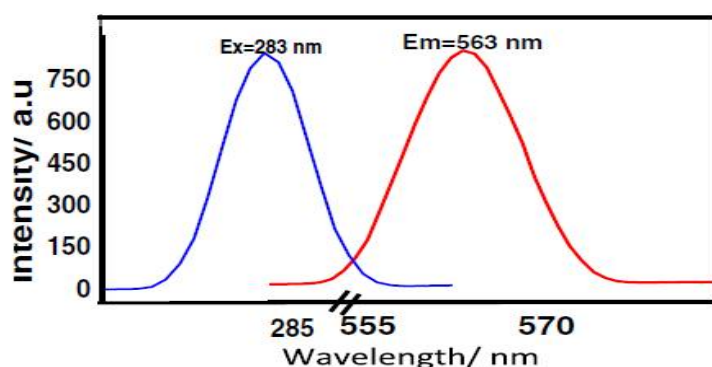
Figure 3.13 Photoluminescence (PL) excitation spectra (blue) of the as prepared Ag NPs under emission wavelength 565 nm and PLE spectrum (red) at λ$_{em}$ = 563 nm under the excitation radiation of λ$_{ex}$ = 285 nm.

The optical properties of the silver nanoparticles depend on both; inter band and intra band transitions between electronic states. FESEM and TEM results indicate that the smaller non-metallic clusters coexist with large metallic nanoparticles. Here, only small metallic particles (cubic crystals) contribute to luminescence phenomine because large metal particle didn't exhibit luminescence due to rapid radiation loss process that makes it hard to compete with effective radioactive process. [58]

3.2 (I) 3.6 Cyclic potentiometeric study

Cyclic voltammetric study has proved to be a successful tool for monitoring the progress of the reaction and reduction mechanism of the Ag^+ ions, using the partial cathodic and anodic reactions proceeding at electrodes. Graphical representation of the cathodic and anodic peak currents vs applied potential (V), was observed for the reaction mixture of the pure 2.0% TA extract and 2.0% TA extract with $AgNO_3$ solution, at 2, 3, 4 and 5 h aging time with the scan rate of 0.1 V s^{-1} (Figure 3.14). It was observed that the anodic peak current decreases on increasing the time of reaction kinetics from 1 h to 5 h. Decrease in anodic peak current with time indicates that an electron transferred from the solution to electrode, which converts Ag^+ ions in the colloidal solution to Ag as a result of reduction reaction. However, reverse occured in oxidation process, where electrons release during the reaction $Ag \rightarrow Ag^+ + e^-$ and that is responsible for the backward reaction. [59] But none of the above investigated reversible couples show the reverse-to-forward peak currents ratio, i.e. $i_{pr}/i_{pf} = 1$. Hence, all the studied cases irreversible with respect to the peak current ratio. The pure TA extract solution exhibited the anodic peak at -0.4 V (at current = 13.0 µA) and cathodic peak at -0.5 V (at current = -7.4 µA). TA-incorporated $AgNO_3$ solution, aged at the different time intervals (1 h, 2 h, 3 h, 4 h and 5 h) exhibited two respective irreversible oxidative peak potentials around -0.5 V and between 0.40 and 0.60 V, are followed by the one reductive wave peak at -0.5 V. The corresponding values of currents for the I- and II - peaks are presented in Table 2. In Figures 3.14a and 3.14b (inset), the first oxidative peak potentials lay around -0.4 to -0.5 V that corresponds to the azo group and aromatic rings. The second peak exsisit between 0.40 and 0.60 V are responsible for the reduction of Ag^+ ion to Ag. [60] Azo group promotes thereduction of Ag^+ to Ag metal NPs. Aging encouraged the depression in current height of I oxidative peak that represents the azo group and aromatic rings were destroyed gradually with time. Simultaneously, increase in the current height of II oxidative peak with aging time, is belongs to the formation of AgNPs formation by the reduction of Ag^+/Ag ($E_{Ag+/Ag}$). Figure 3.14b exhibited the linear raise in current peak height with aging time. Red shift

in peak was observed due to increase in AgNPs concentration, which results in increase in current (Table 2).

Table 2 Current and voltage values of pure 2.0% TA extract and Ag NPs prepared at 1-5 h aging.

Aging of Ag NPs/h	I Peak applied potential/V; Current/A	II Peak applied potential; Current/A
Pure TA	$-0.490: 1.36 \times 10^{-5}$	0.43/0.58: no peak
1	$-0.610:2.00 \times 10^{-7}$	$0.481: 1.360 \times 10^{-7}$
2	$-0.182: 1.890 \times 10^{-7}$	$0.430:5.081 \times 10^{-7}$
3	$-0.173: 1.456 \times 10^{-7}$	$0.439: 8.900 \times 10^{-7}$
4	$-0.133: - 2.010 \times 10^{-7}$	$0.501: 1160 \times 10^{-7}$
5	$-0.083: - 1.93 \times 10^{-7}$	$0.598: 20.70 \times 10^{-7}$
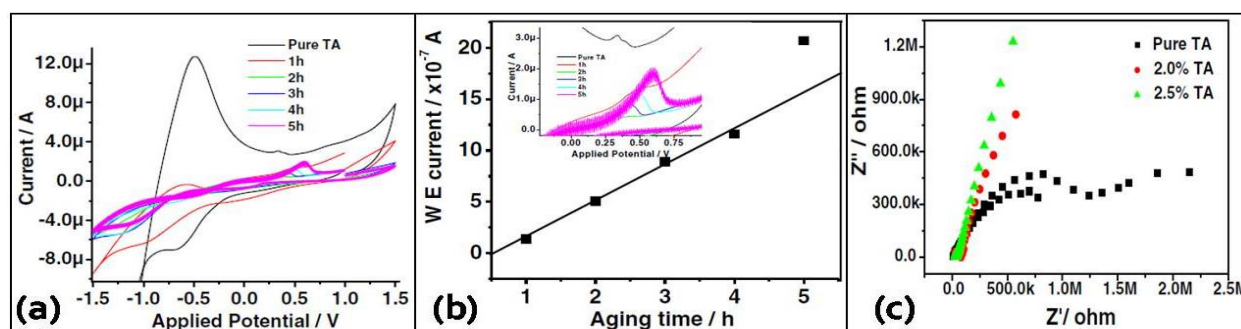
Figure 3.14 Cyclic voltagrams for pure TA and the colloidal AgNPs the formed in 2.0% TA seed extract at different time interval; 1 h, 2 h, 3 h, 4 h and 5 h **(a)** CV plot with aging and **(b)** working electrode current vs aging time plot along with the Inset represents the close up of II peak (belongs to AgNPs) around applied potential between 0.40 and 0.60 V. **(c)** Electrochemical impedance spectroscopy (EIS) plot of pure TA, 2.0% and 2.5% TA seed extract in 0.001 M AgNO$_3$ solution.

3.2 (I) 3.7 Electrochemical impedance spectroscopy (EIS)

Impedance experiments were carried out to get into the kinetic of the electrochemical processes occurring at electrode/electrolyte interface in the absence/ presence of Ag NPs. In these experiments, all the measurements have been reported with respect to the reference Ag/AgCl electrode. The local impedance diagrams (Figure 3.14c), were recorded in terms of the real impedance *Vs* imaginary impedance as a function of frequency over a range from10 kHz to 500 mHz. Complex impedance diagram were recorded in Nyquist modulus format, for Pure TA and

24 h aged Ag NPs that was suspended in 2.0% and 2.5% aqueous TA solution, as shown by Figure 3.14c.

Pristine TA sample comprise of two depressed capacitive semicircle, spread over from the high to low frequency regions. This typical behaviour of the solid metal electrodes corresponds to the non ideal frequency dispersion that related to the surface the inhomogeneities. Rapid linear increase in the real impedance was observed with increase in concentration of TA (2-2.5%) in TA supported-Ag NPs, due to the increase in particle size and decrease in ionic conductivity. This is a clear cut indication of the corrosion inhibition process/proceeds during the production of AgNPs. Moreover, Warburg impedance dropped out at higher frequency because the time scale is so short that diffusion can't manifest itself. At low frequency, the reactants have to diffuse farther that increases the Warburg-impedance.

3.2 (I) 4 CONCLUSION

A nanometal has a remarkable impact on the present century due to its ability to show different physical, electrical, magnetic and optical properties because of their great surface to volume ratio (aspect ratio). Different physical and chemical methods are in fashion to synthesis MNPs. But the biogenesis is the most benign way to synthesis MNPs over the presently used chemical and physical methods. In this study, nanoparticles of silver metal have been successfully fabricated by using aqueous extract of the TA and $AgNO_3$ at varying the concentration of TA and aging time. During the biosynthesis of the Ag nanoparticles, self-assembling of the chemical components (i.e. nicotinic acid and steroidal saponins) of the TA extract's rap around the of Ag^+ ion that leads to the reduction of Ag^+ ion in to Ag NPs in dilteral shapes. TA seeds extract contains nicotinic acid, which attributed to the reduction. Other phythogen altogether leads to the nucleation of the Ag nanoparticles in two shapes (cubes of 5-20 nm and elongated particles of 0.52×2 μm). XRD studies confirmed the purity of these nanosized NPs that crystallized in a cubic and rod shape crystals with growth orientation of the Ag NPs along the 111 plane. Prominent, intense and broad excitonic UV-vis. spectrum peak of the Ag NPs was found at 420-440 nm, attributed to the associated surface plasmonic phenomena. IR spectroscopic studies confirmed that carbonyl group of amino acid residues have strong binding ability with metal suggesting the formation of the layer covering metal nanoparticles and acting as capping agent to prevent agglomeration and providing stability to the medium. Excitation of electrons from occupied d bands into states above the Fermi level is responsible to the green light luminescence of Ag nanoparticles at 563 nm.

Cyclic-voltammetric studies confirms the one electron reduction process of the AgNPs. Silver nanoparticles are successfully synthesised using biosynthesis method that can be further used in water splitting for hydrogen generation and for reduction of organic pollutant PNP to PAP.

3.2 (I) 5 REFERENCES

[1] M. Catauro, M.G. Raucci, F. Gaaetano, A. De Marotta, "Antibacterial and bioactive silver containing $Na_2O \cdot CaO \cdot 2SiO_2$ glass prepared by sol gel method" *J. Mater. Sci. Mater. Med.* **(2004),** 15: 831-840.

[2] J.H. Crabtree, R.J. Burchette, I.T. Siddiqi Ra, B. Huen, L.L. Hadnott, A. Fishman, "The efficacy of silver-ion implanted catheters in reducing peritoneal dialysis-related infections" *Perit. Dial. Int.* **(2003),** 23: 368-374.

[3] A. Krolikowska, A. Kudelski, A. Michota, Bukowska, "SERS Studies on the Structure of Thioglycolic Acid Monolayers on Silver and Gold" *J. Surf. Sci.* **(2003),** 532: 227-232.

[4] G. Zhao, S.J. Stevens, "Multiple parameters for the comprehensive evaluation of the susceptibility of Escherichia coli to the silver ion" *Biometals* **(1998),** 11: 27-32.

[5] N. Duran, P.D. Marcato, O.L. Alves, G.I.H. De Souza, E. Esposito, "Mechanistic aspects of biosynthesis of silver nanoparticles by several Fusarium oxysporum strains" *J. Nanobiotechnol.* **(2005),** (3): 1.

[6] D.S. Balaji, S. Basavaraja, R. Deshpande, D.B. Mahesh, B.K. Prabhakar, A., "Extracellular biosynthesis of functionalized silver nanoparticles by strains of Cladosporium cladosporioides fungus" *Colloids Surf. B* **(2009),** 68: 88-92.

[7] A. Ahmad, P. Mukherjee, D. Mandal, S. Senapati, M.I. Khan, R. Kumar, M. Sastry, "Biotemplated Inorganic Nanostructures: Supramolecular Directed Nanosystems of Semiconductor(*s*)/Metal(*s*) Mediated by Nucleic Acids and Their Properties" *J. Am. Chem. Soc.* **(2002),** 124: 12108.

[8] A. Ahmad, S. Senapati, M.I. Khan, R. Kumar, M. Sastry, "Biotemplated Inorganic Nanostructures: Supramolecular Directed Nanosystems of Semiconductor(*s*)/Metal(*s*) Mediated by Nucleic Acids and Their Properties" *Langmuir* **(2003),** 19: 3550.

[9] A. Ahmad, S. Senapati, M.I. Khan, R. Ramani, V. Srinivas, M. Sastry, "Intracellular synthesis of gold nanoparticles by a novel alkalotolerant actinomycete, Rhodococcus species" *Nanotechnology* **(2003),** 14: 824.

[10] H. Lee, A.M. Purdon, V. Chu, R.M. Westervelt, "Controlled assembly of magnetic nanoparticles from magnetotactic bacteria using microelectromagnets arrays" *Nano Lett.* **(2004),** 4: 995-998.

[11] V. Armendariz, J.L. Gardea-Torresdey, M. Jose-Yacaman, J. Gonzalez, I. Herrera, J.G. Parsons, Proceedings Waste Research Technology Conference at the Kansas City, ***Mariott-Country Club Plaza* (2002),** July 30 Aug 1.

[12] M. Kowshik, S. Ashtaputre, S. Kharrazi, W. Vogel, J. Urban, S.K. Kulkarni, K.M. Paknikar, "Extracellular synthesis of silver nanoparticles by a silver-tolerant yeast strain" ***Nanotechnology* (2003),** 14 (1): 95.

[13] K. Ghule, A.V. Ghule, J.Y. Liu, Y.C.J. Ling, "Microscale size triangular gold prisms synthesized using Bengal Gram beans extract and $HAuCl_4 \cdot 3H_2O$: A green biogenic approach" ***Nanosci. Nanotechnol.* (2006),** 6: 3746-3751.

[14] S. Li, Y. Shen, A. Xie, X. Yu, L. Qiu, L. Zhang, Q. Zhang, "Green synthesis of silver nanoparticles using Capsicum annum L. extract" ***Green Chem.* (2007),** 9: 852-858.

[15] J.L. Gardea-Torresdey, J.G. Parsons, E. Gomez, J. Peralta-Videa, H.E. Troiani, P. Santiago, M. Yacaman, " Formation and growth of Au nanoparticles inside live alfalfa plants" ***J. Nano Lett*. (2002),** 2: 397-401.

[16] I.B. Obot, S.A. Umoren, A.S.J. Johnson, "Sunlight- mediated synthesis of silver nanoparticles using honey and its promising anticorrosion potentials for mild steel in acidic environments" ***Mater. Environ. Sci.* (2013),** 4 (6): 1013-1019.

[17] E.M. Egorova, A.A. Revina, "Synthesis of metallic nanoparticles in reverse micelles in the presence of quercetin" ***Physicochem. Eng. Asp.* (2000),** 168: 87-96.

[18] J. Huang, Q. Li, D. Sun, Y. Lu, X. Yang, H. Wang, Y. Wang, W. Shao, N. He, J. Hong, C. Chen,"Biosynthesis of Silver and Gold Nanoparticles by Novel Sundried Cinnamomum camphora Leaf" ***Nanotechnology* (2007),** 8: 105104.

[19] B. Ankamwar, C. Damle, A. Ahmad, M. Sastry, "Biosynthesis of gold and silver nanoparticles using Emblica Officinalis fruit extract, their phase transfer and transmetallation in an organic solution" ***J. Nanosci. Nanotechnol.* (2005),** 5: 1 665-671.

[20] S.P. Chandran, M. Chaudhary, R. Pasricha, A. Ahmad, M. Sastry, "Synthesis of gold nanotriangles and silver nanoparticles using Aloe vera plant extract" ***Biotechnol. Prog.* (2006),** 22: 577-583.

[21] S.S. Shankar, A. Rai, A. Ahmad, M. Sastry, "Rapid synthesis of Au, Ag and bimetallic Au core-Ag shell nanoparticles using Neem (Azadirachta indica) leaf broth" ***J. Colloid Interf. Sci.* (2004),** 275: 496-502.

[22] R.P. Singh, S. Magesh, C. Rakkiyappan, "Ginger (Zingiber officinale) root extract: a source of silver nanoparticles and their application" ***Int. J. Bioeng. Sci. Technol.* (2011),** 02 (03): 75-80.

[23] K Govindaraju, S Tamilselvan, V Kiruthiga, G Singaravelu, "Antimicrobial activity of silver nanoparticles. Biogenic silver nanoparticles by Solanum torvum and their promising antimicrobial activity" ***J. Biopestic.* (2010)** 3 (1): 394-399.

[24] M. Sundarajan, S. Gowri, "Green synthesis of titanium dioxide nanoparticles by Nyctanthes arbour-tristis leaves extract" ***Chalcogenide Lett.*** **(2011),** 8 (8): 447-451.

[25] S. Maensiri, P. Laokul, J. Klinkaewnarong, S. Phokha, V. Promarak, S. Seraphin, "Indium oxide (In$_2$O$_3$) nanoparticles using Aloe vera plant extract: Synthesis and optical properties" ***J. Optoelectron. Adv. Mater.*** **(2008),** 10 (3): 161-165.

[26] H.M. Gong, L. Zhou, X.R. Su, S. Xiao, S.D. Liu, Q.Q.Wang, "Illuminating dark plasmons of silver nanoantenna rings to enhance exciton-plasmon interactions" ***Adv. Funct. Mater.*** **(2009),** 19: 298-303.

[27] N.P.S. Acharyulu, R.S. Dubey, V. Swaminadham, P. Kollu, S.V.N. Pammi, "Green synthesis of CuO nanoparticles using Phyllanthus Amarus leaf extract and their antibacterial activity against multidrug resistance bacteria" ***Int. J. Eng. Res. Technol.*** **(2014),** 3 (4): 639-641.

[28] S. Ankanna, P. TNVKV, E.K. Elumalai, N. Savithramma, "Production of biogenic silver nanoparticles using Boswellia ovalifoliolata stem bark" ***Dig. J. Nanomater. Biostruct.*** **(2010),** 5 (2): 369-372.

[29] R.H. Ritchie, "Plasma losses by fast electrons in thin films" ***Phys. Rev.*** **(1957),** 106: 874.

[30] W.L. Barnes, A. Dereux, T.W. Ebbesen, "Surface plasmon subwavelength optics" ***Nature*** **(2003),** 424: 824-830.

[31] S.A. Maier, H.A. Atwater, "Plasmonics: localization and guiding of electromagnetic energy in metal/dielectric structures" ***J. Appl. Phys.*** **(2005),** 98: 011101.

[32] S.A. Maier, "Plasmonics Fundamentals and Applications, first ed" ***Springer, New York***, **(2007),** 21-34 and 65-88.

[33] S. Lal, S. Link, N. Halas, "Nano-optics from sensing to waveguiding" ***Nat. Photonics*** **(2007),** 1: 641-648.

[34] X.C. Wang, J.C. Yu, H.Y. Yip, L. Wu, P.K. Wong, S.Y. Lai, "A mesoporous Pt=TiO$_2$ nanoarchitecture with catalytic and photocatalytic functions" ***Chem. Eur. J.*** **(2006),** 11: 2997-3004.

[35] X.B. Cao, L. Gu, L.J. Zhuge, W.J. Gao, W.C.Wang, S.F.Wu, "Template-free preparation of hollow. Sb$_2$S$_3$ microspheres as supports for Ag nanoparticles and photocatalytic properties of the constructed metal– semiconductor nanostructures" ***Adv. Funct. Mater.*** **(2006),** 16: 896-902.

[36] K. Satyavani, T. Ramanathan, S. Gurudeeban, "Green synthesis of silver nanoparticles by using stem derived callus extract of bitter apple Citrullus colocynthis" ***Dig. J. Nanomater. Biostruct.*** **(2011),** 61019-1024.

[37] P. Scherrer, "Bestimmung der Grösse und der inneren Struktur von Kolloidteilchen mittels Röntgenstrahlen" ***Nachr. Ges. Wiss. Göttingen*** **(1918),** 26: 98-100.

[38] J.I. Langford and A.J.C. Wilson, "Scherrer after Sixty Years: A Survey and Some New Results in the Determination of Crystallite Size" *J. Appl. Cryst.* **(1978),** 11: 102-113.

[39] R. Varshney, S. Bhadauria, M.S. Gaur, "Biogenic synthesis of silver nanocubes and nanorods using sundried Stevia rebaudiana leaves" *Adv. Mat. Lett.* **(2010),** 1 (3): 232-237.

[40] K. Jeet, N. Devi, T. Narendra, T. Sunil, S. Lalit, T. Raneev, "Trachyspermum ammi (Ajwain) Comprehensive Review" *Int. Res. J. Pharm.* **(2012),** 3 (5): 133-138.

[41] M. Kjellin, I. Johansson, "Surfactants from Renewable Resources" *John Wiley & Sons,* **(2010)**.

[42] X. Gao, G. Gu, Z. Hu, Y. Guo, X. Fu, J. Song, "A simple method for preparation of silver dendrites colloids Surf" *A Physicochem. Eng. Asp.* **(2005),** 254: 57-61.

[43] A. van Dijken, E.A. Meulenkamp, D. Vanmaeklenbergh, A. Meijerink, "The luminescence of nanocrystalline ZnO particles: the mechanism of the ultraviolet and visible emission" *J. Lumin.* **(2000),** 87-89 454-456.

[44] Y.J. Xing, Z.H. Xi, Z.Q. Xue, X.D. Zhang, J.H. Song, R.M. Wang, J. Xu, Y. Song, S.L. Zhang, D.P. Yu, "Optical properties of the ZnO nanotubes synthesized via vapor phase growth" *Appl. Phys. Lett.* **(2003),** 83: 1689-1691.

[45] W. Haiss, N.T.K. Thanh, J. Aveyard, D.G. Fernig, "Determination of. Size and Concentration of Gold Nanoparticles from UV-Vis Spectra" *Anal. Chem.* **(2007),** 79: 4215-221.

[46] D.C. Oh, T. Suzuki, J.J. Kim, H. Makino, T. Hanada, M.W. Cho, T. Yao, "Electron-Trap Centers in ZnO Layers Grown by Molecular-Beam Epitaxy" *Appl. Phys. Lett.* **(2005),** 86: 032909.

[47] Wriedt, T. Mie Theory 1908-2008, ed. by W. Hergert, T. Wriedt, Universität Bremen. *Bremen* **(2008),** 17-21.

[48] K. Jilie, Y.U. Shaoning, "Fourier Transform. Infrared Spectroscopic Analysis of Protein. Secondary Structures" *Acta Biochim. Biophys. Sin.* **(2007),** 39: 549-559.

[49] N.P.G. Roeges, "A Guide to the Complete Interpretation of Infrared Spectra of Organic Structures" *Wiley, New York*, **(1994)**.

[50] G. Varsanyi, "Assignments of Vibrational Spectra of Seven Hundred Benzene Derivatives" vol. 1, *Halsted Press* **(1974)**.

[51] I.D.G. Macdonald, W.E. Smith, "Orientation of Cytochrome c Adsorbed on a Citrate-Reduced Silver Colloid Surface" *Langmuir* **(1996),** 12: 706-713.

[52] A.M. Fayaz, K. Balaji, M. Girilal, R. Yadav, P.T. Kalaichelvan, R. Venketesan, "Biogenic synthesis of silver nanoparticles and their synergistic effect with antibiotics: a study against gram-positive and gram-negative bacteria" ***Nanomedicine: NBM* (2010),** 6: 103-109.

[53] R. Sathyavathi, M.B. Krishna, S.V. Rao, R. Saritha, D.N. Rao, "Biosynthesis of silver nanoparticles using Coriandrum Sativum leaf extract and their application in nonlinear optics" ***Adv. Sci. Lett.* (2010),** 3: 138-143.

[54] A. Manna, T. Imae, M. Iida, N. Hisamatsu, "Formation of Silver Nanoparticles from a *N*-Hexadecylethylenediamine Silver Nitrate Complex" ***Langmuir* (2001),** 17 (19): 6000-6004.

[55] M.H. Moore, R.L. Hudson, "Infrared study of ion-irradiated N2-dominated ices relevant to Triton and Pluto: Formation of HCN and HNC" ***Icarus* (2003)**161: 486-500.

[56] W. Zheng, D. Jewitt, Y. Osamura, R.I. Kaiser, "Formation of Nitrogen and Hydrogen-bearing Molecules in Solid Ammonia and Implications for Solar System and Interstellar Ices" ***Astrophys. J.* (2008),** 674 (2): 1242.

[57] B.M.V. Romão, C. Pardini, R.C.L. Dutra, F. Burel, "Caracterização por FT-IR de. Agentes de Cura Utilizados em Resinas Epoxídicas-II-Polimercaptana, Poliaminoamida e Amina Modificada" ***Polímeros Ciência Tecnologia* (2003),** 13: 173-180.

[58] J.P. Wilcoxon, J.E. Martin, F. Paraspour, D.F.J. Kelley, "Photoluminescence from nanosize gold clusters" ***Chem. Phys.* (1998),** 108: 9137-9143.

[59] H. Peng, S.X. Hai, G.H. Cheng, "Pternopetalum Franch. represents one of the largest genera of Apiaceae in Asia" ***Acta Phys. -Chim. Sin.* (2004),** 20 (10): 1200-1203.

[60] A. Frattini, N. Pellegri, D. Nicastro, O.D. Sanctis, "Effect *of* amine groups in the synthesis *of* Ag nanoparticles using aminosilanes" ***Mater. Chem. Phys.* (2005),** 94 (1): 148-152.

Chapter 3.2

Synthesis and Characterization of biogenic Ag NPs prepared by using:

(2) Fenugreek (Trigonella Foenum Graecum)

ABSTRACT

In this chapter, we had reported the biosynthesis of 13.42 nm sized silver nanoparticles (AgNPs) using Fenugreek (Methi) seed extract at room temperature. Synthesis of plasmonic AgNPs is carried out by reducing the $AgNO_3$ with the aqueous Fenugreek seed extract. Formation of AgNPs is confirmed by the appearance of a red color due to the prominent localised surface plasmon resonance band in the UV-Visible spectrum around 425 nm. As synthesized AgNPs were characterized by using advance analyses techniques such as: Fourier-transform infrared spectroscopy (FTIR), powder X-ray diffraction (PXRD) studies, scanning electron microscopy (SEM) and transmission electron microscopy (TEM) supported EDX and ATR, etc. And observed optical properties leads to a good optoelectronic material.

Key Words: Aqueous Fenugreek seed extract**,** Ag-nanoparticles**,** LSPR, biogenic synthesis, etc.

3.2 (II) 1 INTRODUCTION

Currently, the noble metals such as Ag, Au, Pd and Pt nanoparticles have been extensively studied due to their unique properties like as a optical, mechanical, electronic, biochemical, polarizability, metallic, [1-3] dielectric [4,5] semiconductor [6,7] magnetic [8,9] antimicrobial as well as antibacterial activities, photocatalytic, surface-enhanced Raman scattering (SERS) and DNA sequencing, etc, which are extensively different from their bulk counterparts. But the hussle free production of the nontoxic metal nanoparticles became a great challenge. Production of the metallic nanoparticles became important due to their uses in many applications such as a photonics, catalysis and electronics, etc. A number of processes have been involved in order to prepare metallic NPs, like as a UV light irradiation, [10,11] microwave irradiation process, [12,13] chemical reduction method, [14-16] photo chemical process, [17,18] electron/light irradiation, [19,20] and sonoelectrochemical method, [21] etc. Microemulsions methods were used for the synthesis of MNPs arrays with chemicals as a precursor along with the large amounts of surfactants as a stabilizing agent. However, the intensive use of solvents and synthetic chemical reactants are harmful for our biological environment as they consumed more energy. Moreover, these methods are not cost effective and they also used the toxic and hazardous chemicals, which may pretend to potential ecological risks in long way. In looking to the high demand of the metal NPs in different facets of life, we need to modify the way to prepare them. For these reasons, it is very attractive to plan the green path for production of nanomaterial research by using natural reactants and of course by without/less consuming the poisonous chemicals.

A bio-mimetic fabrication of the metal nanoparticles involves the bio reduction process by using enzymes, fungus, extracts of different parts of plants such as a stem, root, leaf, seed and fruit, and microorganisms, are recommended as the green alternative to the chemical and physical methods. Silver nanoparticles are produced by different parts of the herbal plants like bark of the neem leaves [22], Juice of Citrus lemon [23] and plant's leaves. Among the noble metal nanoparticles like Ag, Au, Pt, Pd, silver nanoparticles found more beneficial on the grounds of their studies as catalysts, photosensitive components, and localised surface plasmon resonance possessing material, etc.

This chapter, includes the synthesis of the stable AgNPs by using aqueous Fenugreek plant seeds' extract and characterized them using advance analyses techniques. The silver nanoparticles were synthesized by the reduction of silver nitrate solution with fenugreek seed's extract. Fenugreek seeds are golden-yellow in colour; small in size/structure [24] and possess the phytochemicals

such as, alkaloids, steroids, carbohydrates, terpenoids, flavonoids, saponins, anthocyanin, tannins and quinones etc. [25] Which can works as reducing agents as well as a stabilizing/capping agents for the synthesis of the AgNPs. [26] As-synthesized AgNPs were characterized by using different analytical techniques such as: X-ray differaction (XRD), FESEM, transmission electron microscopy (TEM), UV-Vis-spectroscopic, ATR, FTIR, etc.

3.2(II) 2 EXPERIMENTAL METHODS

3.2(II) 2.1 Preparation of the Feenugreek Extract

The fenugreek plant seeds were collected from medicinal garden of Agriculture University campus, Kota, India. The collected seeds were carefully washed by deionised water (DIW) then dried and crushed. Subsequently, 2g fresh Fenugreek seeds were soaked in 50 mL of DIW at room temperature for 24 h, followed by filtration and the extract was kept at 4^oC in refrigeration until it further utilized for the investigations. The extract can be used within 7 days of its preparation.

3.2 (II) 2.2 Synthesis of silver nanoparticle

$AgNO_3$ (99.98%; Merck (Germany)) was purchased and deionised distilled water was used for solution preparation. The chemicals used in the study are of analytical grade and used without any further purification. The aqueous 2.0 mL fenugreek seeds extract was dropwise mixed with 25 ml of freshly prepared 10^{-3} M $AgNO_3$ solution at room temperature. The colour change in $AgNO_3$ solution with aging was observed that is from transparent to dark reddish-brown. On centrifugation the AgNPs powder was obtained, which is well dispersed in DIW to clear the uncoordinated biological material in solution. The purified AgNPs was then dried in oven at 90^oC temperature for 24 h.

3.2 (II) 2.3 Characterization of synthesized AgNPs

The synthesized AgNPs were optically observed by UV-Vis spectroscopy over a range between the wavelength 200 to 800 nm. The morphology and composition of the synthesized AgNPs was observed by SEM investigations and their corresponding EDX. FTIR was performed to trace out the possible phytochemicals present in Ag NPs that responsible for capping and reduction in synthesis of AgNPs by fenugreek seed extract. The XRD result was analysed to check the crystalline nature, purity of the samples, average particle size, and plane of the growth of the AgNPs.

3.2 (II) 3 RESULTS AND DISCUSSION

3.2 (II) 3.1 Optical Analysis

Figure 3.15a, 3.15b and 3.15c, confirmed the formation of AgNPs by change in colour with the AgNO$_3$ solution from transparent to dark reddish-brown with time.
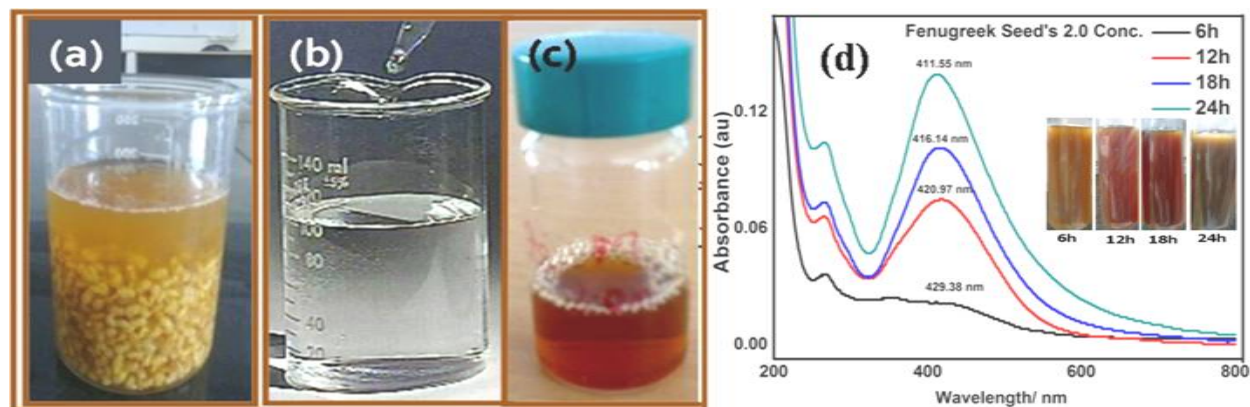
**Figure 3.15 (a)** Soaked FG seed extract, **(b)** pure AgNO$_3$ solution and **(c)** synthesized solution of AgNPs and **(d)** UV-Vis. spectrum of as synthesized AgNPs with aging time 6h,12h,18h and 24h.

3.2 (II) 3.1.1 UV-Visible Analysis

One of the most widely used tool for analysing the particle concentration and size of silver nanoparticles is UV-Visible spectroscopy. Figure 3.15d, graphically represents the UV-Vis absorption spectrum of the as synthesized reddish-brown AgNPs solution, which consist of a one peakat 236 nm ($\pi \rightarrow$n*) and another broad peak from 429 to 411 nm peaks to show blue shift with aging with first excitation due to surface plasmon absorption band ($\pi \rightarrow \pi$*) with the maximum absorbance that signify the existence of the AgNPs with SPR. The effect of aging on UV-Vis spectrum of as synthesized AgNPs with aging time 6h,12h,18h and 24h, demonstrated by Figure 3.15d. First peak of all samples are retained at same position but the first excitation peaks show the blue shift with aging. Therefore, it is important to notice the effect of synthesis time on particle size and concentration that can play an important role in formation of the Ag nanoparticles. The influence of aging of the AgNPs, was evaluated with reaction mixture (inset of Figure 3.15d). Six hour aged sample show small but broad SPR band the indicates, the formation of low concentration of nanoparticles with small size. These results confirmed the formation of silver nanoparticles with increasing concentration and increasing particle size with time. In the present analysis 24 h synthesised samples are taken for study.

3.2 (II) 3.1.2 FTIR/ ATR Analysis

ATR measurement used to recognize the probable phytochemicals present in the plant extract, which are accountable for reducing and capping agent for AgNPs, as shown by the Figure 3.16a. The apparent infrared band was observed at 3330 cm^{-1}, 1635 cm^{-1} and 580/557 cm^{-1}. The strong and broad band at 3330 cm^{-1}, attributed to the O-H (intermolecular/intramolecular) group and N-H band. The intense band at 1635 cm^{-1} belongs to the C=O stretching of amino functional group present in the representative protein, used as capping agent for AgNPs, which causes high stability to AgNPs. The small and broad peaks at 580 cm^{-1} and 557cm^{-1}, are responsible for bonding Ag metal with phytochemicals. Figure 3.16b shown FTIR spectrum of the sample Feenugreek supported AgNPs.
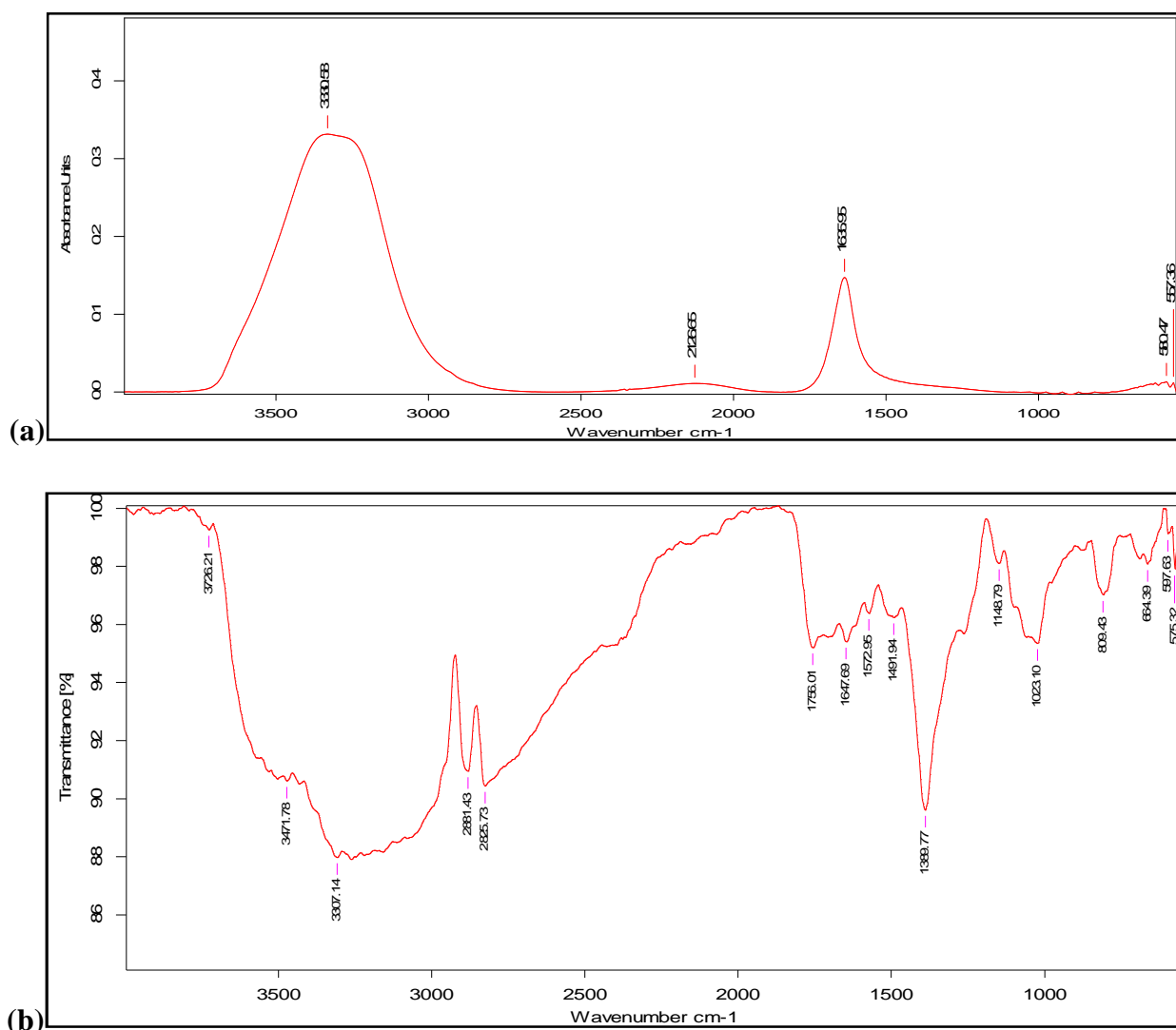

Figure 3.16 (a) ATR spectra and **(b)** FTIR spectra of the AgNPs prepared by Fenugreek plant extract in 24h.

The FTIR absorption bands of Fenugreek supported AgNPs are found at 3726.21, 3471.78 (O-H stretching), 3307.14 (C-H stretching), 2881.43 (C-H stretching), 2825.73, 1756.01 (C-H stretching), 1647.69 (C=O stretching) due to protien, 1572.96 (Aromatic skeletal stretching), 1491.94 (CH$_2$ deformation stretching), 1389.77 (Aliphatic C-H stretching group in methyl and phenol O-H), 1143.79 (C-O-C stretching, C=O stretching), 1023.10 (C-O,C=O, C-H stretching), 809.43,654.39, 597.63 and 575.32 cm^{-1}. The characteristic absorptions peaks at 1143.79 and 1023.10cm^{-1}, were exhibited the presence of polysaccharides and coumarin. The peak ranging from 800 cm^{-1} to 500 cm^{-1}was mainly attributed to the vibration and bending vibration of hydroxyl groups of alcohols and benzene rings and their respective intratcions with Ag NPs [27] a strong IR band at 809.43 cm^{-1} (with pure Fenugreek it is at 793cm^{-1}), is formed due to the inorganic part of fenugreek that mainly consists of phosphate compounds. It could be concluded that of phosphate compounds. The Fenugreek seed contains proteins, fat, fiber, and ash, which is in complete harmony with AACC, 1980. [28]

3.2 (II) 3.2 X-ray diffraction analysis

XRD patterns for the as- synthesized AgNPs were exhibited by the Figure 3.17 in the form of the most distinguished diffraction peaks of silver metal at 2θ = 38.45^o, 45.04^o and 53.90^o, which indicated the presence of the fcc (face centered cubic) crystalline phase of the AgNPs that resembles to the standard JCPDS File No. 00-004-0783 of the metallic silver. No bogus peaks found shows phase purity of the AgNPs. The crystalline particle size of the AgNPs was calculated by using Scherrer equation by using full width half maxima (FWHM) of the strongest diffraction peaks.According to the Scherrer equation, the synthesized sample of AgNPs possesses13.42 nm size. [29,30] The hump in diffractogram is associated with the glass substrate because the sample was dried on glass substrate before running it for XRD analysis. The results express that the Ag ions reduced to Ag^0 by fenugreek plant seed extract under suitable reaction conditions.
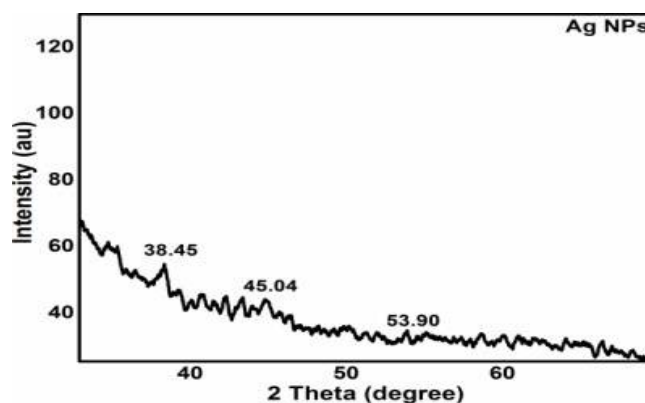
Figure 3.17 XRD diffraction pattern of the Fenugreek supported AgNPs aged at 24h.

3.2 (II) 3.3 TEM, SEM and EDX studies of AgNPs

The size, morphology and structure of the nano particle were also confirmed by the TEM and FESEM images (Figures 3.18a and 3.18b). Morphology of the synthesized samples of the Fenugreek supported AgNPs was studied using different electron microscopic techniques such as SEM, TEM and HRTEM. Particle size (~13 nm) with cubic shape of the as-synthesized AgNPs was traced by using TEM as demonstrated by Figure 3.18a. As grown particle morphology in bilk is shown by the Figure 3.18b.

The elemental chemical composition of the AgNPs was analysed by the SEM supported EDX spectroscopy i.e. Ag ~ 99.36% and C ~ 0.64% (Figure 3.18c). Over all EDX profile exhibits there are no bogus peaks of impurity except carbon, which might becomes from the carbon tape that used to hold the sample during the SEM analysis. So, we can say this method produced the highly purity organic molecules freeAg NPs.
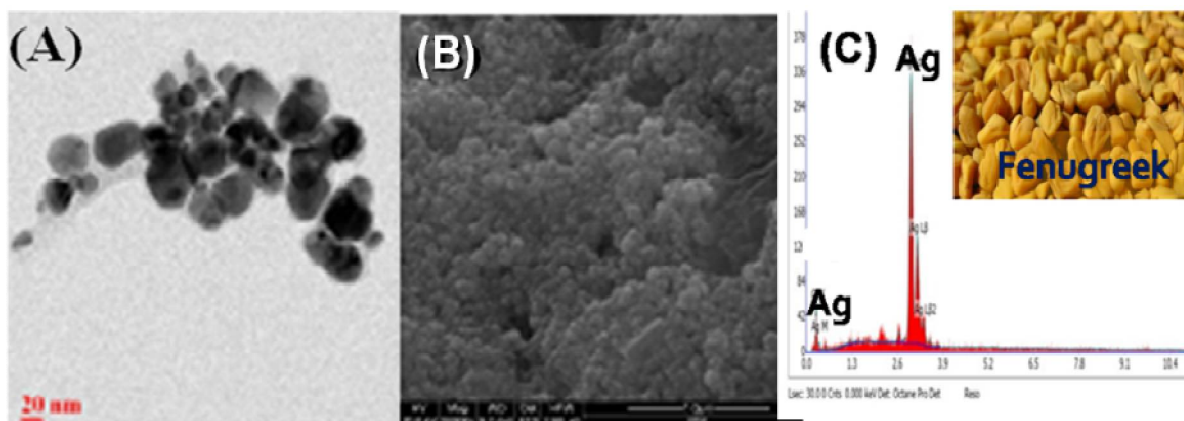
Figure 3.18 (a) TEM image and particle size distribution of AgNPs **(b)** FESEM images of silver nanoparticles, **(c)** corresponding AgNP's EDX profile.

3.2 (II) 4 CONCLUSION

In this chapter, we produced aprooimately 14.00 nm sized AgNPs by using biogenic reducing method, where the aqueous extract of Fenugreek was acted as a green reducing agent without hazarding environment. AgNPs crystallised in cubic crystalline phase. During the biosynthesis of the Ag nanoparticles, self-assembling biochemical of the fenugreek seed extract's covered the Ag^+ ion and leads to the reduction of Ag^+ ion to Ag NPs. As synthesized AgNPs were characterized by Fourier-transform infrared spectroscopy (FTIR), powder X-ray diffraction (PXRD) studies, scanning electron microscopy (SEM) and transmission electron microscopy (TEM) supported EDX and ATR, etc.

3.2 (II) 5 REFERENCES

[1] CJ Murphy, TK Sau, AM Gole, CJ Orendorff, J Gao, L Gou, SE Hunyadi, Li T, "Anisotropic metal nanoparticles: synthesis, assembly, and optical applications" *J Phys Chem B* **(2006),** 109: 13857-13870.

[2] DM Ledwith, D Aherne, JM Kelly, "Approaches to the Synthesis and Characterization of Spherical and Anisotropic Silver Nanomaterials" *Wiley-VCH Verlag* **(2009),** 1: 99-148.

[3] CH Yu, K Tam, ESC Tsang: In Handbook of Metal Physics, Vol. 5, Chapter 5 "Chemical Methods for Preparation of Nanoparticles in Solution" *Elsevier* **(2009),** 113-141.

[4] JK Nelson, "Overview of nanodielectrics: insulating materials of the future. In Proceedings of Electrical Insulation Conference and Electrical Manufacturing Expo" October 2007. *Nashville: EEIC* **(2007),** 229.

[5] MR Baklanov, "In Nanodevices and Nanomaterials for Ecological Security: Chapter 1 Nanoporous Dielectric Materials for Advanced Micro- and Nanoelectronics" *Springer* **(2012),** 3-18.

[6] JZ Zhang, Z Wang, J Liu, S Chen, G Liu, "In Self-Assembled Nanostructures: Chapter 8 Optical, Electronic, and Dynamic Properties of Semiconductor Nanomaterials" *Kluwer Academic Publishers* **(2004),** 201-255.

[7] C Weber, M Richter, S Ritter, A Knorr, "In Semiconductor Nanostructures: Chapter 9 Theory of the Optical Response of Single and Coupled Semiconductor Quantum Dots" *Springer* **(2008),** 189-210.

[8] A Lu, EL Salabas, F Schüth, "Magnetic nanoparticles: synthesis, protection, functionalization, and application" *Angew Chem Int Ed* **(2007),** 461222-1244.

[9] YA Koksharov, "In Magnetic Nanoparticles: Magnetism of nanoparticles: effects of size, shape and interactions" *Wiley-VCH Verlag* **(2009),** 117-196.

[10] AT Le, LT Tam, PD Tam, "Synthesis of oleic acid-stabilized silver nanoparticles and analysis of their antibacterial activity" *Materials Science and Engineering: C* **(2010),** 30(6): 910-916.

[11] H Huang, Y Yang. "Preparation of silver nanoparticles in inorganic clay suspensions" *Composites Science and Technology* **(2008),** 68(14): 2948-2953.

[12] H Yin, T Yamamoto, Y Wada, S Yanagida, "Large-scale and size-controlled synthesis of silver nanoparticles under microwave irradiation" *Materials Chemistry and Physics* **(2004),** 83(1): 66-70.

[13] MN Nadagouda, TF Speth, RS Varma, "Microwave-Assisted Green Synthesis of Silver Nanostructures" *Accounts of Chemical Research* **(2011)** 44 (7): 469-478.

[14] L Suber, I Sondi, E Matijevic, DV Goia, "Preparation and the mechanisms of formation of silver particles of different morphologies in homogeneous solutions" *Journal of Colloid and Interface Sicence* **(2005),** 288(2): 489-495.

[15] K Song, S Lee, T Park, B Lee, "Preparation of colloidal silver nanoparticles by chemical reduction method" *Korean Journal of Chemical Engineering* **(2009),** 26 (1): 153-155.

[16] O Golubeva, O Shamova, D Orlov, T Pazina, A Boldina, V Kokryakov, "Study of antimicrobial and hemolytic activities of silver nanoparticles prepared by chemical reduction" *Glass Physics and Chemistry* **(2010),** 36 (5): 628-634.

[17] M Harada, C Kawasaki, K Saijo, M Demizu, Y Kimura, "Photochemical synthesis of silver particles using water-in-ionic liquid microemulsions in high-pressure CO_2" *Journal of Colloid and Interface Science* **(2010),** 343 (2): 537-545.

[18] M Harada, Y Kimura, K Saijo, T Ogawa, S Isoda, "Photochemical synthesis of silver particles in Tween 20/water/ionic liquid microemulsions" *Journal of Colloid and Interface Science* **(2009),** 339 (2): 373-381.

[19] K Li, FS Zhang, "A novel approach for preparing silver nanoparticles under electron beam irradiation" Journal of Nanoparticle Research **(2009),** 12 (4): 1423-1428.

[20] KA Bogle, "Silver nanoparticles: synthesis and size control by electron irradiation" *Nanotechnology* **(2006),** 17 (13): 3204.

[21] J Zhu, S Liu, O Palchik, Y Koltypin, A Gedanken, "Shape-Controlled Synthesis of Silver Nanoparticles by Pulse Sonoelectrochemical Methods" *Langmuir* **(2000),** 16 (16): 6396-6399.

[22] Aparajita Verma, Mohan Singh Mehata, "Controllable synthesis of silver nanoparticles using Neem leaves and their antimicrobial activity" *Journal of Radiation Research and Applied Sciences* **(2016),** Volume 9, Issue 1, January 109-115.

[23] P Vankar, D Shukla, "Biosynthesis of silver nanoparticles using lemon leaves extract and its application for antimicrobial finish on fabric" *Applied Nanoscience* **(2012),** 1-6.

[24] E Altuntas, E Ozgoz, "Taser of Some physical properties of fenugreek *(Trigonellafoenum-graceum L.)* seeds" ***J Food Eng*** **(2005),** 71: 37-43.

[25] AR Sumayya, Srinivasan Sivagami, Amatullah Nabeelah, "Screening and biochemical quantification of phytochemicals in fenugreek (Trigonella foenum-graecum)" ***RJPBCS*** (**2012),** 3(1): 165-169

[26] R Jani, SA Udipi, PS Ghugre, "Mineral content of complementary foods" ***Indian J Pediatr*** **(2009),** 7637-44.

[27] Doha Samargandi ***J. Chem. Pharm. Res.,*** **(2014),** 6(9): 19-24.

[28] GMS El-Bahy, "FTIR and Raman spectroscopic study of Fenugreek (*Trigonella foenum graecum L.*) seeds" ***Journal of Applied Spectroscopy*** **(2005),** 72 (1): 111-116.

[29] P Scherrer "Bestimmung der Grösse und der inneren Struktur von Kolloidteilchen mittels Röntgenstrahlen" ***Nachr. Ges.Wiss. Göttingen*** **(1918),** 26: 98-100.

[30] JI Langford, AJC Wilson, "Scherrer after Sixty Years: A Survey and Some New Results in the Determination of Crystallite Size" ***J. Appl. Cryst.*** **(1978),** 11: 102-113.

Chapter 3.2

Synthesis and Characterization of biogenic Ag NPs prepared by using:

(III) Tea (Camellia Sinensis) leaves extract

ABSTRACT

Biosynthesis of silver nanoparticles is comparative simple, cheap and environmentally benign alternative to the physical and chemical procedures. Green synthesis of silver nanoparticles from biogenic tools is more compatible, economic viability, effective, easy to scale up and less time consuming process. Tea leaves extract act as a capping agent and reducing agent in the nanoparticles synthesis. This green method is a single step process and good for rapid production of nanoparticles that could be used in many optoelectronics/sensing devices, biomedical and chemical transformation applications. The silver ions reduced to nano silver and show characteristic UV-Vis absorbtion peak at 420 nm. As-prepared AgNPs were characterized by powder X-ray diffraction (PXRD), UV-Visible spectroscopy and Scanning electron microscopy (SEM), Fourier transformer Infrared spectroscopy (FTIR). X-ray diffraction pattern confirmed the formation of face centered cubic crystals of size range of 5-20 nm with prominent SPR peak at 412 nm in UV -Vis spectra.

Key Words: Silver nanoparticles**,** Tea leaves, ecofriendly synthesis, surface plasmon resonance etc.

3.2 (III) 1 INTRODUCTION

Currently, the nanotechnology became a vital tool in current research as well as in other fields. Nanomaterials have been getting considerable attention due to their distinctive physical and chemical properties over their larger-size equivalents. [1-3] Nanostructured silver particles (AgNPs), have been utilised in different fields for example chemical, biological, physical, and medical. [4-6] Recently, the silver nanoparticles have been established to exhibit fascinating antibacterial activities, coating stainless steel metals, sun creams and burn treatments. [7] All noble metal nanoparticles have been produced by chemical reduction method by using different reducing reagents ($NaBH_4$, ascorbate or citrate), [8] reduction via reverse micelles way, [9] radiation cum chemical reduction [10] and thermal decomposition. [11] Many of these methods are expensive, consuming a lot of energy, outcome in low yields, the chemicals, which used in fabrications are toxic and harmful, which affects the human health and environment. [12] Now a day, silver nanoparticles have been prepared by the biological methods by using enzymes, [13] microorganisms, [14] and fungus. [15] The main drawbacks of these methodologies are they need special culture preparation and nonuniform partical size along with their tough separation procedures. [16,17] Silver nanoparticles have also been made-up by using plant extracts as reducing, stablising and capping agents. The major benefits of using plant extracts is it simple reaction route, environmentally benign, cost effective, ease to scale-up, and non-toxic nature. [18-22] A vast range of metal NPs such as Au, [23-27] Ag, [28,29] TiO_2, [30] In_2O_3, [31] ZnO, [32] CuO, [33] etc, have been synthesized using herbal plant extracts. Utilization of plant extract and microbial cells in the synthesis of metal NPs was triggered by the occurrence of the various organic group/compounds such as carbonyl groups, terpenoids, phenolics, flavanones, amines, amides, proteins, pigments alkaloids and other phytochemicals of the plant extract. Tea leaves has a great medicinal and nutrition values because its seed extract consists of the most important compounds in fresh tea leaves responsible for producing Tea with desirable appearance, aroma, flavor, and taste are: polyphenols (flavonoid group, flavanols (catechin (C), epicatechin (EC), epicatechin gallate (ECG), gallocatechin (GC), epigallocatechin (EGC), and epigallocatechin gallate (EGCG) 40%), amino acids (L-Theanine , 6%), enzymes (Polyphenol oxidase and peroxidase), pigments (chlorophylls and carotenoids), carbohydrates (11%), methylxanthines, minerals (25 menerals including fluorine, manganese, arsenic, nickel, selenium, iodine, aluminum, and potassium) and many volatile flavor and aromatic compounds (linalool and linalool oxide are responsible for sweetness; geraniol and phenylacetaldehyde are responsible

for floral aromas; nerolidol, benzaldehyde, methyl salicylate, and phenyl ethanol are responsible for fruity flavors; and trans-2-hexenal, n-hexanal, cis-3-hexenol, and p-ionone are responsible for a Tea's fresh flavour. [34,35] These components undergo changes during tea processing to produce different effect on the body and mind of the drinker. Hence, due to the existence of these biochemical ingredients, tea leaves can be served as the reducing and capping agent without addition of any external stabilizing agent, during the synthesis process of NPs. Silver has long been well-known for its good inhibitory effect towards many bacterial strains/microorganisms and catalytic activity. Therefore, it commonly used in the medical and industrial products such as shampoos, soaps, detergents, shoes, cosmetic products, and toothpaste etc. These are also stuitable for the photocatalytic and pharmaceutical applications.

Here, in this work, a facile and rapid green chemical method was explored for the fabrication of the silver nanoparticles using tea leaves essence. To the best of our knowledge, there is no such report is available, in which the aqueous tea leaves essence is used for the production of AgNPs. As prepared nanoparticles were characterized using XRD, UV-Visible absorption spectroscopy, FESEM, transmission electron microscopy (TEM), EDX and FTIR, etc. Therefore, this study is dedicated to the production of the Ag NPs by biogenic reduction method using aqueous tea leaves extract at ambient conditions.

3.2 (III) 2 EXPERIMETAL

3.2 (III) 2.1 Preparation of the Tea leaves extract

Fresh leaves of Tea plant are carefully washed with water and dried in air for 2h. 20 g of plant leaves are crushed in 50 mL water and filtered first through sterile muslin cloth and then through with Whatman filter paper. This Tea leaves extract is later on used in silver NPs synthesis.

3.2 (III) 2.2 Synthesis of AgNPs

All the chemicals used during this experiment are of analytical reagent grade and used without further purification. Deionised Millipore water (DIW) was used as the solvent throughout the experiment. 2 mL of Tea leaf extract is added to 25 mL of an aqueous solution of 10^{-3} M $AgNO_3$ and kept at room temperature. The solution color changed from pale yellow to dirty greenish red, suggested the formation of Ag NPs. (Figure 3.19) the pure $AgNO_3$ solution and leaf extract have not shown any visible color changes during the incubation period under similar conditions. The formation of AgNPs was monitored and confirmed by UV-visible spectroscopy. As- produced AgNPs were centrifuged at 28,000 rpm speed for 20 min and purified using methanol/ hot water.

The repeated purification is done by giving several washes to the sample by methanol and hot water to remove the plant residues. AgNPs are finally dried at 70°C in muffle furnace for 2h to evaporate methanol/water solvent form solution.

Figure 3.19 Step-wise representation of the synthesis of AgNPs by Tea Leaves' Extract

3.2 (III) 2.3 Characterization of AgNPs

The as-synthesized nanoparticles are characterized by using UV-visible, FTIR, XRD, SEM, TEM, EDX and SAED methods.The powder X-ray diffraction pattern of the biologically synthesized Ag NPs is recorded using XRD Bench-top Powder Diffractometer (Proto Manufacturing Limited). The XRD data is analyzed to find out the crystal structure and average crystal domain size of synthesized Ag NPs. The reduction of silver ions (Ag^+) to Ag NPs (Ag^0) in the reaction mixture is confirmed by a visual color change from pale radish pink to greenish red. The formation of AgNPs is confirmed by UV-visible spectroscopy. The UV spectrum was taken for the reaction mixture after diluting a small aqueous aliquot in solvent. The UV-visible spectral analysis is performed using Shimadzu-1800 UV-Vis spectrometer. The DIW was used as a control. FTIR studies conducted on the as synthesized samples using Jasco FTIR 4100 (Japan) spectrometer. The spectral analysis is performed in the wave number range of 500-4000 cm^{-1}. SEM is analysed on a ZEISS EVO40EP (Germany) microscope and the micrograph images of synthesized AgNPs are recorded. TEM is performed on JEOL/JEM 2100 microscope with an accelerating voltage of 200 kV with a resolution of 0.23 nm.

3.2(III) 3 RESULTS AND DISCUSSION

3.2 (III) 3.1 XRD study

The structural identity and phase purity of the as synthesized AgNPs were studied by PXRD analysis. XRD pattern of AgNPs is shown in Figure 3.20a. This showed three intense peaks in the range of 2θ from 30° to 70°. The peaks at 37.56, 43.54 and 64.06 are indexed to lattice planes of (111), (200) and (220), of AgNP's respectively. These planes represent the cubic crystal system of the Ag NPs that matched well with the standard JCPDS card No. 04-0783 of pure silver. The XRD study confirms that the resultant particles are (FCC) pure silver nanoparticles as no other peaks revealed in XRD pattern. [36] These results also revealed that the crystal growth along the (111) plane was recorded as the highest intensity peak. The experimentally obtained X-ray reflections are consistent with the standard diffraction pattern of the silver (standard JCPDS File No. 00-004-0783 of silver) metal. [37] The ratio between the intensities of the (200) and (111) diffraction peaks and (220) and (111) peaks is also slightly higher than the conventional value (0.48 versus 0.31) and (0.34 versus 0.22). [38] Peak broadening observed in the XRD data was due to the small particle size and associated spin plasmonic resonance phenomena. Absence of any extra peak in the PXRD analysis of synthesized AgNPs, confirms that the as-prepared NPs are pure and there is no traces of precursor salt. The particle size D (11 to 18 nm) is calculated based on the regular broadening of XRD peaks as a function of decreasing crystallite size. [39]

3.2 (III) 3.2 UV-visible spectroscopy

UV-visible spectroscopy is used as a tool to investigate the formation of AgNPs. The UV-visible spectral measurements of reaction mixture at regular intervals during incubation period showed a gradual increase in absorbance with shifting of peak position. The absorbance reached a maximum and almost stabilized after 12 hours of incubation indicating the complete reduction of silver ions to AgNPs. A broad and strong peak in UV spectrum at 420 nm clearly confirmed the formation of AgNPs (Figure 3.20b). This peak may be attributed to the surface plasmon resonance of the AgNPs. [33] Saha *et al.*, reported absorption band for the synthesized silver particles at 420 nm due to the pressure of the colloidal silver. [40]

(a)   **(b)**
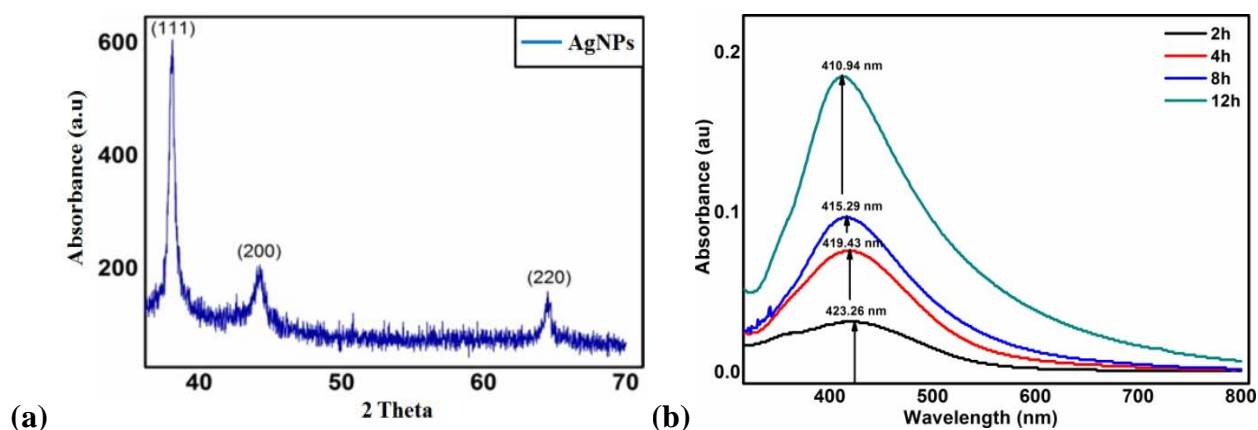
Figure 3.20 Tea leaves extract supported AgNPs X-ray diffraction pattern and UV Vis spectrum taken at a different time intervals (4, 8 and 12h)

A broadening of peak in the range from 380-440 nm is also observed indicating that the nano particles are polydispersed [41] and it was further established by SEM analysis. UV-visible study also verifies the completion of AgNPs formation in nearly 12 hours. Maximum concentration of the silver nanoparticles was obtained after 12 h. The spectra show peaks at 420 nm (4h), 418nm (8h), and 412nm (12h). With the increasing reaction time UV-vis spectra show sharp narrow peak shift at lower wavelength of 420 nm. The SPR band also shows blue shift because the peaks are shifted from 420 nm to 412 nm after 12 h, suggesting that the particle shape strongly influences the SPR band.

The phytochemical and spectral studies reported in previous literatures have established the presence of alkaloids, glucosides, carbohydrates, flavonoids, proteins, steroids, gums and mucilages in the plant extracts. These are responsible for the reduction from Ag^+ to AgNPs. In the present research work, FTIR study of biosynthesized AgNPs is carried out to establish the identity of biomolecules attached to AgNPs surface and their possible involvement in reduction from Ag^+ to Ag^0. FTIR spectrum of biosynthesized AgNPs showed prominent peaks at 3388, 2886, 2066, 1646. 1394, 1239, 1064, 986, 758, 679 and 628 cm^{-1} (Figure 3.21d). The major and broad peak around 3388 cm^{-1} represent the -OH stretching vibrations corresponding to glycosides. The peaks at 2886 and 2820 cm^{-1} are probably due to -C-H stretching and asymmetric bending vibrations of -CH_3 group respectively. The existence of amide group (-NH-CO-) of protein and the aromatic ring structures is revealed by the peaks around 1646 and 1500 cm^{-1}, which represents amide I and amide II of proteins and arises due to carbonyl stretch and –N-H stretch vibrations in the amide linkages shown in Figure 3.21d. Carbonyl group of amino acid residues and peptides of proteins

has the stronger ability to bind metal, so proteins could be the most possible organic moiety for stabilizing the AgNPs in the medium. [42] The -C=O stretching vibration of -COOH group is exposed by peak around 1763 cm^{-1}. The signals located at 1394 and 1064 cm^{-1} indicate the in plane bending vibrations of -OH and C-O-C groups correspondingly. The aliphatic -C-H bending vibration has appeared as a signal at 758 cm^{-1}. The FTIR spectral analysis clearly suggests the presence of biomolecules with functional groups such as -OH, -C=O, -NH-CO-, -COOH, C-O-C, etc, as attachments to AgNPs surface and these biomolecules are possibly involved in reduction of Ag$^+$ to Ag^0 and shape deciding factor.

3.2 (III) 3.3 Electron Microscopy

The surface morphology of as synthesized AgNPs is studied using SEM and TEM techniques. Figure 3.21a shows SEM image of AgNPs. The SEM image reveals that the size of synthesized AgNPs is in the range of 5-10 nm. The nanoparticles tend to agglomerate to form still bigger structures. TEM study indicates that most of the nanoparticles are spherical and oval shape as visible in Figure 3.21b is due to the fact that when a particle is formed, in its initial state, it tries to acquire a shape that corresponds to minimum potential energy. The spherical and oval shapes correspond to the state of minimum potential energy. Other factors that a vital play role in determining the shape of silver nanoparticles i.e. concentration of AgNPs and rate of reaction leads to symmetrical particles and low concentration of silver nitrate solution and slower rate of reaction [43] and higher concentration of silver nitrate [44] leads to anisotropic silver nanoparticles. The size distribution histogram of AgNPs shown in Figure 3.21c suggest that most particles have a size distribution around 7-8 nm.
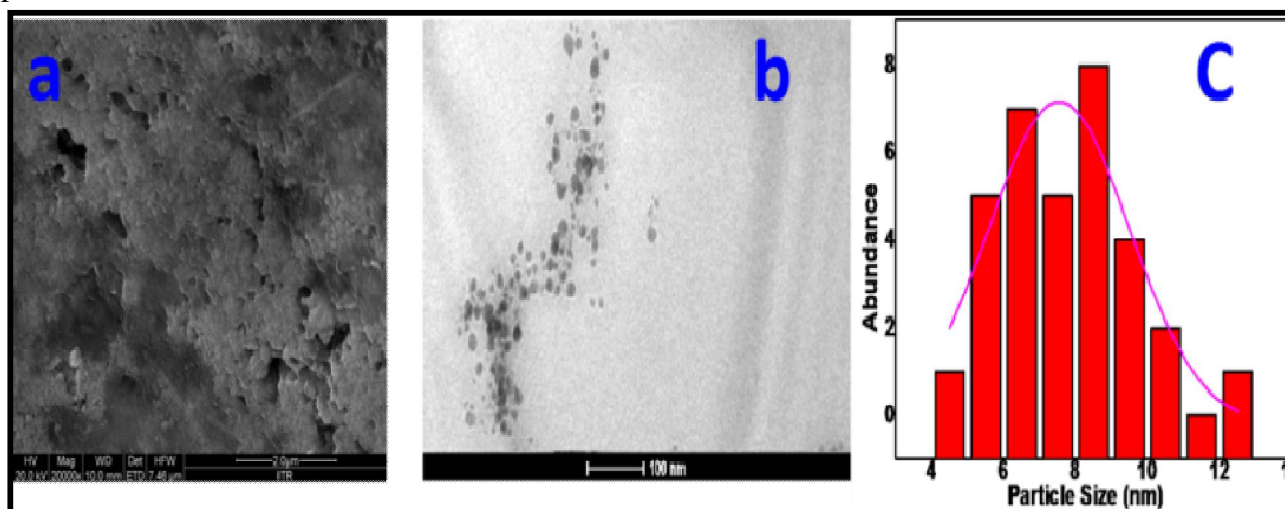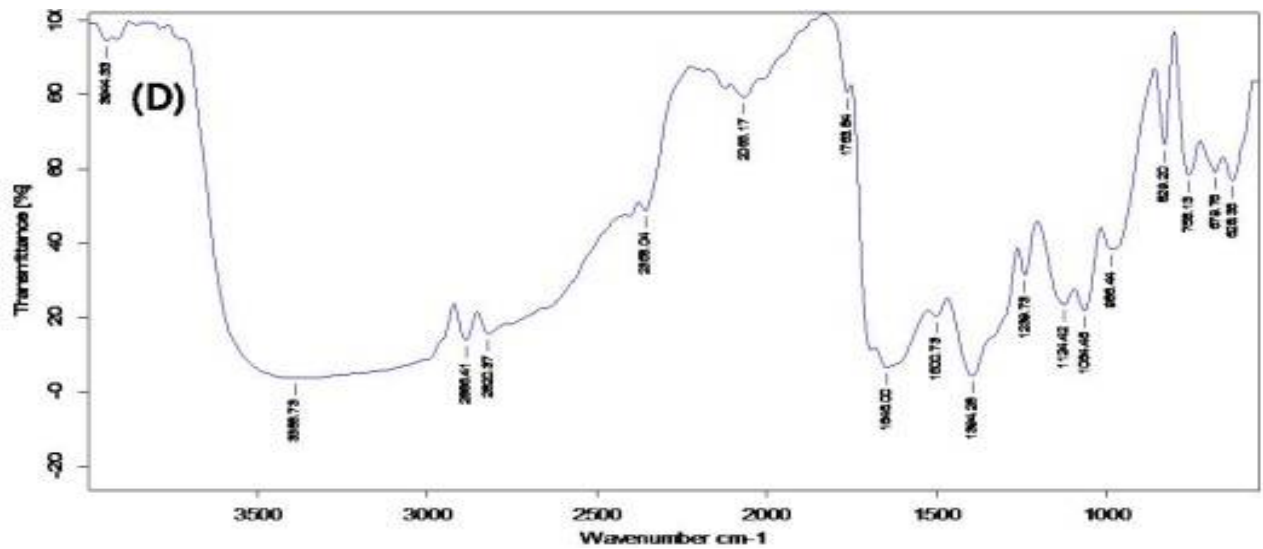
Figure 3.21 Tea supported-AgNPs representing their **(A)** SEM, **(B)** TEM image of respectively **(C)** size distribution histogram obtained from TEM studies and **(D)** FTIR spectrum of AgNPs synthesized from Tea Leaves.

3.2 (III) 3.4 Surface Morphology analysis of AgNPs
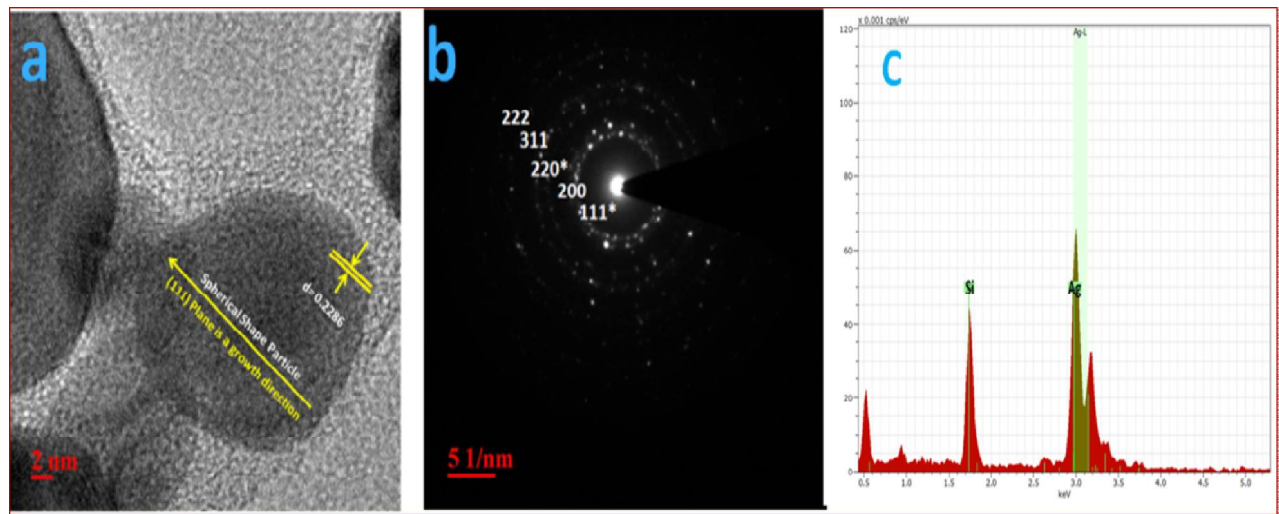
Figure 3.22 (a) HRTEM image of a 12 nm spherical like structure that featuring d-spacing for the 111 plane and **(b)** cross-grating patterns (SAED pattern) consistent with the cubic structure **(c)** EDX spectrum of biogenic Ag NPs.

Figure 3.22a represents the HRTEM images and corresponding SAED pattern of the as synthesized AgNPs. Figure 3.22a. exhibits a high resolution TEM image featuring lattice fringes associated with a d-spacing of 0.2286 nm, consistent with the growth planes (111). The SAED pattern in Figure 3.22b exhibits polycrystalline diffraction rings consistent of (111), (200), (220),

(311) and (222) cubic reflections. The EDS spectra recorded from the silver nanoparticles are shown inset Figure 3.22c, which revealed the information about the particle size and elemental composition of the synthesized Ag NPs. The EDS profile shows a strong silver signal along with weak oxygen and carbon peaks, which may have originated due to the carbon being present in the sample holder. Thus, stable AgNPs in solution up to 4 weeks after synthesis [45,46]. This is another advantage of nanoparticles synthesized using plant extracts over those synthesized using chemical methods.

3.2 (III) 4 CONCLUSION

In this chapter, we report a green approach for the synthesis of Ag nanoparticles using the fresh tea leaves extract. This is a simple, green, cheap and efficient method to synthesize silver nanoparticles at room temperature without using any harmful reducing agents such as sodium borohydrite, EDTA, hydrazine and any capping or dispersing agent. It was found that the green synthesized silver nanoparticles were composed of spherical particles which have high crystallinity. The particles sizes were controlled in the range from 5 to 10 nm.

3.2 (III) 5 REFERENCES

[1] AM Fayaz, "Biogenic Synthesis of Silver Nanoparticles and Their Synergistic Effect with Antibiotics: A Study against Gram-Positive and Gram-Negative Bacteria" ***Nanomedicine: Nanotechnology, Biology and Medicine*** (**2010**), 6: 103-109.

[2] M Vijayakumar, "Biosynthesis, Characterisation and Anti-Bacterial Effect of Plant-Mediated Silver Nanoparticles Using *Artemisia nilagirica*" ***Industrial Crops and Products*** (**2013**), 41: 235-240.

[3] E Alzahrani, K Welham, "Optimization Preparation of the Biosynthesis of Silver Nanoparticles Using Watermelon and Study of Its Antibacterial Activity" ***International Journal of Basic and Applied Sciences*** (**2014**), 3: 392-400.

[4] JY Song, BS Kim, "Rapid Biological Synthesis of Silver Nanoparticles Using Plant Leaf Extracts" ***Bioprocess and Biosystems Engineering*** (**2009**), 32: 79-84.

[5] M Rai, A Yadav, A Gade, "Silver Nanoparticles as a New Generation of Antimicrobials" ***Biotechnology Advances*** (**2009**), 27: 76-83.

[6] A Kumar, "Silver-Nanoparticle-Embedded Antimicrobial Paints Based on Vegetable Oil" ***Nature Materials*** (**2008**), 7: 236-241.

[7] F Furno, "Silver Nanoparticles and Polymeric Medical Devices: A New Approach to Prevention of Infection" ***Journal of Antimicrobial Chemotherapy*** (**2004**), 54: 1019-1024.

[8] LM Liz-Marzán, I Lado-Tourino, "Reduction and Stabilization of Silver Nanoparticles in Ethanol byNonionic Surfactants" ***Langmuir*** (**1996**), 12: 3585-3589.

[9] Y Sun, P Atorngitjawat, MJ Meziani, "Preparation of Silver Nanoparticles via Rapid Expansion of Water in Carbon Dioxide Microemulsion into Reductant Solution" *Langmuir* **(1996),** 17: 5707-5710.

[10] A. Henglein, "Physicochemical Properties of Small Metal Particles in Solution: "Microelectrode" Reactions, Chemisorption, Composite Metal Particles, and the Atom-to-Metal Transition" *The Journal of Physical Chemistry* **(1993),** 97: 5457-5471.

[11] K Esumi, "Preparation and Characterization of Bimetallic Palladium-Copper Colloids by Thermal Decomposition of Their Acetate Compounds in Organic Solvents" *Chemistry of Materials* **(1990),** 2: 564-567.

[12] S Ponarulselvam, C Panneerselvam, K Murugan, N Aarthi, K Kalimuthu, S Thangamani, "Synthesis of Silver Nanoparticles Using Leaves of *Catharanthusroseus* Linn. G. Don and Their Antiplasmodial Activities" *Asian Pacific Journal of Tropical Biomedicine* **(2012),** 2: 574-580.

[13] I Willner, R Baron, B Willner, "Growing Metal Nanoparticles by Enzymes" *Advanced Materials,* **(2006),** 18: 1109-1120.

[14] Y Konishi, K Ohno, N Saitoh, T Nomura, S Nagamine, H Hishida, *"*Bioreductive Deposition of Platinum Nanoparticles on the Bacterium *Shewanella algae" Journal of Biotechnology* **(2007),** 128: 648-653.

[15] XR Zhang, XX He, KM Wang, XH Yang, "Different Active Biomolecules Involved in Biosynthesis of Gold Nanoparticles by Three Fungus Species" *Journal of Biomedical Nanotechnology* **(2011),** 7: 245-254.

[16] D Jain, HK Daima, S Kachhwala, SL Kothari, "Synthesis of Plant-Mediated Silver Nanoparticles Using Papaya Fruit Extract and Evaluation of Their Anti Microbial Activities" *Digest Journal of Nanomaterials and Biostructures* **(2009),** 4: 557-563.

[17] A Saxena, R Tripathi, R Singh, "Biological Synthesis of Silver Nanoparticles by Using Onion (*Allium cepa*) Extract and Their Antibacterial Activity" *Digest Journal of Nanomaterials and Biostructures* **(2010),** 5: 427-432.

[18] ARJ Azar, S Mohebbi, "One-Pot Greener Synthesis of Silver Nanoparticles Using Tangerine Peel Extract: Large-Scale Production" *Micro & Nano Letters* **(2013),** 8: 813-815.

[19] MC Moulton, LK Braydich-Stolle, MN Nadagouda, S Kunzelman, SM Hussain, RS Varma, "Synthesis, Characterization and Biocompatibility of "Green" Synthesized Silver Nanoparticles Using Tea Polyphenols" *Nanoscale* **(2010),** 2: 763-770.

[20] M Dubey, S Bhadauria, B Kushwah, "Green Synthesis of Nanosilver Particles from Extract of *Eucalyptus hybrid* (Safeda) Leaf" *Digest Journal of Nanomaterials and Biostructures* **(2009),** 4: 537-543.

[21] V Parashar, R Parashar, B Sharma, Pandey, AC *Parthenium* "Leaf Extract Mediated Synthesis of Silver Nanoparticles: A Novel Approach towards Weed Utilization" *Digest Journal of Nanomaterials and Biostructures* **(2009),** 4: 45-50.

[22] SS Shankar, A Rai, A Ahmad, M. Sastry, "Rapid Synthesis of Au, Ag, and Bimetallic Au Core-Ag Shell Nanoparticles Using Neem (*Azadirachtaindica*) Leaf Broth" ***Journal of Colloid and Interface Science* (2004),** 275: 496-502.

[23] SS Shankar, A Rai, A Ahmad, M Sastry, "Rapid synthesis of Au, Ag, and bimetallic Au core-Ag shell nanoparticles using Neem (Azadirachta indica) leaf broth" ***J. Colloid Interf. Sci.* (2004),** 275: 496-502.

[24] J Huang, Q Li, D Sun, Y Lu, X Yang, H Wang, Y Wang, W Shao, N He, J Hong, "Biosynthesis of Silver and Gold Nanoparticles by Novel Sundried Cinnamomum camphora Leaf" ***C. Chen, Nanotechnology* (2007),** 8: 105104.

[25] B Ankamwar, C Damle, A Ahmad, M Sastry, "Biosynthesis of gold and silver nanoparticles using Emblica officinalis fruit extract, their phase transfer and transmetallation in an organic solution" ***J. Nanosci. Nanotechnol.* (2005),** 5: 1665-1671

[26] SP Chandran, M Chaudhary, R Pasricha, A Ahmad, M Sastry, "Synthesis of gold nanotriangles and silver nanoparticles using Aloe vera plant extract" ***Biotechnol. Prog*. (2006),** 22: 577-583.

[27] EM Egorova, AA Revina, "Synthesis of metallic nanoparticles in reverse micelles in the presence of quercetin" ***Physicochem. Eng. Asp.* (2000),** 16887-96.

[28] K Govindaraju, S Tamilselvan, V Kiruthiga, G Singaravelu, "Biogenic silver nanoparticles by Solanum torvum and their promising antimicrobial activity" ***J. Biopestic.*** 3 (1): 394-399.

[29] RP Singh, S Magesh, C Rakkiyappan, "Formation of fenugreek (Trigonella foenum-graecum) extract mediated Ag nanoparticles: mechanism and applications" ***Int. J. Bioeng. Sci. Technol.* (2011),** 02 (03): 75-80.

[30] M Sundarajan, S Gowri, "Green synthesis of titanium dioxide nanoparticles by Nyctanthes arbour-tristis leaves extract" ***Chalcogenide Lett.* (2011),** 8 (8): 447-451.

[31] S Maensiri, P Laokul, J Klinkaewnarong, S Phokha, V Promarak, S Seraphin, "Indium oxide (In$_2$O$_3$) nanoparticles using Aloe vera plant extract: Synthesis and optical properties" **J. Optoelectron.** *Adv. Mater.* **(2008),** 10 (3): 161-165.

[32] HM Gong, L Zhou, XR Su, S Xiao, SD. Liu, QQ Wang, "Illuminating dark plasmons of silver nanoantenna rings to enhance exciton-plasmon interactions" ***Adv. Funct.Mater.* (2009),** 19: 298-303.

[33] M A Noginov, G Zhu, M Bahoura, J Adegoke, C Small, BA Ritzo, VP Drachev, VM Shalaev, "The effect of gain and absorption on surface plasmons in metal nanoparticles" ***Appl. Phys. B.*(2007),** 86: 455-60.

[34] Harbowy, E Matthew, A. Balentine Douglas "Tea Chemistry" ***Critical Reviews in Plant Sciences*** (**1997),** 16 (5): 415-480

[35] Ercisli, Sezai, Emine Orhan, Ozlem Ozdemir, Memnune Sengul, Neva Gungor. "Seasonal Variation of Total Phenolic, Antioxidant Activity, Plant Nutritional Elements, and Fatty Acids in Tea Leaves Grown in Turkey" ***Pharmaceutical Biology* (2008),** 46: 683-687.

[36] AS Lanje, SJ Sharma, RB Pode, "Synthesis of Silver Nanoparticles: A Safer Alternative to Conventional Antimicrobial and Antibacterial Agents" *Journal of Chemical and Pharmaceutical Research* **(2010),** 2: 478-483.

[37] R Das, SS Nath, D Chakdar, G Gope, R Bhattacharjee, "Preparation of Silver Nanoparticles and Their Characterization" *Journal of Nanotechnology Online* **(2009),** 51-6.

[38] YG Sun, YN Xia, "Shape-Controlled Synthesis of Gold and Silver Nanoparticles" *Science* **(2002),** 298: 2176-2179.

[39] R Georgekutty, MK Seery, SC Pillai, "A highly efficient Ag-ZnO photocatalyst: synthesis, properties, and mechanism" *The Journal of Physical Chemistry C* **(2008),** 112 (35): 13563-13570.

[40] S Saha, MM Malik, MS Qureshi, "Characterisation and synthesis of silver nano particle using leaf extract of epipremnumaureum" *International Journal of Nanomaterials and Biostructures* **(2012),** 2: 1-4.

[41] R Geethalakshmi, D V L Sarada, "Synthesis of plant-mediated silver nanoparticles using Trianthemadecandra extract and evaluation of their anti microbial activities" *International Journal of Engineering Science and Technology* **(2010),** 2: 970-75.

[42] K. Das Sujoy, Dickinson Calum, Lfir Fathima, F. Brougham Dermot, Marsili Enrico, "Synthesis, characterization and catalytic activity of gold nanoparticles biosynthesized with Rhizopus oryzae protein extract" *Green Chem*.**(2012),** 14: 1322-1334.
[43] SP Chandran, M Chaudhary, R Pasricha, "snthesis of gold nanotriangles and silver nanoparticles using aloe vera plant extract" *Biotechnology progress* **(2006),** vol. 22, No 2 577-583.

[44] I Pastoriza-Santos, LM Liz-Marzan, "Formation and characterization of silver nanoparticles in DMF with shape control" **(2005).**

[45] SS Shankar, A Rai, A Ahmad, M Sastry, "Rapid synthesis of Au, Ag, and bimetallic Au core Ag shell nanoparticles using Neem (Azadirachta indica) leaf broth" *J Colloid Interface Sci* **(2004),** 275: 496-502.

[46] JY Song, BS Kim "Rapid biological synthesis of silver nanoparticles using plant leaf extract" *Bioprocess Biosyst Eng* **(2009),** 3279-84.

Chapter 3.2

Synthesis and Characterization of biogenic Ag NPs prepared by using:

(IV) Shikakai (Acacia Concinna) pods extract

ABSTRACT

Green Synthesis method was employed to synthesis the silver nanoparticles (AgNPs) by aging the mixture of the aqueous extract of the Acacia concinna (Shikakai fruit) and $AgNO_3$ solution at different time interval. Synthesized spherical shaped silver nanoparticles were characterized for their structural, optical and morphological properties. The Fourier transformer infrared (FTIR) spectroscopy reveals the presence of polyphenolic compounds in Acacia Concinna pods extract, which can acts as a reducing agent for the conversion of silver nitrate to silver nanoparticles. The x-ray diffraction (XRD) pattern examine the absence of the impurities that ascertains the higher order purity of the biosynthesized silver nanoparticles. The experimental UV results absorption peak at 419 nm corresponds to surface plasmon resonance property of the silver nanoparticles. The green synthesized silver nanoparticles with average size ranging below 60 nm imaged using (HRTEM) High Resolution Transmission Electron Microscopy. As synthesized AgNPs could be applicable in different types of field such as biomedical, spintronics, optical, home products, etc.

Key Words: Silver Nitrate, Acacia Concinna pods, Nanotechnology, Silver Nanoparticles.

3.2 (IV) 1 INTRODUCTION

The unique features of nanoparticles may lead to play an important role in biomedicine, energy, optics and other health care applications. [1] Among the various nanoparticles, AgNPs are widely investigated ought to be their broad range of applications as antibacterial agent, catalyst and biosensor. Several researches have made attempts for synthesis of AgNPs using chemical reduction, [2] electrochemical reduction and photochemical reduction. [3] To overcome the difficulties of the convential methods of AgNPs synthesis requires more chemicals, large quantities of energy and results in formation of hazardous by products. [4] Some prominent chemical and physical methods have been employed to prepare silver nanoparticles of different sizes and shapes, are: UV irradiation, [5,6] microware irradiation, [7,8] chemical reduction, [9-11] photochemical method, [12,13] electron irradiation, [14,15] and sonoelectrochemical method. [16] However, most of the reported methods involve more than one step, high energy requirement, low material conversions, difficulty in purification, and hazardous nature of the chemicals. The chemical synthesis of nanoparticles may lead to the presence of some toxic chemical species adsorbed on the surface that may have adverse effects to its application. The synthesis of nanoparticles by green method can potentially eliminate this problem. Therefore, there is an urgent need to develop a green process of nanoparticle synthesis.

Green synthesis methods employing either biological microorganism such as bacteria, either intracellularly and extracellularly, fungus and algae or plant extracts have emerged as a simple and alternative to chemical synthesis. The interest in this field has shifted towards green approach. Recently, plant extract assisted syntheses of nanoparticle have attracted interest in the area of nanoscience and technology due to its eco-friendly nature. These approaches focused on the utilization of the environment friendly, cost effective and biocompatible reducing agents for the synthesis of the AgNP's so the green synthesis of the AgNP's has attracted much attention in recent years than the conventional methods of synthesis. [17] The use of plant and their extacts for the synthesis of AgNP's can be advantageous over other biological synthesis process. Nanoparticles produced by the plant extracts are more stable and rate of synthesis is faster than in the case of microorganisms. Some of the plant materials such as leaves, stem, seeds, fruits, latex and barks are involved in metal reduction process so the use of plant extract reduces the cost as well as we do not require any special culture preparation and isolation techniques. [18] The another advantages of using plants and their extracts for the synthesis of metal nanoparticle is that they are easily available, safe to handle and possess a broad variability of metabolites that may aid

in reduction. [19] Considering the advantages of green synthesis over other methods, in the present study, we have synthesized AgNP's by using Acacia Concinna pod's aqueous extract for reduction of Ag^+ ions to Ag^0 from silver nitrate solution. It focuses on the study of the effects of various physicoechemical parameters on AgNPs. We also attempt to investigate about the antimicrobial effect of the synthesized nanoparticles. Acacia concinna, which is a common plant known as shikakai is found abundantly in India and in nearby Indian subcontinents. It belongs to Meliaceae family and is known for its various applications especially its medicinal property. It has been used traditionally for hair care in Indian sub contient. It is one of the ayurvedic medicinal plants. [20] Furthermore, several of organic compounds present in Acacia Concinna extract are namely phenols, saponin, quunine, tannins and flavonoids, which act a reducing agent as well as capping agent and helping in stabilizing the nanoparticles. Acacia Concinna fruit extract is used in the synthesis of various nanoparticles like gold, zinc oxide, silver etc. When silver salt is treated with shikakai pods extract, the silver salt is reduced to AgNPs. The synthesized nanoparticles, which are capped with shikakai extract also, exhibit the enhanced antibacterial activity. The Figure 3.23a shows the Acacia Concinna shrub and Figure 3.23b shows Acacia Concinna pods.

Figure 3.23 [a] Acacia concinna shrub **[b]** Acacia concinna pods

3.2 (IV) 2 EXPERIMENTAL METHODS

3.2 (IV) 2.1 Aqueous extract of Acacia Concinna pods

Sigma-Aldrich grade $AgNO_3$ (99%), was used as purchased without any further purification. All solutions were prepared using deionised water (DIW). All the glassware were washed with cromic acid and distilled water and dried in oven. The petridishes and glasswares were autoclaved before use. Established procedure for the extraction of Acacia Concinna pods was adopted to prepare the aqueous extract [21] and dry pods were washed thoroughly with distilled water to make them free form dust particles surface contamination. Afterwards, sample dried for 24 h in moisture free

atmosphere and 2 gm of this sample was dried and soaked in 50 mL of pure DIW for 24 h. The extract was filtered using Whatmann filter paper No. 42.

3.2 (IV) 2.2 Synthesis of silver nanoparticle

Silver nanoparticles were synthesized using the procedure describe somewhere else. [22] 2.5 mL of the aqueous Acacia Concinna fruit extract was added drop wise into the 25.0 mL of aqueous 0.001 M $AgNO_3$ kept in a boiling tube at room temperature. Subsequently, the mixture was shifted in a desiccator at room temperature for aging (8 h, 16 h and 24 h etc) that leads to a biogenic chemical reduction of Ag^+ ions into Ag NPs. Transparent solution of $AgNO_3$ turns reddish brown with time, which indicates the presence of Ag nanoparticles. Aging added sharpness to the colour shfted toward low wavelength. The effects of physicoehemical parameter were examined by varying the reaction time. Silver nanoparticles in aqueous phase are extremely stable without any precipitation and their stability for long period may be due to antimicrobial properties of this plant. Highly dispersed colloidal Ag NPs were found soluble in water and stable at ambient condition for more than 6 months. After certain aging time, the suspension was centrifuged at 20,000 rpm for 20 min, which resulted in suspended solid. It was washed by distilled water then to be used for further analysis (XRD, HRTEM, UV-vis, FTIR, and PL study) and catalytic activity analysis of Ag NPs.

3.2 (IV) 3 RESULTS AND DISCUSSION

3.2 (IV) 3.1 UV-Vis absorbtion spectrum

Effect of reaction time on the formation of AgNPs was noted by the naked eyes. The change in the colour of solution indicates the formation of Ag nanoparticles. This is the strong indication of the formation of silver nanoparticles the change due to the strong absorption of visible light due to the excitation of the surface plasmonic effect of the AgNPs. [23-26] The inset image of the Figure 3.24, the vials with of differently aged samples (8h, 16h and 24h) are a signal of the growth of silver nanoparticles. The nanoparticle formed after 8h is the beginning of the reaction.The reduction of silver salt to silver ions is happened due to the presence of reducing agents like terpenoids and flavanones etc. AgNPs show yellowish brown colour in aqueous solution due to the excitation of surface plasmon vibrations. It is noticed that the complete colour change appeared after about 24h and thereafter no further change in colour of the reaction mixture occured. This indicates that silver salt present in the reaction mixture has been reduced completely. Then the formation of the silver nanoparticles was examined, and confirmed by the

respective absorption spectra. The absorption spectrum originated due to the strong surface plasmon resonance (SPR). The observed absorption band is size dependent, since SPR band depends on the refractive index of the solution. Figure 3.24 shows the UV-Vis absorption spectra of AgNPs obtained in the range of 250-700 nm at different reaction time.
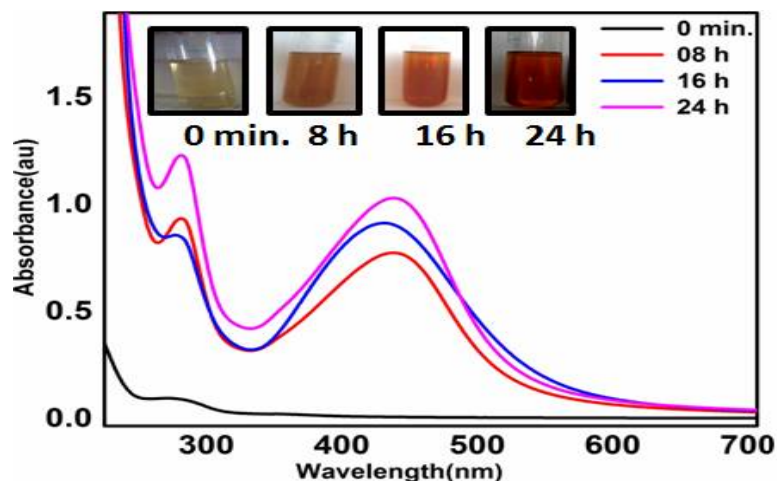

Figure 3.24 UV-visible-NIR spectra of the Ag NPs synthesized from predicted optimum conditions upon dilution of 3.5 times. Inset shows the coloration due to formation of AgNPs with aging.

Silver nanoparticles had free hot electrons, which give surface Plasmon resonance (SPR) absorption band, due to the combination of vibration of electrons of silver nanoparticles with the light wave. In Figure 3.24, we showed the 8 h aged samples with the pronounced SPR peak at 436 nm. That confrms that the prepared AgNPs are smaller in size and uniform in size distribution. It is also observed that there is anincrease in height of the peak with aging that represents the enhancement in the concentration of AgNPs with time. All the spectra displayed in Figure 3.24, showed the polyphenolic peak around 278 nm. We also display the UV- Vis is spectra of the AgNO$_3$ and solution; it has a peak around 217 nm, as expected for Ag$^+$ ions. Changes in colour was observed initially after 3 min of adding the salt solution to the acacia concinna fruit extract. After 24 h, the colour of the solution becomes nearly constant, indicating that no silver salt was left for further reaction. The results are complete correlated with the passage of time, the intensity of the SPR band increased without any shift in peak wavelength. According to the absorption spectra of the spherical AgNPs, as the anisotropy increases the number of peaks increases. In the present study, SPR band suggested that the synthesized nanoparticles are hexagonal top shaped, which is further confirmed by TEM study.

3.2 (IV) 3.2 XRD Analyses

Figure 3.25 showed the XRD profile for Ag nanoparticles synthesized by the pure Acacia Concinna fruit extract. Three main characteristic diffraction peaks of Ag NPs, were observed at 2θ = 38.4°, 44.5° and 64.8°, which corresponds to the major peak (111) along with the very weaks reflections along (200) and (220) crystallographic planes of face-centered cubic (fcc) Ag crystals, (JCPDS 00-004-0783), respectively with the lattice parameter of a = 4.077 Å. No other peaks from different phase were observed showing that the presence of the single phase Ag nanoparticles without forgien element/compound. Because no biomass residue or other crystallographic impurities are observed in the XRD profile. These observations reflected the single phase Ag nanoparticles formation without any adultration. In general, Scherrer equation was used to determine the average crystalline size. [27] The (111) plane was chosen to calculate crystalline particle size, which is measured to be 34.2 nm. [28] This result was also matches well with the TEM study.
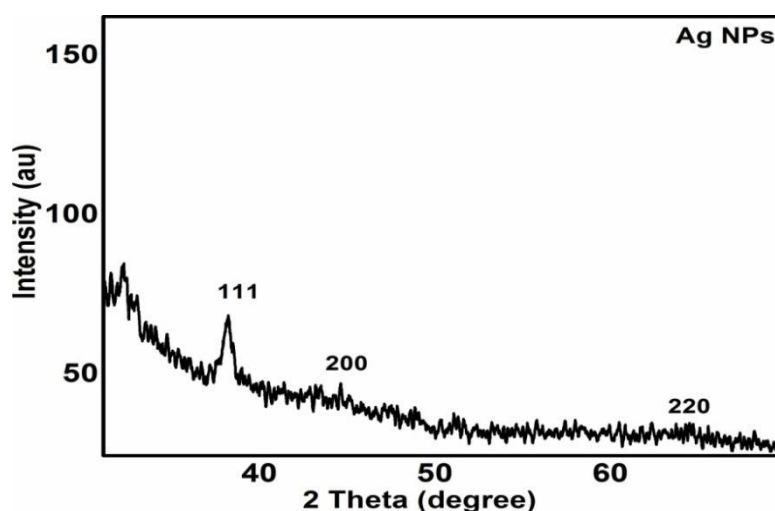
Figure 3.25 XRD patterns for Ag nanoparticles developed in Acacia Concinna pod's extract.

3.2 (IV) 3.3 Transmission electron microscopy (TEM)

Transmission electron microscopy (TEM) has been employed to characterize the size, shape and morphology of the synthesized silver nanoparticles. The TEM and HRTEM images of the silver nanoparticles are shown in Figure 3.26A and 3.26B, respectively. From the image, it is evident that the hexagonal top likes morphology for the silver nanoparticles. The average particles size measured from the TEM image is 40.06 nm, which is in good agreement with the particle size calculated from XRD analysis. TEM corresponding to the SAED pattern is showing the hint of hexagonal structuring of the AgNPs Figure 3.26 C.
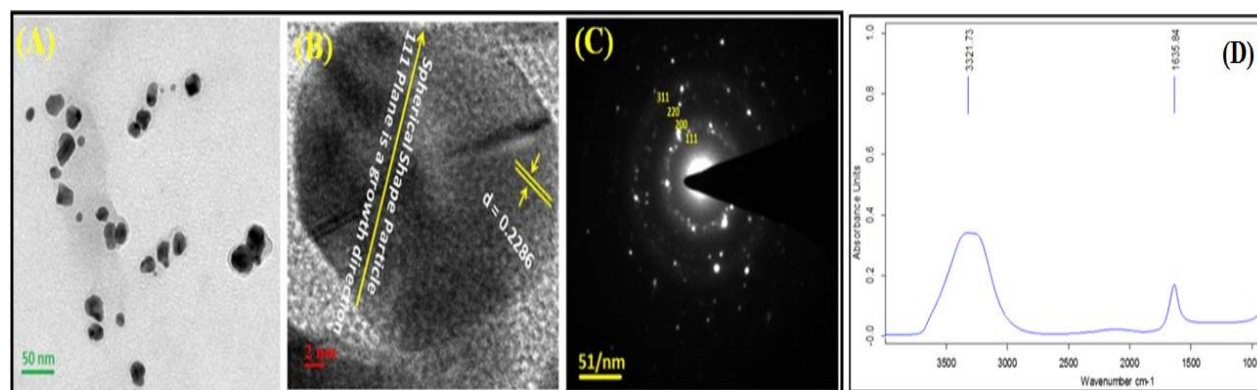
Figure 3.26 (A) TEM and **(B)** HRTEM image of the biogenic Acacia Concinna supported Ag NPs, featuring with the d-spacing along the 111 plan and **(C)** SAED pattern consistent with the hexagonal top shaped structure. **(D)** ATR spectra of 2 % Acacia concinna supported Ag NPs of 24 h.

3.2 (IV) 3.4 ATR measurement

ATR analyses were carried out to identify the possible biomolecules responsible for capping and reducing agent for the Ag nanoparticles synthesized by Acacia Concinna fruit extract. Two obvious infrared bands are observed at 3321cm^{-1} and 1635 cm^{-1}(Figure 3.26 D) that represents the presence of the intermolecular hydrogen bonding (N-H and O-H stretching mode in linkage of the protein) and the C=O /C=C stretching mode in amine aqueous group, in pure Acacia Concinna pods. [29,30] Which indicated the presence of the proteins as capping agent for the silver nanoparticles, which increases the stability of the nanoparticles. [31] The secondary structures of the proteins were not affected during the reduction of Ag$^+$ ions or after binding with Ag nanoparticles. [32] These spectroscopic studies confirmed the presence of the amino acid that develops the strong binding, reducing and stabilizing ability with the metal through carbonyl group.

These IR spectroscopic studies confirmed the presence of the amino acid that develop the strong binding, reducing and stabilizing ability with metal through carbonyl group. Thus, it is concluded

that a layer of the bio-organics was formed around AgNPs to secure the nanoparticles. This layer acts as a capping agent to prevent agglomeration and provides the extra stability in aqueous medium. [33] IR study prove the presence of two kinds of chemicals in Acacia Concinna extract: one, the reducing agents (polyphenols, Acaciac acid (trihydroxymonocarboxylic acid)) that convert Ag^+ ions into Ag nanoparticles and second, the capping agents/surfactant (tannins, flavonoids, oil and fats, qunine, saponin, etc), which can act as an scaffold for controlling size and shape of these nanoparticles.

3.2 (iv) 3.5 PL spectrum

Figures 3.27A and 3.27B, represents PL spectrum of the sample recorded at an excitation wavelength $\lambda_{ex}=283$ nm. Its shows the emission peaks at $\lambda_{em}=564$ nm (green region) at ecitation wavelength $\lambda_{ex}=283$ nm. The broad peak in green region is generated by radial recombination of the photoexcited holes with the electrons in oxygen vacancies. Excitation of the electrons from the occupied d-bands into the states above the Fermi level and successive relaxation of the electrons from an occupied sp-band to the holes takes place by the electron-phonon scattering process directed an energy loss, which is responsible for the visible light luminescence of the Ag nanoparticles. [34] For Ag NPs broad peak in green emission region indicates that Ag NPs have good crystal structure with very few oxygen vacancies. The optical properties of the silver nanoparticles depend on both; interband and intraband transitions between electronic states. FESEM and TEM results indicate that the smaller non-metallic clusters coexist with large metallic nanoparticles. Here, only small metallic particles (cubic crystals) responsible for the photoluminescence because it is hard for large metal particle to compete with effective radioactive process with rapid radiation loss process. Therefore, they didn't exhibit photoluminescence. [35]
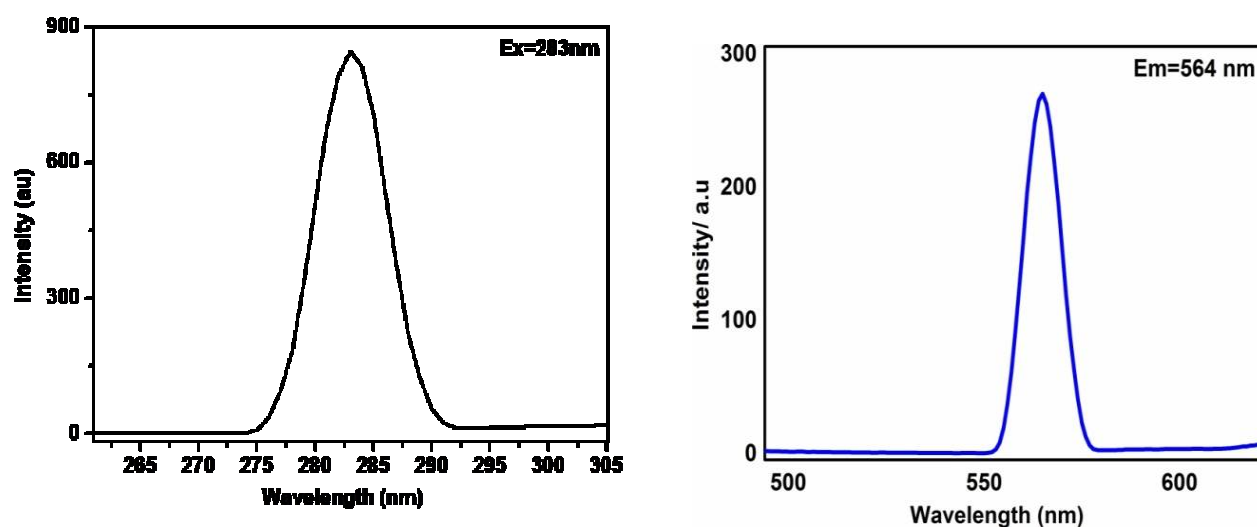
Figure 3.27 Photoluminescence (PL) emission at λ_{em}=564 nm spectra (green) of the as prepared Ag NPs under the excitation radiation of λex = 283 nm.

3.2 (IV) 4 CONCLUSION

AgNPs have been successfully synthesized using a well-known Acacia Concinna pods extract by simple biogenic reducing method. As synthesized AgNPs are crystalline in nature, polydispersed and show SPR band at 436 nm wavelength and a strong PL at around 564 nm. This is a simple, green and efficient method to synthesize silver nanoparticles at room temperature without using any chemical reducing or capping or dispersing agent. It was concluded that the green synthesized silver nanoparticles were composed of spherical nanoparticles, which were highly crystalline. The particles sizes were controlled in the range from 20 to 40 nm.

During the biosynthesis of the Ag nanoparticles, phythogen altogether leads to the nucleation of the Ag nanoparticles in hexagonal top shaped. XRD studies confirmed the purity of these nanosized NPs that crystallized in spherical shaped crystals. Crystal growth orientation of the Ag NPs was found along the 111 plane. Prominent, intense and broad excitonic UV-vis. spectrum peak, of the AgNPs at 390-440 nm, attributed to its surface plasmonic phenomena. IR spectroscopic studies confirmed that carbonyl group of amino acid residues have strong binding ability with metal suggesting the formation of the layer covering metal nanoparticles and acting a capping agent to prevent agglomeration and to provid stability to the medium. Excitation of the electrons from occupied d bands into states above the Fermi level is responsible to the green light luminescence.

3.2 (IV) 5 REFERENCES

[1] A Fayaz, M Balaji, M Girilal, R Yadav, P Thangavelu, KR Venketesan, "Biogenic synthesis of silver nanoparticles and their synergistic effect with antibiotics: a study against gram-positive and gram-negative bacteria" ***Nanomed Nanotechnol. Biol. Med*** **(2010),** 6: 103-109.

[2] K Balantrapu, D Goia, "Silver nanoparticles for printable electronics and biological applications" ***J Mater Res***. **(2009),** 24 (9): 2828-2836.

[3] RK Bera, AK Das, CR Raj, "Enzyme-Cofactor-Assisted Photochemical Synthesis of Ag Nanostructures and Shape Dependent Optical. Sensing of Hg (II) Ions" ***Chem. Mater*** **(2010),** 4505-4511.

[4] AM Awwad, NM Salem, "Green synthesis of silver nano- particles by mulberry leaves extract" ***Nanosci Nanotechno*** **(2011),** 2125-128.

[5] AT Le, LT Tam, PD Tam, "Synthesis of oleic acid-stabilized silver nanoparticles and analysis of their antibacterial activity" ***Materials Science and Engineering: C***. **(2010),** 30 (6): 910-916.
[6] H Huang, Y Yang, "Preparation of silver nanoparticles in inorganic clay suspensions" ***Composites Science and Technology*** **(2008),** 68 (14): 2948-2953.

[7] H Yin, T Yamamoto, Y Wada, S Yanagida, "Large-scale and size-controlled synthesis of silver nanoparticles under microwave irradiation" ***Materials Chemistry and Physics*** **(2004),** 83 (1): 66-70.

[8] MN Nadagouda, TF Speth, RS Varma, "Microwave-Assisted Green Synthesis of Silver Nanostructures" ***Accounts of Chemical Research*** **(2011),** 44 (7): 469-478.

[9] L Suber, I Sondi, E Matijevic, DV Goia, "Preparation and the mechanisms of formation of silver particles of different morphologies in homogeneous solutions" ***Journal of Colloid and Interface Science*** **(2005),** 288 (2): 489-495.

[10] K Song, S Lee, T Park, B Lee, "Preparation of colloidal silver nanoparticles by chemical reduction method" ***Korean Journal of Chemical Engineering***. **(2009),** 26 (1): 153-155.

[11] O Golubeva, O Shamova, D Orlov, T Pazina, A Boldina, V Kokryakov, "Study of antimicrobial and hemolytic activities of silver nanoparticles prepared by chemical reduction" ***Glass Physics and Chemistry***. **(2010),** 36 (5): 628-634.

[12] M Harada, C Kawasaki, K Saijo, M Demizu, Y Kimura, "Photochemical synthesis of silver particles using water-in-ionic liquid microemulsions in high-pressure CO_2" ***Journal of Colloid and Interface Science*** **(2010),** 343 (2): 537-545.

[13] M Harada, Y Kimura, K Saijo, T Ogawa, S Isoda, "Photochemical synthesis of silver particles in Tween 20/water/ionic liquid microemulsions" ***Journal of Colloid and Interface Science*** **(2009),** 339 (2): 373-381.

[14] K Li, FS Zhang, "A novel approach for preparing silver nanoparticles under electron beam irradiation" ***Journal of Nanoparticle Research*** **(2010),** 12(4): 1423-1428.

[15] KA Bogle, "Silver nanoparticles synthesis and size control by electron irradiation" ***Nanotechnology.* (2006),** 17(13): 3204.

[16] J Zhu, S Liu, O Palchik, Y Koltypin, A Gedanken, "Shape-Controlled Synthesis of Silver Nanoparticles by Pulse Sonoelectrochemical Methods" ***Langmuir.* (2000),** 16 (16): 6396-6399.

[17] M Gnanadesigan, M Anand, S Ravikumar, M Maruthupandy, M Syed Ali, V Vijayakumar, AK Kumaraguru; "Antibacterial potential of biosynthesised silver nanoparticles using Avicennia marina mangrove plant" ***Appl. Nanosci.* (2012),** 2: 143-147.

[18] KC Bhainsa, SD Souza, "Extracellular biosynthesis of silver nanoparticles using the fungus Aspergillus fumigates" ***Colloids Surf Biointerfaces* (2006),** 47(2): 160-164.

[19] N Krumov, I.N Perner, S Oder, V Gotcheva, A Angelov, C Posten, "Production of Inorganic Nanoparticles by Microorganisms" ***Chem. Eng. Technol* (2009),** 32(7): 1026-1035.

[20] Y Tezuka, K.Honda, A.H.Banskota, M.M.Thet, S.Kadota, "Kinmoonosides A-C, three new cytotoxic saponins from the fruits of Acacia concinna, a medicinal plant collected in Myanmar" ***J. Nat. Prod* (2000),** 63: 1658-1664.

[21] S Ankanna, P. TNVKV, E.K. Elumalai, N. Savithramma, "Production of biogenic silver nanoparticles using Boswelliaovalifoliolata stem bark" ***Dig. J. Nanomater. Biostruct.* (2010),** 5 (2): 369-372.

[22] J Virkutyte, R.S. Varma, "Fabrication and visible-light photocatalytic activity of novel Ag/TiO$_2$À$_x$Nx photocatalyst" ***New J. Chem*. (2010),** 34: 1094-1096.

[23] MJ Kwon, J Lee, AW Wark, HJ Lee, "Nanoparticles-enhanced surface plasmon resonance detection of proteins at attomolar concentrations: comparing different nanoparticle shape and size" ***Anol chem.* (2012),** 84: 1702-1707.

[24] PC Ray, "Size and shape dependent second order nonlinear optical properties of nanomaterials and their application in biological and chemical sensing" ***Chem Rev* (2010),** 110: 5332-5365.

[25] V Amendola, OM Bakr, F stellacci, "A study of the surface plasmon resonance of silver nanoparticles by the discrete dipole approximation method: effect of shape, size, structure and assembly" ***Plasmonics* (2010),** 5: 85-97.

[26] GV Hartland: "Optical studies of dynamic in noble metal nanostructures"***Chem Rev* (2011),** 111: 3858-3887.

[27] P. Scherrer, "Bestimmung der Grösse und der inneren Struktur von Kolloidteilchen mittels Röntgenstrahlen" ***Nachr. Ges. Wiss. Göttingen* (1918),** 26: 98-100.

[28] J. I. Langford, A.J.C. Wilson, "Scherrer after Sixty Years: A Survey and Some New Results in the Determination of Crystallite Size" ***J. Appl. Cryst.* (1978)** 11 102-113.

[29] T. Wriedt, Mie Theory 1908-2008, ed. by Hergert, W.; Wriedt, "Present developments and interdisciplinary aspects of light scattering, eds" ***T. Universität Bremen. Bremen* (2008),** 17-21.

[30] H Jiale, L Qingbiao, S. Daohua, "Biosynthesis of silver and gold nanoparticles b novel sundried Cinnamomum camphora leaf" ***Nanotechnology.* (2007),** 18 (10): 105-104.

[31] G. Varsanyi, "Assignments of Vibrational Spectra of Seven Hundred Benzene Derivatives" ***Halsted Press* (1974),** vol. 1**.**

[32] I.D.G. Macdonald, W.E. Smith, "Orientation of Cytochrome c Adsorbed on a Citrate-Reduced Silver Colloid Surface" ***Langmuir* (1996),** 12: 706-713.

[33] A.M. Fayaz, K. Balaji, M. Girilal, R. Yadav, P.T. Kalaichelvan, R. Venketesan, *"NanomedicineNanotechnology"* ***Biology and Medicine* (2010),** NBM 6: 103-109.

[34] B.M.V. Romão, C. Pardini, R.C.L. Dutra, F. Burel, "Caracterização por FT-IR de. Agentes de Cura Utilizados em Resinas Epoxídicas-II-Polimercaptana, Poliaminoamida- Amina Modificada" ***Polímeros Ciência Tecnologia* (2003),** 13: 173-180.

[35] J.P. Wilcoxon, J.E. Martin, F. Paraspour, D.F.J. Kelley, "Photoluminescence from nanosize gold clusters" ***Chem. Phys.* (1998),** 108: 9137-9143.

Chapter 3.3

Synthesis and Characterization of Ag @ZnO NRs

ABSTRACT

Nanostructured zinc oxide nanorods (ZnO NR's) are grown through a hydrothermal method followed by the production of silver nanoparticles (AgNPs) through a biogenic reduction process. Afterwards the silver nanoparticle loaded on ZnO NR's to synthesise the Ag@ZnO heterostructured nanorods with an average diameter of 180±5 nm and an average length of 2 μm. High-resolution transmission electron microscopic (HRTEM) study shows the highly crystalline ZnO NRs with a lattice fringe of 2.38 nm, which corresponds to the (011) growth plane of lattice where, Ag NPs embedded with (111) plane. Where, as the average diameter of the AgNPs deposioted on the ZnO NRs is estimated as at 22.5±50 nm nm. As compared to the pristine ZnO NRs, the heterostructured Ag@ZnO nanorod array exhibits the enhanced ultraviolet (UV) absorption at 384 nm, and significant PL emission in the visible region (λ_{em} = 480 nm).

Key Words: ZnO Nanorods; Nanoparticles; plasmonic Ag NPs; Ag@ZnO NPs, XPS, etc

3.3.1 INTRODUCTION

In modern era, nanotechnology is a boon for the researchers. Nanoparticles having a size of 1-100 nm along one dimension are used significantly concern with catalysis chemistry, industrial chemistry, medical chemistry, atomic physics, and moreover it touched the almost all known fields. Nanoparticles are immensely used in all parts of life due to their small size (surface to volume ratio), preferred orientation, optical, chemical, magenetic, physical properties. Broad domain of nanotechnology, includes oxide nanoparticles that can exhibits unique chemical properties owing to their limited size and high density of interfaces or edge at surface sites. [1, 2] ZnO-based semiconductors are always matter of interest for scienctific community. ZnO is a group II–VI semiconductor, which not only has excellent thermal and chemical stability, with high carriers mobility, but also has relatively large excitonic binding energy (60 meV) and it is a direct wide band gap (3.37eV) at room temperature. In addition to above, ZnO also possesses strong piezoelectric properties due to the inherent crystal structure. [3] These characteristics made ZnO semiconductor suitable for applications in electronic, optoelectronic, electrochemical, and electromechanical devices such as light-emitting diodes, [4] photodetectors, [5] photodiodes, [6] gas sensors, [7] solar cells, [8] piezoelectric transducers, [9] and so on. Modification of ZnO properties by incorporation of the metal /elements (dopant) is important to improve the feasibility of these devices in multiple applications. Due to the high aspect ratio (~ equal to 3 to 5) of 1D-ZnO nanostructures, these are considered as the best system to understand the transport mechanism in 1D materials with excellent performance. Like nanowires, ZnO nanorods can also exhibits properties i.e. tuneable optical band gap and morphology, composition and size, high carrier mobility and direct conduction pathway for the flow of excitons. [10] It can also be serve as an better interface between electrodes and fecilitate electrical path for the flow of charge carriers in sensors. [11] ZnO nanorods can be easily grown on number of substrates including, metal, conductive glass, polymers, etc and exhibit low density defects. These are also applicable for the electronic and optoelectronic devices, transparent electrodes, short wavelength lasers, and catalyst (for solar cells, photo-catalytic dye degradation, water splitting etc). [12-22] So Ag metal ion deposition on ZnO NRs can offers good electrical, optical, magnetic and piezoelectric properties, which is vital for their practical applications. In Ag@ZnO NRs, silver (Ag) act as a cocaltalyst to enhance its optical properties of ZnO. Ag ions can act as acceptors in ZnO NRs, existing on substitutional Zn sites or in the interstitial form. In Ag doped -ZnO NRs, the location

of the acceptor level remains contentious. [23] In general, the physical properties of Ag-ZnO NRs are closely related to the deposition parameters and temperature of annealing. Due to these reasons, the hydrothermal method has been widely used to adjust the structural, electrical and optical properties of Ag@ZnO NRs. Ag-coated ZnO nanorods have been used in many applications, such as efficient and cost effective transparent conducting oxide electrodes. In order to test its utility as transparent conducting oxide electrode and antireflection coating, parameters like conductivity and refractive index of the film needs to be investigated in future as reported in literature. [24-26] In these studies, Ag doped ZnO thin films reported to increase in the resistivity in addition to enhancement in the UV emission, and reduction of the optical band gap. [27-29] All Ag-decorated ZnO NRs arrays were used for the electrical or optoelectrical properties. Although, the pure ZnO nanostructures show weak optical features because of point defects such as oxygen vacancy or interstitial Zn. Metal decorated ZnO can be engineered the optical and magnetic properties of the pure ZnO. Therefore, various metals are used to in-cooperate with ZnO to make the n-type and p-type optoelectronic devices. Silver has been reported as the best candidate because of its high solubility, larger ionic size, and minimum orbital energy. [30] Theoretically, among the all reported elements of group I B, copper (0.7 eV) and Au (0.5 eV), had higher ionization energy than Ag (0.4 eV) that will caused silver to be the best candidate for making p-doping in ZnO. [31,32] Recently, experimental and theoretical approaches revealed that when the Ag doped (substitution) into the ZnO lattice, [33] Ag 4d and O 2p orbitals were overlapped to form an impurity band, which can shift the Fermi level toward the valence band maxima and induced p-type character in ZnO. These p-type properties not only depend on Ag content, but also on experimental conditions such as electrochemical growth and post-annealing conditions, etc. [34,35] Electrical properties of the AgNPs-doped ZnO governed by the place Ag in ZnO lattice (substitution and interstitial), where the substitutional sites were more energetically favourable than interstitial sites. Few of the studies reported the effects of silver doping on the photocatalytic activity and antibacterial properties of ZnO. [36-38] The dilute magnetism was also observed for the AgNPs- doped ZnO semiconductor. However, the origin of ferromagnetic properties is still under investigation. But few studies said that the ferromagnetic behaviour of the compound are result of the formation of impurity band, which interacts with the d orbital of nonmagnetic element. Therefore, it can also be used in spintronic applications. [39-41] Here, we synthesised

the nanostructures of ZnO NRs by a simple and low-cost hydrothermal method and AgNPs by biogenic reduction of silver salt. Afterwards the AgNPs decorated on the surface of the ZnO by chrmical bath deposition technique. The aim of this work was to produce p-type semiconductor that can be used in different type of optical applications specially for water splitting and pollutant degeradation.

3.3.2 EXPERIMENTAL

During the fabrication of the heterostructured device, we first, grow ZnO nanorod array using the modified low-temperatured hydrothermal method, as it discussed in section 3.1. [42,43] Synthesis of AgNPs was done by biogenic plant extract reduction of silver salts as it discussed in the section 3.2.To modify the ZnO NRs surface with AgNPs, the mixture of both was stirred at room temperature. And as shown in Scheme 1, the synthesized Ag@ZnO NR were exposed under a UV light (hv) that leads to form electron-hole pairs because when sunlight exposed to ZnO the electron jump from VB (photoholes formed) to CB (photoelectrons formed) of ZnO. In presence of CH_3OH, the holes (h^+) are consumed to produce ethoxy radicals CH_3O^*.
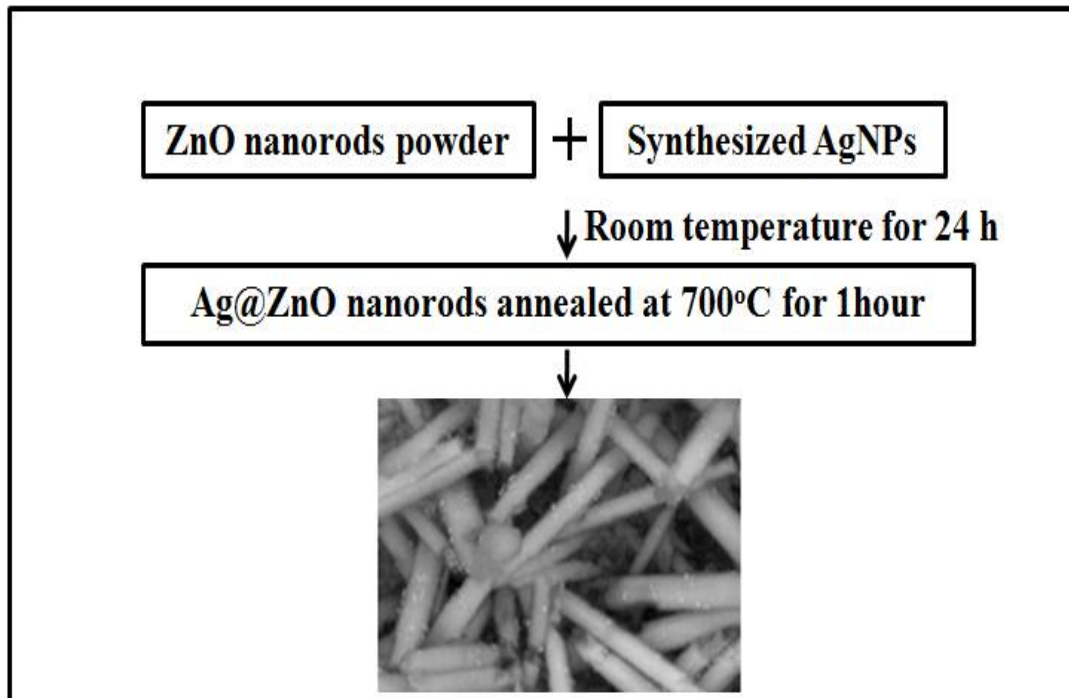
Scheme 1 Flow chart for the preparation of Ag@ZnO nanorods

3.3.3 RESULTS AND DISCUSSION

3.3.3.1 Structural Characterization

The surface morphology and chemical composition of the Ag@ZnO nanorods have been studied by FESEM, HRTEM and SAED analysis. Figure 3.28A shows the FESEM micrograph of the Ag loaded on to the ZnO nanorod substrate. The average diameter of ZnO hexagonal nanorods is estimated as 180±5 nm with their average length of 2 μm. The shape and size of the typical as-grown Ag at the surface of ZnO nanorod are revealed in the TEM micrograph (Figure 3.28B), which is consistent with the result of the FESEM micrograph. The HRTEM micrograph demonstrated by the Figure 3.28C further indicates that the Ag@ZnO nanorods are highly crystalline with a lattice fringe of 2.38 nm, which corresponds to the (011) growth planes of the ZnO crystal lattice. The heterostructures of Ag@ZnO nanorods are clearly shown in TEM (Figure 3.28E). The surface of nanostructured Ag@ZnO NRs are not smooth as it was decorated with Ag NPs. The chemical composition of Ag@ZnO heterostructured nanorods were also determined using EDX neasurement. Figure 3.28f indicate the three elements presence in nanocomposite i.e. Zn, O, and Ag with their % composition (Zn: O : Ag :: 56.86 : 32.53 :10.61 %). It indicates that the large amount of spherical Ag NPs loaded on the ZnO NRs surface. Furthermore, Ag@ZnO NRs were studied by HRTEM that confirms the loading of the average diameter of spherical Ag nanoparticles is estimated at 22.5±5 nm as shown in Figure 3.28C and a small-inset image shows a HRTEM micrograph of Ag@ZnO NRs. In addition, the inter planar and distance between two fringes is measured as 0.95 nm, as it illustrated by the Figure 3.28C, which corresponds to the d-spacing of the [111] crystal plane of Ag NPs. The interface between ZnO NR and Ag NP is highlighted by the white rectangle, shown in figure 3.28E.
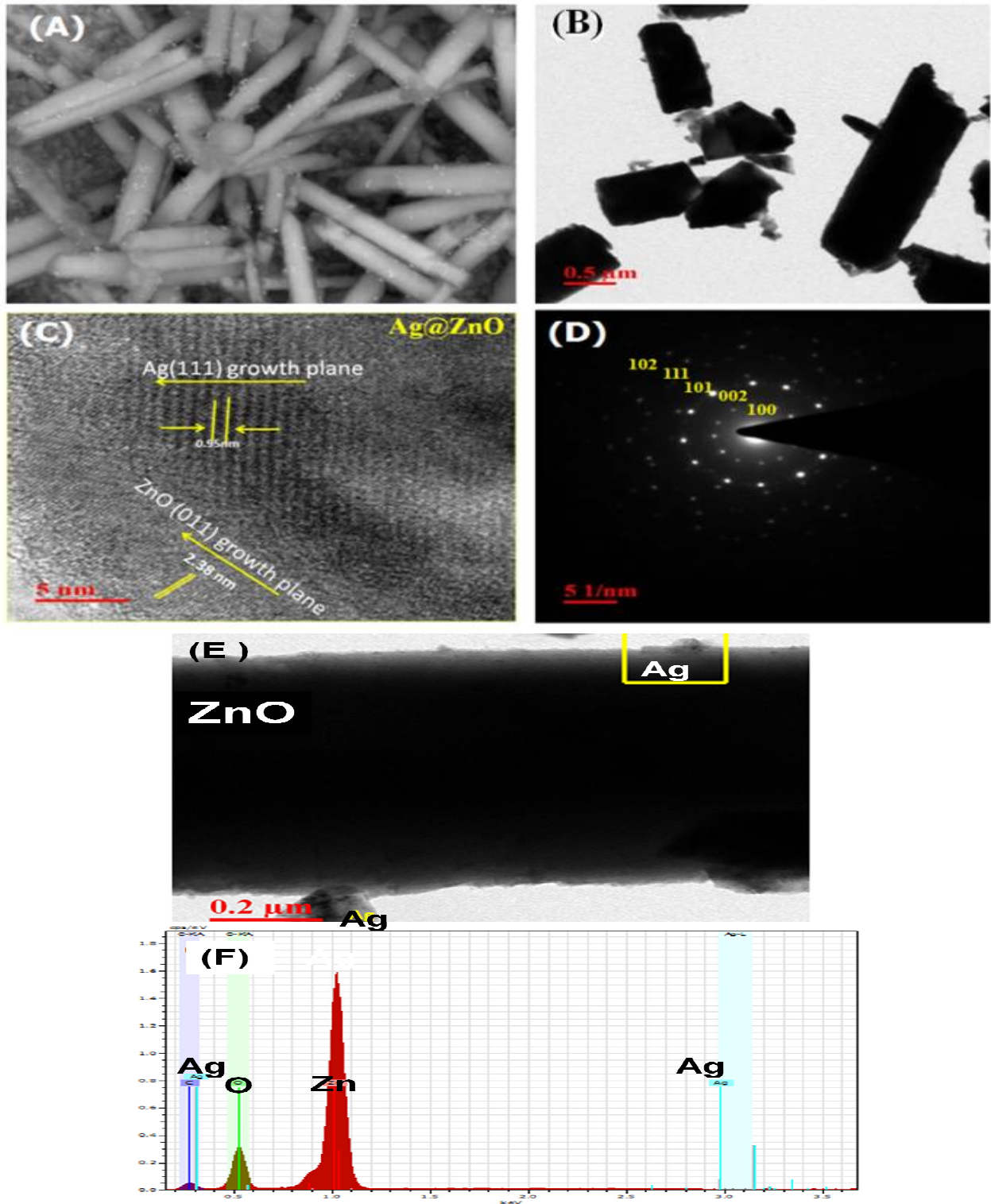
Figure 3.28 (A) FESEM micrograph of aligned Ag@ZnO nanorod, **(B)** TEM micrograph of Ag@ZnO nanorod, **(C)** HRTEM micrograph of the Ag@ZnO nanorod and **(D)** SAED Pattern of Ag@ZnO nanorods, **(E)** TEM micrograph of the single Ag@ZnO nanorod that loaded with nano Ag, **(F)** EDX micrograph of Ag-ZnO nanorods.

The elemental composition was measure through EDXS to find out the purity of AgNPs loaded ZnO NRs and their graphical results are represented in Figure 3.28F which is supported by the TEM instrumentation and shows the amount of nanosilver loaded onto ZnO NRs' surface. These EDX results are also supported by EDXS mapping results shown by the Figure 3.29, which exhibits the distribution of the constituent elements: O, Zn, Ag and carbon. Here, the carbon might be comes from the biochemical present in green reductant, which was disappeared after annealing of these nanocomposite samples.
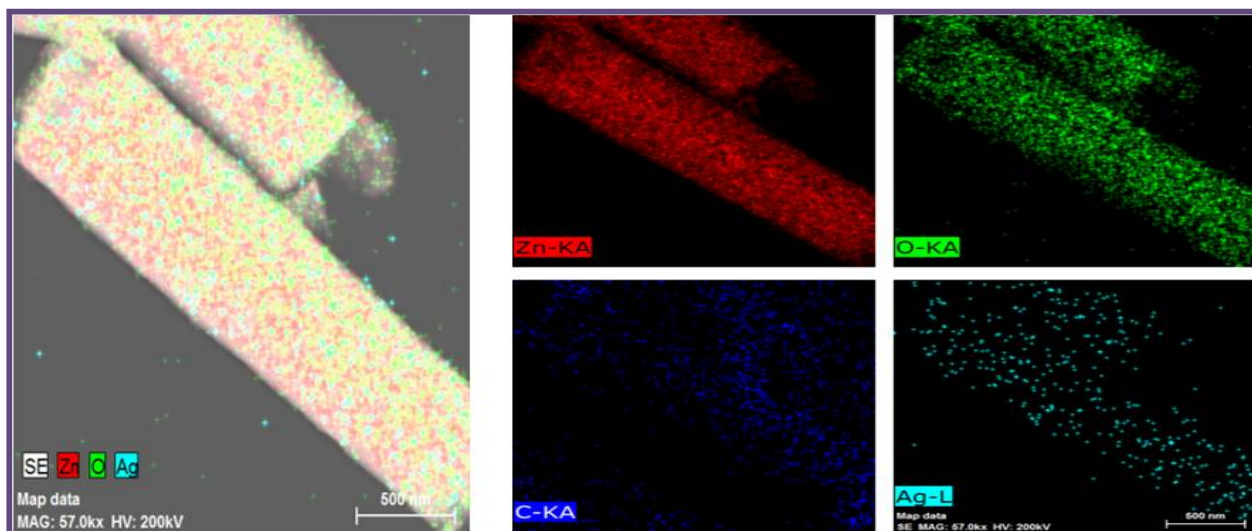
Figure 3.29 EDXS mapping of the Ag@ZnO NRs and elemental mapping, which depicts the distribution of constituents O, Zn, Ag and carbon.

3.3.3.2 UV-Vis ANALYSIS
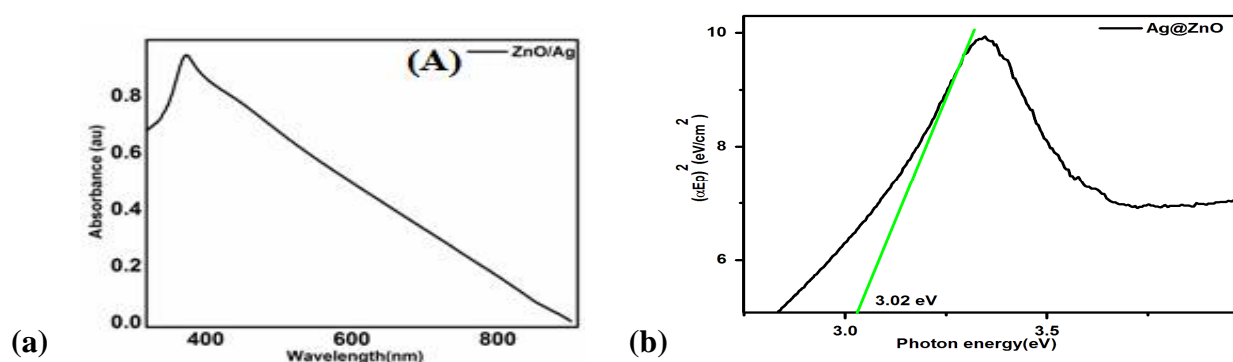
Figure 3.30 (a) the UV-Vis absorption spectra of the synthesized AgNPs@ZnO NRs and **(b)** the Kubelka Munk plot between $(\alpha Ep)^2$ and photon energy that used to determine the band gap for the AgNPs @ ZnO NRs i.e. 3.02 eV.

The UV-visible absorption spectra of the ZnO@Ag NRs samples as shown in Figures 3.30(a) and 3.30(b), was taken in the range of 200-900 nm. Figure 3.30(a) exhibited a strong excitonic peak of Ag NPs decorated ZnO NRs absorption that was existed at 384 nm that is higher than that of the pure ZnO nano rods 368 nm [Chapter 3.1] The peak obtained at 384 nm is assigned to absorption of ZnO NRs and careful investigation shows the presence of Ag NPs peak at 420 nm. The difference in the absorption peak positions of the pure ZnO NRs and Ag NPs/ ZnO NRs, was observed due to the binding of the SPR Ag NPs to the zinc oxide surface. This enriched the absorption peak. Figure 3.30(b) represents the Kubelka Munk plot between $(\alpha Ep)^2$ and photon energy that used to determine the band gap for the AgNPs @ ZnO NRs i.e. 3.02 eV.

3.3.3.3 XRD STUDY

The XRD patterns of the Ag@ZnO nanorods are displayed in Figure 3.31. The diffraction peaks of the ZnO NRs array match as well the typical hexagonal wurzite structure of the ZnO (corresponds to the standard JCPDS card no. 36-1451). The extra peaks located at $2\theta = 38.12°$, 44.28°, 64.25°, and 77.47°, are attributed to the respective crystalline planes (111), (200), (220), and (311) belongs to the Ag NPs i.e. consistent with the standard Ag JCPDS card no. 04-0783. In addition, there is no remarkable shift and intensity change to all diffraction peaks. The ZnO and Ag NPs particle size can be estimated by Scherrer's equation [28]
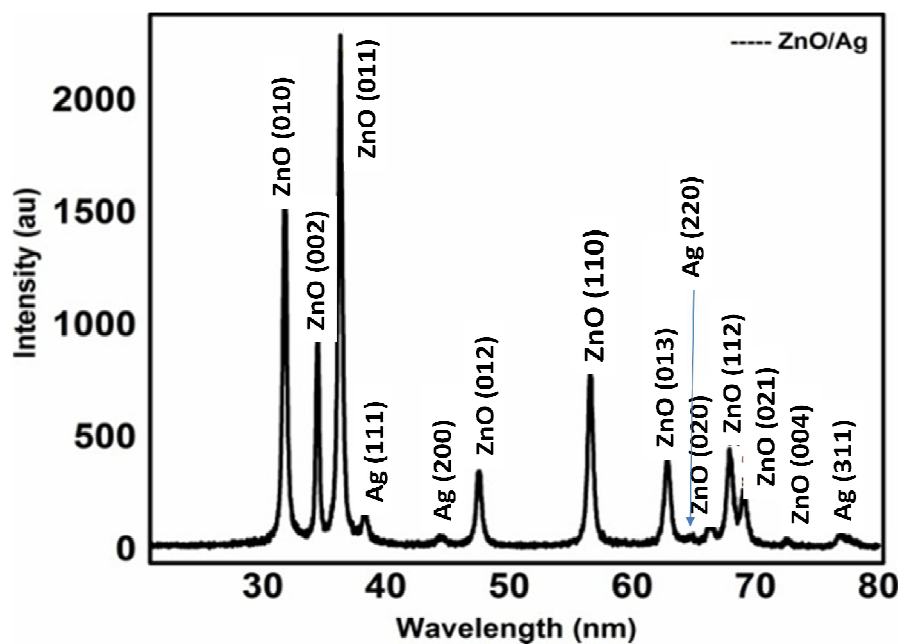

Figure 3.31 XRD profile of the Ag@ZnO nanorods

The average particle size of the Ag NPs deposited on ZnO nanorods is around 22.9 nm which is consistent with the result of TEM and 300 nm diameter of ZnO nanorods was estimated along with their the average length of 2 μm.

3.3.3.4 XPS STUDY

The XPS spectra of as-grown Ag-ZnO NRs was taken for the Zn, Ag, C and O elementsusing the XPS spectrophotometer (Omicron EA 125 spectrometer). High-resolution XPS spectrum of the as-grown Ag@ZnO nanorods is illustrated by the Figures 3.32a, 3.32b, 3.32c and 3.32d. The chemical state of the Ag was characterized by examining Ag-3d levels demonstrated in Figure 3.32a. The Ag peaks ($3d_{3/2}$) located at 367.95 and Ag ($3d_{5/2}$) at 373.51 eV, due to the splitting of the energy about ~6eV that represent the metallic state of silver present in the synthesized samples. [44, 45] Khosravi et. al. [46], have revealed the presence of two different components, which could be attributed to the either metallic Ag or Ag_2O and to an Ag-Zn-O ternary compound. As the binding energy of the Ag-3d for the doped sample compared to the binding energy of the bulk silver sample (367.95 eV for Ag ($3d_{5/2}$) and 373.51 eV for Ag ($3d_{3/2}$) [47] was significantly shifted towards lower binding energy. That result of the interaction between silver and ZnO nanoparticles, which could regulate the position of the Fermi level of silver by the formation of a new Fermi level for metallic silver. Free electrons above the new Fermi level might be tunnelled to the empty conduction band of ZnO. [48] As per present XPS patterns, Ag-3d binding energy was shifted to lower binding energy that can be explained by two processes: In first process, the binding energy of the unit valance silver is much lower than the zero valance silver [49] and the second one is due to the formation of an oxide layer on the surface of silver particles but there is no oxide layer confirmed by the XRD analysis. Due to the high electronegativity of Ag than Zn, electron transfer was assumed to be occured from Zn to the Ag particles, suggested that the chemical bond between ZnO and Ag, which is compensate the defects at ZnO crystal lattice.
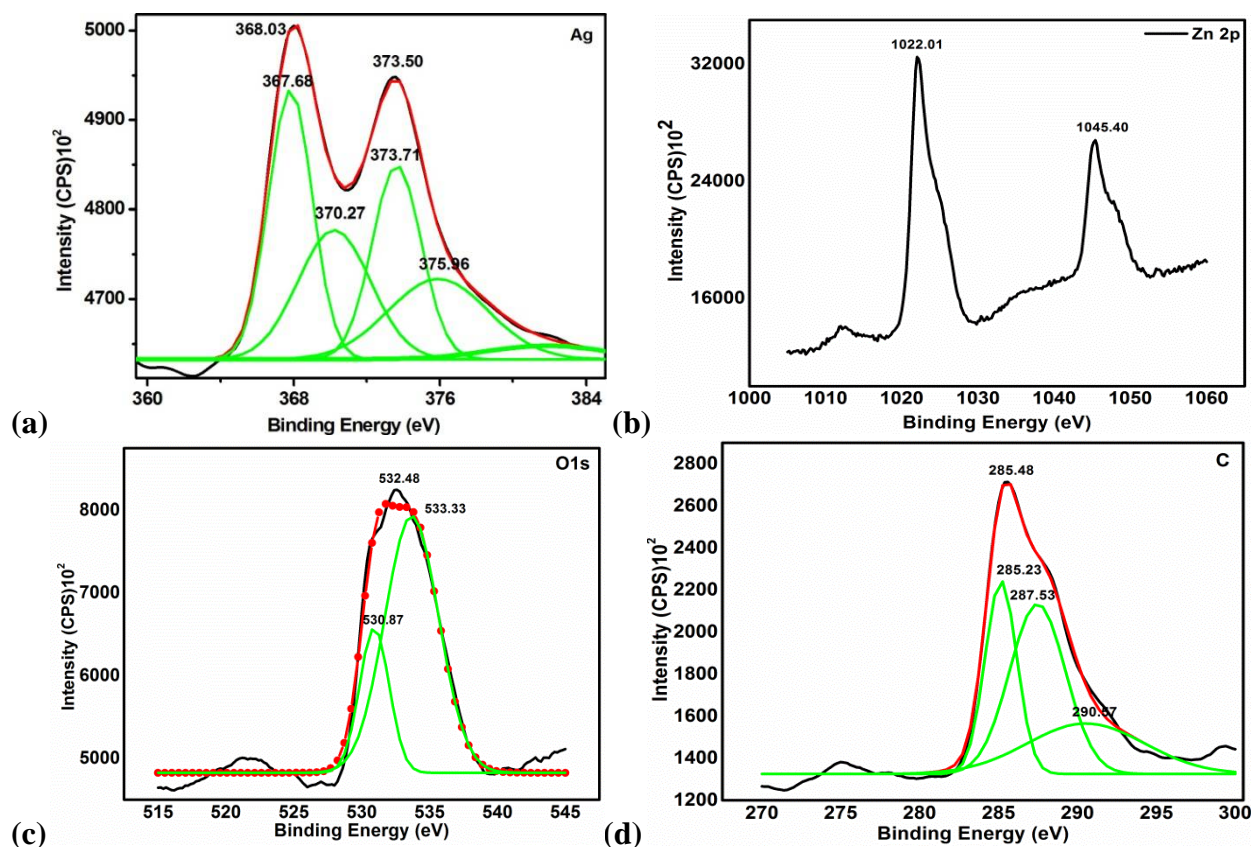
Figure 3.32 XPS spectra of the AgNPs @ZnO sample. **(a)** XPS spectra of Zn 2p **(b)** Ag 3d **(c)** O 1s. and **(d)** C element high-resolution spectra.

When Ag NPs are loaded onto ZnO NRs surface, the positions of the symmetrical peaks of Zn are located at 1022.01 and 1045.40 eV, as demonstrated by the Figure 3.32b. Where, the peaks positions for the sample of pure zinc oxide ascribed to $Zn(2p_{1/2})$ and $Zn(2p_{3/2})$, are located at 1021.67 and 1044.81 eV and corresponding to $Zn(2p_{1/2})$ and $Zn(2p_{3/2})$. [50] The splitting energy of Zn-2p states is about 23 eV, which can be induced from the powerful spin-orbit coupling. Red shift in Zn spectra was observed on silver doping from the binding energy of the standard ZnO (1022.1 eV for $Zn(2p_{1/2})$ and 1045.1 eV for $Zn(2p_{3/2})$), which can be attributed to the charge transfer from Zn^{2+} to O^{2-} due to the presence of the vacancies. [51] These peaks positions confirms the wurtzite structure and Zn^{2+} mode of the Zn atom on the samples. [52] Therefore, due to the charge transfer in the binding energy of XPS spectrum, it can be deduced that the Zn-2p peak shift indicates that oxygen deficiency is the dominant factor versus Zn deficiency in the doped samples in contrast to the pure one. [51]

Figure 3.32c shows the internal levels of the oxygen in both of the nanoparticles. Itis clearly seen that the O-1s curve was asymmetric that can be fitted with two Gaussian peaks (530.87 (I) and 533.33 (II) symmetrically to represent the two different types of oxygen groups in the samples. The peak (I) was located in the lower binding energy in comparison with the peak (II), which was dedicated to O^{2-}ions of Zn-O bonding at crystal lattice due to lattice oygen species. [53] The peak (II) was related to the oxygen vacency due to structural defects. [54] These groups could play a major role in the photocatalytic activity.

It could increase the photocatalytic activity [55] by suppressing the recombination of electron-hole pairs. Silver doping of ZnO led to a shift in the O-1s spectrum toward lower binding energy. The atomic ratio of oxygen vacancy (II) to total oxygen was calculated for pure ZnO, which was equal to 51% and increased by 16% using Ag doping. So, the photocatalytic activity should be increased by silver addition process. Also, decreasing the binding energy of the Zn-2p and O-1s levels with silver doping could be due to the reduction of oxygen vacancy. Decrease in the ratio of Zn/O in the present XPS results for the doped samples compared to the pure sample confirmed the reduced the density of oxygen defects.Figure 3.32d, exhibited the three type of carbon situated at 285.23 (C-C and C-H) 287.53   (O-C-O) and 290.67(O-C=O) eV in XPS profile of the AgNPs@ZnO NRs.The presences of carbon in XPS profile of the compound may be result of the phytochemicals present on the Ag NPs surface and removed on annealing.

3.3.3.5 PL STUDY

Figure 3.33 represents PL spectrum of the sample recorded at the excitation wavelength 281 nm and display deep level emissions (DLE) at about 480 nm in the visible region. This visible emission of ZnO has been frequently ascribed to several intrinsic and extrinsic defects or blue/green radiation is due to the oxygen vacancy with a hole in the valence band. [56-58]

(a) **(b)**
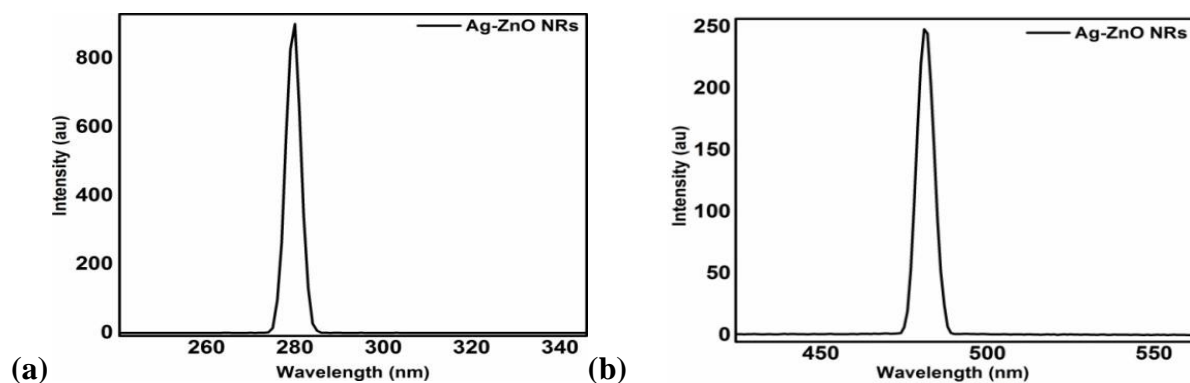
Figure 3.33 (a) Excitation spectra of the Ag@ZnO at λ_{em}= 480 nm. (b) Photoluminescent emission spectra of Ag@ZnO heterostructured nanorodrecorded at λ_{ex}= 281nm.

3.3.4 CONCLUSION

Ag@ZnO heterostructure nanorods with excellent optical properties are successfully prepared through a simple chemical deposition method. The heterostructures of Ag@ZnO was examined by various analytical techniques such as XRD, UV-Vis, SEM, TEM, HRTEM, EDXS, XPS, PL, etc. It is found that the addition of Ag NPs to ZnO surface, results in the formation of zero valent metallic Ag deposited on the surface of ZnO nanorods and the optical properties of Ag@ZnO nanorods is dependent on their structure, especially the heterostructure and oxygen vacancy. The presence of the Ag nanoparticles and oxygen vacancy on the surface of ZnO nanorods promotes the separation of photogenerated electron-hole pairs and thus enhances the optical and photocatalytic activity.

3.3.5 REFERENCES

[1] T.C. Prathna, L.M., N. Chandrasekaran, Ashok M. Raichur and Amitava Mukherjee, "Biomimetic synthesis of Nanoparticles: Science, Technology & Applicability" School of Bio Sciences & *Technology*, VIT University, ***Department of Materials Engg., Indian Institute of Science, India.* (2010),** 1-17.

[2] Deepali Sharma , J.R., B.S. Kaith , Mohinder Kaur, Sapna Sharma "Synthesis of ZnO nanoparticles and study of their antibacterial and antifungal properties" ***Thin Solid Films* (2010),** 5191224-1229.

[3] U. Ozgur, Ya. I. Alivov, C. Liu, A. Teke, M. A. Reshchikov, S. Doan, V. Avrutin, S.-J.Cho, H. Morkoc, "A comprehensive review of ZnO materials and devices" ***J. Appl. Phys.* (2005),** 98: 041301.

[4] N. Saio, H. Hanela, T. Sekiguchi, N. Ohashi, I. Sakaguch, K. Koumoto, "Low-Temperature Fabrication of Light-Emitting Zinc Oxide Micropatterns Using Self-Assembled Monolayers" ***Adv. Mater.*** **(2002),** 14: 418-421.

[5] S. Liag, H. Sheng, Y. Liu, Z. Hio, Y. lu, H. Shen, "ZnO Schottky ultraviolet photodetectors" ***J. Cryst. Growth*** **(2001),** 225: 110-113.

[6] J. Y. Lee, Y. S. Choi, J. H. Kim, M. O. Park, S. Im, "Optimizing n-ZnO/p-Si heterojunctions for photodiode applications" ***Thin solid films*** **(2002),** 403: 553-557.

[7] N. Golego, S. A. Studenik, M. Cocivera, "Sensor Photoresponse of Thin-Film Oxides of Zinc and Titanium to Oxygen Gas" ***J. Electrochem. Soc.*** **(2000),** 147: 1592-1594.

[8] R.J. Hong, K. Helming, X. Jiang, B. Szyszka, "Texture analysis of. Al-doped ZnO thin films prepared by in-line reactive MF magnetron sputtering" ***Appl. Surf. Sci.*** **(2004),** 226 378.

[9] T. Shiosaki and A. Kawabata,"Low-Frequency Piezoelectric-Transducer Applications of ZnO Film" ***Appl. Phys. Lett.*** **(1974),** 25: 10-11.

[10] WI Park, J S Kim, GC Yi, MH Bae, HJ Lee, "Fabrication and electrical characteristics of high-performance ZnO nanorod field-effect transistors" ***Appl. Phys. Lett.*** **(2004),** 85: 5052-5054.

[11] M Jiao, NV Chien, NV Duy, ND Hoa, NV Hieu, K Hjort, H Nguyen, "On-chip hydrothermal growth of ZnO nanorods at low temperature for highly selective NO_2 gas sensor" ***Mater. Lett.*** **(2016),** 169: 231-235.

[12] Q Zhang, CS Dandeneau, X Zhou, G Cao, "ZnO Nanostructures for Dye-Sensitized Solar Cells" ***Adv. Mater.*** **(2009),** 21: 4087-4108.

[13] Y Hames, Z Alpaslan, A Koasemen, S E San, Y Yerli "Electrochemically grown ZnO nanorods for hybrid solar cell applications" ***Sol. Energy*** **(2010),** 84: 426-431.

[14] ML Zhang, F Jin, ML Zheng, J Liu, Z S Zhao, XM Duan, "High efficiency solar cell based on ZnO nanowire array prepared by different growth methods" ***RSC Adv.*** **(2014),** 4: 10462-10466.

[15] A Djurisic, A Ng, X Chen "ZnO nanostructures for optoelectronics: material properties and device applications" ***Prog.Quantum Electron.*** **(2010),** 34: 191-259.

[16] S Chu, G Wang, W Zhou, Y Lin, L Chernyak, J Zhao, J Kong, L Li, J Ren, J Liu "Electrically pumped waveguide lasing from ZnO nanowires" ***Nat. Nanotechnol.*** **(2011),** 6: 506-510.

[17] F T Liu, S F Gao, S K Pei, SC Tseng, C Hsin, J Liu "ZnO nanorod gas sensor for NO_2 detection" ***Journal of the Taiwan Institute of Chemical Engineers*** **(2009),** 405528-532.

[18] M Thambidurai, N Muthukumarasamy, D Velauthapillai, C Lee "Synthesis of garland like ZnO nanorods and their application in dye sensitized solar cells" *Mater. Lett.* **(2013),** 92: 104-107.

[19] L Schlur, A Carton, P Leveque, D Guillon, G Pourroy, "Optimization of a new ZnO nanorods hydrothermal synthesis method for solid state dye sensitized solar cells applications" *J. Phys. Chem.C* **(2013),** 117: 2993.

[20] R Zou, G He, K Xu, Q Liu, Z Zhangand, J Hu "ZnO nanorods on reduced graphene sheets with excellent field emission gas sensor and photocatalytic properties" *J. Mater. Chem. A* **(2013),** 1: 8445-8452.

[21] M Raja, N Muthukumarasamy, D Velauthapillai, R Balasundaraprabhu, S Agilan, T S Senthil " Influence of pH on ZnO nanocrystalline thin films prepared by *sol*-gel dip coating method" *Sol. Energy* **(2014),** 106: 129-135.

[22] J J. Hassan, MA Mahdi, CW Chin, HA Hassan, Z Hassan, "A high-sensitivity room-temperature hydrogen gas *sensor* based on oblique and vertical ZnO nanorod arrays" *Sensors and Actuators B: Chemical* **(2013),** 176: 360-367.

[23] Y. Zhang, "Effects of Ag Doping on the Photoluminescence of ZnO Films Grown on Si Substrates" *J. Phys. Chem. B* **(2005),** 109: 19200-19203.

[24]J. Fan, "The roles played by Ag and Al dopants in controlling the electrical properties of ZnO varistors" *J. Appl. Phys.* **(1995)**77 4795-4800.

[25] L. Xu, G. Zheng, L. Zhao, and S. Pei, "Two different mechanisms on UV emission. enhancement in Ag-doped ZnO thin films" *Journal of Luminescence* **(2015),** 158: 396-400.

[26] A.N. Gruzintsev, V.T. Volkov, and E.E. Yakimov, "Photoelectric properties of ZnO films doped with Cu and Ag acceptor impurities" *Semiconductors* **(2003),** 37: 259-262.

[27] J. Xu, Z.Y. Zhang, Y. Zhang, B.X. Lin, and Z.X. Fu, "Effect of Ag Doping on Optical and Electrical Properties of ZnO Thin Films" *Chin. Phys. Lett.* **(2005),** 22: 2031-2034.

[28] H.S. Kang, B.D. Ahn, J.H. Kim, G.H. Kim, S.H. Lim, H.W. Chang, and S.Y. Lee, "Structural, electrical, and optical properties of p-type ZnO thin films with Ag dopant" *Appl. Phys. Lett.* **(2006),** 88: 202108.

[29] M. Liu, S.W. Qu,W.W. Yu, S.Y. Bao, C.Y. Ma, Q.Y. Zhang, J. He, J.C. Jiang, E.I. Meletis, and C.L. Chen, "Photoluminescence and extinction enhancement from ZnO films embedded with Ag nanoparticles" *Appl. Phys. Lett.* **(2010),** 97231906.

[30] H. Xue, X.L. Xu, Y. Chen, G.H. Zhang, and S.Y. Ma,"Influence of Ag-doping on the optical properties of ZnO films" *Applied Surface Science* **(2008),** 255: 1806-1810.

[31] K. Liu, B. Yang, H. Yan, Z. Fu, M. Wen, Y. Chen, and J. Zuo,"Strong room-temperature ultraviolet emission from nanocrystalline ZnO and ZnO: Ag films grown by ultrasonic spray pyrolysis" *Applied Surface Science* **(2008),** 255: 2052-2056.

[32] M. Ahmad, J. Zhao, J. Iqbal, W. Miao, L. Xie, R. Mo, J. Zhu, "Conductivity enhancement by slight indium doping in ZnO nanowires for optoelectronic applications" *Journal of Physics D: Applied Physics* **(2009),** 42 (16): 165406.

[33] Y. Yan, M. Al Jassim, S.H. Wei, "Doping of ZnO by group-IB elements" *Applied physics letters* **(2006),** 89 (18): 181912-181912.

[34] Y. Ma, G. T. Du, S. R. Yang, Z. T. Li, B. J. Zhao, X. T. Yang, T. P. Yang, Y. T. Zhang, D. L. Liu, "Control of conductivity type in undoped ZnO thin films grown by metalorganic vapor phase epitaxy" *Journal of Applied Physics* **(2004),** 95: (11) 6268-6273.

[35] M. Thomas, W. Sun, J. Cui, "Mechanism of Ag doping in ZnO nanowires by electrodeposition: experimental and theoretical insights" *The Journal of Physical Chemistry C* 116 (10) (2012), 6383-6391.

[36] O. Lupan, L. Chow, L. K. Ono, B. R. Cuenya, G. Chai, H. Khallaf, S. Park, A. Schulte, "Synthesis and characterization of Ag or Sb doped ZnO nanorodsby a facile hydrothermal route" *The Journal of Physical Chemistry* C **(2010),** 114 (29): 12401-12408.

[37] C. Karunakaran, V. Rajeswari, P. Gomathisankar, "Optical, electrical, photocatalytic, and bactericidal properties of microwave synthesized nanocrystalline Ag-ZnO and ZnO" *Solid State Sciences* **(2011),** 13 (5): 923-928.

[38] P. Amornpitoksuk, S. Suwanboon, S. Sangkanu, A. Sukhoom, N. Muensit, J. Baltrusaitis, "Synthesis, characterization, photocatalytic and antibacterial activities of Ag-doped ZnO powders modified with a d-block copolymer" *Powder Technology* **(2012),** 219: 158-164.

[39] T. Chen, Y. Zheng, J.M. Lin, G. Chen, "Study on the photocatalytic degradation of methyl orange in water using Ag/ZnO as catalyst by liquid chromatography electrospray ionization ion-trap mass spectrometry" *Journal of the American Society for Mass Spectrometry* **(2008),** 19 (7): 997-1003.

[40] R. Kumar, D. Rana, A. Umar, P. Sharma, S. Chauhan, M. S. Chauhan, "Ag-doped ZnO nanoellipsoids: Potential scaffold for photocatalytic and sensing applications" *Talanta* (*2015*)**,** 137204-213.

[41] M. He, Y. Tian, D. Springer, I. Putra, G. Xing, E. Chia, S. Cheong, T. Wu, "Polaronic transport and magnetism in Ag-doped ZnO" *Applied Physics Letters* **(2011),** 99 (22): 222511/1-*222511*/3.

[42] SK. Tzeng, MH. Hon, IC. Leu, "Improving the performance of a zinc oxide nanowire ultraviolet photodetector by adding silver nanoparticles" *J Electrochem Soc.* **(2012),** 159 H440-H443.

[43] D. Lin, H. Wu, R. Zhang, W. Pan, "Enhanced photocatalysis of electrospun Ag-ZnO heterostructured nanofibers" *Chem Mater.* **(2009),** 21: 3479-3484.

[44] Y. Ao, J. Xu, D. Fu, C. Yuan, "Preparation of Ag-doped mesoporous titania and its enhanced photocatalytic activity under Uv light irradiation" *Journal of Physics and Chemistry of Solids* **(2008),** 69 (11): 2660-2664.

[45] M. Wu, B. Yang, Y. Lv, Z. Fu, J. Xu, T. Guo, Y. Zhao, "Efficient one-pot synthesis of Ag nanoparticles loaded on n-doped multiphase TiO_2 hollow nanorod arrays with enhanced photocatalytic activity" *Applied Surface Science* **(2010),** 256 (23): 7125-7130.

[46] S. Khosravi-Gandomani, R. Yousefi, F. Jamali-Sheini, N. M. Huang, "Optical and electrical properties of p-type Ag-doped ZnO nanostructures" *Ceramics International* **(2014),** 40 (6): 7957-7963.

[47] Y. Zheng, C. Chen, Y. Zhan, X. Lin, Q. Zheng, K. Wei, J. Zhu, "Photocatalytic activity of Ag/ZnO heterostructure nanocatalyst:correlation between structure and property" *The Journal of Physical Chemistry C* **(2008),** 112 (29): 10773-10777.

[48] Y. Zheng, L. Zheng, Y. Zhan, X. Lin, Q. Zheng, K. Wei, "Ag/ZnO heterostructure nanocrystals: synthesis, characterization, and photocatalysis" *Inorganic chemistry* **(2007),** 46 (17): 6980-6986.

[49] M. Habibi, R. Sheibani, "Preparation and characterization of nanocomposite znoag thin film containing nano-sized Ag particles: influence" *Journal of Sol-Gel Science and Technology* **(2010),** 54 (2): 195-202.

[50] Y. Jin, Q. Cui, K. Wang, J. Hao, Q. Wang, J. Zhang, "Investigation of photoluminescence in undoped and Ag-doped ZnO flower like nanocrystals" *Journal of Applied Physics* **(2011),** 109 (5).

[51] R. K. Sahu, K. Ganguly, T. Mishra, M. Mishra, R. Ningthoujam, S. Roy, L. Pathak, "Stabilization of intrinsic defects at hightemperatures in ZnO nanoparticles by Ag modification" *Journal of colloid and interface science* **(2012),** 366 (1): 8-15.

[52] A. Meng, S. Sun, Z. Li, J. Han, "Synthesis, characterization, and dispersion behavior of ZnO/Ag nanocomposites" *Advanced Powder Technology* **(2013),** 24 (1): 224-228.

[53] J. H. Zheng, J. L. Song, X. J. Li, Q. Jiang, J. S. Lian, "Experimental and first-principle investigation of Cu-doped ZnO ferromagnetic powders" *Crystal Research and Technology* **(2011),** 46 (11): 1143-1148.

[54] R. Al-Gaashani, S. Radiman, A. Daud, N. Tabet, Y. Al-Douri, "XPS and optical studies of different morphologies of ZnO nanostructures prepared by microwave methods" *CeramicsInternational* **(2013),** 39 (3): 2283-2292.

[55] M. N. Chong, B. Jin, C. W. Chow, C. Saint, "Recent developments in photocatalytic watertreatment technology: a review" *Water research* **(2010),** 44 (10): 2997-3027.

[56] C. Karunakaran, J. Jayabharathi, K. Jayamoorthy, P. Vinayagamoorthy, "Inhibition of fluorescence enhancement of benzimidazolederivative on doping ZnO with Cu and Ag" *Journal of Photochemistry and Photobiology A: Chemistry* **(2012),** 247: 16-23.

[57] H. Kumar and R. Rani "Structural and Optical Characterization of ZnO Nanoparticles Synthesized by Microemulsion Route" *International Letters of Chemistry, Physics and Astronomy* **(2013),** 1426-36.

[58] C. Lin and Y. Li, **"**Synthesis of ZnO nanowires by thermal decomposition of zinc acetate dihydrate" *Materials Chemistry and Physics* **(2009),** 113: 334-337.

Chapter 3.4

Synthesis and Characterization of CdS @Co-ZnO NRs

ABSTRACT

CdS@Co-ZnO Nanorods with different end shapes, were synthesised using hydrothermal method by varying the concentration of the aqueous CTAB (17.5, 20, 25, 30, 35 and 40%). The growth mechanism of the preparation is proposed for the Co-ZnO Nanorods (~400 nm broad and 2 mm long). CdS nanocrystals were loaded on to the surface of the Co-ZnO to increase the activity of the ZnO in visible range. Successive surface modification of the one dimensional ZnO nanostructures, reduces the band gaps, after each modification as follows 3.18 eV (ZnO NRs), 3.00 eV (Co-ZnO NRs), 2.48 eV (CdS/ZnO NRs) and 2.25 eV (CdS/Co-ZnO NRs). These heterostructures exhibits the excellent stability, capability to utilize the wide portion of visible light, and suppress the recombination of the photocarriers i.e. light generated photo-electrons and photo holes. As synthesised nanostructures are examined using advance the techniques such as XRD, SEM, EDX, TEM, HRTEM, SAED, UVVis spectroscopy, XAS , etc. It was established that the nanodevice nanocomposite is useful for the optoelectronic devices.

Key words: one dimensional structured Co-ZnO, CdS nano crystal, CdS/Co-ZnO NRs, hydrothermal method, XAS.
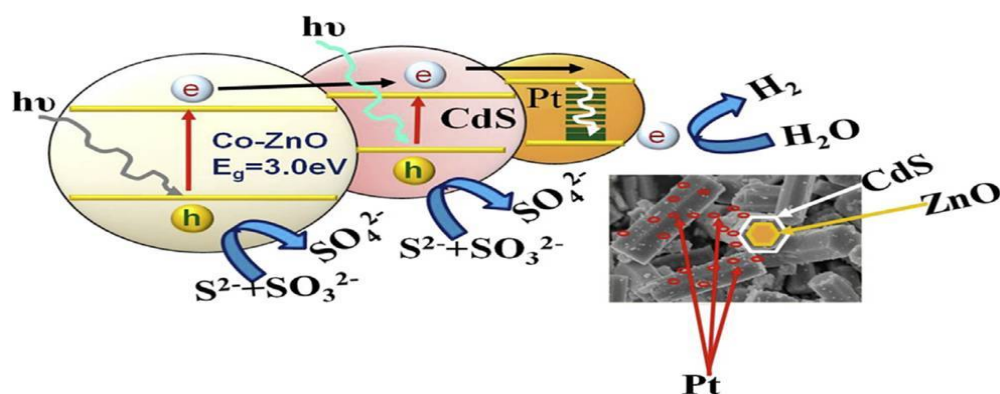
3.4.1 INTRODUCTION

Oxide photocatalysts (ZnO, TiO$_2$, Ga$_2$O$_3$, Nb$_2$O$_3$, In$_2$O$_3$ Fe$_2$O$_3$, SnO$_2$, WO$_3$, NiO, etc.) are comparatively found stable and cost effective photocatalyst. Out of the commercially available wide range of oxide semiconductors, ZnO [1,2] has been selected for the study because of its superb and unique inherent qualities such as low cost, wide availability, viability to change in morphology, large excitonic binding energy (60 me V), deep photon penetration, short diffusion length, low reflectivity, high carrier mobility, good bio-compatibility, etc. Usually, the nanostructures of ZnO possess a large degree of charge character transfer over their bulk counter part that is due to their large surface area to volume ratio, short lateral diffusion length and low reflectivity. [3] Furthermore, doping of transition metals to the semiconductors, used to improve the optical output of these photocatalytic materials. Hence, cobalt doping was employed to modify the surface quality of ZnO. Therefore, it was decided to synthesize nanostructures of ZnO and Co doped ZnO systems for utilizing them for hydrogen generation through water splitting. Consequently, the hydrothermal method [2] was adopted to develop one dimensional (1D) nanorods (NRs) of Co-ZnO by controlling the surfactant (CTAB; cetyltrimethylammonium bromide) concentration in water. Unluckily, neither the ZnO NRs nor Co-ZnO NRs, can exploit sunlight fully due to their wide band gap (WBG) i.e. Eg = 3.2 eV. More often the hetero-assemblies (by incorporation of visible light harvesting moiety to oxides) are made by introducing better light harvesting material (chalcogenide quantum dots/dyes) to nanooxide systems that to enhance their light harvesting capacity. These heterostructure exhibit excellent stability, capability to utilize the wide portion of visible light, and to suppress the recombination of the light generated photo-electrons and photo holes. For this reason, a chalcogenide CdS (Eg = 2.4 eV) was introduced as a sensitizer to ZnO or Co-ZnO NRs. Additionally,1.5% Pt was loaded as co-catalyst to generate reduction site to consume the photoelectrons at the surface of CdS/Co-ZnO NRs. Then this nanomolecular machines i.e. 1.5% Pt/CdS/Co-ZnO NRs, were utilized for photocatalytic water cleavage, in aqueous electrolyte (0.35 M Na$_2$S +0.25 M K$_2$SO$_3$, pH =13.3) under visible light irradiation. [4]

3.4.2 EXPERIMENTAL

3.4.2.1 Synthesis of ZnO and Co-ZnO NRs

Typical synthesis of ZnO or Co-ZnO nanostructures includes two major steps: (i) seed formation and (ii) growth of NRs. First step involves precipitation of Co-doped ZnO NRs were fabricated using pinkish white precipitate of Co-doped ZnO powder obtained by oxidizing 40mL aqueous solution of 0.009 mol (2.67g) of $Zn(NO_3)_2.6H_2O$ and 0.0009 mol (0.262g) of $Co(NO_3)_3.2H_2O$, till the pH of the solution become 7. Subsequently, as-obtained slurry of Co-ZnO (2.2g) was transferred into a Teflon-lined stainless-steel autoclave of 100 cm^3, containing 35 ml of aqueous 1% CTAB by varying surfactant (CTAB) concentration (17.5, 20, 25, 30, 35 and 40%) in reverse micelle hydrothermal method. Then the autoclave was sealed properly and heated at 200°C for 10h in an oven. [5] Here, CTAB-micelles served as the templates in nano crystals growth. Dry 1.4g green solid product was collected by centrifugation of the resulted autoclave solution and their washing several times with distilled water and alcohol. Finally, the sample dried at 80°C for 5h in oven under vacuum. For the synthesis of ZnO NRs, the same synthesis process was adopted without taking cobalt salt.

3.4.2.2 Loading of CdS on to the surface of ZnO and Co-ZnO NRs

Direct sulfurization method was employed to add CdS sensitizer to ZnO and Co-ZnO NRs, Mixture of 0.2g Co-ZnO NRs and 4.0 mM (0.733g) $CdCl_2.5H_2O$ in 30 mL were treated with 0.2M Na_2S (2.6g in 100 mL DIW, 90%, extra pure reagent), and nanoadded until the pH of solution reached up to 7. Respective pinkish white and yellowish green powder of CdS/ZnO NRs and CdS/Co-ZnO NRs were obtained, which was washed thoroughly with hot water and dried in the oven at 60°C for 24h. [6]

3.4.2.3 Co-catalyst addition to CdS-loaded ZnO and CdS/Co-ZnO NRs surface

CdS-loaded ZnO and Co-ZnO NRs were decorated with co-catalyst (1.5% Pt) to facilitate the reduction sites on the photocatalytic surface. Impregnation method was adopted to load 1.5%Pt on CdS/ Co-ZnO and CdS-loaded ZnO surface by continuously stirring of the solution (0.2g CdS/ Co-ZnO and 0.00769g H_2PtCl_6 in 2mL deionised H_2O) in porcelain dish with glass rod, at 60°C temperature. [7] Finally, the sample dried at 60°C for 12h in oven and employed in photocatalytic reaction as nanomolecular photoelectrode.

3.4.3 RESULTS AND DISCUSSION

3.4.3.1 Study of surface morphology

As fabricated nanomolecular device (1.5% Pt/CdS/Co-ZnO NRs) was rigorously characterized at every step of fabrication process, using variety of analytic tools. Morphological images of ZnO NRs, was recorded using a field emission-scanning electron microscope (FESEM; Hitachi S-4000) after every step of advancement. High resolution transmission electron microscope (HRTEM; JEM-2100F, at 200 kV) and corresponding energy-dispersive X-ray (EDX) spectroscopy were used to know the lattice fringes and growth directions by knowing the distance between lattice fringes with and chemical camposition. Selected area electron diffraction (SAED) pattern gives the information about crystallinity product of the hydrothermal process at varying concentration of aqueous CTAB and seeds were examined by using FESEM (Figures. 3.34a, 3.34b, 3.34c, 3.34d and 3.34e). All concentrations of CTAB (17.5, 20, 25, 30, 35 and 40%) were kept greater than its critical micelle concentration (CMC; 0.95 mM) to promote one dimensional (1D) augmentation of Co-ZnO seeds. [8] According to the principle of dynamic salvation, there is a selective adsorption (electrostatic) of the cationic surfactant on the hexagonal facets i.e. (100) and (111) planes, which was also evident from HRTEM images of the Co-ZnO seeds. [9] Dissimilar rate of attachment/detachment of the surfactant on above planes, effectively reduce the energy and growth rate along these planes that allows NRs to grow along (011) plane. [10,11] Bulky cationic surfactant, CTAB plays two major roles in production of one dimensional Co-ZnO structures: (i) as a micellizer, it induces 1D molecular aggregation of micelles in aqueous medium and (ii) as a stabilizer; it stabilizes the micelle-captivated Co-ZnO nanoclusters by preventing their uncontrollable growth. Results of both of these actions collectively promote cylindrical aggregation (wormlike micelle) of ZnO or Co-ZnO seeds (scaffold by CTAB) in opposite directions with time that creates a junction in the middle of the rods (revealed from FESEM images). [12,13]
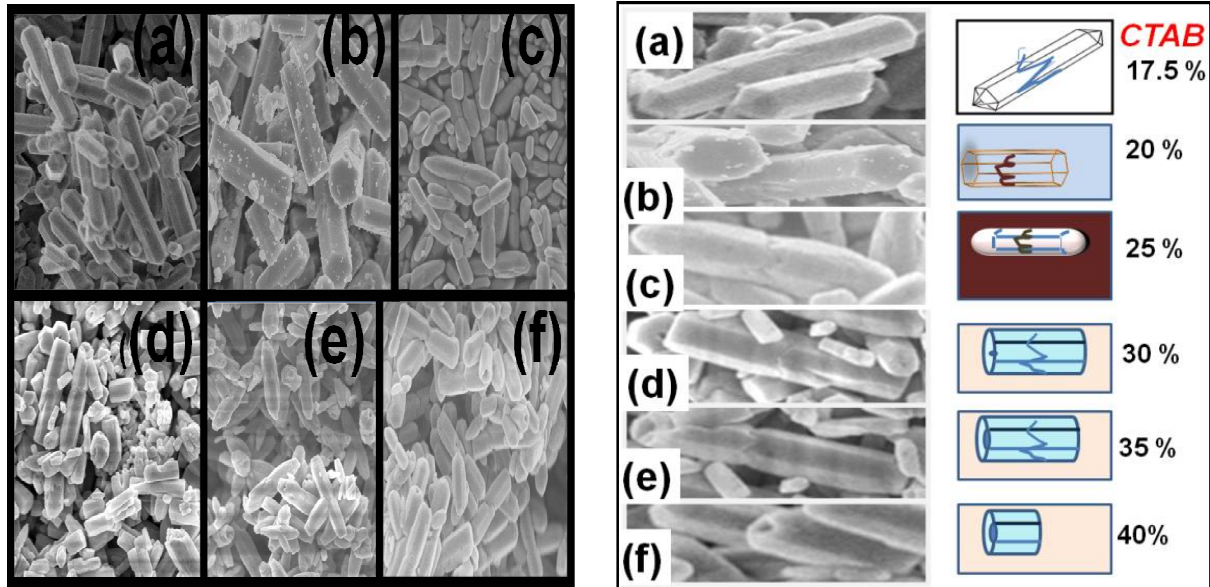
Figure 3.34 FESEM optical images of Co-ZnO at the different stages of the advancement along with their corresponding closeup SEM images of (011) plane of Co-ZnO with morphological sketches, which was fabricated using hydrothermal method on varing surfactant CTAB concentration from (a) 17.5%, (b) 20%, (c) 25%, (d) 30%, (e) 35%, and (f) 40%. Where, 4.5 cm equal to the 6 μm length of the NRs.

The growth process of NRs will continuous till the critical mass of the nanorods of ZnO or Co-ZnO was attained. Afterwards, NRs split into two parts, as illustrated in Figure 3.35e. Final size of the NRs strictly depends on the size of the reaction volume i.e. driven by the radius of the cavity in water droplets with surfactant R_w, which is expressed by the following Equation (1). [14]

$$R_w = 3\ V_{aq}\ [H_2O]/\sigma[s] \qquad\qquad .... (1)$$

Where, $\sigma[s]$ =polar group area of surfactants' head and $V_{aq}[H_2O]$ =volume of water. It means the size of the nanorod can be regulated by changing the volume of water and the polar head area of micelles (controlled by CTAB concentration). Increase in volume of water droplet directed to increase the volume of the surfactant in surfactant-incorporated water droplets. Increase in CTAB concentration tends to increase in head area of polar group. Both of these effects, contribute equally in keeping the size of the Co-ZnO NRs (~400 nm broad and 2 mm long) same even at higher CTAB concentration reactions. FESEM images (Figures 3.34a, 3.34b, 3.34c, 3.34d, and 3.34e) of the Co-ZnO nano architects fabricated at different concentrations of the CTAB and the supporting literature [15], give some significant hints about their physical growth mechanism.

Gradual morphological transformations were observed in finishing-end shape of the Co-ZnO NRs by varying CTAB amount/ concentrations.
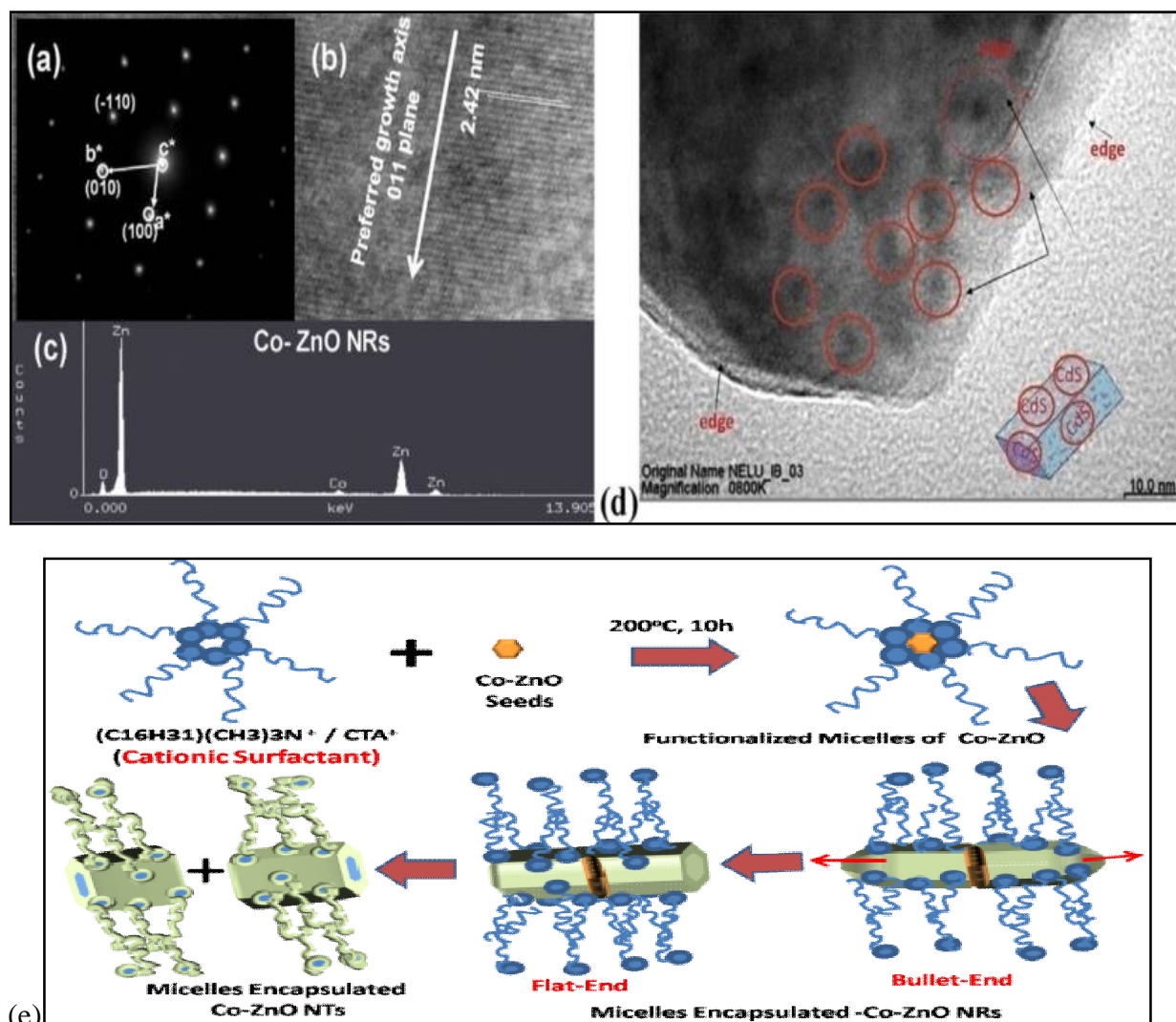
Figure 3.35 HRTEM micrographs of Co-ZnO NRs including the **(a)** SAED pattern, **(b)** lattice fringes, **(c)** EDX analysis. This shows well ordered crystalline planes along with hexagonal packing of atoms and a lattice spacing of 2.42 nm, corresponding to the growth 011-plane of Co doped-ZnO lattice and **(d)** HRTEM image of CdS nanoparticles loaded Co-doped ZnO that revealed the presence of the heterojunction between CdS and Co-doped ZnO. **(e)** Schematic gradual physical growth mechanism for hexagonal faceted Co-ZnO nanorods.

At 17.5, 20, 25, 30, 35 and 40% CTAB concentration, corresponding shuttle-end, flat end, cocoon-end (without hole), cocoon-end (with hole), cocoon-end (with big hole) and cocoon-end (with hole) hexagonal rods were obtained, respectively. Due to the apt salt/surfactant ratio (Co-

ZnO/CTAB =1:0.20) in 20% CTAB [16], the flat-end Co-ZnO NRs were produced. Beyond 20% CTAB concentration, the enhancement in CTAB concentration, promotes the formation of the excess of bromide ions by cleavage of CTAB. These bromide ions induced the chemical inching in nanooxides, which was initiated from the centre of the (011) plane of the hexagonal Co-ZnO NRs and created a hole at centre. The size of this hole increases with CTAB concentration from 50 nm (30% CTAB) to 76 nm (35% CTAB) to 98nm (40% CTAB). Further, whatever may be the concentration of CTAB was used for synthesis; almost same sized (400 nm wide and 2 mm long) hexagonal-nanorods were obtained. SAED pattern (Figure 3.35a) of flat-end Co-ZnO NRs was obtained corresponding to the HRTEM image, which evident the hexagonal orientation of the Lau's spot around central spot, proves the presence of the crystalline single hexagonal phase of the Co-ZnO NRs, which consistent with the X-ray powder diffraction (XRD) results. Lattice fringes, depicted in the HRTEM image (Figure 3.35b), are separated by 2.42 nm distance, illustrate the high crystalline nature of NRs that grow along the (011) plane. EDX profile of the Co-ZnO NRs, possess the Co and Zn peaks that confirms the Co-doping onto ZnO lattice (Figure 3.35c). Figure 3.35d exhibits the HRTEM image of the CdS loaded Co doped ZnO that revealed the presence of the hetero junction between CdS and Co-doped ZnO.

3.4.3.2 XRD analysis

X-ray diffraction patterns of the synthesized samples were recorded on Philips X'Pert MPD-3 diffractometer (mono-chromatizedradiation of Cu Kα (l =0.15418 nm), with the scan rate =0.05^{0}2θs^{-1}, at applied voltage 45 kV and current 40 mA). XRD patterns, as shown in Figures 3.36a, 3.36b and 3.36c, verify crystallization of ZnO and Co-ZnO NRs in a single wurtzite phase. Positions of the diffraction peaks of the ZnO and Co-ZnO NRs, are in good agreement with the standard JCPDS (Joint Committee on Powder Diffraction Standards) card No. 36-1451, which accounts for the hexagonal crystal growth in both samples along the 011 plane.
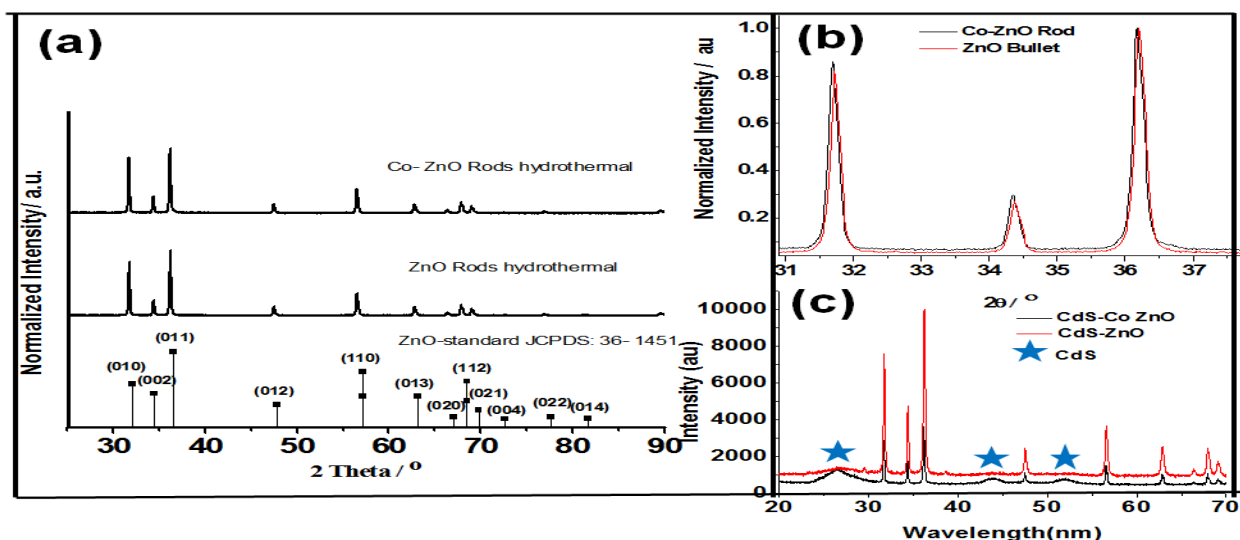
Figure 3.36 Powder XRD patterns of the **(a)** pristine ZnO and Co-ZnO NRs with respect to the standard ZnO (JCPDS card No. 036-1451) with **(b)** (100), (002) and (101) reflections highlighted between the angles 31.0 to 37.5⁰ to demonstrate the insertion of Co in ZnO lattice and **(c)** loading of CdS on ZnO and Co-ZnO surface and star sign assigned to the hexagonal CdS peaks (JCPDS No. 80-0006). First star at lowest angle represents the combined intensities of (100), (002), and (101) peaks, second and third star belongs to (110), and (112) peaks of CdS, respectively.

Diffraction patterns of the pristine ZnO and Co-ZnO NRs, shown by Figure 3.36a, confirmed that both belongs to the P63mC space group and their corresponding lattice parameters are a =b =3.1919 Å, c =5.1908 Å, a = b =90⁰, g =120⁰, at z =4, V =52.8800 Å^3 and a =b =3.1942 Å, c =5.1968 Å, a =b =90⁰, g =120⁰, at z =4, V =52.9600 Å3, respectively. Minor shifting in XRD-peaks of Co-ZnO was found towards lower angles in comparison to the pristine ZnO NRs Figure 3.36b that strongly recommends the incorporation of the slightly bigger ions i.e. Co^{2+} (IR =0.075 nm >Zn$^{2+;}$ IR =0.074 nm) in to ZnO lattice. Value of c/a ratio was estimated as 1.626 (1.633 for ideal tetrahedra) for the Co-ZnO system that reflected the hexagonal packing of the atoms by geometric occupation of ions at the dissimilar sites of slightly distorted tetrahedra. The tetrahedral positions are occupied by anions at four apices and by cations at centre. [17] Another crystal parameter b/c (u) =0.615 (0.375 for an ideal crystal), shows the existence of the anion-cation bond, parallel to the c-axis. c/a parameter follows an inversely proportional relationship with u. Therefore, on decreasing c/a value with respect to ideal tetrahedra, u adjusts itself in such a way that the four tetrahedral distances get balanced through the distortion in tetrahedral angles and distances. Prominent and sharp peak (011) around 2θ=36.26⁰, reconfirms the crystal growth along

(011) plane. Crystalline domain of the flat end Co-ZnO NRs, was calculated using Debye-Sherrer equation i.e. 385 nm, which is quite near to the average size (~400 nm) of the NRs that measured by FESEM images Figure 3.36c expressed the significantly broad XRD peaks of CdS accompanied with regular wurtzite Co-ZnO peaks, in CdS/ZnO NR's sample. In the same sample presence of the first broad peak centred at $2\theta=27^0$ is an aggregation of (100), (002), and (101) peaks of CdS, (110) peak at $2\theta=44^0$, and (112) peak at $2\theta=52.5^0$, are also in good agreement with the standard CdS (JCPDS card No. 80-0006). It proves the successful loading of the hexagonal CdS nanoparticles onto the ZnO NR's and Co-ZnO NR's surface as shown in Figure 3.36c XRD patterns of the all studied samples are shown in Figure 3.36a - 3.36c and following Equation (2) [18], is used to measure the crystallinity of the samples.

$$C_{rt}(\%) = \{(I_{011-}I_{am})/I_{011}\} \times 100 \qquad \ldots\ldots\ldots\ldots\ldots\ldots(2)$$

Where, C_{rt} = the relative crystallinity (in percentage) I_{011}=the highest intensity of the (011) diffraction angle of the crystal lattice (arbitrary unit; au) and I_{am}= is the scattering strength diffracted by the non-crystalline environment (if 2θ is close to angle $21^{0,}$ the unit is similar to I011). The observed crystallinity (ZnO NRs (95.00%), Co-ZnO NRs (94.00%), CdS-ZnO (90.00%) and CdS/Co-ZnO (78.95%) of the all studied samples is decreases with gradual modification in the basic ZnO NRs sample.

3.4.3.3 UV-Vis DRS study

Diffuse reflectance UV-visible absorption spectrum was recorded for the dry and pressed disk samples of powdered ZnO NRs to confirm the doping of Co and deposition of CdS on ZnO NRs, by using UV-visible spectrophotometer (UV-1700, Shimazdu, Japan with UV Probe device). Moisture free $BaSO_4$ was used as a reflectance standard in a UV-Vis diffuse reflectance experiment. Instrumental error was noticed around the wavelength 350 nm due to the shifting of the light source from UV to Visible region, which was found responsible for the noise. Characteristic diffuse reflectance spectra (Figures 3.37a and 3.37b) of the samples illustrate the red shifts in their edges with broadening in the main peak (300-525 nm) on successive advancement (addition of Co or CdS) in the ZnO NRs for making of the hetero-assembly CdS/Co-ZnO NRs.
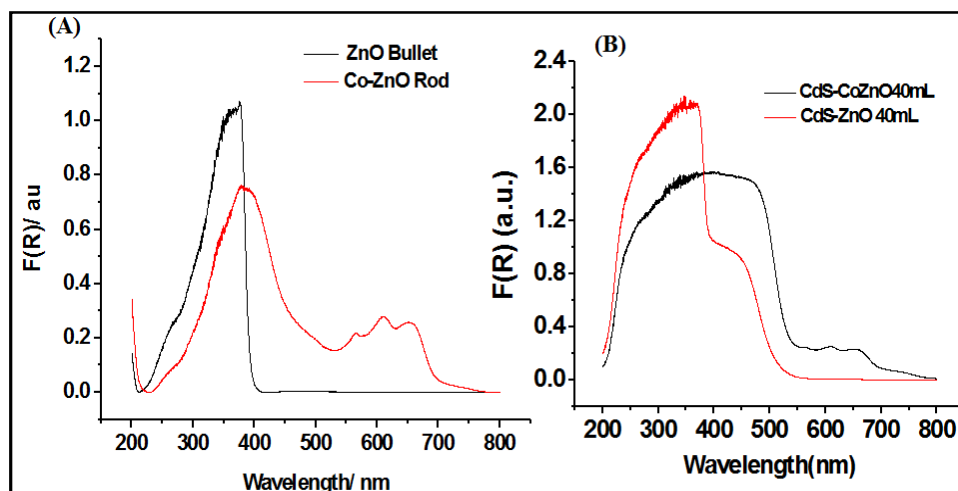
Figure 3.37 Diffuse reflectance spectroscopic Kubelka-Munk plots (F(R) vs wavelength) of pristine ZnO NRs and Co-ZnO NRs **(A)** before and **(B)** after CdS loading.

First excitation peak centred at 450 nm, represents the presence of the CdS. Co^{2+} incorporated samples (Co-ZnO NRs and CdS/Co-ZnO NRs) exhibits a secondary peak around 525 to 700 nm that is attributed to the multiple d-d transitions of Co(II) [19]. Band gap (E_g) of the studied system has been estimated at different stages of the advancement of ZnO NRs using the Kubelka-Munk function F(R) vs wavelength plot (Figures 3.37a and 3.37b). Successive surface modification of ZnO nanostructures reduces their band gaps, as follows 3.18 eV (ZnO NRs), 3.00 eV (Co-ZnO NRs), 2.48 eV (CdS/ZnO NRs) and 2.25 eV (Cd/Co-ZnO NRs). Band gap of the CdS/Co-ZnO NRs, ensures us about the good possibility of using it for photocatalytic hydrogen generation. First excitonic peak of DRS spectrum was utilized to determine the particle size of the sensitizer CdS (ca 5.24 nm) in CdS/Co-ZnO NRs by using following power Equation (3) [20],

$$D = (-6.6521 \times 10^{-8}) \lambda 3 + (1.9557 \times 10^{-4})\lambda^2 - (9.2352 \times 10^{-2})\lambda + (13.29) \ldots\ldots\ldots (3)$$

Where, D (nm) is the size of the CdS nanosensitizer in heterostructure and l (nm) is the first excitonic absorption wavelength i.e. 450 nm for the corresponding sample. It represented that the incorporation of 5.24 nm CdS nanoparticles on Co-ZnO NRs (~400 nm broad and 2 mm long).

3.4.3.4 XAS study

X-Ray absorption spectroscopy (XAS) was used to examine the local electronic environment around the centre atom. XAS (XANES/EXAFS) was recorded at BL-8 dispersive EXAFS beam line at INDUS-2 synchrotron radiation source at RRCAT, Indore. Measurements were made at the

Zn K-edge (9659 eV) in fluorescence mode at room temperature with a seven element HP Ge detector and double crystal Si (111) monochromator. Measurements were performed along the c axis perpendicular to electric field vector and along the c axis in the plane of the electric field vector. The raw X-ray absorption data were analysed using a standard procedure (software program ATHENA) that includes the subtraction of the pre- and post-edge background, edge calibration with a reference Zn foil, and normalization of edge jump. The Fourier transform of the normalized k^3-weighted EXAFS spectra was taken using the program ARTEMIS for k from 2 to 11.5 $Å^{-1}$ and Hanning window function followed by nonlinear least-squares fit between 1.0 and 3.6 Å. Theoretical phase and amplitude functions were calculated using the FEFF (V.8.4) code. This technique identifies the lattice disorders and short range local atomic arrangement around the central atoms, which XRD can't observe. [21]

XAS profiles of the ZnO, Co-ZnO and CdS/Co-ZnO NRs, were recorded at Zn K edge. Typical normalized XAS plot between X-ray absorption cross-section and photonic energy (PE) are displayed in Figure 3.38a-c. XAS profile was divided into four prominent zones with respect to the photonic energy of incoming photons i.e. pre-edge, edge, near-edge (XANES; X-rays absorption near edge spectroscopy) and fine structures (EXAFS; extended X-rays absorption fine structures and NEXAFS; near edge X-ray absorption fine structure) regions. Absence of pre-edge features (ls → 3d; dipole forbidden transition, PE < 9659 eV) in all samples is credited to the fully occupied 3 d^{10} configuration of Zn^{2+} ions [22] and negligible p-band defects. Edge features (ls → 4p) of Co-ZnO shifted towards the higher PE =9660.23 eV with respect to the pure ZnO and CdS/Co-ZnO NRs (PE < 9659 eV) are attributed to the replacement of the high polarity Zn-O bonds by the low polarity Co-O and Co-Zn bonds in Co-ZnO. Eventually, the presence of the highly polar bonds of CdS/Co-ZnO NRs i.e. Cd-O, Cd-S and Zn-S, nullified the shifting in edge. It also confirms the existence of the highly oxidized Zn atoms (>2^+ oxidation state) in Co-ZnO NRs, attributed to the adsorption process [23]. Almost same edge position of the pristine ZnO and CdS/Co-ZnO NRs, signify the retention of similar oxidation state of Zn (2^+) in both. Intense, symmetrical and superimposed white line (WL) peak features of ZnO and Co-ZnO NRs, centred

at 9668.50 eV (10.01 eV/step), are originated due to ls-4p hybridization, reflected the similar electronic surroundings in both the species. Short heighted WL peak of CdS/Co-ZnO NRs, predicts the low degree of anisotropy, and highly disordered arrangement of elements around Zn atom. Electronic transition 1s → 4d in Zn is attributed to the EXAFS features at P E ~ 9668.50 +50 eV. Shoulder peak was observed at 9678.52 eV, followed by the symmetrical third and fourth peaks at PE 9695.96 and 9714.00 eV, respectively for both sample. These fine features reflected that the anions envelop the central Zn atoms in a regular tetrahedral fashion in above two samples.
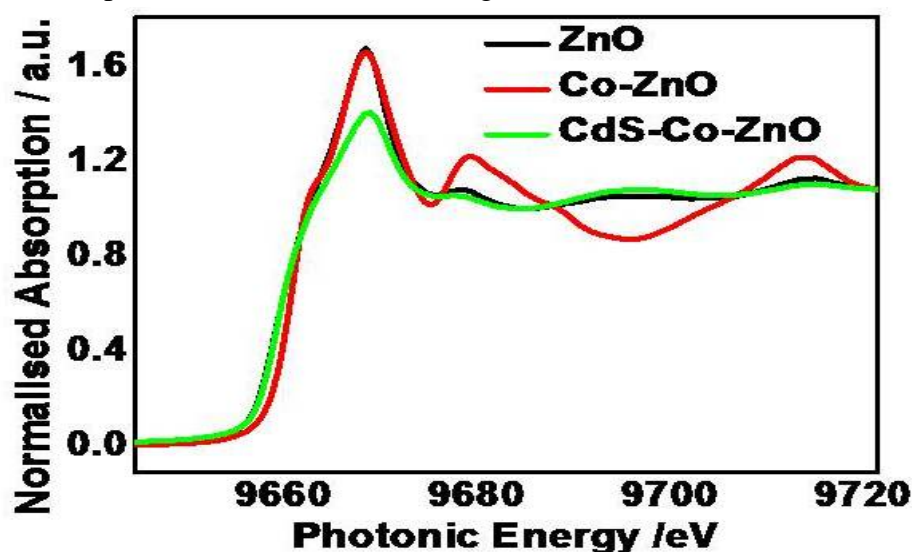
Figure 3.38 Normalized synchrotron-radiation based absorption cross section as a function of photonic energy with the geometry of the c-axis aligned parallel to the electric field vector of the x rays at the Zn K-edge (E = 9659 eV) spectra of **(a)** pristine ZnO NRs, **(b)** Co-ZnO NRs and **(c)** CdS/Co-ZnO NRs, recorded in a florescent mode.

Absence of the 9695.96 eV peak in Co-ZnO, reveals the existence of the cobalt (II) oxide with few Co atoms that substitute zinc in the ZnO system [24]. It stimulates the distorted tetrahedral surrounding around Zn and deviation in the lattice parameters. NEXAFS features for ZnO and CdS/Co-ZnO NRs, coincide within 1 eV PE range, suggesting that both have similar regular tetrahedral environment of anions for Zn atoms. The results also suggested about the distorted tetrahedral arrangement in the Co-ZnO system, where the metallic species Co (II) and Zn are at the centre of the tetrahedra and anions (O^{2-}) are situated at the four apexes of the tetrahedra.

NEXAFS features of the all examined systems were refined by keeping typical k^3- weight Age in the range of 3.5-12 $Å^{-1}$ and using software FEFF (V-7) (Figures 3.39a and 3.39b). [25] Respective refined parameters (least squares refined R-factor, mean first-shell metal- oxygen bond length, coordination number, and Debye-Waller factor) are extracted for ZnO (3.8wt%, 1.99(8) Å, 5.10 and 0.96 $\times 10^{-2}$ $Å^2$), Co-ZnO (4.10wt%, 2.01(4) Å, 5.40 and 0.82 $\times 10^{-2}$ $Å^2$) and CdS- Co-ZnO (4.20wt%, 1.95(7) Å, 5.80 and 0.86 10^{-2} $Å^2$).
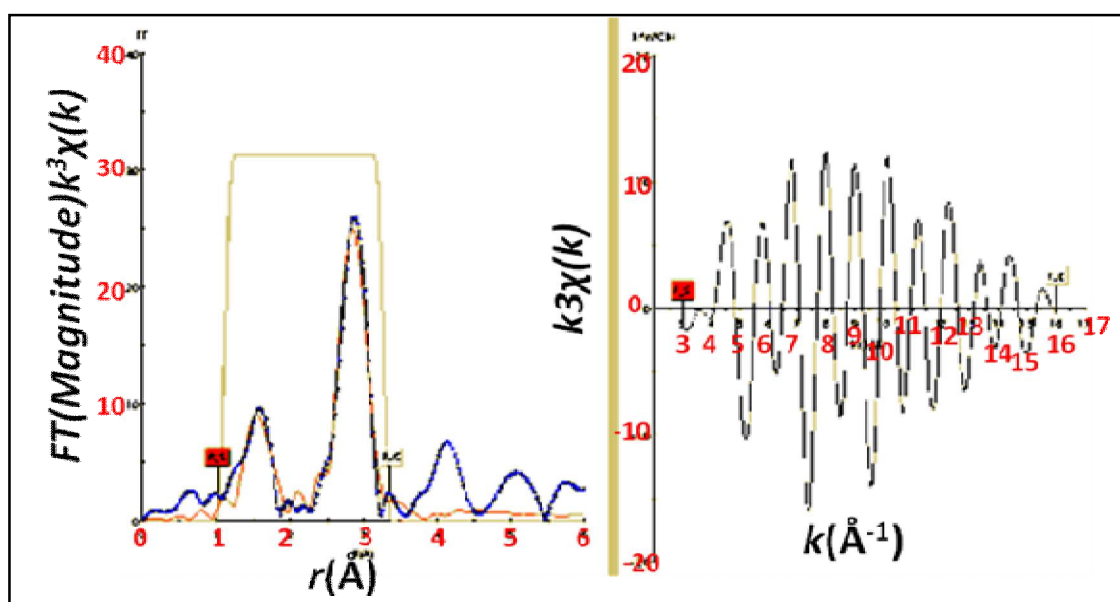
Figure 3.39 It shows the **(a)** Fourier-transformed magnitudes of the extended XAFS (EXAFS) oscillations in the Zn K-edge XAS spectra as a function of the phase-uncorrected interatomic distance R (nm), and fitting for the pure wurtzite phase of CdS/Co-ZnO NRs. The solid blue lines represent experimental data and red lines the calculated values are fits to the parameter. **(b)** The k^3-weighted EXAFS $Å^{-1}$) corrected for phase shifts.

3.4.4 CONCLUSION

Current work is focused on the surfactant (CTAB)-controlled low cost fabrication of the ZnO NRs via reverse-micelles synthesis. This study gives us and focused on the performance of the nanomolecular photoelectrode of ZnO NRs by gradual surface modification for hydrogen production efficiency. A good correlation between atomic arrangement around Zn atom and light harvesting capacity of the modified ZnO NRs has been established. Defects developed on Co-ZnO

NR's surface, may act as recombination centres for the photocarriers. These defects were suppressed by the decoration of flat-end Co-ZnO NRs with visible light sensitizer CdS. Heterocouple Cds/Co-ZnO NRs, show a good compatibility of nanoparticles of CdS with Co-ZnO NRs.

3.4.5 REFERENCES

[1] N Chouhan, L Yeh, SF Hu, RS Liu, WS Chang, KH Chen, "CdSe(QDs)@ ZnO nanotubes as an effective photoanode" *Chem Commun* **(2011),** 47: 3493-5.

[2] XH Wang, YC Zhang, WL He, MK Zhu, B Wang, H Yan, "Hydrothermal synthesis of zinc oxide powders with controllable morphology" *Ceram Int* **(2004),** 30: 93-7

[3] A Wolcott, WA Smith, TR Kuykendall, YP Zhao, JZ Zhang, "Photoelectrochemical generation of hydrogen from water splitting based on dense and aligned TiO_2 nanorod arrays" *Small* **(2008),** 5 (1): 104-11.

[4] JF Reber, K Meier, "Photochemical hydrogen production with platinized suspensions of cadmium sulfide and cadmium zinc sulfide modified by silver sulphide" *J Phys Chem* **(1986),** 90 (5): 824-34.

[5] D Chu, YP Zeng, DL Jiang, "Hydrothermal synthesis and optical properties of Pb^{2+} doped ZnO nanorods" *Mater Lett* **(2006),** 60: 2783-5.

[6] G Larramona, C Chone, A Jacob, D Sakakura, B Delatouche, D Pere, "Nanostructured photovoltaic cell of the type titanium dioxide, cadmium sulfide thin coating, and copper thiocyanate showing high quantum efficiency" *Chem Mater* **(2006),** 18 (6): 1688-96.

[7] X Wang, G Liu, GQ Lu, HM Cheng, "Stable photocatalytic hydrogen evolution from water over ZnO-CdS coreeshell nanorods" *Int J Hydrogen Energy* **(2010),** 35: 8199-205.

[8] HC Gao, RX Zhu, XY Yang, SZ Mao, S Zhao, JY Yu, "Properties of polyethylene glycol (23) lauryl ether with cetyltrimethylammonium bromide in mixed aqueous solutions studied by self-diffusion coefficient NMR" *Colloid Interface Sci* **(2004),** 273(2): 626-31.

[9] YD Yin, AP Alivisatos, "Colloidal nanocrystal synthesis and the organic inorganic interface" *Nature* **(2005),** 437: 664-70.

[10] E Faeibold, B Michels, G Waton, "Micellar growth study by micocalorimetry in CTAB solutions" *J Phys Chem* **(1996),** 100: 20063-7.

[11] PJ Missel, NA Mazer, MC Carey, GB Benedek, "Influence of alkali-metal counterion identity on the sphere-to-rod transition in alkyl sulfate micelles" *J Phys Chem* **(1989),** 93: 8354-66.

[12] H Rehage, H Hoffmann, "Rheological properties of viscoelastic surfactant systems" *J Phys Chem* **(1988),** 92: 4712-9.

[13] G Porte, J Appell, J Poggi, "Experimental investigations on the flexibility of elongated cetylpyridinium bromide micelles" ***J Phys Chem*** **(1980),** 84(23): 3105-10.

[14] J Appell, G Porte, A Khatory, A Kern, SJ Candau, "Static and dynamic properties of a network of wormlike surfactant micelles (Cetylpyridinium chlorate in sodium chlorate brine)" ***J Phys II*** **(1992),** 2(5): 1045-52.

[15] M Pileni, "Reverse micelles as microreactors" ***J Phys Chem*** **(1993),** 97(27): 6961-74.

[16] WJ Kim, SM Yang, "Preparation of mesoporous materials from the flow-induced microstructure in aqueous surfactant solutions" ***Chem Mater*** **(2000),** 12: 3227-35.

[17] H Karzel, W Potzal, M Kofferlein, W Schiessl, M Steiner, U Hiller, "Lattice dynamics and hyperfine Interactions in ZnO and ZnSe at high external pressures" ***Phys Rev, B Condens Matter*** **(1996),** 53: 11425-39.

[18] N Chouhan, CC Lin, S-F Hu, R-S Liu, "Earth-free GaZnON phosphor prepared by combustion for white light-emitting diodes" ***J Mater Chem C*** **(2015),** 3: 1473-9.

[19] (a) X Qiu, M Miyauchi, H Yu, H Irie, K Hashimoto, "Visiblelight- driven Cu(II)-($_{Sr1-y}$Nay)(Ti$_{1-x}$Mox)O$_3$ photocatalysts based on conduction band control and surface ion modification" ***J Am ChemSoc*** **(2010),** 132: 15259-67. (b) H Yu, H Irie, K Hashimoto. "Conduction band energy level control of titanium dioxide: toward an efficient visible lightsensitive photocatalyst" ***J Am Chem Soc*** **(2010),** 132: 6898-9. (c) H Irie, K Kamiya, T Shibanuma, S Miura, DA Tryk, T Yokoyama. "Visible light-sensitive Cu(II)-grafted TiO$_2$ photocatalysts: activities and x-ray absorption Fine structure analyses" ***J Chem Phys C*** **(2009),** 113: 10761-6.

[20] WW Yu, L Qu, W Guo, X Peng, "Experimental determination of the extinction coefficient of CdTe, CdSe, and CdS nanocrystals" ***Chem Mater*** **(2003),** 15: 2854-60.

[21] JJ Rehr, RC Albers, "Theoretical approaches to x-ray absorption fine structure" ***Rev Mod Phys*** **(2000),** 72(3): 621-54.

[22] WJ Kim, SM Yang, "Preparation of mesoporous materials from the flow-induced microstructure in aqueous surfactant solutions" ***Chem Mater*** **(2000),** 12: 3227-35.

[23] T Yamamoto, "Assignment of pre-edge peaks in k-edge x-ray absorption spectra of 3d transition metal compounds: electric dipole or quadurpole?" ***X-Ray Spectrom*** **(2008),** 37: 572-84.

[24] S Krishnamurthy, C Guinness, LS Dorneles, M Venkatesan, JMD Coey, JG Lunney, "Soft x-ray spectroscopic investigation of ferromagnetic co-doped ZnO" ***J Appl Phys*** **(2006),** 99 08M111, 3 pages.

[25] EA Stern. Theory of EXAFS. In: DC Koningsberger, R Prins, "X-ray absorption: principles, applications, techniques of EXAFS, SEXAFS and XANES" ***New YorkWiley-Interscience*** **(1988),** Ch. 8.618-708.

Chapter 4

Applications of the synthesized systems in Chapter 3:

4.1 Pt/Ag/ZnO NRs and Pt/CdS/ZnO NRs for Water Splitting

4.2 Ag NPs used for Pollutant P-Nitro Phenol (PNP) Degradation into P-Amino Phenol
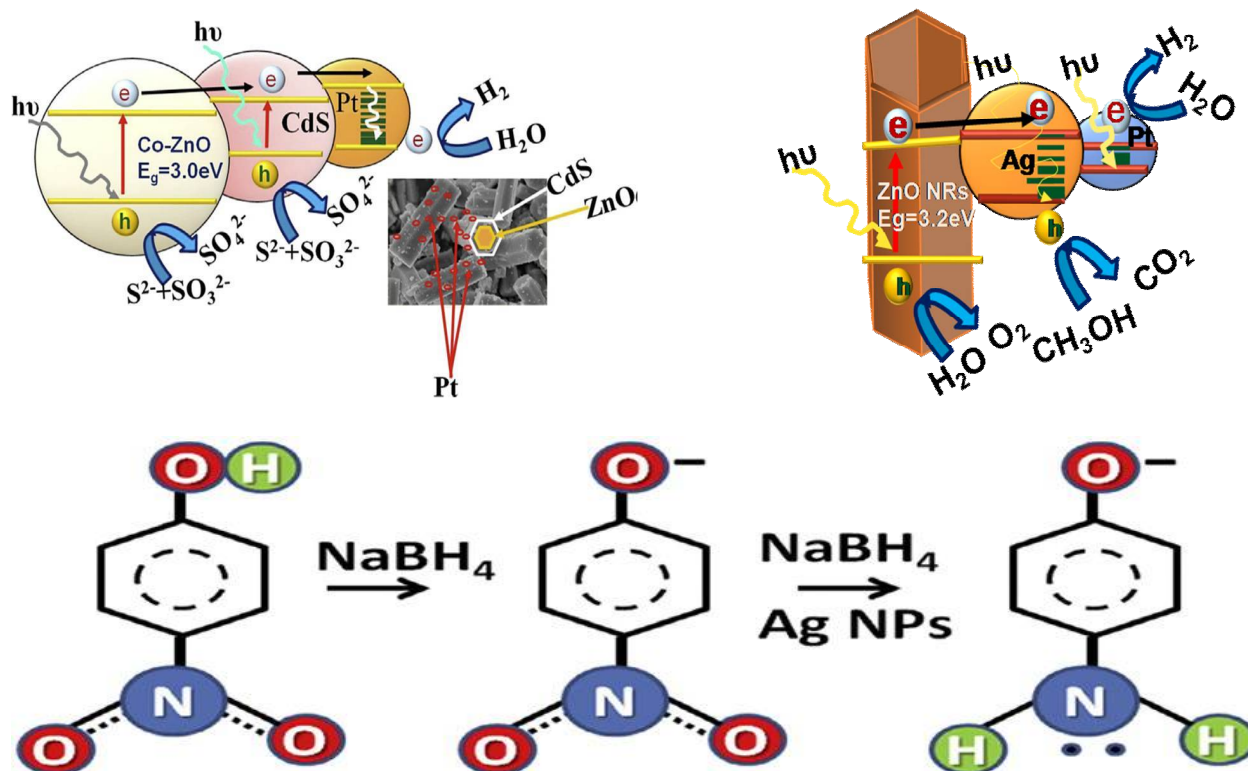
Chapter 4

4.1 Pt/Ag/ZnO NRs and Pt/CdS/ZnO NRs for Water Splitting

ABSTRACT

We had utilised the all as-synthesized systems in Chapter 3 for photocatalytic water splitting and hydrogen generation. These systems are Pt/Ag NPs @ ZnO NRs with four different AgNPs and Pt/CdS@ZnO NRs as molecular devices. Electron sacrificial electrolyte CH_3OH (pH=7.0) and $Na_2S+K_2SO_3$ solution (pH =13.5), were used for above mentioned systems under the irradiation of AM1.5 G light for four or seven hours, respectively. The Pt/Ag NPs @ ZnO NRs systems show amount of hydrogen release as: Pt/Ag(TA)@ZnO (204.60 mol h^{-1} g^{-1}), Pt/Ag(AC)@ZnO (78.1580 mol h^{-1} g^{-1}), Pt/Ag(Tea)@ZnO (33.9639 mol h^{-1} g^{-1}) and Pt/Ag(FG)@ZnO (27.7400 mol h^{-1} g^{-1}). A nice correlation was established between the first excitation UV-Vis peak of Ag NPs, particle shape and size of AgNPs (all samples had the same ZnO NRs) with the hydrogen production efficiency of the molecular device. In another case of Pt/CdS/Co-ZnO NRs, the defects developed on Co-ZnO NR's surface, may act as recombination centres for the photocarriers. And after the decoration of the Co-ZnO NR's with the visible light sensitizer CdS, the concentration of the defects on the flat-end Co-ZnO NRs was suppressed. In a heterocouple CdS/Co-ZnO NRs, a good compatibility of nanoparticles of CdS with Co-ZnO NRs, is found. Gradual increase in the photocatalytic hydrogen evolution activity of the devices was monitored with surface modification, such as 1.5% Pt/ZnO (10.20 mmol/hg, AQY =0.30%), 1.5% Pt/Co-ZnO (22.56 mmol/hg, AQY =0.66%), 1.5% Pt/CdS/ZnO (50.57 mmol/hg, AQY =1.49%) and 1.5% Pt/CdS/Co-ZnO NRs (67.20 mmol/hg, AQY = 1.98%).

Key words: Pt/CdS@Co-ZnO, Pt/Ag NPs @ ZnO NRs Electron sacrificial electrolyte CH_3OH (pH=7.0), $Na_2S+K_2SO_3$ solution (pH =13.5), photocatalytic water splitting, hydrogen generation.

4.1.1 INTRODUCTION

Hydrogen is the most compatible and clean fuel on the planet in terms of energy economy and ecological health of the planet. [1-3] Unfortunately, the large amount of the H_2 is produced by the carbon containing conventional fuel resources that release the enormous amount of CO_2 in atmosphere. Beside this, nature has provided us a carbon - free abundant source of hydrogen in form of water at almost free of cost. Cleavage of water in presence of the photocatalyst (a semiconductor of appropriate band gap) and sunlight can produce the hydrogen in an eco-friendly manner. Although, the sunlight and water comes free of cost to us but the fabrication cost, stability and efficiency of the photocatalysts are the main thrust areas for the large scale hydrogen production. At some extent oxide photocatalysts (ZnO, TiO_2, Ga_2O_3, Nb_2O_3, In_2O_3 Fe_2O_3, SnO_2, WO_3, NiO, etc) were found fit in above criteria. Out of the commercially available wide range of oxide semiconductors, ZnO [4,5] has been selected for the study because of its superb and unique inherent qualities such as low cost, wide availability, viability to change in morphology, large excitonic binding energy (60 Me V), deep photon penetration, short diffusion length, low reflectivity, high carrier mobility, good bio-compatibility, etc. Usually, the nanostructures of ZnO have a large degree of charge transfer over their bulk counter part that is due to their large surface area to volume ratio, short lateral diffusion length and low reflectivity.[6] Few of the notable ZnO systems that accounts for photocatalytic water splitting are : N-doped ZnO nanowires ($\eta=4\%$),[7] CdTe sensitized ZnO nanorods ($\eta=1.98\%$),[8] CdSe sensitized ZnO nanotubes, [4] GaN-ZnO ($\eta=5.2\%$), [9] ZnS-ZnO core-shell (STH =0.38%), [10] TiO_2 shell ZnO core NPs ($\eta=0.17\%$),[11] $ZnO/ZnO/Cr$,[12] Si/ZnO core shell nanowires ($\eta=0.035\%$), [13] ZnO and Fe_2O_3 modified TiO_2 fibers (0.12 ml/min mg), [14] etc. Furthermore, the doping of transition metals to the semiconductors, used to improve the optical output of these photocatalytic materials. The effect of the different transition metals (Fe, Co, Ni, Cu, Zn, In, etc) on the photocatalytic activity of oxide semiconductor was studied for splitting of water into hydrogen and oxygen under UV irradiation. [15,16] In nonoxide semiconductor category, nanocomposite Ni-doped InN/GaZnON and Ni-doped CdS nanoparticles are a good example of the semiconductor that release 2.23 mmol $h^{-1}g^{-1}$ and 25.848 mmol/(h g) of H_2, respectively, under visible light irradiation. [17,18] Hence, cobalt doping was employed to modify the surface quality of ZnO. Therefore, it was decided to synthesize nanostructures of ZnO and Co-doped

ZnO systems for water splitting and hydrogen generation. Consequently, the hydrothermal method, [5] was adopted to develop one dimensional (1D) nanorods (NRs) of Co-ZnO by controlling the surfactant (CTAB; cetyltrimethylammonium bromide) concentration in water. Unluckily, neither the ZnO NRs nor Co-ZnO NRs, can able to exploit the sunlight fully due to their wide band gap (WBG) i.e. Eg = 3.2 eV. More often the hetero-assemblies (by incorporation of the visible light harvesting moiety to oxides) are made by introducing better light harvesting material (chalcogenide quantum dots/dyes) to nanooxide systems that to enhance their light harvesting capacity. A small amount of the state of art hetero-assemblies are mentioned here i.e. $H_4Nb_6O_{17}$/CdS, Pt/TiO_2/Zn-porphyrin, ZnO/Erythrosine, $Pt/SrTiO_3$:Rh/$BiVO_4$, Fe_2O_3/WO_3, ZnO/CdSe, TiO_2/CdS, etc, which was also used for water splitting. [19-28] These heterostructures exhibit excellent stability, capability to utilize the wide portion of the visible light, and suppress the recombination of the light generated photo-electrons and photo holes. For this reason, we had synthesised the following systems: (i) AgNPs@ZnONRs and (ii) chalcogenide CdS (Eg=2.4 eV) sensitized ZnO or Co-ZnO NRs, for hydrogen generation using photocatalytic water splitting. Additionally, 1.5% Pt was loaded as co-catalyst to generate reduction sites for consuming the photoelectrons at the surface of Ag@ZnO and CdS/Co-ZnO NRs. Then this nanomolecular machines i.e. 1.5% Pt/Ag@ZnO NRs (four systems with different Ag produced AgNPs) and 1.5% Pt/CdS/Co-ZnO NRs, were utilized for photocatalytic water cleavage, in aqueous electrolyte (0.35 M Na_2S +0.25 M K_2SO_3 at pH =13.3 for CdS sensitizer or 20% CH_3OH for Ag with LSPR) under 300W Xe light source irradiation. [29]

4.1.2 EXPERIMENTAL
4.1.2.1 Synthesis of Photocatalyst for water splitting

Here, we synthesised and characterised the five different systems i.e. (i) Ag(TA)@ZnO (ii) Ag(Fenugreek)@ZnO (iii) Ag(Tea)@ZnO (iv) Ag(Acacia Concinna/Shikakai)@ZnO and (v) CdS@Co-ZnO, those methods are discussed in detail in Chapter 3. In which, we had first prepared Ag nanoparticles with four different routes along with ZnO, Co-doped ZnO, CdS@ Co doped ZnO. Afterwards, Ag@ZnO and CdS@ZnO, will be made by (loading of Ag NPs on ZnO NRs and CdS NPs on ZnO/Co-ZnO NRs) impregnation method.

4.1.2.2 Photocatalytic hydrogen production

The catalyst (0.3 g) was suspended in 120 mL of aqueous electrolyte (0.35 M Na_2S +0.25 M K_2SO_3 at pH =13.3 for CdS sensitizer or 20% CH_3OH for Ag with LSPR) in a double walled-Pyrex glass reaction cell (volume ~120 mL, with water jacket) that was sealed with a rubber septum. To expel the air content from the solution, the sample was purged with Ar for 1 h prior to start the photochemical reaction. Ar gas flows continuously in inner jacket, to maintain 1 atm pressure of the solution. Temperature of the outer jacket was set at 25^0C. The suspension was irradiated with a 300 W Xe lamp (>420 nm, light intensity 1×10^{22} photons per hour Xe lamp-HX1, Model PE300UV, ISS, USA). All the experiments are carried out under ambient conditions. Photocatalytic responses were hourly monitored in terms of the amount of hydrogen generated at 1-7h time intervals, using gas chromatograph (Shimazdu, Japan, thermal conductivity detector and molecular sieve with 5 A columns) throughout the course of the reaction. Photocatalytic cleavage of water was carried out in presence of the hole-scavenger electrolyte (0.35 M Na_2S + 0.25 M K_2SO_3 at pH =13.3 for CdS sensitizer or 20% CH_3OH for Ag with LSPR in pH=7.0 solution), under the irradiation of 1 Sun (100 mW/cm^2, AM1.5 G) visible light, as demonstrated in the Figure 1.
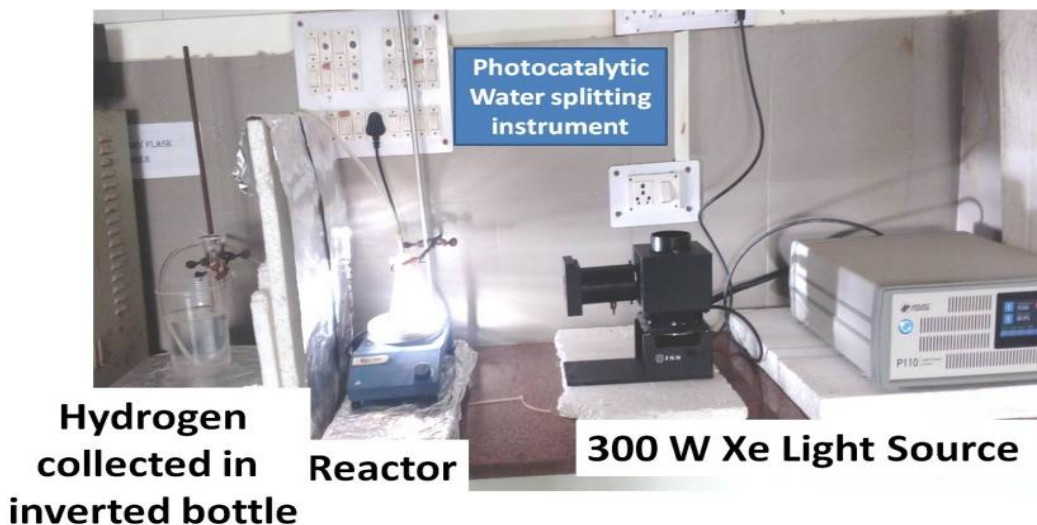
Figure 1 Instrumental set up for hydrogen generation through water splitting.

Ideal gas equation is used to calculate the number of moles of the hydrogen released since the hydrogen gas has very small density, it is usually not practical to collect the gas and find its

mass. For gases that are not particularly soluble in water, it is possible to collect the evolved gas by displacement of the water from a container. The setup for the collection of a gas over water involves a gas collection container that filled with water and inverted over a reservoir of the water. The gas evolved from the reaction is collected by attaching one end of a hose to the reaction container and inserting the other up into the inverted gas collection graduated bottle. As the gas is created, it will displace water from the bottle. The volume of gas can be determined by the amount of water that was displaced by the gas. The volume of gas collected and the gas laws (equation 1) can be used to calculate the number of moles of gas collected.

$$PV = nRT \qquad \ldots\ldots\ldots\ldots (1)$$

Where: P = Pressure of the gas, V = Volume of water displaced, n = number of moles of gas, R = the ideal gas constant and T = the temperature of the gas.

4.1.3 RESULT AND DISCUSSION

Rough and hexagonal crystalline surface of the Ag@ZnO and CdS/Co-ZnO, was loaded with co-catalyst (Pt) to facilitate the active sites for the oxidation (photo hole rich) and reduction (photoelectron rich) of water. These active sites suppress the recombination of the photoelectric current carriers i.e. photoelectrons and photo holes. Hole-scavenger electrolyte was used to avoid the photooxidation of CdS or Ag nanoparticles present in the nanomolecular device by the irreversible consumption of photogenerated holes that prohibited the oxidation of water. [30] We had examined below mentioned total four systems i.e. (i) Ag (Trachyspermum Ammi)@ZnO (ii) Ag (Trigonella foenum graecum/Fenugreek)@ZnO (iii) Ag (Tea)@ZnO (iv) Ag (Acacia Concinna/Shikakai)@ZnO and (v) CdS@Co-ZnO and discussed in detail.

4.1.3.1 Ag(TA)@ ZnO NRs

Nanocomposite Ag(TA)@ ZnO NRs (0.30g) was homogeneously dispersed in 20% methanol (hole scavenger electrolyte) and exposed to the 300W Xe lamp for photocatalytic water splitting that leads to generate the hydrogen gas, which was half hourly checked in terms of the amount of

the hydrogen released continuously for 4 hours. Pristine ZnO NRs were modified in terms of four following stages i.e. ZnO NRs, Pt/ ZnO NRs, Ag(TA)@ZnO NRs and Pt/Ag(TA)@ZnO NRs. Their corresponding release of hydrogen was monitored as: 5.0000, 13.5037, 102.3000 and 204.6000 mol $h^{-1}g^{-1}$ and shown by the Figure 2.
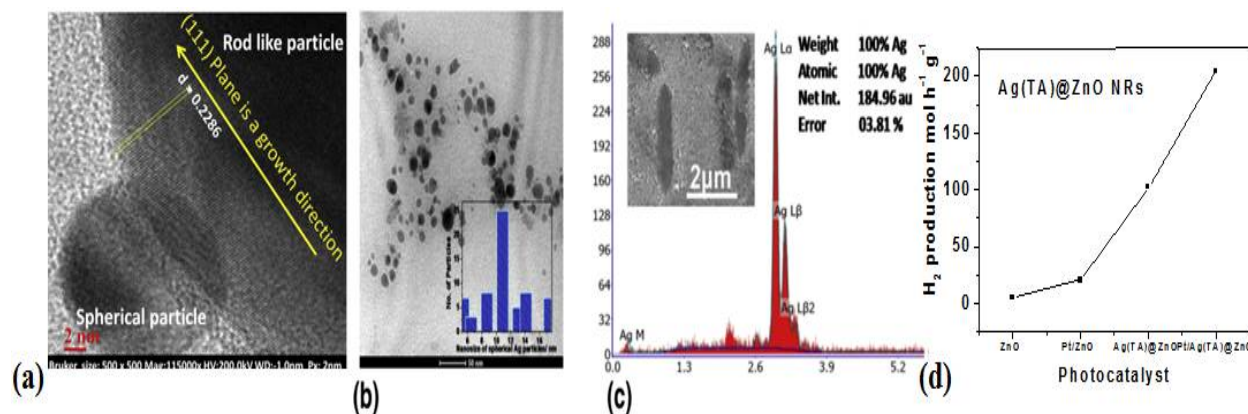
(a) Figure 2 Ag(TA)@ ZnO NRs **(a)** HRTEM image with lattice fringes, **(b)** TEM image along with particle size distribution **(c)** EDX profile along with long particle at inset. **(d)** Comparative water splitting efficiency of the ZnO NRs, Pt/ ZnO NRs, Ag(TA)@ZnO NRs and Pt/Ag(TA)@ZnO NRs.

4.1.3.2 Ag(Fenugreek)@ ZnO NRs

Nanocomposite Ag(Fenugreek)@ ZnO NRs (0.30g) was well dispersed in 20% methanol (hole scavenger electrolyte) was mixed and exposed to the 300W Xe lamp for photocatalytic water splitting that leads to generate the hydrogen gas, which was half hourly checked in terms of the amount of the hydrogen released continuously for 4 hours. Pristine ZnO NRs were modified in terms of the following four stages i.e. ZnO NRs, Pt/ ZnO NRs, Ag(FG)@ZnO NRs and Pt/Ag(FG)@ZnO NRs. Their corresponding release of hydrogen was monitored as: 5.0000, 13.5037, 20.4670, and 27.7400 mol $h^{-1}g^{-1}$ and shown by the Figure 3.
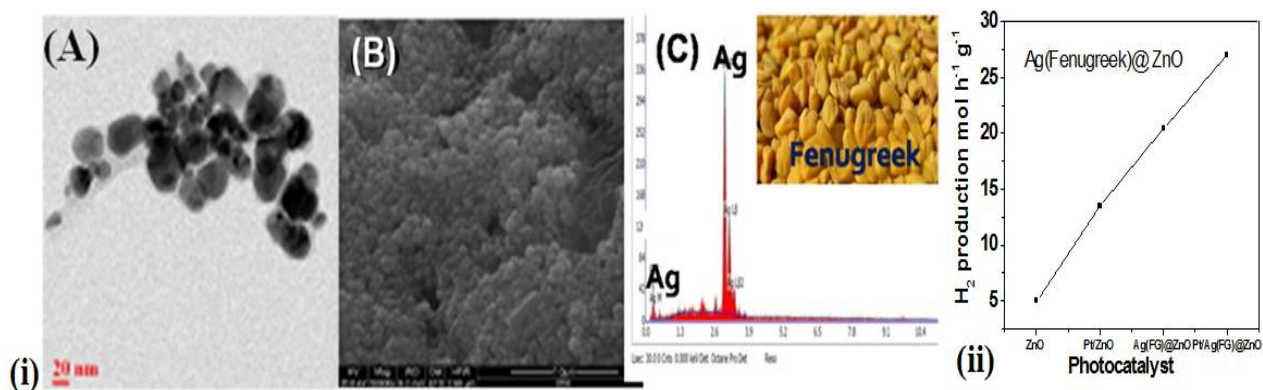
Figure 3 Comparative water splitting efficiency of the ZnO NRs, Pt/ ZnO NRs, Ag(TA)@ZnO NRs and Pt/Ag(TA)@ZnO NRs.

4.1.3.3 Ag(Tea)@ZnO

Nanocomposite Ag(Tea)@ ZnO NRs (0.30g) was equally dispersed in 20% methanol (hole scavenger electrolyte) by stirring the solution and exposed to the 300W Xe lamp for photocatalytic water splitting that leads to generate the hydrogen gas, which was half hourly observed in terms of the amount of the hydrogen released continuously for 4 hours. Pristine ZnO NRs were modified in terms of following four stages i.e. ZnO NRs, Pt/ ZnO NRs, Ag(FG)@ZnO NRs and Pt/Ag(FG)@ZnO NRs. Their corresponding release of hydrogen was monitored as 5, 13.5037, 20.467 and 33.9639 mol $h^{-1}g^{-1}$ and shown by the Figure 4. The silver ions reduced to nano silver and show characteristic UV-Vis absorbtion peak at and 412nm 420 nm. size distribution around 7-8 nm, (Figures 4a, 4b and 4c).
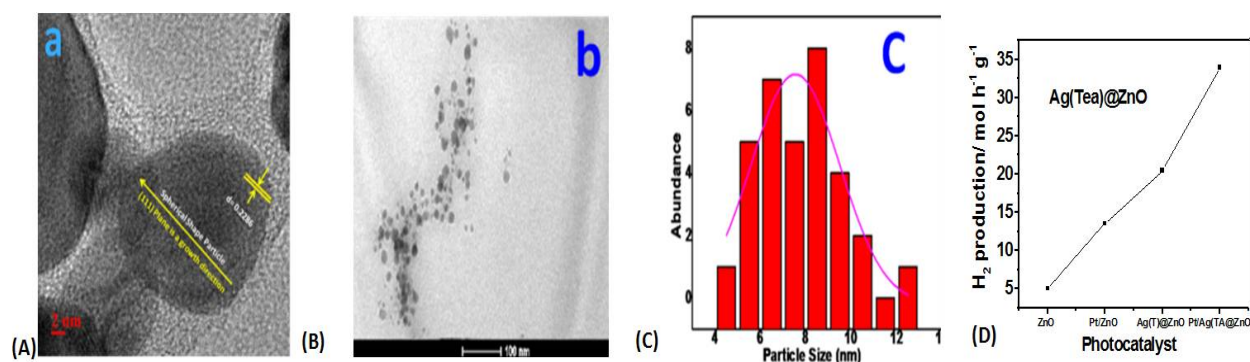
Figure 4 (a) Particle size distribution along with HRTEM and TEM images and **(b)** comparative water splitting efficiency of the ZnO NRs, Pt/ZnO NRs, Ag(Tea)@ZnO NRs and Pt/Ag(Tea)@ZnONRs.

4.1.3.4 Ag(Acacia Concinna)@ZnO

Nanocomposite Ag(Acacia Concinna)@ ZnO NRs (0.30g) was equally dispersed in 20% methanol (hole scavenger electrolyte) and irradiated with the 300W Xe lamp for photocatalytic water splitting that leads to generate the hydrogen gas, which was half hourly monitored in terms of the amount of the hydrogen released continuously for 4 hours. Pristine ZnO NRs were modified in terms of the following four stages i.e. ZnO NRs, Pt/ ZnO NRs, Ag(FG)@ZnO NRs and Pt/Ag(FG)@ZnO NRs. Their corresponding release of hydrogen for above systems was monitored as: 5.000, 13.5037, 61.3800 and 78.1580 mol $h^{-1}g^{-1}$ and shown by the Figure 5.
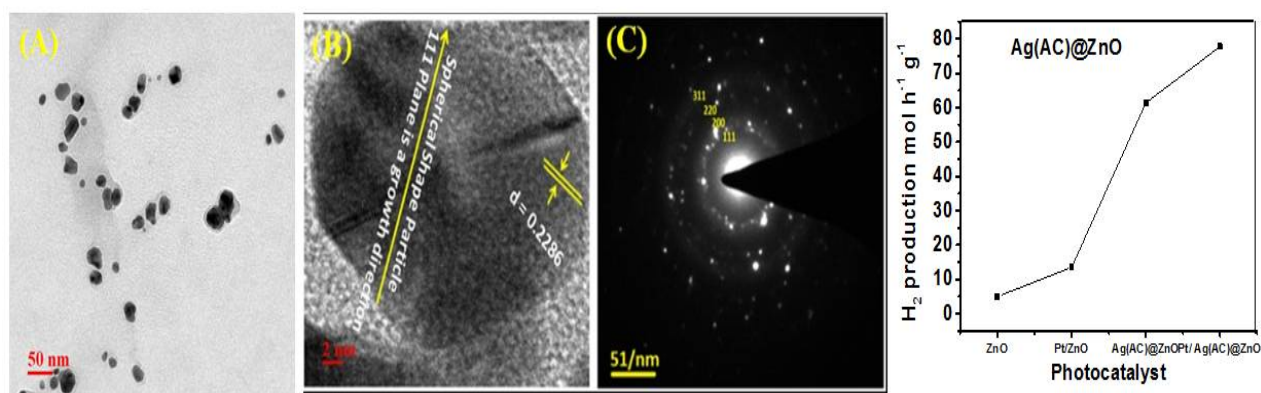
Figure 5 .TEM, HRTEM images and SAED pattern of the Acacia Concinna supported Ag NPs comparative water splitting efficiency of the ZnO NRs, Pt/ZnO NRs, Ag(TA)@ZnO NRs and Pt/Ag(TA)@ZnO NRs.

4.1.3.5 Water splitting mechanism for the all molecular photocatalytic devices i.e. Ag@ ZnO systems

When the sunlight falls on the surface of the molecular photocatalytic devices i.e. Pt loaded Ag@ ZnO then the electron (energised from sunlight) jumped from the valance band to conduction band. This process leads to enrich the conduction band with electrons and left valance band with high concentration of holes. Electrons of the conduction band (ZnO) flow towards the surface of the AgNPs presented at the surface of ZnO and ultimately come to the Pt surface and holes stay at valance band. The separation of the carriers leads to reduce and oxidise the water as hydrogen and oxygen-gases production, respectively via water splitting process. Here, cocatalyst (Ag) supported ZnO works as anode and Pt (co- cocatalyst) act as a cathode.

(a)

(b)
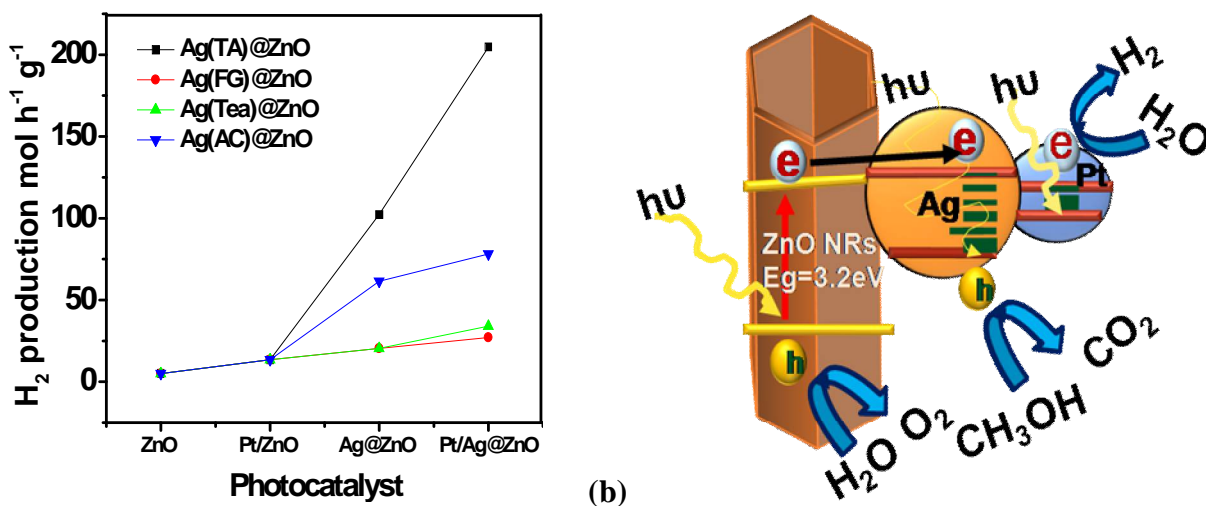
Figure 6 Photocatalytic hydrogen production via water splitting of Ag @ZnO NRs using different type of Ag NPs where, silver nanoparticles stands for **(i)** Ag NPs (Trachyspermum Ammi)@ZnO NRs **(ii)** Ag NPs (Trigonella foenum graecum/ Fenugreek)@ZnO NRs **(iii)** Ag(Tea) NPs @ZnO NRs **(iv)** Ag(Acacia Concinna/Shikakai)@ZnO NRs. **(b)** Electron transfer mechanism for Ag NPs @ZnO NRs systems that applied for water splitting.

As per electron transfer mechanism predicted in Figure 6b, it is demonstrated that the holes induced the oxidation of methanol (sacrificial electrolyte) at nanorods of ZnO and Ag surface, where Pt surface induced the reduction of water to generate hydrogen.[2, 4] The system wise results are shown in Table 1. In looking the results that shown in Table 1 and Figure 6a, it can be predicted that the Pt/Ag(TA)@ZnO show the highest efficiency in terms of hydrogen production (204.60/ mol h^{-1} g^{-1}). Afterwards, the efficiency order follows the following order: Pt/Ag(AC)@ZnO (78.1580 mol h^{-1} g^{-1}), Pt/Ag(Tea)@ZnO (33.9639 mol h^{-1} g^{-1}) and Pt/Ag(FG)@ZnO (27.7400 mol h^{-1} g^{-1}). Position of first excitation peak with the particle shape and size are important to correlate the efficiency of the molecular device. Therefore, we can conclude as the higher the position of first excitation peak on wavelength and lower the particle size can result in the high efficiency of hydrogen generation.

The tentative chemical reactions responsible for hydrogen evolution by photocatalytic cleavage of the water, are given by the Equations (2-5), under the 300 W Xe light exposure:

$$Pt/Ag@ZnO + hv(radiation) \rightarrow e^{-}(Pt/Ag@ZnO) + h^{+}(ZnO@Ag/Pt) \tag{2}$$

$$Cathode\ (Pt/Ag@ZnO)\ 2H_2O + 2e^{-} \rightarrow 2OH^{-} + H_2 \tag{3}$$

$$Anode\ (ZnO@Ag/Pt)\ CH_3OH + 2OH^{-} + H_2O + 6h^{+} \rightarrow CO_2 + 2H_2O + 4H^{+} \tag{4}$$

$$6\ OH^{-} + CH_3OH + 6H^{+} \rightarrow HCHO + HCOOH + H^{+} \tag{5}$$
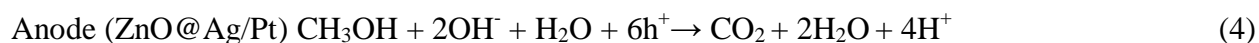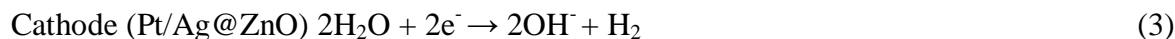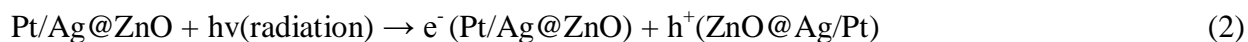
Table 1 A correlation between the various parameters of molecular device and their corresponding hydrogen generation.

S. L.	Type of silver nanoparticles	Particle size	Shape of the particle	Position of 1st excitonic peak	Hydrogen generated with Pt/ AgNPs@ ZnONRs / mol h^{-1} g^{-1}
1.	Ag(Ajwain)	12.478	Cubic + Rods	446 nm	204.6000
2.	Ag(Fenugreek)	13.420	Spherical	425 nm	27.7400
3.	Ag(Tea)	7.0 - 8.000	Spherical	420 nm	33.9639
4.	Ag(Shikakai)	23.420	Hexagonal top shaped structure	436 nm	78.1580

All of above systems show good hydrogen generation quality of course without any noticeable degradation in the photocatalytic devices.

4.1.3.6 Pt/CdS@Co-ZnO

Nanocomposite heteromolecular devices of Pt/CdS@Co-ZnO at their different stages of advancement, 1.5% Pt/ZnO, 1.5% Pt/Co-ZnO, 1.5% Pt/CdS/ZnO and 1.5% Pt/CdS/Co-ZnO, was documented exhibits the corresponding amount of H_2 evolved, such as 10.20, 22.56, 50.57 and 67.20 mmol/H_2 $g^{-1}h^{-1}$, respectively (Figures 7a and 7b). All of above systems show good hydrogen generation quality of course without any noticeable degradation in the photocatalytic

devices under the presence of the electron sacrificial electrolyte $Na_2S+K_2SO_3$ solution (pH =13.5) under the irradiation of AM1.5 G light. The electrolyte $Na_2S+K_2SO_3$ solution (pH =13.5) used to stop the photo degradation of the sensitizer CdS. Quantitative rise is observed in the rate of H_2 evolved with the each step of the advancement on ZnO NRs, which follows a quadratic relation y =1.022(03) x^2+14.734(15)x-6.900(16) and satisfy 3/2 order kinetics for advancement paradigm of nanomolecular device (Figure 7b). Apparent quantum yield (AQY) was estimated for the tested device using Equation (6) by the assumption of that the all incident photons are absorbed during the photochemical reactions. [31]
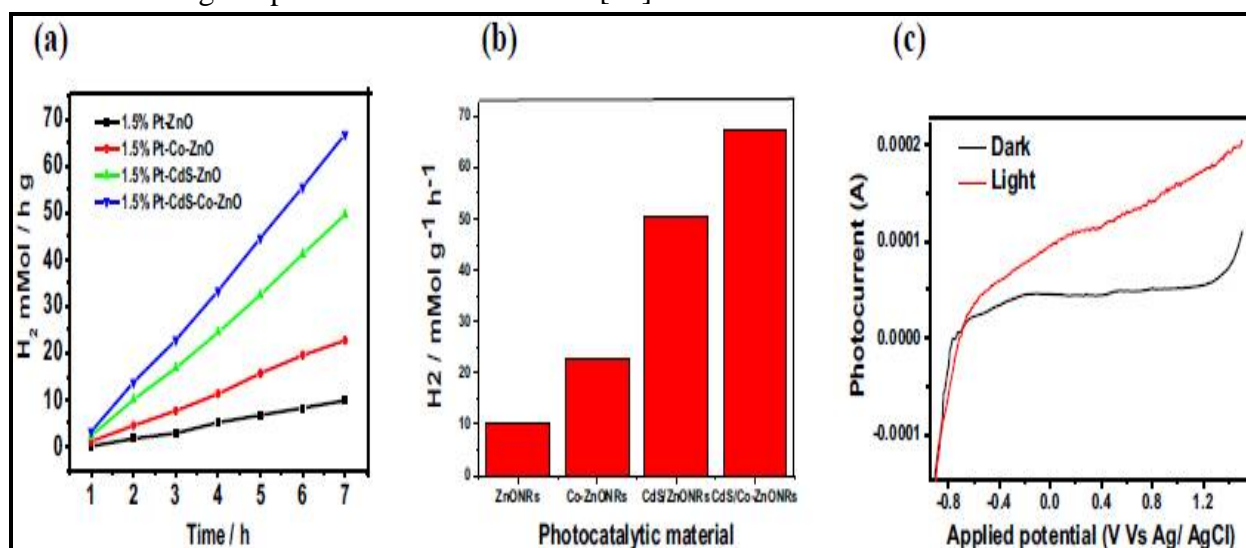
Figure 7 (a) H_2 production by photocatalytic cleavage of water using molecular devices of 1.5% Pt/ZnO NRs, 1.5% Pt/Co/ZnO NRs, 1.5% Pt/CdS/ZnO NRs, and 1.5% Pt/CdS/Co-ZnO NRs; **(b)** Bar plot of gradual increase in the rate of H_2 evolved after 7 h for each advancement. **(c)** I-V plot for CdS/Co-ZnO NRs in the electrolyte $Na_2S+K_2SO_3$ solution (pH =13.5) under AM1.5 G illumination, recorded at zero bias voltage at 25 ^{0}C temperature in the applied potential range -1.0 to +1.5 V (vs Ag/AgCl electrode). Exposure area of the sample is 1 cm^2.

AQY (%) = ([Number of H_2 molecules evolved×2]×100) /[Number of incident photons]   ….(6)

Where, the number of incident photons was 4.48×10^{24} photon h^{-1}, measured using a Si photodiode, at 420 nm wavelength. Corresponding water splitting ability of the device was estimated in terms of AQY at 420 nm. These were found to be 0.30, 0.66, 1.49 and 1.98%, respectively for above mentioned systems (1.5% Pt-ZnO, 1.5% Pt/Co-ZnO, 1.5% Pt/CdS/ZnO and 1.5% Pt/CdS-Co-ZnO). Reproducibility of these systems against their photocatalytic water splitting ability was checked thrice by using the same photocatalytic material, (suspended particles in aqueous electrolyte) after their five times washing with the pure de-ionized water and drying at 100 ^{0}C for 1 h. Electrochemical analyzer [Auto lab potentiostat model PGSTAT30] in the midst of software GPES (general purpose electrochemical study) manager, was used to monitor the photovoltaic responses of the test samples. Power density of the light source was controlled at 100 mWcm^{-2} (AM1.5 G), using thermopile (Gentec (ε) Solo-2, Model-UP12E105-H5 ISS, USA) at the beginning and checked at end of the each PEC run. Pyrex glass photoelectrochemical (PEC) cell with water jacket was well equipped with a small quartz window and conventional three electrode-system, comprising of a saturated calomel electrode (SCE) as reference electrode, a Pt flag as counter electrode and uniform film of the sample loaded on fluorine doped tin oxide (FTO) substrate (using doctor blade method) as the working electrode (WE). A wide potential window with a width of 1.5 V (-0.9 to +0.6 V) recorded during photovoltaic study of 1.5% Pt/CdS/Co-ZnO NRs device, was attributed to a good electron exchange quality of the system (Fig. 7c). [32] Significantly, no saturation in photocurrent was observed at applied positive potentials, which indicates efficient charge separation upon light illumination that is responsible for higher hydrogen evolution amount. [33] On the basis of this study and other supportive analytical evidences, [7,34] the most plausible overall photocatalytic water splitting mechanism for the nano device (1.5% Pt/CdS/Co/ZnO NRs) in presence of hole sacrificial electrolyte under visible light exposure, is suggested and illustrated by Figures 8.

Accordingly, during the electron transfer, when the surface of the device was illuminated with light, an electron was excited from VB to CB, which generates a pair of photohole and photoelectron in corresponding VB and CB of Co-ZnO. Nascent photoelectrons of the CB (Co-ZnO) are transported to the CB of quantum confined nano-sized sensitizer (CdS). This electron arrived at the junction of Pt/electrolyte interface by passing through the electron-pool of the metallic Pt.
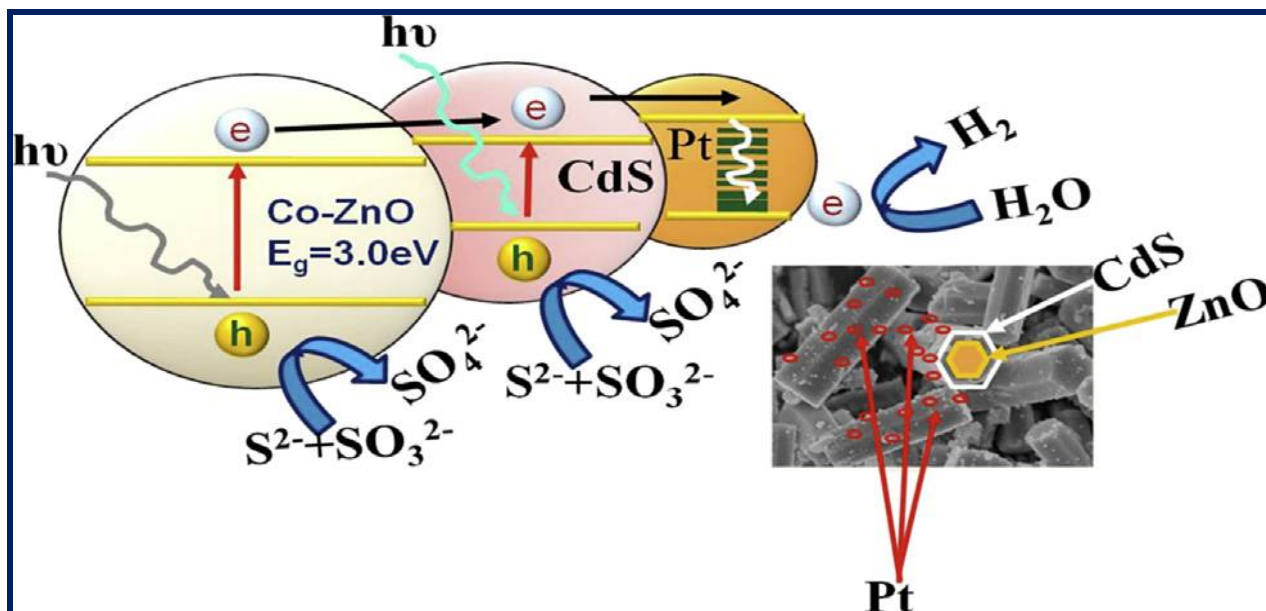
Figure 8 Electron transfers mechanism for the photocatalytic water splitting using the nanomolecular device i.e. 1.5% Pt-CdS/Co-ZnO NRs.

At the interface of material surface with Pt and water, the photoelectrons interact with H^+ ions [35] of the solution and liberated the nascent H that combined with another nascent H atom to generate H_2 gas. Holes accumulated at VB of Co-ZnO and CdS responsible for the degradation of the scavenger electrolyte by photocatalytic cleavage of the water, are given by the Equations (7-9) on photo exposure:

$$CdS/Co\text{-}ZnO + hv \rightarrow e^{-}(CdS/Co-ZnO) + h^+(CdS/Co-ZnO) \qquad ....(7)$$

$$\text{Cathode: } 2H_2O + 2e^- \rightarrow 2OH^- + H_2 \qquad ....(8)$$

$$\text{Anode: } SO_3^{2-} + S^{2-} + 2OH^- + 1.5H_2O + 6h^+ \rightarrow 1.5S_2O_3^{2-} + SO_4^{2-} + 4H^+ \qquad ....(9)$$

$$\text{Overall Redox Reaction: } S^{2-} + SO_3^{2-} + 5H_2O \rightarrow 5H_2 + 2SO_4^{2-} \qquad ....(10)$$
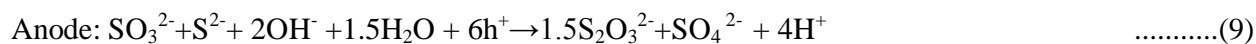
4.1.4 CONCLUSION

In short, this study gives us an inside view of the photocatalytic water splitting of two type of systems: (A) Ag @ZnO NRs using different type of Ag NPs [where, silver nanoparticles (i)Ag NPs (Trachyspermum Ammi) @ZnO NRs (ii)Ag NPs(Trigonella foenum graecum/

Fenugreek)@ZnO NRs (iii) Ag NPs (Tea) @ZnO NRs (iv) Ag NPs (Acacia Concinna/Shikakai)@ZnO NRs] and (B) CdS@Co-ZnO. System A i.e. AgNPs@ ZnO NRs dispersed in 20% CH_3OH (electron sacrificial electrolyte) under the 300W Xe light source for 4h to perform the reduction of water and generation of the hydrogen gas. The results exhibited that the AgNPs@ ZnO NRs after Pt loading i.e. Pt/Ag(TA)@ZnO, showed the highest efficiency in terms of hydrogen production (204.60/ mol h^{-1} g^{-1}), that followed by the Pt/Ag(AC)@ZnO (78.1580 mol h^{-1} g^{-1}), Pt/Ag(Tea)@ZnO (33.9639 mol h^{-1} g^{-1}) and Pt/Ag(FG)@ZnO (27.7400 mol h^{-1} g^{-1}). Ag NPs with the different particle shape and size, play an important role in correlating the hydrogen generation efficiency of the molecular device, where the ZnO NRs are taken in the same proportion in all cases. Therefore, we can conclude as the higher the position of first excitation peak on wavelength axis and lower particle size can result in the high efficiency of hydrogen generation In case of system B, a good correlation between atomic arrangement around Zn atom and light harvesting capacity of the modified ZnO NRs has been established, in terms of the water splitting. Defects developed on Co-ZnO NR's surface, may act as recombination centres for the photocarriers. The concentration of the defects on the flat-end Co-ZnO NRs was suppressed by its decoration with the visible light sensitizer CdS. Heterocouple CdS/Co-ZnO NRs, show a good compatibility of nanoparticles of CdS with Co-ZnO NRs. Whole molecular assembly was utilised as a photoelectrode after Pt-loading for hydrogen generation via water splitting in the electron sacrificial electrolyte i.e. $Na_2S+K_2SO_3$ solution (pH =13.5) under the 300 W Xe light exposure. (hydrogen evolved amount, apparent quantum yield) Gradual increase in the photocatalytic activity of the devices was recorded with surface modification, such as 1.5% Pt/ZnO (10.20 mmol/hg, AQY =0.30%), 1.5% Pt/Co-ZnO (22.56 mmol/hg, AQY =0.66%), 1.5% Pt/CdS/ZnO (50.57 mmol/hg, AQY =1.49%) and 1.5% Pt/CdS/Co-ZnO NRs (67.20 mmol/hg, AQY = 1.98%), which can execute a excellent job of water splitting better than pristine samples. Time dependent hydrothermal synthesis CdS/Co/ZnO NRs is in progress to explore the relationship between their photocatalytic hydrogen generation efficiency and atomic arrangement. Therefore, it can be established the SPR effect of Ag NPs and sensitizer CdS increase the efficiency of the ZnO NRs of the hydrogen generation via water splitting.

4.1.5 REFERENCES

[1] M Balat, "Potential importance of hydrogen as a future solution to environmental and transportation problems" ***Int J Hydrogen Energy*** (**2008**), 33: 4013-29.

[2] N Chouhan, RS Liu, "Electrochemical technologies for energy storage and conversion" In: Liu RS, Zhang L, Sun X, Liu H, Zhang J, editors, "Electrochemical technologies for energy storage and conversion" ***1. Weinheim, Germany: Wiley-VCH*** (**2012**), Chap. 1: 23-33.

[3] JM Ogden, "Prospectus of building a hydrogen energy Infrastructure" ***Annu Rev Energy Environ*** (**1999**), 24: 227-79.

[4] N Chouhan, L Yeh, SF Hu, RS Liu, WS Chang, KH Chen, "CdSe(QDs)@ ZnO nanotubes as an effective photoanode" ***Chem Commun*** (**2011**), 47: 3493-5.

[5] XH Wang, YC Zhang, WL He, MK Zhu, B Wang, H Yan, "Hydrothermal synthesis of zinc oxide powders with controllable morphology" ***Ceram Int*** (**2004**), 30: 93-7.

[6] A Wolcott, WA Smith, TR Kuykendall, YP Zhao, JZ Zhang, "Photoelectrochemical generation of hydrogen from water splitting based on dense and aligned TiO_2 nanorod arrays" ***Small*** (**2008**), 5 (1): 104-11.

[7] X Yang, A Wolcott, G Wang, A Sobo, RC Fitzmorris, F Qian, "Nitrogen-doped ZnO nanowire arrays for photoelectrochemical water splitting" ***Nano Lett*** (**2009**), 9 (6): 2331-6.

[8] HM Chen, CK Chen, YC Chang, CW Tsai, RS Liu, SF Hu, "Quantum dot monolayer sensitized ZnO nanowirearray photoelectrodes: true efficiency for water splitting" ***Angew Chem*** (**2010**), 122(34): 6102-5.

[9] K Maeda, K Teramura, D Lu, T Takata, N Saito, Y Inoue, "Photocatalyst releasing hydrogen from water" ***Nature*** (**2006**), 440 295.

[10] A Kushwaha, M Aslam, "ZnS shielded ZnO nanowire photoanodes for efficient water splitting" ***Electrochim Acta*** (**2014**), 130: 222-31.

[11] M Liu, CY Nam, CT Black, J Kamcev, L Zhang, "Enhancing water splitting activity and chemical stability of zinc oxide nanowire photoanodes with ultrathin titania shells" ***J Phys Chem C*** (**2013**), 117: 13396-402.

[12] S Shen, CX Kronawitter, J Jiang, P Guo, L Guo, SS, "A ZnO/ZnO: Cr isostructural nanojunction electrode for Photoelectrochemical water splitting" ***Nano Energy*** (**2013**), 2: 958-65.

[13] J Ji, W Zhang, H Zhang, Y Qiu, Y Wang, Y Luo, "High density Si/ZnO core/shell nanowire arrays for photoelectrochemical water splitting" *J Mater Sci Mater Electron* **(2013),** 24 (9): 3474-80.

[14] NAM Barakat, A Taha, M Motlak, MM Nassar, MS Mahmoud, SS Al-Deyab, "ZnO &Fe_2O_3-incoportaed TiO_2 nanofibers as super effective photocatalyst for water splitting under visible light radiation" *Appl Catal A General* **(2014),** 481: 19-26.

[15] A Hameed, MA Gondal, ZH Yamani, "Effect of transition metal doping on photocatalytic activity of WO_3 for water splitting under laser illumination: role of 3d-orbitals" *Catal Commun* **(2004),** 5 (11): 715-9.

[16] R Sasikala, AR Shirole, V Sudarsan, Jagannath, C Sudakar, R Naik, "Enhanced photocatalytic activity of indium and nitrogen co-doped TiO_2-Pd nanocomposites for hydrogen generation" *Appl Catal A General* **(2010),** 377(1-2): 47-54.

[17] X Hou, S Jiang, Y Li, J Xiao, Y Li, "Ni-doped InN/GaZnON composite, catalyst for overall water splitting under visible light irradiation" *Int J Hydrogen Energy* **(2015),** 40 (45): 15448-53.

[18] H Wang, W Chen, J Zhang, C Huang, L Mao, "Nickel nanoparticles modified CdSe A potential photocatalyst for hydrogen production through water splitting under visible light irradiation" *Int J Hydrogen Energy* **(2015),** 40 (1): 340-5.

[19] K Hashimoto, T Kawai, T Sakata, "Hydrogen production with visible light by using dye sensitized TiO_2 powder" *Nouv J Chim* **(1983),** 7: 249-53.

[20] S Tawkaew, Y Fujishiro, S Yin, T Sato, "Synthesis of cadmium sulfide pillared layered compounds and photocatalytic reduction of nitrate under visible light irradiation" *Colloids Surf A* **(2001),** 179: 139-44.

[21] EA Malinka, GL Kamalov, SV Vodzinskii, VI Melnik, ZI Zhilina, "Hydrogen production from water by visible light using zinc porphyrin-sensitized platinized titanium dioxide" *J PhotochemPhotobiol A* **(1995),** 90: 153-8.

[22] T Shimidzu, T Iyoda, Y Koide. "An advance visible light induced water reduction with dye sensitised semiconductor powder catalyst" *J Am ChemSoc* **(1985),** 107: 35-41.

[23] H Kato, M Hori, R Konta, Y Shimodaira, A Kudo, "Construction of Z scheme type heterogeneous photocatalysis systems for water splitting into H_2 and O_2 under visible light irradiation" *Chem Lett* **(2004),** 33 (10): 1348-9.

[24] X Wang, G Liu, GQ Lu, HM Cheng, "Stable photocatalytic hydrogen evolution from water over ZnO-CdScoreeshell nanorods" *Int J Hydrogen Energy* **(2010),** 35 8:199-205.

[25] D Chu, YP Zeng, DL Jiang, "Hydrothermal synthesis and optical properties of Pb^{2+} doped ZnO nanorods" *Mater Lett* (**2006,**) 60: 2783-5.

[26] BC Cheng, YH Xiao, GS Wu, LD Zhang. "Controlled growth and properties of one-dimensional ZnO nanostructures with Ce as activator/dopant" *Adv Funct Mater* (**2004,**) 14 (9): 913 9.

[27] SM Zhou, XH Zhang, XM Meng, SSK Wu, T Lee. "Enhancement of UV luminescence in sol-gel prepared ZnO thin films by incorporation of Mg" *Phys Status Solidi A* (**2005,**) 202(3): 405-10.

[28] CX Xu, XW Sun, ZL Dong, MB Yu, YZ Xiong, JS Chen, "Magnetic nanobelts of iron-doped zinc oxide" *Appl Phys Lett* (**2005,**) 86: 173110. 3 pages.

[29] JF Reber, K Meier, "Photochemical hydrogen production with platinized suspensions of cadmium sulfide and cadmium zinc sulfide modified by silver sulphide" *J Phys Chem* (**1986,**) 90 (5): 824-34.

[30] J Neamtu, G Georgescu, T Malaeru, NG Gheorghe, RM Costescu, I Jitaru, "Atomic structure and magnetic properties of cobalt doped ZnO thin films prepared by the sol-gel method", *Dig J NanomaterBiostr* (**2010**) 5:873-85.

[31] AL Ankudinov, B Ravel, JJ Rehr, SD Conradson, "Real-space multiple-scattering calculation and interpretation of x-rayabsorption near-edge structure" *Phys. Rev B* (**1998,**) 58: 7565-76.

[32] M Sathish, B Viswanathan, RP Viswanath, "Alternate synthetic strategy for the preparation of CdS nanoparticles and its exploitation for water splitting" *Int J Hydrogen Energy* (**2006,**) 31: 891-8.

[33] R Konta, T Ishii, H Kato, A Kudo, "Photocatalytic activities of Noble metal ion doped $SrTiO_3$ under visible light irradiation" *J Phys Chem B* (**2004,**) 108 (26): 8992-5.

[34] WC Poh, KP Loh, WD Zhang, S Tripathy, JS Ye, FS Sheu, "Biosensing properties of diamond and carbon nanotubes" *Langmuir* (**2004,**) 20: 5484-92.

[35] G Lindbergh, D Simonsson, "Inhibition of cathode reactions in sodium hydroxide solution containing chromate" *J ElectrochemSoc* (**1991,**) 36: 1985-94.

Chapter 4

4.2 Ag NPs used for Pollutant P-Nitro Phenol (PNP) Degradation into P-Amino Phenol

ABSTRACT

Plasmonic silver nanoparticles (AgNPs, size=3-50 nm) were synthesized by biogenic reduction of aqueous $AgNO_3$ using aqueous Trachyspermum ammi (TA, Ajwain) seeds extract. Increase in concentration of TA, accelerated the reduction rate of Ag^+ and affected the AgNPs particle size. Pronounce effect of the AgNP's aging (24, 48 and 72 h) was exhibited by the systems on Ag particle concentration/size and their corresponding catalytic activity. As-synthesized 24, 48 and 72 h aged-Ag NPs, were tested for their catalytic reduction activity towards the conversion of p-nitro phenol to p-aminophenol in excess of $NaBH_4$. 48h-aged Ag NPs show highest catalytic activity for conversion of p-nitrophenol to p-aminophenol in excess of $NaBH_4$ in terms of rate (r =0.34539 min^{-1}) with the complete reduction time of 12 min.

Key Words: Ag Nanoparticles, green synthesis (Trachyspermum Ammi), p-nitrophenol, p-aminophenol, $NaBH_4$, etc.
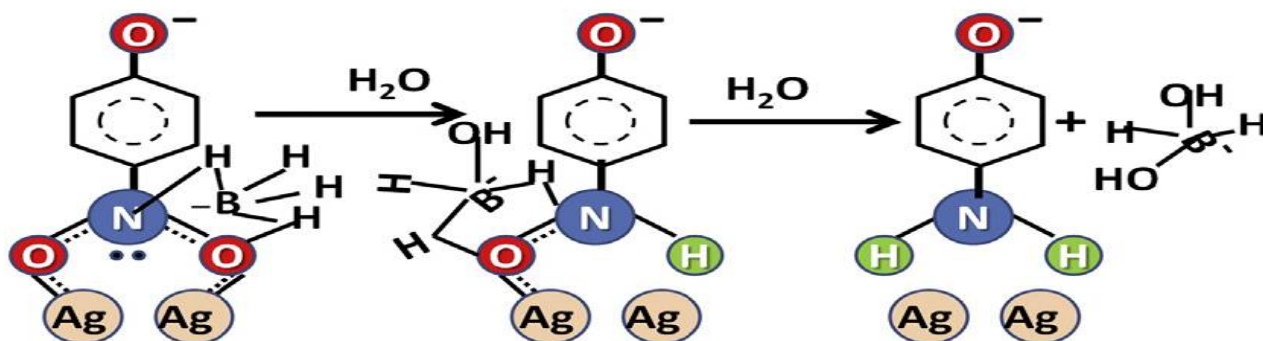
4.2.1 INTRODUCTION

The silver nanoparticles exhibits quite good antibactericidal, antiviral, anti-inflammatory, antiangiogenic, anti tumor, anti-oxidative properties against the bacterial strains/ microorganisms along with the biological and chemical sensing, imaging, drug carrier, diagnosis of the cancer/HIV/AIDS and catalytic activity. Therefore, it commonly used in medical and industrial products that can directly get in touch with the human body, such as shampoos, soaps, detergent, shoes, cosmetic products, and toothpaste, besides photocatalytic and pharmaceutical applications. Moreover, superiority of the nanosilver particles over other candidates of the same class is already established in terms of the small losses in optical frequency during the surface-plasmon propagation, high conductivity, thermal and chemical stability at ambient conditions, lesser costlier price than other noble metals such as gold and platinum, high primitive character, and wide range of visible light absorption, etc. Which, prompt us to select silver as a plasmonic material for this study. Tiny nano-particles of the noble metals under light exposure can possess the localised spin plasmonics resonance (LSPR) character, are known as plasmonics material. Free electrons integrated with the photon energy produces a LSPR [1-5] on exposing nano-particles of noble metals to sunlight. Therefore, NPs of the noble metals will be work as the energetic centres on catalyst for the thermal redox reaction that can entrap, scatter, and ponder the light [6-8], due to the fast charge transfer and bring about enhanced activities. Pure Ag NPs, as well as some chemically modified Ag NPs has also been in trend that to be used in various applications such as: cleaning water, catalyst, sensor, optoelectronic properties, eradication of organic pollutants (dye phenol,etc), etc. Out of which the removal of organic pollutants (nitrophenol) from waste water is quite fascinating as the 4-nitrophenol (PNP) is a low water-soluble and highly stable chemical that used to be found in waste water, produced by explosive- and dye-industries. Environmental Protection Agency of United States rated nitrophenols as the highly polluted chemical among the top 114 organic pollutants. It adversely affects the human and animal organs like liver, kidney, blood and central nervous system, skin, etc.[9] Moreover, the degradation of PNP to non dangerous product is difficult due to its high stability. Therefore, the study for catalytic reduction of hazardous PNP to benign 4-aminophenol (PAP) becomes a remarkable echnique in terms of nitrophenol-pollution mitigation process. [10] PAP is a very fascinating chemical as it can be used in production of analgesic and antipyretic drugs,

photographic developer, corrosion inhibitor, anti-corrosion lubricant, and many more applications. It can be produced by reduction of PNP to PAP using reducing agents at room temperature. Aforementioned reaction is a thermodynamically feasible process as it involves E_0 for PNP/PAP = -0.76 V and H_3BO_3/BH_4^- = -1.33 V versus NHE. But this reaction is kinetically restricted by nature and never produce PAP as end product but generate an intermediate i.e. p-nitrophenolate ion in absence of the catalyst. Metal, were often used to catalyse the above reaction Here, the metal NPs or modified metal NPs can serve as catalysts to transfer electrons from metal ions to the PNP and smoothen the way to be converted into the PAP by reducing activation energy requirements. Few outstanding examples of the metal NPs used for catalytic reduction of PNP into PAP in presence of excess of $NaBH_4$ are Ag NPs-decorated polyaniline nanofibers (AgNPs/PANINFs) nanocomposites, [11] SiO_2-coated graphene oxide nanosheets, decorated with Ag nanoparticles, [12] Pd/CuO NPs, [13] Ag NPs synthesized by using of Theobroma cacao L. seed extract, etc. Where, PNP absorbed on the catalytic surface of metal NPs and reduce PNP in presence of $NaBH_4$, result in the production of PAP. Hence, this study is devoted to the fabrication of the Ag NPs by biogenic reduction method using aqueous TA seed extract at ambient conditions. Finally, the biogenic Ag NPs produced by varying concentration and aging time and used to reduce p-nitrophenol to p-aminophenol in excess of $NaBH_4$. The reaction mechanism for this reaction is also suggested on the basis of the characterisation. Effect of aging/particle size on catalytic activity and rate of reaction will also be discussed.

4.2.2 Reduction of p-nitro phenol

The light yellow colour of 0.05 mM p-nitrophenol turns to yellow green upon incorporation of the alkaline 15 mM sodium borohydride solution. But under such conditions PNP didn't convert into PAP, until the addition of AgNPs. The peak intensity was quantitatively observed by using UV-Vis spectrophotometer (Model 3000^+ of Lab India) with a time gap of 3m in a scanning range of 200-800 nm at room temperature of 25 °C with scan speed of 250nm per minute. The reduction of p-nitrophenol with $NaBH_4$ was monitored using UV-Vis absorption spectroscopy by use of 1 mL of 15 mM $NaBH_4$ (aqueous solution) mixed with 1.7 mL of 0.2 mM 4-nitrophenol (aqueous) and 0.1 mL of 100 mgL^{-1} of AgNPs, poured in to a 5 mL quartz cell for optical observations.

4.2.3 Catalytic reduction of p-nitrophenol using NaBH₄ and AgNPs

Currently, the AgNPs has been extensively observed in the field of chemical catalysis. In eradication of nitrophenol pollution AgNPs are proved to be a remarkable material. In order to evaluate the catalytic activity of the AgNPs (synthesized by using Trachyspermum ammi (Ajwain) seed extract; aged at 24 h, 48 h and 72 h) for the reduction of PNP (0.05mM) to PAP in aqueous sodiumborohydride (15mM). The reaction was monitored at room temperature in absence and presence of AgNPs. The reaction progress was spectrophotometrically examined by recording the absorption spectra at various time interval. The main absorption peaks of PNP were found at 258 and 316.5 nm due to $\pi \to \pi^*$ and $n \to \pi^*$ transition, respectively. The treatment of this solution with freshly prepared aqueous solution of NaBH₄ result in disappearance of $\pi \to \pi^*$ nm peak and red shift of the first excitation peak of PNP from 316.5 nm to 401.5 nm, due to the formation of 4-nitrophenolate ion in the solution, which was demonstrated by optical spectra in Figure 1a and its schematic presentation is demonstrated by Scheme 1.

The peak position at 401.5 nm in absence of AgNPs remains unaltered even after the month long aging because of a huge kinetic barrier exist due to large potential difference between the donor and acceptors that decreases the feasibility of this reaction for the reduction process. [14] Interestingly, on addition of a freshly prepared biogenic AgNPs (0.1 mL, 100 mgL^{-1}) to the mixture of PNP and sodiumborohydride solution, the intensity of the 4-nitrophenolate peak at 401.5 nm, start decreasing development of new peak at 300nm nm wavelength was confirmed the catalytic reduction of PNP to PAP and its mechanism is shown by the Scheme 1. [15] The whole reduction process of the PNP in 24, 48 and 72 h aged samples of AgNPs, was completed in 10, 12 and 18 min, respectively. As it revealed by the naked eyes the disappearance of the yellow colour of the PNP (Figures 1b, 1c and 1d) into colorless solution. Simultaneously, the peak position of the 24 h, 48 h and 72 h aged samples in absence of AgNPs, were observed at 401, 400 and 402 nm, respectively (Figure 1e). This confirms the particle size reduces from 24 h aging to 48 h aging but its increases after 72 h aging.
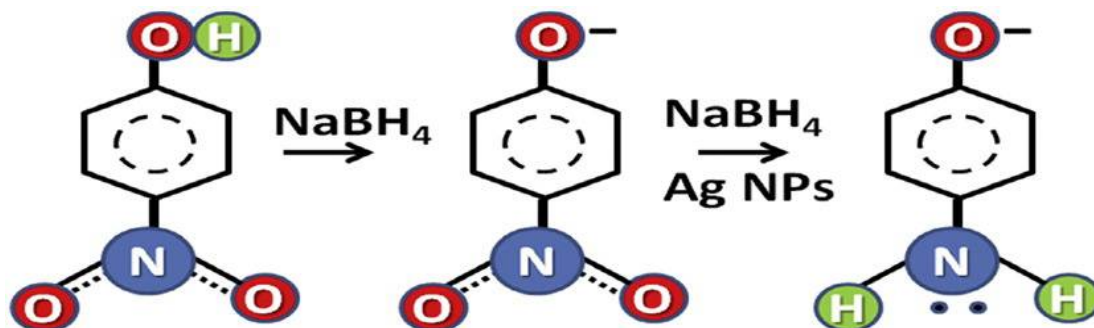
Scheme 1 Schematic reaction for the reduction of p-nitrophenol to p-aminophenol.

Table 3 Comparison of the catalytic efficiency of our system with respect to reaction time, concentration (AgNPs, NaBH$_4$ and PNP) and rate of reaction, with few state of art AgNPs and modified AgNPs systems, showing same reduction.

Catalytic System	Conc. PNP	Conc. Of NaBH$_4$	Nanoparticles	Red. time	Catalytic rate	Ref.
Calcium-Alginate-Stabalised Ag and Au NPs	0.10mM	2.5 ml of 0.1 M	1.2 g/L Ag	8 min	0.14-0.20 $\times$ 10^{-5} min^{-1}	[22]
AgNP-PG-5K	0.12 M	12mM	25µg m L^{-1}	11min	5.50 $\times$ 10-3 s^{-1}	[23]
Al2O3@Ag7,8 QCs	7.00 mM	160 mM	50 mg m L^{-1}	18min	8.23 $\times$ 10-3 s^{-1}	[24]
Ag–P (NIPAM-co-Aam)	0.061 mM	9.15 mM	37.18 mg mL^{-1}	25min	0.1713 s^{-1}	[25]
CNFs/AgNPs composite	0.12 mM	5 mM	1.0 mg m L^{-1}	8min	6.2 $\times$ 10-3 s^{-1}	[26]
Breynia Rhamnoides supported Ag and Au nanoparticles	2.00 mM	0.03 M	0.5 mL AgNPs or AuNPs	- 11min	4.06 $\times$ 10-3 s^{-1} (AgNPs) 9.19 $\times$ 10-3 s^{-1} (AuNPs)	[27]
TCD supported Ag NPs	2 mmol	0.03 M	300 µL	75min	0.05 s^{-1}	[28]
AgNPs	5 mM	160 mM	0.67 mg mL^{-1}	20min	3.28 $\times$ 10-3 s^{-1}	[29]
AgNPs/PANINFs nanocomposites	5 mM	160 mM	0.67 mg m L^{-1}	3 min	21.39 $\times$ 10-3 s^{-1}	[30]
TA-supported biogenic Ag NPs	0.05 mM	15 mM	10 µg m L^{-1}	12 min	5.756 $\times$ 10-3 s^{-1}	This Work
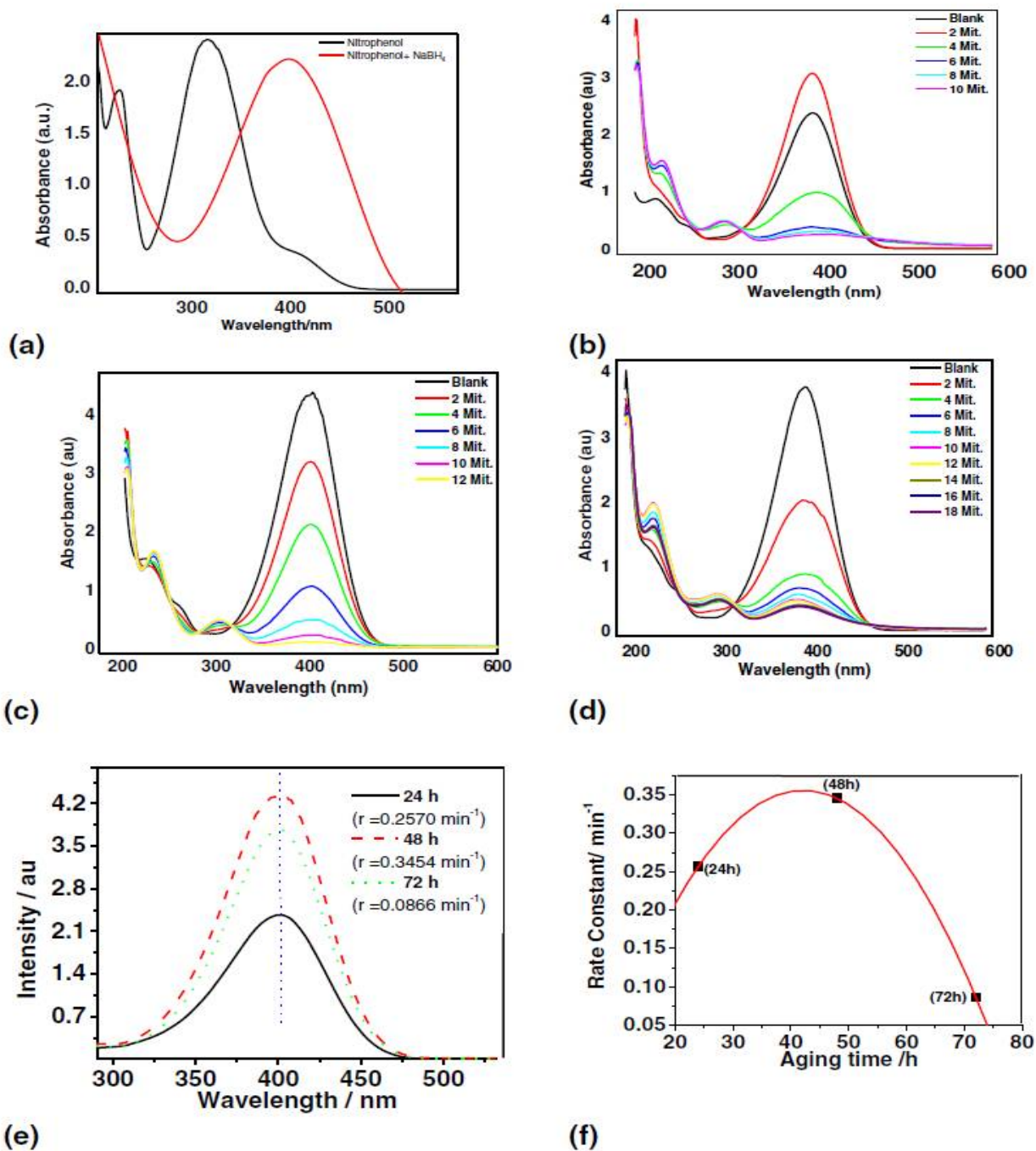
Figure 1 (a) Red shift observed in UV–visible spectrum of 4-nitrophenol (Black) when it reduced to 4-nitrophenolate ions (401.5 nm) (Red) with $NaBH_4$; catalytic reduction of 4-nitrophenol in $NaBH_4$ solution to 4-aminophenol (300 nm peak), was observed on the addition of AgNPs at the time interval (b) 24 h (c) 28 h and (d) 72 h. (e) peak position of the aged samples in absence of AgNPs and (f) Rate constant vs aging time plot. Where, the concentration of various reactants are taken as [0.05 mM PNP]; [0.1 mL of 100 mgL^{-1} AgNPs] and [15 mM $NaBH_4$].
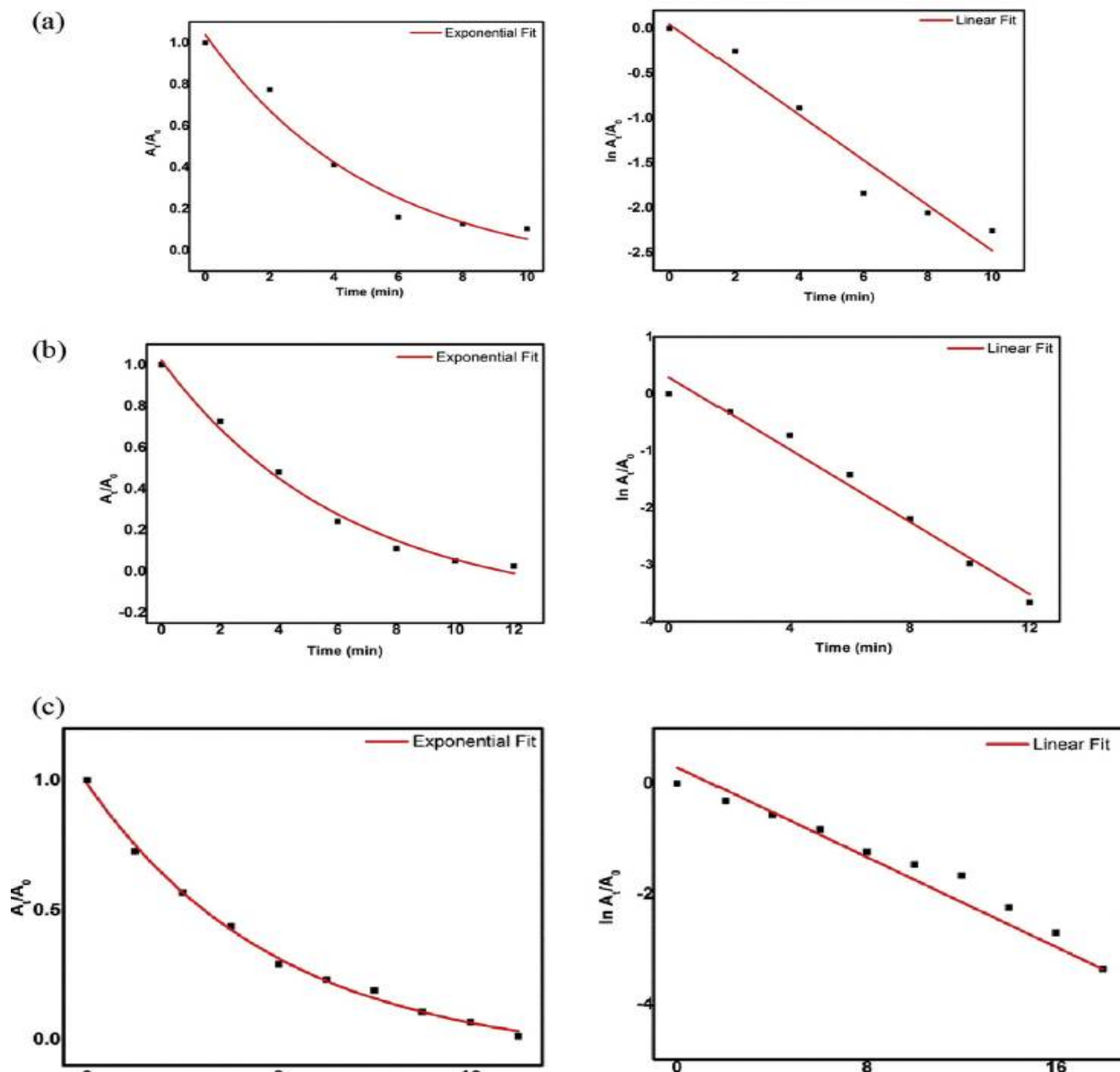
Figure 2 Plot of (i) A_t/A_0 vs time and (ii) ln (A_t/A_0) vs time for the reduction of p-nitrophenol at (a) 24 h, (b) 48 h and (c) 72 h aging. Where, [0.05mMPNP]; [0.1 mL of 100mgL^{-1} AgNPs] and [15 mM NaBH$_4$].

Catalytic action of AgNPs is shown for the above reduction process, lower down the activation energy that leads to the formation of PAP by following a pseudo-first-order rate kinetics with respect to PNP. Effect of aging ((a) 24 h, (b) 48 h and (c) 72 h) revealed on AgNPs catalytic activity (as A_t/A_0 vs time and (ii) ln (A_t/A_0) vs time plots) against the reduction process of PNP

in terms of the rate of reaction. The apparent catalytic rate constant ($k_{24}=0.25709\text{min}^{-1}$, $k_{48}=0.34539\text{min}^{-1}$ and $k_{72}=0.0866\text{min}^{-1}$) was calculated for the reduction process at 24 h, 48 h and 72 h, using the slope of the plot between logarithm of the observed optimum absorbance and time, which are represented by Figures 2a, 2b and 2c, respectively.
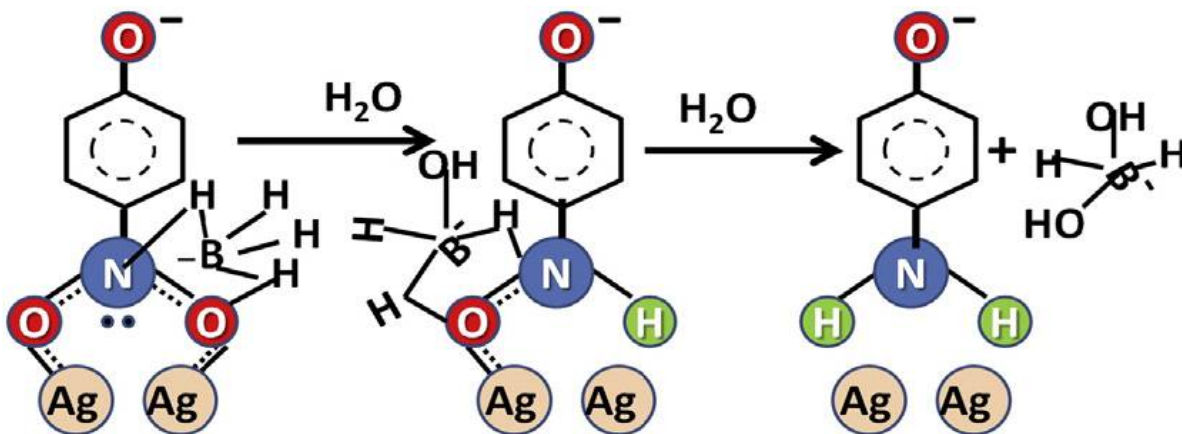
Scheme 2 Reduction mechanism of p-nitro phenol to p-aminophenol in presence of the aqueous NaBH₄ and Ag NPs.
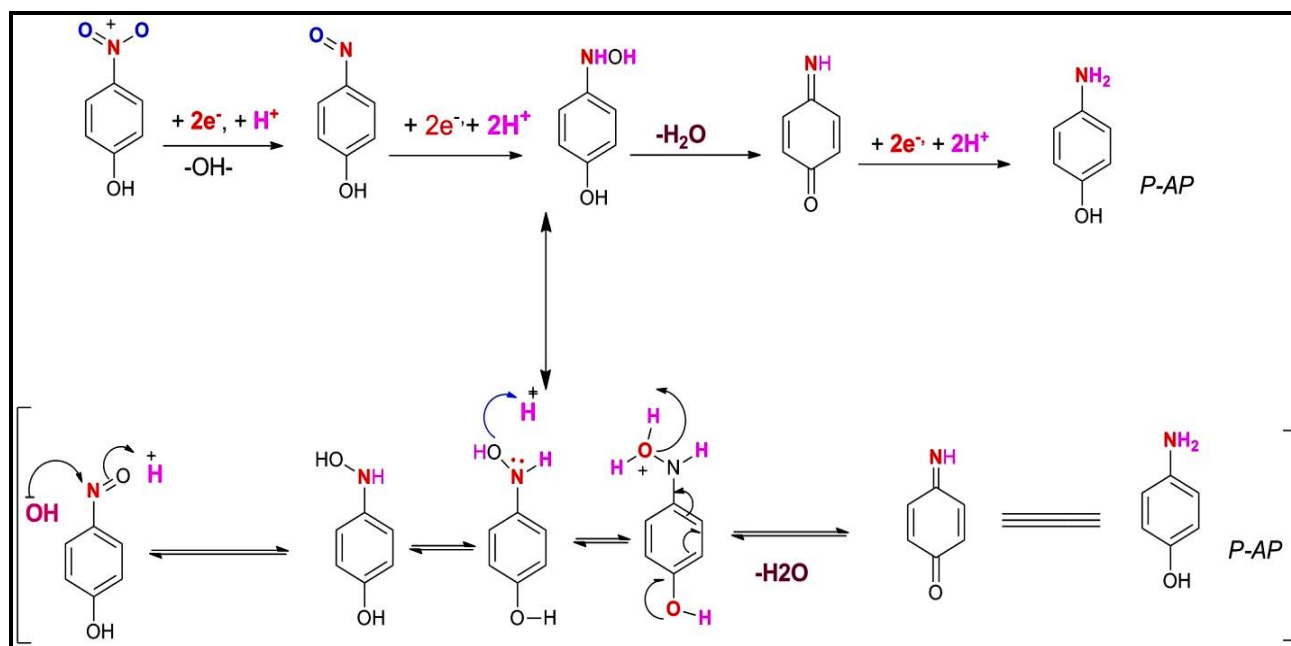
Scheme 3 Conversion of 4-nitrophenol to 4 aminophenol in the presence of Ag nanoparticles, proposed by Anand etal.

The catalytic action of Ag nanoparticles is corresponds to its' size, shape and well dispersion. A probable mechanism for the catalytic conversion of 4-nitrophenol to 4-aminophenol is shown in scheme 3, was proposed by K. Anand *et al*., [16] with slight modification. During the catalytic action, of the PNP molecule are initially chemisorbed at the (100) surface of the AgNPs through two oxygen atoms of the nitro group of p-nitro phenolate ion. That may create a pentagonal Ag-O-N-O-Ag cyclic intermediate that may react with BH_4^- ion and decomposed into PAP, as illustrated by Scheme 2. Binding of organic molecules to metal surfaces and their reduction process has been extensively model by Newns [17] and later on expanded by Hammer and Nørskov. [18-22] After executing our experiment we compare the efficiency of our results with respect to reaction time (12 min), concentration and rate of reaction (5.756×10^{-3} s^{-1}), with some of the recent state of art AgNPs and modified AgNPs systems such as; Calcium-Alginate-stabilised Ag and Au NPs, Ag/NP-PG-5K (PG: polyguanidino oxanorbornenes (PG), 5 K and 25 kDa), $Al_2O_3@Ag$, QCs, Ag-P (NIPAM-co-Aam; NIPAM: Nisopropylacrylamide), CNFs (carbon nano fibres)/AgNPs composite, Breynia Rhamnoides supported Ag and Au Nanoparticles, TCD (TCD: trisodium citrate dihydrate (HOC(COONa) $(CH_2COONa)_2 \cdot 2H_2O$)) supported Ag NPs, chemically reduced Ag NPs, AgNPs/PANINFs nanocomposites (PANINFs: polyaniline nano fibres), etc., as shown as Table 3 [23-29]. And it was found that our system is performing better than above mentioned systems. Reason behind the superiority can be given on the basis of Garcia-Vidal and Pendry's model, the smaller metallic particles and higher content of NPs gave higher enhancement in efficiency [30]. Moreover, TA supported-AgNPs shown the high catalytic activity that will be sustain till the three successive cycles of reduction reactions and would greatly promoted for their industrial applications.

4.2.4 CONCLUSION

As synthesized AgNPs, were used successfully to completely catalyse the reduction of notorious pollutant PNP to PAP in presence of excess $NaBH_4$, which was kinetically toughest reaction in absence of catalyst. The study of effect of AgNPs particle size on PNP reduction catalytical activity was observed. The results showed that the 48 h-aged AgNPs prepared in 2.0% TA extract, exhibited the optimum catalytic efficiency in comparision to the many state of art catalytic systems.

4.2.5 REFERENCES

[1] S. Ankanna, P. TNVKV, E.K. Elumalai, N. Savithramma, "Production of biogenic silver nanoparticles using Boswellia ovalifoliolata stem bark" ***Dig. J. Nanomater. Biostruct.*** **(2010),** 5 (2) 369-372.

[2] R.H. Ritchie, "Plasma Losses by Fast Electrons in Thin Films" **Phys. Rev. (1957)** 106: 874.

[3] W.L. Barnes, A. Dereux, T.W. Ebbesen, "Surface Plasmon Sub wavelength Optics" ***Nature*** **(2003),** 424: 824-830.

[4] S.A. Maier, H.A. Atwater, "Plasmonics: localization and guiding of electromagnetic energy in metal/dielectric structures" ***J. Appl. Phys.*** **(2005),** 98: 011101.

[5] S.A. Maier, "Plasmonics Fundamentals and Applications" ***first ed. Springer*****, New York, (2007),** 21-34 and 65-88.

[6] S. Lal, S. Link, N. Halas, ***Nat. Photonics*** **(2007),** 1: 641-648.

[7] X.C. Wang, J.C. Yu, H.Y. Yip, L. Wu, P.K. Wong, S.Y. Lai, "A mesoporous Pt=TiO₂ nanoarchitecture with catalytic and photocatalytic functions" ***Chem. Eur. J.*** **(2006),** 11: 2997–3004.

[8] X.B.Cao, L. Gu, L.J.Zhuge, W.J.Gao, W.C. Wang, S.F.Wu, "Template-free preparation of hollow Sb_2S_3 microspheres as supports for Ag nanoparticles and photocatalytic properties of the constructed metal- semiconductor nanostructures" ***Adv.Funct.Mater.*** **(2006),** 16: 896-902.

[9] J. Virkutyte, R.S. Varma, "Fabrication and visible-light photocatalytic activity of novel $Ag/TiO_2À_xN_x$ photocatalyst" ***New J. Chem.*** **(2010),** 34: 1094-1096.

[10] T. Vincent, E. Guibal, "Influence of experimental parameters on nitrophenol degradation" ***Langmuir*** **(2003),** 19: 8475-8483.

[11] G. Chang, Y. Luo,W. Lu, X. Qin, A.M. Asiri, A.O. Al-Youbi, X. Sun, "Ag. Nanoparticles Decorated Polyaniline Nanofibers: Synthesis, Characterization, and. Applications Toward

Catalytic Reduction of 4-Nitrophenol and Electrochemical. Detection of H_2O_2 and Glucose" ***Catal. Sci. Technol.*** **(2012),** 2: 800-806.

[12] W. Lu, Y. Luo, G. Chang, X. Sun, "Synthesis of functional SiO_2-coated graphene oxide nanosheets decorated with Ag nanoparticles for H_2O_2 and glucose detection" ***Biosens. Bioelectron.*** **(2011),** 26: 4791-4797.

[13] M. Nasrollahzadeh, S.M. Sajadi, A. Rostami-Vartooni, M. Bagherzadeh, "Green synthesis of Pd/CuO nanoparticles by Theobroma cacao L. seeds extract and their catalytic performance for the reduction of 4-nitrophenol and phosphine-free" ***J. Colloid Interface Sci.*** **(2015),** 448: 106-113.

[14] N. Pradhan, A. Pal, T. Pal, "Silver nanoparticle catalyzed reduction of aromatic nitro compounds" ***Colloids Surf. A Physicochem. Eng. Asp.*** **(2002),** 196: 247-257.

[15] Z.D. Pozun, S.E. Rodenbusch, E. Keller, K. Tran, W. Tang, K.J. Stevenson, G.J. Henkelman, "Systematic Investigation of p-Nitrophenol Reduction by Bimetallic Dendrimer Encapsulated Nanoparticles" ***Phys. Chem. C*** **(2013),** 117: 7598-7604.

[16] K. Anand, R.M. Gengan, A. Phulukdaree, A. Chuturgoon, "Agroforestry waste Moringa oleifera petals mediated green synthesis of gold nanoparticles and their anti-cancer and catalytic activity" ***Journal of Industrial and Engineering Chemistry,*** **(2015),** 21: 1105-1111.

[17] D.M. Newns, "Self-Consistent Model of Hydrogen Chemisorption" ***Phys. Rev.*** **(1969),** 178: 1123-1135.

[18] B. Hammer, J.K. Nørskov, "Self-Consistent Model of Hydrogen Chemisorption" ***Nature*** **(1995),** 376: 238-240.

[19] B. Hammer, Y. Morikawa, J.K. Nørskov, "CO Chemisorption at Metal Surfaces and Overlayers" ***Phys. Rev. Lett.*** **(1996),** 76 2141-2144.

[20] B. Hammer, J.K. Nørskov, "Electronic factors determining the reactivity of metal surfaces" ***Surf. Sci.*** **(1995),** 343: 211-220.

[21] B. Hammer, J.K. Nørskov, "Erratum to Electronic factors determining the reactivity of metal surfaces" ***Surf. Sci.*** **(1996),** 359: 306.

[22] B. Hammer, "Special sites at noble and late transition metal catalysts" ***Top. Catal.*** **(2006),** 37: 3-16.

[23] S. Saha, A. Pal, S. Kundu, S. Basu, T. Pal, " Photochemical Green Synthesis of Calcium-Alginate-Stabilized Ag and Au Nanoparticles and Their Catalytic Application to *4*-Nitrophenol Reduction " ***Langmuir*** **(2010),** 26 (4): 2885-2893.

[24] B. Baruah, G.J. Gabriel, M.J. Akbashev, M.E. Booher, "Facile synthesis of silver nanoparticles stabilized by cationic polynorbornenes and their catalytic activity in 4-nitrophenol reduction" ***Langmuir*** **(2013),** 29 (13): 4225-4234.

[25] A. Leelavathi, B.T.U. Rao, T. Pradeep, "Supported quantum clusters of silver as enhanced catalysts for reduction" ***Nanoscale Res. Lett.*** **(2011),** 6: 123.

[26] R. Begum, Z.H. Farooqi, E. Ahmed, K. Naseem, S. Ashraf, A. Sharif, R. Rehan, "Catalytic reduction of 4-nitrophenol using silver nanoparticles engineered poly(N-isopropylacrylamide-co-acrylamide) hybrid microgels" ***Appl. Organomet. Chem.*** **(2016)** 1-8.

[27] P. Zhang, C. Shao, Z. Zhang, M. Zhang, J. Mu, Z. Guo, Y. Liu, "In situ assembly of well-dispersed Ag nanoparticles (AgNPs) on electrospun carbon nanofibers (CNFs) for catalytic reduction of 4-nitrophenol" ***Nanoscale*** **(2011),** 3: 3357-3363.

[28] A. Gangula, R.K. Podila, M. Ramakrishna, L. Karanam, C. Janardhana, A.M. Rao, "Catalytic reduction of 4-nitrophenol using biogenic gold and silver nanoparticles derived from Breynia rhamnoides" ***Langmuir*** **(2011),** 27 (24): 15268-15274.

[29] F.A. Al-Marhaby, R. Seoudi, "Preparation and characterization of silver. nanoparticles and their use in catalytic reduction of 4-nitrophenol" ***World J. Nanosci. Eng.*** **(2016),** 6: 29-37.

[30] H. Hu, Z. Wang, L. Pan, S. Zhao, S.J. Zhu, "Ag-coated $Fe_3O_4@SiO_2$ three-ply composite microspheres: synthesis, characterization, and application in detecting melamine with their surface-enhanced Raman scattering" ***Phys. Chem. C*** **(2010),** 114:7738-7742.

Fabrication of the Nanomolecular Devices of ZnO for Solar Hydrogen Production

Summary

Submitted by

Rajesh Kumar Meena

Under the supervision of

Dr. Neelu Chouhan
Head and Associate Professor
Department of Pure & Applied Chemistry
University of Kota, Kota (Rajasthan)

Submitted to
University of Kota, Kota
MBS Road, Vivekananda Nagar, Kota (Rajasthan)-324005
www.uok.ac.in

2018

Energy is the basic need of the mankind. Current resources of energy are not sufficient to satisfy the energy requirement of human rescores. Moreover, perpetual energy resource-war among countries, disturbed ecological balance of the earth, soaring prices. Global warming due to vichele and industrial air pollution that responsible for the associated climate changes, inextricable link between nuclear weapons and nuclear power, consumer awareness, abundant and cheap renewable energy resources, are the major driving forces behind the shifting of energy trend from conventional to renewable fuels. Free and abundant availability of sustainable energy resources like, water and solar energy, adds volume to the field of sustainable energy sources. Nature split water via photosynthesis process in plants, to produce oxygen and glucose. That inspired us to impersonate the same phenomena in producing hydrogen by substituting plant's chlorophyll with apt catalyst in photocatalytic water splitting and photoelectron catalytic water splitting. Similarly artificial water splitting can generate oxygen and hydrogen using appropriate and sun light. Hydrogen, produced via photocatalytic water splitting, is a clean fuel (without greenhouse gases production), because on oxidation of hydrogen water is produced which is not harmful for nature and human being energy security (can be produced from abundant sources), economic growth, high efficiency (75% fuel efficiency), portability (Car tanks, micro fuel), can do wonders in energy world. Photo water splitting (PWS) or photoelectron chemical water splitting (PECWS) is the most promising technology to produce H_2 energy directly from renewable source water and solar light at photocatalytic surface. The splitting of water into molecular hydrogen and oxygen by light irradiation is one of the most fascinating ways for the photochemical conversion and storage of energy. Therefore, we prepare less toxic metal nanoparticles using different chemical and green synthesis methods, which is a great challenge of recent time. We focus to maximize the usage of environmental friendly materials for generating metal nanoparticles. The synthesized materials was rigorously analysed through advance analytical techniques such as, UV-Visible spectrophotometer, FTIR spectrophotometer, XRD, FESEM, HRTEM, EDS, PL, Cyclic voltmeter, etc. As synthesized nanomaterials used for solar H_2 production by water splitting and pollutant degradation. This study became contemporary in context of present energy scenario.

The present thesis describes the synthesis of metal nanoparticles like as a metal oxide, metal

sulphide, noble metals and their composite etc. As synthesized metal oxide molecular devices was used for hydrogen production through water splitting and strengthening our technological capabilities in designing the photocatalyst for efficient water splitting with a promise of giving competitive solutions for the production of clean fuel (i.e.H_2) at large scale. It will resolve the present current energy crisis without damaging our precious environment anymore. The entire research work is divided into six chapters.

The **first chapter** deals with introduction of this research work, objective, scope and application of the research work. This chapter deals with review on the potential thrust for the material scientists to develop an ultimate material with appropriate band edge positions and adequate stability for the photocatalytic water cleavage processes.[1] This is expected to offer new horizons in the development of visible-light-driven photocatalysis, for achieving overall water splitting.[2] A number of metal oxides containing d^0-transition metal cations (e.g., Ti^{4+}, Zr^{4+}, Nb^{5+}, Ta^{5+}, and W^{6+}) or d^{10}-typical metal cations (e.g., Zn^{2+}, Ga^{3+}, In^{3+}, Ge^{4+}, Sn^{4+}, and Sb^{5+}) with metal titanates, oxynitrides, oxysulphides, etc,[3-12] have been reported as active photocatalysts for overall water splitting. Unfortunately, beside the wide domain of photocatlysts most of them fail on the criteria of stability, cost, and efficiency under visible light (altogether). Methods to overcome this limitation by controlling the energy structure using nano solid solutions (ZnO-ZnS) between semiconductor photocatalysts of wide and narrow band gaps or to develop the one dimensional nanomaterials of apt band gap oxide-semiconductors and their sensitization with short band gap visible light driven catalyst.[13] Synthetic techniques like epitaxial growth,[14] sol-gel[15] reduction by natural products[16], hydrothermal,[17,18] will definitely do great help in this felid by enhancing their structural qualities. In this regard, we propose a below mentioned strategy, which involves to build up the infrastructure for study and literature survey along with the fabrication of the apt semiconductor (doped with elements C, N, S, P, B, F or transition metal ions)[19-24] and used these assemblies as a photoanode and loaded them with sensitizer (quantum dots)[25-29] and utilised noble metal[30] as a counter electrode i.e. photocathode. Semiconductor quantum dots, such as CdS, CdSe, CdTe, and InP, etc,[31-35] found compatible to be assembled on metal oxide semiconductor nanostructures as sensitizers of photoelectrodes.[36-40] This combination would be tested as a functionalized molecular device for the cleavage of water.

This chapter also sheds light on the development of silver nanoparticles with different sizes and shapes, using methods such as UV irradiation,[41,42] microware irradiation,[43,44] chemical reduction,[45-47] photochemical method,[48,49] electron irradiation,[50,51] and sonoelectrochemical method, etc.[52] However, most of the reported methods involve more than one step, high energy requirement, low material conversions, difficulty in purification, and hazardous chemicals. The chemical synthesis of nanoparticles may lead to the presence of some toxic chemical species adsorbed on the surface that may have adverse effects in its application. The synthesis of nanoparticles by green method can potentially eliminate this problem. Therefore, there is an urgent need to develop a green process of nanoparticle synthesis. Green synthesis methods employed either biological microorganisms or plant extracts and emerged as a simple and alternative to chemical synthesis. Green synthesis provides advancements over chemical methods as it is environment friendly, cost effective, and easily scaled up for large scale synthesis. Generally, the green synthesis method involves three main steps, (1) solvent medium selection, (2) environmental benign reducing agent selection, and (3) non-toxic substances for nanoparticles stability selection. The synthesis of nanoparticles by using plant extracts can be advantageous over other biological processes because it eliminates the elaborate process of maintaining cell cultures and can be suitably scaled up for large scale production under non-aseptic environments.

The **second chapter** describes with the fundamental experimental part along with chemicals basic information. This chapter divided into two sections. The first (A) section of this chapter deals with the description of various characterization techniques which are most important to characterize the synthesized nanocatalyst. This section also describes the basic theories and principles associated with the main analytical methods, i.e. electron microscopy UV-Visible spectrophotometer, FTIR spectrophotometer, XRD, FESEM, HRTEM, EDS, PL, Cyclic voltmeter, electronic balance, pH meter, used throughout the study. UV-Visible spectrophotometer and FTIR spectrophotometer were frequently employed to analyze the progress of reaction and identification of the synthesis nanoparticle. The second (B) section is deals with the details of the reagents, chemicals and their solutions with other specifications employed in kinetic study of various suitable reactions.

The **third chapter** deals with the synthesis part of ZnO nanorods and green synthesis of Ag nanoparticles, which divided into two sections. In the first **(A) section,** we discuss about synthesis process and optical properties of ZnO nanorods by hydrothermal method using in a reagent solution of zinc acetate, zinc nitrate and HMT in a hydrothermal reactor. This was sealed in an autoclave and heated to $90^{\circ}C$ to grow nanorods. Their physical growth mechanism on FTO substrate by an aqueous solution growth method was traced in the light of PL, FESEM and HRTEM studies. The nanorod of the ZnO has been analyzed by using X-ray diffraction analysis and UV visible DRS measurement. Similarly in the **Second (B)** chapter divided into four sections basis on preparation method of silver nanoparticles from silver metal ion using different plant extract using as a reducing agent. The first section (a) of this chapter deals with the description of synthesized spherical and rod shaped silver nanoparticles by green synthesis method (with use of Ajwain seed extract in aqueous medium) and characterize it with physicochemical techniques. Section b, c and d, used to synthesize the spherical silver nanoparticles, using Fenugreek, Tea leaves and Acacia concinna fruit extract. The progress of the reaction was is investigated by X-ray diffraction, transmission electron microscopy, UV-Visible spectrophotometer, FTIR spectrophotometer. And now **Section (C)** we synthesized silver decorated nanorods of ZnO i.e. Ag/ZnO hetrostructures and study the optical properties. Effect of variation of morphology, size and shape, temperature, was also studied. On the basis of results, the nanorods growth mechanism was proposed. And now **Section (D)** Synthesis part of metal (Co) doped ZnO nanorods, which is further divided into three sections. The synthesis and mechanism of visible light harvesting section (A) Co-doped ZnO nanorods, (B) CdS/Co-doped ZnO nanorods and (C) Pt/CdS/Co-doped ZnO nanorods molecular devices. All prepared by hydrothermal method using cationic surfactant cetyltrimethylammonium bromide (CTAB). Their physical growth mechanism was traced in the light of FESEM and HRTEM studies.

The **fourth chapter** deals with the synthesis part of biosynthesized Ag@ZnO NRs (i) Ag(Ajwain)@ZnO   (ii) Ag(Fenugreek)@ZnO (iii) Ag(Tea)@ZnO   (iv) Ag(Acacia Concinna/Shikakai)@ZnO and metal (Co) doped ZnO nanorods, which is further divided into three sections. The synthesis and mechanism of visible light harvesting section (A) Co-doped ZnO nanorods, (B) CdS/Co-doped ZnO nanorods and (C) Pt/CdS/Co-doped ZnO nanorods molecular devices. All prepared by hydrothermal method using cationic surfactant

cetyltrimethylammonium bromide (CTAB). Their physical growth mechanism was traced in the light of FESEM and HRTEM studies. A strong correlation between their electronic structural arrangement and photocatalytic activity was established. Broad and uniform UV-vis. diffuse reflectance spectral peaks were found between 525 and 700 nm, which were attributed to the d-d transition of Co^{2+} ion. Successful loading of the nano-sized sensitizer CdS onto the Co-ZnO NRs' surface, contributes to the band gap reduction in CdS/Co-ZnO NRs (E_g = 2.25 eV) sample. X-ray absorption spectroscopy confirms the presence of the lower degree structural disorders in CdS/Co-ZnO NRs with respect to the pristine ZnO and Co-ZnO NRs. It was found that the gradual modification in pristine ZnO NRs enhances the photocatalytic activity. Finally, the hetero-assembly, 1.5% Pt/CdS/Co-ZnO NRs, exhibited excellent photocatalytic responses in terms of quantum efficiency (1.98%) and hydrogen generation capacity (67.20 mmol/H_2 g) under 1 Sun (1.5AM G) light exposure.

In the second part of this chapter deals with the green synthesis of silver nanoparticles are used for pollutant degradation like as 4-nitrophenol to 4-aminophenol reduction. Finally, the products were used to degrade the 4-nitrophenol.

REFERENCES

1. Doorslaer X V, Dewulf J, Langenhove H V, Demeestere K, *Sci. Total. Environ.* 2014; 500-501: 250.
2. Bouki C, Venieri D, Diamadopoulos E. *Ecotoxicol. Environ. Saf.* 2013; 91:1.
3. Kümmerer K. *Chemosphere,* 2009; 75: 417.
4. Adriaenssens N, Coenen S, Versporten A, Muller A, Minalu G, Faes C, Vankerckhoven V, Aerts M, Hens N, Molenberghs G, Goossens H. *J. Antimicrob. Chemother.* 2011; 66:47.
5. Grave K, Greko C, Kvaale M K, Torren-Edo J, Mackay D, Muller A, Moulin G. *J. Antimicrob. Chemother.* 2012; 67:3001.
6. Watkinson A J, Murby E J, Costanzo S D. *Water Res.* 2007; 41: 4164.
7. Kummerer K.; Al-Ahmad A.; Mersch-Sundermann V. *Chemosphere,* 2000; 40: 701.
8. Gudaganatti M S, Hanagadakar M S, Kulkarni R M, Malladi R S, Nagarale R K. *Prog. React. Kinet. Mech.* 2012; 37: 366.
9. Patgar M B, Nandibewoor S T, Chimatadar S A. *Cogent Chemistry,* 2015; 1: 1.
10. Zhang H, Huang C H. *Environ. Sci. Technol.* 2005; 39: 4474.
11. Zhang H, Chen W-R, Huang C-H, *Environ. Sci. Technol.* 2008; 42: 5548.
12. Wang P, Yi-Liang H, Ching-Hua C H. *Water Res.* 2010; 44: 5989.
13. Dodd M C, Shah A D, Gunten U V, Huang C-H. *Environ. Sci. Technol.* 2005; 39:7065.
14. De Witte B, Dewulf J, Demeestere, Langenhove H. *J. Hazard. Mater .*2009; 161:701.
15. Nanda N, Mayanna S M, Gowda N M M. *Int. J. Chem. Kinet.* 1999; 3:153.

16. Nanda N, Kumar P, Malini. *Int. J. Pharm. Sci. Rev. Res.* 2013; 23:388.
17. Adegoke O A, Balogun B B. *Int. J. Pharm. Sci. Rev. Res.* 2010; 4:1.
18. Ebraheem S A M, Elbashir A A. *American Academic & Scholarly Research Journal.* 2012; 4:89.
19. Pavagada R J, Kanakapura B, Nagaraju R, Okram Z D, Kanakapura B V. *J. Appl. Spectrosc.* 2011;78:383.
20. Diab N, Abu-Shqair I, Al-Subu M, Salim R. *International Journal of Chemistry,* 2013; 34:1388.
21. Khan A A P, Asiri A M, Azum N, Rub M A, Khan A, Al-Youbi O A. *Ind. Eng. Chem. Res.* 2012; 51: 4819.
22. Shrivastavaa A, Singh A K, Sachdev N, Shrivastava D R, Katre Y, Singh S P, Singh M, Mejuto J C. *J. Mol. Catal. A: Chem.* 2012; 1.
23. Khan A A P, Khan A, Asiri A M, Khan S A. *J. Mol. Liq.* 2016; 218: 604.
24. Padavathil H T, Mavalangi S, Nandibewoor S T. *American International Journal of Research in Science, Technology, Engineering & Mathematics,* 2013; 3:63.
25. Yang B, Kookana R S, Williams M, Kumar A. *J. Hazard. Mater.*2016; 320.
26. Zhou Z, Jiang J-Q. *Chemosphere,* 2015; S119:95.
27. Kulkarni R M, Hanagadakar M S, Malladi R S, Biswal H S, Cuerda-Correa E M. *Desalination and Water Treatment.* 2015; 57:1.
28. Naik P N, Chimatadar S A, Nandibewoor ST. *Ind. Eng. Chem. Res.* 2009; 48:2548.
29. Badi S S, Tuwar S M. *Res. Chem. Intermed.* 2015; 41:7827.
30. Law M., Greene,L.E., Johnson,J.C., Saykally R and Yang P. *Nat. Mater.*, 2005; 4: 455.
31. Nozik A.J. and Miller J., *Chemical Reviews*, 2010; 110: 11
32. Si H.Y., Sun,Z.H., Zhang H.L., *Eng. Aspects*, 2008.
33. Gao X.F., Li,H.B., Sun,W.T., Chen Q., Tang F.Q., Peng,L.M., *J. Phys. Chem. C,* 2009; 113**:**18.
34. Hao Ming Chen, Chih Kai Chen, Chih-Jung Chen, Liang-Chien Cheng, Pin ChiehWu, Bo Han Cheng,You Zhe Ho, Ming Lun Tseng,Ying-Ya Hsu, Ting-Shan Chan, Jyh-Fu Lee, Ru-Shi Liu, and Din Ping Tsa, *ACS Nano*, 2012; *6* :8.
35. H.M. Chen, C.K. Chen, Y.C. Chang, C.W. Tsai, R.S. Liu, S.F. Hu, W.S. Chang, and K. H. Chen, *Angew. Chem. Int. Ed.* 2010; 49.
36. J. Hensel , G. M. Wang , Y. Li , J. Z. Zhang , *J. Phys. Chem. C*, 2010; 114:1.
37. Jingfei Luan * and Jianhui Chen *Materials*, 2012; *5*.
38. Gongming Wang, Yichuan Ling and Yat Li* *Nanoscale*, 2012; 4.
39. Hao Ming Chen,† Chih Kai Chen,† Chun Che Lin,† Ru-Shi Liu,*,† Heesun Yang,‡ Wen-Sheng Chang,§ Kuei-Hsien Chen,∥ Ting-Shan Chan,# Jyh-Fu Lee,# and Din Ping Tsai *J. Phys. Chem. C*, 2011; 115.
40. Le A-T, Tam LT, Tam PD, et al. *Materials Science and Engineering: C.* 2010; 30:6.
41. Huang H, Yang Y. *Composites Science and Technology*. 2008; 68:14.
42. Yin H, Yamamoto T, Wada Y, Yanagida S. *Materials Chemistry and Physics*. 2004; 83:1.

43. Nadagouda MN, Speth TF, Varma RS. *Accounts of Chemical Research*. 2011; 44:7.

44. Suber L, Sondi I, Matijevic E, Goia DV. *Journal of Colloid and Interface Science*. 2005; 288:2.

45. Song K, Lee S, Park T, Lee B. *Korean Journal of Chemical Engineering*. 2009; 26:1.

46. Golubeva O, Shamova O, Orlov D, Pazina T, Boldina A, Kokryakov V. *Glass Physics and Chemistry*. 2010; 36:5.

47. Harada M, Kawasaki C, Saijo K, Demizu M, Kimura Y. *Journal of Colloid and Interface Science*. 2010; 343:2.

48. Harada M, Kimura Y, Saijo K, Ogawa T, Isoda S. *Journal of Colloid and Interface Science*. 2009; 339:2.

49. Li K, Zhang F-S. *Journal of Nanoparticle Research*. 2010; 12:4.

50. Bogle KA, et al. *Nanotechnology*. 2006; 17:13.

51. Zhu J, Liu S, Palchik O, Koltypin Y, Gedanken A. *Langmuir*. 2000; 16:16.

APPENDIX-A

Distinctions anD awarDs

1. **International Best Research Scholar Award 2018** for contributed to a great extent in the field of Nanotechnology, by International Science Community Association (ISCA) Venu: Rashtriya Sanskrit Vidyapeetha, Tirupati, Andhra Pradesh, India on Monday, 8th May 2018.

2. **International Young Scientist Award 2018 in** 4th International Young Scientist Congress (IYSC-2018) organized by International Science Community Association (ISCA) in collaboration with Rashtriya Sanskrit Vidyapeeth, Tirupati, Andhra Pradesh, India on 8th & 9th May 2018.

3. **Campus Ambassador** of University of Kota in **"APOGEE" The Annual Technical Festival of Bits Pilani** Organized by Birla Institute of Technology & Science, Pilani on March 2015, 2017 and Feb 2018.

4. **Best Poster Presentation Award** during International Conference on Recent Trends in Chemical Sciences (ICRCS-2017) Organized by Department of Chemistry, Govt. Engineering College Bikaner, Rajasthan, India Jan 12-13, 2017.

5. **Best Appreciation Award** during National Symposium Global Environmental Challenges: Present Scenario (GECPS-2017) Organized by Department of Botany, University of Rajasthan, Jaipur, India 21st Jan 2017.

6. **Dr. S. K. Banerji** Award in UGC-Sponsored National Conference on Modern Trends in Chemical Sciences Organized by Department of Chemistry, Faculty of Science, Mohan Lal Sukhadia University, Udaipur, Rajasthan 30th - 31st January 2016.

7. **Young Scientist Award 2016 in 92nd Annual Indian Chemical Society (ICS)** organized by Department of Chemistry, Institute of Science, GITAM University, Visakhapatnam, Andhra Pradesh during 27-29 Dec. 2016.

APPENDIX B

LIST OF PUBLICATION(S)/COMMUNICATION(S)

(1) Rajesh Kumar Meena & Neelu Chouhan, "Rapid Biosynthesis of Silver Nanoparticles using Fenugreek Seeds" Proceeding of 3rd International Conference on *"Advance Trends in Engineering, Technology and Research" (ICATETR-2014) held at Balkrishna Institute of Technology, IPR-15, Kota on 22-24 Dec.2014 pp 376-378.*

(2) Neelu Chouhan* & **Rajesh Kumar Meena,** "Biosynthesis of Silver Nanoparticles Using Trachyspermum Ammi and Evaluation of Their Antibacterial Activities" *J. Pharm. Biochemical Sciences,* 2015, 6(2): (B) 1077-1086 publisher STRP, (IF=2.958) e-ISSN: 2320-1924.

(3) Rajesh Kumar Meena and Neelu Chouhan, "Biosynthesis of Silver Nanoparticles from Plant (Fenugreek Seeds) Reducing Method and their Optical Properties" *Research Journal of Recent Sciences*, Vol. 4(IVC-2015), 1-5 (2015) ISSN 2277-2502.

(4) Rajesh Kumar Meena and Neelu Chouhan "ZnO Nanoparticles Synthesized by a Novel Approach at Room Temperature and Antibacterial activity" *American International Journal of Research in Formal, Applied & Natural Sciences,* 11(1), June-August 2105, pp. 68-72.

(5) Neelu Chouhan, Rakshit Ameta, **Rajesh Kumar Meena**, Niranjan Mandawat, and Rahul Ghildiyal, "Visible light harvesting Pt/CdS/Co-doped ZnO nanorods molecular device for hydrogen generation" *International Journal of Hydrogen Energy,* 41(4) 2016, 2298-2306 (Elsewhere publications) (IF= 3.659) (doi:10.1016/j.ijhydene.2015.11.019)

(6) Rajesh Kumar Meena & Neelu Chouhan, "Synthesis and characterization of Flower-shaped Ag@ZnO nanocomposite and Antibacterial Activities" **Proceeding of** National Conference on "Green Chemistry and Sustainable Technologies for Society 2016" **(NCGCSTS-2016)** *held at* Government Women Engineering College, Ajmer on – 11-12, Jan.2016 pp-16-18.

(7) Rajesh Kumar Meena & Neelu Chouhan, "Biosynthesis of silver nanoparticles (Tea Leaves) reducing   method and there optical properties, **Research** *Journal of Recent Sciences,* Vol. 5(11), 39-43, November 2016.

(8) Rajesh Kumar Meena & Neelu Chouhan, **"**ZnO Nanoparticles synthesized by precipitation method and Optical properties" ISST *Journal of Applied Chemistry***, Vol. 7(2), (July - December 2016), p.p. 7-10.

(9) Neelu Chouhan, Rakshit Ameta, **Rajesh Kumar Meena**, "Biogenic Silver Nanoparticle from *Trachyspermum Ammi* (*Ajwain*) Seeds Extract used in Catalytic Reduction of p-Nitrophenol to p-Aminophenol in excess of $NaBH_4$" ***Journal of Molecular Liquids,*** *230 (2017) 74-84.*

(10) Rajesh Kumar Meena, Niranjan Kumar Mandawat, Neeta Gurbani and Neelu Chouhan, "Synthesis of ZnO Nanoparticles for Organic Pollutant Degradation" ***International Journal of Advance Research in science and Engineering,*** *Vol. No 6(01), January 2017 P.P 802-808.*

(11) Rajesh Kumar Meena, Kahkashan Ansari, Nawal Kishor and Neelu Chouhan "Green synthesis of silver nanoparticles using acacia concinna plant extract and their antibacterial activity" ***Research Journal of Recent Sciences,*** (2018) Vol. **7(3),** 1-6.

Publications Book Chapter:

1. Co-Author of **SOLAR ENERGY CONVERSION AND STORAGE Photochemical Modes:** Some Photochemical Modes, Chapter 8 Hydrogen: An Alternative fuel Neelu Chouhan, **Rajesh Kumar Meena** and R. S. Liu, Apple Academics Press CRC Press, a Taylor & Francis Group, Florida- USA. 2015 (978-48-224630-8)

APPENDIX C

LIST OF SEMINAR/SYMPOSIUMS/ CONFERENCES

1. **Indo-Swedish Symposium on Strategic Knowledge on Climate Change** (Designing Climate-Smart Water adaptation Strategies for Sustainable Development) Organized by Department of Pure and Applied Chemistry, University of Kota, Kota (India) October 09, 2012.

2. **International Workshop on Chemistry for a Sustainable Future jointly** Organized by Department of Chemistry , University of Rajasthan, jaipur & Malaviya National Institute of Technology, jaipur in Collaboration With Green Chemistry Network Centre, Department of Chemistry, University of Delhi (India) December 10-12, 2012.

3. **Indian chemical society Convention (*49th Annual Convention of Chemists 2012*)** Organized by Department of Applied Science, National Institute of Technical Teacher's Training and Research, Bhopal, Madhya Pradesh (India) December 12–15, 2012.

4. **19th ISCB International Conference (ISCBC-2013) titled "Recent Advances and Current Trends in Chemical and Biological Science"** jointly Organized by Indian Society of Chemistry & Biologists, Lucknow (UP) India and Deptt. Of Chemistry, Mohanlal Sukhadia University, Udaipur (Rajasthan) India March 2-5, 2013.

5. **Board of Research in Nuclear Sciences (BRNS) Sixth School on Analytical Chemistry (SAC-6)** Organised By Association of Environmental Analytical Chemistry of India (AEACI), C/O Analytical Chemistry Division, Bhabha Atomic Research Centre, Trombay, Mumbai, India During May 13-20, 2013.

6. **International Conference on Interdisciplnary Areas With Chemical Sciences (ICIACS2013)** Organized by Panjab University, Chandigarh In Association With Institute of Nano Science and Technology (INST), Mohali, (India) 30th Oct- 1st Nov 2013.

7. **DAE-BRNS Conference on organic devices the future ahead (ODeFA) 2014** organized by Technical Physics Division Bhabha Atomic Research Center, Mumbai on 3rd to 6th March 2014.

8. **"IVCr workshop on X-ray diffraction systems and related applications"** Containing XRD basics, experimental techniques & data analysis using Highscore Plus software Organized by University of Delhi, India on 25-26th Sep 2014.

9. **National Conference on Material Science (NCMS-2014)** *Organized by Department of Physics, Mewar University Gangrar, Chittorgarh-312901 (Rajasthan) India* on Oct. 17-18, 2014.

10. **National Seminar on "Recent Advancements in Protection of Environment and its Management Issues" (NSRAPEM-2015)** Organized by Maharishi Arvind College of Engineering & Technology, Ranpur, Kota on 27-28 February 2015.

11. **2nd International Virtual Congress (IVC-2015)** Organized by International Science Congress Association, and presented a scientific paper "Biosynthesis of Silver Nanoparticles from Plant (Fenugreek Seeds) Reducing Method and their Optical Properties" ISBN 978-93-83520-98-1.

12. **52nd Annual Convention of Chemists 2015 And International Conference on Recent Advances in Chemical Sciences** Organized by JECRC University, Jaipur, Rajasthan December 28–30, 2015.

13. **National Conference on "Green Chemistry and Sustainable Technologies for Society2016"** Organized by Government Women Engineering College, Ajmer, January 11-12, 2016.

14. **UGC-Sponsored National Conference on Modern Trends in Chemical Sciences** Organized by Department of Chemistry, Faculty of Science, Mohan Lal Sukhadia University, Udaipur, Rajasthan 30th – 31st January 2016.

15. **International Conference on Frontiers at the Chemistry Allied Sciences Interface (FCASI-2016)** Organized by Department of Chemistry, University of Rajasthan, Jaipur 25-26 April, 2016.

16. **3rd International Virtual Congress (IVC-2016)** Organized by International Science Congress Association, and presented a scientific paper "Biosynthesis of Silver Nanoparticles (Tea Leaves') Reducing Method and their Optical Properties" ISBN 978-93-83520-98-1.

17. INUP **"Familiarization Workshop on "Nanofabrication Technologies"** Organized by Electronics & Communication Engineering Department, Malaviya National Institute of Technology, Jaipur, Rajasthan 26-27 August 2016.

18. National Conference on **Frontiers in Chemical Sciences** (NCFCS-2016) in association of Indian Chemical Society, Kolkata Organized by Department of PG Studies & Department of Chemistry, Pacific University, Udaipur (Raj.) 4th October 2016.

19. **National Conference and workshop on Green Chemistry teaching and technology (NCWGC- 2016)** Organized by Department of Chemistry, Faculty of Science, Mohan Lal Sukhadia University, Udaipur, Rajasthan 20 Oct. 2016.

20. **2nd International Conference on Soft Material (ICSM-2016)** Organized by Department of Physics Malaviya National Institute of Technology (MNIT), Jaipur, Dec 12-16, 2016.

21. **92nd Annual Indian Chemical Society organized by** Department of Chemistry, Institute of Science, GITAM University, Visakhapatnam, Andhra Pradesh during 27-29 2016.

22. **International Conference on Recent Trends in Chemical Sciences (ICRCS-2017)** Organized by Department of Chemistry, Govt. Engineering College Bikaner, Rajasthan, India Jan 12-13, 2017.

23. **National Symposium Global Environmental Challenges: Present Scenario (GECPS-2017)** Organized by Department of Botany, University of Rajasthan, Jaipur, India 21st Jan 2017

24. "Synthesis of ZnO Nanoparticles for Organic Pollutant degradation" Rajesh Kumar Meena[1], Niranjan Kumar Mandawat[2], Neeta Gurbani[3], Neelu Chouhan[4]* **International Conference on Innovative Research in Science, Technology and Management (ICIRSTM-17)** Modi Institute of Management & Technology, Dadabari, Kota, Rajasthan 22-23 Jan 2017. **Conference proceeding in Page 802-808, ISSN (o) 2319-8354**

25. Presented of Research Work in "**Nano India 2017"** Conference Organized by Indian Institute Of Technology Delhi, New Delhi during 15-16 March 2017.

26. UGC-Sponsored One Week Short-term Course on **Separation Techniques and Instrumental Method of Analysis** from January 30, 2017 to February 4, 2017 at University of Kota, Kota, Rajasthan.

27. **Anveshan Students' Research Convention (West Zone)** organized by association of Indian Universities and hosted by Nims University Rajasthan on 7th-8th March 2017.

28. **National Symposium on Nano Science & Technology (NSNST-2017)** from 2nd - 4th july 2017 conducted by the Centre for Nano Science and Engineering, Indian Institute of Science, Bangalore.

29. **CRSI-ACS** Symposium in Chemistry July 30, 2017 Organized by CSIR-Indian Institute of Chemical Technology, Tarnaka, Hyderabad, India.

30. International Conference on **Frontiers at the Chemistry – Allied Science Interface (FCASI-2017)** Organized by Centre of Advanced Study, Department of Chemistry University of Rajasthan, Jaipur (INDIA) Supported by UGC, New Delhi; DST, Govt.

of India, New Delhi CRSI-Rajasthan Chapter; ISCB-Jaipur Chapter; RSC-North India Section.

31. **4th International Virtual Congress (IVC-2017)** Organized by International Science Congress Association, and presented a scientific paper "Green Synthesis of Silver Nanoparticles using Acacia Concinna extract and their Antibacterial activity" ISBN 978-93-83520-98-1.

32. **International Conference of Advancing Green Chemistry:** Building a Sustainable Tomorrow 3-4 Oct 2017 Organized by Green Chemistry Network Centre, Department of Chemistry, University of Delhi, Delhi. "Green Synthesis of Metal nanoparticles using Plant extract" by Reducing method and Optical Properties Presented by Rajesh Kumar Meena and Neelu Chouhan*

33. **International Conference on Nano and Functional Materials**- Interface between Science & Engineering (NFM-2017) jointly Organized by Department of Chemistry, BITS Pilani, Pilani campus and Materials Research Society of India (MRSI) Rajasthan Chapter, held between 16-18 November 2017.

34. **7th International Science Congress (ISC-2017)** 8th & 9th December 2017 jointly organized by International Science Community Association & College of Science and Technology, Rinchending, Phuentsholing, Chukkha, Bhutan, "Synthesis of flower-like ZnO nanostructures and Optical properties by Hydrothermal process" Rajesh Kumar Meena and Neelu Chouhan*

35. **54th Annual Convention of Chemists 2017** Organized by Uka Tarsadia University, Bardoli, Surat, Gujarat December 23-25, 2017 (AEC (AP)-06 Green Synthesis of silver nanoparticles by using Black pepper extract for catalytic reduction of organic pollutant Rajesh Kumar Meena and Neelu Chouhan*

36. **54th Annual Convention of Chemists 2017** Organized by Uka Tarsadia University, Bardoli, Surat, Gujarat December 23-25, 2017 (IAC (AP)-03 "Synthesis of flower shape ZnO nanostructure and optical properties for dyes degradation" Rajesh Kumar Meena and Neelu Chouhan*

37. **4th International Young Scientist Congress (IYSC-2018)** organized by International Science Community Association (ISCA) in collaboration with Rashtriya Sanskrit Vidyapeeth, Tirupati, Andhra Pradesh, India on 8th & 9th May 2018.

APPENDIX D

ReseaRch Publ ication (s)

Rapid Biosynthesis of Silver Nanoparticles using Fenugreek Seeds

Rajesh Kumar Meena[1] & Neelu Chouhan*[1]
*[1]Department of Pure & Applied Chemistry, University of Kota, Kota, Rajasthan, India.
Corresponding author's Email address- niloochauhan@hotmail.com

Abstract- The present study focus on green chemistry in the synthesis of silver nanoparticles (AgNPs) by silver nitrate and utilizing the bio components of seeds extract of fenugreek plant. The optical properties of the as prepared nanoparticles of size 100-200 nm, were characterized for by using TEM, UV – visible spectroscopy and FTIR spectroscopy. The Fourier transformer infrared spectroscopy reveals the presence of polyphenolic compounds in fenugreek seeds extract which acts as a reducing agent for the transformation of silver nitrate into silver nanoparticles. The experimental absorption peak at 419nm corresponds to surface plasmon resonance belongings of silver nanoparticles.

Keywords: Silver nitrate, Polyphenols, Fenugreek seeds, Nanotechnology, Silver nanoparticles.

I. INTRODUCTION

Introduction and Experimental

The silver nanoparticles are popular as the multifunctional inorganic nanoparticles and can be synthesized by simple and ecofriendly methods. The synthesis of nanoparticles of noble metals such as silver exhibited significantly distinct chemical, physical and biological properties from their bulk counterparts over the past decade. Traditionally, Silver is expansively used as a disinfecting agent and in some countries it is also used as an ingredient in cuisine [1]. In recent years, various chemical methods have been replaced by biological for the synthesis of silver nanoparticles [2, 3]. Green chemistry, has developed as a naive and possible another to more complex chemical synthetic protocols to obtain Silver nanoparticles Therefore, a growing attention towards the biosynthesis of the metal nanoparticles using organisms like yeast, honey plant extracts, enzymes, etc, is noticed. Among these organisms, plants seem to be the best candidate and they are suitable for large scale biosynthesis of nanoparticles. Nanoparticles produced by plants are more stable, and the rate of synthesis is faster than that in the case of other organisms. Colleagues and Sastry [4] pioneered the consumption of plant extracts to synthesize nanoparticles and have reported syntheses of nanoparticles at rates on par with chemical reagents. Various metallic nanoparticles of gold, zinc, palladium, silver etc., are being synthesized using biological systems [5]. Uchida et al., [6], Kumar and Munsted [7] recommended that the antimicrobial activity of Ag may be due to the binding of the Ag^+ cation to electron donor groups in biological molecules containing oxygen, sulphur or nitrogen (e.g. enzymes) which, in turn, results in the loss of their function. The present attempt is to use fenugreek seeds for reducing silver nitrate salts to metallic silver. Because of their inherent antimicrobial abilities, Fenugreek seeds are useful and cost effective, possesses photochemicals such as polyphenols and alkaloids that can be used as a reducing agent in the synthesis of metal nanoparticles.

II. Experimental Details:

Chemicals: All chemicals were of analytical grade (AR) and used as purchased without any further purification. Analytical grade chemicals such as, $AgNO_3$ (silver nitrate, $\geq99.0\%$, Merck), and Ethyl alcohol (SD fine-chem limited) were used in the study. All solutions were prepared using deionised Millipore water.

Characterization: Morphology and elemental composition of the sample was checked using scanning electron microscopy (FESEM, JEOL JSM-6700F). The optical absorptions of the mixtures of seeds extract and colloidal solution of $AgNO_3$ (sample solutions) were evaluated in 10 mm optical path length quartz cuvettes. The characteristic absorption peak of AgNPs were examined using UV-visible spectrum, recorded using UV-Vis spectroscopy (LABINDIA UV- Visible 3000+) in the range between 250 – 800 nm. In order to identify the groups of the phytochemicals capped on the surface of the AgNPs. Fourier Transform Infra-red spectroscopy (Bruker -Tensor Model) was used to study the bonding environment of the AgNPs in Fenugreek extract in the range of 4000 to 400 cm^{-1}. Dried and purified powders of AgNPs in KBr pellets were then the subjected to FTIR spectroscopic measurement.

Preparation of Dried Fenugreek Seeds:

The fresh fenugreek plant seeds were exposed to the sun until they were totally dried. The fenugreek plant seed extraction was prepared by boiling a mixture of 5 g of fenugreek dried seeds into sterile distilled water in an Erlenmeyer flask for 5 min and filtered through Whatman filter paper. The filtrate was further filtered through 0.6 μm sized filters. The solution was decanted and stored at 4°C; it was used within a week of its preparation. The extract used for the reduction of silver ions to silver nanoparticle.

Biosynthesis of Silver Nanoparticles:

The filtrate, fenugreek seeds extract (FSE), was then added to the silver nitrate solution drop wise, at a ratio of 4:1 as reported earlier [8]. Then this mixture was refluxed at room temperature for 24 to 48 hours to obtain colloidal silver nanoparticles (Fig.1a and 1b) which are further dried and stored for characterization. Then aqueous solution of 0.001M$AgNO_3$ was used in the synthesis of silver nanoparticles by bioreduction of Ag+ ions in the solution. AgNPs were centrifuged at 10,000 rpm for 15 min. The process of centrifugation and dispersion in sterile distilled

water was repeated three times to ensure better separation of free entities from the metal nanoparticles. The AgNPs solution kept at room temperature for 24 hours.


(a)   (b)
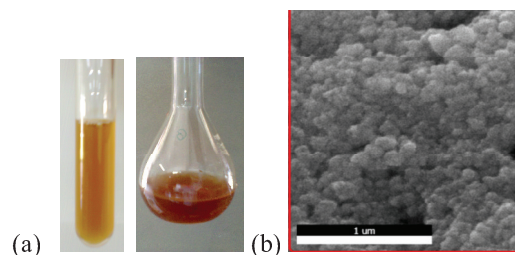
Figure 1a represents the Fenugreek seed extract (yellow) and 15days aged Fenugreek supported silver nanoparticles (dark pink) (b) TEM image of AgNPs.

III. Results and Discussion

Fig. 1a., shows the colloidal solutions of the extract, and the mixtures of extract and AgNO$_3$ solution, colour change from golden yellow to reddish yellow occurs by adding the AgNO$_3$ solution into the extract, which indicates the presence of Ag nanoparticles. Microscopic studies illustrated the formation of cubical AgNPs of size 100-200 nm as shown by FESEM imaging (Fig. 1b). **Figure 2** exhibits the distinctive absorption peak in UV-visible spectroscopy for Ag nanoparticles become visible around 400 nm of the optical range due to surface plasmon resonance [9-10]. This absorption identifies the formation of Ag nanoparticles in a colloidal solution. Data revealed an appearance of surface plasmon resonance peak (SPR) at the 419nm, the wavelength corresponds to silver nanoparticles formation.
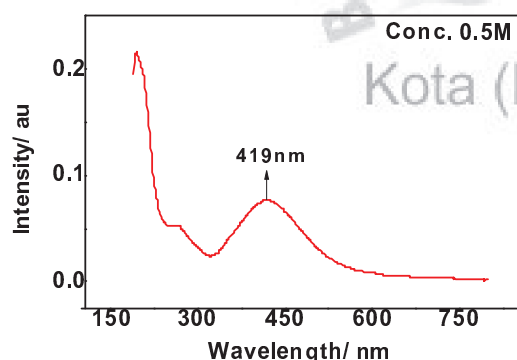
Figure 2. UV Visible spectrum of silver nanoparticles (24 h).

FTIR Analysis of Silver Nanoparticles after Bioreduction: To identify the probable biomolecules responsible for the reduction of the Ag$^+$ ions and ex-capping of the bio-reduced silver nanoparticles synthesized using fenugreek seed extract. FTIR studies were carried out and the representative spectrum of the nanoparticles obtained in the present study is presented in **Figure 3**. Amongst them, the absorption peak at something like 2800, 1572, 1399, 1148 cm^{-1} can be assigned as absorption peaks.
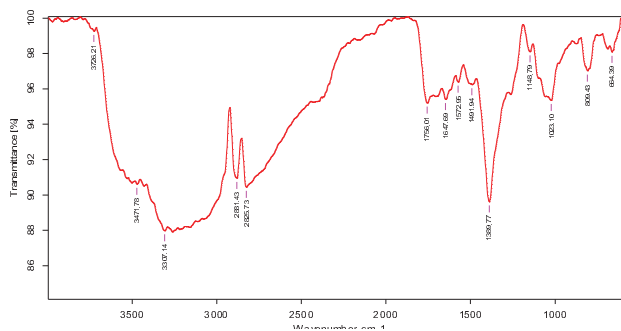
Figure 3. FTIR spectrum of fenugreek supported silver nanoparticles

The broad peak obtained at the 2800 cm^{-1} suggests the presence of organic acid groups which maintain the higher fungicidal efficacy of silver nanoparticles as already mentioned above under reference that fenugreek plant has fungicidal organic acids like ferulic acid, coumaric acid and proto catechuic acid, etc. Peak at 1399 cm^{-1} assigned to the amides and amines. The narrow peaks at 1572 and 1491 cm^{-1}, clearly evidence the attendance of stretches of C=C-C and C-H bonds in aromatic rings that are found in coumaric acid, ferulic acid. Another peak at the 1148 cm^{-1} attributes the antifungal activity further suitable to the presence of compounds from fenugreek seed extract that have ether and ester forming C=O setups [11-13]. So FTIR results confirm the presence of the phytochemicals such as polyphenols (-OH group), carbonic acids present in the FSE caps the silver nanoparticles surface, there by restricting the aggregation of silver nanoparticles and stabilize them.

IV. Conclusions

Although the reduction process during the formation of fenugreek seeds extract mediated Ag nanoparticles takes hours to days, but Ag nanoparticles thus produced were of almost uniform size, which is a most wanted requirement for their utilization. Mechanism of formation of the fenugreek seeds extract mediated Ag nanoparticles has been derived from the experimental observations. To the best of our knowledge this is the best information of the observations of the unique structures of fenugreek seeds extract mediated Ag nanoparticles. This opens a way to understand the synthesis mechanism of Ag nanoparticles formed from other plant seeds extracts.

References

1. S.C.G. Kiruba Daniel, B. Nazeema Banu, M. Harshiny, K. Nehru, P. Sankar Ganesh, S. Kumaran and M. Sivakumar, "Ipomea carnea-based silver nanoparticle synthesis for antibacterial activity against selected human pathogens," *J of Expt. Nanosci.,* pp. 1-13, 2012.

2. T. L. Riddin, M. Gericke and C. G. Whiteley, "Analysis of the Inter- and Extracellular Formation of Platinum Nanoparticles by Fusarium oxysporum. sp. Lycopersicum Using Surface Response Methodology," *Nanotechnology*, Vol. 17, No. 14, pp. 3482-3489, 2006.

3. K. B. Narayana and N. Sakthivel, "Biological Synthesis of Metal Nanoparticles by Microbes," *Advances in Colloids and Interface Science*, Vol. 156, No. 1-2, pp. 1-13, 2010.

4. S. P. Chandran, M. Chaudhary, R. Pasricha, A. Ahmad and M. Sastry, "Synthesis of Gold Nano Triangles and Silver Nanoparticles Using Aloe Vera Plant Extract," *Bio- technology Progress,* Vol. 22, No. 2, pp. 577-583, 2006.

5. M. Sastry, A. Ahmad, K. M. Islam and R. Kumar, "Bio- synthesis of Metal Nanoparticles Using Fungi and Acti- nomycetes," *Current Science*, Vol. 85, No. 2, pp. 162-170, 2003.

6. M. Uchida, T. Yamamoto and A. Taniguchi, "Reaction of Silver Ions and Some Aminoacids," *J of Antibacterial and Antintifungal Agents,* Vol. 31, No. 11, pp. 695-704, 2003.

7. R. Kumar and H. Münstedt, "Silver Ion Release from Antimicrobial Polyamide/Silver Composites," *Biomaterials,* Vol. 26, No. 14, pp. 2081-2088, 2005.

8. Devasena T., Gayathri R. andTamilarasi K., Fenugreek mediated biosynthesis of silver nanoparticles and their characterization for biomedical applications, *Biomed*, 30, 2, 192-197, 2010.

9. U. Kreibig, M. Vollmer, *Springer Series in Material Science,* 25 (1995) 50.

10. Anupam R., Kalyani K., Anjan M., and Nandan B., Highly Cytotoxic (PA-1), less Cytotoxic (A549) and antimicrobial activity of a green synthesized silver nanoparticle using *Mikania cordata* Int J of Advances Res, 2013,1, 193 - 198.

11. V. Bansal, D. Rautaray, A. Bharde, K. Ahire, A. Sanyal, A. Ahmad, *et al.*, "Fungus-Mediated Biosynthesis of Sil- ica and Titania Particles," *Journal of Materials Chemistry*, Vol. 15, No. 26, pp. 2583-2589, 2005.

12. J. Huang, Q. Li, D. Sun, Y. Lu, Y. Su, X. Yang, *et al.*, "Biosynthesis of Silver and Gold Nanoparticles by Novel Sundried Cinnamomum Camphora Leaf," *Nanotechnol- ogy*, Vol. 18, No. 10, 2007.

13. R. Sanghi and P. Verma, "Biomimetic Synthesis and Characterisation of Protein Capped Silver Nanoparticles," *Bioresource Technology*, Vol. 100, No. 1, pp. 501- 504, 2009.

Dr. Neelu Chouhan, after obtaining a PhD degree in Organic conductors from the M. L. Sukhadia University Udaipur, undertook research on various topics. She has been teaching physical chemistry at the University of Kota, Kota. Her main research interests are in field of organic conductors, kinetic studies of phenols, nanomaterial and related fields. She heads a research group, which carried out computational and experimental studies on catalysis by nanomaterials. Her research on nanoscale materials also includes theoretical and experimental studies on quantum dots and their size-dependent properties to be used in photocatalytic water splitting for hydrogen production as well as semiconductor devices and sensors. Prof. Chouhan has over 20 research publications in international journals of well repute. She has delivered invited several talks at scientific conferences. She regularly reviews manuscripts for many international journals, including those published by the American Chemical Society, Royal Society of Chemistry and Elsevier.

Rajesh Kumar Meena did his B.Sc. (2009) and M.Sc. (2011) in Inorganic Chemistry from Department of Chemistry, Rajasthan University, Jaipur, India. He is currently pursuing Ph.D. under the guidance of Associate Prof. Dr. Neelu Chouhan at the Department of Pure and Applied Chemistry, University of Kota, Kota India. His research interests include Nanoscience, Quantum dots, Nanoparticles synthesized and their applications in Photocatalytic Water Splitting for Hydrogen Production as well as semiconductor devices, sensors and biomedical area.

Research Article   **Biochemistry**

BIOSYNTHESIS OF SILVER NANOPARTICLES USING TRACHYSPERMUM AMMI AND EVALUATION OF THEIR ANTIBACTERIAL ACTIVITIES

NEELU CHOUHAN[1] & RAJESH KUMAR MEENA[2]

[1]Associate Professor, Department of Pure & Applied Chemistry, University of Kota, Kota, Rajasthan, India,
[2]Research Scholar, Department of Pure & Applied Chemistry, University of Kota, Kota, Rajasthan, India,

ABSTRACT

Bio-chemical reduction method was employed to synthesise the silver nanoparticles (Ag NPs) by aging the mixture of the aqueous extract of the *Trachyspermum Ammi* (TA, Ajwain) seeds and $AgNO_3$ solution at different time interval. Reaction time of $AgNO_3$ and TA could accelerate the reduction rate of Ag^+ and affect AgNPs size and concentration of NPs. X-ray diffraction (XRD) studies confirms the formation of pure AgNPs that crystallized into the cubic shape particles of size 36nm. Surface plasmon resonance band centred at 420-430 nm was recognised as the first exitonic peak of UV-Vis absorption spectra that confirmed the presence of the AgNPs. FTIR results TA supported AgNPs showed decrease in intensity of peaks at 3497 and 1695 cm^{-1} with respect to the pure TA indicating the involvement of NH_2, O-H, carbonyl group and C=C stretching in formation of TA-AgNPs aggregates. The C-O-C and C-N stretching suggested the presence of the bonding between the phytochemicals and AgNPs. TA extract play a role of capping and reducing agent for converting silver ions into silver nanoparticles. Pronounce effect of the aging on AgNPs concentration and particle size, was exhibited by the system. As synthesized AgNPs was characterized using transmission electron microscopy (TEM), UV- Vis spectrophotometer (UV-Vis), Fourier transformation infrared (FTIR) spectroscopy and XRD. Study demonstrated the inside view of the most probable mechanism of the biosynthesis of AgNPs and the potent antagonistic activity against bacteria, which possess potential applications in medicine and pharmaceutical fields.

KEYWORDS: Biogensis, surface plasmonic resonance, Fourier transformation infrared spectroscopy, silver nanoparticles, antagonistic activity

NEELU CHOUHAN
Associate Professor, Department of Pure & Applied Chemistry,
University of Kota, Kota, Rajasthan, India,
niloochauhan@hotmail.com

*Corresponding author

INTRODUCTION

Nanotechnology plays a vital role in engineering and manipulating of the size particles at the nano level ranging from approximately 1-100 nm.[1] The importance of the nanotechnology in a variety of fields such as food, health care and feed, cosmetics, biomedical science, environmental health, chemical industries, drug and gene delivery, power science, electronics, mechanics, and space industries,[2] has been already established. It also has extensively been used for the treatments of diabetes,[3] cancer,[4] allergy,[5] inflammation,[6] and infection,[7] etc. In recent years the trend of the green synthesis of NPs is growing due to the number of its advantages over chemical synthesis methods such as simplicity, mild reaction conditions and cost effectiveness.[8] Moreover, it is compatible for biomedical and food applications and this technique eliminates the use of high pressure, temperature, energy and toxic chemicals.[9, 10] The growing need of environmental friendly production of nanoparticles forced researchers to choose the green way for their fabrication. Various metallic nanoparticles,[11] because of their remarkable properties over their bulk counter parts, used in the variety of applications.[12] Biological methods are more beneficial than the most popularly used photochemical reduction, chemical reduction, electrochemical reduction, heat evaporation, etc.[13] In biological method, the plant extract has been used as reducing and capping agent for the production of nanoparticles[14] due to their reducing properties.[15] The change in properties of the nanoparticles such as size, distribution, and morphology of the nanoparticles are clearly observed with biomaterial.[16] Various nanoparticles like gold, silver, copper, iron, palladium, zinc, quantum dots (CdS, ZnS) are synthesized using variety of biochemicals. Silver nanoparticles are selected for the study among the above mentioned nanoparticles because of their several unbeatable properties such as optical, chemical, electronic, photo electro chemical, catalytic, magnetic, antibacterial, and antimicrobial activity. Silver nanoparticle acts as antimicrobial agent can be used in medical applications such as blood collecting vessels, coated capsules, band aids, biological

labeling, etc.[23] The silver is non-toxic to animal cells and highly toxic to bacteria, and other microorganisms (E-coli, Pseudomonas aeruginosa, Staphylococcus aureus, etc). Therefore, nanosilver is considered as a safe, effective and valuable bactericidal metal to be used for medical purpose.[24-26] In present work, we used biogenic method for synthesis of silver nanoparticle, which are usually non-toxic, low cost, usage less amount of chemicals, environmental friendly workable at mild temperature and pressure conditions. Plants in general used for green synthesis of AgNPs are, *Zea mays*[27], *Azadirachta indica* (Neem)[28], *Medicago sativa* (Alfa alfa)[29,30], *Aloevera*[31], *Emblica officinalis* (Amla)[32], *Capsicum annuum*[33], *Geranium* sp.[34,35], *Diopyros kaki*[36], *Magnolia kobus*[37] and *Coriandrum* sp.[38], etc. Different parts of plant like leaf, stem, flower, seed and skin of the fruits were already used for the synthesis of AgNPs. Plant extract-coated nanoparticles, has medical advantageous, can be used in drugs and cosmetic applications.[39] *Trachyspermum Ammi* (TA) belongs to the family of *Apiaceae* plants, commonly known as Ajwain. TA is a climbing herbaceous annual plant found in throughout India and has been served as an antibacterial and carminative drug in the traditional medicines.[40] TA consists of the fatty acids, proteins, flavonoids and alkaloids that promotes antioxidant, antimicrobial, anti inflammatory and immune stimulant activity.[41] The current investigation focused on the synthesize of AgNPs, using the aqueous seeds extract of TA at different experimental conditions and their application in antibacterial activity against the *Bacillus subtilis*, *Staphylococcus aureus* and *Escherichia coli* at room temperature. Work will contribute in establishing the importance of plant sources and implementing green chemistry in synthesis of nano metal particles for the future research.

MATERIALS AND METHODS

(1) Materials
Aqueous extract of TA seeds was used to synthesize AgNPs, using the method mentioned elsewhere.[42] Dry seeds were washed thoroughly with distilled water to make

them free form dust particles and surface contamination and dried in sunlight for week long time. Afterwards 2 gm dried seeds were soaked in to 50 mL of pure deionised water for 24 h. The extract was filtered using whatmann filter paper No.42. The filtrate was centrifuged at 2000 rpm for 20 min, and the suspended solid was used for further analysis.

(2) Chemicals

Analytical grade chemicals from different suppliers such as $AgNO_3$ (silver nitrate, ≥99.0%, Merck), $Zn(NO_3)_2.6H_2O$ (zinc nitrate hexahydrate 98%; Sigma Aldrich), were used as purchased without any further purification. All solutions were prepared with deionised water (DIW).

(3) Synthesis of Silver Nanoparticles

Silver nanoparticles were synthesized using the following procedure. Firstly, the aqueous 10^{-3} M $AgNO_3$ solution was prepared in 250 mL of deionised water. Secondly, 2.5 mL of concentrated TA seeds extract was added drop wise into the 25 mL $AgNO_3$ solution that kept at room temperature for after 2 minutes, 7h, 24h, 7day's, 21day's etc, respectively. During aging of $AgNO_3$ in TA extract, electron transfer from the solution to the Ag^+, was responsible for the electrical conduction in colloids and final conversion of Ag^+ ions into Ag nanoparticles. Reverse process occurs in oxidation process, where electrons get lost during reaction.

(4) Optical Properties of Ag Nanoparticles

Ultraviolet-visible spectroscopy (UV-Vis) refers to the absorption of light in the UV-visible spectral region i.e. 200-900 nm that directly affects the perceived colour of the involved chemicals. In this region of the electromagnetic spectrum, molecules undergo electronic transitions. UV-Vis absorption spectrum was taken using a (LABINDIA UV-Visible 3000⁺) spectrophotometer, where the cuvette path length was set to 1.0 cm and DIW was used for background subtraction. UV-VIS absorption spectra have been proven a sensitive tool to get the information about the formation of silver nanoparticles. Because an intense absorption peak of silver nanoparticles exhibited in certain region (~ 420 nm) that attributed to the surface

plasmonic resonance (it describes the collective excitation of the conduction electrons in a metal) excitation. This technique can characterize the silver dendrites, colloids and surfaces.

(5) pH Analysis

The pH was determined by using digital pH meter (Systronics; Model-ERMA). In making of the AgNPs process the pH of TA extract and $AgNO_3$ solution gradually became acidic (pH=7 to pH=5) within 24h time that revealed in the form of the reduction in pH of studied sample.

(6) XRD Analysis

The redispersed silver nanoparticles were kept in an oven at 60°C for 24h in order to obtain the dry powdered AgNPs of high purity. As synthesized silver nanoparticles, were used for phase identification and the crystallinity check using powder XRD. The diffracted intensities were recorded from 35 º to 90 º of 2 theta angles. XRD analysis was performed using an X'Pert Pro X-ray diffractometer operated at a voltage of 40 kV and a current of 30 mA with Cu K_{α} radiation.

(7) FTIR Analysis

In order to collect solid biomass of the seed residue or synthesised compound, the corresponding solution of 100 ml was centrifuged at 20,000 rpm for 10 min. This was followed by the drying of the AgNPs at 60°C. As obtained sample of the synthesised silver nanoparticles, was subjected to FTIR analysis in the range of 400 to 4000 cm^{-1} using Bruker -Tensor Model FTIR spectrophotometer in the diffuse reflectance mode at a resolution of 4cm^{-1} in KBr pellets.

(8) TEM Analysis

The TEM measurement was done using JEOL model 1200Ex microscope operated at an accelerating voltage of 80kV. Samples were prepared by placing 3-4 drops of the well dispersed Ag nanoparticles in alchohol on a 300-mesh carbon coated Cu grid (EM sciences) and allowing the liquid to evaporate in air. For Ag nanoparticles the particle size distribution was based on 30 randomly selected particles. The TEM image was taken with very high resolution and MATLAB analysis gives the pixel depth of the image

equal to 24 bits and the image format as JPEG. The TEM Images have been taken at National Chemical Laboratory, Pune, India.

RESULTS

(1) Optical Properties with UV Visible Spectroscopy

Biosynthesis of the silver nanoparticles was confirmed on the basis of the colour developed in solution during the course of reaction (transparent to pink) and change in pH (7 to 5) of solutions. The intensity of colour interprets the degree of bio-reduction of AgNPs due to addition of reducing agent. As the plant extract of TA seeds mixed in the aqueous solution of the silver ion complex, it started to change the colour (from transparent to deep reddish violet) due to reduction of silver ion, which may be the indication of formation silver nanoparticles, as shown in Figs 1 (a) and 1 (b). Colour of silver colloid is attributed to surface plasmon resonance (SPR) phenomena arising due to the collective oscillation of the free conduction electrons induced by an interacting electromagnetic field. [43] Therefore, the formation of AgNPs was primarily recorded on the basis of the surface plasmonic resonance/first exitonic peak in UV-visible spectroscopy.
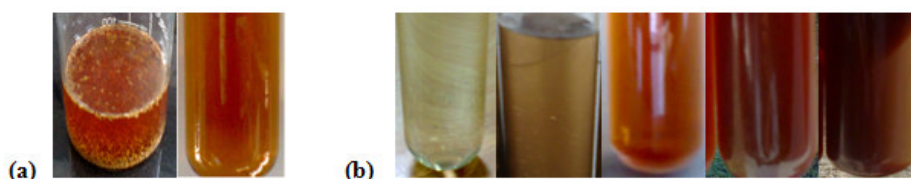
Figure 1
(a) Pure TA seed aqueous extract and filtered extract of TA (b) Synthesis of TA-Ag NPs at different aging time such as after 2 minutes, 7h, 24h, 7day's, and 21day's.

The deep reddish violet coloured sample powder was dissolved in DIW and sonicated for10 min, was taken in cuvette and exposed to UV-visible radiation for monitoring of the absorbance with respect to the DIW. Surface plasmon resonance phenomena, attributed to the first exitonic peak at different wavelength for different nanoparticles solution. It is reported in the literature [44-53] that typical AgNPs shows the characteristic SPR at the wavelength in the range of 380-440nm. Fig 2 exhibited the SPR peak at the wavelength of 422 nm, which verified the presence of AgNPs in the solution. This is absent in neat TA extract solution. The SPR absorbance is sensitive to the nature, concentration, size and shape of the particles present in the solution and also depends upon their inner particle distance and the surrounding media.
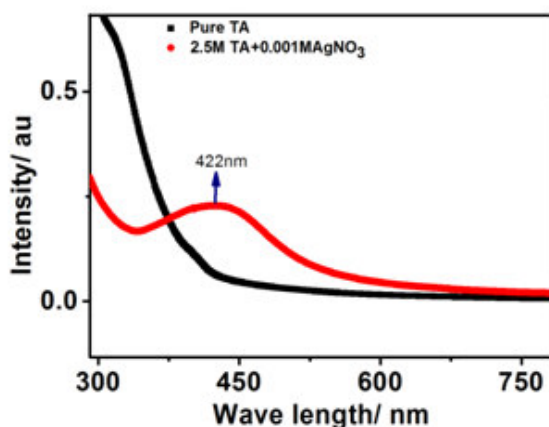
Figure 2
UV-visible spectrum of pure TA extract (black) and silver nanoparticles (red).

(2) XRD Pattern

XRD patterns of the synthesized AgNPs are shown by Fig 3, where four major peaks appeared. The peak position explains crystal parameters along with the translational symmetry, namely size and shape of the unit cell, whereas the peak intensities gives the details about the electron density inside the unit cell. These XRD patterns correspond to the cubic crystal structure which is in agreement with the standard JCPDS file No. 00-004-0783 and indicates that the synthesized nanoparticles are crystallised in a pure form without any impurities. The Braggs reflections observed in the XRD pattern at 2θ = 38.142°, 44.514°, 65.146° and 77.274° (Fig 3) which can be indexed to the (200), (220), (311) and (222) planes of pure silver, respectively. A strong diffraction peak was ascribed to the 32.23 facets of silver. The results thus illustrate that AgNPs was crystallized in face centered cubic symmetry of space group Fm-3m (Space group number: 225) along the point group m3m (O_h). Williamson-Hall plot (sin θ Vs β cos θ, where, θ in radians) was used to determine the particle size of the NPs, i.e. 36 nm.
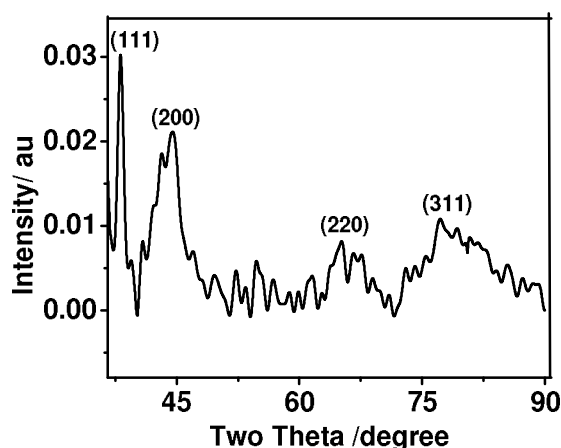
Figure 3
XRD Plot of Silver Nanoparticles

(3) FTIR Analysis

The FTIR measurements were carried out to identify the possible bio molecules present in dispersion of AgNPs that was responsible for the reduction of the Ag^+ ions. The spectrum as shown in the Fig.4 indicates the major peak at 3428.45 cm^{-1} (pure TA) resembles the presence of the intermolecular hydrogen bond in pure TA where, sharp and well defined peaks at 3723.95 cm^{-1} and 3664.86 cm^{-1} attributed to the intra-molecular hydrogen bond in AgNPs. [54] In addition to this, other peaks were obtained at 1695 cm^{-1}, 1047 cm^{-1} and minor peaks at 2876 cm^{-1}, 1539 cm^{-1}, 676 cm^{-1}, are corresponding to alkene C=C stretch, alcoholic C–O stretch, asymmetric and symmetric stretching and wagging vibrations of CH_2 group, NH_2, O-Ag-O stretching, which plays a major role in the synthesis of TA mediated silver nanoparticles. These bonds tethered AgNPs with organics present in TA and reduce Ag^+ ion.
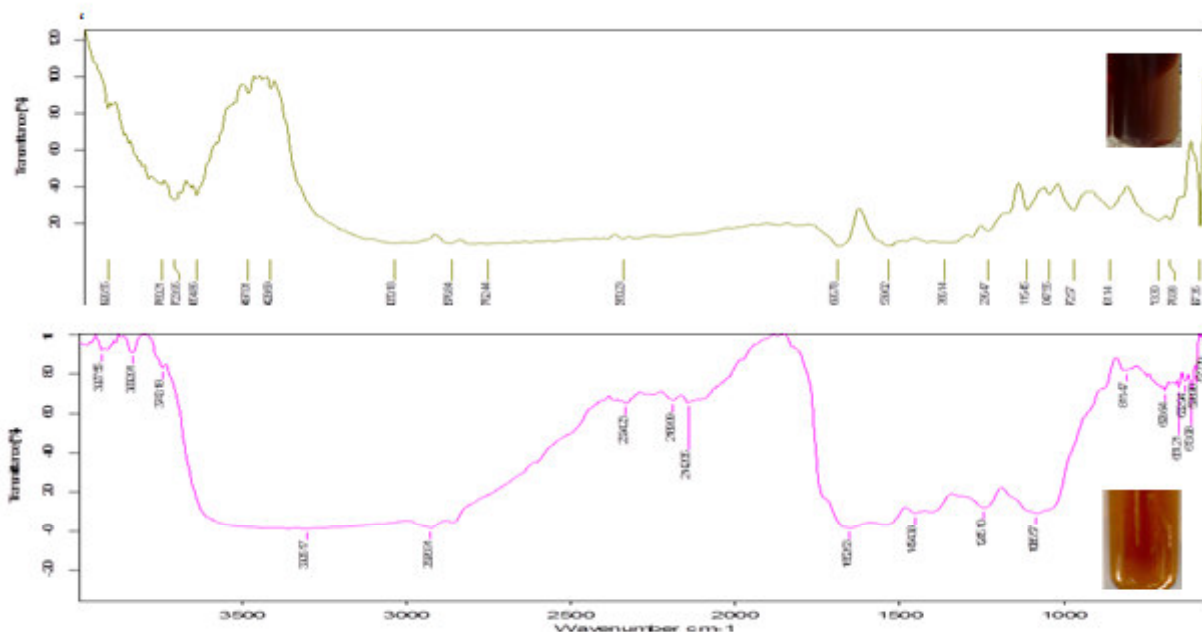
Figure 4
FTIR Spectrum of Pure Ajwain Extract (Pink) and Silver Nanoparticles (Black)

(4) TEM Analysis:

TEM image shown in Figs 5a and 5b reveals that there is formation of poly-disperse spherical particles with non uniform distribution and bar plot revealed the particle size distribution of AgNPs i.e. between 1-10 to 30-40, respectively. It was revealed that the nanoparticles formed were of different sizes and particle size was found to be 8nm, 14nm, 24nm and 36nm and the mean size of about 22nm which lies in the nano range. Difference in average particle size obtained from XRD and TEM observed because edges of particles are not well defined in TEM images.
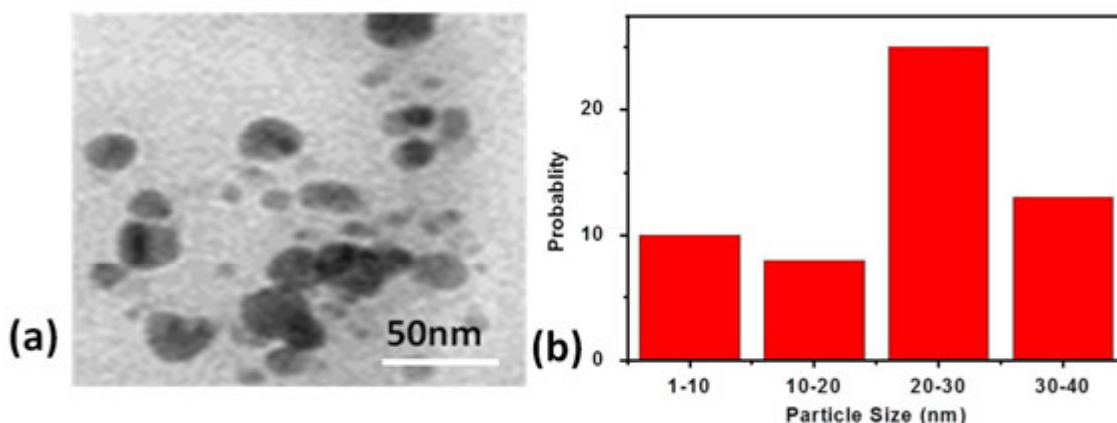
Figure 5
(a) TEM image of poly-disperse silver nanoparticles
(b) Average particle sizes of silver nanoparticles

(5) Antagonistic activity of silver nanoparticles against bacteria

The TA seeds reduce the silver salts and produced silver nanoparticles by stabilizing and capping the nanoparticles with the plant peptides. The antimicrobial activity of the nanoparticles is thus enhanced due to the presence of plant proteins and

phytochemicals. The antimicrobial activity of silver nanoparticles was studied against Bacillus subtilis, Staphylococcus aureus and Escherichia coli and Table 1 represents the comparative activities in terms of inhibition zone i.e 17, 16 and 14, respectively. Study demonstrated that the AgNPs show best antagonistic activity of silver nanoparticles against Bacillus subtilis.

Table 1
Antagonistic activity of silver nanoparticles against bacteria

Organism	Zone of inhibition (mm)
Bacillus subtilis	17
Escherichia coli	16
Staphylococcus aureus	14

CONCLUSION

The present green synthetic method is a low cost approach of synthesizing AgNPs at ambient condition. The size and structure of obtained NPs were characterized by FTIR, TEM, UV absorption, and XRD. Our results have shown that the ajwain seeds aqueous extract is the easy, economic and eco-friendly way to synthesize metallic nanoparticles. The antagonistic activity of silver nanoparticles was studied. It was experimentally evident that the Ag nanoparticles found effective against the bactericidal activity of the Bacillus subtilis, Staphylococcus aureus and Escherichia coli. Thus, this study proves to be an effective and economical method. Moreover; this plant mediated synthesis method represents a considerable improvement in the preparation of AgNPs because of various advantages such as reduced reaction time, no need of additional capping agent, and better control over their size and shape. There are bulks of the investigations which have been carried at research laboratories in small scale whereas there are no reports on pilot plants or industrial scale fabrication of nanomaterials using natural products. However, we believe that there are good opportunities for developing large scale synthesis using greener processes.

ACKNOWLEDGMENT

REFERENCES

1. Majumder R. Waste to health: Bioleaching of nanoparticles from e-waste and their medical applications. Indian J Appl. Research, 3(2): 2249-555X. 2, (2013).
2. Korbekandi H., Iravani S. Silver Nanoparticles. Nanotechnology and Nanomaterials, 3: 5-16, (2012).
3. Singh J., Basarkar A., Poly (lactide-co-glycolide)- polymethacrylate nanoparticles for intramuscular delivery of plasmid encoding interleukin-10 to prevent autoimmune diabetes in mice. Pharm Res., 26: 72–81, (2009).
4. Brigger I., Dubernet C., Couvreur P. Nanoparticles in cancer therapy and diagnosis. Adv Drug Deliv Rev., 64: 24–36, (2012).
5. Roy K., Mao H.Q., Huang S.K., Leong K.W. Oral gene delivery with chitosan-DNA nanoparticles generates immunologic protection in a murine model of peanut allergy. Nat. Med., 5: 387–391, (1999).
6. Wilson D.S., Dalmasso G., Wang L., Sitaraman S.V., Merlin D., Murthy N. Orally delivered thioketal nanoparticles loaded with TNF-α–siRNA target inflammation and inhibit gene expression

in the intestines. Nat. Mater, 9: 923–928, (2010).

7. Morley K.S., Furno F., Wong B., Arnold P.L., Sharp B.L., Howdle S.M. Silver nanoparticles and polymeric medical devices: a new approach to prevention of infection. J Antimicrob Chemother, 54: 1019–1024, (2004).

8. Mano Priya M, Karunai Selvia B, John Paul J.A. Green Synthesis of Silver Nanoparticles from the Leaf Extracts of Euphorbia Hirta and Nerium Indicum. Digest. J. Nanomat. Biostruct, 6(2): 869 – 877, (2011).

9. SudhaLakshmi G. Y., Banu F., Ezhilarasan, Arumugam, Sahadevan. Green Synthesis of (Ag-Np) Silver Nanoparticles from Cleome Viscosa: Synthesis and Antimicrobial Activity, IPCBEE 5: 334-337, (2011).

10. Tagad C.K., Dugasanic S.R., Aiyer R., Parkc S., Kulkarni A., Sabharwal S. Green synthesis of silver nanoparticles and their application for the development of optical fiber based hydrogen peroxide sensor. Sensors and Actuators B, 183: 144– 149, (2013).

11. Christopher L, Kitchens D., Hirt E., Scott M., Husson A. A., Vertegel. Synthesis, Stabilization, and Characterization of Metal Nanoparticles. The Graduate School of Clemson University, Dissertation Thesis, 1-183, (2010)

12. Salam H.A., Rajiv P., Kamaraj M., Jagadeeswaran P., Gunalan S., Sivaraj R. Plants: Green Route for Nanoparticle Synthesis. Inter.Res.J.Bio. Sci., 1(5): 85-90, (2012).

13. Geoprincy G., Vidhyasrr B.N., Poonguzhali U., Nagendra Gandhi N, Renganathan S. A review on green synthesis of silver nano particles. Asian. J. Pharma. Clini.res, 6(1): 8 –12, (2013).

14. Awwad A.M., Nidà M. Green Synthesis of Silver Nanoparticles by Mulberry Leaves Extract. Nanoscience and Nanotechnology, 2(4): 125-128, (2012).

15. Jagtap U.B., Bapat V.A. Green synthesis of (Ag-Np) silver nanoparticles via Artocarpus heterophyllus Lam. Seed extract and its antibacterial activity. Industrial Crops and Products, 46: 132– 137, (2013).

16. Nethradevi C., Sivakumar P., Renganathan S., Green synthesis of silver nanoparticles using Datura metel flower extract and evaluation of their antimicrobial activity. Inter. J. Nanomat.Biostruct, 2(2): 16 –21, (2012).

17. Raveendran P., Fua J., Wallen S. L. A simple and green method for the synthesis of Au, Ag, and Au–Ag alloy nanoparticles. Green Chemistry, 8: 34–38, (2006).

18. Subhankari I., Nayak P. L. Synthesis of Copper Nanoparticles Using Syzygium aromaticum (Cloves) Aqueous Extract by Using Green Chemistry. World Journal of Nano Science & Technology, 2(1): 14-17, (2013).

19. Canizal G., Schabes-Retchkiman P. S., Pal U., Liu H. B., Ascencio J. A. Controlled synthesis of ZnO nanoparticles by bioreduction. Materials Chemistry and Physics, 97: 321–329, (2006).

20. Konishi Y., Ohno K., Saitoh N., Nomura T., Nagamine S., Hishida H., Takahashi Y., Uruga T. Bioreductive De- position of Platinum Nanoparticles on the Bacterium She- wanella Algae. Journal of Biotechnology, 128(3): 648-653, (2007).

21. Petla R. K., Vivekanandhan S., Misra M., Mohanty A. K.; Satyanarayana N.. Soybean (Glycine max) Leaf Extract Based Green Synthesis of Palladium Nanoparticles. Journal of Biomaterials and Nanobiotechnology, 3: 14-19, (2012).

22. Bai H. J., Zhang Z. M., Guo Y., Yang G. E. Biosynthesis of cadmium sulfide nanoparticles by photosynthetic bacteria Rhodopseudomonas palustri. Colloids and Surfaces B: Biointerfaces, 70(1): 142-146, (2009).

23. Geoprincy G., Saravanan P., Gandhi N., Renganathan S. A novel approach for studying the combined antimicrobial effects of (Ag-Np) silver nano particles and antibiotics through disk diffusion method and agar over layer method. Digest. J. Nanomat. Biostruct., 6(4): 1557-1565, (2011).

24. Venkataraman D., Babu R.S., Bilal M., Kalimuthu K., Gurunathan S. Biosynthesis of silver nanocrystals by

Bacillus licheniformis. Colloids Surf B. 65(1): 150-153, (2008).

25. Wijnhoven S.W.P., Peijnenburg W.J.G.M., Herberts C.A., Hagens W.I., Oomen A.G., Heugens E.H.W. Nano–silver: a review of available data and knowledge gaps in human and environmental risk assessment. Nano toxicology 3: 109, (2009).

26. Wagner V., Klueh U., Johnson A., Kelly S., Bryers J.D. Efficacy of silver-coated fabric to prevent bacterial colonization and subsequent device-based biofilm formation. J. Biomed. Mater. Res, 53 (6): 621–631, (2000).

27. Choi S. M. , Seo M. H., Kim H. J., Kim W. B. Synthesis and characterization of graphene-supported metal nanoparticles by impregnation method with heat treatment in H_2 atmosphere. Synthetic Metals,161: 2405– 2411, (2011).

28. Shankar S., Rai S., Ahmad A., Sastry M. Rapid synthesis of Au, Ag, and bimetallic Au core-Ag shell nanoparticles using Neem (Azadirachta indica) leaf broth. J. Colloid Interface Sci., 275: 496–502, (2004).

29. Gardea-Torresdey J. L., Gomez E., Peralta-Videa J., Parsons J. G., Troiani H. E., Santiago P. Formation and growth of Au nanoparticles inside live alfalfa plants. Nano Lett., 2: 397–401, (2002).

30. Gardea-Torresdey J. L., Gomez E., Peralta-Videa J., Parsons J. G., Troiani H. E., Santiago P. Alfalfa sprouts: a natural source for the synthesis of silver nanoparticles. Langmuir, 19: 1357–1361, (2003).

31. Chandran S.P., Chaudhary M., Pasricha R., Ahmad A., Sastry M. Synthesis of gold nanotriangles and silver nanoparticles using *Aloe vera* plant extract. Biotechnol. Prog., 22: 577–583, (2006).

32. Amkamwar B., Damle C., Ahmad A., Sastry M. Biosynthesis of gold and Ag nanoparticles using Emblica officinalis fruits extract, their phase transfer and transmetallation in an organic solution. J Nanosci. Nanotechnol., 5: 1665-1671, (2005).

33. Li S., Shen Y., Xie A., Yu X., Qiu L., Zhang L., Zhang Q. Synthesis of silver nanoparticles using. Capsicum annum L.

extract. Green Chemistry, 9: 852–858 (2007).

34. Shankar S. S., Ahmad A., Sastry M. Geranium Leaf Assisted Biosynthesis of Silver Nanoparticles. Biotechnol. Progress, 19: 1627–1631, (2003).

35. Vijayakumara M., Priya K., Nancy F.T., Noorlidah A., Ahmed A.B. A. Biosynthesis, characterisation and anti-bacterial effect of plant-mediated silver nanoparticles using Artemisia nilagirica. Industrial Crops and Products, 41: 235–240, (2013).

36. Gan P. P., Ng S. H., Huang Y., Fong S., Li Y., Green synthesis of gold nanoparticles using palm oil mill effluent (POME): A low-cost and eco-friendly viable approach. Bioresource Technology, 113: 132–135, (2012).

37. Song J.Y., Hyeon-Kyeong H.K., Kim B.S. Biological synthesis of gold nanoparticle using Magnolia kobus and Dipyros kaki leaf extracts. Process Biochem, 44: 1133-1138, (2009).

38. Narayanan K. B., Sakthivel N. Coriander leaf mediated biosynthesis of gold nanoparticles. Materials Letters, 62: 4588–4590, (2008).

39. Mallikarjuna K., Narasimha G., Dillip G.R., Praveen B., Shreedhar B., Shree Lakshmi C. Green Synthesis of Silver Nanoparticles Using Ocimum Leaf Extract and Their Characterization. Digest J. Nanomat. Biostruct, 6(1): 181–186, (2011).

40. Lather A., Chudhary A. K., Gupta V., Bansal P., Bansal R. Phytochemistry and Pharmacological Activities of Capparis zeylanica: an overview. Inter.J.Pharma.Anal.Res, 1(2): 384-389, (2010).

41. Dhabale P.N., Shrikhande V.N., Sakharkar D.M. Physicochemicals and Phytochemicals Evaluation of Capparis Zeylanica Linn. Inter. J. Pharma.Sci.Res, 3(1): 198-200, (2012).

42. Rajathi K., Sridhar S. Green Synthesized Silver Nanoparticles from the Medicinal Plant Wrightia Tinctoria and its Antimicrobial Potential. Inter. J.Chem.Tech. Res.; 5(4): 1707-1713, (2013).

43. Mulvaney P. Surface plasmon spectroscopy of nanosized metal

particles. Langmuir, 12(3): 788–800, (1996).

44. Shankar S.S., Rai A., Ahmad A. Sastry M. Rapid synthesis of Au, Ag, and bimetallic Au core-Ag shell nanoparticles using neem (Azadirachta indica) leaf broth. J Colloid Interf Sci, 275: 496-502, (2004).

45. Shahverd A.R., Shahvedi S.M.H.R., Jamalifar H., Nohi A.A. Rapid synthesis of silver nanoparticles using culture supernatants of Enterobacteria: a novel biological approach. Biochem, 42(5): 919-923, (2007).

46. Liu F.K. A high-efficiency capillary electrophoresis-based method for characterizing the sizes of Au nanoparticles J Chromatogr A, 1167: 231-235, (2007).

47. Fayaz M., Girilal M., Venkateshan R., Kalaichelvan P.T. Biosynthesis of anisotropic gold nanoparticles using Maduca longifolia extract and their potential in infrared absorption. Colloids Surf B : Biointerfaces, 88: 287-291, (2011).

48. Quang D.V., Sarawade P.B., Hilonga A., Kim J.K., Chai Y.G., Sang K., Jae Y.R., Hee T.K. Preparation of amino functionalized silica micro beads by dry method for supporting silver nanoparticles with antibacterial properties. Colloid Surf A : Physicochemical and Engineering Aspects, 389: 118-126, (2011).

49. Mustafa M.H.K, Eman H.I., Fatama E.M. Biosynthesis of Au nanoparticles using olive leaf extract: 1st Nano Updates. Arabian J Chem, 5(4): 431-437, (2012).

50. Mohanan V.S, Soundarapondian K. Green synthesis of gold nanoparticles using Citrus fruits (Citrus limon, Citrus reticulata and Citrus sinensis) aqueous extract and its characterization. Spectrochimia Acta A: Molecular and Biomolecular Spectroscopy, 102: 15-23, (2013).

51. Kannan B.N., Natarajan S. Biological synthesis of metal nanoparticles by microbes. Adv Colloidal Interf Sci, 156: 1-13, (2010).

52. Chunekar K.C., Pandey G.S. Ed. Hindi Commentary of Bhavaprakash Nighantu of Karpuradi Verga. Chaukhambha, Varanasi, India, 380-383, (1960).

53. Jagtap U.B., Bapat V.A. Green synthesis of silver nanoparticles using A Atrocarpus heterophyllus Lam. Seed extract and its antibacterial activity. Ind Crops Prod, 46: 132-137, (2012).

54. Jilie K., Shaoning Y. Fourier Transform Infrared Spectroscopic Analysis of Protein Secondary Structures. Acta Biochim. Biophys. Sin. 39(8): 549-559, (2007).

Biosynthesis of Silver Nanoparticles from Plant (Fenugreek Seeds) Reducing Method and their Optical Properties

Rajesh Kumar Meena and Neelu Chouhan[*]
Department of Pure and Applied Chemistry, University of Kota, Kota-324005 Rajasthan, INDIA

Abstract

In this paper, we synthesied the spherical silver nanoparticles (AgNPs) of 50-90 nm size, using $AgNO_3$ solution and the aqueous extract of Fenugreek plant seeds, which can act as a reducing, stablising and capping agent, at ambient condition. The formation of silver nanoparticles was confirmed by the XRD pattern and first excitonic peak of UV Vis. spectra that was supported by the change in colour of the solution (from colourless to dark pink). As synthesised Ag nanoparticles were characterized with the help of UV-Vis absorption spectroscopy analysis, Fourier Transform Infrared (FTIR) analysis, X-ray diffraction analysis (XRD), Scanning Electron Microscopy (SEM) analysis.

Keywords, Fenugreek seed, bioreduction, AgNPs.

Introduction

In recent research, nanotechnology plays a vital role our day to day life becuase it can not only engineer shape and size of metal but the basic properties (chemical, physical, mechanical, optical and catalytic, etc) may also be changed in the useful manner[1]. Nanotechnology has achieve the importance in different fields such as health care, food and feed, cosmetics, energy science, electronics, mechanics, space industries, environmental health, biomedical science, chemical industries, drug and gene delivery[2]. It also have expansively been achieved for the treatments of cancer[3], diabetes[4], allergy[5], infection[6] and inflammation[7]. Green chemistry is an enhancement and development in such a fields, design, implementation of chemical products and processes to reduce the use and generation of substances that are harmful to human health and environment[8]. There are many ways to synthesize nanoparticles such as solid reaction, co-precipitation, chemical reaction, and sol gel method etc. In recent years green synthesis of NPs has a number of advantages over chemical synthesis, such as cost effectiveness and simplicity,. Moreover it is compatible for food applications and biomedical, and this method eliminates the use of toxic chemicals, temperature, energy and high pressure[9,10]. The growing need of environment friendly nanoparticles has attracted lots of researchers to use green synthesis methods of a variety of metal nanoparticles[11] due to their interesting, motivating, attractive and remarkable properties with a variety of applications over their bulk material[12]. Considering the chemical reduction methods, photochemical reduction, electrochemical reduction and heat evaporation etc., the biological method is more beneficial and advantageous[13]. In this biosynthesis method, the plant extract has been used as reducing agent and capping agent for the synthesis of nanoparticles[14] due to their reducing properties[15]. Some properties such as size, morphology and distribution of the particles are clearly obtained from the nanoparticles[16].

The synthesis of silver nanoparticles has been synthesized using green methods which are less usage of chemicals, non-toxic and low cost and Environmental friendly. Plants used for green Synthesis of silver nanoparticles like using plant extracts have been reported in *Argemone maxicana*[17],*Ocimum*[18],*Cleome Viscosa*[19], *Trigonella foenum-graecum*[20], *Cycas*[21], *Eucalyptus hybrida*[22], *Iresine herbstii*[23], *Avena sativa*[24], *Lantana camara*[25], *Citrus limon*[26], *Calotropis gigantean*[27] *Achillea wilhemsii*[28], *Tagetes erecta*[29] Trachyspermum ammi[30]. Zea mays[31], Azadirachta indica (Neem)[32], Medicago sativa (Alfa alfa)[33,34], Aloevera[35], Emblica officinalis (Amla)[36], Capsicum annuum[37], Geranium sp.[38,39], Diopyros kaki[40], Magnolia kobus[41] and Coriandrum sp.[42], etc.,. All the parts of the plant like leaf, stem, flower, seed and skin of the fruits were used earlier for the synthesis of AgNPs. Plants have been used for the synthesis of nanoparticles were coated by the plant extract which has medical benefits and can be used as drug and cosmetic applications[43]. The various nanoparticles like Ag[44], Au[45], Fe[46], Pd[47], ZnO/Au and ZnO/Ag[48] nanoparticles as well as quantum dots CdS[49], among these, Silver nanoparticles places a major role because it has a number of important properties such as optical, electronic, chemical, photo electro chemical, catalytic, magnetic, antibacterial, and biological labelling, antimicrobial, catalytic. Silver nanoparticle acts as antimicrobial agent which finds applications in medical field such as AgNPs coated blood collecting vessels, coated capsules, band aids etc[50]. The silver is non-toxic to animal cells and highly toxic to bacteria, and other microorganisms (E-coli, Pseudomonas aeruginosa, Staphylococcus aureus). Due to these phenomena it is considered to be safe and effective bactericidal metal[51-53].

In this report, Fenugreek is a self pollinating annual leguminous bean which belongs to Fabaceae family[54] commonly known as Indian methi, It is one of the most ancient medicinal herbs[55]. Fenugreek seeds are the most important and useful part of

fenugreek plant. The fenugreek, plant mainly shows the presence of saponin and alkaloids are anti-nutritional factors[56]. The current investigation focuses on the aqueous seeds extract of Fenugreek used to synthesize AgNPs using different experimental conditions and thereby enhancing the importance of plant sources and implementing green chemistry for the future research.

Material and Methods

Preparation of Dried Biomass, The seeds of Fenugreek Seeds were collected from herbal garden of University of Rajasthan Campus, Rajasthan, India. The seeds were thoroughly washed with deionised distilled water and crushed. The powder was further used for preparation of 10 g/L aqueous seeds extract. This extract was filtered and stored at 4°C until further use for present investigation.

Chemicals: Silver nitrate (AgNO₃) was purchased from Sigma-Aldrich. Deionised distilled water was used throughout the experiment. All other chemicals were of analytical grade.

Synthesis of nanoparticles: For biosynthesis of nanoparticles, 2.0 ml plant seeds extract was mixed with 25 ml of freshly prepared silver nitrate 10^{-3} M AgNO₃ solution was prepared in 250 mL of deionised water in a sterile conical flask and kept in dark condition at room temperature. The reaction mixture was incubated for 30 min or till colour change to dark pink was observed. The nanoparticles were then synthesized by drying at 90°C.

Characterization of nanoparticles: The syntheised nanoparticles were characterized using UV-Vis Spectroscopy (LABINDIA UV- Visible 3000⁺) over a range of 200-800 nm. The topography of the nanoparticles was studied by SEM (Scanning Electron Microscope) analysis. FTIR (Fourier Transform Infrared Spectroscopy) was performed to obtain wide spectrum of nanoparticles over a narrow range. This method gives us information about plant peptides that have covered the particles during synthesis procedure. The XRD (X-Ray Diffraction Analysis) was performed to note the size of the obtained nanoparticle.

Results and Discussion

Synthesis and characterization of silver nanoparticles, Aqueous seed extract of Fenugreek acts as a reducing agent[57] which reduces metallic silver to nanosilver and hence the colour change was obtained figure-1. It is well known that silver nanoparticles exhibit reddish pink colour in aqueous solution due to excitation of surface plasmon vibrations in silver nanoparticles. Ag^{2+} ions of silver nitrate are found to be reduced to Ag atoms. It is generally recognized that UV-Vis spectroscopy could be used to examine size and shape controlled nanoparticles in aqueous suspensions. Figure 1 show the UV-Vis spectrum recorded from the reaction medium after 24 hours and gives rise to an absorption band at 420 nm.
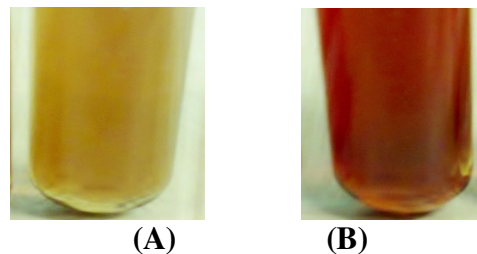
Figure-1
(A) Aqueous seed extract (B) Aqueous extract and silver nitrate after incubation

The synthesized nanoparticles were characterized using FTIR, SEM, XRD and UV Vis spectroscopy analysis. The reduction of silver ions to nano silver was monitored and confirmed using UV spectra. After the colour change was obtained a small aliquot of sample was diluted with distilled water and subjected to UV analysis. The characteristic peak value for silver nanoparticles is between 400-580nm. Figure-2.
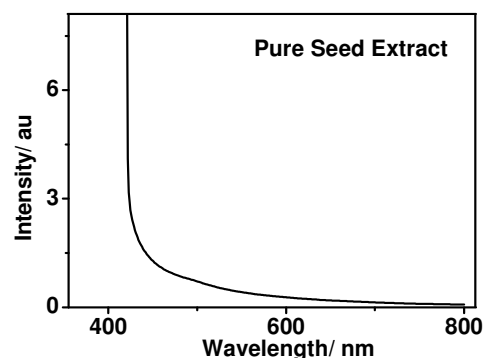
(A)
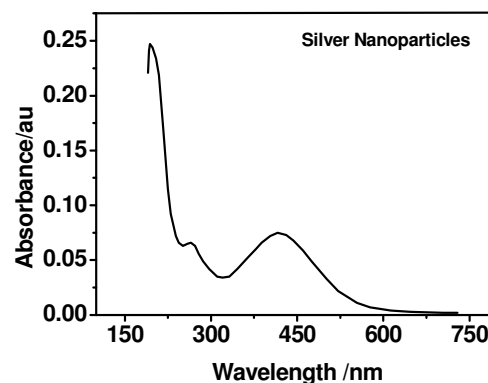
(B)
Figure-2
UV Vis spectra of (A) Pure Seed Extracts (B) Silver nanoparticles produced by extract of Fenugreek Seeds

The spectrum of the sample was obtained for wavelength range in-between 400nm to 580nm. The λ max of the nanoparticles was observed at 470nm. This is because of a phenomenon called Surface Plasmon Resonance (SPR) exhibited by silver nanoparticles. The silver nanoparticles oscillate when exposed to electromagnetic radiation and this oscillation gives a typical peak value[58]. The SEM (FESEM, JEOL JSM-6700F) image of the nanoparticles represents the topography of the particles is shown in image figure-3.
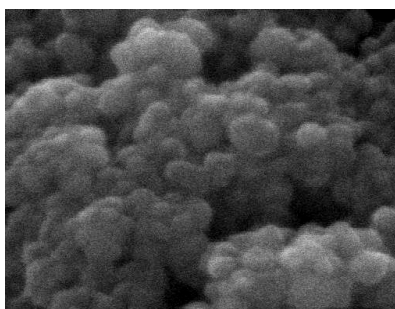
Figure-3
SEM image of silver nanoparticles produced by Fenugreek seeds extract

The SEM image suggests the presence of roughly spherical silver nanoparticles. The incidence of Xrays on the powdered nanoparticles gives a particular pattern which helps to characterize the nanoparticles as shown in the XRD graph figure-4.
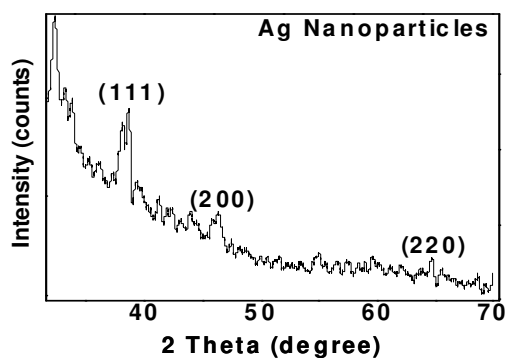
Figure-4
XRD pattern of the silver nanoparticles produced by extract of Fenugreek seeds

XRD (manual mode) was used to characterize the AgNp. The 2d angle is converted to the diameter using the Scherrer formula $(Dp = K\lambda /\beta 1/2 \cos\theta)$. The size of silver nanoparticles synthesised by green synthesis was estimated to be around 20-50 nm. FTIR (Bruker -Tensor Model) analysis also gives a set of peak values unique for the sample along with information of the plant peptides that are present in the sample as the plant extract acts as a reducing agent figure-5. FTIR analysis is used to confirm the presence of plant peptides visible due to the bending produced by amide bonds[59].
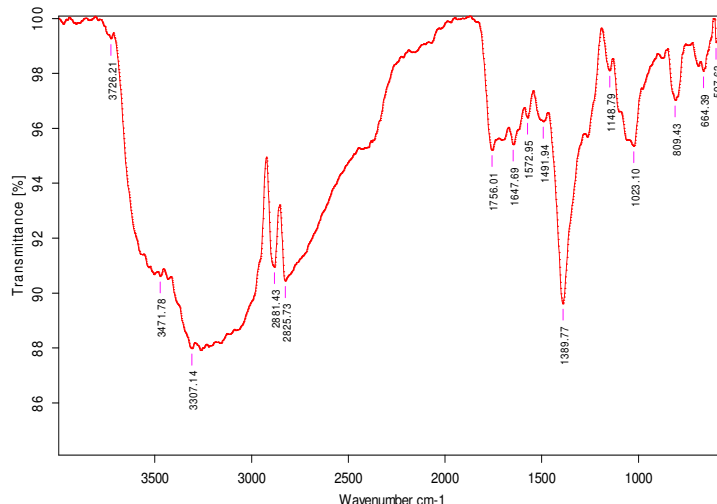
Figure-5
FTIR spectra of nanoparticles synthesized by extract of Fenugreek seeds

Biological synthesis of silver nanoparticles is an alternative to chemical synthesis and it used the reducing properties of biological products for synthesis of silver nitrate to nanosilver. Biological synthesis of nanoparticles has been previously reported using plant seed extracts. The phytochemical in the seed reduce the silver salts and not only produce silver nanoparticles but also stabilize it by capping the nanoparticles with the plant peptides. The antimicrobial activity of the nanoparticles is thus enhanced due to the presence of plant proteins and phytochemical.

Conclusion

In this present study the synthesis of silver nanoparticles was synthesized by biological method using Fenugreek seed extract which acts as a reducing agent to reduce silver metal to nanosize particles. The synthesized silver nanoparticles were subjected to analysis such as SEM, UV Vis Spectroscopy, XRD, and FTIR in order to characterize them. To the best of our knowledge this is the best information of the observations of the unique structures of fenugreek seeds extract mediated Ag nanoparticles. This opens a way to understand the synthesis mechanism of Ag nanoparticles formed from other plant seeds extracts.

Reference

1. Alqudami A and Annapoorni S., Fluorescence from metallic silver and iron nanoparticles prepared by exploding wire technique, *Plasmonics.*, **2(1)** 5-13 **(2007)**

2. Korbekandi H and Iravani S., Silver Nanoparticles, *Nanotechnology and Nanomaterials*, **3,** 5-16 **(2012)**

3. Brigger I, Dubernet C, Couvreur P., Nanoparticles in cancer therapy and diagnosis, *Adv Drug Deliv Rev.*, **64,** 24–36 **(2012)**

4. Basarkar A, Singh J. Poly (lactide-co-glycolide)-polymethacrylate nanoparticles for intramuscular delivery of plasmid encoding interleukin-10 to prevent autoimmune diabetes in mice, *Pharm Res*., **26**, 72–81 **(2009)**

5. Roy K, Mao HQ, Huang SK and Leong KW, Oral gene delivery with chitosan-DNA nanoparticles generates immunologic protection in a murine model of peanut allergy, *Nat. Med.*, **5**, 387–391 **(1999)**

6. Furno F, Morley KS, Wong B, Sharp BL, Arnold PL, Howdle SM et al. Silver nanoparticles and polymeric medical devices, a new approach to prevention of infection, *J Antimicrob Chemother*., **54**, 1019–1024 **(2004)**

7. Wilson DS, Dalmasso G, WangL, Sitaraman SV, Merlin D and Murthy N., Orally delivered thioketal nanoparticles loaded with TNF-α–siRNA target inflammation and inhibit gene expression in the intestines, *Nat. Mater.*, **9**, 923–928 **(2010)**

8. Mano Priya M, Karunai Selvia B, John Paul JA. Green Synthesis of Silver Nanoparticles from the Leaf Extracts of Euphorbia Hirta and Nerium Indicum, *Digest.J. Nanomat. Biostruct*., **6(2)**, 869–877 **(2011)**

9. Chandrakant K, Tagad, Sreekantha Reddy Dugasanic, Rohini Aiyer, Sungha Parkc, Atul Kulkarni and Sushma Sabharwal., Green synthesis of silver nanoparticles and their application for the development of optical fiber based hydrogen peroxide sensor, *Sensors and Actuators B*., **183**, 144–149 **(2013)**

10. Yamini Sudha Lakshmi G, Fouzia Banu, Ezhilarasan, Arumugam, Sahadevan., Green Synthesis of Silver Nanoparticles from Cleome Viscosa, *Synthesis and Antimicrobial Activity.*, **5 (2011)**

11. Christopher L, Kitchens Douglas E, Hirt Scott M, Husson Alexey A and Vertegel., Synthesis, Stabilization, and Characterization of Metal Nanoparticles, The Graduate School of Clemson University, **(2010)**

12. Hasna Abdul Salam, Rajiv P, Kamaraj M, Jagadeeswaran P, Sangeetha Gunalan and Rajeshwari Sivaraj., Plants, Green Route for Nanoparticle Synthesis, *Inter.Res.J.Bio. Sci*., **1(5)**, 85-90 **(2012)**

13. Geoprincy G, Vidhyasrr BN, Poonguzhali U, Nagendra Gandhi N, Renganathan S., A review on green synthesis of silver nano particles, *Asian.J.Pharma.Clini.res*., **6(1)**,8–12 **(2013)**

14. Akl M Awwad1, Nidà M., Green Synthesis of Silver Nanoparticles by Mulberry Leaves Extract, *Nanoscience and Nanotechnology*., **2(4)**, 125-128 **(2012)**

15. Umesh B. Jagtap, Vishwas A. Bapat., Green synthesis of silver nanoparticles using Artocarpus heterophyllus Lam.

Seed extract and its antibacterial activity, *Industrial Crops and Products*., **46**, 132– 137 **(2013)**

16. Nethra Devi C, Sivakumar P and Renganathan S., Green synthesis of silver nanoparticles using Datura metel flower extract and evaluation of their antimicrobial activity, *Inter.J. Nanomat.Biostruct*., **2(2)**, 16–21 **(2012)**

17. Singh D. Jain, M.K. Upadhyay, N. Khandelwal and H.N. Verma., Green Synthesis Of Silver Nanoparticles Using Argemone Mexicana Leaf Extract And Evaluation Of Their Antimicrobial Activities., *Digest Journal of Nanomaterials and Biostructures,* **5(2)**, 483-489 **(2010)**

18. Mallikarjun K, Narsimha G, Dillip GR, Praveen B, Shreedhar B, Lakshmi S, Reddy VS and Raju DP., Green synthesis of silver nanoparticles using Ocimum leaf extract and their characterization. *Digest J Nanomat Biostruct*., **6(1)**, 181-186 **(2011)**

19. Yamini Sudha Lakshmi.G Singapore., Green Synthesis of Silver Nanoparticles from Cleome Viscosa, Synthesis and Antimicrobial Activity, *International Conference on Bioscience, Biochemistry and Bioinformatics IPCBEE*., 5 **(2011)**

20. R.P. Singh, S. Magesh, C., Rakkiyappan formation of fenugreek (Trigonella foenum-graecum) extract mediated Ag Nanoparticles, mechanism and applications, *International Journal of Bio-Engineering Sciences & Technology-IJBEST*., **2(3),** 283-294 **(2011)**

21. Anal K. Jha K. Prasad., Green Synthesis of Silver Nanoparticles Using Cycas Leaf, *International Journal of Green Nanotechnology, Physics and Chemistry*., **1**, 110–117 **(2010)**

22. Manish dubey, Seema bhadauria, B.S. Kushwah., Green synthesis of nanosilver particles from extract of Eucalyptus hybrida (safeda) leaf, *Digest Journal of Nanomaterials and Biostructures*., **4(3)**, 537–543 **(2009)**

23. Dipankar C, Murugan S., The green synthesis, characterization and evaluation of the biological activities of silver nanoparticles synthesized from Iresine herbstii leaf aqueous extracts, *Colloids*., **98**,112-119 **(2012)**

24. V. Armendariz, I. Herrera, J.R. Peralta-Videa et al., Size controlled gold nanoparticle formation by Avena sativa biomass, use of plants in nanobiotechnology, *Journal of Nanoparticle Research*., **6(4)**, 377–382 **(2004)**

25. Thirumurugan A et al., Biological synthesis of silver nanoparticles by Lantana camara leaf extracts, *International Journal of Nanomaterials and Biostructures*., **2(4)** 65-69 **(2012)**

26. Prathna TC and Chandrasekaran N and Raichur, Ashok M and Mukherjee, Amitava., Biomimetic synthesis of silver nanoparticles by Citrus limon (lemon) aqueous extract and theoretical prediction of particle size, *In,*

Colloids and Surfaces B, Biointerfaces., **82(1)**, 152-159 **(2011)**

27. J. Sivakumar, C.Premkumar, P. Santhanam and N. Saraswathi., Biosynthesis of Silver Nanoparticles Using Calotropis gigantean Leaf, *African Journal of Basic & Applied Sciences*., **3(6)**, 265-270 **(2011)**

28. Javad karimi andeani, Hojjatollah kazemi, Sasan mohsenzadeh, Afsanehs afavi., Biosynthesis of gold nanoparticles using dried flowers extract of achillea wilhelmsii plant, *Digest Journal of Nanomaterials and Biostructures.*, **6(3)** 1011-1017 **(2011)**

29. krishnamurthy NB, Nagaraj , Barasa malakar, liny P, and Dinesh R., Green synthesis of gold nanoparticles using tagetes erecta l.(mari gold) flower extract & evaluation of their antimicrobial activities, *International Journal of Pharma and BioSciences*., **3(1)**, 212-221 **(2012)**

30. Chouhan Neelu and Meena Rajesh Kumar., Biosynthesis of silver nanoparticles using Trachyspermum ammi and evaluation of their antibacterial activities, *Int J Pharm Bio Sci*., **6(2)**,1077–1086 **(2015)**

31. Choi S.M., Seo M.H., Kim H.J. and Kim W.B., Synthesis and characterization of graphene-supported metal nanoparticles by impregnation method with heat treatment in H$_2$ atmosphere, *Synthetic Metals*., **161**, 2405– 2411 **(2011)**

32. Shankar S., Rai S., Ahmad A. and Sastry M., Rapid synthesis of Au, Ag, and bimetallic Au core-Ag shell nanoparticles using Neem (Azadirachta indica) leaf broth, *J.Colloid Interface Sci*., **275**, 496–502 **(2004)**

33. Gardea-Torresdey J. L., Gomez E., Peralta-Videa J., Parsons J.G., Troiani H.E. and Santiago P., Formation and growth of Au nanoparticles inside live alfalfa plants, *Nano Lett*., **2**, 397–401 **(2002)**

34. Gardea-Torresdey J.L., Gomez E., Peralta-Videa J., Parsons J.G., Troiani H.E. and Santiago P., Alfalfa sprouts, a natural source for the synthesis of silver nanoparticles, *Langmuir.,* **19**, 1357–1361 **(2003)**

35. Chandran S.P., Chaudhary M., Pasricha R., Ahmad A. and Sastry M., Synthesis of gold nanotriangles and silver nanoparticles using Aloe vera plant extract, *Biotechnol. Prog*., **22**, 577–583 **(2006)**

36. Amkamwar B., Damle C., Ahmad A., Sastry M., Biosynthesis of gold and Ag nanoparticles using Emblica officinalis fruits extract, their phase transfer and transmetallation in an organic solution, *J Nanosci. Nanotechnol*., **5**, 1665-1671 **(2005)**

37. Li S., Shen Y., Xie A., Yu X., Qiu L., Zhang L. and Zhang Q., Synthesis of silver nanoparticles using. Capsicum annum L. Extract, *Green Chemistry*., **9**, 852–858 **(2007)**

38. Shankar S. S., Ahmad A. and Sastry M., Geranium Leaf Assisted Biosynthesis of Silver Nanoparticles, *Biotechnol. Progress*., **19**, 1627–1631 **(2003)**

39. Vijayakumara M., Priya K., Nancy F.T., Noorlidah A. and Ahmed A.B.A., Biosynthesis, characterisation and antibacterial effect of plant-mediated silver nanoparticles using Artemisia nilagirica, *Industrial Crops and Products*., **41**, 235–240 **(2013)**

40. Gan P. P., Ng S. H., Huang Y., Fong S. and Li Y., Green synthesis of gold nanoparticles using palm oil mill effluent (POME), A low-cost and eco-friendly viable approach, *Bioresource Technology.,* **113**, 132–135 **(2012)**

41. Song J.Y., Hyeon-Kyeong H.K. and Kim B.S., Biological synthesis of gold nanoparticles using Magnolia kobus and Dipyros kaki leaf extracts, *Process Biochem*., **44**, 1133-1138 **(2009)**

42. Narayanan K.B. and Sakthivel N., Coriander leaf mediated biosynthesis of gold nanoparticles, *Materials Letters.*, **62**, 4588–4590 **(2008)**

43. Mallikarjunaa K, Narasimhab G, Dillipa GR, Praveenb B, Shreedharc B and Sree Lakshmic C et al., Green Synthesis of Silver Nanoparticles Using Ocimum Leaf Extract and Their Characterization, *Digest.J.Nanomat.Biostruct*., **6(1)**, 181–186 **(2011)**

44. Song JY and Kim BS., Rapid biological synthesis of silver nanoparticles using plant leaf extracts, *Bioprocess Biosyst Eng.*, **32**, 79-84 **(2009)**

45. Huang J, Li Q, Sun D, Lu Y, Su Y, Yang X, Wang H, Wang Y, Shao W, He N, Hong J, Chen C., Biosynthesis of silver and gold nanoparticles by using novel sun-dried Cinnamomum camphora leaves, *Nanotechnol*., **18**, 105-104 **(2007)**

46. Pattanayak M and Nayak PL., Green Synthesis and Characterization of Zero Valent Iron Nanoparticles from the Leaf Extract of Azadirachta indica (Neem), *World Journal of Nano Science & Technology*., **2(1)**, 06-09 **(2013)**

47. Nadagouda M.N. Varma R.S., Green synthesis of silver and palladium nanoparticles at room temperature using coffee and tea extract, *Green Chem*., **10**, 859–862 **(2008)**

48. Fageria P., Gangopadhyay S. and Pande S., Synthesis of ZnO/Au and ZnO/Ag nanoparticles and their photocatalytic application using UV and visible light. *RSC Adv*., **4**, 24962–24972 **(2014)**

49. Ahmad, P. Mukherjee, D. Mandal, S. Senapati, M.I. Khan, R. Kumar and M. Sastry., Enzyme Mediated Extracellular Synthesis of CdS Nanoparticles by the Fungus, Fusariuoxysporum, *J.Am. Chem. Soc*., **124**,12108–12109 **(2002)**

50. Geoprincy G, Saravanan P, NagendraGandhi N and Renganathan S., A novel approach for studying the

combined antimicrobial effects of silver nano particles and antibiotics through agar over layer method and disk diffusion method, *Digest.J.Nanomat.Biostruct*, **6(4)**, 1557-1565 **(2011)**

51. Kalimuthu K, Babu RS, Venkataraman D, Bilal M and Gurunathan S., Biosynthesis of silver nanocrystals by Bacillus licheniformis, *Colloids Surf B.*, **65(1)**, 150-153 **(2008)**

52. Wijnhoven SWP, Peijnenburg WJGM, Herberts CA, Hagens WI, Oomen AG and Heugens EHW et al., Nano–silver, a review of available data and knowledge gaps in human and environmental risk assessment, *Nano toxicology.*, **3**, 109-138 **(2009)**

53. Klueh U, Wagner V, Kelly S, Johnson A and Bryers JD., Efficacy of silver-coated fabric to prevent bacterial colonization and subsequent device-based biofilm formation, *J. Biomed. Mater. Res.*, **53(6)**, 621–631 **(2000)**

54. Balch PA Prescription for dietary wellness (2nd edn). Penguin group, New York 15-17 **(2003)**

55. Thomas JE, Bandara M, Lee EL, Driedger D and Acharya S., Biochemical monitoring in fenugreek to develop functional food and medicinal plant variants, *N Biotechnol.*, **28**, 110-117 **(2011)**

56. Jani R, Udipi SA. and Ghugre PS Mineral content of complementary foods, *Indian J Pediatr* **76**, 37-44 **(2009)**

57. Thombre RS, Mehta S, Mohite J and Jaisinghani P., Synthesis of silver nanoparticles and its cytotoxic effect on THP-1 cancer cell line. *International Journal of Pharma and Biosciences.* **4(1)**,184-192 **(2013)**

58. Smitha SL, Nissamudeen KM, Philip D and Gopchandran KG., Studies on surface Plasmon resonance and photoluminescence silver nanoparticles, *Spectrochim. Acta A.*, **71(1)**, 186–190 **(2008)**

59. Jing A, Wang D, Luo Q and Yuan X., Antimicrobial active silver nanoparticles and Silver/polystyrene core-shell nanoparticles prepared in room-temperature ionic liquid, *Materials Science and Engineering C*, **29(6)**,1984–1989 **(2009)**

ZnO Nanoparticles Synthesized by a Novel Approach at Room Temperature and Antibacterial activity

Rajesh Kumar Meena[1] and Neelu Chouhan[*2]
[1,2]Department of Pure & Applied Chemistry,
University of Kota, Kota-324005 Rajasthan, India

Abstract: *Applications of metal oxide nanoparticles in research and health-related applications, metal oxide nanoparticles are increasingly being developed through cheaper and more user-friendly approaches. We have formulated a simple route to synthesize zinc oxide nanoparticles (ZNPs) by a hydrothermal method at near-room temperatures. The results are analyzed by X-ray diffraction, transmission electron microscopy, FTIR and ultraviolet-visible absorption spectroscopy. Highly significant antimicrobial activity against medically important Gram-positive (S.aureus) and Gram-negative (Escherichia coli) bacteria by these ZNPs. we can postulate that our fabricated ZNPs may be useful as antimicrobial agents in antiseptic creams and lotions for the treatment of skin diseases.*

Index Terms: *Nanoparticles, hydrothermal method, antimicrobial activity etc.*

I. Introduction

ZnO Semiconductors with magnitude in the nanometer region are important because their electrical, optical and chemical properties can be tuned by varying the size of particles. Optical properties are of great importance for relevance in optoelectronics, photovoltaics and biological sensing. Various chemical synthetic methods have been developed to prepare such nanoparticles. Zinc Oxide (ZnO) is a exclusive material with a direct band gap (3.37eV) and large exciton binding energy of 60me[1-2]. It has been normally used in near-UV emission, gas sensors, transparent conductor and piezoelectric application[3 - 7]. Most of the ZnO crystals have been synthesized by conventional high temperature solid state method which is energy consuming and difficult to manage the particle properties as well as similar methods that are used for the fabrication of ZNPs include the sol–gel method, facile hydrothermal method, solution method, electric current heating method; solvothermal method, self-propagating high-temperature synthesis method, spontaneous nucleation method, spray pyrolysis, gas-phase reaction method, laser ablation method and thermal evaporation[8–21]. Hydrothermal technique is a promising substitute synthetic method because of the low process temperature and very easy to control the particle size. The hydrothermal process have several advantage over other growth processes such as use of simple equipment, catalyst-free growth, low cost, large area uniform fabrication, environmental friendliness and less hazardous. The low down reaction temperatures create this method an gorgeous one for microelectronics and plastic electronics[22]. This method has also been successfully employed to prepare nanoscale ZnO and other luminescent materials. The particle properties such as morphology and size can be controlled via the hydrothermal process by adjusting the reaction temperature, time and concentration of precursors. In this consider, several reports are obtainable that are neither feasible nor cost effective. The hydrothermal preparation of ZnO/Au and ZnO/Ag nanoparticles at 80^0C for 5 hours[23] and flower-like ZnO nanorods is masintained at more than 120°C, for several hours, at basic medium[24] chrysanthemum-like ZnO nanorods are formed in the presence of sodium dodecyl sulfate at 120°C for 24 hours[25] and 10 hours,[26,27] and the preparation of flower-like ZnO microstructures was conducted via sonochemical treatment for 1 hour.[28]

The present study focuses on the hydrothermal synthesis of ZnO nanopowders. The hydrothermal synthesis of ZnO powders has four advantages (1) powders with nanometer-size can be obtained by this method (2) the reaction is carried out under moderate situations (3) powders with different morphologies by adjusting the reaction situation and (4) the as-prepared powders have different properties from that of the bulk. In this present work, we have reported the synthesis of ZnO nanoparticles using hydrothermal method and characterized its structural, morphological properties. Additionally we have performed the electrochemical activity of the synthesized ZnO.

II.   Materials and Experimental Methods:

Materials:
Zinc acetate dihydrate $Zn(CH_3COO)_2 \cdot 2H_2O)$ and sodium hydroxide pellets (NaOH) were purchased from Sigma- Aldrich and were all used without further purification and Double distilled water was used as the solvent.

Synthesis of Zinc Oxide Nanoparticles: 5g of $Zn(CH_3COO)_2 \cdot 2H_2O)$ and 10ml (5M) of NaOH were dissolved into 100 mL of distilled water. After the mixture are magnetically stirred for 4h at room temperature and then slowly being cooled to room temperature, obtained powders were collected by centrifugation and washed with distilled water and absolute ethanol. The powders were finally dried at 60 °C for 12 h.

Optical Properties: Ultraviolet-visible spectroscopy (UV-Vis) refers to absorption spectroscopy in the UV-Visible spectral region. That means it uses beam in the visible and adjacent (near-UV and near-infrared (NIR)) ranges. The absorption in the visible range openly affects the perceived colour of the chemicals involved. In this region of the electromagnetic spectrum generate by the electronic transitions. In this time uv-vis absorption spectra was takened using a (LABINDIA Uv- Visible 3000+) spectrophotometer where the cuvette path length was set to 1.0 cm. The particles were dissolved in methanol, and solution was placed in a quarts cuvettes.

pH Analysis
The pH was determined by using Digital pH meter Systronics. The pH of the reduced solution with Nanoparticle synthesized was found to be basic. After reduction the pH of sample was found to increase and move towards the basic range.

Structure and morphology:

Powder X-Ray Diffraction: XRD patterns of the powdered samples were obtained on a Phillips X'Pert materials research diffractometer using secondary monochromated Cu Kα radiation (λ = 1.54060 A°) at 40 Kv/50mA. Samples were supported on a glass slide. Measurements were taken using a glancing angle of incidence detector at an angle of 2 for 2θ values over 10–80 in steps of 0.05 with a scan speed of 0.012.

TEM analysis: The TEM measurement was done with JEOL model 1200Ex instrument operated at an accelerating voltage of 80kV. Samples were prepared by placing 3-4 drops of the well dispersed Zn nanoparticles samples on a 300-mesh, carbon coated Cu grid (EM sciences) and allowing the liquid to evaporate in air. For Zn nanoparticles the particle size distribution was based on 30 randomly selected particles. The TEM image was taken with very high resolution and MATLAB analysis gives the pixel depth of the image equal to 24bits and the image format as JPEG. The TEM Images have been taken from National Chemical Laboratory, Pune, India.

Fourier Transform Infrared (FTIR) Spectroscopy: FTIR analysis range 4000 to 400 cm^{-1} using Bruker - Tensor Spectrum in the diffuse reflectance mode at a resolution of $4cm^{-1}$ in KBr pellets. The powder sample was placed on a sample holder and the spectrum was recorded.

III.   Results and discussions

Synthesis of silver nano particles:
Structural Characterization:
XRD patterns of the ZnO nanoparticles prepared by hydrothermal method is shown in Figure 1, which indicates the ZnO has hexagonal wurtzite phase structure The peak and relative intensities obtained for the ZnO competition with the reported JCPDS data[29] and no other attribute peaks were observed other than ZnO. The x-ray diffraction information were recorded by using Cu Kα radiation (1.5406 A^o). The intensity data were collected over a 2θ range of 20-80°. In addition, the peaks (100), (002), and (101) clearly indicate formation of pure wurtzite structure of ZnO.[30] Therefore, the XRD pattern showed that samples were formed in single phase. The high intensity of (100) peak at 31° suggested the growth of ZNPs along the easy direction of crystallization.[31] No other peaks related to impurities were detected in the XRD spectra, confirming the pure form of the synthesized ZNPs. The expected grain size of the ZnO nanoparticles was estimated with the help out of Scherrer equation using the diffraction intensity of (101) peak. x-ray diffraction studies confirmed that the synthesized materials were ZnO nanoparticles with wurtzite phase and all the diffraction peaks agreed. The mean grain size (D) of the particles was resolute from the XRD line broadening measurement via Scherrer equation.

$$D=0.89\lambda / (\beta Cos\theta)$$

Where λ is the wavelength (Cu Kα), β is the full width at the half- maximum (FWHM) of the ZnO (101) line and θ is the diffraction angle. A specific line broadening of the diffraction peaks is suggested that the synthesized materials are in nanometer series and the average grain size of ZnO is determined using Scherrer equation[32] and it was found to be around 50 nm.
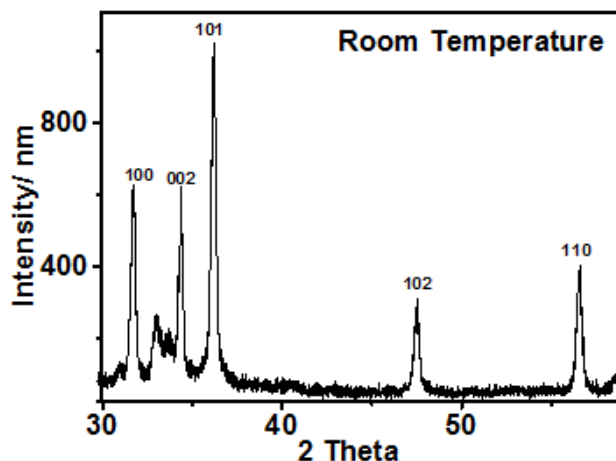
Figure 1. XRD pattern of ZnO nanoparticles

FT-IR spectrum of ZnO nanoparticles (Figure 2) showed significant absorption peaks at 3372 and 1577, 573 cm^{-1}. The absorption band at 573 cm^{-1} was assigned to Zn-O stretching vibration. The weak band near 1577 cm^{-1} is assigned to H-O-H bending vibration mode were presented due to the adsorption of moisture, when FTIR sample disks were prepared in an open air atmosphere. These observations provided the evidence for the presence of hydration in the structure and intense broad band near 3372 cm^{-1} represents the hydrogen bonded O-H stretching vibration.
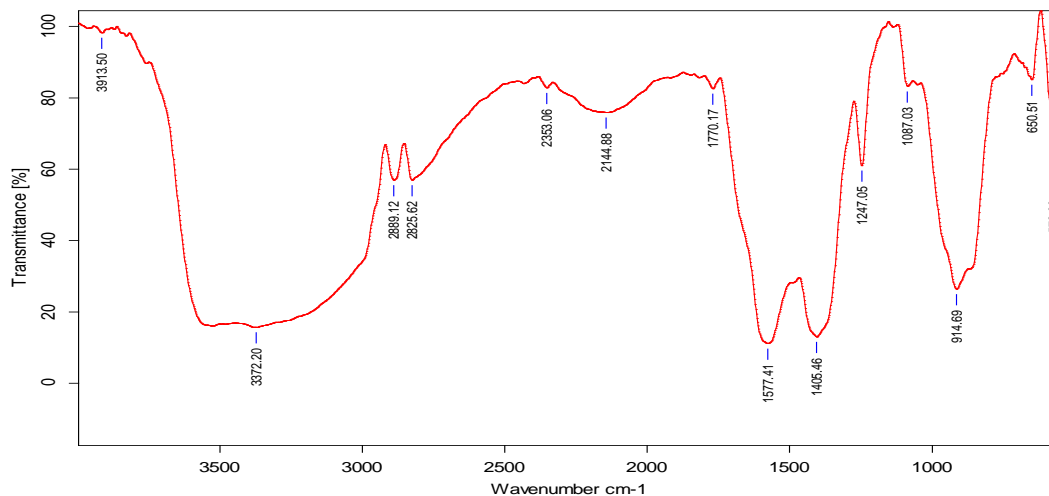
Figure 2. FT-IR spectrum of ZnO nanoparticles

Figure 3 shows the TEM image and equivalent selected-area electron diffraction (SAED) pattern of the ZnO nanoparticles synthesized at room temperature for 4h from 5M NaOH. TEM image confirms the formation of ZnO nanoparticles and it has an average size about 50 nm.
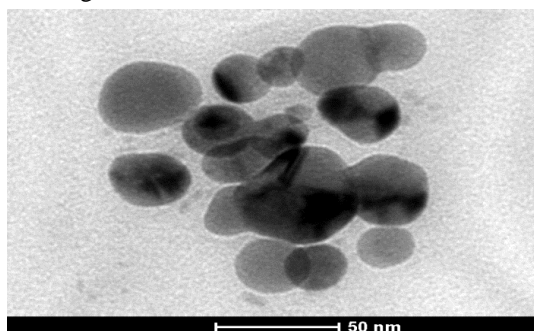
Figure 3 TEM Images of ZnO Nanoparticles

Size evolution of semiconducting nano particles become very essential to explore the properties of the materials. UV-Visible absorption spectroscopy is widely used technique to examine the optical properties of nano sized particles. The prepared zinc oxide white Crystalline powder was not soluble in water and almost in all organic solvents. ZnO nano particles UV-Visible spectra recorded by dispersed in methanol solution and sonicated for 5 to 10 min. Fig. 4 shows the absorption spectroscopy of the ZnO nanoparticles in the uv-spectral region. ZnO

exhibits a sharp band at 354 nm, which corresponds to the formation of ZnO nanoparticles. From the absorption spectrum of ZnO nanoparticles an approximate optical band gap can be derived using the following equation:

$$\alpha Ep^{\frac{1}{4}} K(Ep-Eg)^{1/2}$$
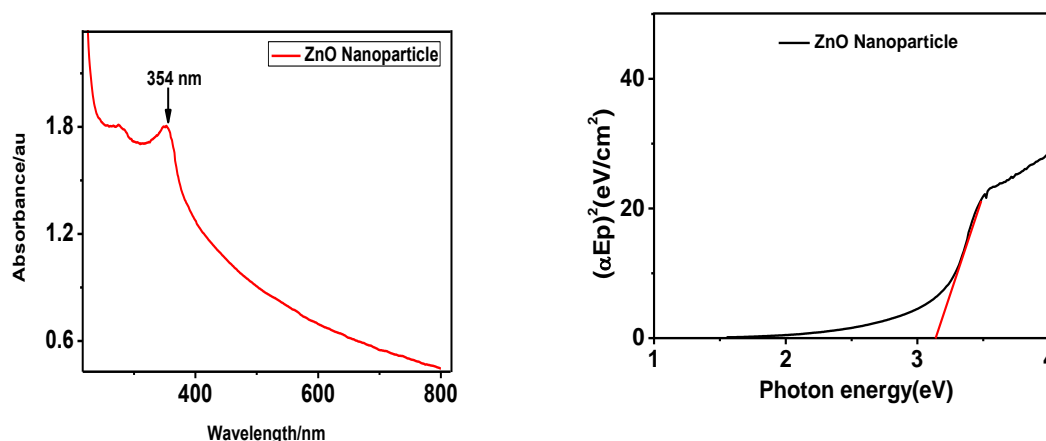
Fig.4. UV-Visible spectra of ZnO nanoparticles synthesized at room temperature

where, α stands for the absorption coefficient, K is a constant, Ep is the discrete photo energy, and Eg is the band gap energy. A classical Tauc approach is further employed to estimate the Eg value of ZnO nanoparticles.[33-35]A plot of $(\alpha Ep)^2$ vs. Ep is shown within the inset of Fig. 4. The extrapolated straight line of this plot meets the Ep axis. Which represents the absorption edge energy corresponds to the band gap (Eg) of the material. The band gap value of ZnO from the experimental data was calculated to be 3.12eV, which is in good agreement with the value reported in the literature.[36]

IV.   Antibacterial Activity

The antibacterial property of the ZnO was evaluated against Gram-ve Escherichia coli and Gram +ve bacteria *S. aureus* using agar well diffusion method. In agar well diffusion method the ZnO nanoparticles showed significant antibacterial activity on bacterial strains Gram-ve and Gram +ve bacteria and Table 1 represents the comparative activities in terms of inhibition zone i.e 16 and 14, respectively. Study demonstrated that the ZnNPs show best antagonistic activity of Zinc nanoparticles against Escherichia coli.

Organism	Zone of inhibition (mm)
Escherichia coli	16
Staphylococcus aureus	14

Table: 1   Antagonistic activity of silver nanoparticles against bacteri*a*

V.   Conclusion

ZnO powder was successfully synthesized by novel approach at room temperature. The crystallite size calculated from the XRD is 50 nm is in good agreement with TEM results. FT-IR results confirm that the presence of Zn-O at 573cm^{-1} as well as UV-visible Spectroscopy. the absorption spectrum was 354 nm show the blue shift compared to bulk ZnO. The antibacterial activity of ZnO Nanoparticles was confirmed by Zone of inhibition. As the diameter of the zone of inhibition is high, we can conclude that ZnO is also a very effective antibacterial agent. ZnO Nanoparticles are effective against both the bacteria which gives a conclusion that it is effective against gram +ve and gram –ve bacteria. Therefore we can conclude that ZnO Nanoparticles is a very effective antibacterial agent.

References

[1]   Qiuxiang Z, Ke Y, Wei B, Qingyan W, Feng X, Ziqiang Z, Ning D, Yan S, "Synthesis, optical and field emission properties of three different ZnO nanostructures", Materials Letters; 2007, 61, 3890.

[2]   Gyu-Chul Y, Chunrui W. and Won Il P. "ZnO nanorods: synthesis, characterization and applications" Semicond. Sci. Technol; 2005, 20, S22.
[3]   Morkoc H, Strite S, Gao G B, Lin M E, and Sverdlov B, and M. Burns, "Large-band-gap SIC, Ill-V nitride, and II-VI ZnSe-based semiconductor device technologies", J.Appl. Phys; 1994 ,76, 1363.
[4]   Yuzhen L, Lin G, Huibin X, Lu D, Chunlei Y, Jiannong W, Weikun G, and Shihe Y, Ziyu W, "Low temperature synthesis and optical properties of small-diameter ZnO nanorods", J. Appl. Phys; 2006, 99, 114302.
[5]   Hachigo A, Nakahata H, Higaki K, Fujii S and Shikata S-I, "Heteroepitaxial growth of ZnO films on diamond (111) plane by magnetron sputtering", Appl. Phys. Lett; 1994,65, 2556.
[6]   Spanhel L and Anderson M A, "Semiconductor Clusters in the Sol-Gel Process: Quantized Aggregation, Gelation, and Crystal Growth in Concentrated ZnO Colloids", J.Am. Chem. Soc; 1991, 113, 2826.
[7]   Bagnall D M, Chen Y F, Shen M Y, Zhu Z, Goto T and Yao T, "Room temperature excitonic stimulated emission from zinc oxide epilayers grown by plasma-assisted MBE", J.Cryst. Growth; 1998, 184/185, 605.
[8]   Zhao H, Su X, Xiao F, Wang J, Jian J. Synthesis and gas sensor properties of flower-like 3D ZnO microstructures. Materials Science and Engineering: B. 2011;176(7):611–615.
[9]   Bahnemann DW, Kormann C, Hoffmann MR. Preparation and characterization of quantum size zinc oxide: a detailed spectroscopic study. J Phys Chem. 1987;91(14):3789–3798.
[10]   Spanhel L, Anderson MA. Semiconductor clusters in the sol-gel process: quantized aggregation, gelation, and crystal growth in concentrated zinc oxide colloids. J Am Chem Soc. 1991;113(8):2826–2833.
[11]   Tokumoto MS, Pulcinelli SH, Santilli CV, Briois V. Catalysis and temperature dependence on the formation of ZnO nanoparticles and zinc acetate derivatives prepared by the sol-gel route. J Phys Chem B. 2003;107(2):568–574.
[12]   Meulenkamp EA. Synthesis and growth of ZnO nanoparticles. J Phys Chem B. 1998;102(29):5566–5572.
[13]   Sivakumar R, Tsunoda T, Kuroki Y, Okamoto T, Takata M. ZnO nanowire growth by electric current heating method: a study on the effect of substrate temperature. Mater Chem Phys. 2012;134(1):345–349.
[14]   Bilecka I, Elser P, Niederberger M. Kinetic and thermodynamic aspects in the microwave-assisted synthesis of ZnO nanoparticles in benzyl alcohol. ACS Nano. 2009;3(2):467–477.
[15]   Chen Y, Yu R, Shi Q, Qin J, Zheng F. Hydrothermal synthesis of hexagonal ZnO clusters. Mater Lett. 2007;61(22):4438–4441.
[16]   Hwang CC, Lin CS, Wang GP, Peng CH, Chung SL. A self-propagating high-temperature synthesis method for synthesis of zinc oxide powder. J Alloys Compd. 2009;467(1–2):514–523.
[17]   Yu Q, Fu W, Yu C, et al. Fabrication and optical properties of large-scale ZnO nanotube bundles via a simple solution route. J Phys Chem C. 2007;111(47):17521–17526.
[18]   Zhao W, Song X, Yin Z, Fan C, Chen G, Sun S. Self-assembly of ZnO nanosheets into nanoflowers at room temperature. Mater Res Bull. 2008;43(11):3171–3176.
[19]   Haile SM, Johnson DW Jr, Wiseman GH, Bowen HK. Aqueous precipitation of spherical zinc oxide powders for varistor applications. J Am Ceram Soc. 1989;72(10):2004–2008.
[20]   Zhang S, Yao S, Li J, Zhao L, Wang J, Boughton RI. Growth habit control of ZnO single crystals in molten hydrous alkali solutions. J Cryst Growth. 2011;336(1):56–59.
[21]   Umar A, Kim SH, Suh EK, Hahn YB. Ultraviolet-emitting javelin-like ZnO nanorods by thermal evaporation: growth mechanism, structural and optical properties. Chem Phys Lett. 2007;440(1–3):110–115.
[22]   Lee. C.Y, Tseng T. Y, Li. S. y, Lin.P. Effect of phosphorus dopant on photoluminescence and field-emission characteristics of Mg0.1Zn0.9O nanowires", J. Appl. Phys; 2006, 99, 024303.
[23]   Fageria P., Gangopadhyay S. and Pande S. Synthesis of ZnO/Au and ZnO/Ag nanoparticles and their photocatalytic application using UV and visible light. RSC Adv., 4, 24962–24972 (2014).
[24]   Zhang H, Yang D, Ji Y, Ma X, Xu J, Que D. Low temperature synthesis of flowerlike ZnO nanostructures by cetyltrimethylammonium bromide-assisted hydrothermal process. J Phys Chem B. 2004;108(13): 3955–3958.
[25]   Yin H, Xu Z, Wang Q, Bai J, Bao H. Study of assembling ZnO nanorods into chrysanthemum-like crystals. Mater Chem Phys. 2005;91(1): 130–133.
[26]   Ni Y, Wu G, Zhang X, et al. Hydrothermal preparation, characterization and property research of flowerlike ZnO nanocrystals built up by nanoflakes. Mater Res Bull. 2008;43(11):2919–2928.
[27]   Li F, Hu L, Li Z, Huang X. Influence of temperature on the morphology and luminescence of ZnO micro and nanostructures prepared by CTAB-assisted hydrothermal method. J Alloys Compd. 2008;465(1–2): L14–L19.
[28]   Li H, Ni Y, Hong J. Ultrasound-assisted preparation, characterization and properties of flower-like ZnO microstructures. Scr Mater. 2009;60(7):524–527.
[29]   JCPDS Card No. 36-1451
[30]   Rekha K, Nirmala M, Nair MG, Anukaliani A. Structural, optical, photocatalytic and antibacterial activity of zinc oxide and manganese doped zinc oxide nanoparticles. Physica B Condens Matter. 2010;405(15):3180–3185.
[31]   Lin HF, Liao SC, Hung SW. The dc thermal plasma synthesis of ZnO nanoparticles for visible-light photocatalyst. J Photochem Photobiol A Chem. 2005;174(1):82–87.
[32]   Klug H P and Alexander L E. X-ray diffraction Procedures for polycrystalline and Amorphous Materials, 1st edn, chapter 9, Wiley, New York; 1st edition, 1954.
[33]   Wong E. M and. Searson. P. C. ZnO quantum particle thin films fabricated by electrophoretic deposition. Appl. Phys. Lett.; 1999;74(20): 2939-2941.
[34]   Brus. L, Electronic wave functions in semiconductor clusters: experiment and theory. J. Phys. Chem. 1986;90(12): 2555-2560.
[35]   Ghobadi. N, Band gap determination using absorption spectrum fitting procedure Int.Nano Lett. 2013;1186/2228-5326-3-2.
[36]   Chandrappa K. G. and Venkatesha T. V. Electrochemical generation of cubic shaped nano Zn2SnO4 photocatalysts. Nano-Micro Lett. 2010; 4(14): 19-22.

Visible light harvesting Pt/CdS/Co-doped ZnO nanorods molecular device for hydrogen generation

Neelu Chouhan [a],*, Rakshit Ameta [b], Rajesh Kumar Meena [a],[1], Niranjan Mandawat [a],[1], Rahul Ghildiyal [c]

[a] Department of Pure and Applied Chemistry, University of Kota, MBS Road, Near Kabir Circle, Kota 324005, Rajasthan, India
[b] Department of Chemistry, PAHER University, Udaipur 313003, Rajasthan, India
[c] Display Materials Laboratory, Applied Physics Department, Faculty of Technology and Engineering, M. S. University of Baroda, Baroda 390002, Gujarat, India

ARTICLE INFO

ABSTRACT

Co-doped ZnO nanorods (Co–ZnO NRs) were synthesized by hydrothermal method using cationic surfactant cetyltrimethylammonium bromide (CTAB). Their physical growth mechanism was traced in the light of FESEM and HRTEM studies. A strong correlation between their electronic structural arrangement and photocatalytic activity was established. Broad and uniform peaks were found between 525 and 700 nm in UV–Vis. diffuse reflectance spectra, which were attributed to the d–d transition of Co^{2+} ion. Successful loading of the nano-sized sensitizer CdS onto the Co–ZnO NRs' surface, contributes to the band gap reduction in CdS/Co–ZnO NRs ($Eg = 2.25$ eV) sample. X-ray absorption spectroscopy confirms the presence of the lower degree structural disorders in CdS/Co–ZnO NRs with respect to the pristine ZnO and Co–ZnO NRs. Gradual modification in pristine ZnO NRs enhances the photocatalytic activity. Hetero-assembly of 1.5% Pt/CdS/Co–ZnO NRs, exhibited excellent photocatalytic responses in terms of quantum efficiency (1.98%) and hydrogen generation capacity (67.20 mmol/H_2 g) under 1 Sun (1.5AM G) light exposure.

Introduction

Hydrogen is the most compatible and clean fuel on the planet in terms of energy economy and ecological health of the planet [1–3]. Unfortunately, the large amount of the H_2 is produced by the carbon containing resources that release enormous amount of CO_2 in atmosphere. Beside this, nature has provided us a carbon-free abundant source of hydrogen in form of water almost free of cost. Cleavage of water in presence of the photocatalyst (a semiconductor of appropriate band gap) and sunlight, can produce hydrogen in an eco-friendly manner. Although, sunlight and water, comes free of cost to us but the cost, stability and efficiency of the

---

photocatalysts are the main thrust areas for the large scale hydrogen production. At some extent oxide photocatalysts (ZnO, TiO$_2$, Ga$_2$O$_3$, Nb$_2$O$_3$, In$_2$O$_3$ Fe$_2$O$_3$, SnO$_2$, WO$_3$, NiO, etc.) were found fit in above criteria. Out of the commercially available wide range of oxide semiconductors, ZnO [4,5] has been selected for the study because of its superb and unique inherent qualities such as low cost, wide availability, viability to change in morphology, large excitonic binding energy (60 meV), deep photon penetration, short diffusion length, low reflectivity, high carrier mobility, good bio-compatibility, etc. Usually, the nanostructures of ZnO have a large degree of charge transfer over their bulk counterparts that is due to their large surface area to volume ratio, short lateral diffusion length and low reflectivity [6]. Few of the notable ZnO systems that accounts for photocatalytic water splitting are N-doped ZnO nanowires ($\eta = 4\%$) [7], CdTe sensitized ZnO nanorods (1.98%) [8], CdSe sensitized ZnO nanotubes [4], GaN-ZnO (5.2%) [9], ZnS–ZnO core–shell (STH = 0.38%) [10], TiO$_2$ shell ZnO core NPs ($\eta = 0.17\%$) [11], ZnO/ZnO:Cr [12], Si/ZnO core shell nanowires (0.035%) [13], ZnO and Fe$_2$O$_3$ modified TiO$_2$ fibres (0.12 ml/min mg) [14], etc. Furthermore, doping of transition metals to the semiconductors, used to improve the optical output of these photocatalytic materials. The effect of different transition metals (Fe, Co, Ni, Cu, Zn, In, etc) on the photocatalytic activity of oxide semiconductor was studied for splitting of water into hydrogen and oxygen under UV irradiation [15,16]. In nonoxide semiconductors category, nano-composite Ni-doped InN/GaZnON and Ni-doped CdS nanoparticles are a good example of semiconductor that release 2.23 μmol h^{-1} and 25.848 mmol/(h g) of H$_2$, respectively, under visible light irradiation [17,18].

Hence, cobalt doping was employed to modify the surface quality of ZnO. Therefore, it was decided to synthesize nanostructures of ZnO and Co doped ZnO systems for water splitting and hydrogen generation. Consequently, the hydrothermal method [5] was adopted to develop one dimensional (1D) nanorods (NRs) of Co–ZnO by controlling the surfactant (CTAB; cetyltrimethylammonium bromide) concentration in water. Unluckily, neither the ZnO NRs nor Co–ZnO NRs, can exploit sunlight fully due to their wide band gap (WBG) i.e. E$_g$ = 3.2 eV. More often the hetero-assemblies (by incorporation of visible light harvesting moiety to oxides) are made by introducing better light harvesting material (chalcogenide quantum dots/dyes) to nanooxide systems that to enhance their light harvesting capacity. A small amount of the state of art hetero-assemblies are mentioned here as H$_4$Nb$_6$O$_{17}$/CdS, Pt/TiO$_2$/Zn-porphyrin, ZnO/Erythrosine, Pt/SrTiO$_3$:Rh/BiVO$_4$, Fe$_2$O$_3$/WO$_3$, ZnO/CdSe, TiO$_2$/CdS, etc, which was also used for water splitting [19–28]. These heterostructures exhibit excellent stability, capability to utilise the wide portion of visible light, and suppress the recombination of the light generated photo-electrons and photoholes. For this reason, a chalcogenide CdS (E$_g$ = 2.4 eV) was introduced as a sensitizer to ZnO or Co–ZnO NRs. Additionally,1.5% Pt was loaded as co-catalyst to generate reduction site to consume the photoelectrons at the surface of CdS/Co–ZnO NRs. Then this nanomolecular machines i.e. 1.5% Pt/CdS/Co–ZnO NRs, were utilised for photocatalytic water cleavage, in aqueous electrolyte (0.35 M Na$_2$S + 0.25 M K$_2$SO$_4$, pH = 13.3) under visible light irradiation [29].

Experimental

Synthesis of ZnO and Co–ZnO NRs

Typical synthesis of ZnO or Co–ZnO nanostructures includes two major steps: (i) seed formation and (ii) growth of NRs. First step involves precipitation of Co–ZnO seeds by oxidation of aqueous nitrates for zinc and cobalt in 10:1 ratio, using liquid ammonia. Afterwards, Co–ZnO seeds (2 g; green powder) were utilised to harvest NRs, by varying surfactant (CTAB) concentration (17.5, 20, 25, 30, 35 and 40%) in reverse micelle hydrothermal method at 200 °C for 10 h, reported earlier [25]. Here, CTAB-micelles served as the templates in nanocrystals growth. For the synthesis of ZnO NRs, the same synthesis process was adopted without taking cobalt salt.

Loading of CdS on to the surface of ZnO and Co–ZnO NRs

Direct sulfurization method was employed to add CdS sensitizer to ZnO and Co–ZnO NRs, described somewhere else [30]. Respective pinkish white and yellowish green powder of CdS/ZnO NRs and CdS/Co–ZnO NRs were obtained, which was washed thoroughly with hot water and dried in the oven at 60 °C for 24 h.

Co-catalyst addition to CdS/Co–ZnO NRs surface

CdS-loaded ZnO and Co–ZnO NRs, were decorated with co-catalyst (1.5% Pt) to facilitate the reduction sites on the photocatalytic surface, by impregnation method [24]. Finally, the sample was dried at 60 °C for 12 h in oven and used as such for photocatalytic cleavage of water.

Results and discussion

Study of surface morphology

As fabricated nanomolecular device (1.5% Pt/CdS/Co–ZnO NRs) was rigorously characterised at every step of fabrication process, using variety of analytic tools. Morphological images of ZnO NRs, was recorded using a field emission-scanning electron microscope (FESEM; Hitachi S-4000) after every step of advancement. High resolution transmission electron microscope (HRTEM; JEM-2100F, at 200 kV) and corresponding energy-dispersive X-ray (EDX) spectroscopy, were used to know the lattice fringes and growth directions from selected area electron diffraction (SAED) pattern and elemental ratio. Products of hydrothermal process at varying concentration of aqueous CTAB and seeds, were examined by using FESEM (Fig. S1). All concentrations of CTAB (17.5, 20, 25, 30, 35 and 40%) was kept greater than its critical micelle concentration (CMC; 0.95 mM) to promote one dimensional (1D) augmentation of Co–ZnO seeds [31]. According to the principle of dynamic solvation, there is a selective adsorption (electrostatic) of the cationic surfactant on the hexagonal facets i.e. (100) and (111) planes, which was also evident from HRTEM images of Co–ZnO seeds [32]. Dissimilar rate of attachment/detachment of surfactant on above planes, effectively reduce the energy

and growth rate along these planes that allows NRs to grow along (011) plane [33,34]. Sterically bulky cationic surfactant, CTAB plays two major roles in production of one dimensional Co–ZnO structures: (i) As micellizer, it induces 1D molecular aggregation of micelles in aqueous medium and (ii) As stabilizer, it stabilises the micelle-captivated Co–ZnO nanoclusters by preventing their uncontrollable growth. Results of both of these actions collectively promote cylindrical aggregation (wormlike micelle) of ZnO or Co–ZnO seeds (scaffold by CTAB) in opposite directions with time that creates a junction in the middle of the rods (revealed from FESEM images) [35,36]. The growth process of NRs will continuous till the critical mass of the nanorods of ZnO or Co–ZnO, was attained. Afterwards, NRs split into two parts, as illustrated in Fig. 1. Final size of the NRs strictly depend on the size of the reaction volume i.e. driven by the radius of the cavity in water droplets with surfactant R_w, which is expressed by the following Equation (1) [37].

Radius of the cavity in water droplets with surfactant
$$R_w = 3 \, V_{aq}[H_2O]/\sigma[s] \quad (1)$$

where, $\sigma[s]$ = polar group area of surfactants' head and $V_{aq}[H_2O]$ = volume of water. It means the size of the nanorod can be regulated by changing the volume of water and the polar head area of micelles (controlled by CTAB concentration). Increase in volume of water droplet directed to increase the volume of the surfactant in surfactant-incorporated water droplets. Increase in CTAB concentration tends to increase in head area of polar group. Both of these effects, contribute equally in keeping the size of the Co–ZnO NRs (~400 nm broad and 2 μm long) same even at higher CTAB concentration reactions.

FESEM images (Fig. S1a and b) of the Co–ZnO nano-architects fabricated at different concentrations of the CTAB and the supporting literature [38], give some significant hints about their physical growth mechanism. Gradual morphological transformations were observed in finishing-end shape of the Co–ZnO NRs with augmentation in CTAB amount/concentrations. At 17.5, 20, 25, 30, 35 and 40% CTAB concentration, corresponding shuttle-end, flat end, cocoon-end

(without hole), cocoon-end (with hole), cocoon-end (with big hole) and cocoon-end (with hole) hexagonal rods were obtained, respectively. Due to the apt salt/surfactant ratio (Co–ZnO/CTAB = 1:0.20) in 20% CTAB [39], the flat-end Co–ZnO NRs were produced. Beyond 20% CTAB concentration, the enhancement in CTAB concentration, promotes the formation of excess of bromide ions by cleavage of CTAB. These bromide ions induced chemical inching in nanooxides, which was initiated from the centre of the (011) plane of the hexagonal Co–ZnO NRs and created a hole at centre. The size of this hole increases with CTAB concentration from 50 nm (30% CTAB) to 76 nm (35% CTAB) to 98 nm (40% CTAB). Further, whatever may be the concentration of CTAB was used for synthesis, almost same sized (400 nm wide and 2 μm long) hexagonal-nanorods were obtained.

SAED pattern (Fig. 2a) of flat-end Co–ZnO NRs was obtained corresponding to the HRTEM image, which evident the hexagonal orientation of the Lau's spot around central spot, proves the presence of the crystalline single hexagonal phase of the Co–ZnO NRs, consistent with X-ray powder diffraction (XRD) results. Lattice fringes, depicted in the HRTEM image (Fig. 2b), are separated by 2.42 nm distance, illustrate the high crystalline nature of NRs that grow along the (011) plane. EDX profile of the Co–ZnO NRs, possess the Co and Zn peaks that confirms the Co-doping onto ZnO lattice (Fig. 2c). Fig. 2d exhibits the HRTEM image of CdS loaded Co doped ZnO that revealed the presence of the heterojunction between CdS and Co-doped ZnO.

XRD analysis

X-ray diffraction patterns of the synthesised samples were recorded on Philips X'Pert MPD-3 diffractometer (monochromatized radiation of Cu K_α (λ = 0.15418 nm), scan rate = 0.05° 2θ s^{-1}, at applied voltage 45 kV and current 40 mA). XRD patterns, shown in Fig. 3a–c, verify crystallisation of ZnO and Co–ZnO NRs in a single wurtzite phase. Positions of diffraction peaks of the ZnO and Co–ZnO NRs, are in good agreement with the standard JCPDS (Joint Committee on Powder Diffraction Standards) card No. 36–1451, which
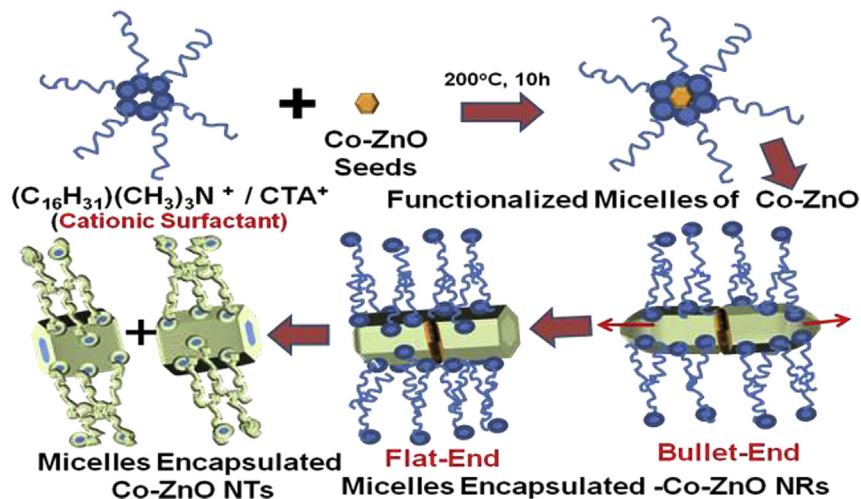

Fig. 1 – A schematic gradual physical growth mechanism for hexagonal faceted Co–ZnO nanorods.
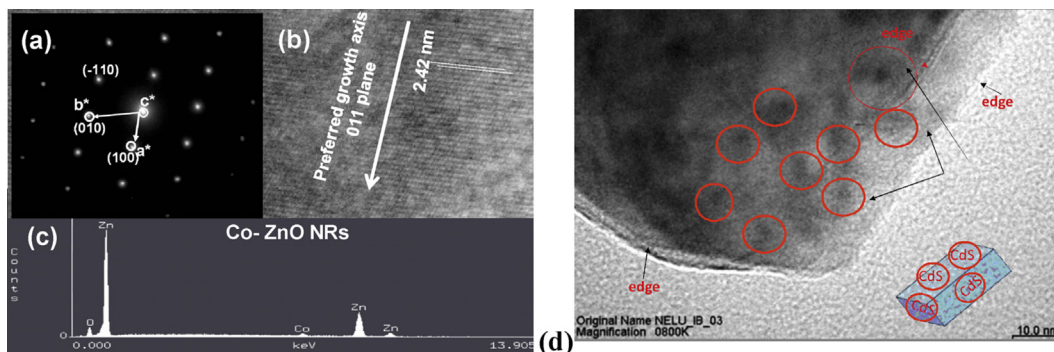
Fig. 2 – HRTEM micrographs of Co–ZnO NRs including the (a) SAED pattern, (b) lattice fringes, (c) EDX analysis. This shows well ordered crystalline planes along with hexagonal packing of atoms and a lattice spacing of 2.42 nm, corresponding to the growth 011-plane of Co doped-ZnO lattice and (d) HRTEM image of CdS nanoparticles loaded Co-doped ZnO that revealed the presence of the heterojunction between CdS and Co-doped ZnO.
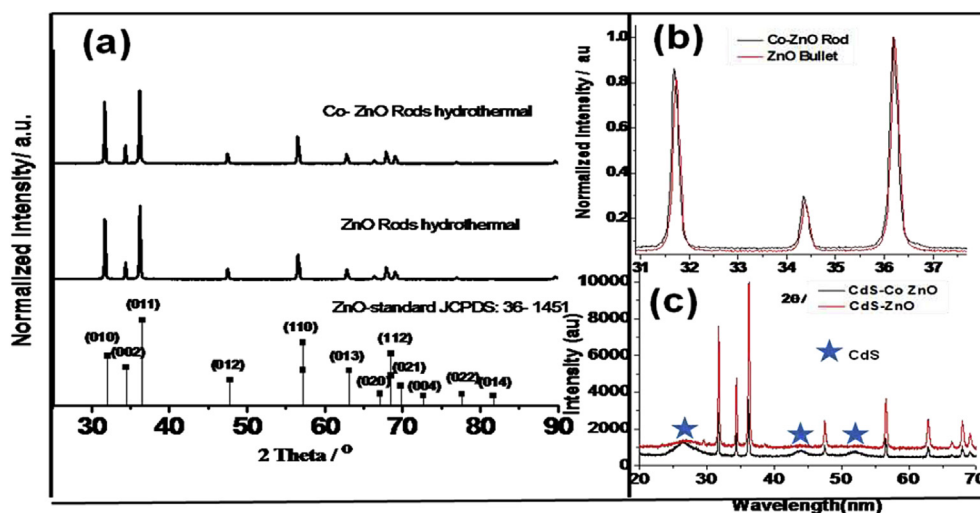
Fig. 3 – Powder XRD patterns of the (a) pristine ZnO and Co–ZnO NRs with respect to standard ZnO (JCPDS card No. 036-1451) with (b) (100), (002) and (101) reflections highlighted between the angles 31.0–37.5° to demonstrate the insertion of Co in ZnO lattice and (c) loading of CdS on ZnO and Co–ZnO surface and star sign assigned to the hexagonal CdS peaks (JCPDS No. 80-0006). First star at lowest angle represents the combined intensities of (100), (002), and (101) peaks, second and third star belongs to (110), and (112) peaks of CdS, respectively.

accounts for the hexagonal crystal growth in both samples along the 011 plane. Diffraction patterns of the pristine ZnO and Co–ZnO NRs, shown by Fig. 3a, confirm that both belongs to the P6$_3$mC space group and their corresponding lattice parameters are a = b = 3.1919 Å, c = 5.1908 Å, α = β = 90°, γ = 120°, at z = 4, V = 52.8800 Å^3 and a = b = 3.1942 Å, c = 5.1968 Å, α = β = 90°, γ = 120°, at z = 4, V = 52.9600 Å^3, respectively. Minor shifting in XRD-peaks of Co–ZnO was found towards lower angles in comparison to the pristine ZnO NRs (Fig. 3b) that strongly recommends the incorporation of the slightly bigger ions i.e. Co^{2+} (IR = 0.075 nm > Zn^{2+}; IR = 0.074 nm) into ZnO lattice. Value of c/a ratio was estimated as 1.626 (1.633 for ideal tetrahedra) for the Co–ZnO system that reflected the hexagonal packing of the atoms by geometric occupation of ions at dissimilar sites of slightly distorted tetrahedra. The tetrahedral positions are occupied by anions at four apices and by cations at centre [40].

Another crystal parameter b/c (u) = 0.615 (0.375 for an ideal crystal), shows the existence of the anion–cation bond, parallel to the c-axis. c/a parameter follows an inversely proportional relationship with u. Therefore, on decreasing c/a value with respect to ideal tetrahedra, u adjusts itself in such a way that the four tetrahedral distances get balanced through the distortion in tetrahedral angles and distances. Prominent and sharp peak (011) around 2θ = 36.26°, reconfirms the crystal growth along (011) plane. Crystalline domain of the flat end Co–ZnO NRs, was calculated using Debye-Sherrer equation i.e. 385 nm, which is quite near to the average size (~400 nm) of the NRs that measured by FESEM images. Fig. 3c expressed the significantly broad XRD peaks of CdS accompanied with regular wurtzite Co–ZnO peaks, in CdS/Co–ZnO NR's sample. In the same sample presence of the first broad peak centred at 2θ = 27° is an aggregation of (100), (002), and (101) peaks of CdS, (110) peak at 2θ = 44°, and (112) peak at 2θ = 52.5°, are also in

good agreement with the standard CdS (JCPDS card No. 80-0006). It proves the successful loading of the hexagonal CdS nanoparticles onto the ZnO NR's and Co—ZnO NR's surface as shown in Fig. 3c. XRD patterns of the all studied samples are shown in Fig. 3a—c and following Equation (2) [41], is used to measure the crystallinity of the samples.

$$C_{rt}(\%) = \{(I_{011} - I_{am})/I_{011}\} \times 100 \qquad (2)$$

where, C_{rt} = the relative crystallinity (in percentage); I_{011} = the highest intensity of the (011) diffraction angle of the crystal lattice (arbitrary unit; au); and I_{am} = the scattering strength diffracted by the non-crystalline environment (if 2θ is close to angle $21°$, the unit is similar to I_{011}). The observed crystallinity (ZnO NRs (95.00%), Co—ZnO NRs (94.00%), CdS/ZnO (90.00%) and CdS/Co—ZnO (78.95%)) of the all studied samples is decreases with gradual modification in the basic ZnO NRs sample.

UV—Vis DRS study

Diffuse reflectance UV—visible absorption spectrum was recorded for the dry and pressed disk samples of powdered ZnO NRs to confirm the doping of Co and deposition of CdS on ZnO NRs, by using UV—visible spectrophotometer (UV-1700, Shimazdu, Japan with UV Probe device). Moisture free $BaSO_4$ was used as a reflectance standard in a UV—Vis diffuse reflectance experiment. Instrumental error was noticed around the wavelength 350 nm due to the shifting of the light source from UV to Visible region, which was found responsible for the noise. Characteristic diffuse reflectance spectra (Fig. 4a and b) of the samples illustrate the red shifts in their edges with broadening in the main peak (300—525 nm) on successive advancement (addition of Co or CdS) in the ZnO NRs for making of the hetero-assembly CdS/Co—ZnO NRs. First excitation peak centred at 450 nm, represents the presence of the CdS. Co^{2+}-incorporated samples (Co—ZnO NRs and CdS/Co—ZnO NRs) exhibits a secondary peak around 525—700 nm that is attributed to the multiple d—d transitions of Co(II) [42]. Band gap (E_g) of the studied system has been estimated at different stages of the advancement of ZnO NRs using the Kubelka—Munk function F(R) vs wavelength plot (Fig. 4a and b). Successive surface modification of ZnO nanostructures reduces their band gaps, as follows 3.18 eV (ZnO

NRs), 3.00 eV (Co—ZnO NRs), 2.48 eV (CdS/ZnO NRs) and 2.25 eV (CdS/Co—ZnO NRs). Band gap of the CdS/Co—ZnO NRs, ensures us about the good possibility of using it for photocatalytic hydrogen generation.

First excitonic peak of DRS spectrum was utilized to determine the particle size of the sensitizer CdS (ca 5.24 nm) in CdS/Co—ZnO NRs by using following power Equation (3) [43],

$$D = (-6.6521 \times 10^{-8})\lambda^3 + (1.9557 \times 10^{-4})\lambda^2 - (9.2352 \times 10^{-2})\lambda + (13.29)$$

$$(3)$$

where, D (nm) is the size of the CdS nanosensitizer in heterostructure, and λ (nm) is the first excitonic absorption wavelength i.e. 450 nm for the corresponding sample. It represented that the incorporation of 5.24 nm CdS nanoparticles on Co—ZnO NRs (~400 nm broad and 2 μm long).

XAS study

X-Ray absorption spectroscopy (XAS), was used to examine the local electronic environment around the centre atom. XAS (XANES/EXAFS) was recorded at BL-8 dispersive EXAFS beamline at INDUS-2 synchrotron radiation source at RRCAT, Indore. Measurements were made at the Zn K-edge (9659 eV) in fluorescence mode at room temperature with a seven-element HPGe detector and double crystal Si (111) monochromator. Measurements were performed along the c axis perpendicular to electric field vector and along the c axis in the plane of the electric field vector. The raw X-ray absorption data were analysed using a standard procedure (software program ATHENA) that includes the subtraction of the pre- and post-edge background, edge calibration with a reference Zn foil, and normalization of edge jump. The Fourier transform of the normalized k^3-weighted EXAFS spectra was taken using the program ARTEMIS for k from 2 to 11.5 $Å^{-1}$ and Hanning window function followed by a nonlinear least-squares fit between 1.0 and 3.6 Å. Theoretical phase and amplitude functions were calculated using the FEFF (V. 8.4) code.

This technique identifies the lattice disorders and short-range local atomic arrangement around the central atoms, which XRD can't observe [44]. XAS profiles of the ZnO, Co—ZnO
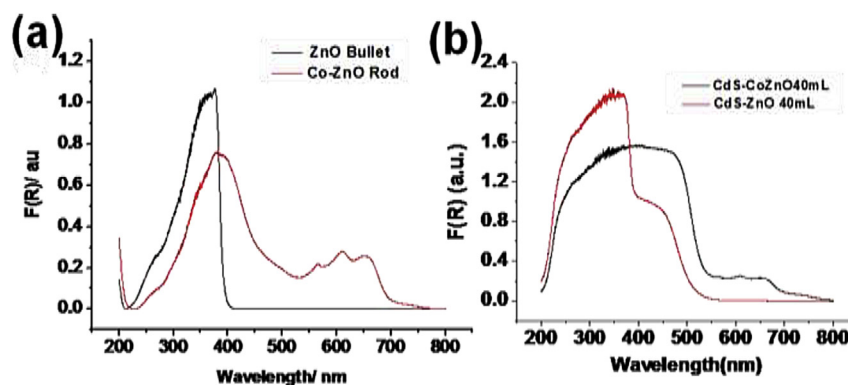

Fig. 4 — Diffuse reflectance spectroscopic Kubelka-Munk plots (F(R) vs wavelength) of pristine ZnO NRs and Co—ZnO NRs (a) before and (b) after CdS loading.

and CdS/Co—ZnO NRs, were recorded at Zn K edge. Typical normalized XAS plot between X-ray absorption cross-section and photonic energy (PE) are displayed in Fig. 5a—c. XAS profile was divided into four prominent zones with respect to the photonic energy of incoming photons i.e. pre-edge, edge, near-edge (XANES; X-rays absorption near edge spectroscopy) and fine structures (EXAFS; extended X-rays absorption fine structures and NEXAFS; near edge X-ray absorption fine structure) regions. Absence of pre-edge features (ls → 3d; dipole forbidden transition, PE < 9659 eV) in all samples are credited to the fully occupied 3 d^{10} configuration of Zn^{2+} ions [39] and negligible p-band defects. Edge features (ls → 4p) of Co—ZnO shifted towards the higher PE = 9660.23 eV with respect to the pure ZnO and CdS/Co—ZnO NRs (PE = 9659 eV) are attributed to the replacement of the high polarity Zn—O bonds by the low polarity Co—O and Co—Zn bonds in Co—ZnO.

Eventually, the presence of the highly polar bonds of CdS/Co—ZnO NRs i.e. Cd—O, Cd—S and Zn—S, nullified the shifting in edge. It also confirms the existence of the highly oxidised Zn atoms (>2 + oxidation state) in Co—ZnO NRs, attributed to the adsorption process [45]. Almost same edge position of the pristine ZnO and CdS/Co—ZnO NRs, signify the retention of similar oxidation state of Zn (2+) in both. Intense, symmetrical and superimposed white line (WL) peak features of ZnO and Co—ZnO NRs, centred at 9668.50 eV (10.01 eV/step), are originated due to ls-4p hybridization, reflected the similar electronic surroundings in both the species. Short heighted WL peak of CdS/Co—ZnO NRs, predicts the low degree of anisotropy, and highly disordered arrangement of elements around Zn atom [6]. Electronic transition 1s → 4d in Zn is attributed to the EXAFS features at P E ~ 9668.50 + 50 eV. Shoulder peak was observed at 9678.52 eV, followed by the symmetrical third and fourth peaks at PE 9695.96 and 9714.00 eV, respectively for both sample. These fine features reflected that the anions envelop the central Zn atoms in a regular tetrahedral fashion in above two samples. Absence of the 9695.96 eV peak in Co—ZnO, reveals the existence of the cobalt (II) oxide with few Co atoms that substitute zinc in the ZnO system [46]. It stimulates the distorted tetrahedral surrounding around Zn and deviation in the lattice parameters

[45]. NEXAFS features for ZnO and CdS/Co—ZnO NRs, coincide within 1 eV PE range, suggesting that both have similar regular tetrahedral environment of anions for Zn atoms. The results also suggested about the distorted tetrahedral arrangement in the Co—ZnO system, where the metallic species Co (II) and Zn are at the centre of the tetrahedra and anions (O^{2-}) are situated at the four apexes of the tetrahedra. NEXAFS features of the all examined systems were refined by keeping typical k^3-weightage in the range of 3.5—12 $\mathring{A}^{-1}$ and using software FEFF (V-7) (Fig. S2a and b) [47]. Respective refined parameters (least-squares refined R-factor, mean first-shell metal—oxygen bond length, coordination number, and Debye-Waller factor) are extracted for ZnO (3.8wt%, 1.99(8)$\mathring{A}$, 5.10 and 0.96 × 10^{-2} $\mathring{A}^2$), Co—ZnO (4.10wt%, 2.01(4)$\mathring{A}$, 5.40 and 0.82 × 10^{-2} $\mathring{A}^2$) and CdS/Co—ZnO (4.20wt%, 1.95(7)$\mathring{A}$, 5.80 and 0.86 × 10^{-2} $\mathring{A}^2$).

Photocatalytic hydrogen production

The catalyst (0.3 g) was suspended in 140 mL of aqueous electrolyte of 0.35 M Na_2S and 0.25 M K_2SO_3 in a double walled-Pyrex glass reaction cell (volume ~220 mL, with water jacket) that was sealed with a rubber septum. To expel the air-content from the solution, the sample was purged with Ar for 1 h prior to start the photochemical reaction. Ar gas flows continuously in inner jacket, to maintain 1 atm pressure of the solution. Temperature of the outer jacket was set at 25 °C. The suspension was irradiated with a 300 W Xe lamp (>420 nm, light intensity 1 × 10^{22} photons per hour Xe lamp-HX1, Model PE300UV, Perkin Elmer). All the experiments are carried out under ambient conditions. Photocatalytic responses were hourly monitored in terms of the amount of hydrogen generated at 1—7 h time intervals, using gas chromatograph (Shimazdu, Japan, thermal conductivity detector and molecular sieve with 5 A columns) throughout the course of the reaction. Photocatalytic cleavage of water was carried out in presence of the hole-scavenger electrolyte (0.25 M K_2SO_3 + 0.35 M Na_2S) solution of 13 pH, under the irradiation of 1 Sun (100 mW/cm^2, AM1.5 G) visible light. Rough and hexagonal crystalline surface of the CdS/Co—ZnO, loaded with co-catalyst (Pt) to facilitate the active sites for the oxidation (photohole rich) and reduction (photoelectron rich) of water. These active sites suppress the recombination of the photoelectric current carriers i.e. photoelectrons and photoholes. Hole-scavenger electrolyte was used to avoid the photooxidation of CdS nanoparticles present in the nanomolecular device by irreversible consumption of photogenerated holes that prohibited the oxidation of water [48]. Corresponding amount of H_2 evolved without any noticeable degradation of the photocatalytic devices, such as 1.5% Pt/ZnO, 1.5% Pt/Co—ZnO, 1.5% Pt/CdS/ZnO and 1.5% Pt/CdS/Co—ZnO, was recorded as 10.2, 22.56, 50.57 and 67.20 mmol/H_2 g, respectively (Fig. 6a). Quantitative rise in the rate of H_2 evolved, was noticed after each step of the advancement on ZnO NRs, which follows a quadratic relation y = 1.022(03) x^2 + 14.734(15) x − 6.900(16) and satisfy 3/2 order kinetics for advancement paradigm of nanomolecular device (Fig. 6b). Apparent quantum yield (AQY) was estimated for the tested device using Equation (4) with the assumption that all of the incident photons are absorbed during the photochemical reactions [49].

Fig. 5 — Normalized synchrotron-radiation based absorption cross section as a function of photonic energy with the geometry of the *c*-axis aligned parallel to the electric field vector of the x rays at the Zn K-edge (E = 9659 eV) spectra of (a) pristine ZnO NRs, (b) Co—ZnO NRs and (c) CdS/Co—ZnO NRs, recorded in a florescent mode.
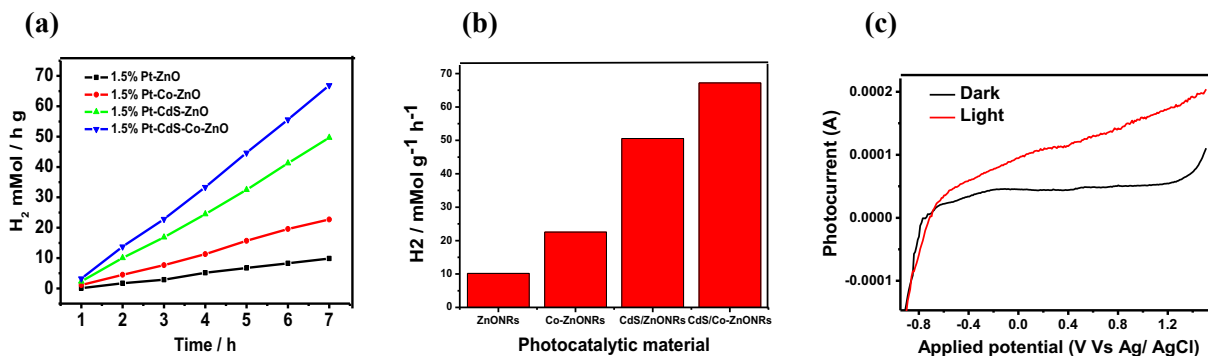
Fig. 6 – (a) Comparative rate of H_2 evolution by photocatalytic cleavage of water using molecular devices of 1.5% Pt/ZnO NRs, 1.5% Pt/Co–ZnO NRs, 1.5% Pt/CdS/ZnO NRs, and 1.5% Pt/CdS/Co–ZnO NRs; (b) Bar plot of gradual increase in the rate of H_2 evolved after 7 h for each advancement. (c) I–V plot for CdS/Co–ZnO NRs in electrolyte solution (pH = 13.5) under AM1.5 G illumination, recorded at zero bias voltage at 25 °C temperature in the applied potential range −1.0 to +1.5 V (vs Ag/AgCl electrode). Exposure area of the sample ~1 cm^2.

$$AQY\ (\%) = \left([\text{Number of } H_2 \text{ molecules evolved} \times 2] \times 100 \right) / [\text{Number of incident photons}] \quad (4)$$

where, the number of incident photons was 4.48×10^{24} photon h^{-1}, measured using a Si photodiode, at 420 nm wavelength. Corresponding water splitting ability of the device was estimated in terms of AQY at 420 nm. These were found to be 0.30, 0.66, 1.49 and 1.98%, respectively for above mentioned systems (1.5% Pt/ZnO, 1.5% Pt/Co–ZnO, 1.5% Pt/CdS/ZnO and 1.5% Pt/CdS/Co–ZnO). Reproducibility of these systems against their photocatalytic water splitting ability was checked thrice by using the same photocatalytic material (suspended particles in aqueous electrolyte) after their five times washing with the pure de-ionized water and drying at 100 °C for 1 h.

Electrochemical analyzer (Auto lab potentiostat model PGSTAT30) in the midst of software GPES (general purpose electrochemical study) manager, was used to monitor the photovoltaic responses of the test samples. Power density of the light source was controlled at 100 mWcm^{-2} (AM1.5 G), using thermopile (Gentec (ε) Solo-2, Model-UP12E105-H5) at the beginning and checked at end of the each PEC run. Pyrex glass photoelectrochemical (PEC) cell with water jacket was well equipped with a small quartz window and conventional three electrode-system, comprising of a saturated calomel electrode (SCE) as reference electrode, a Pt flag as counter electrode and uniform film of the sample loaded on fluorine-doped tin oxide (FTO) substrate (using doctor blade method) as the working electrode (WE). A wide potential window with a width of 1.5 V (−0.9 to + 0.6 V) recorded during photovoltaic study of 1.5% Pt/CdS/Co–ZnO NRs device, was attributed to good electron exchange quality of the system (Fig. 6c) [50]. Significantly, no saturation in photocurrent was observed at applied positive potentials, which indicates efficient charge separation upon light illumination that is responsible for higher hydrogen evolution amount [51].

On the basis of this study and other supportive analytical evidences [7,52], the most plausible overall photocatalytic water splitting mechanism for the nanodevice (1.5% Pt/CdS/Co–ZnO NRs) in presence of hole sacrificial electrolyte under visible light exposure, is suggested and illustrated by Fig. 7.

During electron transfer, when the surface of the device was illuminated with light, an electron was excited from VB to CB, which generates a pair of photohole and photoelectron in corresponding VB and CB of Co–ZnO. Nascent photoelectrons of CB (Co–ZnO) are transported to the CB of quantum confined nano-sized sensitizer (CdS). This electron arrived at the junction of Pt/electrolyte interface by passing through the electron-pool of the metallic Pt. At the interface, photoelectrons interacts with H^+ ions [53] of the solution and liberates nascent H that combined with another nascent H atom to generate H_2 gas. Hole accumulated at VB of Co–ZnO and CdS, were consumed by hole-scavenger electrolyte. Major chemical reactions [54], responsible for hydrogen evolution by photocatalytic cleavage of the water, are given by the Equations (5–8).

On photo − exposure : $CdS/Co − ZnO + hv → e^-(CdS/Co − ZnO) + h^+(CdS/Co − ZnO)$

$$(5)$$

Cathode : $2HO + 2e^- → 2OH^- + H_2$ $\quad (6)$

Anode : $SO_3^{2-} + S^{2-} + 2OH^- + 1.5H_2O + 6h^+ → 1.5S_2O_3^{2-} + SO_4^{2-} + 4H^+$

$$(7)$$
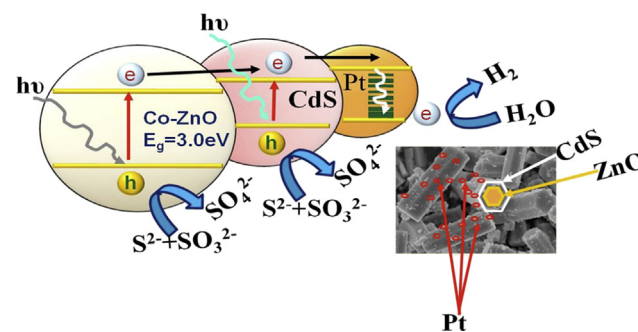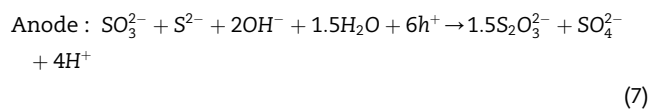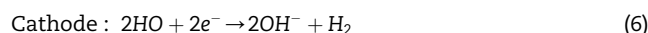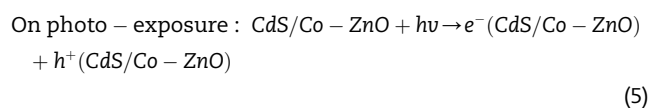
Fig. 7 – Electron transfer mechanism for the photocatalytic water splitting using the nanomolecular device i.e. 1.5% Pt/CdS/Co–ZnO NRs.

Overall Redox Reaction : $S^{2-} + SO_3^{2-} + 5H_2O \xrightarrow{h\nu} 5H_2 + 2SO_4^{2-}$ (8)

Conclusion

In short, this study gives us an inside view of the surfactant (CTAB)-controlled low cost fabrication of the ZnO NRs via reverse-micelles synthesis. Current work is focused on the performance of the nanomolecular photoelectrode of ZnO NRs by gradual surface modification for hydrogen production efficiency. A good correlation between atomic arrangement around Zn atom and light harvesting capacity of the modified ZnO NRs has been established. Defects developed on Co–ZnO NR's surface, may act as recombination centres for the photocarriers. These defects were suppressed by the decoration of flat-end Co–ZnO NRs with visible light sensitizer CdS. Heterocouple CdS/Co–ZnO NRs, show a good compatibility of nanoparticles of CdS with Co–ZnO NRs. Whole molecular assembly was utilised as a photoelectrode after Pt-loading for hydrogen generation via water splitting. Gradual increase in the photocatalytic activity of the device was recorded with modification, such as 1.5% Pt/ZnO (10.20 mmol/hg, AQY = 0.30%), 1.5% Pt/Co–ZnO (22.56 mmol/hg, AQY = 0.66%), 1.5% Pt/CdS/ZnO (50.57 mmol/hg, AQY = 1.49%) and 1.5% Pt/CdS/Co–ZnO NRs (67.20 mmol/hg, AQY = 1.98%), which can execute a job of water splitting better than pristine samples. Time dependent hydrothermal synthesis CdS/Co–ZnO NRs is in progress to explore the relationship between their photocatalytic hydrogen generation efficiency and atomic arrangement.

Acknowledgement

Appendix A. Supplementary data

Supplementary data related to this article can be found at http://dx.doi.org/10.1016/j.ijhydene.2015.11.019.

REFERENCES

[1] Balat M. Potential importance of hydrogen as a future solution to environmental and transportation problems. Int J Hydrogen Energy 2008;33:4013–29.

[2] Chouhan N, Liu RS. Electrochemical technologies for energy storage and conversion. In: Liu RS, Zhang L, Sun X, Liu H, Zhang J, editors. Electrochemical technologies for energy storage and conversion, 1. Weinheim, Germany: Wiley-VCH; 2012. p. 23–33. Chap. 1.

[3] Ogden JM. Prospectus of building a hydrogen energy Infrastructure. Annu Rev Energy Environ 1999;24:227–79.

[4] Chouhan N, Yeh L, Hu SF, Liu RS, Chang WS, Chen KH. CdSe(QDs)@ ZnO nanotubes as an effective photoanode. Chem Commun 2011;47:3493–5.

[5] Wang XH, Zhang YC, He WL, Zhu MK, Wang B, Yan H. Hydrothermal synthesis of zinc oxide powders with controllable morphology. Ceram Int 2004;30:93–7.

[6] Wolcott A, Smith WA, Kuykendall TR, Zhao YP, Zhang JZ. Photoelectrochemical generation of hydrogen from water splitting based on dense and aligned TiO_2 nanorod arrays. Small 2008;5(1):104–11.

[7] Yang X, Wolcott A, Wang G, Sobo A, Fitzmorris RC, Qian F, et al. Nitrogen-doped ZnO nanowire arrays for photoelectrochemical water splitting. Nano Lett 2009;9(6):2331–6.

[8] Chen HM, Chen CK, Chang Y-C, Tsai C-W, Liu R-S, Hu S-F, et al. Quantum dot monolayer sensitized ZnO nanowire-array photoelectrodes: true efficiency for water splitting. Angew Chem 2010;122(34):6102–5.

[9] Maeda K, Teramura K, Lu D, Takata T, Saito N, Inoue Y, et al. Photocatalyst releasing hydrogen from water. Nature 2006;440:295.

[10] Kushwaha A, Aslam M. ZnS shielded ZnO nanowire photoanodes for efficient water splitting. Electrochim Acta 2014;130:222–31.

[11] Liu M, Nam C-Y, Black CT, Kamcev J, Zhang L. Enhancing water splitting activity and chemical stability of zinc oxide nanowire photoanodes with ultrathin titania shells. J Phys Chem C 2013;117:13396–402.

[12] Shen S, Kronawitter CX, Jiang J, Guo P, Guo L, Mao SS. A ZnO/ZnO: Cr isostructural nanojunction electrode for photoelectrochemical water splitting. Nano Energy 2013;2:958–65.

[13] Ji J, Zhang W, Zhang H, Qiu Y, Wang Y, Luo Y, et al. High density Si/ZnO core/shell nanowire arrays for photoelectrochemical water splitting. J Mater Sci Mater Electron 2013;24(9):3474–80.

[14] Barakat NAM, Taha A, Motlak M, Nassar MM, Mahmoud MS, Al-Deyab SS, et al. ZnO & Fe_2O_3-incoportaed TiO_2 nanofibers as super effective photocatalyst for water splitting under visible light radiation. Appl Catal A General 2014;481:19–26.

[15] Hameed A, Gondal MA, Yamani ZH. Effect of transition metal doping on photocatalytic activity of WO_3 for water splitting under laser illumination: role of 3d-orbitals. Catal Commun 2004;5(11):715–9.

[16] Sasikala R, Shirole AR, Sudarsan V, Jagannath, Sudakar C, Naik R, et al. Enhanced photocatalytic activity of indium and nitrogen co-doped TiO_2–Pd nanocomposites for hydrogen generation. Appl Catal A General 2010;377(1–2):47–54.

[17] Hou X, Jiang S, Li Y, Xiao J, Li Y. Ni-doped InN/GaZnON composite, catalyst for overall water splitting under visible light irradiation. Int J Hydrogen Energy 2015;40(45):15448–53.

[18] Wang H, Chen W, Zhang J, Huang C, Mao L. Nickel nanoparticles modified CdS–A potential photocatalyst for hydrogen production through water splitting under visible light irradiation. Int J Hydrogen Energy 2015;40(1):340–5.

[19] Hashimoto K, Kawai T, Sakata T. Hydrogen production with visible light by using dye sensitized TiO_2 powder. Nouv J Chim 1983;7:249–53.

[20] Tawkaew S, Fujishiro Y, Yin S, Sato T. Synthesis of cadmium sulfide pillared layered compounds and photocatalytic reduction of nitrate under visible light irradiation. Colloids Surf A 2001;179:139—44.

[21] Malinka EA, Kamalov GL, Vodzinskii SV, Melnik VI, Zhilina ZI. Hydrogen production from water by visible light using zinc porphyrin-sensitized platinized titanium dioxide. J Photochem Photobiol A 1995;90:153—8.

[22] Shimidzu T, Iyoda T, Koide Y. An advance visible light induced water reduction with dye sensitised semiconductor powder catalyst. J Am Chem Soc 1985;107:35—41.

[23] Kato H, Hori M, Konta R, Shimodaira Y, Kudo A. Construction of Z scheme type heterogeneous photocatalysis systems for water splitting into H_2 and O_2 under visible light irradiation. Chem Lett 2004;33(10):1348—9.

[24] Wang X, Liu G, Lu GQ, Cheng HM. Stable photocatalytic hydrogen evolution from water over ZnO—CdS core—shell nanorods. Int J Hydrogen Energy 2010;35:8199—205.

[25] Chu D, Zeng YP, Jiang DL. Hydrothermal synthesis and optical properties of Pb^{2+} doped ZnO nanorods. Mater Lett 2006;60:2783—5.

[26] Cheng BC, Xiao YH, Wu GS, Zhang LD. Controlled growth and properties of one-dimensional ZnO nanostructures with Ce as activator/dopant. Adv Funct Mater 2004;14(9):913—9.

[27] Zhou SM, Zhang XH, Meng XM, Wu SSK, Lee T. Enhancement of UV luminescence in sol-gel prepared ZnO thin films by incorporation of Mg. Phys Status Solidi A 2005;202(3):405—10.

[28] Xu CX, Sun XW, Dong ZL, Yu MB, Xiong YZ, Chen JS. Magnetic nanobelts of iron-doped zinc oxide. Appl Phys Lett 2005;86:173110. 3 pages.

[29] Reber JF, Meier K. Photochemical hydrogen production with platinized suspensions of cadmium sulfide and cadmium zinc sulfide modified by silver sulphide. J Phys Chem 1986;90(5):824—34.

[30] Larramona G, Chone C, Jacob A, Sakakura D, Delatouche B, Péré D, et al. Nanostructured photovoltaic cell of the type titanium dioxide, cadmium sulfide thin coating, and copper thiocyanate showing high quantum efficiency. Chem Mater 2006;18(6):1688—96.

[31] Gao HC, Zhu RX, Yang XY, Mao SZ, Zhao S, Yu JY, et al. Properties of polyethylene glycol (23) lauryl ether with cetyltrimethylammonium bromide in mixed aqueous solutions studied by self-diffusion coefficient NMR. Colloid Interface Sci 2004;273(2):626—31.

[32] Yin YD, Alivisatos AP. Colloidal nanocrystal synthesis and the organic—inorganic interface. Nature 2005;437:664—70.

[33] Faeibold E, Michels B, Waton G. Micellar growth study by micocalorimetry in CTAB solutions. J Phys Chem 1996;100:20063—7.

[34] Missel PJ, Mazer NA, Carey MC, Benedek GB. Influence of alkali-metal counterion identity on the sphere-to-rod transition in alkyl sulfate micelles. J Phys Chem 1989;93:8354—66.

[35] Rehage H, Hoffmann H. Rheological properties of viscoelastic surfactant systems. J Phys Chem 1988;92:4712—9.

[36] Porte G, Appell J, Poggi J. Experimental investigations on the flexibility of elongated cetylpyridinium bromide micelles. J Phys Chem 1980;84(23):3105—10.

[37] Appell J, Porte G, Khatory A, Kern A, Candau SJ. Static and dynamic properties of a network of wormlike surfactant micelles (Cetylpyridinium chlorate in sodium chlorate brine). J Phys II 1992;2(5):1045—52.

[38] Pileni M. Reverse micelles as microreactors. J Phys Chem 1993;97(27):6961—74.

[39] Kim WJ, Yang SM. Preparation of mesoporous materials from the flow-induced microstructure in aqueous surfactant solutions. Chem Mater 2000;12:3227—35.

[40] Karzel H, Potzal W, Kofferlein M, Schiessl W, Steiner M, Hiller U, et al. Lattice dynamics and hyperfine Interactions in ZnO and ZnSe at high external pressures. Phys Rev, B Condens Matter 1996;53:11425—39.

[41] Chouhan N, Lin CC, Hu S-F, Liu R-S. Earth-free GaZnON phosphor prepared by combustion for white light-emitting diodes. J Mater Chem C 2015;3:1473—9.

[42] (a)Qiu X, Miyauchi M, Yu H, Irie H, Hashimoto K. Visible-light-driven Cu(II)—$(Sr_{1-y}Na_y)(Ti_{1-x}Mo_x)O_3$ photocatalysts based on conduction band control and surface ion modification. J Am Chem Soc 2010;132:15259—67.
(b)Yu H, Irie H, Hashimoto K. Conduction band energy level control of titanium dioxide: toward an efficient visible-light-sensitive photocatalyst. J Am Chem Soc 2010;132:6898—9.
(c)Irie H, Kamiya K, Shibanuma T, Miura S, Tryk DA, Yokoyama T, et al. Visible light-sensitive Cu(II)-grafted TiO_2 photocatalysts: activities and x-ray absorption Fine structure analyses. J Chem Phys C 2009;113:10761—6.

[43] Yu WW, Qu L, Guo W, Peng X. Experimental determination of the extinction coefficient of CdTe, CdSe, and CdS nanocrystals. Chem Mater 2003;15:2854—60.

[44] Rehr JJ, Albers RC. Theoretical approaches to x-ray absorption fine structure. Rev Mod Phys 2000;72(3):621—54.

[45] Yamamoto T. Assignment of pre-edge peaks in k-edge x-ray absorption spectra of 3d transition metal compounds: electric dipole or quadurpole? X-Ray Spectrom 2008;37:572—84.

[46] Krishnamurthy S, McGuinness C, Dorneles LS, Venkatesan M, Coey JMD, Lunney JG, et al. Soft x-ray spectroscopic investigation of ferromagnetic co-doped ZnO. J Appl Phys 2006;99:08M111. 3-pages.

[47] Stern EA. Theory of EXAFS. In: Koningsberger DC, Prins R, editors. X-ray absorption: principles, applications, techniques of EXAFS, SEXAFS and XANES. New York: Wiley-Interscience; 1988. p. 618—708. Ch. 8.

[48] Neamtu J, Georgescu G, Malaeru T, Gheorghe NG, Costescu RM, Jitaru I, et al. Atomic structure and magnetic properties of cobalt doped ZnO thin films prepared by the sol-gel method. Dig J Nanomater Biostr 2010;5:873—85.

[49] Ankudinov AL, Ravel B, Rehr JJ, Conradson SD. Real-space multiple-scattering calculation and interpretation of x-ray-absorption near-edge structure. Phys. Rev B 1998;58:7565—76.

[50] Sathish M, Viswanathan B, Viswanath RP. Alternate synthetic strategy for the preparation of CdS nanoparticles and its exploitation for water splitting. Int J Hydrogen Energy 2006;31:891—8.

[51] Konta R, Ishii T, Kato H, Kudo A. Photocatalytic activities of Noble metal ion doped $SrTiO_3$ under visible light irradiation. J Phys Chem B 2004;108(26):8992—5.

[52] Poh WC, Loh KP, Zhang WD, Tripathy S, Ye JS, Sheu FS. Biosensing properties of diamond and carbon nanotubes. Langmuir 2004;20:5484—92.

[53] Lindbergh G, Simonsson D. Inhibition of cathode reactions in sodium hydroxide solution containing chromate. J Electrochem Soc 1991;36:1985—94.

[54] Reber JF, Meier K. Photochemical production of hydrogen with zinc sulfide suspensions. J Phys Chem 1984;88(24):5903—13.

Synthesis and Characterization of Flower-shaped ZnO/Ag Nanocomposite and Antibacterial Activities

Rajesh Kumar Meena, Neelu Chouhan*,

Department of Pure and Applied Chemistry, University of Kota, MBS Road Near Kabir Circle, Kota

*niloochauhan@hotmail.com , 1988rajeshmeena@gmail.com

Abstract

A simple, fast, cost-effective, hydrothermal method, for synthesizing zinc oxide nanoparticles in aqueous media was established and tested for the antibacterial activites. Nanocomposite ZnO/Ag flower shaped particles were prepared in water. The as-synthesized ZnO/Ag nano flowers have investigated by X-ray powder diffractometer (XRD), scanning electron microscopy (SEM) for used to characterize the structural and the chemical features of the ZnO/Ag nano flower. The flower shaped nano particle method is fast, simple, convenient, economical, and environmentally benign. On the basis of our shape-control of the ZnO nanostructures, growth mechanisms were also proposed. We believe this technique will be readily adopted in realizing other forms of various nanostructured materials.

Key words: Nanoparticle, Hydrothermal Method and XRD, and FESEM.

Introduction

The shape of semiconductor nanostructures has involved extensive attention for potential applications due to their chemical and physical properties which are determined by morphology, size, and dimensions.(1) Thus, the shape control of semiconductor nanostructures has been the topic of intensive investigation in recent materials chemistry. ZnO is one of the most important multifunctional semiconductors with its wide direct energy band gap of 3.37eV and its large exciton binding energy (about 60 meV). As a result, various ZnO nanostructures, including nanobelts,(2) nanotubes,(3) nanowires,(4) and nanodisks,(5) have been reported for potential applications.(6) In addition to the conventional vapor-phase methods of vapour transport and condensation, metal-organic chemical vapor deposition and solution phase thermal evaporation methods have been developed as alternative ways to synthesize ZnO nanomaterials nanostructures with different shapes and dimensions. A hydrothermal method(7) is a widely used technique that can control the shape and dimension of ZnO nanostructures among all solution-based approaches. Unlike conventional vapor-phase methods, the hydrothermal method can produce various ZnO nanostructures at a relatively low temperature (below 200°C) using simple equipments; however, the reaction time required for the growth of ZnO nanostructures is too long (usually from a few hours to several days). Therefore, the development of a simple and fast synthetic route that can control the shape of ZnO nanostructures under ambient conditions remained an important topic of investigation. In this consider, several reports are obtainable that are neither feasible nor cost effective. The hydrothermal preparation of ZnO/Au nanoparticles at 80°C for 5 hours(8) and flower-like ZnO nanorods is masintained at more than 120°C, for several hours, at basic medium(9) chrysanthemum-like ZnO nanorods are formed in the presence of sodium dodecyl sulfate at 120°C for 24 hours,(10) and 10 hours,(11,12) and the preparation of flower-like ZnO microstructures was conducted via sonochemical treatment for 1 hour(13).

The present study focuses on the hydrothermal synthesis of ZnO/Ag nanocomposite powder. The hydrothermal synthesis of nanomaterials powders has four advantages (i) powders with nanometer-size can be obtained by this method (ii) the reaction is carried out under moderate situations (iii) powders with different morphologies by adjusting the reaction situation and (iv) the as-prepared powders have different properties from that of the bulk. In this present work, we have reported the synthesis of ZnO/Ag nanomaterials using hydrothermal method and characterized its structural, morphological properties.

Materials and Experimental Methods

ZnO/Ag nanoflowers, and nanospheres were fabricated in a hydrothermal convention technique. All chemical reagents were used without further purification. Zinc acetate dihydrate $Zn(CH_3COO)_2 \cdot 2H_2O$, 98% and CTAB

were used as zinc cation and hydroxide anion precursors, respectively, for the synthesis of ZnO/Ag nanoflowers and nanospheres. In case of ZnO/Ag composite nanoflowers, a mixture of zinc acetate dihydrate solution (90 mL) CTAB and NaOH(10 mL), the solution with continuous stirring respectively at 6h 90°C temperature. Then ZnO nanoflower- and nanosphere-containing solution was prepared and filtered, and then the resulting powder particles were washed and dried. Then as-synthesized white ZnO powder was dispersed well in water and AgNO$_3$ was added on the above dispersed ZnO solution and continuous stirring. The whole solution was stirred well for ~2h so that the AgNO$_3$ was adsorbed well on ZnO surface. Afterwards, the AgNO$_3$ adsorbed ZnO precipitate were collected and washed several times with water to drain out the excess AgNO$_3$ from the solution. Then composite of ZnO/Ag particles and as a result yellow coloured precipitate was observed. Finally, this yellow colour powder was collected and washed with deionised water twice and dried well for further characterization. The morphology of the as-prepared ZnO nanostructures was observed by field emission scanning electron microscope. The crystal structures of the nanocomposite were investigated by X-ray diffraction.

Structure and Morphology

Powder X-Ray Diffraction

The phase and the crystallinity of the samples were determined by powder x-ray diffraction (PXRD) using a Mini Flex II diffractometer with Cu-Kα radiation at 25°C with 2θ values ranging from 20-80° and scanning rate of 2° per min.

FESEM analysis

The surface morphology of as-synthesized nanoparticles was characterized using a commercial FESEM instrument from FEI Nova NanoLab combined with focused ion beams for SEM characterization.

Results and Discussion

ZnO/Ag nanocomposite was prepared by a simple hdrothermal method. The phase and the crystallinity of the samples were determined by powder x-ray diffraction Fig. 1 and Surface morphology of the samples was studied by FESEM and their images are shown in respectively Fig. 2. As can be seen, ZnO/Ag flower like Nanocaomposite consist of highly aggregated flower like particles of different sizes.

X-Ray Diffraction

The produced powder was investigated by X-ray powder diffraction patterns of ZnO/Ag nanoparticles calcined are illustrated in Fig. 1. All peaks can be well indexed to the zincite phase of ZnO/Ag nanocomposite. No peaks from any other phase of ZnO.

SEM analysis

The morphological analysis of the as-synthesized ZnO/Ag nanoflower composite has been studied using a field emission scanning electron microscopy (FESEM). Surface morphology of the samples was studied by SEM and their images are shown in Fig. 2. As can be seen, ZnO/Ag nanostructures consist of highly aggregated nanoflower of different sizes. It is clear and changes in the surface morphology of the nanomaterials take place at different pH. Moreover, ZnO nanostructures are composed of nearly nanoflower and Ag nanoparticles deposits on surface on nanoflower like structures.

Antagonistic activity of ZnO/Ag nanomaterials against bacteria

The antibacterial property of the ZnO/Ag nanomaterials was evaluated against Gram-ve Escherichia coli and Gram +ve bacteria S. aureus with agar well diffusion method. In agar well diffusion method the ZnO/Ag nanocomposite showed significant antibacterial activity on bacterial strains Gram-ve and Gram +ve bacteria and Table 1 represents the relative activities in terms of inhibition zone i.e 15 and 13, respectively. Study demonstrated that the ZnO/Ag show best antagonistic activity of ZnO/Ag nanomaterials against Escherichia coli.

| Organism	Zone of inhibition
Escherichia coli	15
Staphylococcus aureus	13
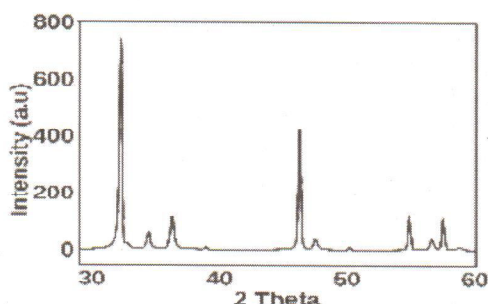
Figure .1. Powder X-ray diffraction (PXRD) patterns of ZnO/Ag nanocomposites

Figure. 2.FESEM images of ZnO/ Ag nanostructure synthesis

Conclusion

In the present study, ZnO/Ag nanocomposites were readily prepared at hydrothermal method from zinc nitrate hexahydrate, CTAB and NaOH in aqueous medium. The calcined Nanoflower like ZnO/Ag Nanocamposite material had been characterized using SEM, which could provide information with regard to surface area of the nanoparticles had a irregular, polyhedra morphology and mixed with some spherical morphology, chunky particles. We expect that this hydrothermal technique can be readily adopted in realizing other forms of various nanostructured materials.

Acknowledgment

References

1. Alivisatos, A. P. *Science* 271, **(1996)**, 933–937.

2. Zhang, B. P.; Binh, N. T.; Wakatsuki, K.; Segawa, Y.; Yamada, Y.; Usami, N.; Kawasaki, M.; Koinuma, H. *Appl. Phys. Lett.* 84, (4), 4098–4100.

3. Pan, Z. W.; Dai, Z. R.; Wang, Z. L. *Science* , 291, **(2001)**, 1947–1949.

   Kong, Y. C.; Yu, D. P.; Zhang, B.; Fang, W.; Feng, S. Q. *Appl. Phys. Lett.* 78, **(2001)** 407–409.

   Xu, C. X.; Sun, X. W.; Dong, Z. L.; Yu, M. B. *Appl. Phys. Lett.* 85, **(2004)**, 3878–3880.

6. Huang, M. H.; Mao, S.; Feick, H.; Yan, H.; Wu, Y.; Kind, H.; Weber, E.; Russo, R.; Yang, P. *Science* 292, **(2001)**, 1897–1899.

7. Law, M.; Greene, L. E.; Jhonson, J. C.; Saykally, R.; Yang, P. *Nat. Mater.* 4, **(2005)**, 455–459.

8. Fageria P., Gangopadhyay S. and Pande S. Synthesis of ZnO/Au and ZnO/Ag nanoparticles and their photocatalytic application using UV and visible light. *RSC Adv.*, 4, **(2014)**, 24962–24972 .

9. Zhang H, Yang D, Ji Y, Ma X, Xu J, Que D. Low temperature synthesis of flowerlike ZnO nanostructures by cetyltrimethylammonium bromide-assisted hydrothermal process. *J Phys Chem B.*, 108 (13) **(2004)**, 3955–3958.

10. Yin H. Xu Z. Wang Q. Bai J. Bao H. Study of assembling ZnO nanorods into chrysanthemum-like crystals. *Mater Chem Phys.* 91(1) **(2005)**, 130–133.

11. Ni Y, Wu G, Zhang X, et al. Hydrothermal preparation, characterization and property research of flowerlike ZnO nanocrystals built up by nanoflakes. *Mater Res Bull.*, 43 (11) **(2008)**, 2919–2928.

12. Li F, Hu L, Li Z, Huang X. Influence of temperature on the morphology and luminescence of ZnO micro and nanostructures prepared by CTAB-assisted hydrothermal method. *J Alloys Compd.*, 465 (1–2) **(2008)**, L14–L19.

13. Li H, Ni Y, Hong J. Ultrasound-assisted preparation, characterization and properties of flower-like ZnO microstructures. *Scr Mater.*, 60 (7) **(2009)**, 524–527.

Biosnthesis of Silver Nanoparticles (Tea Leaves') Reducing Method and their Optical Properties

Rajesh Kumar Meena and Neelu Chouhan[*]
Department of Pure and Applied Chemistry, University of Kota, Kota- 324005 Rajasthan, India
niloochauhan@hotmail.com

Abstract

In this study, we report the synthesis of silver nanoparticles (AgNPs) by using a simple green synthesis method. 30 nm sized AgNPs prepared by using tea extract and Ag salt at normal room temperature. The AgNPs synthesized via this one-pot greener approach, can be used as a promising material in different fields such as cosmetics, foods, medicine and pollutant degradation, etc. This environment benign did not use of any extra capping or reducing agent or template. As synthesized nanoparticles were evidenced by advance analysis techniques such as: UV-Vis spectroscopy, transmission electron microscopy (TEM), powder X-ray diffraction (PXRD) and fourier transform infrared (FTIR) spectroscopy, etc. X-ray analysis exhibits that the pure silver nanoparticles were grown in a single phase (face-centered cubic structure). Particle size was confirmed by the TEM images of the well dispersed sample. This method can also be facilitated for other metals such as gold (Au), copper (Cu), palladium (Pd) and platinum (Pt).

Keywords: Tea leaves, Capping agent, Bioreduction, AgNPs.

Introduction

Nanosciences is an emerging field of research nowadays because of its wide range application in the field of electronics[1-3] fuel cells, batteries, agriculture, food industry, and medical sciences[4]. Nobel metal nanoparticles *e.g.,* Au, Ag, Pd and Pt are prepared through different techniques and their characterizations expose interesting properties make them greatly significant for research. The nanoparticles synthesized through chemical method cannot be considered as an environment benign because of their hazardous effect on human health, but in recent times the fabrication of NPs by green synthesis method has pulled the interest amongst researchers because of its ecofriendly character. The synthesis of noble metal NPs using greener routes is a major agenda of nowadays scientific research[5]. Silver nanoparticles are also extensively studied owing to their unique properties such as excellent electrical and thermal conductivity and non-linear optical behaviour and catalytic activity, chemical stability antifungal and antimicrobial effects[6]. Indeed many reports are there on the synthesis of metal NPs using a variety of methods like microorganisms[7] and plant extracts.

Greener synthetic approaches for the synthesis of metal NPs have attracted considerable interest. It reduces the utilization and generation of hazardous chemicals that can be produced by different type of physical and chemical method, which are not good for living being and environment[8]. Moreover, the green production of NPs has a numeral benefits over pure chemical methods because it is a comparatively cost effective, healthy and easy to handle method. Therefore, green synthetic methology has attracted enormous attention of researcher's to

synthesize a range of metal NPs[9] due to their fascinating, and outstanding properties with respect to their bulk counterparts[10,11]. Among the various practicing green methods, biogenesis is a promising method for the synthesis of metal NPs, in which the extract of different part of the plant has been used for reduction of metal ions[12-14]. Every part of the plants such as leaf, stem, flower, bark, leaves' and skin of the fruits can be employed for the production of metal nano particles. The excess of reports have been documented recently stating the wide range of nanoparticles production using plant extracts such as Ag,[15] Au,[16] Fe,[17] Pd,[18] ZnO/Au and ZnO/Ag,[19] quantum dots CdS,[20] etc. Here, we have synthesized the silver nanoparticles via biogenesis by utilising tea leaves'.

Here, we have introduced the convenient and simple route to synthesize the silver nanoparticles using biogenesis. The applications of AgNPs include in the numerous areas such as electronic, optical, catalytic, chemical, photo-electrochemical, magnetic, antibacterial, and biological labelling. It also has been proved an efficient antimicrobial, antifungal, antioxidant agent in medical field. Due to their non-toxic action towards animal cells and highly toxic activity towards bacteria including microorganisms like Pseudomonas Aeruginosa, E-coli, Staphylococcus Aureus etc. Ag NPs are referred to be the protected and effective bactericidal metal[21-23].

Within this report we mainly focus on the Tea aqueous leaves' extract as they are the most significant and valuable piece of this plant. The tea extract contains few important phyto-chemicals i.e. nicotinic acid, proteins, lipids, ploy-phenols, saponins and alkaloids[24]. These were used to synthesize AgNPs via a

convenient and highly reproducible method. The most important benefit of this process is, necessity of any external capping and reducing agent can also be eliminated, synthesis can occur at room temperature and aqueous medium synthesis.

Materials and Methods

Required materials: Clean tea leaves were collected from tea garden of Agriculture University Kota. Silver nitrate ($AgNO_3$) was purchased from Merck, Germany. All of the chemicals used in the study are of analytical grade and used without any purification. Deionised water was used throughout in the experiment to prepare all the solutions.

Preparation of Dried Biomass: 2gm of tea leaves were collected and transferred to a beaker containing 25 ml of deionised water. The combination was thoroughly agitated for the complete night via a magnetic stirrer. The extract was then filtered to achieve the deep pink coloured solution. The liquor was centrifuged and filtered one more time to remove impurities. This extract was further filtered and stored at 4^oC until the use for current study.

Synthesis of nanoparticles: For green synthesis of silver nanoparticles, 2.0ml aqueous tea leaves' extract was taken for the reaction. Freshly prepared 25 mL of 10^{-3} M silver nitrate solution was mixed drop by drop into the plant extract. The reaction mixture filtered was incubated in dark and at ambient temperature till the colour of the solution transformed from colourless to light green. Afterwards the AgNPs were dried at 90^oC.

Characterization of nanoparticles: The synthesised nanoparticles were carefully characterized by means of advance analytical techniques. The absorption spectra were recorded using UV-Vis spectroscopy (Schimadzu UV- 1600 model *2010*) over a range of wavelength i.e. 200-800 nm, where water is used as a reference. The surface morphology of the AgNPs was examined using a JEOL-2010F TEM operating with electron beam of energy of 200 kV. FTIR (UV 3000+ *Lab India, 2011*) was examined to achieve broad spectrum of nanoparticles over a narrow series. This process gives us information regarding phytochemicals that have enclosed the particles through synthesis method. The XRD investigations were performed using Rigaku (*Ultima IV*) diffractometer with Cu-Kα radiation at 25^oC to determine the phase purity and the crystal structure of the NPs.

Results and Discussion

Synthesis and characterization of silver nanoparticles: Aqueous tea leaves' extract act as a reducing agent as well as capping agent during the silver nanoparticle production. Which reduces silver ions to nano silver hence, the colour will be change from light pink to green, as shown in Figure-1. The appearance of the aqueous silver nanoparticles was light green

in colour due to excitation of surface plasmon vibration in silver nanoparticles.[25] UV-Vis spectroscopy could be used to examine size and shape controlled by nanoparticles in aqueous suspensions. The peak attributed to the surface plasmon resonance is observed at 460 nm. The broad UV-Vis- absorption spectrum of the sample was obtained between the wavelength range in 200nm-800nm. Figures-2 and 3, shows the corresponding UV-Vis spectrum recorded for pure Tea extract and mixture of Tea with $AgNO_3$ after 24 hours aging that gives rise to the two absorption bands: first around 280 nm (π-π* transition) and second the characteristic first excitonic UV peak between 340-580nm (d-d transition) with a well defined peak at 460 nm, as shown in figure Figure-2 and 3. The first excitonic UV peak the nanoparticles was experimentally obtained due to the surface plasmon resonance (SPR) exhibited by silver nanoparticles. Which will caused when AgNP solution exposed to electromagnetic radiation and resulted oscillation gives a typical peak value.[26]
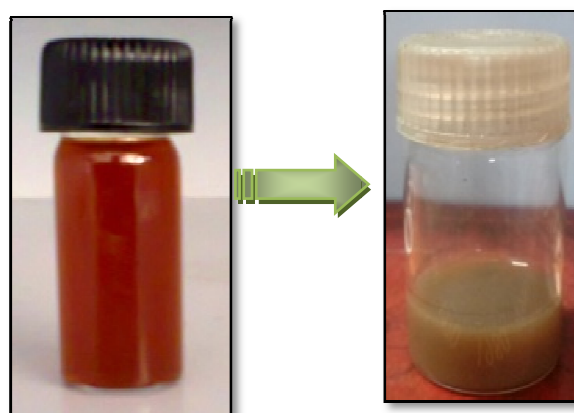

Figure-1
**(a) Aqueous Tea leaves' extract (b) AgNPs after24h incubation**
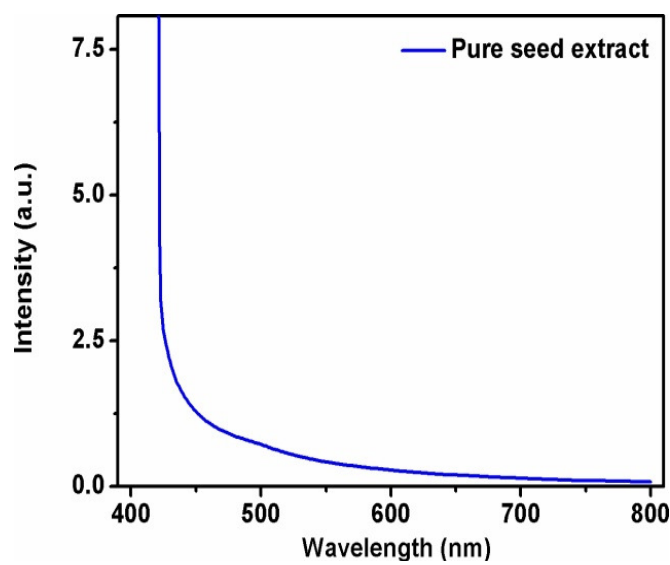
Figure-2
**Uv-Vis spectra of pure Tea leaves extract**
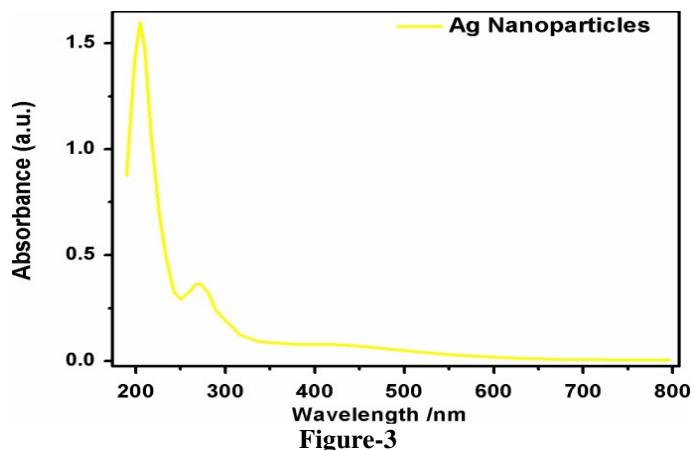
Figure-3
Silver nanoparticles produced by extract of Tea leaves

TEM image of the NPs corresponds to the topography of the AgNPs (Figure-4), which exhibits the particle size in between 20-50 nm and recommended the presence of approximately spherical silver nanoparticles in the solution. The Transmission Electron Micrograph image indicates the dispersity and morphology of the silver nanoparticles. These particles are rounded in shape and distributed in smaller and bigger size zones. These silver nanoparticles may be due to the capping of phytochemicals such as polyphenols or due to the formation of the cluster.
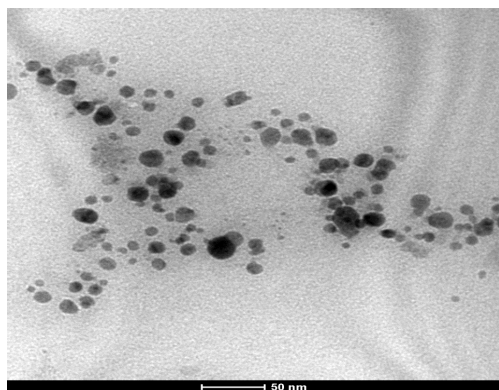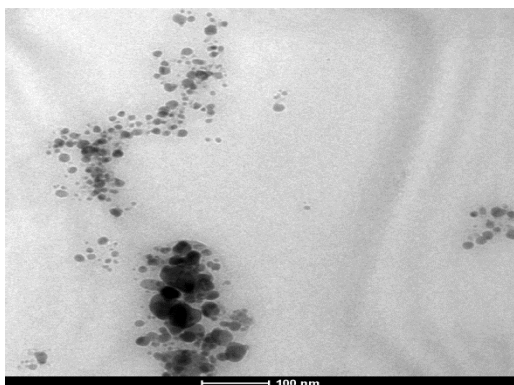
Figure-4
TEM images of AgNPs produced by Tea leaves' extract

The XRD patterns of the powdered silver nanoparticles taken using CuK$_\alpha$ radiation (λ= 1.5418 Å) gives major peaks at 38.09°, 44.12° and 64.37° that can be indexed to the (111), (200) and (220) planes of a cubic crystal system (a=4.0686Å) and corresponding well with the standard JCPDS file No.04-0783 of pure silver metal. Broadness in patterns reflected the small particle size of the AgNPs and spin plasmonic resonance phenomena (Figure-5).
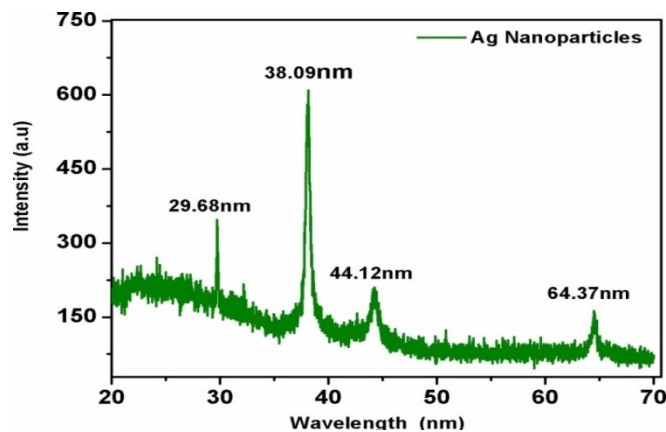
Figure-5
XRD plot of synthesized AgNPs via extract of tea leaves'

The Debye-Scherrer formula (D_p = Kλ /β1/2 cosθ with K=0-89, λ=wavelength of the radiation, β=full width at half maximum, θ = incident angle of radiation beam, D_p=particle size) was also used for calculation of the particle size i.e. ~ 20-50 nm. FTIR investigation also gives a series of peaks for the AgNPs sample belong to the sequence of the phytochemicals present in the sample that acts as a reducing agent (Figure-6). FTIR investigations on the biosynthesized AgNPs was passed out in the range of 4000-500 cm^{-1} wave number to make out the most likely interactions between the Ag ions and phytochemicals present in tea leaves' extract that used to stabilize the AgNPs. Figure-6 definite the existence of plant peptides visible due to the bending formed by amide bonds. AgNPs exhibits prominent peaks at 3379.76, 1696.45 and 1648.73 cm^{-1}, representing the contribution of N-H stretching vibrations, N-H bending vibrations and C=O stretching vibrations that refers to the Tea-AgNPs aggregates. The C-N and C-O-C stretching vibration suggested the existence of a lot of phytochemicals on the surface of the NPs.

Green production method of AgNPs is an additional way to chemical and physical synthesis methods and it is used to reduce metal ion of silver to nano silver. Green Synthesis of the silver nanoparticles has been earlier reported using plant's leaves' extracts as well as different kind of plant body parts. The phytochemicals present in the leaves' extract, which are responsible for reducing the silver salts and producing stable silver nanoparticles without using any capping agent[27]. Furthermore, the antimicrobial, antifungal and antioxidant activities of the nanoparticles are also improved by the existence of the phytochemicals.
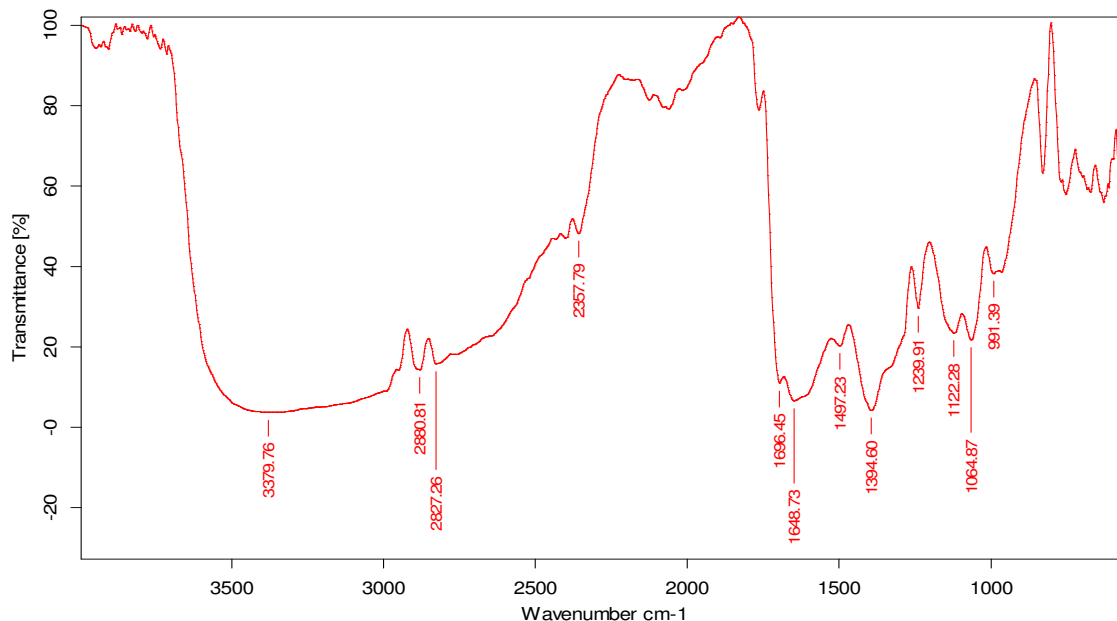
Figure-6
FTIR spectra of AgNPs synthesized by plant tea leaves' extract

Conclusion

In this current study we have planned and an ecofriendly synthesis of AgNPs using tea leaves' extracts via biological method, in which tea leaves' extract act as a reducing agent. In green synthesis method, tea leaves' extract are responsible for reduction of silver metal to nano size. The synthesized silver nanoparticles were subjected to advance analysis technique such as a TEM, XRD, Uv-Vis spectroscopy and FTIR in order to characterize them.

The formation of nanoparticles as well as size was also confirmed by UV-Vis spectroscopy; while crystalline properties of the nanoparticles and average particle size is investigated by XRD analysis and the TEM image show visibly the formation of nanoparticles. To the best of our information this is the unique information of the explanation that lead the path to produce the tea mediated AgNPs. These research works are further extended to investigate the synthesis and optical properties of AgNPs formed by the other plant leaves' extracts.

Acknowledgment

References

1. Alqudami A. and Annapoorni S. (2007). Fluorescence from metallic silver and iron nanoparticles prepared by exploding wire technique. *Plasmonics*., 2(1), 5-13.

2. Korbekandi H. and Iravani S. (2012). Silver Nanoparticles. *Nanotechnology and Nanomaterials*., 3, 5-16.

3. Brigger I., Dubernet C. and Couvreur P. (2002). Nanoparticles in cancer therapy and diagnosis. *Adv Drug Deliv Rev*., 64, 24-36.

4. Basarkar A. and Singh J. Poly. (2009). Poly (lactide-co-glycolide)-polymethacrylate nanoparticles for intramuscular delivery of plasmid encoding interleukin-10 to prevent autoimmune diabetes in mice. *Pharm Res*., 26, 72-81.

5. Roy K., Mao H.Q., Huang S.K. and Leong K.W. (1991). Oral gene delivery with chitosan-DNA nanoparticles generates immunologic protection in a murine model of peanut allergy. *Nat. Med*., 5, 387-391.

6. Wilson D.S., Dalmasso G., Wang L., Sitaraman S.V., Merlin D. and Murthy N. (2010). Orally delivered thioketal nanoparticles loaded with TNF-α–siRNA target inflammation and inhibit gene expression in the intestines. *Nat. Mater*., 9, 923-928.

7. Mano Priya M., Karunai Selvia B. and John Paul J.A. (2011). Green Synthesis of Silver Nanoparticles from the Leaf Extracts of Euphorbia Hirta and Nerium Indicum. *Digest .J. Nanomat. Biostruct*., 6(2), 869-877.

8. Li S., Shen Y., Xie A., Yu X., Qui L., Zhang L. and Zhang Q. (2007). Green synthesis of silver nanoparticles using *Capsicum annuum* L. extract. *Green Chem.*, 9, 852.

9. Christopher L., Kitchens, Douglas E., Hirt, Scott M., Husson, Alexey A. and Vertegel (2010). Synthesis, Stabilization, and Characterization of Metal Nanoparticles. The Graduate School of Clemson University.

10. Salam H.A., Rajiv P., Kamaraj M., Jagadeeswaran P., Gunalan S. and Sivaraj R. (2012). Plants: Green Route for Nanoparticle Synthesis. *Inter.Res.J.Bio. Sci.*, 1(5), 85-90.

11. Geoprincy G., Vidhyasrr B.N., Poonguzhali U., Gandhi N. and Renganathan S. (2013). A review on green synthesis of silver nano particles. *Asian.J.Pharma.Clini.res*, 6(1), 8-12.

12. Akl M. Awwad and Nida M. (2012). Green Synthesis of Silver Nanoparticles by Mulberry Leaves Extract. *Nanoscience and Nanotechnology*, 2(4), 125-128.

13. Umesh B.J. and Vishwas A.B. (2013). Green synthesis of silver nanoparticles using Artocarpus heterophyllus Lam. Leaves' extract and its antibacterial activity. *Industrial Crops and Products*, 46, 132-137.

14. Nethra Devi C., Sivakumar P. and Renganathan S. (2012). Green synthesis of silver nanoparticles using Datura metel flower extract and evaluation of their antimicrobial activity. *Inter.J. Nanomat.Biostruct*, 2(2), 16-21.

15. Song J.Y. and Kim B.S. (2009). Rapid biological synthesis of silver nanoparticles using plant leaf extracts. *Bioprocess Biosyst Eng.*, 32, 79-84.

16. Huang J., Li Q., Sun D., Lu Y., Su Y., Yang X., Wang H., Wang Y., Shao W., He N., Hong J. and Chen C. (2007). Biosynthesis of silver and gold nanoparticles by using novel sun-dried Cinnamomum camphora leaves. *Nanotechnol.*, 18, 105-104.

17. Pattanayak M. and Nayak P.L. (2013). Green Synthesis and Characterization of Zero Valent Iron Nanoparticles from the Leaf Extract of *Azadirachta indica* (*Neem*). *World Journal of Nano Science & Technology*, 2(1), 6-9.

18. Nadagouda M.N. and Varma R.S. (2008). Green synthesis of silver and palladium nanoparticles at room temperature using coffee and tea extract. *Green Chem.*, 10, 859-862.

19. Fageria P., Gangopadhyay S. and Pande S. (2014). Synthesis of ZnO/Au and ZnO/Ag nanoparticles and their photocatalytic application using UV and visible light. *RSC Adv.*, 4, 24962-24972.

20. Ahmad A., Mukherjee P., Mandal D., Senapati S., Khan M.I., Kumar R. and Sastry M. (2002). Enzyme Mediated Extracellular Synthesis of CdS Nanoparticles by the Fungus, Fusariuoxysporum. *J.Am. Chem. Soc.*, 124, 12108-12109.

21. Kalimuthu K., Babu RS., Venkataraman D., Bilal M. and Gurunathan S. (2008). Biosynthesis of silver nanocrystals by Bacillus licheniformis. *Colloids Surf B.*, 65(1), 150-153.

22. Wijnhoven S.W.P., Peijnenburg W.J.G.M., Herberts C.A., Hagens W.I., Oomen A.G. and Heugens E.H.W et al. (2009). Nano-silver: a review of available data and knowledge gaps in human and environmental risk assessment. *Nano Toxicology*, 3, 109-138.

23. Klueh U., Wagner V., Kelly S., Johnson A. and Bryers JD. (2000). Efficacy of silver-coated fabric to prevent bacterial colonization and subsequent device-based biofilm formation. *J. Biomed. Mater. Res.*, 53(6), 621-631.

24. Jani R., Udipi S.A. and Ghugre P.S. (2009). Mineral content of complementary foods. *Indian J Pediatr*, 76, 37-44.

25. Mulvaney P. (1996). Surface plasmon spectroscopy of nanosized metal particles. *Langmuir*, 12, 788-800.

26. Abu Bakar N.H.H, Ismail J. and Abu Bakar M. (2007). Synthesis and Characterization of Silver Nanoparticles in Natural Rubber. *Mater. Chem. Phys.*, 104, 276-283.

27. Meena R.K. and Chouhan N. (2015). Biosynthesis of Silver Nanoparticles from Plant (Fenugreek Leaves') Reducing Method and their Optical Properties. *Research Journal of Recent Sciences*, 4(IVC-2015), 1-5.

ZnO NANOPARTICLES SYNTHESIZED BY PRECIPITATION METHOD AND OPTICAL PROPERTIES

Rajesh Kumar Meena and Neelu Chouhan
Department of Pure & Applied Chemistry, University of Kota, Kota-324005 Rajasthan, India
E-mail: 1988rajeshmeena@gmail.com, niloochauhan@hotmail.com

ABSTRACT

The aim of this study was to achieve and characterize ZnO nanoparticles by precipitation method. $Zn(NO_3)_2$, NaOH were used as precursors for the synthesis. NaOH was dissolved in distilled water at a concentration of 1.0 M with agitation to the desired reaction temperature at 40°C. The powder was characterized by by X-ray diffraction, transmission electron microscopy, FTIR and ultraviolet-visible absorption spectroscopy. Nano ZnO particles were obtained with crystallite size between 20 and 40 nm (FESEM and XRD). The results of UV-Vis spectrometry show that highly significant antimicrobial activity against medically important Gram-positive (S.aureus) and Gram-negative (Escherichia coli) bacteria by these ZNPs. we can postulate that our fabricated ZNPs may be useful as antimicrobial agents in antiseptic creams and lotions for the treatment of skin diseases.

Iindex Terms: Nanoparticles, Precipitation method, Antimicrobial activity etc.

I. INTRODUCTION

Zinc oxide is a chemical compound found naturally in the mineral called zincite and has attracted much attention in recent times due to its low cost and because it can be obtained by simple techniques [1]. ZnO crystallizes in the characteristic wurtzite hexagonal structure where oxygen and zinc atoms are spatially arranged in a particular manner that O atoms are arranged in a closed hexagonal arrangement, while the Zn atoms interest the centre of the distorted tetrahedron configuration [2]. Moreover, it is a semiconductor material of the II-VI group with a large energy gap around Eg=3.2eV, as well as large range of excitation energy and controlled electrical conductivity [3], and when doped with transition metals exhibits the ferromagnetic phenomenon at room temperature, and because of that it has attracted greatly importance due to their potential applications in "spintronics" [4]. Nano crystalline powders – due to their average particle size below 100 nm may show different behaviours resulting from a higher surface energy due to the large surface area and the wider gap between the conduction band and valence band, effects characteristic of sizes close to the atoms. These phenomena may increase the potential use of the material, including optical, chemical, and electromagnetic among other properties. Therefore, because of its exceptional physical as well as chemical characteristics [5], the nano zinc oxide (ZnO) is an important raw material for many applications as the design of gas sensors, varistors, luminescent oxides [6], rubber, ceramics, paints and others [7]. The ZnO is unsolvable in water and ethanol but is soluble in dilute mineral acids and is a fine powder, white or slightly yellow. In large amount of quantities and high purity it is recommended for use in the pharmaceutical, food and cosmetic industries [8]. Zinc oxide is a transition metal as well as semi-metal that can react with both acids and bases providing water and salt. Because ZnO presents intermediate properties in-between acid and basic oxides it can perform as both acid and basic oxide [9]. It is an intrinsic n-type semiconductor material.

That crystallizes in the hexagonal crystal system; it is relatively economical, presents low toxicity, and is very effective in protecting against UV rays. ZnO is an excellent material for the fabrication of sunscreen, because it absorbs ultraviolet (UV) rays and combat the potential problems associated with sun exposure.

Many methods have been described in the literature for the production of ZnO nanostructures such as laser ablation [10], electrochemical depositions [11], chemical vapour deposition [12], hydrothermal methods [13] thermal decomposition [14], sol–

gel method [15], and combustion method [16,17]. Recently, ZnO nanoparticles were prepared by ultrasound [18], two-step mechanochemical-thermal synthesis [19], co-precipitation [20], anodization[21], microwave-assisted combustion method [22], and electrophoretic deposition [23]. Rodrigues-Paez et al. synthesized zinc oxide nanoparticles with different morphologies by controlling different parameters of the precipitation process such as solution concentration, pH, and washing medium etc. [24] In the present study, ZnO nanostructures were synthesized using a simple precipitation method. Zinc nitrate and sodium hydroxide were used as precursors to formulate ZnO nanostructures. The prepared samples were characterized by the purity of the sample was tested by X-ray diffraction (XRD) and scanning electron microscopy (SEM), The band gap energies of the samples were calculated from diffuse reflectance spectroscopy. The morphology, crystallite size, and optical properties of ZnO nanostructures were investigated, and an attempt was made to correlate the optical properties of ZnO with morphology and crystallite size.

II. EXPERIMENTAL PROCEDURE

A. Materials

Zinc nitrate $Zn(NO_3)_2$ and sodium hydroxide were used in the experiments. All the chemicals used were of Sigma- Aldrich and were all used without further purification and Double distilled water was used as the solvent.

B. Synthesis of ZnO Nanoparticles

To the aqueous solution of zinc nitrate $Zn(NO_3)_2$, sodium hydroxide solution was added slowly dropwise in a molar ratio of 1:2 under vigorous stirring, and the stirring was continued for 12h.The resulting solution was heated under constant stirring at the 40°C reaction temperature. The precipitate obtained was filtered and washed thoroughly with deionised water. The precipitate was dried in an oven at 100°C and ground to fine powder using agate mortar. The powder obtained from the above method was calcined at 300°C for 2h.

III. RESULTS AND DISCUSSION

Figure 1 shows XRD patterns of the ZnO nanoparticles prepared by precipitation method is shown in Figure 1, which indicates the ZnO has hexagonal wurtzite phase structure The peak and relative intensities obtained for the ZnO competition with the reported JCPDS data.[25] The x-ray diffraction information were recorded by using Cu Kα radiation (1.5406 A°). The intensity data were collected over a 2θ range of 20-80°.
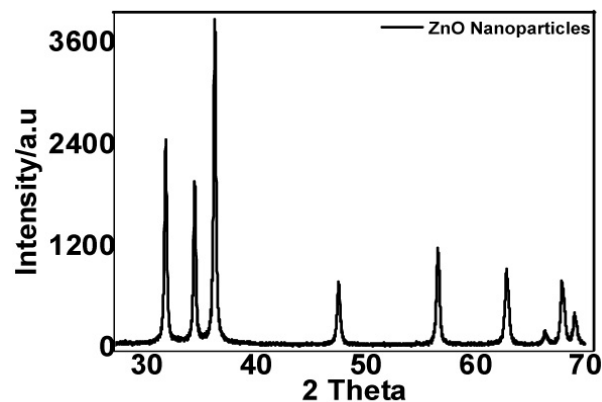

Figure 1. XRD pattern of ZnO nanoparticles

In addition, the peaks (100), (002), and (101) obviously indicate formation of pure wurtzite structure of ZnO.[26] Therefore; the XRD pattern showed that samples were formed in single phase. The high intensity of (100) peak at 31° suggested the growth of ZNPs along the easy direction of crystallization.[27] No other peaks related to impurities were detected in the XRD spectra, confirming the pure form of the synthesized ZNPs. x-ray diffraction studies confirmed that the synthesized materials were ZnO nanoparticles with wurtzite phase and all the diffraction peaks agreed. The mean grain size (D) of the particles was resolute from the XRD measurement via Scherrer equation.

$$D = 0.89\lambda / (\beta Cos\theta)$$

Where λ is the wavelength (Cu Kα), β is the full width at the half- maximum (FWHM) of the ZnO (101) line and θ is the diffraction angle. A definite line broadening of the diffraction peaks is recommended that the synthesized materials are in nanometer series and the average grain size of ZnO is determined using Scherrer equation and it was found to be around 50 nm.
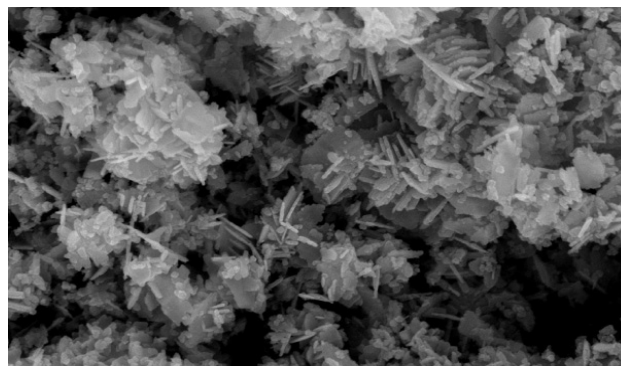

Figure 2. High resolution SEM image of the (101) plane of the wurtzite structure for the condition $Zn(NO_3)_2$, at 40°C room temperature

Figure 2 shows a high resolution SEM image – and detail at higher magnification – using zinc nitrate as a precursor with synthesis temperature of 90°C. The image shows the basal plane (101) of the wurtzite structure, which has a higher growth rate. SEM image showed relatively more uniform polyhedral nanoparticle formed with diameter range 10-50nm.
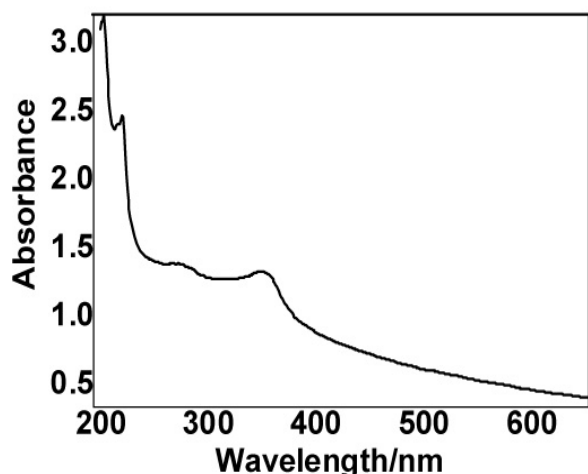

Figure 3. UV-Visible spectra of ZnO nanoparticles synthesized at 40ºC room temperature

Finally, Figure 3 shows the UV-Vis spectrum for the synthesis condition using zinc nitrate as precursor, synthesis at room temperature. It is possible to see a strong absorbance at near uv regions 300~400nm, showing that the synthesis resulted in photosensitive samples in the UV region.

IV. ANTIBACTERIAL ACTIVITY

The antibacterial property of the ZnO nanoparticles was evaluated against Gram-ve Escherichia coli and Gram +ve bacteria *S. aureus* using disk diffusion method. In disk diffusion method the ZnO nanoparticles showed significant antibacterial activity on bacterial strains Gram-ve and Gram +ve bacteria and below this Table 1 represents the comparative activities in terms of inhibition zone i.e 18 and 15, respectively. These Studies verified that the ZnO NPs show best antagonistic activity against Escherichia coli.

Table: 1 Antagonistic activity of silver nanoparticles against bacteria

Organism	Zone of inhibition (mm)
Escherichia coli	18
Staphylococcus aureus	15

V. CONCLUSION

ZnO nanoparticles with wurtzite structure were obtained from a precipitation method quickly and easily, using zinc nitrate. The results of the crystallite size calculations by the FWHM method from the XRD spectra showed that for the (101) plane the crystallite size is a function of the of precursor and the synthesis temperature. The smallest crystallite size is depends on using a precursor in the highest synthesis temperature, 40°C. Images of high resolution SEM show that zinc oxide nanoparticles were obtained with sizes close to 50 nm (300 Å) for the basal plane (101).

VI. REFERENCES

[1] Koudelka, L.; Horak, J.; Jariabka, P. Morphology of polycrystalline ZnO and its physical properties. Journal Materials Science, v.29, n.6, p.1497-1500, (2004).

[2] Martins, J.B.L.; Sambrano, J.R.; Vasconcellos, L.A.S.; Longo, E.; Taft, C.A. Análise teórica da interação de CO, CO2 e NH3 com ZnO. Química Nova, v.27, n.1, p.10-16, (2004).

[3] Look, D.C.; Reynolds, D.C.; Jones, R.L.; Litton, C.W.; Cantwell, G.; Eason, D.B. Characterization of homoepitaxial p-type ZnO grown by molecular beam epitaxy. Applied Physics Letters, v.81, n.10, p.1830-1832, (2002).

[4] Prellier, W.; Fouchet, A.; Mercey, B. Oxide-diluted magnetic semiconductors: A review of the experimental status. Journal of Physics Condensed Matter, v.15, R1583, (2003).

[5] Kwon, Y.J.; Kim, H.K.; Lim, C.S.; Shim, K.B. Characterization of ZnO nanopowders synthesized by the polymerized complex method via an organochemical route. Journal of Ceramic Processing Research, v.3, n.3, p.146-149, (2002).

[6] Ravi, V.; Pasricha, R.; Dhage, S.R. Synthesis of fine particles of ZnO at 100°C. Materials Letters, v.59, p.779-781, (2004).

[7] Perez-lopes, O.W.; Faria, A.C.; Marcilio, N.R.; Bueno, J.M.C. The catalytic behaviour of zinc oxide prepared from various precursors and by different methods. Materials Reserch Bulletin, (2005).

[8] Ramalho, M.A.F. Avaliação da proporção de ácido cítrico/metal no tamanho da partícula de ZnO preparados pelo método de Pechini. In: Congresso Brasileiro de Ciência e Engenharia de Materiais, (2004).

[9] Horak, J.; Kouldelka, L. J Mater Sci., v.29, p.1497, (1994).

[10] carisoreanu, N, Metai, DG, Dinescu, G, Epurescu, G, Ghica, C, Nistor, LC, Dinescu, M: Properties of ZnO thin films prepared by radio-frequency plasma beam

assisted laser ablation. Appl. Surf. Sci. 247, 518–525 (2005)

[11] Chang, S, Yoon, SO, Park, HJ, Sakai, A: Luminescence properties of Zn nanowires prepared by electrochemical etching. Mater. Lett. 53, 432–436 (2002)

[12] Wu, JJ, Liu, SC: Low-temperature growth of well-aligned ZnO nanorods by chemical vapor deposition. Adv. Mater. 14, 215–218 (2002)

[13] Ni, YH, Wei, XW, Hong, JM, Ye, Y: Hydrothermal synthesis and optical properties of ZnO nanorods. Mater. Sci. Eng., B, Solid State Mater. Adv. Technol 121, 42–47 (2005)

[14] Wang, RC, Tsai, CC: Efficient synthesis of ZnO nanoparticles, nanowalls, and nanowires by thermal decomposition of zinc acetate at a low temperature. Appl. Phys. A. 94, 241–245 (2009)

[15] Ristiac, M, Musiac, S, Ivanda, M, Popoviac, S: Sol–gel synthesis and characterization of nanocrystalline ZnO powders. J. Alloys Compd. 397, L1–L4 (2005)

[16] Badhuri, S, Badhuri, SB: Enhanced low temperature toughness of Al2O3-ZrO2 nano/nano composites. Nanostrct. Mater. 8, 755–763 (1997)

[17] Lamas, DG, Lascalea, GE, Walsoc, NE: Synthesis and characterization of nanocrystalline powders for partially stabilized zirconia ceramics. J. Eur. Ceram. Soc. 18, 1217–1221 (1998)

[18] Khorsand, Z, Abid, A, Majid, WH, Wang, HZ, Yousefi, R, Golsheikh, M, Ren, ZF: Sonochemical synthesis of hierarchical ZnO nanostructures. Ultrasonic Sonochemistry 20, 395–400 (2013)

[19] Rajesh, D, Vara Lakshmi, B, Sunandana, CS: Two-step synthesis and characterization of ZnO nanoparticles. Physica B-Cond. Mater. 407, 4537–4539 (2012)

[20] Singh, O, Kohli, N, Singh, RC: Precursor controlled morphology of zinc oxide and its sensing behavior. Sens. Actuators B. 178, 149–154 (2013)

[21] Shetty, A, Nanda, K: Synthesis of zinc oxide porous structures by anodisation with water as an electrolyte. Appl. Phys. A. 109, 151–157 (2012)

[22] Kooti, M, Nagdhi Sedish, A: Microwave-assisted combustion synthesis of ZnO nanoparticles. J. Chem (2013).

[23] Vazquez, A, Lopez, IA, Gomez, I: Growth mechanism of one-dimensional zinc sulfide nanostructures through electrophoretic deposition. J. Mater. Sci 48, 2701–2704 (2013)

[24]. Rodrigues-Paez, J, Caballero, AC, Villegas, M, Moure, C, Duran, P, Fernandz, JF: Controlled precipitation methods: formation mechanism of ZnO nanoparticles. J. Eur. Ceram. Soc. 21, 925–930 (2001)

[25] JCPDS Card No. 36-1451

[26] Rekha K, Nirmala M, Nair MG, Anukaliani A. Structural, optical, photocatalytic and antibacterial activity of zinc oxide and manganese doped zinc oxide nanoparticles. Physica B Condens Matter;405(15):3180–3185 (2005)

[27] Lin HF, Liao SC, Hung SW. The dc thermal plasma synthesis of ZnO nanoparticles for visible-light photocatalyst. J Photochem Photobiol A Chem.;174(1):82–87 (2005).

CrossMark
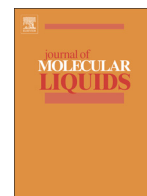
Biogenic silver nanoparticles from *Trachyspermum ammi* (*Ajwain*) seeds extract for catalytic reduction of *p*-nitrophenol to *p*-aminophenol in excess of NaBH₄

Neelu Chouhan [a,*], Rakshit Ameta [b], Rajesh Kumar Meena [a]

[a] *Department of Pure and Applied Chemistry, University of Kota, Kota 324005, India*
[b] *Department of Chemistry, PAHER University, Udaipur 313003, India*

A B S T R A C T

Plasmonic silver nanoparticles (AgNPs, size = 3–50 nm) were synthesized by biogenic reduction of aqueous AgNO₃ using *Trachyspermum ammi* (TA, *Ajwain*) seeds extract. Increase in concentration of TA, accelerated the reduction rate of Ag^+ and affected the AgNPs particle size. Pronounce effect of the AgNP's aging (24, 48 and 72 h) on particle concentration/size and their corresponding catalytic activity, was exhibited by the systems. Surface plasmonic resonance band centered between 420 and 430 nm wavelength, recognized as first exitonic peak of UV–vis absorption spectra of Ag NPs, was used to estimate the particle size (10–30 nm) of Ag NPs, which was consistent with the particle size observed with the FESEM (5–20 nm) and XRD observations (12.74 nm). XRD analysis also indicated that the silver nanoparticles were crystallized in the cubic crystal pattern. However, some cubic/rod like patterns grown along the 111 plane, was also observed by FESEM and HRTEM. ATR (Attenuated total reflectance) profile of aging of TA supported Ag NPs, exhibited the decrease in intensity of 3394, 1716 and 1618 cm⁻¹ peaks with respect to the pristine TA extract sample. That reflects the increase in particle concentration with time (24–48 h). These peaks correspond to the O—H group, carbonyl group and C =C stretching along with C—O—C and C—N stretching in TA-AgNPs aggregates. ATR and IR results suggested the presence of the reducing agent/phytochemicals (nicotinic acid, thymol, sugars, proteins, saponin, etc) incorporated NPs. Impedance study revealed that the rate of charge transfer in TA-Ag NPs aggregates is inversely proportional to the concentration of TA that confirms the stability of the Ag NPs in water. These biogenic Ag NPs are also characterized using transmission electron microscopy (TEM) and their corresponding energy dispersive X-ray analysis (EDX), electrochemical impedance spectroscopy (EIS), cyclic voltammetry (CV) studies, etc. On the basis of the above observations and optoelectronic characteristics, the most probable mechanism of biogenesis of the stable Ag NPs, is suggested. As-synthesized 24, 48 and 72 h aged Ag NPs, were tested for their catalytic reduction activity towards the conversion of *p*-nitro phenol to *p*-aminophenol in excess of NaBH₄. 48 h-aged Ag NPs show highest catalytic activity for conversion of *p*-nitrophenol to *p*-aminophenol in excess of NaBH₄ in terms of rate (r = 0.34539 min⁻¹) with complete reduction time 12 min.

1. Introduction

Recently, metal nanoparticles have attracted immense attention of researchers over their bulk counterparts due to their versatile applicability in different areas [1–4]. These are magnetic, electronic, electrochemical, antimicrobial, corrosion, inhibition and optical performances. Because of their unmatched superb qualities, they can affect human life in various avatars such as biosensors, nano-molecular optoelectronic devices, bio-mimetic materials, catalysts in biomedicine, industrial and environmental fields. There are two most well-liked approaches for fabrication of nanoparticles. First is bottom to top or small to big approach, where the NPs gain the final shape by addition of small building blocks and prepared using supercritical liquid medium, templates, spinning, plasma or fire sparing, pyrolysis, sol-gel process, biological method, chemical vapour deposition, atomic condensation, etc. The second approach is top to bottom approach, which involves mechanical milling, electrochemical explosion, laser ablation, chemical etching, etc. Where, bigger particle cut down into small particles of different shapes. Morphology (shape and size) of the nanoparticles' is very important for deciding their optical, electronic, magnetic, and catalytic properties. These novel properties can be engineered by controlling the dimensions of metal nanoparticles. Beside

 * Corresponding author.
   E-mail addresses: niloochauhan@hotmail.com, neeluchouhan@uok.ac.in
(N. Chouhan).

the conventional practices of synthesizing metallic nanoparticles i.e. physical and chemical methods, the biogenic production is a better option due to its ease of fabrication via green route with non-toxic and non-poisonous ingredients, biocompatibility, mild reaction conditions, low cost, simplicity and eco-friendly nature of reaction, are the benefits of the biogenic synthesis. Therefore, this can be used as an economic and valuable alternative for the large scale production of metal nanoparticles. Biological materials/tools adopted in this method are fungi [5–7], bacteria [8–10], Bengal gram bean [11], yeasts [12], *Capsicum annuum* [13], quercetin [14], biomass of oat (*Avena sativa*) and wheat (*Triticum aestivum*) [15], honey [16], plants' extract, etc.

A wide range of metal NPs such as Au [17–21], Ag [22–23], TiO_2 [24], In_2O_3 [25], ZnO [26], CuO [27], etc, have been synthesized using herbal/ plant extracts. Several plants have been explored for the synthesis of metal NPs including medicinal plants [26]. Use of plant extract and microbial cells in the synthesis of metal NPs, was triggered by existence of the several organic group/compounds such as carbonyl groups, terpenoids, phenolics, flavonones, amines, amides, proteins, pigments alkaloids and other reducing agents of the plant extract. In this research work, an aqueous seed extract of *Trachyspermum ammi* (TA; *Ajwain*) has been used to grow the metal (silver) nanoparticles. This plant is the native of Egypt and cultivated in Iran, Iraq, Afghanistan, Pakistan and India. TA has a great medicinal and nutrition values because its seed extract consists of carbohydrates (—CHO, —OH), glucosides (6-O-β-glucopyranosyl oxythymol), oleoresin, saponin, phenols, volatiles (thymol, γ-terpinmene, para-cymene, α- and β-pinene, dipentene), proteins, fat, fibres, and minerals (P, Fe, Ca, etc). Furthermore, prominent principle oils such as, carvone (46%), dillapiole (9%) and limonene (38%) along with reducing agents (nicotinic acid), are also present in TA. Therefore, due to the presence of these biochemical ingredients, TA can be served as the reducing and capping agent without addition of any external stabilizing agent, during the synthesis process of NPs.

Silver has long been famous for its good inhibitory effect towards many bacterial strains/microorganisms and catalytic activity. Therefore, commonly used in medical and industrial products that directly come in to the contact with the human body, such as shampoos, soaps, detergent, shoes, cosmetic products, and toothpaste, besides photocatalytic and pharmaceutical applications. Moreover, superiority of the nanosilver particles over other candidates of the same class is already established in terms of the small losses in optical frequency during the surface-plasmon propagation, high conductivity and stability at ambient conditions, less costlier price than other noble metals such as gold and platinum, high primitive character, and wide range of visible light absorption, etc. Which, prompt us to select silver as a plasmonic material for this study. Tiny nano-particles of the noble metals with localised spin plasmonic resonance (LSPR) are known as plasmonic material. Free electrons integrated with the photon energy produces a LSPR [28–32] on exposing nano-particles of noble metals to sunlight. Therefore, NPs of the noble metals will be act as the active centres on catalyst for the thermal redox reaction that can trap, scatter, and concentrate light [33–35], due to the fast charge transfer and result in enhanced activities.

Pure Ag NPs, as well as some chemically modified Ag NPs has also been in trend that to be used in various applications such as: cleaning water, catalyst, sensor, optoelectronic properties, eradication of organic pollutants, etc. Out of which removal of organic pollutants (nitrophenols) from waste water is very important. 4-Nitrophenol (PNP) is a highly stable and low water-soluble chemical that used to be found in waste water that produced by explosive- and dye-industries. Environmental Protection Agency of United States rated nitrophenols highly polluted chemical among the top 114 organic pollutants. It adversely affects the human and animal organs like liver, kidney, blood and central nervous system, skin, etc [36]. Moreover, the degradation of PNP to nondangerous product is difficult due to its high stability. Therefore, the study for catalytic reduction of hazardous PNP to benign 4-aminophenol (PAP) becomes a remarkable step in terms of nitrophenol-pollution mitigation [37]. PAP is very fascinating

chemical as it can be used in production of analgesic and antipyretic drugs, photographic developer, corrosion inhibitor, anti-corrosion lubricant, and many more applications. It can be produced by reduction of PNP to PAP in sodium borohydride at room temperature. Aforementioned reaction is a thermodynamically feasible process as it involves E^0 for PNP/PAP $= -0.76$ V and $H_3BO_3/BH_4^- = -1.33$ V versus NHE. But this reaction is kinetically restricted by nature and never produce PAP as end product but generate an intermediate i.e. *p*-nitrophenolate ion in absence of the catalyst. Metal NPs or modified metal NPs, were used to catalyse the above reaction. Few prominent e example, Ag NPs-decorated Polyaniline nanofibers (AgNPs/PANINFs) nanocomposites [38], SiO_2-coated graphene oxide nanosheets, decorated with Ag nanoparticles [39], Pd/CuO NPs [40], synthesized by using of *Theobroma cacao* L. seed extract, etc, were used for catalytic reduction of PNP into PAP in presence of excess of $NaBH_4$. The metal NPs can serve as catalysts to transfer electrons from ion to the PNP. Both absorbed on the catalyst surface and result in the production of PAP.

Hence, this study is devoted to the fabrication of the Ag NPs by biogenic reduction method using aqueous TA seed extract at ambient condition. Consequently, as-synthesized Ag NPs were rigorously investigated using advance techniques i.e. XRD (X-ray diffraction), UV–vis spectrophotometry, FTIR and ATR spectroscopy, scanning electron microscopy (SEM) and their corresponding energy dispersive X-ray analysis (EDX), transmission electron microscopy (TEM), high resolution transmission electron microscopy (HRTEM), photoluminescence emission (PLE), cyclic voltammetry and electrochemical impedance spectroscopy (EIS), etc. Finally, the biogenic Ag NPs were used to reduce *p*-nitrophenol to *p*-aminophenol in excess of $NaBH_4$ and reaction mechanism for this reaction is also suggested. Effect of aging/particle size on catalytic activity and rate of reaction will also be discussed.

2. Results and discussion

2.1. Crystallography of Ag NPs

The powder XRD patterns of the Ag NPs exhibited the major diffraction peaks at 37.554°, 43.751° 64.021° and 76.949° (Fig. 1).

One sharp and strong peak at 37.554°, followed by the other small peaks can be index by (111), (200), (220) and (311) planes of a cubic crystal system (a = 4.0686 Å) that matched well with the standard JCPDS card No. 04-0783 of pure silver. These results attributed to the orientation of the crystal growth along the 111 plane. Peak broadening noticed in XRD data of the silver nanoparticles was dedicated to the small particle size and spin plasmonic resonance phenomena. No bogus Bragg reflections were observed in the pattern due to crystallographic impurities in the sample, which reflected the presence of the 100% pure silver metal in the sample [41]. Ag NPs was crystallized in face centered cubic symmetry of the space group Fm-3m (Space group number: 225) and point group m3m. Debye Scherrer equation
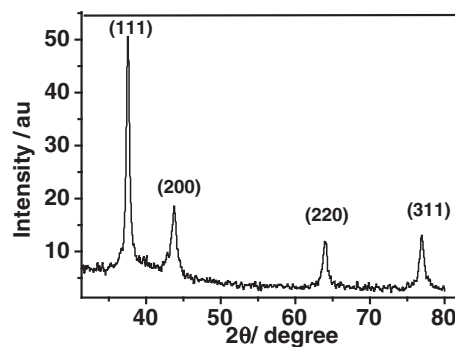

Fig. 1. XRD pattern of biogenic TA supported Ag NPs with reference to the standard JCPDS file No. 04-0783 of pure Ag.

corresponding to the XRD profile (Fig. 1) was used to calculate the particle size of the NPs, i.e. 12.74 nm, by utilizing following relationship (Eq. (1)).

$$B_r \mathrm{Cos}\theta = \frac{k\lambda}{L} \qquad\qquad (1)$$

where, θ = half of the diffraction angle, λ = wavelength of the incident X-ray beam, L = average crystallite size ($\perp$ *to surface* of specimen), k (constant) = 0.94 [$k \in$ (0.89, 1.39)] and B_r = full width at half maximum.

FESEM and TEM images along with the corresponding EDX profile exhibited by Fig. 2a, b and c, which reveal the information about the surface morphology, particle shape/size and elemental composition of the synthesized Ag NPs. Flocculated surface visualised by the FESEM and TEM images, indicates a uniformly dispersed colloidal silver NPs in sample. Fig. 2c corresponds to the EDXS profile of the Ag NPs, collected at 3.2 KeV and used to exhibit the chemical composition of the silver NPs i.e. 100% pure Ag without any foreign contaminants. On minute observation of the TEM micrographs, it was found that the Ag NPs crystallized in two shapes i.e. features in the form of the dark cubes of size 5–20 nm (inset of Fig. 2a) and transparent gray elongated cylinderical particles of size 0.480 × 2 μm (inset of Fig. 2c). Where, the dark cubic structures dominated over the rod shape structures. These features are result of the interaction between some of the interesting biochemicals present in aqueous TA extract and AgNO₃. One of the chief bio-constituent of TA is the surfactant; saponin (present as 38% limonene with cmc = 0.5–0.8 g/L) [42], which induces micellization process and captivate silver ions through hydrophobic force, resulting into reduction in entropy. When the concentration of surfactant is higher than CMC, entropy penalty for Ag ions assembly formation is lesser than the entropy penalty for caging of Ag ions by surfactant into water. That causes the electrostatic interaction between surfactant and Ag ions that leads to elongated structures. Hydrophobic group of the surfactant sequestrated into the centre, which solubilised in bulk Ag ions by the virtue of head's group interaction with solvent and hydrophilic part extended away from the centre. Moreover, position strongly affects the micellisation process by reducing its surface and interfacial tension [43]. The carboxylic group belongs to saponin (responsible for stabilizing the silver nanoparticles) fasten to the hydrophobic aglycone part of the molecule, which dissociates slowly. It leads to grow molecular self assembling of surfactant around Ag NPs in a one dimensional way and induce the formation of the elongated filamentous nanoclusters.

The extract also contains the carboxylic/phenolic group attached to the different moieties i.e. nicotinic acid, thymol, sugars, proteins, etc. that also highly influence the surface activity, foam ability, and emulsifying ability of the surfactant. These carboxylic/phenolic groups dissociate into aqueous phase and form free carboxyl/phenoxide anions, which increase the solubility of molecule in water and promote the formation of cubical Ag NPs.

Fig. 3a and b, represents the HRTEM images and corresponding SAED pattern of the as synthesized AgNPs. Fig. 3a exhibits a high resolution TEM image featuring lattice fringes associated with a d-spacing of 0.2286 nm, consistent with the growth planes 111. The SAED pattern in Fig. 3b exhibits polycrystalline diffraction rings consistent with 111, 200, 220, 311 and 222 cubic reflections.

2.2. Optical characterization

Presence of the Ag NPs, grown at different concentrations of TA and growth time, was successfully examined using UV-vis absorption spectrum (Fig. 3a and b). UV spectra shown in Fig. 3c, revealed the production of AgNPs in TA extract (Red line), where TA extract in absence of AgNO₃ didn't exhibit any peak in region 350–550 nm (Black line). Silver NPs exhibited an intense, small and broad absorption peak due to the surface plasmon (it describes the collective excitation of the conduction electrons in a metal) excitation [44].

All of the absorption spectra possess two prominent peak maximas; first at 200 nm and second around 420–450 nm. Strong peak around 200 nm, usually caused by the general transition of electrons between the valence and conduction bands of Ag NPs. Second, broad but short peak found within the range of excitonic transitions between 415 and 460 nm, depending on TA extract concentration, structural, and aging conditions [45–47]. Fig. 4a confirmed the formation of the Ag NPs at different concentrations (0.5, 1.0, 1.5, 2.0 and 2.5% (w/v)) of TA at fixed AgNO₃ concentration i.e. 0.001 M AgNO₃ and 1 h aging. The increase in intensity of the first excitonic peak at 446, 445, 446, 452, and 452 nm along with the broadness of the peak on raising the TA concentration, was observed. Furthermore, 2.0 and 2.5% TA concentrated samples has shown the same pattern and peak maxima (452 nm) (Fig. 4a). Therefore, 2.0% TA samples were taken for optimisation through aging. The effect of aging on Ag NPs grown in 2.0% of TA was explored by varying the growth time (24 h, 36 h and 48 h); on peak position viz. 448, 446 and 446 nm as shown in Fig. 4b [48]. The height of the first excitation peak for 24 h and 36 h aged samples are similar but rise in the peak height with 48 h aged sample confirmed the increase in concentration of Ag NPs. Blue shift in peaks on aging, indicated a decrease in size of the Ag NPs. UV spectrum for 2.0% TA sample aged at 48 h and pure TA extract is demonstrated in Fig. 4c. The presence of broad first excitonic peak between 333.7 and 650 nm (3.72–1.98 eV) at peak maxima at $\lambda_{\max}$ = 446 nm (2.78 eV), confirms the formation of Ag NPs. Broadening to the optical absorption spectrum of Ag NPs, was originated by SPR absorption. The surface plasmon resonance (SPR) is the coherent excitation of all the 'free' electrons within the conduction band. Because the SPR prohibits to give rise to the intensity of the absorption peak for very small Ag NP clusters. Hence, the short and broad peaks were
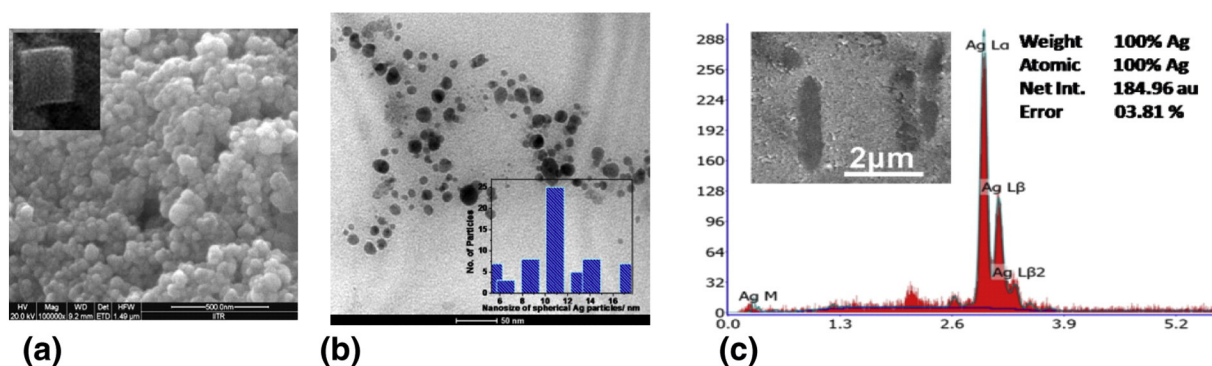

Fig. 2. (a) FESEM images of silver nanoparticles, (b) TEM image and particle size distribution of Ag NPs and (c) corresponding EDX profile. Inset images (in a and c) are the magnified TEM images of square and elongated Ag NPs.
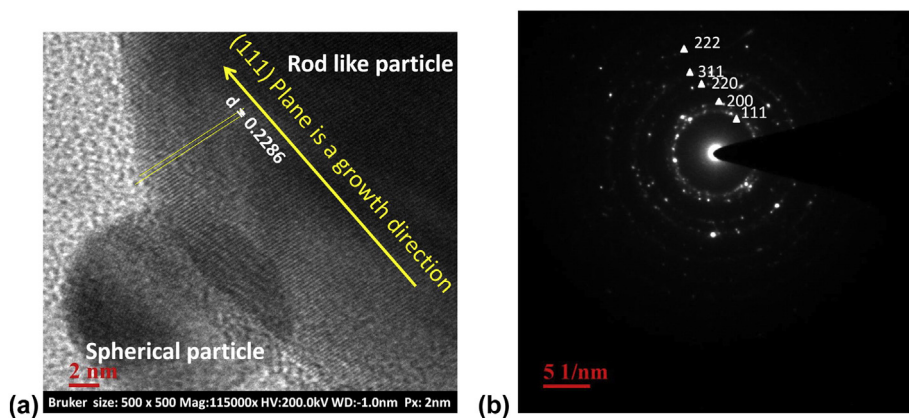
Fig. 3. HRTEM image of a 12.78 nm spherical and rod like structure that featuring d-spacing for the 111 plane and cross-grating patterns (SAED pattern) consistent with the cubic structure for biogenic Ag NPs.

observed. Such absorption spectra can be explained by Mie theory [49]. Mie theory describes the scattering of light (in various directions with varying efficiency) by small particles (an aggregation of material) that constitutes a region with refractive index, different from the refractive index of its surroundings.

2.3. IR spectroscopic investigation

Fig. 5 demonstrates the ATR (Attenuated total reflectance) spectrum of TA-stabilised Ag NPs that was used to study the effect of aging on bonding environment of the Ag NPs in presence of the phytochemicals that belongs to TA. Respective IR peaks of N—H or O—H and υ C $=$ O groups, were observed at different aging period i.e. 24 h (3315.74 & 1637.36 cm^{-1}), 36 h (3314.32 & 1635.59 cm^{-1}) and 48 h (3313.64 & 1635.69 cm^{-1}). Gradual shifting of peaks towards low wave number was observed for the TA and AgNO$_3$ mixture with aging, signifies the increase in bulkiness (heavier the molecule, lesser the frequency or wave number) of the molecular self assembly of TA due to the formation of the cluster of Ag NPs. It was also justified by the FTIR study, which was carried out (Fig. 6) on the biosynthesized Ag NPs and pure TA in the range of the wave number 4000–500 cm^{-1}. This technique is also used to recognize the most probable interactions between the Ag ions and phytochemicals present in TA with time and the role of the chemical constituents of TA in stabilization of Ag NPs. Pure 2.5% TA gave peaks at the wave number of 3918.14, 3876.04, 3832.59, 3770.15, 3308.45, 2926.98, 2368.65, 2331.20, 2237.03, 2132.62, 1652.2, 1453.87, 1245.57, 1085.17, 806, 693.40 and 604.85 cm^{-1}.

2.5% TA stabilised AgNPs exhibits prominent peaks at the wave number 3926.55 (w), 3760.21 (w), 3723.95 (s), 3664.86 (s), 3497.01 (w), 3428.69 (w), 3060.18 (b), 2876.84 (w), 2762.44 (vw), 2350.23 (vw),

1695.78 (s), 1539.02 (w), 1366.14 (vw,b), 1236.47 (w), 1115.45 (s), 1047.55 (w), 972.57 (s), 861.14 (s), 713.30 (b,s), 676.98 (b,s) and 587.36 (vs) cm^{-1}. The respective functional groups of these peaks along their most probable biomolecular species are shown in Table 1. Similar to the ATR results, the shifting of the IR peaks towards the lower frequencies was observed due to the formation of the TA stabilised-Ag NPs. Characteristic broad band at 3308.45 cm^{-1}, represents the presence of the intermolecular hydrogen bonding in pure TA. Where, the sharp and well defined peaks at 3723.95 s and 3664.86 s in TA stabilised Ag NPs, are attributed to the intra-molecular hydrogen bond [50]. Absorption peak at 3428.69 cm^{-1} belongs to the OH stretching of alcohols and phenolic groups in TA stabilised Ag NPs. The frequencies due to stretching modes of CH$_2$ group are generally found in the region of 3000–2800 cm^{-1}. The IR bands at 3060.18, 2876.84 and 1366.14 (vw,b) cm^{-1} may be associate with the asymmetric and symmetric stretching/wagging vibrations of CH$_2$ group, respectively.

Distinctive peak at 3060.18 cm^{-1}, was attributed to the polysubstituted benzenes and aromatic CH$_2$ stretching vibrations [51, 52]. Sharp absorption band at 1695.78 cm^{-1} suggested the presence of amide group [53], due to the carbonyl stretch of the proteins that strongly adsorbed the metal nanoparticles. TA supported Ag NPs exhibits the strong bands at 972.57 and 861.14 cm^{-1}, identified as twisting and rocking modes of CH$_2$ bending. The secondary structures of proteins were not affected during the reaction with Ag$^+$ ions or after binding with Ag nanoparticles [54]. These IR spectroscopic studies confirmed the presence of the amino acid that develop the strong binding, reducing and stabilizing ability with metal through carbonyl group. Thus, it is concluded that a layer of the bio-organics have formed on AgNPs to secure the nanoparticles. This layer acts as a capping agent
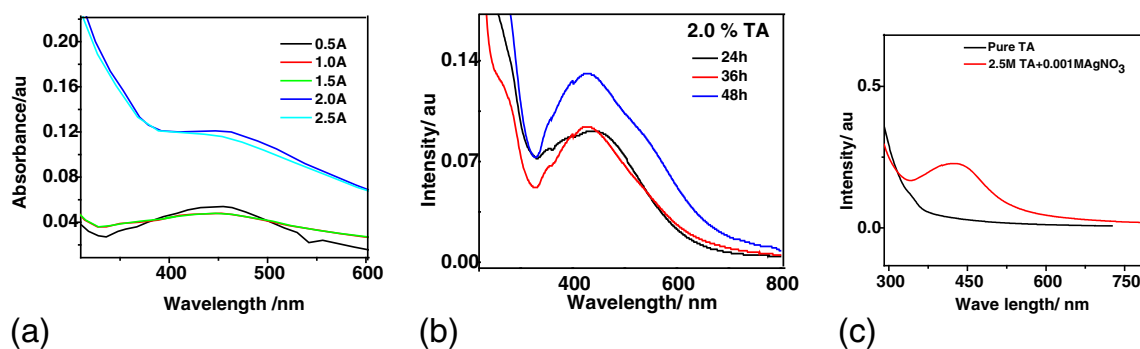
Fig. 4. UV–vis diffuse reflectance spectra of the (a) as-prepared Ag NPs at different concentrations of TA i.e. 0.5, 1.0, 1.5, 2.0 and 2.5%, (b) TA supported Ag NPs on aged at different time i.e. 24 h, 36 h, and 48 h and (c) comparative spectra of 2.5 M Pure TA (Black solid line) and Ag NPs synthesized by mixing of 2.5 M TA and 0.001 M AgNO$_3$ (Red solid line). (For interpretation of the references to colour in this figure legend, the reader is referred to the web version of this article.)
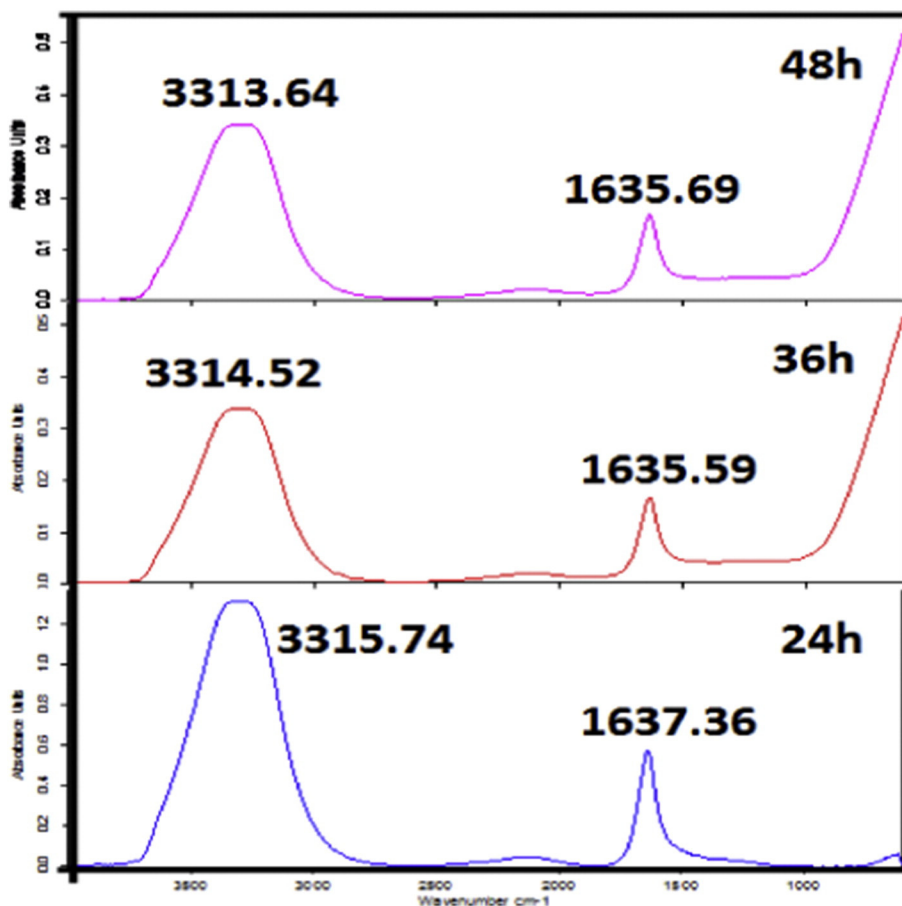
Fig. 5. ATR spectra of 2.5% TA supported Ag NPs with aging of 24 h, 36 h and 48 h.

to prevent agglomeration and provides the extra stability in aqueous medium [55]. The spectra also show peaks at 1321 and 1580 cm^{-1}, attributed to ν-C—N and δ-NH$_2$, respectively [56]. The position and relative intensity of these bands change with respect to the pure amine (2083, 1514 cm^{-1}) [57,58]. The variation in the —NH$_2$ and —NH infrared bands suggests the links between the nanoparticles. The bands at 1120 and 1480 cm^{-1} are typical of the ν-C—OC, δs-CH$_2$ and δa-CH$_3$ vibrations, respectively [59]. The aromatic C—H out-of-plane deformations were observed in the range 720–1000 cm^{-1}. The out-of-plane and in-plane deformation of the phenyl ring are observed below 1000 cm^{-1} and these modes are not pure but contain a significant

contribution from other modes and are substituent sensitive also, the spectral positions of the weaker γ-CH near 900 cm^{-1} correlates well with electron donating or electron attracting properties of the substituent. The CH in-plane deformations (δ-CH) were obtained at 972.57 s and 1047.55 cm^{-1} in the IR spectrum. Aromatic nitro compounds show a C—N stretching vibration near 870 cm^{-1}. In the present study, the ν-CN is available at 861.14 cm^{-1} in the IR spectrum. The vibration modes of the various functional groups are variant with respect to the formation of the complex and to the adsorption at the nanoparticles surface. It is suggested that the alkyl chains adopted the stretched conformation irrespective of the complex formation. Stretching also confirms
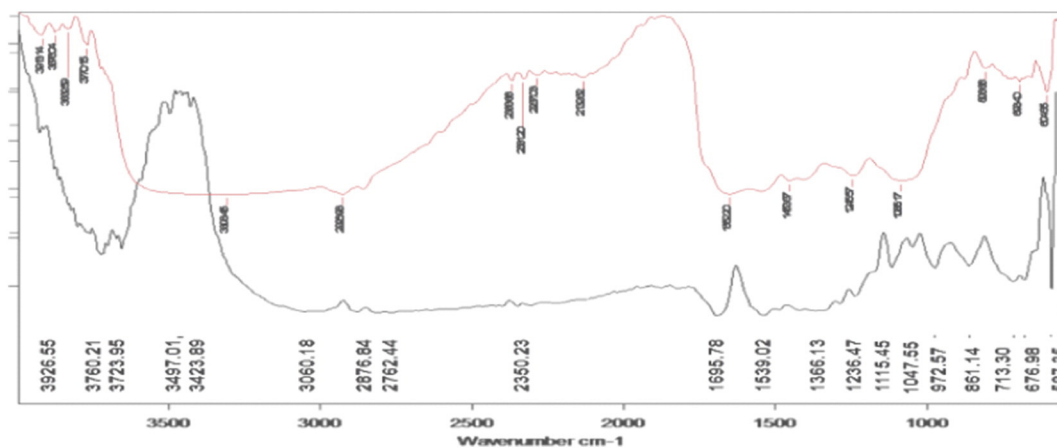

Fig. 6. FTIR spectrum of the 2.5% pure TA (Red solid line) extract and Ag NPs stabilised in 2.5% TA (Black solid line). (For interpretation of the references to colour in this figure legend, the reader is referred to the web version of this article.)

Table 1
Representative functional groups and their corresponding biomolecules with respect to the FTIR peak positions (in wave number) for the 2.5% TA stabilised AgNPs.

Wavenumber (cm^{-1})	Functional groups	Associated biomolecules
587.35	CCC out of plane bending P—O bending	PO$_4^{3-}$
676.98	C—S str. O—Ag—O str.	Thiol, sulfide
713.30	N—H bonded, secondary amide	Carvone
861.14	C—O str.	Epoxide
972.57	C—H out of the plane bend	Trans RHC=CHR', fat oil
1047.55	Alkane, C—O str. P—O str.	Lipids, saponin
1115.45	C—O, C—N, C—C str.	Lipid, amino acid sugars
1236.47	C=S str.	(RO)$_2$C=S, thioketone
1366.13	S=O str., ν-C—N	(RO)$_2$SO$_2$, sulfuric ester, nicotinic acid
1539.02	C=N (plus C =C), δ-NH$_2$ str. Aromatic ring str.	Aromatic ring, pyrimidines, thymol
1695.78	Primary amide, carboxylate C—O stretch, conjugated ketones H O—H bending HO—H	Proteins, thymol, nicotinic acid, p-cymene
2350.23	NH$_2^+$, NH$^+$ str.	Nicotinic acid
2762.44	C—H str., —C(=O)H, aldehyde	Carbohydrates
2876.84	—CH$_2$— stretch (s), C—H str. methine	Aliphatic methylene group, limonene
3060.18	Alkane, aromatic C—H stretch	Lipids, saponin, polystyrene
3428.69	Asym. N—H str., carboxylate C—O sym. and asym. str. Bonded/non-bonded OH group	Alcohols and phenols, thymol, nicotinic acid
3497.01	Intra- or inter-molecular bonded OH	Saponin
3664.86	Free OH, primary NH amines asymmetric	Amino acids
3723.95	Free OH	Saponin
3760.21	Free OH	Saponin
3926.55	C—H stretch of aromatic combination	All aromatic rings

the interband and intraband transitions between electronic states of silver. IR study prove the presence of two kinds of chemicals in TA extract: one the reducing agent (nicotinic acid, polyphenols) that convert Ag$^+$ ions into Ag nanoparticles and second the capping agents/surfactant (carvone, thymols, sugars, proteins, lipids, saponin, etc), which can act as an scaffold for controlling size and shape of these nanoparticles, as it was mentioned in SEM/TEM/HRTEM study segment of this paper.

2.4. Visible photoluminescence

Fig. 7 illustrated the excitation and emission spectra of biogenic silver nanoparticles that synthesized at 48 h aging AgNPs in 2.0% TA. Excitation spectra of the as-prepared Ag NPs was obtained at λ_{ex} = 289 nm
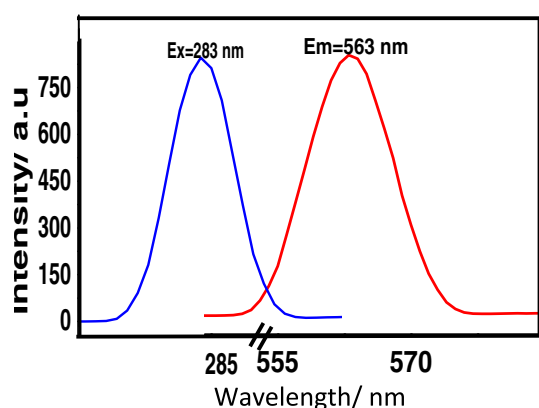
Fig. 7. Photoluminescence (PL) excitation spectra (blue) of the as prepared Ag NPs under emission wavelength 565 nm and PLE spectrum (red) at λ_{em} = 563 nm under the excitation radiation of λ_{ex} = 285 nm. (For interpretation of the references to colour in this figure legend, the reader is referred to the web version of this article.)

under the emission radiation of 565 nm and sharp PL emission spectrum of green light at λ_{em} = 563 nm was found under the excitation of λ_{ex} = 285 nm. Excitation of electrons from the occupied d-bands into the states above the Fermi level and successive relaxation of electrons from an occupied sp-band to the holes takes place by the electron-phonon scattering process directed an energy loss, which is responsible for the visible light luminescence of the Ag nanoparticles [60]. The optical properties of the silver nanoparticles depend on both; interband and intraband transitions between electronic states. FESEM and TEM results indicate that the smaller non-metallic clusters coexist with large metallic nanoparticles. Here, only small metallic particles (cubic crystals) contribute to luminescence because large metal particle didn't exhibit luminescence due to rapid radiation less process that is hard to compete with effective radioactive process [61].

2.5. Cyclic potentiometeric study

Cyclic voltammetric study has proved to be a successful tool for monitoring the progress of the reaction and reduction mechanism of the Ag$^+$ ions, using the partial cathodic and anodic reactions proceeding at electrodes. Graphical representation of the cathodic and anodic peak currents vs applied potential (V), was observed for the reaction mixture of pure 2.0% TA extract and 2.0% TA extract with AgNO$_3$ solution, at 2, 3, 4 and 5 h aging and scan rate of 0.1 V s^{-1} (Fig. 8).

It was observed that the anodic peak current decreases on increasing the time of reaction kinetics from 1 h to 5 h. Decrease in anodic peak current with time indicates that an electron transferred from the solution to electrode, which converts Ag$^+$ ions in the colloidal solution to Ag as a result of reduction reaction. However, reverse occurs in oxidation process, where electrons release during the reaction Ag $\rightarrow$ Ag$^+$ + e$^-$ and that is responsible for the backward reaction [62]. But none of the above investigated reversible couples show the reverse-to-forward peak currents ratio, i_{pr}/i_{pf} = 1. Hence, all these cases are irreversible with respect to the peak current. The pure TA extract solution exhibited the anodic peak at -0.4 V (at current = 13.0 μA) and cathodic peak at -0.5 V (at current = -7.4 μA). TA-incorporated AgNO$_3$ solution, aged at the different time intervals (1 h, 2 h, 3 h, 4 h and 5 h) exhibited two respective irreversible oxidative peak potentials around -0.5 V and between 0.40 and 0.60 V, are followed by the one reductive wave peak at -0.5 V. The corresponding values of currents of I and II peaks are presented in Table 2. In Fig. 8 (a and b (inset)), the first oxidative peak potentials around -0.4 to -0.5 V correspond to the azo group and aromatic rings. The second peak around between 0.40 and 0.60 V are responsible for the reduction of Ag$^+$ ion to Ag [63]. Azo group promotes the reduction of Ag$^+$ to Ag metal. Aging encouraged the depression in current height of I oxidative peak that represents the azo group and aromatic rings were destroyed gradually. Simultaneously, increase in the current height of II oxidative peak with aging time, is belongs to the formation of AgNPs formation by reduction of Ag$^+$/Ag (E$_{Ag+/Ag}$). Fig. 8b exhibited the linear raise in current peak height with aging time. Red shift observed in peak was observed due to increase in concentration of AgNPs, result in increase in current (Table 2).

2.5.1. Electrochemical impedance spectroscopy (EIS)

Impedance experiments were carried out to get insight of the kinetic of the electrochemical processes occurring at electrode/electrolyte interface in the absence and presence of Ag NPs. In these experiments, all the measurements have been reported with respect to the reference Ag/AgCl electrode. The local impedance diagrams (Fig. 9) were recorded in terms of the real impedance vs imaginary impedance as a function of frequency over a frequency range of 10 kHz to around 500 mHz. Complex impedance diagram were recorded in Nyquist modulus format, for Pure TA and 24 h aged Ag NPs that was suspended in 2.0% and 2.5% aqueous TA solution, as shown by Fig. 9.
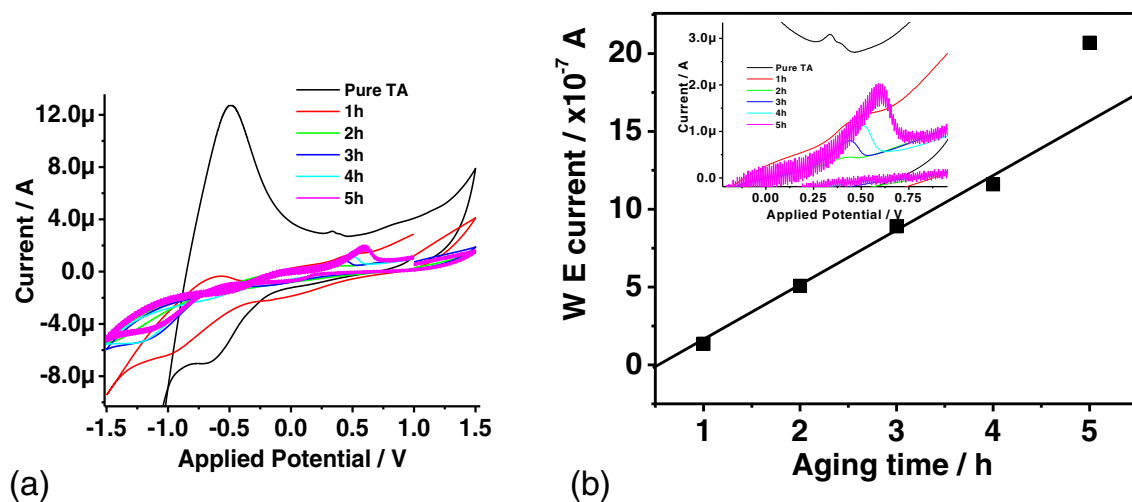
Fig. 8. Cyclic voltagrams for pure TA and the colloidal Ag NPs the formed in 2.0% TA seed extract at different time interval; 1 h, 2 h, 3 h, 4 h and 5 h (a) bird eye view and (b) working electrode current vs aging time plot along with the Inset represents the close up of II peak (belongs to AgNPs) around applied potential between 0.40 and 0.60 V.

Pristine TA sample comprise of two depressed capacitive semicircle, spread over from the high to low frequency regions. This typical behaviour of the solid metal electrodes corresponds to the non ideal frequency dispersion that related to the surface the inhomogeneities. Rapid linear increase in real impedance was observed with increase in concentration of TA (2–2.5%) in TA supported-Ag NPs, due to the increase in particle size and decrease in ionic conductivity. This is a clear indication of inhibition in the corrosion process that might be aspected during the production of AgNPs. Moreover, Warburg impedance dropped out at higher frequency because the time scale is so short that diffusion can't manifest itself. At low frequency, the reactants have to diffuse farther that increases the Warburg-impedance.

2.6. Catalytic reduction of p-nitrophenol using NaBH₄ and AgNPs

In recent years one of the most important applications of the AgNPs has been observed in catalysis of chemical reactions. Even in eradication of nitrophenol pollution it proved remarkable. In order to evaluate the catalytic activity of the AgNPs (synthesized by using *Trachyspermum ammi* (*Ajwain*) seed extract; aged at 24 h, 48 h and 72 h) for the reduction of PNP (0.05 mM) to PAP in aqueous sodium borohydride (15 mM). The reaction was monitored at room temperature in absence and presence of AgNPs. The reaction progress was spectrophotometrically examined by recording the absorption spectra at various time interval. The main absorption peaks of PNP were found at 258 and 316.5 nm due to $\pi \to \pi^*$ and $n \to \pi^*$ transition, respectively. The treatment of this solution with freshly prepared aqueous solution of NaBH₄ result in disappearance of 258 nm peak and shift of the first excitation peak of PNP from 316.5 nm to 401.5 nm, due to the formation of 4-nitrophenolate ion in the solution, which was demonstrated by optical spectra in Fig. 10a and its schematic presentation is demonstrated by Scheme 1.

The peak position at 401.5 nm in absence of AgNPs, remains unaltered even after the month long aging because of a huge kinetic barrier

development due to large potential difference between the donor and acceptors that decreases the feasibility of this reaction for the reduction process [64]. Interestingly, on addition of a freshly prepared biogenic AgNPs (0.1 mL, 100 mgL⁻¹) to the mixture of PNP and sodium borohydride solution, the intensity of the 4-nitrophenolate peak at 401.5 nm, start decreasing. The whole reduction process of the PNP in 24, 48 and 72 h aged samples of AgNPs, was completed in 10, 12 and 18 min, which was revealed by naked eyes through the disappearance of the yellow colour of the PNP (Fig. 10b,c and d). Simultaneously, the appearance of a new peak at 300 nm wavelength, was confirmed the catalytic reduction of PNP to PAP and its mechanism is shown by the Scheme 1 [65]. Peak position of the 24 h-, 48 h- and 72 h-aged samples in absence of AgNPs, were observed at 401, 400 and 402 nm, respectively (Fig. 10e). This confirms the particle size reduces from 24 h aging to 48 h aging and afterwards its increases at 72 h aging.

Catalytic action of AgNPs in above reduction process, lower down the activation energy that leads to the formation of PAP by following a pseudo-first-order rate kinetics with respect to PAP. Effect of aging revealed on AgNPs's catalytic activity for the PNP reduction process in terms of rate of reaction (Fig. 10f). The apparent catalytic rate constant ($k_{24} = 0.25709 \text{ min}^{-1}$, $k_{48} = 0.34539 \text{ min}^{-1}$ and $k_{72} = 0.0866 \text{ min}^{-1}$) was calculated for the reduction process at 24, 48 and 72 h, using the slope of the plot between logarithm of the observed optimum absorbance and time, which are represented by Fig. 11a, b and c, respectively.

During the catalytic action, AgNPs are initially chemisorbed at the (100) surface of the PNP molecule through two oxygen atoms of the

Table 2
Current and voltage values of pure 2.0% TA extract and Ag NPs prepared at 1–5 h aging.

| Aging of Ag NPs/h	I peak applied potential/V; current/A	II peak applied potential/V; current/A
Pure TA	−0.490; 1.36 × 10⁻⁵	0.43/0.58; no peak
1	−0.610; 2.00 × 10⁻⁷	0.481; 1.360 × 10⁻⁷
2	−0.182; 1.890 × 10⁻⁷	0.430; 5.081 × 10⁻⁷
3	−0.173; 1.456 × 10⁻⁷	0.439; 8.900 × 10⁻⁷
4	−0.133; −2.010 × 10⁻⁷	0.501; 11.60 × 10⁻⁷
5	−0.083; −1.943 × 10⁻⁷	0.598; 20.70 × 10⁻⁷
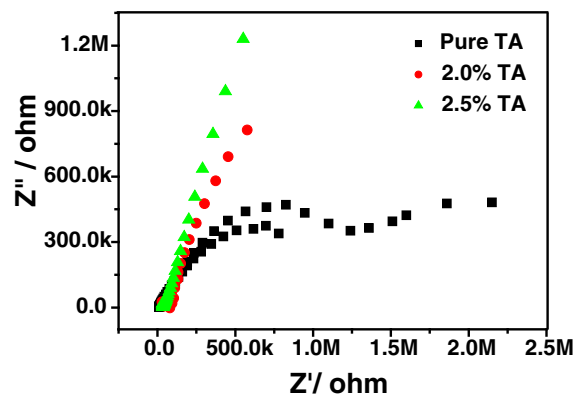
Fig. 9. Electrochemical impedance spectroscopy (EIS) plot of pure TA, 2.0% and 2.5% TA seed extract in 0.001 M AgNO₃ solution.
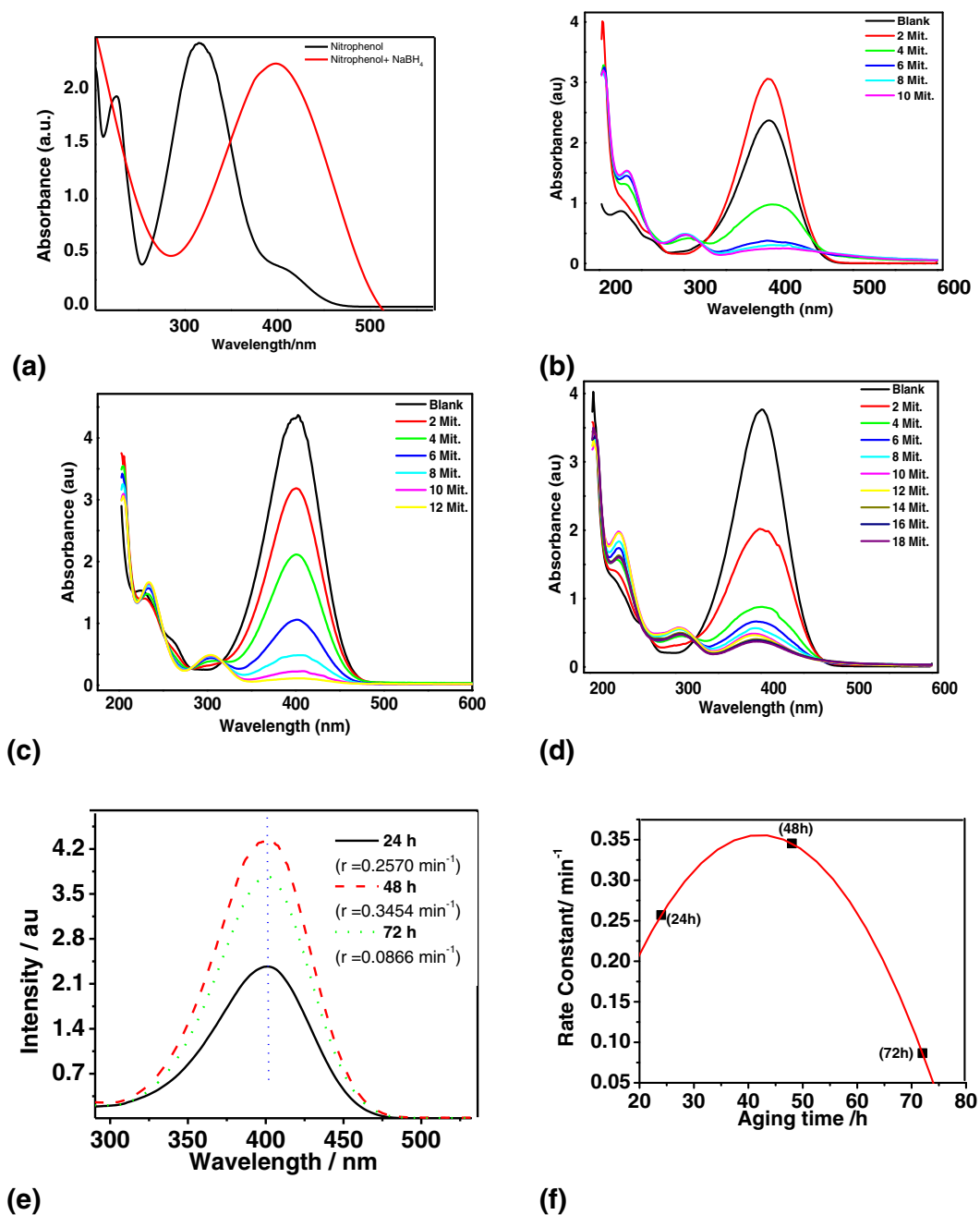
Fig. 10. (a) Red shift observed in UV–visible spectrum of 4-nitrophenol (Black) when it reduced to 4-nitrophenolate ions (401.5 nm) (Red) with NaBH$_4$; catalytic reduction of 4-nitrophenol in NaBH$_4$ solution to 4-aminophenol (300 nm peak),was observed on the addition of AgNPs at the time interval (b) 24 h (c) 28 h and (d) 72 h. (e) peak position of the aged samples in absence of AgNPs and (f) Rate constant vs aging time plot. Where, the concentration of various reactants are taken as [0.05 mM PNP]; [0.1 mL of 100 mgL^{-1} AgNPs] and [15 mM NaBH$_4$]. (For interpretation of the references to colour in this figure legend, the reader is referred to the web version of this article.)

nitro group of *p*-nitro phenolate ion. That may create a pentagonal Ag—O—N—O—Ag cyclic intermediate that may react with BH$_4^-$ ion and decomposed into PAP, as illustrated by Scheme 2. Binding of organic molecules to metal surfaces and their reduction process has been
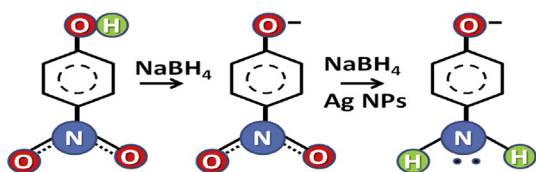
Scheme 1. Schematic reaction for the reduction of *p*-nitrophenol to *p*-aminophenol.

extensively modeled by Newns [66] and later expanded upon by Hammer and Nørskov [67–71].

After executing our experiment we compare the efficiency of our results with respect to reaction time (12 min), cost and rate of reaction (5.756 × 10^{-3} s^{-1}), with some of the recent state of art AgNPs and modified AgNPs systems such as; Calcium-Alginate-Stabilised Ag and Au NPs, AgNP-PG-5K (PG: polyguanidino oxanorbornenes (PG), 5 K and 25 kDa), Al$_2$O$_3$@Ag$_{7,8}$ QCs, Ag–P (NIPAM-co-Aam; NIPAM: N-isopropylacrylamide), CNFs (carbon nano fibres)/AgNPs composite, Breynia Rhamnoides supported Ag and Au Nanoparticles, TCD (TCD: trisodium citrate dihydrate (HOC(COONa) (CH$_2$COONa)$_2$·2H$_2$O)) supported Ag NPs, chemically reduced Ag NPs, AgNPs/PANINFs nanocomposites (PANINFs: polyaniline nano fibres), etc (Table 3) [38,72–78].
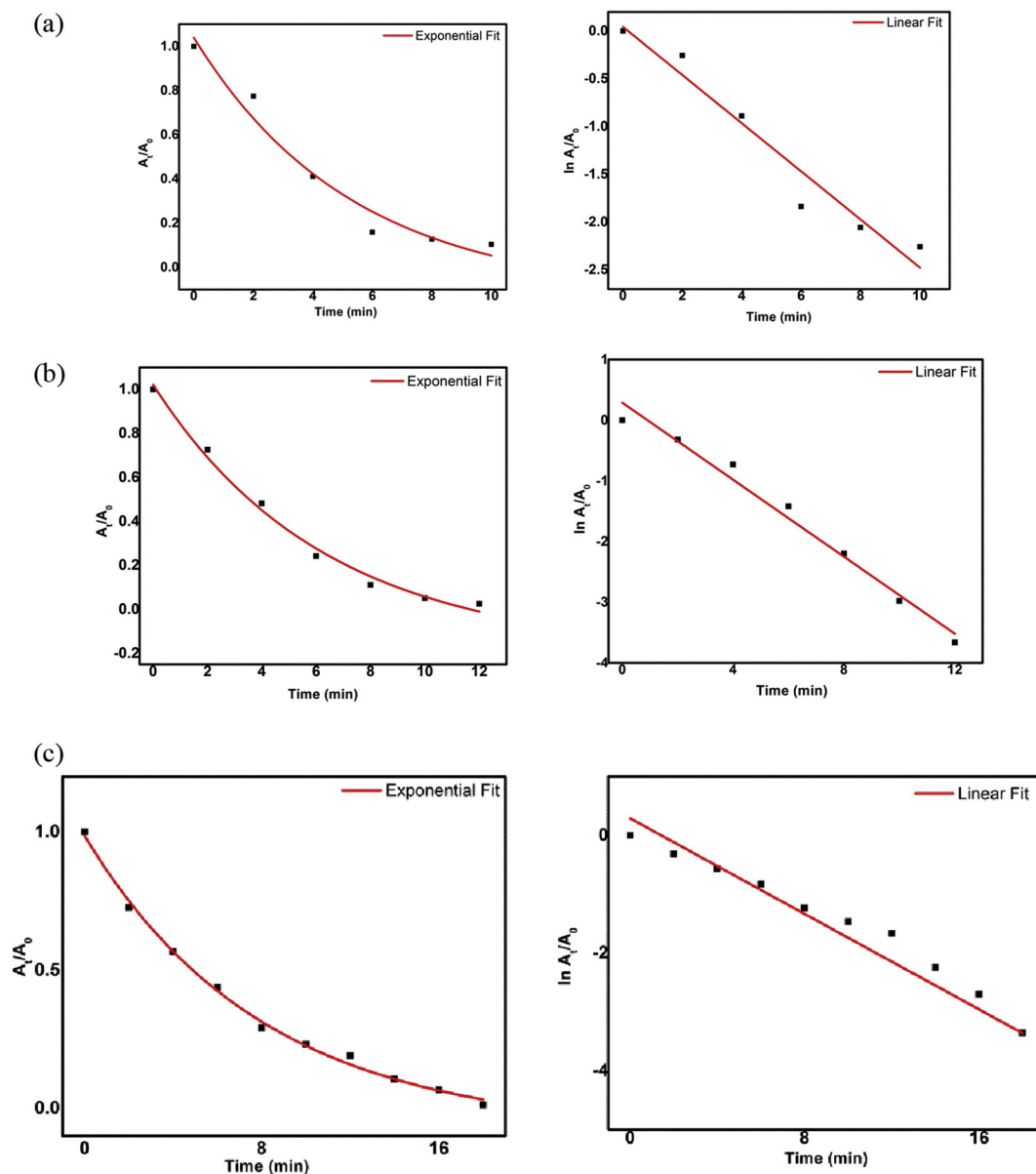
Fig. 11. Plot of (i) A_t/A_0 vs time and (ii) ln (A_t/A_0) vs time for the reduction of *p*-nitrophenol at (a) 24 h, (b) 48 h and (c) 72 h aging. Where, [0.05 mM PNP]; [0.1 mL of 100 mgL^{-1} AgNPs] and [15 mM NaBH$_4$].

And it was found that our system is better than above mentioned systems. Reason behind the superiority can be given on the basis of Garcia–Vidal and Pendry's model, the smaller metallic particles and higher content of NPs gave higher enhancement in efficiency [79]. Moreover, TA supported-AgNPs with high catalytic activity could be easily recovered by sedimentation upon three successive cycles of reduction reactions, and would greatly promote their industrial application.
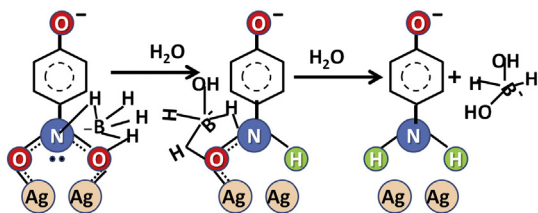
Scheme 2. Reduction mechanism of *p*-nitro phenol to *p*-aminophenol in presence of the aqueous NaBH$_4$ and Ag NPs.

3. Conclusion

Nanotechnology has a remarkable impact on the present century due to its ability to convert materials into their nanosized counterparts. At nano-level, drastic changes in the chemical, physical, electrical and optical properties of the metals, is observed because of their great surface to volume ratio, prominent random motion, negligible gravitational forces and dominating electromagnetic forces. Biogenesis is the most benign way to synthesis the nanoparticles of metals rather than the presently chemical and physical methods in practice. In this study, nanoparticles of silver metal have been successfully fabricated by using aqueous extract of the TA and AgNO$_3$ at varying the concentration of TA and aging time. During the biosynthesis of the Ag nanoparticles, self-assembling of the chemical components (i.e. nicotinic acid and steroidal saponins) of the TA extract's around the of Ag$^+$ ion that leads the reduction of Ag$^+$ ion in Ag NPs. TA seeds extract contains nicotinic acid, which attributed to the reduction. These phythogen altogether leads to the nucleation of Ag nanoparticles in two shapes (cubes of 5–20 nm and elongated particles of 0.52 × 2 μm). XRD studies confirmed the purity of

Table 3
Comparison of the catalytic efficiency of our system with respect to reaction time, cost and rate of reaction, with few state of art AgNPs and modified AgNPs systems.

Catalytic system	Conc. PNP (M)	Conc. of NaHB$_4$	Nano particles	Reduction time	Catalytic rate	Reference
Calcium-Alginate-Stabilised Ag and Au NPs	0.10 mM	2.5 mL of 0.1 M	1, 2 g/L Ag	8 min	0.14–0.20×10^{-5} min^{-1}	[71]
AgNP-PG-5K	0.12 mM	12 mM	25 µg	11 min	5.50×10^{-3} s^{-1}	[72]
Al$_2$O$_3$@Ag$_{7,8}$ QCs	7.00 mM	160 mM	50 mg	18 min	8.23×10^{-3} s^{-1}	[73]
Ag–P (NIPAM-co-Aam)	0.061 mM	9.15 mM	37.18 mg ml^{-1}	25 min	0.1713	[74]
CNFs/AgNPs composite	0.12 mM	5 mM	1.0 mg	8 min	6.2×10^{-3} s^{-1}	[75]
Breynia Rhamnoides supported Ag and Au nanoparticles	2.00 mM	0.03 M	0.5 mL AgNPs or AuNPs	–	4.06×10^{-3} s^{-1} (AgNPs)	[76]
				11 min	9.19×10^{-3} s^{-1} (AuNPs)	
TCD supported Ag NPs	2 mmol	0.03 M	300 µL	75 min	0.05 s^{-1}	[77]
Ag NPs	5 mM	160 mM	0.675 mg mL^{-1}	20 min	3.28×10^{-3} s^{-1}	[78]
AgNPs/PANINFs nanocomposites	5 mM	160 mM	0.675 mg m L^{-1}	3 min	21.39×10^{-3} s^{-1}	[78]
TA-supported biogenic Ag NPs	0.05 mM	15 mM	10 µg	12 min	5.756×10^{-3} s^{-1}	This work

PG: polyguanidino oxanorbornenes (PG), 5 K and 25 kDa; NIPAM: N-isopropylacrylamide; TCD: trisodium citrate dihydrate (HOC(COONa)(CH$_2$COONa)$_2$·2H$_2$O).

these nanosized NPs that crystallized in a cubic and rod shaped crystals. Crystal growth orientation of the Ag NPs was found along the 111 plane. Prominent, intense and broad excitonic UV–vis. spectrum peak of the Ag NPs at 420–440 nm, attributed to its surface plasmonic phenomena. IR spectroscopic studies confirmed that carbonyl group of amino acid residues have strong binding ability with metal suggesting the formation of layer covering metal nanoparticles and acting as capping agent to prevent agglomeration and providing stability to the medium. Excitation of electrons from occupied d bands into states above the Fermi level is responsible to the green light luminescence of Ag nanoparticles at 563 nm. Cyclic-voltammetric studies confirm the one electron reduction process of the AgNPs. As synthesized AgNPs, were used successfully to completely catalyse the reduction of notorious pollutant PNP to PAP in presence of NaBH$_4$, which was kinetically hard reaction in absence of catalyst. The study of effect of AgNPs particle size on PNP reduction catalytical activity was observed. That results the 48 h-aged AgNPs prepared in 2.0% TA extract, show the optimum catalytic efficiency in term of high reaction with respect to many state of art catalytic systems.

4. Experimental

4.1. Aqueous extract of TA seeds

Analytical grade AgNO$_3$ (99%, Merck), was used as purchased without any further purification. All solutions were prepared using deionised Millipore water (DMW). Established procedure for the extraction of *Trachyspermum ammi* (*Ajwain*) seeds was adopted to prepare the aqueous extract [28] and dry seeds were washed thoroughly with distilled water to make them free form dust particles and surface contamination and dried for 24 h in moisture free atmosphere. Afterwards 2 g dried seeds were soaked in 50 mL of pure DMW for 24 h. The extract was filtered using Whatmann filter paper No. 42.

4.2. Synthesis of silver nanoparticle

Silver nanoparticles were synthesized using the procedure describe somewhere else [36]. 2.5 mL of the aqueous TA seeds' extract was added drop wise into the 25.0 mL of aqueous 0.001 M AgNO$_3$, kept in a 50 mL boiling tube, at room temperature. Afterwards, the mixture was shifted in a desiccator at room temperature for aging (7 h, 24 h, 48 h, 7 days, 14 days, 21 days, etc) that leads to a biogenic chemical reduction of Ag$^+$ ions into Ag NPs. Transparent solution of AgNO$_3$ turns pink with time, which indicates the presence of Ag nanoparticles. Aging added sharpness to the colour. Silver nanoparticles in aqueous phase are extremely stable without any precipitation and their stability for long period may be due to antimicrobial properties of this plant. Highly dispersed colloidal Ag NPs were found soluble in water and stable at ambient condition for more than 6 months. After certain aging time, the suspension was centrifuged at 20,000 rpm for 20 min, which resulted in suspended solid. It was washed by hot DMW thrice prior

to be used for further analysis (XRD, TEM, FESEM with EDX, UV–vis, FTIR, PLE, and cyclic voltammetric study) and catalytic activity analysis.

5. Characterization

5.1. Optical measurement

The Ag NPs were analyzed by X-ray diffraction (XRD) using a Bruker D2 Phase diffractometer that was operated in transmission mode with CuK$_\alpha$ radiation ($\lambda = 1.5418$ Å). The data were collected over the 2θ range from 20° to 90° at the interval of 0.02° with a counting time of 30 s per step. UV–visible absorption spectra were measured in the range of 200–800 nm by periodic sampling of 1 mL aliquot, in spectrophotometer (LAB India, UV 3000$^+$). The particle size of the Ag NPs was also monitored by considering the position of the first excitonic peak of the spectra. The FTIR spectra of the synthesized nanoparticles (in form of KBr pellet), were recorded in transmission mode at the frequency range between 4000 and 400 cm^{-1} with the resolution of 4 cm^{-1}, by using FTIR spectrophotometer (Tensor-27 Bruker, Germany with software OPUS version 5.1) for solid and ATR spectrophotometer (T-alpha, Bruker) for liquid sample. PL spectra were observed using a spectrofluorimeter (Shimazdu Model RF-5301; along with software PC-IV) equipped with a 150 W Xe lamp and a Hamamatsu R928 photo-multiplier tube at room temperature. The excitation and emission spectra were recorded at fixed slit width i.e. 5 nm. Morphology and elemental composition of the sample was checked using scanning electron microscopy (FESEM, JEOL JSM-6700F) and their corresponding energy dispersive X-ray spectrum (EDXS, OXFORD), respectively. EDXS measurement was carried out with the same instrument by focusing a particular area of the samples. TEM and HRTEM micrographs were recorded using an electron microscope (CM12, PHILIPS). The images were analyzed on the basis of the shape, size and crystallinity of Ag NPs at accelerating voltage of 200 kV. Samples were prepared by placing 3–4 drops of the well dispersed Ag NPs in ethyl alcohol samples on a 300-mesh, carbon coated Cu grid (EM Sciences) and afterwards allowing the liquid to evaporate in air. For Ag NPs, the particle size distribution was based on 30 randomly selected particles.

5.2. Electrochemical measurements

Electrochemical experiments were conducted in a conventional three-electrode glass cell of capacity 100 mL, using a potentiostat/galvanostat (Auto Lab-PGSTAT 204 Metrohm, equipped with the software NOVA 3.1). Pt-tipped carbon electrode, Pt-wire and a saturated Ag-AgCl electrode, were used as a working, counter and reference electrodes, respectively. In these experiments, all the potentials were reported against the Ag/AgCl reference electrode in naturally aerated and unstirred solutions at 303 K. Impedance measurements were made at corrosion potentials over a frequency range of 100 kHz–10 mHz, with a signal amplitude perturbation of 5 mV.

5.3. Reduction of p-nitro phenol

The light yellow colour of 0.05 mM p-nitrophenol turns to yellow-green upon incorporation of the alkaline 15 mM sodium borohydride solution. But under such conditions PNP didn't convert into PAP, until the addition of AgNPs. The peak intensity was quantitatively observed by using UV–Vis spectrophotometer (Model 3000⁺ of Lab India) with a time gap of 3 min. in a scanning range of 200–800 nm at room temperature of 25 °C with scan speed of 250 nm per minute. The reduction of p-nitrophenol with NaBH$_4$ was monitored using UV–vis absorption spectroscopy in 1 mL of 15 mM NaBH$_4$ (aqueous solution) was mixed with 1.7 mL of 0.2 mM 4-nitrophenol (aqueous solution) and 0.1 mL of 100 mgL^{-1} of AgNPs than the mixture was poured in a 5 mL quartz cell for optical observations.

Acknowledgements

References

[1] M. Catauro, M.G. Raucci, F. Gaaetano, A. De Marotta, J. Mater. Sci. Mater. Med. 15 (2004) 831–840.
[2] J.H. Crabtree, R.J. Burchette, I.T. Siddiqi Ra, B. Huen, L.L. Hadnott, A. Fishman, Perit. Dial. Int. 23 (2003) 368–374.
[3] A. Krolikowska, A. Kudelski, A. Michota, Bukowska, J. Surf. Sci. 532 (2003) 227–232.
[4] G. Zhao, S.J. Stevens, Biometals 11 (1998) 27–32.
[5] N. Duran, P.D. Marcato, O.L. Alves, G.I.H. De Souza, E. Esposito, J. Nanobiotechnol. 3 (2005) 1.
[6] D.S. Balaji, S. Basavaraja, R. Deshpande, D.B. Mahesh, B.K. Prabhakar, A. Venkataraman, Colloids Surf. B 68 (2009) 88–92.
[7] A. Ahmad, P. Mukherjee, D. Mandal, S. Senapati, M.I. Khan, R. Kumar, M. Sastry, J. Am. Chem. Soc. 124 (2002) 12108.
[8] A. Ahmad, S. Senapati, M.I. Khan, R. Kumar, M. Sastry, Langmuir 19 (2003) 3550.
[9] A. Ahmad, S. Senapati, M.I. Khan, R. Ramani, V. Srinivas, M. Sastry, Nanotechnology 14 (2003) 824.
[10] H. Lee, A.M. Purdon, V. Chu, R.M. Westervelt, Nano Lett. 4 (2004) 995–998.
[11] V. Armendariz, J.L. Gardea-Torresdey, M. Jose-Yacaman, J. Gonzalez, I. Herrera, J.G. Parsons, Proceedings – Waste Research Technology Conference at the Kansas City, Mariott-Country Club Plaza July 30–Aug 1, 2002.
[12] M. Kowshik, S. Ashtaputre, S. Kharrazi, W. Vogel, J. Urban, S.K. Kulkarni, K.M. Paknikar, Nanotechnology 14 (1) (2003) 95.
[13] K. Ghule, A.V. Ghule, J.Y. Liu, Y.C.J. Ling, Nanosci. Nanotechnol. 6 (2006) 3746–3751.
[14] S. Li, Y. Shen, A. Xie, X. Yu, L. Qiu, L. Zhang, Q. Zhang, Green Chem. 9 (2007) 852–858.
[15] J.L. Gardea-Torresdey, J.G. Parsons, E. Gomez, J. Peralta-Videa, H.E. Troiani, P. Santiago, M. Yacaman, J. Nano Lett. 2 (2002) 397–401.
[16] I.B. Obot, S.A. Umoren, A.S.J. Johnson, Mater. Environ. Sci. 4 (6) (2013) 1013–1019.
[17] E.M. Egorova, A.A. Revina, Physicochem. Eng. Asp. 168 (2000) 87–96.
[18] J. Huang, Q. Li, D. Sun, Y. Lu, X. Yang, H. Wang, Y. Wang, W. Shao, N. He, J. Hong, C. Chen, Nanotechnology 8 (2007) 105104.
[19] B. Ankamwar, C. Damle, A. Ahmad, M. Sastry, J. Nanosci. Nanotechnol. 5 (2005) 1665–1671.
[20] S.P. Chandran, M. Chaudhary, R. Pasricha, A. Ahmad, M. Sastry, Biotechnol. Prog. 22 (2006) 577–583.
[21] S.S. Shankar, A. Rai, A. Ahmad, M. Sastry, J. Colloid Interf. Sci. 275 (2004) 496–502.
[22] R.P. Singh, S. Magesh, C. Rakkiyappan, Int. J. Bioeng. Sci. Technol. 02 (03) (2011) 75–80.
[23] K. Govindaraju, S. Tamilselvan, V. Kiruthiga, G. Singaravelu, J. Biopestic. 3 (1) (2010) 394–399.
[24] M. Sundarajan, S. Gowri, Chalcogenide Lett. 8 (8) (2011) 447–451.
[25] S. Maensiri, P. Laokul, J. Klinkaewnarong, S. Phokha, V. Promark, S. Seraphin, J. Optoelectron. Adv. Mater. 10 (3) (2008) 161–165.
[26] H.M. Gong, L. Zhou, X.R. Su, S. Xiao, S.D. Liu, Q.Q. Wang, Adv. Funct. Mater. 19 (2009) 298–303.
[27] N.P.S. Acharyulu, R.S. Dubey, V. Swaminadham, P. Kollu, S.V.N. Pammi, Int. J. Eng. Res. Technol. 3 (4) (2014) 639–641.
[28] S. Ankanna, P. TNVKV, E.K. Elumalai, N. Savithramma, Dig. J. Nanomater. Biostruct. 5 (2) (2010) 369–372.
[29] R.H. Ritchie, Phys. Rev. 106 (1957) 874.
[30] W.L. Barnes, A. Dereux, T.W. Ebbesen, Nature 424 (2003) 824–830.
[31] S.A. Maier, H.A. Atwater, J. Appl. Phys. 98 (2005) 011101.
[32] S.A. Maier, Plasmonics Fundamentals and Applications, first ed. Springer, New York, 2007 pp 21–34 and 65–88.
[33] S. Lal, S. Link, N. Halas, Nat. Photonics 1 (2007) 641–648.
[34] X.C. Wang, J.C. Yu, H.Y. Yip, L. Wu, P.K. Wong, S.Y. Lai, Chem. Eur. J. 11 (2006) 2997–3004.
[35] X.B. Cao, L. Gu, L.J. Zhuge, W.J. Gao, W.C. Wang, S.F. Wu, Adv. Funct. Mater. 16 (2006) 896–902.
[36] J. Virkutyte, R.S. Varma, New J. Chem. 34 (2010) 1094–1096.
[37] T. Vincent, E. Guibal, Langmuir 19 (2003) 8475–8483.
[38] G. Chang, Y. Luo, W. Lu, X. Qin, A.M. Asiri, A.O. Al-Youbi, X. Sun, Catal. Sci. Technol. 2 (2012) 800–806.
[39] W. Lu, Y. Luo, G. Chang, X. Sun, Biosens. Bioelectron. 26 (2011) 4791–4797.
[40] M. Nasrollahzadeh, S.M. Sajadi, A. Rostami-Vartooni, M. Bagherzadeh, J. Colloid Interface Sci. 448 (2015) 106–113.
[41] K. Satyavani, T. Ramanathan, S. Gurudeeban, Dig. J. Nanomater. Biostruct. 6 (2011) 1019–1024.
[42] R. Varshney, S. Bhadauria, M.S. Gaur, Adv. Mat. Lett. 1 (3) (2010) 232–237.
[43] K. Jeet, N. Devi, T. Narendra, T. Sunil, S. Lalit, T. Raneev, Int. Res. J. Pharm. 3 (5) (2012) 133–138.
[44] M. Kjellin, I. Johansson, Surfactants from Renewable Resources, John Wiley & Sons, 2010.
[45] X. Gao, G. Gu, Z. Hu, Y. Guo, X. Fu, J. Song, Colloids Surf. A Physicochem. Eng. Asp. 254 (2005) 57–61.
[46] A. van Dijken, E.A. Meulenkamp, D. Vanmaeklenbergh, A. Meijerink, J. Lumin. 87–89 (2000) 454–456.
[47] Y.J. Xing, Z.H. Xi, Z.Q. Xue, X.D. Zhang, J.H. Song, R.M. Wang, J. Xu, Y. Song, S.L. Zhang, D.P. Yu, Appl. Phys. Lett. 83 (2003) 1689–1691.
[48] W. Haiss, N.T.K. Thanh, J. Aveyard, D.G. Fernig, Anal. Chem. 79 (2007) 4215–4221.
[49] D.C. Oh, T. Suzuki, J.J. Kim, H. Makino, T. Hanada, M.W. Cho, T. Yao, Appl. Phys. Lett. 86 (2005) 032909.
[50] Wriedt, T. Mie Theory 1908–2008, ed. by Hergert, W.; Wriedt, T. Universität Bremen. Bremen, 2008, pp. 17–21.
[51] K. Jilie, Y.U. Shaoning, Acta Biochim. Biophys. Sin. 39 (2007) 549–559.
[52] N.P.G. Roeges, A Guide to the Complete Interpretation of Infrared Spectra of Organic Structures, Wiley, New York, 1994.
[53] G. Varsanyi, Assignments of Vibrational Spectra of Seven Hundred Benzene Derivatives, vol. 1, Halsted Press, 1974.
[54] I.D.G. Macdonald, W.E. Smith, Langmuir 12 (1996) 706–713.
[55] A.M. Fayaz, K. Balaji, M. Girilal, R. Yadav, P.T. Kalaichelvan, R. Venketesan, Nanomedicine: NBM 6 (2010) 103–109.
[56] R. Sathyavathi, M.B. Krishna, S.V. Rao, R. Saritha, D.N. Rao, Adv. Sci. Lett. 3 (2010) 138–143.
[57] A. Manna, T. Imae, M. Iida, N. Hisamatsu, Langmuir 17 (19) (2001) 6000–6004.
[58] M.H. Moore, R.L. Hudson, Icarus 161 (2003) 486–500.
[59] W. Zheng, D. Jewitt, Y. Osamura, R.I. Kaiser, Astrophys. J. 674 (2) (2008) 1242.
[60] B.M.V. Romão, C. Pardini, R.C.L. Dutra, F. Burel, Polímeros Ciência Tecnologia 13 (2003) 173–180.
[61] J.P. Wilcoxon, J.E. Martin, F. Paraspour, D.F.J. Kelley, Chem. Phys. 108 (1998) 9137–9143.
[62] H. Peng, S.X. Hai, G.H. Cheng, Acta Phys. -Chim. Sin. 20 (10) (2004) 1200–1203.
[63] A. Frattini, N. Pellegri, D. Nicastro, O.D. Sanctis, Mater. Chem. Phys. 94 (1) (2005) 148–152.
[64] N. Pradhan, A. Pal, T. Pal, Colloids Surf. A Physicochem. Eng. Asp. 196 (2002) 247–257.
[65] Z.D. Pozun, S.E. Rodenbusch, E. Keller, K. Tran, W. Tang, K.J. Stevenson, G.J. Henkelman, Phys. Chem. C 117 (2013) 7598–7604.
[66] D.M. Newns, Phys. Rev. 178 (1969) 1123–1135.
[67] B. Hammer, J.K. Nørskov, Nature 376 (1995) 238–240.
[68] B. Hammer, Y. Morikawa, J.K. Nørskov, Phys. Rev. Lett. 76 (1996) 2141–2144.
[69] B. Hammer, J.K. Nørskov, Surf. Sci. 343 (1995) 211–220.
[70] B. Hammer, J.K. Nørskov, Surf. Sci. 359 (1996) 306.
[71] B. Hammer, Top. Catal. 37 (2006) 3–16.
[72] S. Saha, A. Pal, S. Kundu, S. Basu, T. Pal, Langmuir 26 (4) (2010) 2885–2893.
[73] B. Baruah, G.J. Gabriel, M.J. Akbashev, M.E. Booher, Langmuir 29 (13) (2013) 4225–4234.
[74] A. Leelavathi, B.T.U. Rao, T. Pradeep, Nanoscale Res. Lett. 6 (2011) 123.
[75] R. Begum, Z.H. Farooqi, E. Ahmed, K. Naseem, S. Ashraf, A. Sharif, R. Rehan, Appl. Organomet. Chem. (2016) 1–8.
[76] P. Zhang, C. Shao, Z. Zhang, M. Zhang, J. Mu, Z. Guo, Y. Liu, Nanoscale 3 (2011) 3357–3363.
[77] A. Gangula, R.K. Podila, M. Ramakrishna, L. Karanam, C. Janardhana, A.M. Rao, Langmuir 27 (24) (2011) 15268–15274.
[78] F.A. Al-Marhaby, R. Seoudi, World J. Nanosci. Eng. 6 (2016) 29–37.
[79] H. Hu, Z. Wang, L. Pan, S. Zhao, S.J. Zhu, Phys. Chem. C 114 (2010) 7738–7742.

SYNTHESIS OF ZnO NANOPARTICLES FOR ORGANIC POLLUTANT DEGRADATION

Rajesh Kumar Meena[1*], Niranjan Kumar Mandawat[2], Neeta Gurbani[3], Neelu Chouhan[4*]

[1,2,3,4]*Department of Pure & Applied Chemistry, University of Kota, Kota, Rajasthan, (India)*

ABSTRACT

In this research work, we have synthesized an effective water filtration system based on the photocatalytic performance of semiconducting dense nanoparticles under natural sunlight. The present study, focus on the photocatalytic activity of nanostructures semiconductor like zinc oxide (ZnO) was prepared by sol-gel methods on the degradation of organic dye such as methylene blue that was investigated. Synthesized ZnO nanoparticles are characterized and study of morphology structure and stability of the synthesized ZnO nanoparticles were studied using scanning electron microscope (FESEM), UV-spectro photometer and Fourier Transform Infrared (FTIR) spectroscopy. The results depicted that the synthesized nanoparticles are moderately stable, roughly spherical with maximum particles in size range within 40-50 nm in diameter.

Key Words: Organic pollutant FTIR, XRD, FESEM etc.

I INTRODUCTION

Environmental contaminants similar to dyes, pesticides and heavy metals in water require remediation and probable removal to make the water it for human consumption. A lot of research is established to purify water from its contaminants, a most important portion of which are organic in nature. Further, the photocatalytic degradation of organic pollutants from water using semiconducting materials has attracted a lot of attention. Such semiconductors are increasingly used for oxidation or degradation of organic dyes and other contaminants particularly in industrial wastewater. The basic mechanism for this remediation is primarily based on the oxygen defects on the surface of the semiconducting materials which when activated by photon irradiation are used to destroy the organic contaminants. The various advantages that the process has are (a) the photocatalytic reaction is not specific to compounds and, therefore, is capable of destroying a spectrum of organic chemicals like hydrocarbon fuels, halogenated solvents, surfactants, pesticides and many hazardous organic chemicals,[1,2] (b) this process is very effective mostly owing to the process of its removal, oven achieving a complete degradation, (c) the process is very resistant to toxicity etc., (d) the process can be applied equally well to liquid (e.g. wastewater and contaminated groundwater) and gaseous streams (e.g. VOC emission), and finally (e) there is a potential to utilize solar energy as reported in this particular work.[3–5] Most photo degradation is still accomplished by exposure to UV radiation although UV sources consume considerable amount of energy.

In the past two decades, zinc oxide has paying much attention with respect to the degradation of different pollutants due to its high stability, photosensitivity and wide band gap. Most researchers have earlier used ZnO in a nano-powder form dispersed in industrial water for the photo-degradation of organic pollutants. Further, it has been reported that ZnO has a higher photocatalytic efficiency compared to TiO2 in the degradation of several organic contaminants in both acidic and basic media, which has attracted researchers to explore the properties of zinc oxide in many photocatalytic reactions.[6-8] Zinc oxide is consideration to be as a low cost alternative photocatalyst to TiO_2 for degradation of organics in aqueous solutions. The dispersion and surface area of zinc oxide, which depend on the synthesis method, are significant factors for determining its photocatalytic activity for pollutant degradation. Zinc oxide NPs can be synthesis by various type of methods, such as, alkali precipitation, hydrothermal synthesis, thermal decomposition, spray pyrolysis and microwave irradiation, organo-zinc hydrolysis, plasma heat-decomposing, etc. Composites of zinc oxide and silica nanoparticle could be created through coprecipitation route; in this case, the zinc oxide could be covered on the silica nanoparticle surface[9].Photocatalyst is besides called photochemical catalyst and the function is parallel to the chlorophyll in the photosynthesis. In a photocatalytic scheme, photo-induced molecular transformation or reaction takes place at the surface of catalyst. A basic photocatalytic reaction on the generation of electron–hole pair and its destination is as follows: when a photocatalyst is illuminated by the light stronger than its band gap energy, electron–hole pairs diffuse out to the surface of photocatalyst and participates in the chemical reaction with electron donor and acceptor. Those free electrons and holes transform the neighboring oxygen or water molecules into OH free radicals with super strong oxidization. It can oxygenolyse various kinds of organic compounds and some parts of minerals. It may also deoxidize harmful substances like formaldehyde, benzene and ammonia into CO_2 and water free of toxic, harm, and odor. Therefore, photocatalyst may kill viruses, germs, pollen, epiphytes and the like and may decompose formaldehyde, benzenes, ammonia, and other harmful gases, and it will not bring secondary environmental pollution [10]. The degradation of the pollutants catalyzed by ZnO has been studied broadly. ZnO is known of the important photocatalysts because of its unique advantages, high photocatalytic activity, such as its low price and nontoxicity etc.[11, 12]

II MATERIALS AND METHODS

2.1 Materials

Zinc nitrate and citric acid were purchased from Sigma- Aldrich and were all used without further purification and Double distilled water was used as the solvent during this process.

2.2 Synthesis of Zinc Oxide Nanoparticles

ZnO NPs were prepared by the sol-gel method. Firstly from Sigma- Aldrich of zinc nitrate and citric acid were selected as original materials without any purification. 0.5837 g citric acid and 0.826 g zinc nitrate were dissolved into DIW water. In which citric acid acted as both stabilizer and mineralizer. After stirring for 1h, the mixture solution aged in the next 14 h at near room temperature. Then the mixture solution was evaporated and concentrated until changing to wet-gel at 90℃ water-bath. Then the wet-gel was put into drying oven at 120℃

for 6h, and then the formed mixture was calcined at 500℃ for 3h, and the ZnO nanospheres material was achieved for further characterization.

2.3 Optical Properties

UV-Visible spectroscopy (UV-Vis) refers to absorption spectroscopy in the UV-Visible spectral region. That means it uses beam in the visible and adjacent (near-UV and near-infrared (NIR)) ranges. . In this time uv-vis absorption spectra was takened using a (LABINDIA Uv- Visible 3000+) spectrophotometer where the cuvette path length was set to 1.0 cm. The particles were dissolved in DIW water, and solution was placed in a quarts cuvettes. The absorption in the visible range openly affects the perceived colour of the chemicals involved. In this region of the electromagnetic spectrum generate by the electronic transitions.

2.4. Powder X-Ray Diffraction

XRD patterns of the powdered samples were obtained on a Phillips X'Pert materials research diffractometer using secondary monochromated Cu Kα radiation (λ = 1.54060 A°) at 40 Kv/50mA. Samples were supported on a glass slide. Measurements were taken using a glancing angle of incidence detector at an angle of 2 for 2θ values over 10–70 in steps of 0.05 with a scan speed of 0.012.

2.5. FESEM analysis

The FESEM image was taken with very high resolution and MATLAB analysis gives the pixel depth of the image equal to 24bits and the image format as JPEG. The FESEM Images have been taken from MNIT Jaipur, Rajasthan, India.

2.6. Fourier Transform Infrared (FTIR) Spectroscopy

FTIR analysis range 4000 to 400 cm$_{-1}$ using Bruker -Tensor Spectrum in the diffuse reflectance mode at a resolution of 4cm^{-1} in KBr pellets. The powder sample was placed on a sample holder and the spectrum was recorded.

III RESULTS AND DISCUSSION

3.1 UV-Visible Analysis

UV-Visible absorption spectroscopy is widely used technique to examine the optical properties of nano sized particles. The prepared zinc oxide white crystalline powder was not soluble in water and almost in all organic solvents. ZnO nano particles UV-Visible spectra recorded by dispersed in methanol solution and sonicated for 5 to 10 min. Fig. 4 shows the absorption spectroscopy of the ZnO nanoparticles in the UV-spectral region. ZnO exhibits a sharp band at 354 nm, which corresponds to the formation of ZnO nanoparticles.
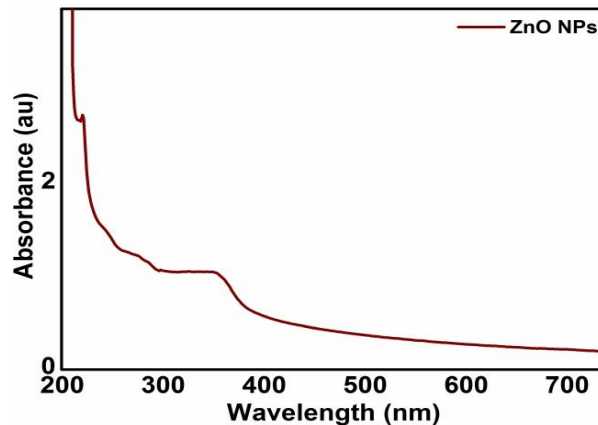
Fig.1. UV-Vis. spectra of ZnO NPs synthesized by sol-gel method

3.2 XRD Analysis

The crystal structures of the synthesized samples were determined by powder X-ray diffraction (XRD) using a copper Kα radiation source at 40 kV and 200 mA in steps of 0.02. Data were recorded ranging from 10° to 70°. Fig. 2 showed the XRD patterns of as-synthesized samples obtained by sol-gel method whose reflection peaks can be readily indexed with the wurtzite ZnO (JCPDS No. 79-2205). Prepared ZnO nanospheres were obtained by the sol-gel method, the crystal structure of ZnO was shown in Fig. 3, which belonged to the wurtzite structure. It can be seen that lattice parameters were a=0.3249 nm and c=0.5206 nm.
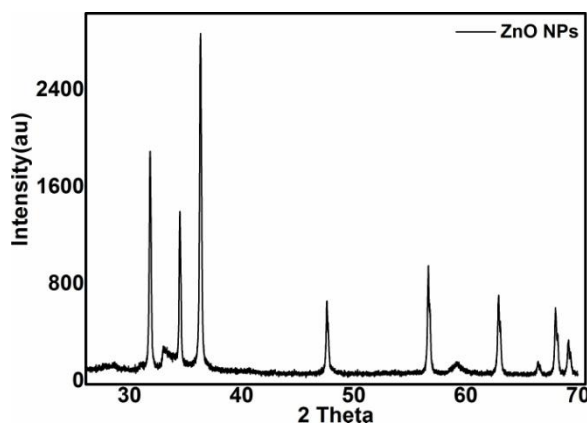
Fig.2. XRD spectra of ZnO synthesized by: sol-gel method   **Fig.3. Crystal structure of ZnO**
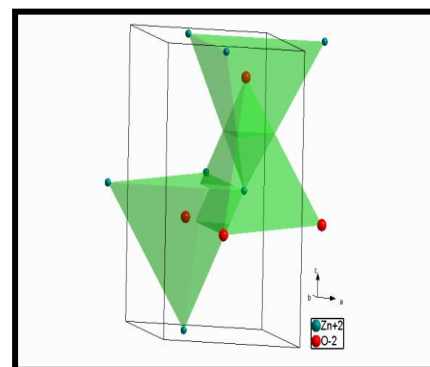
3.3 Morphology Analysis:

SEM images of the products were shown in Fig. 4. ZnO NPs was prepared by sol-gel method calcined at 500℃ for 3 hours and pH was 8. SEM image showed relatively more uniform ZnO NPs prepared by sol-gel method look like nanospheres, with diameter range 10-50nm.
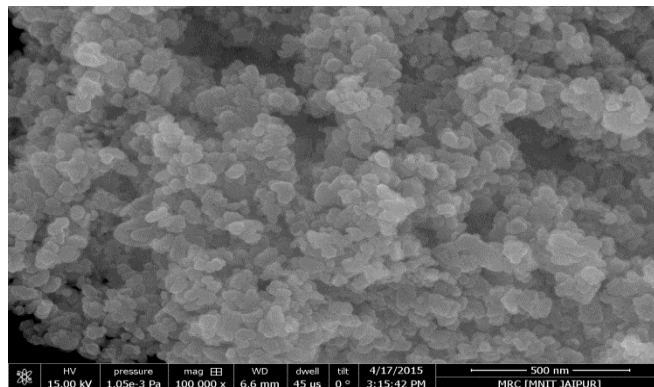

Fig.4. SEM image of ZnO NPs produced by the Sol-gel method

3.4 FTIR Analysis

FT-IR spectrum of ZnO nanoparticles (Fig. 5) showed significant absorption peaks at 573 and 1577, 3372cm^{-1}. The absorption band at 573 cm^{-1} due to Zn-O stretching vibration mode. The weak band near 1577 cm^{-1} is assigned to H-O-H bending vibration mode were presented due to the adsorption of moisture, when FTIR sample disks were ready in an open air atmosphere. These explanations provided the evidence for the presence of hydration in the structure and intense broad band near 3372 cm^{-1} represents the hydrogen bonded O-H stretching vibration mode.
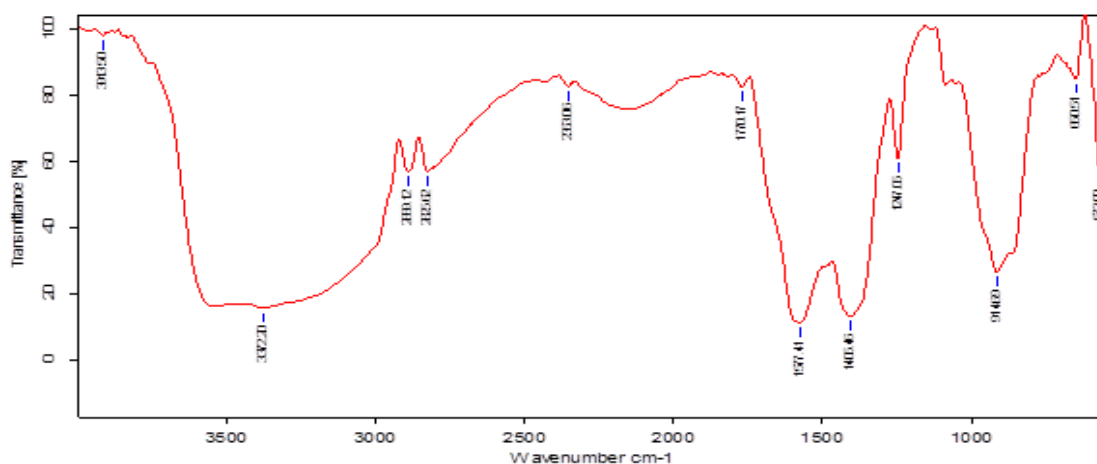

Fig.5 FTIR spectra of synthesized ZnO NPs

International Journal of Advance Research in Science and Engineering

Vol. No.6, Issue No. 01 , January 2017

www.ijarse.com

IJARSE
ISSN (O) 2319 - 8354
ISSN (P) 2319 - 8346

3.6 Photocatalytic activity of ZnO NPs

Photocatalytic activity of ZnONPs was investigated by measuring the photocatalytic degradation of methylene blue in water under the illumination of UV light. The ZnO nanoparticles of 50 nm in common particle size were chosen for the evaluation of photocatalytic activity. As shown in Fig. 6, it was found that the ZnO nanoparticles were effective on the degradation of the methylene blue. Higher photocatalytic activity of the ZnO nanoparticles is considered due to the higher surface area of the ZnO nanoparticles. At higher surface area, larger contact area between photocatalyst and target material can be obtained. It also meant that higher degree of UV light absorption could occur at the smaller particle size in the test solution.
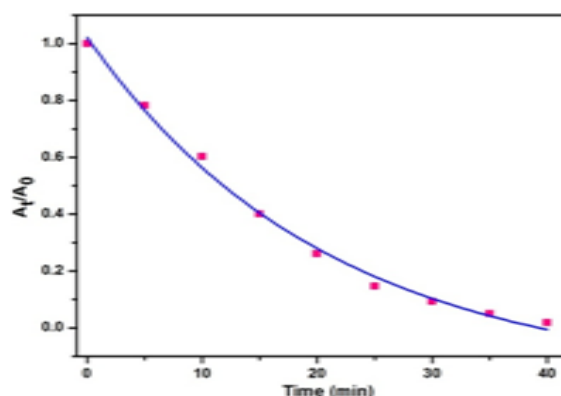
Fig.6. Effect of catalyst loading on the photodegradation of methylene blue using ZnO nanoparticles.

lV. CONCLUSION

In this present study, ZnO NPs have been successfully synthesized using Zinc nitrate and citric acid solution as precursors via sol-gel approach. By carefully controlling the process window, various morphologies of ZnO particles such as disk like and spherical NPs could be produced. The crystallite size calculated from the XRD is 50 nm. FT-IR results confirm that the presence of Zn-O at $573 cm^{-1}$ as well as UV-visible Spectroscopy the absorption spectrum was 374 nm absorbed. The photo degradation of methylene blue using ZnO spherical nanoparticles process was investigated. In which catalysts may further enhance the photocatalytic activity due to its high surface to volume ration which will facilitate the better adsorption of dyes.

V. ACKNOWLEDGMENT

REFERENCES

[1] R. Venkatadri and R. W. Peters, Chemical oxidation technologies: ultraviolet light/hydrogen peroxide, Fenton's reagent, and titanium dioxide-assisted photocatalysis, Hazard. *Waste Hazard. Mater.,* 10(2), 1993, 107–149.

[2] M. R. Hoffmann, S. T. Martin, W. Choi and D. W. Bahnemann, Environmental applications of semiconductor photocatalysis, *Chem. Rev.,* 95(1), 1995, 69– 96.

[3] A. L. Pruden and D. F. Ollis, Photoassisted heterogeneous catalysis: the degradation of trichloroethylene in water, *J. Catal.,* 82(2), 1983, 404–417.

[4] C. Kormann, D. W. Bahnemann and M. R. Hoffmann, Photolysis of chloroform and other organic molecules in aqueous titanium dioxide suspensions, *Environ. Sci. Technol.,* 25(3), 1991, 494–500.

[5] J. C. Crittenden, J. Liu, D. W. Hand and D. L. Perram, Photocatalytic oxidation of chlorinated hydrocarbons in water, *Water Research,* 31(3), 1997, 429–438.

[6] M. Muruganandham and J. J. Wu, Synthesis, characterization and catalytic activity of easily recyclable zinc oxide nanobundles, *Appl. Catal., B,* 80(1), 2008, 32–41.

[7] J. C. Lee, S. Park, H.-J. Park, J.-H. Lee, H.-S. Kim and Y.-J. Chung, Photocatalytic degradation of TOC from aqueous phenol solution using solution combusted ZnO nanopowders, *J. Electroceram.,* 22(1–3), 2009, 110–113.

[8] A. A. Khassin, T. M. Yurieva, V. V. Kaichev, V. I. Bukhtiyarov, A. A. Budneva, E. A. Paukshtis and V. N. Parmon, Metal– support interactions in cobalt-aluminum co-precipitated catalysts: XPS and CO adsorption studies, *J. Mol. Catal. A: Chem.,* 175(1), 2001, 189–204.

[9] Wenzhong Sh., Zhijie L ., Hui W., Yihong L., Qingjie G., Yuanli Z., Photocatalytic degradation for methylene blue using zinc oxide prepared by codeposition and sol–gel methods. *Journal of Hazardous Materials.* 152: 2008, 172–175.

[10] Comparelli R., Fanizza E., Curri M L., Cozzi P D., Mascolo G., Agostiano A., Photodegradation of methylene blue using Ta-doped ZnO nanoparticle. *Appl. Catal. B: Environ.* 60: 2005, 1–11.

[11] Akyol A., Yatmaz H C., Bayramoglu M., Photocatalytic degradation of reactive brilliant blue X-BR in aqueous solution using quantum-sized ZnO. *Appl. Catal. B: Environ.* 54: 2004, 19–24.

[12] Liu H Q., Yang J X., Liang J H., Huang Y X., Tangz C Y., Photo-degradation of methylene blue using Ta-doped ZnO nanoparticle. *J. Am. Chem. Soc.* 91: 2008, 1287–1291.

Short Communication

Green synthesis of silver nanoparticles using acacia concinna plant extract and their antibacterial activity

Rajesh Kumar Meena, **Kahkashan Ansari**, **Nawal Kishor** and **Neelu Chouhan**[*]
Department of Pure, Applied and Chemistry, University of Kota, Kota, Rajasthan, India
niloochauhan@hotmail.com

Abstract

Rapid synthesis of AgNPs by plant of Acacia concinna fruit extract. Synthesis of Ag Nps has been planned as a valuable and eco-friendly approach. This research work are cost effective as well as eco-friendly i.e reduction method using the fruit extract of acacia concinna plant and aqueous silver nitrate solution, for the preparation of the AgNPs. This plant extract act as both reducing and capping agent. The essential ingredients liable variables are triterpenes, flavonoids and eugenol, are present in the fruit extract that used for the formation of AgNPs. After the reduction process silver (Ag$^+$) ions was monitored, it showed the formation of Ag NPs using UV-visible spectrophotometry, which exhibits the absorption peak around at 430 nm. The sizes of nanoparticles were calculated by transmission electron microscopy (TEM) and X-ray diffraction (XRD). In addition, by using Agar-Well Diffusion Method, the antimicrobial activity of synthesized AgNPs was investigated by against Escherichia coli. For the conversion of Ag$^+$ to AgNPs at room temperature, this method could be proved a better substitute to chemical synthesis method without the contribution of any hazardous to environment.

Keywords: Eco friendly, TEM, UV-visible, XRD, diffusion method etc.

Introduction

Recently, synthesis of noble metal NPs such as Au, Ag, Pd and Pt and their study are given much importance[1-3]. Their physical as well as chemical properties are look like different from the bulk materials which fascinate the current research field[4]. Noble metal nanoparticles are of much significance owing to their optical, electronic and magnetic as well as catalytic behavior. Mainly PXRD technique is used to study the phase and purity of nanomaterials. In this research work, we discussed about the easy, low cost and room temperature synthesis of metal AgNPs. The as prepared AgNPs are of 2-20 nm size and their respective results are exhibited by TEM analysis. To prepare nanoparticles on solid support materials, including diverse lithographic techniques, vacuum depositionl, diffusion, electrophoretic chemical and electrochemical deposition of the metal NPs etc.[5-8] a range of synthetic techniques has been adopted. For consistent morphology and size of NPs, there are a variety of techniques like vacuum deposition of metal, diffusion, lithography etc and but they all are not cost-effective. The appropriate, simplest and economical approaches to synthesize nanomaterials are using the green and environmentally benign method.

Currently, the green synthetic method has gained fabulous persuade in large-scale biosynthesis process than physical and chemical process due to environmental concerns. The green synthesis of NPs is a clean, nontoxic, nonhazardous, cost-effective and environmentally friendly approach. The biological synthesis process includes use of the plant (or) and microbes (fungi, bacteria, algae) for the synthesis. Due to adverse microbial culture protection the use of plant extract is more significant than using microbes, time-consuming and cost-effective. In this research work, we have confirmed the synthesis of AgNPs via green synthesis method using *Acacia Concinna* plant extract. We have also investigated using UV-Vis spectroscopy, ATR, biological activity against Gram (-) ve (Escherichia coli (E. coli) bacteria, PXRD data. The PXRD results were correlated with TEM results.

Materials and methods

Silver nitrates (99.99%) were purchased from sigma Aldrich and *Acacia concinna* plant fruit extract as a green reducing agent and all valuable glassware's were cleaned with distilled water during the experiment.

Aqueous extract of Acacia concinna fruit: Acacia concinna plant fruit were collected from University of Rajasthan, Jaipur, Rajasthan, and cleaned with distilled water and dry at normal room temperature and grind to make it powder. 2 gm of *Acacia concinna* fruit powder was dissolved with 50 mL of distilled water and kept for 12 h, afterwards the extracts were filtered by whatman paper and stored at 4°C for further nanoparticles synthesis process.

Synthesis of silver nanoparticle: Firstly 10 ml of *Acacia concinna* plant fruit extract and freshly 10 mM silver nitrate solution prepared in a separate beaker. Secondly, silver nitrate

solution was stirred for half an hour and afterwards the plant fruit extract was drops wise added to aqueous $AgNO_3$. The titration was carried out for reducing of Ag^+ ions to Ag nanoparticles. The obtain solution is dissolved for on 15 minutes and then incubated at near room temperature for 24 h. The change in color was observed in the solution that confirms the formation of the NPs in the solution.

Figure 1: Acacia concinna fruit.

Separation of AgNPs: The synthesized Ag NPs was separated by centrifugation technique at 4000 rpm for 30 min. For further settlement of particles the supernatant material was transferred to a beaker and frequent centrifugation process was carried out to clean AgNPs. The obtained synthesized pellet was dry in an oven and stored for further characterizations.

Characterization: The absorption spectra of samples were observed at 200-800 nm wavelengths using by UV-visible spectrophotometer (LAB India, UV 3000^+). Using FTIR spectrum, the synthesized NPs were analyzed for the existence of biomolecules (Thermo Scientific Nicolet 380 FTIR Spectrometer). In transmission mode at the frequency range between 4000 and 400 cm^{-1} with the resolution of 4 cm^{-1}, the IR spectra of the synthesized nanoparticles were recorded by using ATR spectrophotometer (T-alpha, Bruker) for liquid sample. The nature of Ag nanoparticles is crystalline as evaluated by X-ray diffraction method. The synthesized Ag nanoparticles study on size, shape and the size distribution of nanoparticles of colloidal solution were analyzed by transmission electron microscopy (JEOL JEM2100 TEM).

Estimation of antibacterial activity: The antibacterial activities of synthesized Ag NPs, from the relevant plant extracts were successfully against Gram (-) ve (Escherichia coli (E. coli) bacteria for investigation. The microorganisms use in the study are purchase from the market. Disc diffusion method[9] was featured for trying of plant extract and their synthesized respective Ag NPs solution. The discs were soaking with distilled water, plant extract, pure $AgNO_3$ solution and solution containing AgNPs of each type individually. Then the discs were air dry at room temperature. The plates containing nutrient agar media were ready by swabbing them with the microbial cultures. The discs were located in the subsequent manner, disc soaked with distilled water as negative control, disc soaked with plant extract, disc soaked with 1 mM silver nitrate solution and disc soaked with solution of synthesized AgNPs. The dishes were incubated at 37°C for 24 to 48 h. Then, the maximum zone of inhibition was experimental and calculated for analysis beside of microorganism.

Results and discussion

Effect of reaction time on the formation of AgNPs, by visual observation was noted, when Acacia concinna fruit extract is added to aqueous silver salt ($AgNO_3$), colour will be changed from pale yellow to yellowish brown and lastly show the brown colour, as shown in Figure-2. By the reduction of silver salt, the optically observed and vary in colour of the solution indicates the creation of metal silver nanoparticles.
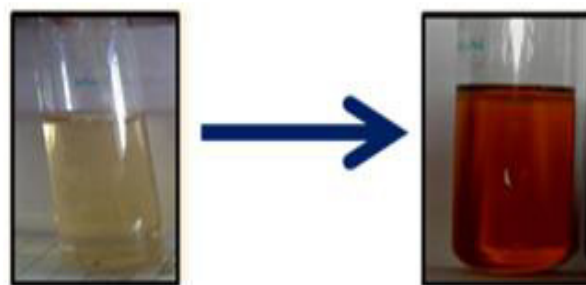

Figure-2: Shows the coloration due to formation of Ag NPs.
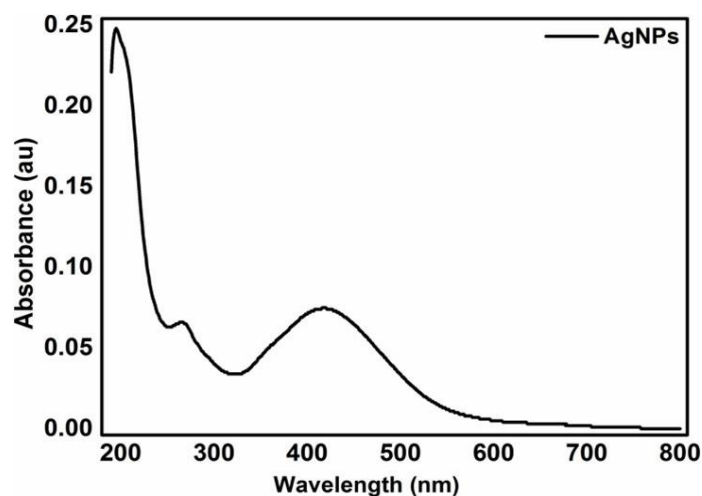

Figure-3: UV-visible spectra of the synthesized Ag NPs from predicted optimum conditions upon dilution of 3.5 times. Inset Figure shows the coloration due to formation of Ag NPs.

Synthesized AgNPs show the yellowish brown colour from pale yellow solution due to the excitation of (SPR) surface plasmon resonance. The change in color was appeared initially after 3

min. of adding the salt solution to the acacia concinna fruit broth. After 24 h, the colour of the solution becomes stable, which indicates that no silver salt was missing in solution for further reaction. In the present study, the synthesized nanoparticles are spherical in shape as suggested by SPR band, which is further confirmed by TEM study. Then the synthesized silver nanoparticles was examined and showed a broad adsorption peak around at 430 nm, which is liable for the Ag[10] and confirmed by respective absorption spectra. The synthesized AgNPs are uniform size distribution and absorption maximum is practically observed at around 430 nm. Due to the strong surface plasmon resonance (SPR) the UV absorption spectrum appeared, i.e., Silver nanoparticles responsible for surface Plasmon resonance (SPR) absorption band, due to the combined vibration of electrons of synthesized AgNPs in resonance with light wave. The resulted absorption spectra are size dependent and SPR band depends on the refractive index of the solution. Figure-3 spectra of the absorption due to the synthesis of AgNPs which is appeared from the reaction of acacia concinna fruit extract with AgNO$_3$ solution recorded in between the range of 200-800 nm.
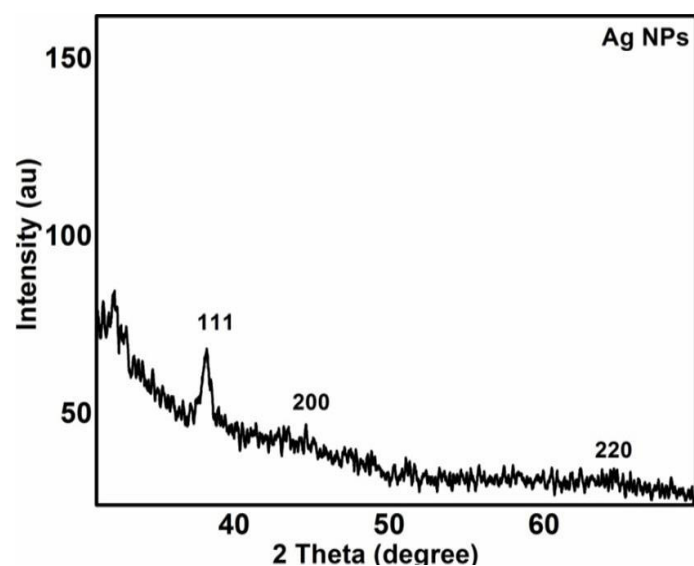

Figure-4: Shows XRD patterns for Ag nanoparticles.

Figure-4 Acacia concinna fruit extract broth containing AgNPs were centrifuged at 20,000 rpm for 20 min and to get rid of any unwanted impurities, the sterile distilled water was used for during this process. The purified pellet was then dried at 60°C at 12h and the sample was characterized by the X-ray diffraction (XRD) using a Bruker D2 Phase diffractometer that was operated in transmission mode with CuKα radiation (λ = 1.5418 Å). At the interval of 0.02° with a counting time of 30 s per step, the data were collected over the 2θ range from 20° to 90°. Figure-4 shows XRD results for synthesized Ag nanoparticles by pure acacia concinna fruit extract. Three major distinguishing diffraction peaks for AgNPs were experimental at 2θ = 38.4, 44.5, 64.8 which correspond to the (111), (200) and (220) crystallographic planes of face-centered cubic Ag crystals,

respectively (JCPDS 00-004-0783) with a lattice parameter of a = 4.077 Å. In general, the crystallite size of Ag NPs is related to width of XRD peaks and Debye-Scherrer equation used for determines average crystallite size. To calculate crystalline size the (111) plane was chosen. The average particle size of synthesized AgNPs is found to be 3.42 nm from Debye-Scherrer equation. This result was consistent with the TEM study.
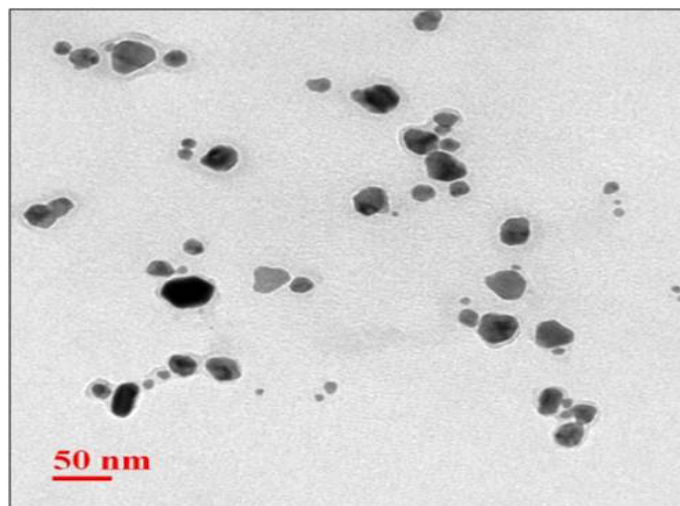

Figure-5: TEM images of synthesized AgNPs.

In Figure-5 TEM image of the Ag NPs corresponds to the topography, which particle size exhibits in between 2-20 nm and suggested the presence of approximately spherical size of silver nanoparticles. The image indicates the dispersity and morphology of the Ag NPs. These particles are distributed in smaller and bigger size zones and rounded in shape and size. These synthesized Ag NPs may be due to the capping agent as well as phytochemicals such as polyphenols or due to the formation of the cluster.

The present biomolecules are liable for capping agent as well as proficient stabilization of the AgNPs by ATR investigation. The IR spectrum of synthesized AgNPs shows the intense powerful bands around at 3315.79 and 1637.36 cm^{-1} are identified for O-H stretching, H-bond and C=C stretch respectively. The IR spectrum of plant extract has exposed in Figure-6. The IR bands located at 3315.79 cm^{-1} and 1634.37 cm^{-1}, clearly show significant variance among the spectral positions of IR bands due to the reduction process. The analysis of IR band peaks confirmed the absorbed alkaloids, phenols as well as terpenoids on the surface of AgNPs[11].

The IR results also provided and show an idea with reference to biomolecules approach at different functionalities. The probable mechanism designed for the reduction of Ag$^+$ to AgNPs be able of explained as: The present phenolic OH groups are in hydrolysable, and tannins can form transitional complexes with suitable Ag$^+$ ions, which for that reason go through oxidation to quinone forms. This results in the successive form of Ag$^+$ to Ag nanoparticles[12].
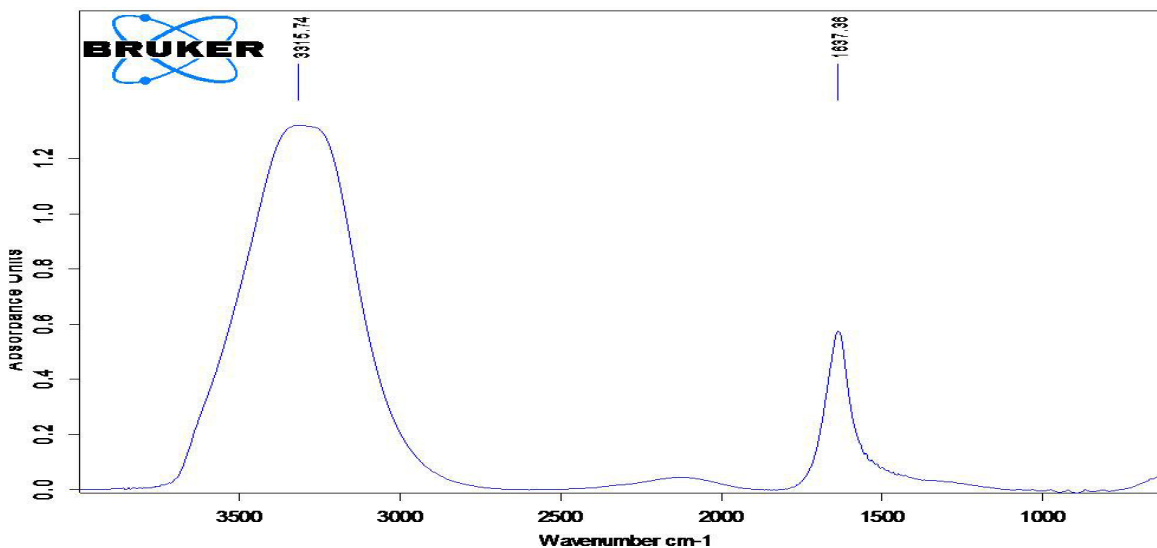
Figure-6: ATR spectrum of biosynthesized AgNPs.

Antibacterial activities: In the present research study of the antibacterial activity of the AgNPs which is analysed against E.Coli bacterial colony presented from sample is exposed in following information (Figure-7). Different quantities of synthesized AgNPs (2, 4, 8 and 10mg) are further to the agar dishes containing bacterial colony. The dishes are visible for each dilution and bacterial colony is observed results after incubating the agar plates overnight at 37°C. Zone of approval is experiential maximum at 10 mg of AgNPs. The antibacterial activity results show due to modify in the bacteria cell membrane permeability as well as degradation of enzymes in bacteria by synthesized AgNPs. The result zone of inhibition increased as well as increases the concentration of AgNPs.
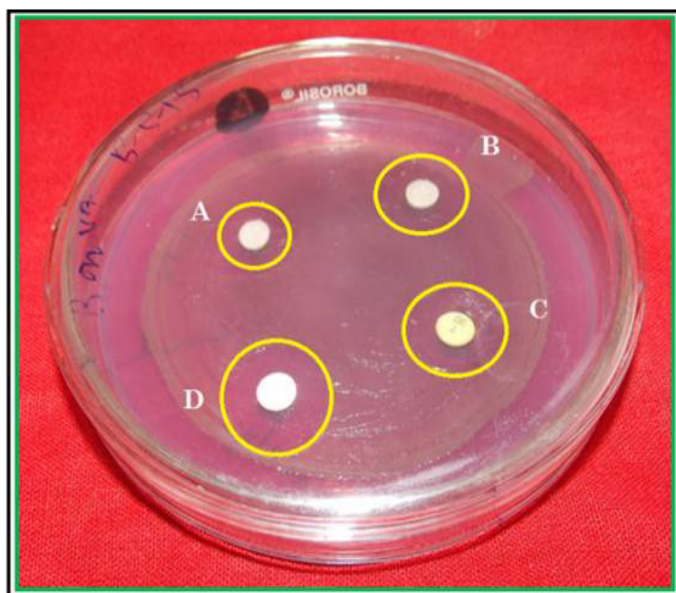

Figure-7: The inhibition zones of Ag NPs against *E.coli on nutrient agar. Where, the samples A, B, C and D are the as synthesized AgNPs in 2, 4, 8 and 10mg, respectively.*

Conclusion

In this report, we have synthesized AgNPs using Acacia Concinna plant extract via a biological method. Here the plant extract useful for reducing agent as well as stabilizing. Which are responsible for silver metal to nano-size (2-20 nm) and to stabilize the NPs. The as-synthesized AgNPs were examined using TEM, XRD, UV-Vis, and FTIR. The formation of nanoparticles, as well as size, was investigated by using UV-Vis spectroscopy. The crystal structure of the nanoparticle as well as average particle size of the NPs were investigated by PXRD analysis and further the shape and size were demonstrated by TEM analysis. This research work can be further extended to explore the synthesis and optical properties of AgNPs using other plant extracts which can be of medicinal use.

Acknowledgment

References

1. Nath S.S., Chakdar D., Gope G. and Avasthi D.K. (2008). #Characterizations of CdS and ZnS Quantum Dots Prepared by Chemical Method on SBR Latex.# *Journal of Nanotechnology Online*, 4, 1-6.

2. Cao G. (2004). #Nanostructures and Nanomaterials: Synthesis, Properties and Applications.# Imperial College Press, London.

3. Ahmadipour M., Venkateswara Rao K. and Rajendar V. (2012). #Formation of Nanoscale Mg(x) Fe (1-x) O (x = 0.1, 0.2, 0.4) Structure by Solution Combustion: Effect of Fuel to Oxidizer Ratio.# *Journal of Nanomaterials*.

4. Wang X., Zhuang J., Peng Q. and Li Y. (2004). #A General Strategy for Nanocrytsal Synthesis.# *Nature*, 437, 121-124.

5. Xu B. and Kevan L. (1991). #Formation of silver ionic clusters and silver metal particles in zeolite rho studied by electron spin resonance and far-infrared spectroscopies.# *The Journal of Physical Chemistry*, 95(3), 1147-1151.

6. Foss C.A., Tierney M.J. and Martin C.R. (1992). #Template Synthesis of Infrared-Transparent Metal Microcylinders: Comparison of Optical Properties with the Predictions of Effective Medium Theory.# *Journal of Physical Chemistry B*, 96(22), 9001-9007.

7. Foss C.A., Hornyak G.L., Stockert J.A. and Martin C.R. (1994). #Template-Synthesized Nanoscopic Gold Particles: Optical Spectra and the Effects of Particle Size and Shape.# *Journal of Physical Chemistry B*, 98(11), 2963-2971.

8. Bo X. and Kevan L. (1992). #Formation of Alkali Metal Partides in Alkali Metal Cation Exchanged X Zeollte Exposed to Atka Metat Vapor: Control of Metat Particle Identity.# *Journal of Physical Chemistry B*, 96, 2642-2645.

9. Bao Q., Zhang D. and Qi P. (2011). #Synthesis and characterization of silver nanoparticle and graphene oxide nanosheet composites as a bactericidal agent for water disinfection.# *J Colloid Interface Sci.,* 360(2), 463-470.

10. Muthukrishnan S., Bhakya S., Kumar T.S. and Rao M.V. (2015). #Biosynthesis, characterization and antibacterial effect of plant-mediated silver nanoparticles using *Ceropegia thwaitesii*-An endemic species.# *Ind Crops Prod.,* 63, 119-124.

11. Nithya Deva Krupa A. and Raghavan V. (2014). #Biosynthesis of Silver Nanoparticles Using *Aegle marmelos* (Bael) Fruit Extract and Its Application to Prevent Adhesion of Bacteria: A Strategy to Control Microfouling.# *Bioinorg Chem Appl,* 8.

12. Fayaz A.M., Balaji K., Girilal M., Yadav R., Kalaichelvan P.T. and Venketesan R. (2010). #Biogenic synthesis of silver nanoparticles and their synergistic effect with antibiotics: a study against gram-positive and gram-negative bacteria.# *Nanomedicine: Nanotechnology, Biology and Medicine*, 6(1), 103-109.